Proceedings



10th U.S. Army Gun Dynamics Symposium



April 23-26, 2001
Austin, Texas

BENET LABS

10TH U.S. ARMY GUN DYNAMICS SYMPOSIUM

PROCEEDINGS

Proceedings from a symposium sponsored by the Institute for Advanced Technology and Benét Laboratories, held April 23-26, 2001, in Austin, Texas.

Edited by
Dr. Mehmet Erengil

DISTRIBUTION STATEMENT A
Approved for Public Release
Distribution Unlimited

20020718 233

Published by:
Institute for Advanced Technology
The University of Texas at Austin
3925 W. Braker Lane, Suite 400
Austin, TX 78759-5316
(512) 232-4400

April 2002

IAT.CW 0065

The Institute for Advanced Technology (IAT) hosted this symposium under the sponsorship of Benét Laboratories of TACOM-ARDEC.

The views and conclusions contained in this document are those of the contributor concerned, and should not be interpreted as presenting the official policies or position, either expressed or implied, of the Department of the Army or the U.S. Government unless so designated by other authorized documents. Citation of manufacturer's or trade names does not constitute an official endorsement or approval of the use thereof. The U.S. Government is authorized to reproduce and distribute reprints for Government purposes notwithstanding any copyright notation hereon.

Contents

Preface vii
Symposium Organization viii

INVITED PRESENTATION
Overview on the German R&D Programs on ETC Gun Technologies for Main Battletank Weaponization
T. H.G.G. Weise 1

STRUCTURAL DYNAMICS OF CONVENTIONAL GUNS
On the Design of Magneto Rheological Recoil Dampers for Fire Out of Battery Control
M. Ahmadian and R. Appleton 9

Muzzle Motion Measurements for the M198 When Fired at 30 and 45 Degrees
J. M. Garner, B. J. Guidos, and B. J. Patton 25

A Fire Out of Battery Tank Gun: Theory and Simulation
E. Kathe and R. Gast 37

Robust Control Design for the Elevation Axis Stabilization of the M256E1 Long Gun
V. R. Marcopoli, M. S. Ng, and C. R. Wells 49

A Chatter Box: Investigation of Dynamic Response across a Gap
G. P. O'Hara 67

Propagation of Longitudinal Waves in a Gun Barrel
I. Randrianangaly, J. Renard, B. Campion, and E. Petitpas 80

Main Battle Tank Flexible Gun Tube Disturbance Model - Three Segment Model
H. J. Sneck 92

Discussion of Fire Out of Battery Test Results
M. Tedesche, R. Durocher, and M. Gully 107

GUN DYNAMICS CONTRIBUTION TO ACCURACY AND PERFORMANCE
Smart Isolation Mount for Airborne Guns
D. Allaei, D. J. Tarnowski, M. S. Mattice, and R. Testa 121

The Dynamic Modelling of a Novel Design of 120mm APFSDS Training Round
D. N. Bulman and J. G. Ferries 133

Adaptive Gun Barrel Vibration Absorber
A. G. Littlefield and E. L. Kathe 140

A Shot Accuracy Model for Predicting the Firing Performance of a Direct Fire Weapon System
D. W. Lodge and A. M. Dilkes 152

Comparison between the M256 120-mm Tank Cannon Jump Test Experiments and ARL's Gun Dynamics Simulation Codes for Prototype KE
J. F. Newill, B. J. Guidos, and C. D. Livecchia 160

Launch Dynamics of the 120-mm M831A1 HEAT Training Projectile
J. F. Newill, J. M. Garner, K. P. Soencksen, and C. P. R. Hoppel 176

The Influence of Projectile Mass upon Precision
E. M. Schmidt and H. L. Edge 193

Comparison of the 120-mm M831A1 Projectile's Experimental Launch Dynamic Data with Hydrocode Gun-Projectile Dynamic Simulations
K. P. Soencksen, J. F. Newill, J. M. Garner, and P. Plostins 200

INTERIOR BALLISTICS: GAS DYNAMICS, WEAR AND EROSION, THERMAL EFFECTS

Modeling of Barrel/Projectile Interaction in a Rotating Band
P. C. T. Chen and M. Leach 213

Gun Tube Surface Kinetics and Implications
P. J. Conroy, M. J. Nusca, C. Chabalowski, and W. Anderson 224

Internal Ballistics Analysis for the RAVEN Propulsion System
S. Dunn, J. French, D. Coats, E. Kathe, R. Dillon, S. Sopok, and M. Witherell 236

Recoil Reduction Using Propellant Gas
E. Kathe 247

Relative Erosivity of Nitramine Gun Propellants with Thermoplastic/Elastomer Binder Systems
C. S. Leveritt, P. J. Conroy, and A. W. Johnson 258

Cannon Coating Erosion Modeling Achievements
S. Sopok, S. Dunn, P. O'Hara, D. Coats, G. Pflegl, and C. Rickard 265

ELECTROMAGNETIC LAUNCH DYNAMICS AND INTEGRATED LAUNCH PACKAGES

Inductiveless Rail Launchers for Long Projectiles
Y. A. Dreizin 279

On the Parasitic Mass of Launch Packages for Electromagnetic Guns
M. J. Hinton, N. R. Cooper, D. Haugh and M. A. Firth 291

Use of the SIMBAD Gun Dynamics Code for Modelling the In-Bore Dynamics of EM Launchers
D. W. Lodge and A. M. Dilkes 305

Results of a Study for a Long Range Coilgun Naval Bombardment System
S. Shope, J. Alexander, W. Gutierrez, R. Kaye, M. Kniskern, F. Long, D. Smith, B. Turman, B. Marder, A. Hodapp Jr., and R. Waverik 320

Critical Velocity of Electromagnetic Gun In Response to Projectile Movement
J. T. Tzeng 332

HIGH PERFORMANCE MATERIALS FOR CONVENTIONAL AND ELECTROMAGNETIC LAUNCHERS

Reinforced Metal Structural Jackets for Advanced Gun Barrels
J. M. Burnett, H. Gigerenzer, E. Pennell, and C. Dampier 341

Investigation of Tungsten, Copper, and Silver Alloys with Indium at the Rail-Armature Interface on a Railgun Test Bench
D. Gillich and W. Maier 355

Concepts for Fieldable Electromagnetic Gun Barrels
M. J. Hinton, A. Howard, N. R. Cooper, D. K. Wallington and M. A. Firth 369

Large Caliber Gun Tube Materials Systems Design
J. S. Montgomery and R. L. Ellis 385

IN-BORE DIAGNOSTICS, TESTING AND INSTRUMENTATION

Off the Shelf Technology for Gun Barrel Straightness Measurement
J. Garner, T. Marrs, T. Erline, and M. Bundy 398

Performance Enhancement and Health Monitoring of a Medium Caliber Gun System Using Optical Fiber Bragg Grating Sensors
C. LaVigna, J. Bowlus, H. Kwatny, S. Chen, H. Zhang, and S. Cytron 406

Investigating UHF Telemetry for Electromagnetic Launchers
S. Levinson , L. Burke, M. Erengil, and J. Faust 418

Use of an Instrumented 120mm Projectile for Obtaining In-bore Gun Dynamics Data
D. W. Lodge and A. M. Dilkes 433

Visual Characterization of Wear in Large Caliber Weapons
D. Salafia 444

Stereo at the Speed of Light: High-Speed Digital Stereo Imaging at up to 100 Million Frames per Second
D. R. Snyder, E. R. Chenette, R. D. Hudson, R. P. Young Jr., D. W. Gardner, and P. E. Nebolsine 454

Complete Bore Centerline Extractor and Surface Mapper
R. Von Wahlde, T. Erline, M. Kregel, and M. Bundy 465

NOVEL LAUNCH TECHNIQUES

Optimizing a Slingatron-Based Space Launcher Using MATLAB®
M. Bundy, G. Cooper, and S. Wilkerson 474

Numerical Simulations of the Slingatron
G. R. Cooper, D. A. Tidman, M. Bundy, and S. Wilkerson 491

Slingatron: A High Velocity Rapid Fire Sling
D. A. Tidman 509

Author Index 527

Preface

This volume contains the papers presented at the 10th U.S. Army Gun Dynamics Symposium held in Austin, Texas on April 23-26, 2001. The contents of this volume, as well as the invited talks, are also published in an accompanying CD-ROM.

Initiated in 1976, the biennial Gun Dynamics Symposium has been providing a forum for discussion of applied research and engineering solutions in collective disciplines of structural dynamics, interior ballistics, exterior ballistics, advanced materials, and multidisciplinary design optimization for high-performance cannon weaponry. In this 10th Symposium, the technical committee has expanded the scope of the meeting and integrated electromagnetic gun discussions with conventional weapons systems and, for the first time, implemented a peer review process. Each technical paper in this volume has undergone peer review by experts in their respective fields of research. A special note of thanks goes to the members of the technical committee for supporting and enabling these changes. The authors are commended for keeping to the schedule imposed by the review process.

The 10th Gun Dynamics Symposium was attended by 114 scientists and engineers representing the United States and the European countries. The Institute for Advanced Technology (IAT) hosted this symposium under the sponsorship of the Benét Laboratories of TACOM-ARDEC. Mr. Eric Kathe (TACOM-ARDEC Benét Laboratories) was the Symposium Chairman; and Dr. Mehmet E. Erengil (IAT) and Dr. Peter Plostins (Army Research Laboratory, ARL) were the Technical Chairmen. The technical agenda included 39 oral presentations and 13 poster presentations. A series of invited speakers discussed a broad spectrum of relevant topics including research and development efforts and engineering applications in both U.S. and European programs.

The keynote addresses were given by Dr. Hans Mark (DDR&E) and LTG Paul Kern (Military Deputy, ASAALT). Invited talks featured presentations by distinguished speakers Dr. Marilyn Freeman (DARPA), Mr. Richard Hassenbein (TACOM-ARDEC Benét Laboratories), Mr. Michael Hermanson (UDLP), Professor Mike Hinton and Mr. David Wallington (DERA, UK), LTC Albert Tanner (ARL), and Dr. Thomas H.G.G. Weise (Rheinmetall W&M GmbH, Germany). In addition, Mr. Robert Sackheim (NASA-MSFC) moderated a special panel discussion on "Gun Launch to Orbit." The expert panel included Mr. John Cole (NASA-MSFC), Dr. Miles Palmer (SAIC), Dr. Ian McNab (IAT), and Dr. Edward Schmidt (ARL). The panel discussion was one of the highlights of the meeting.

The programmatic changes implemented in this symposium — namely the inclusion of electromagnetic gun technology within the conventional weapons systems community and the peer review process — have both proven to be extremely successful. The electromagnetic gun technology promises an undeniably revolutionary improvement in weapons systems capabilities. Cross-fertilization of ideas within the entire gun community could only help accelerate the implementation of this technology. I not only look forward to future symposia organizers to embrace the programmatic changes implemented here but also challenge the leadership to seize upon this opportunity and help accelerate the development of electromagnetic gun weapons systems.

Last, but not least, I am fully indebted to Ms. Michelle Ramsey and Ms. Janet Monaco who worked diligently to coordinate all aspects of the symposium and assemble these proceedings. The success of the symposium is largely due to their dedicated commitment and attention to detail. Thank you both!

Mehmet E. Erengil
Technical Co-Chairman
Institute for Advanced Technology

10TH U.S. ARMY GUN DYNAMICS SYMPOSIUM

Austin, Texas
April 23-26, 2001

Symposium Chairman

Eric Kathe

Technical Chairmen

Mehmet Erengil
Peter Plostins

Committee Members

Edward Alexander
David Bauer
Larry Burton
Robert Dillon
Roger Ellis
Ron Gast
Frank Hoogterp
Joel Leifer
William Oberle
Mohan Palathingal
Chadee Persad
Edward Schmidt
John Vasilakis
James Wildman

Organizing Committee

Mehmet Erengil
Eric Kathe
Janet Monaco
Michelle Ramsey

Overview on the German R&D Programs on ETC Gun Technologies for Main Battletank Weaponization

Thomas H.G.G. Weise
Rheinmetall W&M GmbH
Heinrich-Erhardt-Strasse 2, D-29345 Unterlüß
Federal Republic of Germany

Abstract

In order to improve the performance of large calibre guns for main battlefield tank applications a wide range of R&D programs have been performed in Germany on electric and electrically supported barrel guns since 1980. In the beginning pure electric gun technologies were investigated including rail, coil and electrothermal acceleration methods. A large calibre 105mm electrothermal gun demonstrator supplied by a 30 MJ capacitive pulsed power supply system was introduced in 1995. Muzzle velocities up to 2.4 km/s were optained with this set-up resulting in muzzle energies up to 5.8 MJ. The missing perspective on solving the energy density requirements of the pulsed power supply technology for a system realization led to the termination of these programs in the beginning of 1996.

Due to its limited electrical energy requirements the technology of ETC guns has been investigated during the last years with high priority. It is the goal to provide a future main battle tank gun with increased firepower for integration into the next generation of combat fighting vehicles. Current R&D programmes result in a demonstration of the interior ballistic performance of the different ETC concepts. 120mm ETC demonstrators are used to perform this demonstration.

The presentation gives a short briefing on the results of the former investigations on pure electric guns and introduces the background for deciding to terminate these efforts. In the following an overrview on the R&D Structure of the German programs on ETC and its related technology fields is presented. Basic investigations led to the definition of different ETC concepts for the realization of electrothermal plasma ignition methods and electrothermal combustion control of ETC tailored propellants and charge designs. Based on the results of 105mm firings and of interior ballistic simulations a 120mm ETC cartridge was designed and investigated experimentally. First 120mm firing results will be given.

The presentation concludes in giving an outlook on the perspectives of the performance of ETC technologies and its power supply technologies in order to provide the access to increased firepower and survivability of existing and succeeding main battle tank systems without leaving the currently introduced boundary conditions of the large calibre weapons.

1 Introduction

Improved protection technologies by active and reactive armor as well as by increased hardeness of armor plating technologies define the requirements of the performance of future tank guns. Improved missile technologies as well as multiple low cost cruise missile attacks will be the challenges for future anti air defence guns. Military operations in urban terrains define new requirements for medium calibre guns for future vehicles.

For the existing conventional guns a high level of lethality has to be provided which can be obtained i.e. from improved temperature insensitive propellants. Future guns have to provide a significantly higher lethality which can be obtained from advanced propulsion and gun technologies. These requirements have been adressed by the R&D programmes on electric and

electrically supported guns.

2 Electric Gun Programs

In order to met the requirements of future tank guns and close the gap between gun performance and armor plating technologies electric guns with their potential of realizing very high muzzle velocities were investigated within several R&D programmes in the past. In the US these programmes concentrated on the rail gun technology. Laboratory systems were set-up demonstrating muzzle velocities with 2kg projectiles of to up to 3.000 m/s in calibre 90mm [1]. In Germany electrothermal gun technologies were investigated. In 1995 105mm shots were demonstrated firing 2kg projectiles to up to 2.400 m/s [2]. Due to the missing perspective of realising high energy density pulsed power supply technologies for integration into a combat fighting vehicle in the short and mid term time frame several nations including the USA and Germany decided to proceed the investigations with the Electrothermal-Chemical Gun Technology (ETC).

3 R&D Programmes on ETC Technologies

3.1 Goal of the 120mm R&D Program

It was the goal of the German R&D program phase 1 (1995-1999) on ETC guns to demonstrate a muzzle energy of at least 14 MJ out of a 120mm Gun within the boundary conditions of the conventional set-up in terms of maximum breech pressure (670 MPa), volume of the charge chamber (10l), projectile travel length (6m), muzzle pressure (<100MPa) and mass of projectile (8,4 kg). The demonstration of this muzzle energy should be performed by using ETC technologies with available propellants. In addition the results of basic investigations should predict the performance potential of new propellant formulations and charge designs with ETC technology. An evaluation of the results obtained from the investigations on the gun performance and on the pulsed power supply technology should result in the short and medium term availability of ETC technologies within the boundary conditions of existing and future large calibre combat fighting vehicle systems.

3.2 Basic Considerations

ETC technologies opens the opportunity to reconsider the limited success of past conventional investigations under aspects of

- perfect ignition properties
- electrothermal enhancement of propellant conversion
- access to new high energetic propellant formulations
- access to charge designs with increased loading densities.

From these properties a significant improvement of the interior ballistic gun performance can be obtained at limited and realistic electric energy requirements.

The electrothermal energy conversion via approximately massless and volumeless high power plasmas which are arranged in the propellant set-up of the cartridge with a high degree of geometrical flexibility can be used efficiently without time delay for the ignition of the propellant as well as for its combustion control.

The large variety of the properties of the plasma ignition processes which are not given from conventional pyrotechnics enable the development of charge designs with increased performance as well as of new high performance powder formulations based on Nitramin and RDX chemicals. Further advantages are gained from the ETC technologies by the possibility of adjusting the ignition performance directly before or during the development of the shot as well as controlling the combustion during the burning phase of the propellant. These properties can be applied i.e. for a temperature compensation of the propellant.

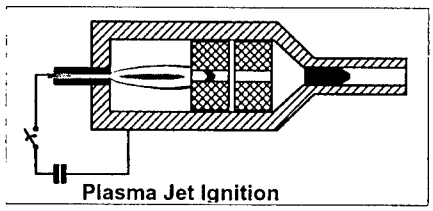
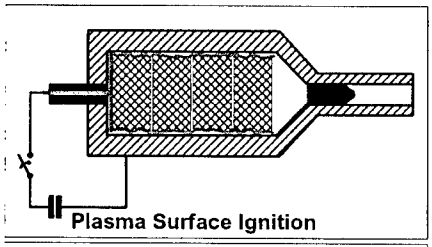
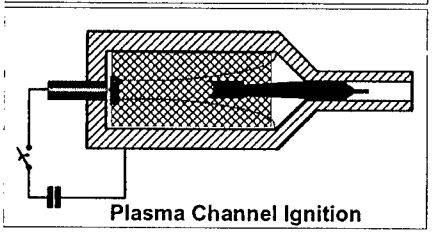


Fig. 1 gives three different plasma ignition methods schematically. The Plasma Jet Ignition is characterized by a so called plasmaburner which is located in the breech of the charge chamber. Supplying this plasmaburner with electrical energy a high temperature plasmajet is generated and directed into the propellant set-up in the charge chamber. The form and the length as well as the ignition power of the plasmajet can be adjusted by the geometry of the plasmaburner and by the pulsehape of the electric energy supply. The plasmajet interacts with the propellant and results in ignition and combustion enhance-ment during the pressure generation phase. A proper design of the plasmaburner and a good matching of the electrical power pulse can lead to large lengths of the plasmajet. The properties of this method are of interest for solving the ignition of modular charges for artillery guns. The application for large calibre tank gun charges has been investigated with minor success.



The Plasma Surface Ignition realises a plasma coating around the propellant set-up. By this the propellant is ignited from the inner surface of the combustible cartridge case to the inside of the charge set-up over the total lenght of the charge without any time delay in the axial direction. This method opens the access to very compact charge designs i.e. coated propellant discs with very high loading densities.

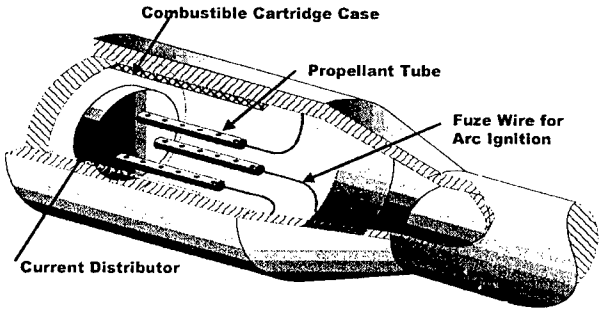


The last method is given by the Plasma Channel Ignition system. Several plasma channels

Fig. 1: Electrothermal Plasma Ignition Methods

thin wires which are located within thin walled propellant tubes. The interaction of these plasma channels leads to the ignition of the propellant. By the electrical energy supply the ignition power is adjusted and in addition, a combustion enhancement can be realized over the entire time period of propellant burning.

The application of the plasma ignition methods for improving the interior ballistic performance requires detailled knowledge of the interaction processes between the plasma and the propellant. The energy transfer mechanism from the plasma to the propellant is provided mainly via radiation processes. Therefore the energy is transmitted into a large volume without any significant time delay. Plasmas are of low mass and of low volume requirements. In particular the plasma channel ignition method is characterized by its high degree of geometrical flexibility. By the electrical energy supply ignition power can be adjusted. Furtheron the propellant combustion can be enhanced during the burning period. The application of these properties is the basis for the assessment of charge designs with increased interior ballistic performance due to increased loading density or new propellant formulations or a



combination of both.

Fig. 2: Large Calibre Cartridge Set-Up with Plasma Channel Ignition (schematically)

Fig. 2 shows the set-up of a three channel plasma ignition system within a large calibre gun cartridge schematically. The plasma ignition system is installed within a conventional cartridge with combustible cartridge case. The stub case is modified by a high voltage feed through with a current distributing conductor. Exploding wires which are located within thin walled propellant tubes are igniting the plasmas in several channels. By the interaction of these plasma channels with the propellant ignition and combustion enhancement are performed.

3.3 Experimental Results obtained from 105mm ETC Firings

A first validation of the large calibre ETC concepts was performed with a 105mm ETC gun. Fig. 3 gives a view on the gun and on the ETC cartridge set-up with their main parameters.

The gun is characterized by a charge chamber volume of 6.44 l and a projectile travel length of 6.24 m. The maximum operation pressure is 500 MPa. ETC cartridges made from inert plastic material were used in this gun. Several pressure sensors are located in the charge chamber and along the barrel.

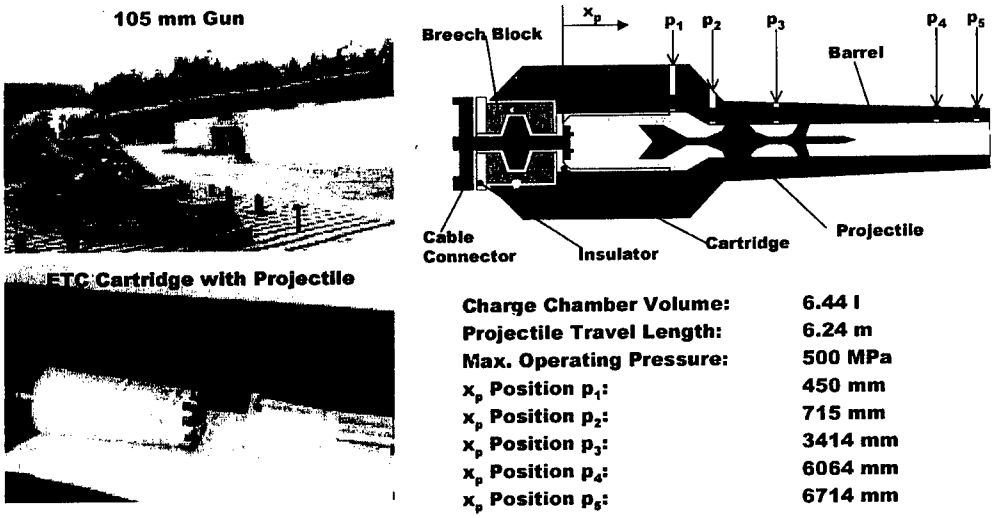
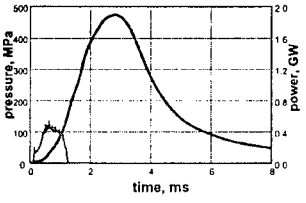


Fig. 3.: Set-Up of the 105mm ETC Gun

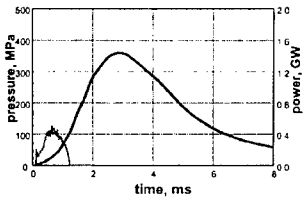
A variety of test firings were performed in the 105mm gun.

Tests with granular propellant made from NENA formulations show the excellent interior ballistic performance of this propellant due to its high impetus. Fig. 4 gives the results of two characteristic experiments conducted with two different web sizes of the propellant grains as well as a summary of all test performed with this concept.



Shot data

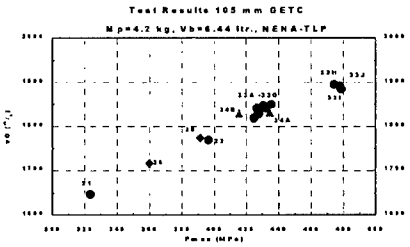
Projectile Mass:	4.2 kg
Mass of Propellant:	5.76 kg
Web Size:	1.3 mm
el. Energy Input:	391 kJ
Muzzle Velocity:	1896 m/s
Muzzle Energy:	7.55 MJ
Overall efficiency:	29.6 %



Shot data

Projectile Mass:	4.2 kg
Mass of Propellant:	5.76 kg
Web Size:	1.5 mm
el. Energy Input:	347 kJ
Muzzle Velocity:	1716 m/s
Muzzle Energy:	6.18 MJ
Overall efficiency:	23.4 %

Summary of results



Standard Deviation t_2:	37.3 µs
Standard Deviation p_{max}:	3.6 MPa

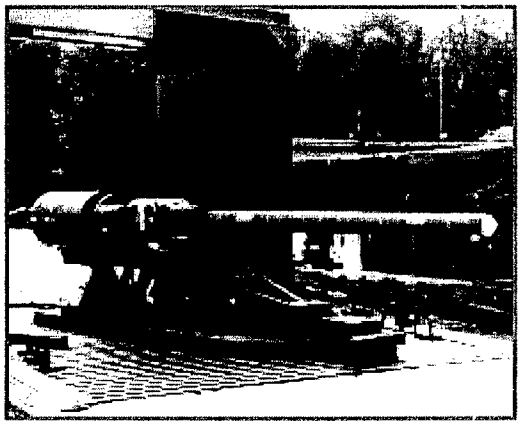
Fig. 4: Characteristic Results of 105mm Test Firings with granular NENA Propellant and single Pulse Plasma Channel Ignition

4.2kg projectiles were accelerated to up to 1.900m/s. A one pulse Plasma Channel Ignition was applied with an electrical energy input of about 400kJ only at a propellant temperature of approximately 21°C. A standard deviation of the ignition delay times of only 37.3µs as well as a standard deviation of 3.6 MPa of the maximum pressure values show the excellant performance of the plasma ignition method even with LOVA type propellants.

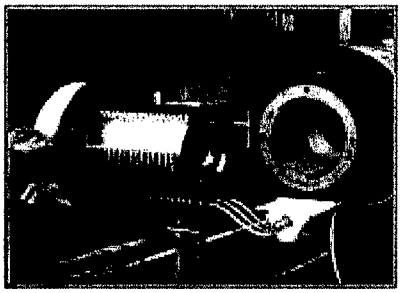
3.4 Experimental Results obtained from 120mm ETC Firings

The 120mm ETC gun being used for the performance demonstration is shown in fig. 5. The gun platform equals those which has already been used for the 105mm firings.

System View



Breech Block System



Technical Data

Calibre Length:	L55
Projectile Travel:	6 m
Volume Charge Chamber:	10 l
max. Operation Pressure:	700 MPa
Design Pressure:	800 MPa

Fig. 5: Set-Up of the 120mm ETC Gun

A 120mm L55 barrel is assembled in the breech block. The breech block system consists of a bajonet joint. The electrical connection to the pulsed power supply system is realized by coaxial cables. Projectiles of approximately 8.4 kg are accelerated in the 6m long barrel. The volume of the charge chamber is approximately 10 l. The maximum operation pressure of this test gun is 700 MPa and the design pressure is 800 MPa.

Up to now a variety of firings have been performed with a granular NENA propellant charge at two different propellant temperatures. Fig. 6 gives the measured signals of a characteristic shot in which the 8.4 kg projectile was accelerated to a muzzle energy of 14 MJ at a propellant temperature of 50°C.

Discharge current, plasma voltage, breech pressure and energy absorbing power are plotted versus time. The duration of the electric pulse igniting the propellant is 1.2 ms. The maximum discharge current is 12.5 kA. 0.3 ms after igniting the electric discharge the voltage signal shows the characteristic peak due to the explosion of the fuze wires.

In the following time period the plasma voltage increases from about 4 kV to a maximum of about 16 kV at the end of the electric discharge pulse.

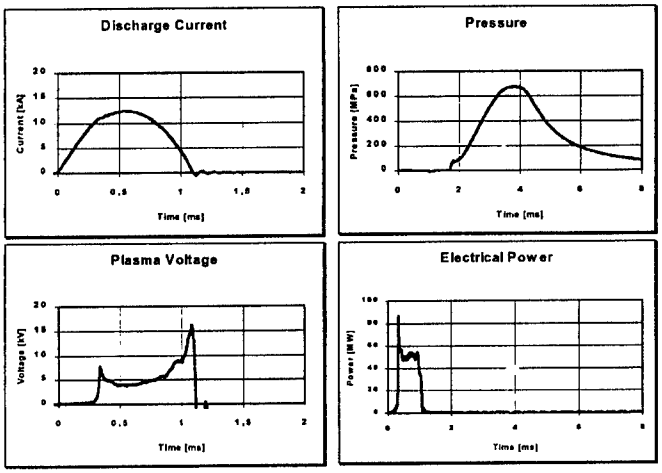


Fig 6: Measurements of a characteristic NENA Firing

The breech pressure starts rising at about 1.8 ms and reaches its maximum of 670 MPa at t = 3.8 ms. The average power of the energy absorption is about 50 MW. For igniting the charge an electric energy of only 39 kJ is released into the plasma channels.

Table 1 gives an overview on the main results of the NENA firings obtained at two different propellant temperatures in comparision to the performance of the LKEII cartridge which provides the current maximum performance level of conventional 120mm ammunition.

With the NENA1 propellant muzzle energies of 14 MJ are demonstrated at propellant temperatures of 21°C and 50°C. The temperature compensation is performed by an increase of the electrically released energy to 110 kJ. The firings with the NENA2 propellant which differs by its larger web size from the NENA1 propellant are performed at 50°C up to now.

Charge	Vo [m/s]		Wo [MJ]		El. Energy [kJ]	
	21°C	50°C	21°C	50°C	21°C	50°C
LKE II	1,750	1,830	12.8	14.0		
ETC NENA1	1,822	1,831	13.9	14.0	110	39
ETC NENA2		1,839		14.1		101

Table 1: Results of 120mm NENA Firings

A further increase of the muzzle velocity to 1.839 m/s is obtained with a slightly increased

amount of electrically released energy of 101 kJ.

By a proper design of the Plasma Channel Ignition and the adjustment of the electric ignition pulseshape the requirements of electric energy for igniting the NENA charge set-up are significantly reduced in the 120mm cartridge. It is expected that energies of only several 100 kJs are sufficient for a fully temperature compensated performance of NENA charge set-ups in a 120mm cartridge providing gun applicable ballistics with high firepower due to the properties of the electrothermal plasma ignition method.

4 Medium Calibre Gun Investigations

First investigations on ETC technologies for medium calibre guns have been performed at Rheinmetall. It is the goal to provide a plasma ignition system for rapid firing guns with the lowest requirements of the electric energy consumption. The current investigations therefore concentrate on the development of a plasma ignition system which is combined with pyrotechnics. First ignition experiments in closed vessels indicate that the electric energy can be further reduced with this approach without loosing the properties of the plasma ignition. In the next step improved propellant formulations and charge set-ups will be tested in order to explore the potential of this method in terms of muzzle velocity increase without decreasing barrel lifetime.

5 Pulsed Power Supply Development

In order to provide proper pulsed power supply technology for the ETC gun developments R&D programs on critical components have been under conductance since 1998. High energy discharge capacitors have been developed with energy densities up to 2MJ/m³ based on conventional metallized film technology and certified for ETC application. Optical triggered semiconducting switches are in the final testing phase. Compact high power charging devices will be available in 2002. Based on these components a first pulsed power system is in the final design stage and will be completed in the beginning of 2002 in order to be used for the large calibre ETC demonstrations at the end of the R&D phase II.

6 Summary and Conclusion

The results of the basic investigations, the theoretical simulations and the experimental firings in the large calibre guns show the important properties of the ETC ignition technology in terms of:

- ignition system with low mass, high geometric flexibility, low volume requirements and short energy transfer times at high interaction temperatures
- adjustable ignition power influencing the whole ignition process
- temperature compensation properties
- combustion control properties
- access to high loading densities by volume effect of plasma radiation

By applying these properties the currently existing performance of conventional 120mm gun technologies could be achieved and slightly improved already during the first phase of the German ETC program. Further increase of the loading density in combination with the application of high energetic propellants, i.e. NENA, will lead to a further improvement of the interior ballistic performance in the 120mm gun. Muzzle energies of more than 15 MJ at muzzle volocities of more than 1.900 m/s can be expected during the running phase of the German ETC program.

The limited requirements of electric energy of only several 100 kJ per shot lead to feasible solutions for the realisation of the power supply technology based on the progress

obtained from the R&D programmes performed on the energy density improvement [3,4]. The bandwidth of ETC technologies and its electric energy requirements opens the access to increased firepower and survivability of existing and succeeding main battle tank systems without leaving the currently introduced boundary conditions of the large calibre weapons.

Acknowledges

This work is performed under contract of the German BWB and we greatfully thank our contractors for their support.

References

[1] McNab, I.R. et.al. Experiments with the Green Farm Electric Gun Facility, IEEE Transaction on Magnetics, Vol. 31, pp. 338-343, 1995

[2] Weise, Th. et.al. Setup and Performance of a 105mm Electrothermal Gun, IEEE Transactions on Magnetics, Volume 33, Pages 345-349, 1997

[3] Wisken, H. et.al. High Energy Density Capacitors for ETC Gun Applications, 10th EML-Symposium, San Francisco, 2000 (to be published)

[4] Wisken, H. et al. Light activated Semiconductors for ETC Pulsed Power Applications, 10tn EML-Symposium, San Francisco, 2000 (to be published)

On the Design of Magneto Rheological Recoil Dampers for Fire Out of Battery Control

Mehdi Ahmadian
Associate Professor and Director
Advanced Vehicle Dynamics Laboratory
Department of Mechanical Engineering, MC-0238
Virginia Tech
Blacksburg, Virginia 24061
(540) 231-4920/ - 9100 (fax)
ahmadian@vt.edu

Randall Appleton
Associate Engineer
Advanced Systems Development
United Defense, L.P.
Minneapolis, MN 55421-1238
(763) 572-4929
randall_appleton@udlp.com

ABSTRACT

The application of magneto rheological dampers for controlling recoil dynamics is examined, using a recoil demonstrator that includes a 0.50-caliber gun and a MR damper (referred to as "recoil demonstrator"). Upon providing a brief background on MR dampers and fire out of battery dynamics, we will describe the recoil demonstrator, along with some of the test results from the laboratory and field-testing from the MR damper on the recoil demonstrator. The test results indicate that the MR damper is able to effectively control the recoil dynamics, and provide a different force-stroke curve for different amounts of current supplied to the damper. The current to the damper is used to energize the magneto rheological fluid within the damper and provide different amounts of damping force. Based on the recoil control results achieved by the damper, a technique is suggested for using MR dampers for fire out of battery. The technique, which consists of two stages, is described in detail along with the potential role of MR damper in each stage. Finally, our plans for field-testing the suggested fire out of battery method, using the recoil demonstrator and the MR damper, is briefly discussed.

INTRODUCTION

Conventional recoil mechanisms in larger guns are traditionally comprised of a hydraulic type system. The design of these systems has been used for years in many different ways. For example, the M198 shown in Figure 1 is a 155 mm towed howitzer used in a general support role for the U.S. Marine Corps Air Ground task forces and Army light infantry divisions. The M198 has a conventional split trail carriage and utilizes a hydraulic recoil mechanism [1].

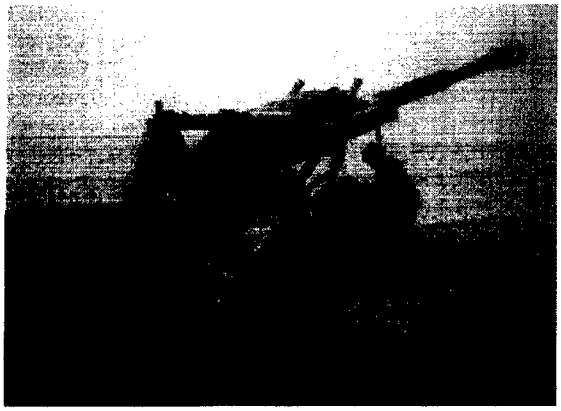


Figure 1. M198 155 mm Towed Howitzer (adapted from [1])

In addition to a towed howitzer configuration, large caliber cannons are also transported by means of a self-propelled vehicle, as in the case of Figure 2, the XM2001 or what it is commonly known as the Crusader Self-Propelled Howitzer (SPH) [1]. The Crusader SPH is a 155 mm fully automatic self-propelled howitzer, which utilizes a hydraulic type recoil system.



Figure 2. XM2001 – 155 mm Crusader Self-Propelled Howitzer (adapted from [1])

As the United States Military defines it direction for the 21st Century, it is asking the defense industry to create lighter and more mobile vehicles, while increasing overall systems effectiveness and firepower. As shown in Figure 3, one of the ways to reduce the total weight is the extensive use of titanium, such as in the 155 mm Ultra-lightweight Field Howitzer (designated the XM777 Lightweight 155 mm Towed Howitzer), making it just over one half of the weight of its predecessor, the M198 [2 – 3].

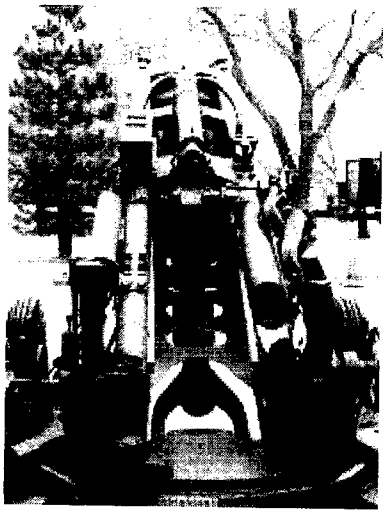


Figure 3. XM777 Lightweight 155 mm Towed Howitzer (adapted from [2])

Based on requests from the US Army, the Crusader Self-Propelled Howitzer has also been trimmed down to a prototype vehicle weight of 40 tons. This lighter platform will allow the Crusader Field Artillery System (the SPH and RSV – Re-supply Vehicle) to be transported aboard the same aircraft (C5 or C17) [4].

The common element among the future weapons—as well as improvement to existing weapons—that are considered by the U.S. Department of Defense are more lethal power and lighter weight. In order to achieve such goals, new recoil technologies must be employed in these weapons to increase their lethal power to weight ratio. This study will discuss one such technology, namely an advanced magneto-rheological damper, that is capable of sensing the recoil force and stroke of the gun and providing the optimal damping force for mitigating the recoil energy, and more importantly react to the fault modes of firing out-of-battery. Specifically, the primary purpose of this study is to

highlight the application of a magneto-rheological damper for controlling the recoil dynamics, using a 0.50 caliber gun that is installed in a test apparatus, called here the "recoil demonstrator." Further, this study intends to discuss a control strategy that can be used for accommodating a fire out-of-battery recoil system and deal with the firing faults modes that may occur.

After providing a brief background on MR dampers and fire out-of-battery dynamics, we will describe the test system that was used for this study, along with some of our test results. This is followed by a discussion on fire out-of-battery control, in which we will suggest an approach for controlling MR dampers for assisting FOOB recoil and, more importantly, deal with the firing fault modes.

BACKGROUND ON MR DAMPERS

Magneto-rheological (MR) dampers have been widely studied for vehicle suspension applications, as seen in the studies included in references [5 – 8]. Most of these studies consider the application of MR dampers for primary or secondary suspensions of the vehicle, and attempt to take advantage of the properties of MR dampers to more effectively control the dynamics and handling of the vehicle. For most vehicles, it is possible to show that through relatively simple control techniques, one is able to provide a more effective compromise between the ride and handling dynamics of the vehicle. In vehicle applications the relative velocities across the damper, due to the suspension motion, are generally in the range of 0 to 25 inches per second (in/s). The maximum range is commonly experienced during severe dynamics, such as sudden vehicle maneuvers or high-velocity input from the road, such as hitting a pothole.

Other systems that can benefit from the application of MR dampers are those involving shock loading. These are commonly systems that due to a large impact load, experience a sudden shock, such as the recoil dynamics that occur upon firing a gun. As described in many past studies—such as [9 – 11]—the dynamic compromise that commonly occurs in shock loading is maintaining the shock forces within the maximum force that the system can sustain, while not exceeding the maximum stroke of the components that absorb the shock (commonly called the "shock absorber" mechanism). For small shock absorber stroke, large forces must be sustained by the system; and

conversely for small shock forces, large strokes must be accommodated by the shock absorber mechanism. To provide a more favorable compromise between recoil force and stroke, several studies have examined closed-loop controlled recoil systems [12 – 14]. The vast majority of these studies have shown that theoretically it is possible to have a closed-loop recoil control system. This study will extend such results by providing the results of a series of experiments conducted on a gun recoil demonstrator

FIRE OUT-OF-BATTERY DYNAMICS

The circumstances that have led to the necessity for a fire out-of-battery system involves the challenge of designing a large caliber gun recoil system that is able to handle higher impulse munitions while at the same time reducing the recoil force that the vehicle feels through the trunnion pins. The necessity for higher impulse rounds is to have the ability to defeat threats at greater distances. Lower recoil loads through the trunnion pins will allow the vehicle to be lighter which translates into greater mobility, deployabilitly, and range.

The first step to understanding the issues is to look at the governing engineering equations. When applied to gun design, the conservation of momentum law dictates that the momentum that the bullet and propellant receive during the firing of the gun will be equal and opposite to the impulse the recoiling mass must absorb. This recoiling impulse translates to the energy that is absorbed by the gun mount, which ultimately appears as a recoil force on the trunnion pins.

For a typical large gun which has a recoil system, such as shown in the M198, XM777, and the Crusader SPH, a first order approximation of the equations that govern the recoil are:

$$(M_{bullet} + \tfrac{1}{2} M_{propellant}) * V_{bullet} = (M * V)_{recoiling\ mass} \quad (1)$$

Eq. (1) above is used to calculate the recoil mass velocity. With this, the recoiling energy can be calculated and equated to the required recoil force needed over the recoil stroke:

$$\tfrac{1}{2} (M_{recoiling\ mass}) * (V_{recoiling\ mass})^2 = \text{Recoil Force}_{Constant} * \text{Distance}_{Acting\ Force} \quad (2)$$

The military has a need to create lighter and more mobile artillery systems, while at the same time developing higher performance level munitions. These more lethal munitions, required to reach targets at much farther distances, demand much higher muzzle velocities, causing greater impulses to be absorbed by the system, and ultimately higher recoil forces seen at the trunnion pins. Various methods have been used and proven to reduce these recoil forces in the past. These include a long recoil stroke design that has the disadvantage of needing a very large swept volume for the recoiling parts. Another approach is the use of a muzzle brake that redirects the exiting propellant gas and thus its momentum as much as possible to the rearward direction of the gun. Muzzle brakes, although widely used, can only redirect the gas impulse and can thus never reduce more than that from the firing loads. Since the largest part of the recoil impulse is due to the bullet impulse, other means must also be used.

A fire out-of-battery (FOOB) mechanism can reduce the firing impulses by imparting a forward momentum (momentum opposite of recoil) of the recoiling parts before ignition. The FOOB mechanism effectively adds another term to Eq. (1):

$$((M_{bullet} + \tfrac{1}{2} M_{propellant}) * V_{bullet}) - ((M_{bullet,\ propellant,\ recoiling\ mass}) * (V_{forward})) = (M * V)_{recoiling\ mass} \quad (3)$$

In looking at Eq. (3), it becomes obvious that the entire firing impulse can be theoretically cancelled, and thus result in no recoil loads, if the forward velocity of the recoiling mass prior to firing can be high enough. Due to engineering limitations, a 50% reduction in recoil force is currently considered the practical limit. Figure 4 shows the contrasts between a conventional recoil system and a fire out-of-battery recoil system.

Figure 4a shows the three steps involved in a conventional recoil cycle. Step A1 is ignition from the in-battery position, Step A2 is recoil, and Step A3 is counter-recoil. Δx is defined as the maximum allowable recoil distance. Figure 4b shows the four steps involved in a FOOB recoil cycle. Step B1 is the loading position (Battery Position) and is the start of the run-up from the battery position. Step B2 is ignition, Step B3 is recoil, and Step B4 is counter-recoil.

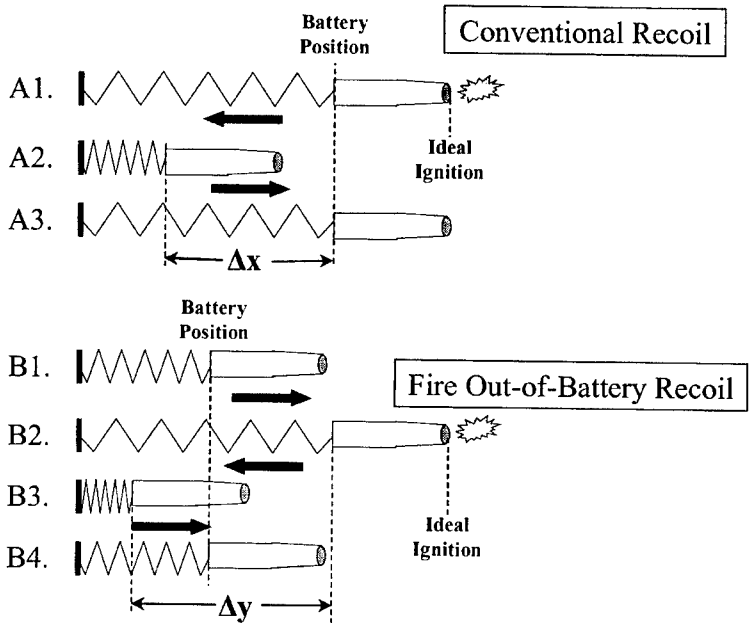


Figure 4. Conventional vs. FOOB Recoil firing sequence;
(a) Conventional firing; (b) FOOB rccoil firing

The FOOB recoil system must be designed to handle the highest impulse munitions. The total stroke Δy, forward and rearward of the battery position, will correspond to this impulse level. The US Army and others have successfully tested this fire out-of-battery system in the past, yet there are two major concerns.

First, in order to correctly utilize the advantages of a FOOB recoil system, it is necessary to consistently predict the ignition time. Conventional ignition systems, while sufficient for their use with conventional recoil systems, are not precise enough to gain the desired results from a FOOB system. Research has been completed and successful testing has shown that the use of an Electro-Thermal Chemical (ETC) Ignition system significantly reduces the standard deviation in ignition time over that of conventional ignition. Figure 5 shows a diagram of successful 120 mm ETC Ignition testing completed by the Armament Systems Division, United Defense, L. P, in conjunction with the US Army's Army Research Laboratory.

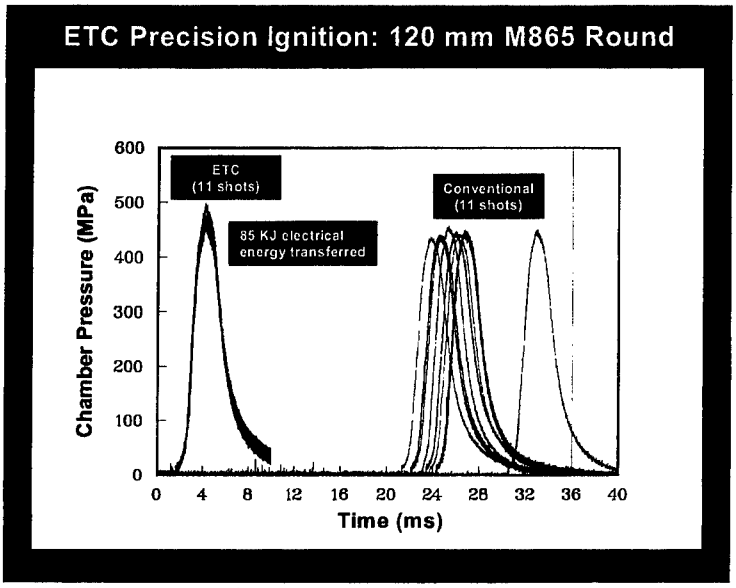


Figure 5. ETC 120 mm Testing

Second, the FOOB recoil mechanism must account for ignition error. The areas of concern are pre-fire (defined in Figure 6a), hang-fire (defined in Figure 6b), and misfire (defined in Figure 6c).

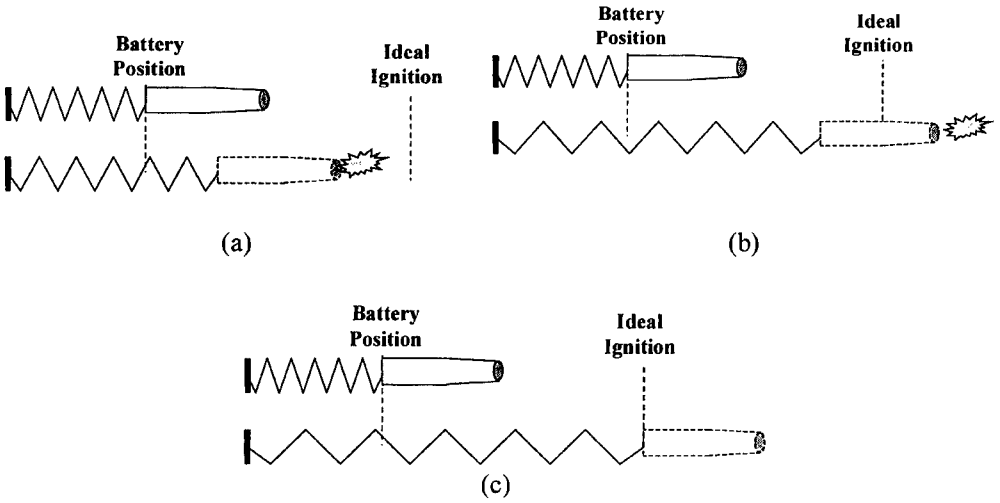


Figure 6. Definition of fault modes associated with Fire Out of Battery:
(a) pre-fire; (b) hang-fire; (c) misfire

In any of these three cases, when generating the momentum required to offset the recoiling impulse, if ignition does not take place at the precise time desired, the recoil system has to be designed to manage this firing impulse and forward momentum. If one of these cases occurs, the system must respond appropriately so that the gun does not damage itself.

The requirements of a Fire Out-of-Battery system are as follows:

1) A recoil system capable of absorbing the impulse from the required munitions
2) A system capable of accelerating the recoiling mass forward (direction opposite of recoil)
3) An ignition system capable of insuring precise and consistent firing times
4) A real time control device able to respond to fault modes associated with FOOB (hang-fire, pre-fire, and misfire)

While the first three requirements have been successfully demonstrated by the Army and ETC Ignition, the last one has yet to have undergone significant full scale testing. With the use of magneto-rheological technology and an active controller, a MR recoil system may be designed to sense normal firing conditions and the fault modes associated with FOOB and respond accordingly to and absorb the required impulse.

TEST SYSTEM

The test system that we designed and built for the purpose of this study is shown in Figure 7. It uses a 0.50 caliber, single-action, Browning Machine Gun (BMG) rifle that is mounted to a slider block. The slider block moves back on a pair of linear bearings, as the gun recoils. To the aft of the recoil slider is mounted a MR damper that is used to damp out the recoil dynamics of the gun. As will be described later, we are able to change the recoil force and displacement, based on the amount of damping force that is generated by the MR damper.

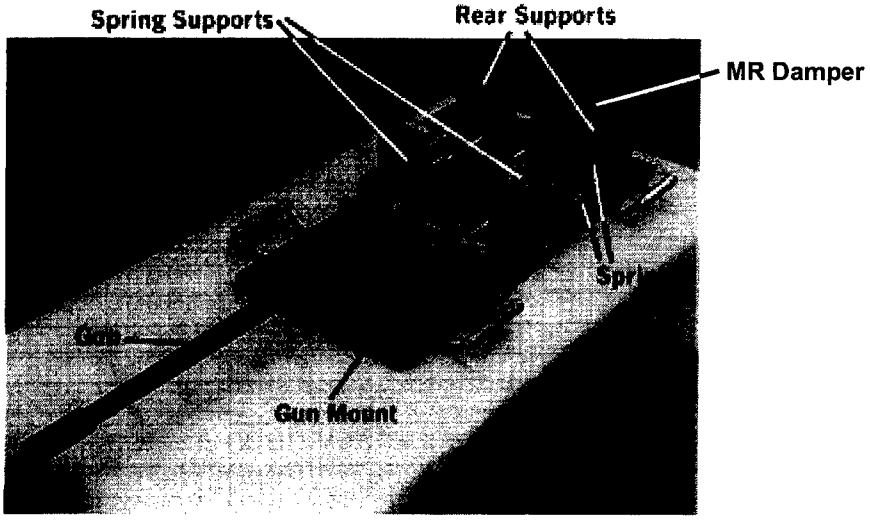


Figure 7. Magneto-Rheological Damper Test Device for Recoil Control

The detail of the MR damper that was designed and fabricated for this study is included in [15]. The damper includes a double-ended piston that can move in the cylinder, guided by two seals that are incorporated into two end caps attached at each end of the piston. In addition to guiding the piston rod, the seals are designed such that they maintain the MR fluid within the piston. A small circumferential clearance (gap) between the piston and the damper body provides the means for energizing the MR fluid, as it passes through the gap due to the movement of the piston within the cylinder. As the MR fluid is activated by a different magnetic flux density, it offers a different amount of resistance to the motion of the piston, therefore providing different damping forces. The larger the magnetic flux density is, the higher the fluid resistance to the piston and the larger the damping force. The magnetic flux density is controlled by the amount of electrical current supplied to a coil designed in the piston.

TEST RESULTS

In order to establish the force-velocity (or damping) characteristics of the MR damper that we had designed for the recoil demonstrator, we conducted a series of tests in a hydraulic material testing machine. In each test, the damper piston was moved at a

given sinusoidal velocity relative to the piston, and the resistance force due to this motion was recorded. The peak values for the force and velocity, plotted in Figure 8, provide the curves that characterize the damper. Although we recognize the importance of testing the damper at velocities sufficiently high to characterize recoil velocities, our test machine was not capable of generating such velocities. Additionally, our attempts to create such velocities through a rig with a drop weight proved unreliable. Therefore, we decided on characterizing the damper at velocities as high as possible with our test machine, and used the results to estimate the damper behavior at the higher recoil velocities. As will be shown later, this approach proved to be reasonably satisfactory.

As shown in Figure 8, when no current is supplied to the damper, the damping force is relatively minimal (38 lb at 22 in/s). This is a desirable characteristic since the low forces when the damper is not powered provide a larger damping force range, defined as the difference between the damping force at a given velocity for the maximum and zero voltage. The larger the damper force range is, the higher the ability of the damper to affect the dynamic of the system in which it is used. As voltage to the damper is increased, the damping force increases, nearly proportionally. For a supplied voltage of 6 V, the MR damper was able to provide approximately 470 lb of force for velocities larger than 22 in/s. We determined this amount of force to be sufficient for our recoil demonstrator.

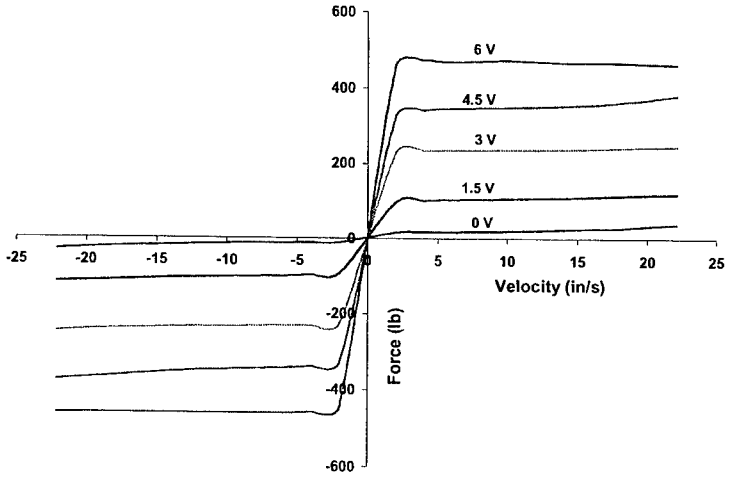


Figure 8. Damping Curves for the Gun Recoil MR Damper at Different Voltages

Although not shown in Figure 8, we tested the damper at voltages much greater than 6V, in order to determine how much more force the damper can generate at higher voltages, and also determine the saturation voltage of the damper. The saturation voltage is defined as the voltage at which no significant increase in damping force is observed as the voltage increases. Our test results showed that the MR damper was able to provide nearly a maximum of 700 lb force at 12 V, which proved to be our saturation voltage.

Field Testing

A series of field tests were conducted to evaluate the effectiveness of the MR damper explained earlier for controlling gun recoil. The data collected in each test included the recoil force and stroke. The recoil force was measured using a force transducer that was installed at the connection of the MR damper to the recoil slider. The force transducer is an Integrated Circuit Piezoceramic (ICP) force transducer manufactured by PCB Piezotronics, model number ICP 201B04,. It can measure dynamic forces in compression to a maximum of 5000 lb, and has a sensitivity of 5 mV/lb. The recoil stroke was measured by a Linear Variable Differential Transformer (LVDT) connected to the recoil slider. The recoil force and stroke data were recorded, using a 2-channel dynamic signal analyzer, model number HP-35665A, manufactured by Hewlett Packard.

Figure 9 shows the recoil force vs. recoil stroke for different voltages supplied to the MR damper. As was mentioned earlier, the coil resistance was approximately 3 Ohms; therefore, if desired, the voltages shown in all figures can be converted to current. For instance, 3 Volts corresponds to 1 Ohm and 6 Volts corresponds to 2 Ohms. As is expected, Figure 9 shows that the initial peak of the recoil force increases as the damper force increases (through increasing the voltage supplied to the damper). The increase in recoil force appears to be nonlinearly dependent to the increase in damping force, with larger increases observed at higher voltages to the damper.

The recoil stroke is inversely proportional to the damping force—again exihibiting a nonlinearly dependency to the damping force—as shown in Figures 10. For larger damping forces, the recoil stroke is shortened significantly (less than ½ of the maximum recoil stroke designed into our demonstrator at 6V), whereas for smaller damping forces the change in recoil stroke appears to be far smaller. When no current

was supplied to the damper, the gun recoil exceeded the 4 inch allowable stroke designed into the demonstrator and hit the elastomeric bumpers installed at the end of the travel, as indicated in Figure 10.

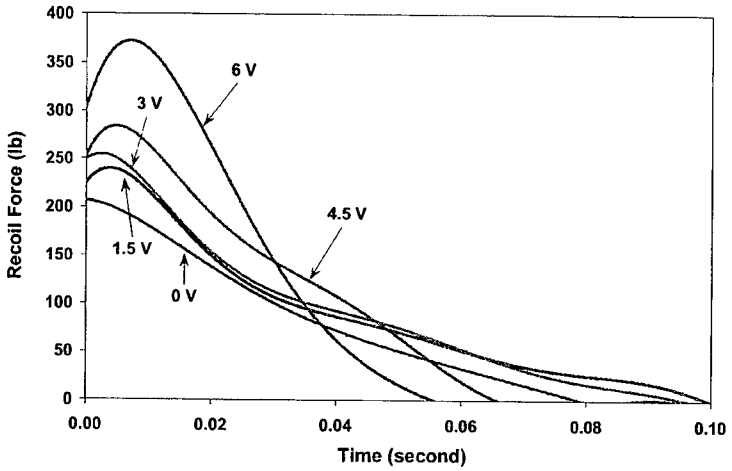


Figure 9. Recoil Force-Recoil Spectrum (Curve-Fitted)

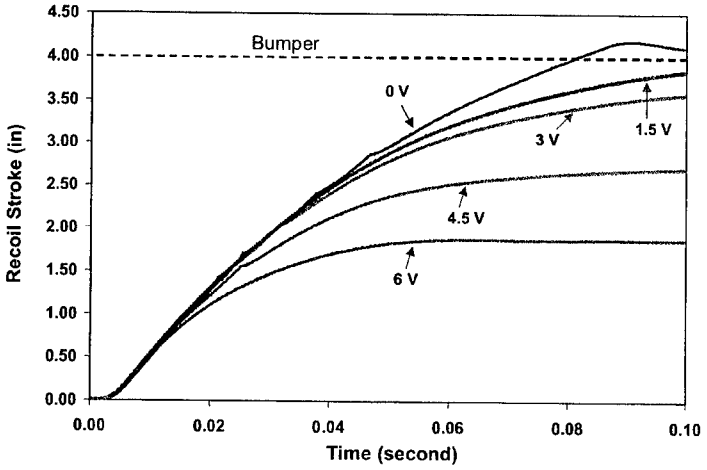


Figure 10. Recoil Force Time Profile

FIRE OUT OF BATTERY CONTROL

Considering the dynamic performance of MR dampers, as stated above, we are considering in our research the fire out of battery control shown in Figure 11. The first stage begins in the maximum displaced position where the gun is latched and loaded. After the round is loaded, the system is unlatched, allowing the gun to propel forward to a predisposed ignition position. The second stage begins with ignition and continues throughout the full recoil stroke (It is important to note that this testing fixture was designed to demonstrate the effectiveness of FOOB, and not designed to re-latch at the Stage 1 initial position as described above. After ignition, the gun recoils rearward until the recoil force is overcome by the spring force, at which point the system changes direction and slams into the front stops).

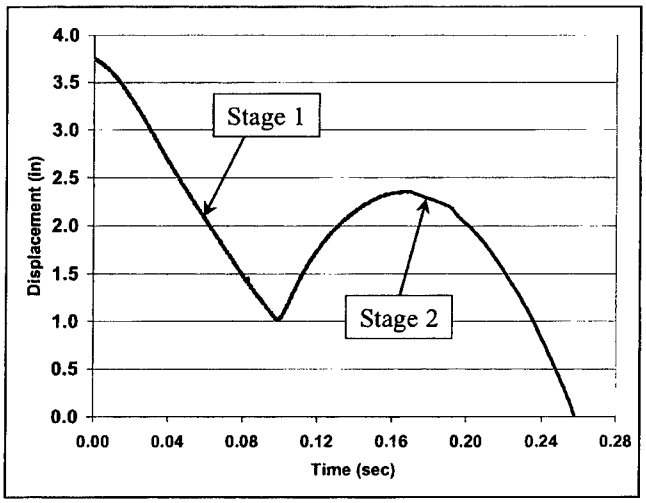


Figure 11. Displacement of the Gun during the Two-Stage FOOB Recoil Process

By sensing the position and velocity of the recoil assembly, we select the most dynamically advantageous position to fire out-of-battery, therefore ensuring lower peak forces, as shown in Figure 12. The recoil stroke and velocity measurements just mentioned above are also used to sense any firing faults, in which case the MR damper is used to react to the dynamics caused by such faults. For instance, incase of a misfire, the

MR damper can be fully energized to counteract the forward momentum of the gun and reduce the impact forces as it returns into the battery position.

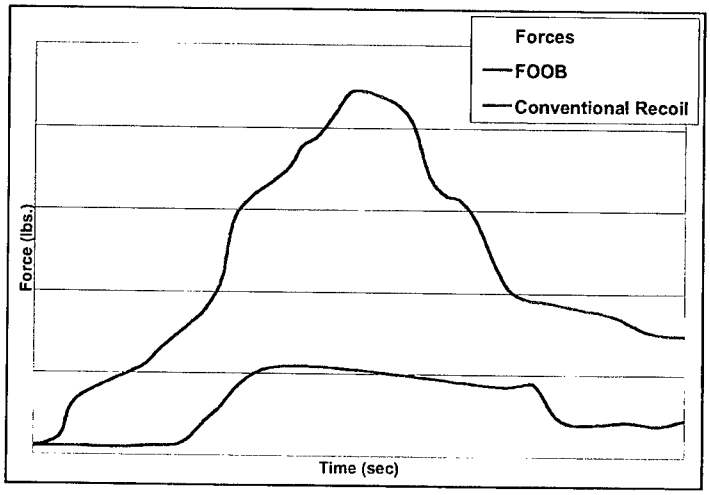


Figure 12. Force Comparison of FOOB and Conventional Recoil

We are currently in the process of implementing the above control technique in our recoil demonstrator. The initial laboratory testing that has been performed on the system indicates promising results. In the near future, we intend to conduct a series of field tests to further evaluate the potential of the MR dampers and the proposed FOOB control technique.

SUMMARY

The application of magneto-rheological dampers for controlling recoil dynamics was examined, using a recoil demonstrator that included a 0.50-caliber gun and a MR damper (referred to as "recoil demonstrator"). Upon providing a brief background on MR dampers and fire out-of-battery dynamics, we described the recoil demonstrator, along with some of the results that have been obtained from testing the MR damper as well as field testing the recoil demonstrator. The test results indicate that the MR damper is able to effectively control the recoil dynamics, and provides a different force-stroke curve for different amounts of current supplied to the damper. The current to the damper is used to energize the magneto rheological fluid within the damper and provide different amounts of damping force. Based on the recoil control results achieved by the damper, a

technique was suggested for using MR dampers for fire out of battery. The technique, which consists of two stages, was described in detail along with the potential role of MR damper in each stage. Finally, our plans for field-testing the suggested fire out of battery method, using the recoil demonstrator and the MR damper, was briefly discussed.

REFERENCES

1. Foss, C. F. Jane's Armour and Artillery 2000-2001, 21st Edition, 2000.
2. Cullen, T., and Foss, C. F., Jane's Armour and Artillery Upgrades 2000-2001, 13th Edition, 2000.
3. http://www.army-technology.com/projects/ufh/index.html
4. http://www.army-technology.com/projects/crusader/index.html
5. Carlson, J. D., and Chrzan, M. J., 'Magneto rheological Fluid Dampers,' Patent No. 5,277,281, Jan 11, 1994.
6. Carlson, J. D., Catanzarite, D. M., and Clair, K. A. St., 'Commercial Magneto rheological Fluid Devices,' *International Conference On Electro-Rheological, Magneto rheological Suspensions and Associated Technology*, Sheffield, 10-14 July, 1995.
7. Ahmadian, M. and Ahn, Y. K., "Performance Analysis of Magneto-Rheological Mounts," *Journal of Intelligent Material Systems and Structures*, Vol. 10, No. 3, pp. 248-256, March 2000.
8. Simon, D. E. and Ahmadian, M., "Application of Magneto-Rheological Dampers for Heavy Truck Suspensions," *Proceedings of the 32nd International Symposium on Automotive Technology and Automation (ISATA)*. Vienna, Austria, June 1999.
9. Chen, Ching Jen, "Fluid Mechanics and Thermodynamics of Recoil Mechanisms," US Army Armament Research and Development Command, Dover NJ, September 1963.
10. Research and Development of Material, AMCP 706-342, "Engineering Design Handbook—Carriages and Mounts Series Recoil Systems," US Army Material Command, Washington DC, September 1963.
11. Hajihosseinloo, M.A., Hooke, C.J., and Walton, D., "Gun Recoil System Performance Measurement and Prediction," Proceedings of the Institution of Mechanical Engineers, Part C: Mechanical Engineering Science, V. 203, N. 2, pp. 85-92, 1989.
12. George, Steven, "Microprocessor Control Recoil Mechanism," STAR (Simulation Technology and Automation Resources Team) Report No. 003-88, Close Combat Armament Center, Systems Integration Division, Dover NJ, March 1988.
13. Jumper, George Y. and Floroff, Stephen G., "Feasibility of a Microprocessor Controlled Recoil Mechanism for Large Caliber Artillery Weapons," Technical Report ARLCD-TR-85007, ARDEC, Picatinny Arsenal NJ, May 1985.
14. George, Steven, "Microprocessor Microprocessor Control Recoil Mechanism," STAR (Simulation Technology and Automation Resources Team) Report No. 029-87, Close Combat Armament Center, Systems Integration Division, Dover NJ, March 1987.
15. Ahmadian, M., Poynor, J.C., "An Evaluation of Magneto-Rheological Dampers for Controlling Gun Recoil Dynamics," *Shock and Vibration*, accepted for publication, in press.

MUZZLE MOTION MEASUREMENTS FOR THE M198 WHEN FIRED AT 30 AND 45 DEGREES

James M. Garner, Bernard J. Guidos, and Brendan J. Patton

U.S. Army Research Laboratory, Aberdeen Proving Ground, MD 21005-5066

The U.S. Army is reducing the weight of its 155-mm artillery system in order to meet increased operational thresholds for mobility, survivability, deployability, and sustainability. The XM777 lightweight 155-mm howitzer is being developed to replace the M198 howitzer for both the Army and the Marine Corps. Certain launch characteristics, such as jump and recoil effectiveness, are important in the design process and are being quantified. The M198 system provides the performance standards against which to compare those of the XM777. To contribute to a baseline characterization database, elevated firings of the M198 howitzer were conducted in which the muzzle motion was measured and quantified in terms of a jump model. This paper describes the experimental firings and presents highlights of the results and analysis.

INTRODUCTION

The U.S. Army's effort to reduce artillery system weight as well as the desire to achieve first round hit has intensified the need for more detailed understanding of factors that affect artillery accuracy. Gun dynamics are relevant in these endeavors because gun-projectile interactions influence the initial conditions for the round's trajectory. Recent experiments conducted by the U.S. Army Research Laboratory (ARL) included measurements of gun dynamics contributions to jump for the M198 artillery system in flat fire [1] using established proximity probe technology [2, 3]. Such measurements had not been made earlier because the gun dynamics had been considered to have minimal influence on accuracy and precision errors for artillery systems. Because artillery systems have traditionally been considered area weapons, precision has not been the limiting factor in characterizing system effectiveness. In fact, gun dynamics effects are modeled in the precision equation by a term broadly used for a spectrum of influences, including gun elevation, charge, and occasion-to-occasion factors [4].

Lightweight systems such as the XM777 can be expected to have increased gun tube motion during launch compared to existing heavier systems. The quantification of such differences is a measure of performance, and the baseline system against which to compare is the M198 howitzer. The baseline characterization process began with previous measurements of M198 muzzle motion in flat fire [1]. Recently, the database has been extended to include M198 muzzle motion measurements for elevated firings. This paper describes the recent elevated firings and presents highlights of the results and analysis, including some comparisons to the flat-fire results.

EXPERIMENTAL PROCEDURE AND SETUP

The experiment was conducted at ARL's Transonic Experimental Facility (TEF) located at Aberdeen Proving Ground. Figure 1 shows the M198 towed howitzer, elevated at 45° (800 mils) quadrant elevation (QE), along with the support platform and muzzle instrumentation. The platform, an existing standard steel frame radiography (x-ray) fixture approximately 10 ft high, 10 ft wide, and 8 ft long, served as a rugged, immobile mount. A smaller steel frame, approximately 5 ft high, was attached to the main platform and served as a mount for the instrumentation.

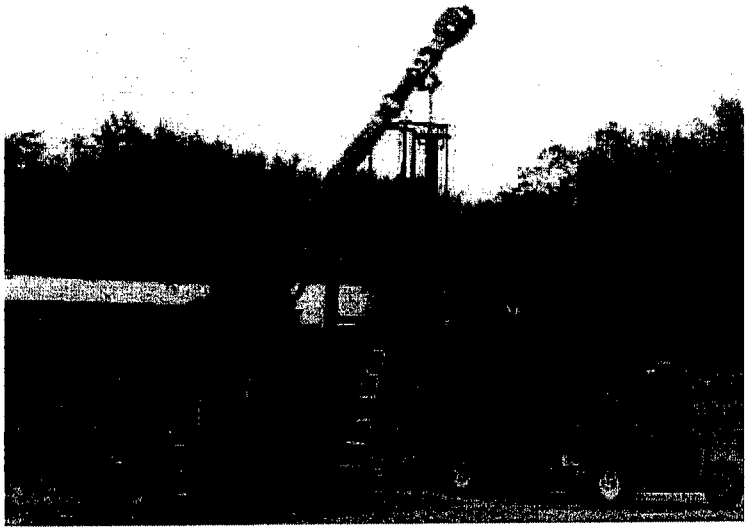


Figure 1. M198 Howitzer Mount at 45° Elevation and Test Setup.

Figure 2 is an expanded view of the M198 gun tube, muzzle, muzzle brake, and instrumentation. Eight eddy probes were mounted in two stations of four probes each within a mounting ring at distances of 170 mm and 380 mm from the muzzle. A pressure probe was clamped to the gun tube approximately 50 mm from the first muzzle brake exit vent, providing a pressure signal for initiating the data acquisition. This data "trigger" started the data recorders such that eddy probe voltage signals are retained for a time span of approximately 20 ms. This time is apportioned such that tube motion before and after shot exit is recorded. The muzzle probe signal is most useful for determining when shot exit occurs, but was also found to be an indicator of obturation consistency.

Eddy probes, also referred to as proximity probes, measure the change in distance from the probe to the tube surface by sensing changes in the magnetic flux through their coil area. The probes are calibrated to correlate their outputs to various offset distances. The probe outputs are recorded, filtered, and transformed into proximity histories. The proximity histories are combined to provide quantities that characterize the gun dynamics for individual shots. Quantities of interest for this study included histories of tube expansion, centerline lateral displacement, muzzle pointing angle, and muzzle crossing velocity.

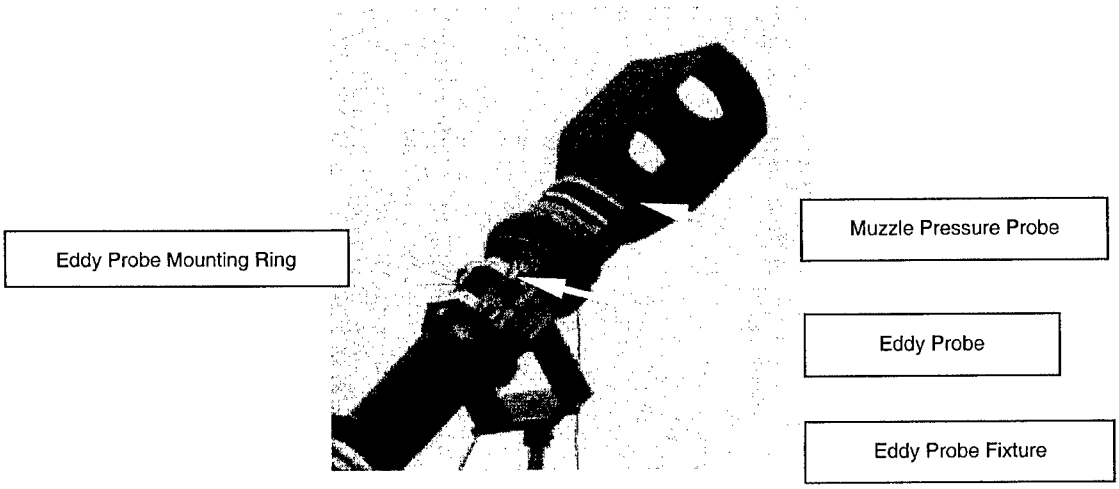


Figure 2. View of Muzzle and Instrumentation.

At shot exit, the instantaneous values of muzzle pointing angle and crossing velocity jump are two components of the jump model used in earlier firings [1]. Each jump quantity is a vector angle having an azimuth (horizontal) and elevation (vertical) component, typically on the order of 1 mrad or less.

The experiment consisted of five firings each of M107 and M549 projectiles. Table 1 lists the nominal physical properties of the projectiles. Firings were conducted in an alternating sequence of projectile type, with six shots at 45° (800 mils) QE and four shots at 30° (534 mils) QE, as shown in Table 2. All rounds were fired using Charge 7W. A Weibel MSL 60037 three-coordinate tracking radar was used to record the trajectories of the rounds and to provide muzzle velocity and impact ranges. The radar results are not included in here for brevity.

Table 1. Projectile Physical Properties.

Physical Property	M107	M549
Length	667 mm	873 mm
Mass	42 kg	43.6 kg
Center-of-Gravity (from nose)	420 mm	518 mm
Axial Moment of Inertia	0.144 kg-m^2	0.149 kg-m^2
Transverse Moment of Inertia	1.20 kg-m^2	1.5 kg-m^2

Table 2. Summary of Test Firings and Launch Velocities.

QE = 45°			QE = 30°		
Round No.	Round Type	Velocity (m/s)	Round No.	Round Type	Velocity (m/s)
35344	M107	567	35350	M107	567
35345	M549	566	35351	M549	566
35346	M107	568	35352	M107	571
35347	M549	566	35353	M549	565
35348	M107	567			
35349	M549	563			

RESULTS

Figure 3 shows the muzzle pressure probe voltage signal obtained for round 35348. The voltage history is shown for a 5 ms interval within the approximately 20 ms in-bore time experienced by the projectile. Zero on the time scale is the time at which a manually specified voltage signal threshold is reached and data recording begins. The precursor reaches the muzzle probe at –3.2 ms, registering a maximum signal level of 0.22 volts. For this shot, the muzzle probe triggered the recording timer as the main blast registered a first maximum signal level of 0.33 volts. The overall positive phase time duration of the main blast is approximately 0.3 ms. Concurrently, shot exit is defined here as the time at which the obturator loses contact with the muzzle and the main blast uncorks. Figure 3 shows that shot exit occurs at 0.136 ms for shot 35348. A method for determining shot exit time from eddy probe data was developed during the study and is described subsequently.

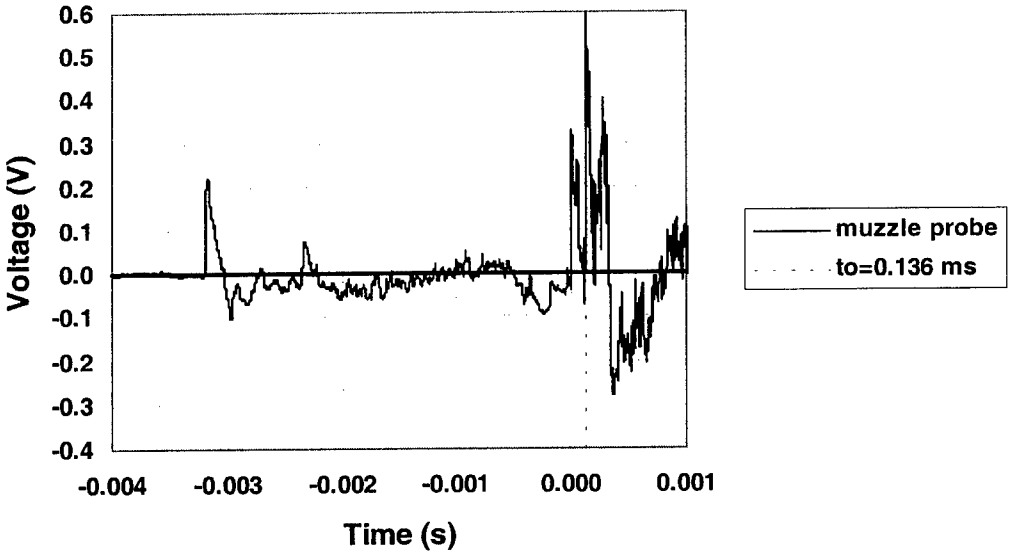


Figure 3. Muzzle Pressure Probe Voltage Signal, Round 35348.

Figure 4 shows reduced eddy probe signals that represent the relative gun tube diameter between opposite probes. The relative gun tube diameter is the difference between the measured proximity of opposite probes, with a negative slope representing an expanding gun tube. The relative gun tube diameter for each pair of opposite probes drops markedly as the gun tube expands due to the large pressure increase associated with obturator passage. The result shows that the gun tube diameter expands by approximately 0.1 mm as the high pressure region passes by. The rearward set of probes experience tube expansion at approximately –1 ms and the forward set of probes experience tube expansion at approximately -0.7 ms.

It was found in this study that the tube expansion recorded at the two eddy probe stations can be used to accurately identify shot exit in the muzzle probe signal already shown in Figure 3. Published and unpublished results from the ARL jump test of the 155-mm Howitzer in flat-fire [1], which had near-muzzle x-rays, were used in this study to validate the use of tube expansion signals to accurately identify shot exit. It was assumed that the in-bore projectile velocity was

constant between the eddy probe rig and the muzzle. The time interval between the two eddy probe stations could be determined accurately enough to calculate the launch velocity to within 20 m/s of the value measured by radar or near-muzzle x-rays (or given by the Army firing table value for the M107 with a 7W charge is 568 m/s [5]). Using the determined launch velocity, the elapsed time between obturator passage and shot exit could be calculated. It was found that shot exit time calculated using the velocity as determined from the tube expansion consistently agreed with that obtained using x-ray position data to within 20 μs for the flat-fire shots. This amount of accuracy is considered here to be adequate for defining shot exit and evaluating the muzzle state at that time.

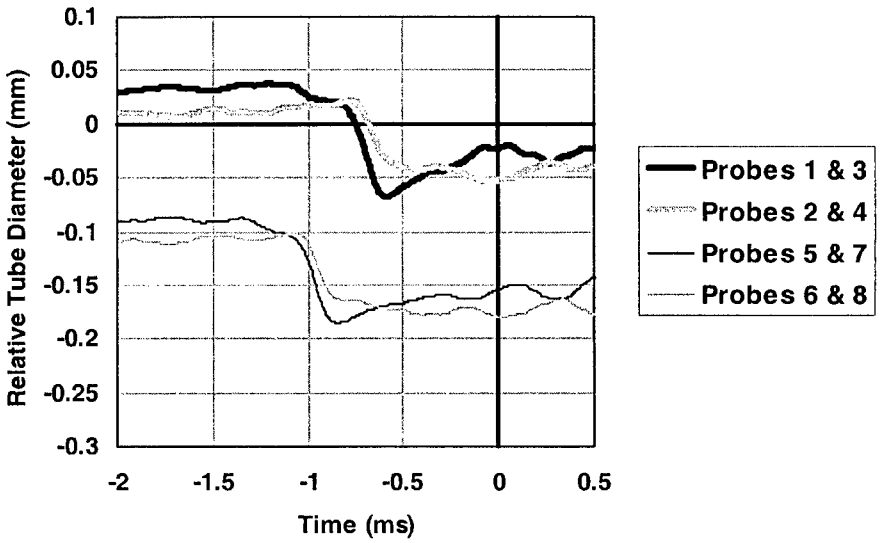


Figure 4. Tube Expansion at Eddy Probe Stations, Round 35348.

The shot exit calibration study showed that obturator passage in tube expansion plots, such as those in Figure 4, can be identified by the slight but distinct change in slope of the steep curve in the rapid expansion region. For round 35348, this occurs 75 μs prior to the first minimum in relative tube diameter being reached. Using this procedure, the shot exit time was determined individually for each shot, and the associated time scales were shifted such that time zero corresponded to shot exit. The resulting adjusted time scales are used in the presentation of all subsequent results.

Interestingly, Figure 3 shows that shot exit occurred for round 35348 *after* the timing trigger was initiated, demonstrating that the blast signal that initiated the timing trigger was associated with leakage through the obturator seal rather than the uncorking of the main blast. Seven out of nine shots for which both eddy probe and muzzle pressure probe data were available showed similar or greater leakage. A quantitative consideration of obturator leakage and its effects (if any) on the observed behaviors of the individual rounds is not included in this paper but may be addressed in the future.

Figure 5 and Figure 6 shows the tube centerline displacement in elevation at the forward eddy probes (170 mm from the muzzle) for the two M107 and two M549 shots at 30° QE and 45° QE , respectively. Comparison is made to round 34340, a flat-fire shot from the earlier M198 flat-fire test [1]. The elevation displacement coordinate is located in a vertical plane and oriented perpendicular to the individual pre-trigger line of fire, positive upward. The tube centerline movement of the flat-fire shot has many of the same characteristics as the 30° QE shots, but noticeably amplified. The flat-fire shot registers tube centerline movement downward, but does not reach a minimum until 1 to 2 ms later than the 30° QE shots. Strong upward displacement occurs, and like the 30° QE shots, it creates the same noticeable saddle point at –5 to –6 ms with the motion peaking at 3 ms prior to shot exit. Unlike the 30° QE shots, the centerline displacement moves upward enough to register a positive value. Less lateral displacement does not, strictly speaking, mean that less disturbance is present because the measurement location could conceivably be located at a node that masks larger motion. If the gun tube disturbances are considered to mainly transitory, though, then the 30° QE shots could be considered to have less overall vertical motion than the flat-fire shot.

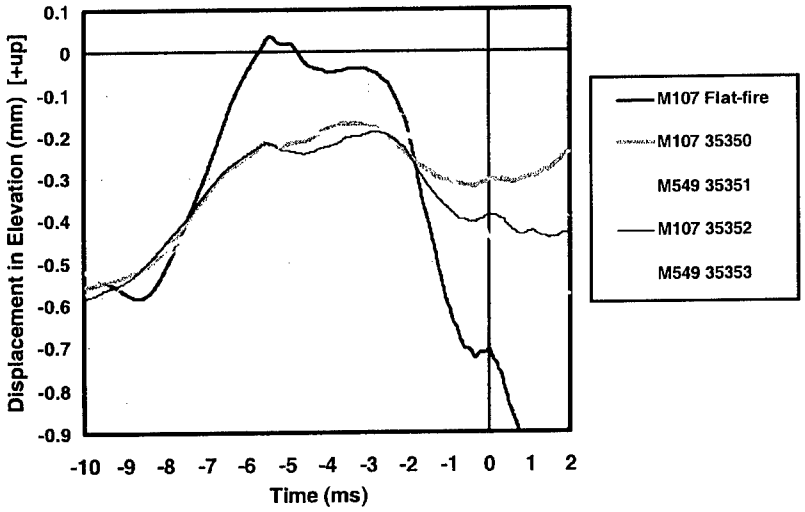


Figure 5. Tube Centerline Displacement in Elevation, Forward Probes, 30° QE.

Figure 6 shows that all 45° QE shots register tube centerline displacement in elevation more similar to the 30° QE shots than to the flat-fire shot, with the flat-fire shot showing considerably more lateral motion in the elevation coordinate. It can be conjectured that the barrel elevation plane displacement should be larger in flat-fire mode since forces at the muzzle would have the longest lever arm to act against the damping/restoring force from the equilibrators. As the gun is elevated, the horizontal distance between the tube CG and the equilibrator attachment is reduced, and the barrel transverse motion is also reduced.

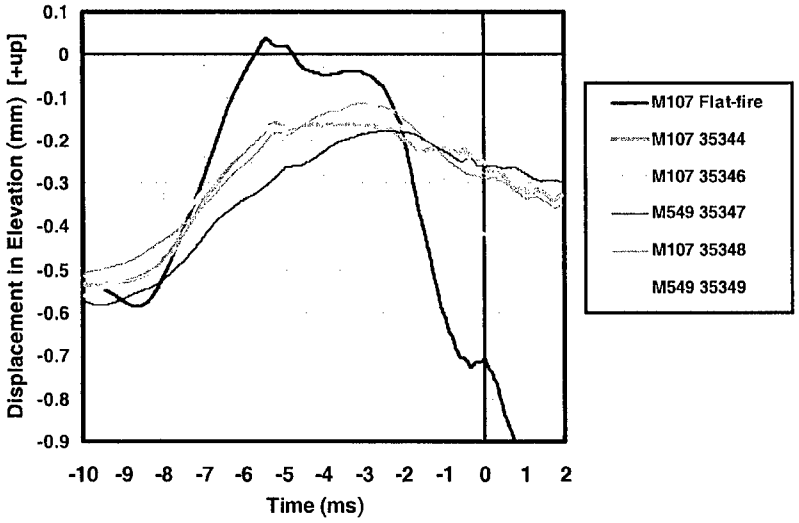


Figure 6. Tube Centerline Displacement in Elevation, Forward Probes, 45° QE.

Figure 7 and Figure 8 show the tube centerline displacement in azimuth at the forward eddy probes for the shots at 30° and 45° QE, respectively. Flat-fire round 34340 is again included in both plots for additional comparison. The azimuth displacement coordinate is assumed to be located in a horizontal plane and oriented perpendicular to the individual pre-trigger line of fire, positive to the gunner's right. In all cases, the displacement in azimuth is noticeably less than the displacement in elevation throughout the in-bore part of the launch. The flat-fire shot shows distinct maximum displacements to the right at 7 ms and 2 ms prior to shot exit. The two M107 shots at 30° QE show similar behavior to the flat-fire shot, except that the peaks are slightly shifted in time and less pronounced. The two M549 shots at 30° QE barely fail to register a maximum at 2 ms prior to shot exit, and displacement continues to the right through shot exit. None of the shots at 45° QE exhibit a noticeable peak or saddle point at 2 ms prior to shot exit.

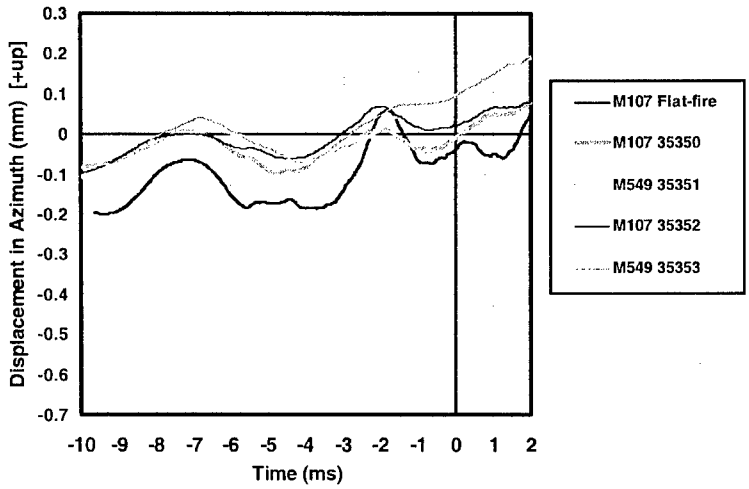


Figure 7. Tube Centerline Displacement in Azimuth, Forward Probes, 30° QE.

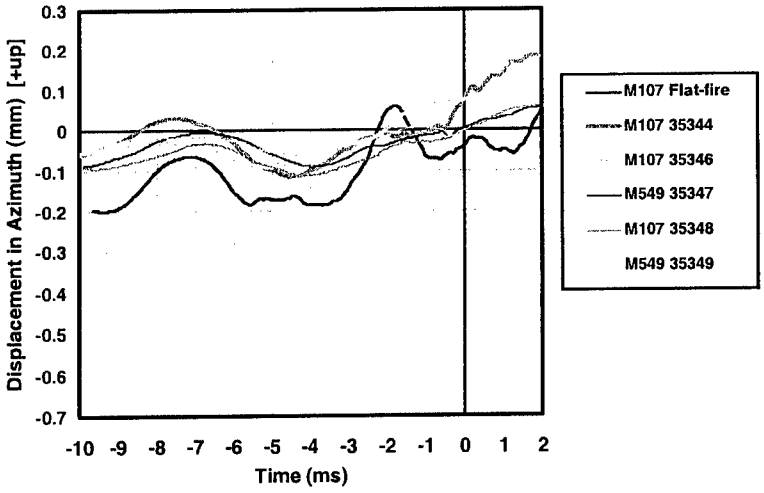


Figure 8. Tube Centerline Displacement in Azimuth, Forward Probes, 45° QE.

Figure 9and Figure 10 show the muzzle pointing angle in elevation for the shots at 30° and 45° QE, respectively, with flat-fire round 34340 included in both plots. Figure 11 and Figure 12 show the muzzle pointing angle in azimuth for the shots at 30° and 45° QE, respectively. In all cases, the muzzle pointing angle in elevation shows larger overall magnitudes and amplitudes than in azimuth. The shots at 45° QE show noticeably smaller shot-to-shot variability throughout the in-bore event than the 30° QE for pointing angle in elevation, with both types of projectiles maintaining a similar history. At 30° QE , the two M549 shots exhibit pointing angles in elevation that are noticeably different than the M107 shots. The pointing angle in azimuth shows small and uneventful histories in all cases.

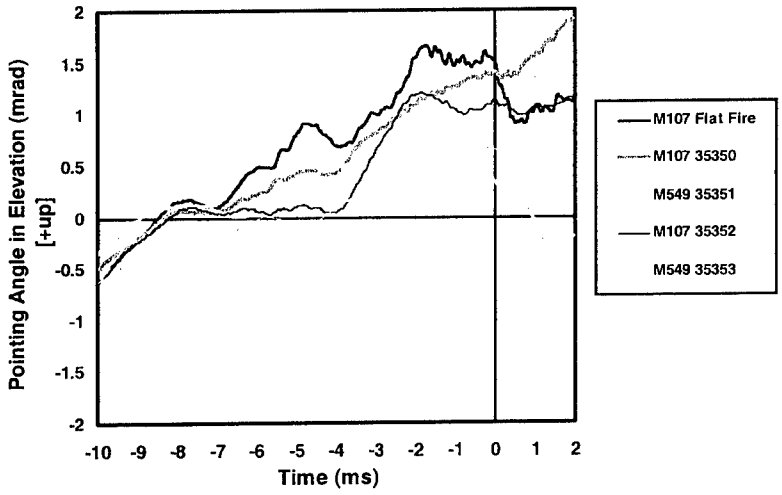


Figure 9. Muzzle Pointing Angle in Elevation, 30° QE.

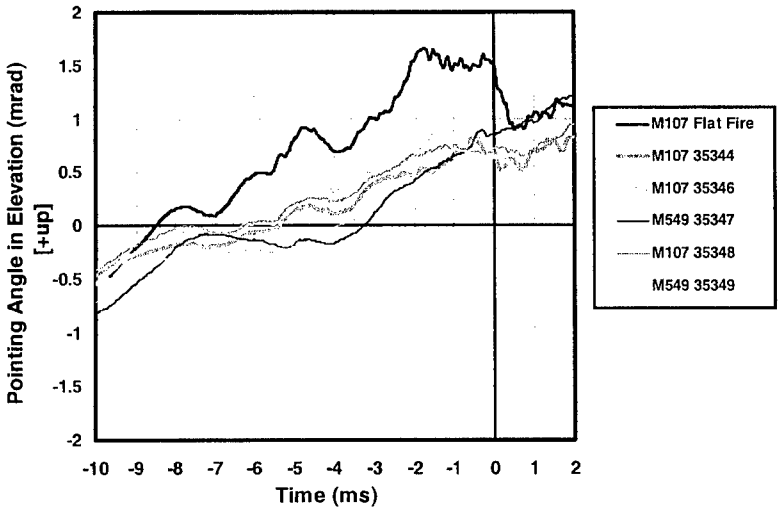


Figure 10. Muzzle Pointing Angle in Elevation, 45° QE.

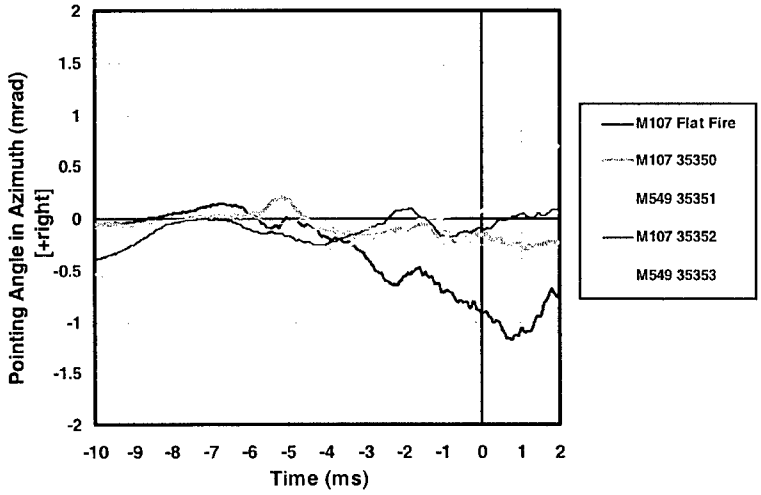


Figure 11. Muzzle Pointing Angle in Azimuth, 30° QE.

The muzzle pointing angle jump and muzzle crossing velocity jump are contributions to total jump included in the jump model presented previously [1]. Both quantities are evaluated at shot exit. The muzzle crossing velocity jump is the lateral displacement at the muzzle (calculated using the displacement at the forward probe location and the muzzle pointing angle) divided by the projectile launch velocity. Table 3 shows the individual muzzle pointing angle and crossing velocity jump for the nine flat-fire shots, along with the mean and standard deviation of the entire group. Table 4 shows the same quantities for the 30° and 45° QE firings.

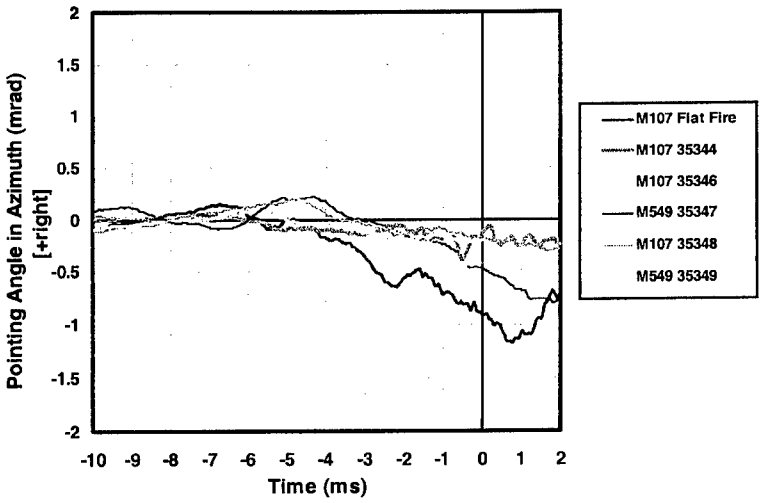


Figure 12. Muzzle Pointing Angle in Azimuth, 45° QE.

Table 3. Muzzle Pointing Angle and Crossing Velocity Jump Components, Flat-fire Shots.

Flat-Fire Shots					
ROUND	TYPE	pax	pay	cvx	cvy
34538	M107	-0.89	0.74	0.58	-0.58
34539	M107	-0.98	0.93	0.10	-0.02
34540	M107	-0.91	1.52	-0.16	-0.06
34541	M107	-0.56	1.44	0.56	0.06
34542	M107	-1.04	1.16	0.11	-0.56
34543	M107	-0.96	1.08	-0.17	0.17
34546	M107	-1.11	1.07	-0.43	-0.46
34547	M107	-0.81	0.98	0.34	-0.12
34537	M107	-0.56	0.82	0.02	-0.42
Mean	-	-0.87	1.08	0.11	-0.22
Std	-	0.20	0.26	0.34	0.28

Table 4. Muzzle Pointing Angle and Crossing Velocity Jump Components, Elevated Shots.

800 mils (45°) QE						534 mils (30°) QE					
ROUND	TYPE	pax	pay	cvx	cvy	ROUND	TYPE	pax	pay	cvx	cvy
35344	M107	-0.14	0.68	0.85	0.07	35350	M107	-0.16	1.41	0.24	0.30
35346	M107	-0.20	0.63	-0.10	-0.31	35351	M549	0.07	0.34	0.30	-0.50
35347	M549	-0.48	0.85	-0.05	0.02	35352	M107	-0.09	1.13	0.05	0.39
35348	M107	-0.18	0.71	0.07	0.26	35353	M549	-0.25	0.65	0.04	-0.11
35349	M549	-0.42	0.72	0.23	-0.05						
Mean	-	-0.28	0.72	0.20	0.00	Mean	-	-0.11	0.88	0.16	0.02
Std	-	0.15	0.08	0.38	0.21	Std	-	0.14	0.48	0.13	0.41

Figure 13 shows the muzzle pointing angle jump for all shots, including nine available flat-fire shots. All three elevation groups show pointing angle jump component means in the second quadrant (i.e., with the gun muzzle pointing up and to the left at shot exit). The pointing angle jump mean for the flat-fire shots is noticeably to the left of the elevated firings. There is less of a difference, if any, between the pointing angle means of the 30° QE and 45° QE shots. The pointing angle for the two M107 shots at 30° QE appears noticeably higher in elevation than the two M549 shots at the same QE, although the trends would be difficult to even statistically detect with so few shots. The standard deviation of the elevation component of the pointing angle is noticeably smaller for the 45° QE shots than the other two elevations. However, the standard deviation in elevation for the 30° QE shots is affected by the aforementioned difference between the two projectile types.

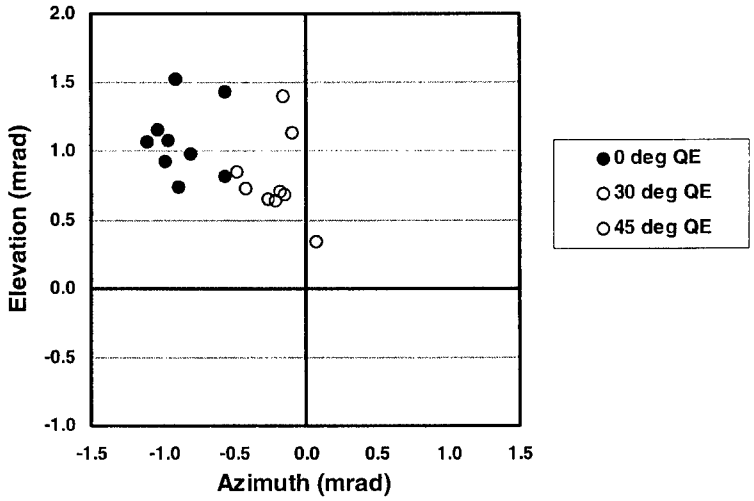


Figure 13. Muzzle Pointing Angle, All Shots.

Figure 14 shows the muzzle crossing velocity jump for all shots, including the nine available flat-fire shots. The elevated firings can not easily be separated based on their crossing velocity values. The exception to this is the crossing velocity value for elevation. The elevated firings have a positive mean elevation crossing velocity, while the flat fire values have a negative mean. The implication is that overall, the firing behavior is only subtly affected by elevation changes, and retains its basic character.

The accuracy of the muzzle pointing angle is estimated to be within ±0.025 mrad, and the accuracy of the muzzle crossing velocity jump is estimated to be within ±0.1 mrad. The exception is five shots lacking data from one probe (rounds 35344, 35347, 35349, 35351, 35352), in which the data reduction was accomplished by assuming that the relative tube diameter was circumferentially invariant at the affected axial location. For those five shots, the accuracy is of the pointing angle is estimated to be within ±0.05 mrad, and the accuracy of the crossing velocity jump is estimated to be within ±0.2 mrad.

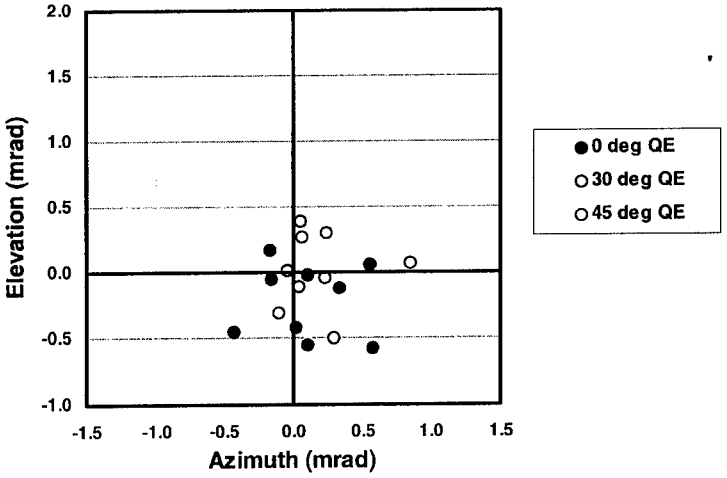


Figure 14. Muzzle Crossing Velocity Jump, All Shots.

CONCLUSIONS

The observed effect of 30° and 45° gun elevation firings was a general reduction of transverse muzzle motion compared to previous flat-fire measurements during the in-bore phase of the event. Specific characteristics of muzzle lateral displacement and pointing angle behavior during the in-bore phase were shared between firings at the three different elevations, but became less pronounced as the elevation increased. In all cases, the muzzle motion parameters were larger and more variable in elevation than azimuth during the in-bore phase. At shot exit, though, little difference between the elevation and azimuth components of the muzzle pointing angle jump and muzzle crossing velocity jump were apparent. The largest difference was a rightward shift in the mean muzzle pointing angle of the elevated firings compared to the flat firings. Differences in the variability of the muzzle pointing angle jump and muzzle crossing velocity jump, if any, were undetectable because of the small number of shots. The shots at 30° QE showed a possible difference in behavior between the two projectile types, with the muzzle pointing angle jump and muzzle crossing velocity jump noticeably higher for the two M107 shots compared to the two M549 shots. Methodology for identifying shot exit using eddy probe tube expansion measurements unexpectedly revealed obturation leakage in seven out of the nine shots. A quantitative consideration of obturator leakage and its effects (if any) on the observed behaviors of individual rounds was not included here but may be addressed in the future.

REFERENCES

1. J. Garner, B. Guidos, K. Soencksen, D. Webb, "Flat Fire Jump Performance of a 155-mm M198 Howitzer," ARL-TR-2067, U.S. Army Research Laboratory, Aberdeen Proving Ground Maryland, Sep 1999.
2. J. Bornstein, I. Celmins, P. Plostins, E. Schmidt, "Techniques for the Measurement of Tank Cannon Jump," BRL-MR-3715, U.S. Army Ballistic Research Laboratory, Aberdeen Proving Ground Maryland, Dec 1988.
3. J. Bornstein, B. Haug, "Gun Dynamics Measurements for Tank Gun Systems," BRL-MR-3688, U.S. Army Ballistic Research Laboratory, Aberdeen Proving Ground Maryland, May 1988.
4. Kogler, T. "The 155-mm Ultralightweight Field Howitzer: Indirect Fire Precision," ARL-MR-265, U.S. Army Research Laboratory, Aberdeen Proving Ground Maryland, July 1995.
5. U.S. Army Firing Table "FT 155-AM-2" Headquarters Department of the Army Washington D.C., Mar 1983.

A FIRE OUT OF BATTERY TANK GUN: THEORY AND SIMULATION

E. Kathe and R. Gast[1]

[1] *U.S. Army Benét Labs TACOM-ARDEC, Watervliet Arsenal, NY 12189*

As part of the Army's Army After Next effort, a radical departure for tank gun recoil was undertaken at TACOM-ARDEC's Benet Laboratories to engineer a soft recoil tank gun. Such a leap in technology may be required to enable a lightweight future combat system to withstand the recoil imparted by a large caliber gun; especially during fire on the move. Although soft recoil is not new to smaller caliber guns and howitzers, implementation for a large caliber tank gun is unprecedented. The theoretical foundations of this recoil management technology will be presented in this paper. Experimental test results of 105mm fire out of battery tank gun demonstrator will be presented in a seperate paper within these proceedings.

INTRODUCTION

The extreme lethality goals of the future combat system (FCS) program require innovative armament solutions to circumvent traditional engineering barriers. Fire Out-Of-Battery (FOOB) recoil constitutes a recoil momentum management technology inspired by the need to meet the requirements of the Army's Objective Force.

One of the clearest operational requirements of any FCS vehicle is the need to be tactically transportable via a C130 class aircraft such as the C130J. Although less clear in engineering specifications, the lethality requirements for FCS vehicles are substantial; in many respects the lethality must be greater than that attained by the M1A2 series main battle tank. Engineering projections for future large caliber gun main armament solutions indicate that launch momentum in the neighborhood of 35,000 N·s (approximately 8,000 $lb_f \cdot s$) may be anticipated. This magnitude is approximately 15% higher than incurred when firing the current state-of-the-art 120mm M829A2 round from the M1A2. A concept image of such a vehicle is depicted in Fig. 1. The image is intentionally vague to avoid skewing the community towards preferred configurations and inadvertently inhibiting novel approaches.

Integration of a main armament system with recoil momentum greater than that developed by the current main battle tank with a future vehicle with a mass less than one third that of the main battle tank will prove an armament engineering challenge that will require unprecedented solutions. (For the case at hand, the FCS exceeds the Ogorkiewicz limit of 900 Ns/tonne [2] by a factor of two.) FOOB recoil (also commonly termed "soft recoil") is one proposed solution path.

HISTORICAL PRECEDENT

The first known application of FOOB recoil is attributable to the French Schneider-Ducrest canon de 65 de Montagne Modele 1906 [3].

Table I presents a listing of modern US Army howitzer FOOB gun efforts as provided by noted ARDEC recoil engineer Steve Floroff [3]. Much of the advancement in US FOOB recoil efforts over the past three decades may be attributed in part to Ken Wynes, of Rock Island Arsenal, IL.

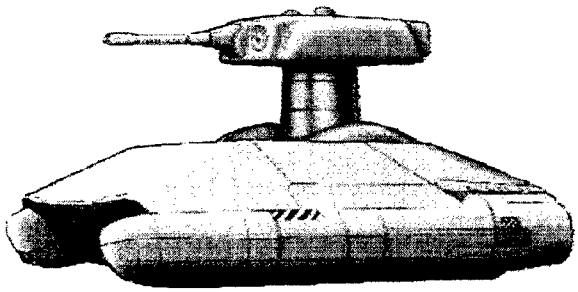


Fig 1. Artists conception of a future combat system vehicle employing a large caliber gun main armament [1].

Table I: Modern US Howitzer FOOB Efforts.

1957	Modified M101	Proof of concept towed howitzer employing FOOB
1965	Test Fixture	Fabrication and test of first ground-up FOOB weapon
1971-1978	M204	Development and type classification of FOOB howitzer [4]. Only six were made.
1975-1976	LCSR	Large caliber soft recoil gun effort. Revealed ignition delay challenges.
1995-1996	VIPER	Moderate use of FOOB to mitigate high zone recoil [5].
1997-1999	ATLAS Test Bed I	Advancement of VIPER for the Advanced Technology Light Artillery System (ATLAS)

ANALYSIS

BASIC EQUATIONS GOVERNING RECOIL

Newton's second law equates the acceleration of an inertial body to the force required to accelerate it (1). Integration of Newton's second law in space for a free body determines the kinetic and imparted energy. Equation (2) results in the familiar result that the kinetic energy of an object may be computed as one half the mass of the object multiplied by the square of its velocity. Imparted energy may be computed as the integral of force over its applied length, as shown in (3), which by the equality of (1) is equivalent to (2). Integration of Newton's second law in time for a free body determines the momentum. Momentum may be computed as the integral of force over time, which is equivalent to the product of an object's mass and its change in velocity (4).

$$\vec{F}(t) = m\vec{a}(t) \tag{1}$$

$$\Delta KE = KE(t_f) - KE(t_f) = \int_{\vec{x}(t_o)}^{\vec{x}(t_f)} m\vec{a}(t)\cdot d\vec{x} = \frac{1}{2}m\left[\vec{v}(t_f)\cdot\vec{v}(t_f) - \vec{v}(t_o)\cdot\vec{v}(t_o)\right] \tag{2}$$

$$\Delta E = E(t_f) - E(t_f) = \int_{\vec{x}(t_o)}^{\vec{x}(t_f)} \vec{F}\cdot d\vec{x} \tag{3}$$

$$\Delta\vec{I} = \vec{I}(t_f) - \vec{I}(t_o) = \int_{t_o}^{t_f} \vec{F}(t)dt = \int_{t_o}^{t_f} m\vec{a}(t)\,dt = m\left[\vec{v}(t_f) - \vec{v}(t_o)\right] = m\,\Delta\vec{v} \tag{4}$$

Where:

- $\vec{a}$ *is the acceleration of the object*
- E *is the imparted energy*
- $\vec{F}$ *is the applied force*
- KE *is the kinetic energy of the object*
- $\vec{I}$ *is the momentum imparted*
- m *is the mass of the object (assumed constant)*
- t *is time*
- t_o *is the time at the commencement of the event*
- t_f *is the time at completion of the event*
- $\vec{v}$ *is the velocity of the object*
- $\vec{x}$ *is the displacement of the object relative to an inertial reference frame*
- $\bar{\bullet}$ *an over-bar denotes a vector quantity*
- Δ *indicates the change between the commencement and completion of the event*

It is worthy of note that displacement, velocity, acceleration, force, and momentum are vector quantities. For typical analysis of a gun it is known that the recoil forces of interest, projectile motion, recoil motion, and momentum all lay parallel to the centerline of the gun barrel. (The effect of bore centerline flexure and misalignment may be considered to have a negligible effect on recoil energy and momentum for the purpose of this discussion.) Therefore, the magnitudes of the vector quantities are often used in computations without reference to their actual form as vectors. This is a valid simplification and will be understood to be the case when the over-bar notation is not used in later equations. Erroneous concepts to dissipate or redirect momentum using forces internal to the system (FCS vehicle) may arise when this is not understood.

In the case of determining the muzzle energy of a launch mass, (3) is used with the ballistic force applied over the traverse of the gun. It is worthy to note that a subtle assumption often made in computing the muzzle energy using (3) is that the launcher recoils so little during the launch, that the difference between the launch length relative to the recoiling gun and that of an earth inertial reference frame is negligible. In fact, the recoiling gun will pull away from the projectile during launch, decreasing the effective launch length by a percentage that may be closely approximated by dividing the sum of the projectile mass and half the propellant mass by the mass that recoils with the cannon, when no significant external forces are applied to the gun. (This will later be derived in (10).)

This motion of the recoiling cannon becomes manifest as its kinetic energy of recoil. The recoil energy is imparted to the gun by the rearward expansion of the propellant gases as the chamber recoils rearward, thus the kinetic energy of recoil is extracted from the internal energy of the propellant gases effecting a modest reduction in their pressure. The resulting degradation in muzzle velocity is discernible; however, from a parametric design perspective it has little affect on ballistic performance for realistic gun systems. (For example, simple NOVA [6] analysis of the M256/M829A2 indicates that doubling the recoiling mass of the gun (from about 1,800 Kg) will increase the muzzle velocity by just less than one quarter of one percent and thus increase the muzzle energy by nearly a half a percent.) Management of this recoil momentum and energy, and its effects on the fighting vehicle, is critical to the success of any future combat system.

Fire out of battery

Fire out of battery is a technique to dramatically reduce the trunnion loads of recoil by pre-accelerating the recoiling cannon mass forward —prior to firing. Taken to its logical extreme, half of the launch momentum may be imparted prior to firing. Using (4) and (2) it may be determined that the recoil system must provide one fourth of the traditional recoil kinetic energy up-front. Upon firing, the momentum imparted to the cannon will reverse its velocity. The first half of the launch momentum will bring the pre-accelerated cannon to rest while the second half will impart rearward momentum of equal magnitude and kinetic energy to that endowed during pre-acceleration. A recoil system that dissipates no energy may thus extract the kinetic energy of recoil from the latter half of a previous firing and store it to pre-accelerate the next firing. A low friction recoil system utilizing highly pre-loaded and soft springs would work exceedingly well in this application.

The advantage of fire out of battery is that the recoil stroke and/or trunnion load may be dramatically reduced. Holding one constant, the other may be reduced by a factor of four. Disadvantages of fire out of battery include misfire and hang-fire handling, and degradation in accuracy.

Some simple relationships

Although it is true that the recoil motion and energy imparted to a cannon during firing will reduce the muzzle velocity somewhat, the effect tends to be very small, less than a percent. Therefore, the launch momentum imparted to a recoiling gun by a given bullet will also tend to remain nearly constant regardless of the recoil motion of the gun. Assuming the recoil momentum imparted by a given round to be independent of recoil motion will allow for a simplified discussion of the governing relationships between the system parameters.

An additional simplification in the present study is to assume that the recoil momentum imparted to the gun results in a discrete change in the recoil velocity of the recoiling cannon. This may be considered a free-recoil assumption while the ballistic forces are applying the momentum to the gun. (If the change in velocity were instantaneous this

would be the Dirac delta function, $\delta(t)$ approximation.) Because of accuracy concerns, current tank gun design philosophy is to approach free-recoil in practice by delaying the application of recoil forces until the bullet has left the gun [7]; or at least until bending waves caused by any asymmetries in the recoil loading cannot reach the muzzle prior to shot-exit [8]. Since the majority of the launch momentum is imparted prior to shot-exit, it may be seen that the free-recoil assumption is approached in practice. This assumption becomes compromised as the energy imparted to or extracted from the recoiling gun during the ballistic event by external loads (such as recoil cylinders) begins to become comparable to the energy imparted or extracted by the ballistic event itself. As the ballistic loads tend to be at least an order of magnitude greater than the recoil cylinder loads, the free-recoil assumption remains quite viable even for gun systems that do not allow for free-recoil. FOOB guns for example do not allow for free-recoil. For the simulation to be presented in Fig 5.b, this has a 2% effect on the change in recoil velocity during firing.

Computing Recoil Velocity and Energy

Using the above two assumptions, the change in recoil velocity (from the commencement of ignition of the round to the completion of blow-down) may be computed using (4) as shown below in (5). For a gun initially at rest (Fire in Battery), this may then be related to the kinetic energy of recoil using (2) as shown in (6).

$$\Delta\vec{v}_r = \bar{I}_L \Big/ m_r \qquad (5)$$

$$\vec{v}_r(t_o) = 0 \Rightarrow \Delta KE_r = \frac{1}{2} m_r \left|\Delta\vec{v}_r\right|^2 = \frac{1}{2} m_r \left|\vec{I}_L \Big/ m_r\right|^2 = \frac{1}{2m_r}\left|\vec{I}_L\right|^2 \qquad (6)$$

Where: I_L *is the launch momentum imparted (often termed the impulse of the round) including any muzzle brake effects*

m_r *is the recoiling mass (gun barrel, breech, etc.)*

$\vec{v}_r$ *is the velocity of the recoiling mass*

ΔKE_r *is the kinetic energy of recoil*

As (6) makes clear, the kinetic energy of recoil is inversely proportional to the recoiling mass, and increases to the square of launch momentum. Thus, efforts to produce lightweight cannons inevitably results in recoil challenges. Similarly, seemingly modest increases in recoil momentum result in substantial increases in the kinetic energy of recoil. (The loss of thermal mass for burst fire is another significant issue for lighter weight barrels.)

The momentum transferred to the recoiling cannon during the launch of a projectile is subsequently imparted to the platform to which the gun is mounted. Recoil systems allow the recoiling cannon to move within the gun mount, and apply braking loads to bring it to rest over a longer period of time than the ballistic event. Typically, the time for the cannon to be brought to rest is an order of magnitude longer than the in-bore time of the bullet. Thus, the recoil loads may be much lower than the ballistic loads while still satisfying the conservation of momentum.

Of principle concern to the armament engineer is the recoil stroke length that must be dedicated to allow the cannon to be brought to rest using reasonable recoil forces. This trade-off between the magnitude of recoil forces and the extent of recoil stroke is determined by the magnitude of the kinetic energy that must be extracted by the applied recoil load. The extracted energy (3) must be equal to the kinetic energy of recoil (2) and (6) by the equality of Newton's second law (1). Using current variable orifice hydraulic brake technology, the recoil system for a given gun may be tailored to provide a nearly flat force versus stroke profile –for the highest momentum (worst case) round fired. (For modern tank guns, the force is intentionally kept low for a very brief time for accuracy considerations as mentioned earlier.) For rounds of lesser momentum, the maximum loads are always lower than for the worst case, however they tend to fall off in force as the gun traverses its recoil stroke. Therefore, a simplifying assumption that may be approached in design practice is to assume free recoil of the gun until shot exit followed by a

step function recoil force until the recoiling gun is brought to rest –for the highest impulse round to be fired. The accuracy of this assumption is not high, but is perhaps a good estimate to within ten to twenty percent. Under this assumption the integration of (3) degrades to integration over a rectangular region. Thus, the product of the recoil force and the stroke over which this force is applied must be equal to the kinetic energy of recoil.

Computing In-Bore Free Recoil Stroke

The free recoil stroke of the gun up to shot exit may be computed by noting that the center of mass of a system cannot change due to the action of internal forces alone. Thus, the motion of the recoiling barrel may be related to the motion of the mass of the projectile and the propellant gases up to shot exit using an inertial reference frame in which the initial recoil velocity immediately prior to ignition is zero. (For a stationary FIB gun, an earth inertial reference frame would suffice.) These motions may be tracked using a selection of variables as depicted in Fig 2.

$$\bar{x}_r(t)m_r + \bar{x}_c(t)m_c + \bar{x}_p(t)m_p = 0 \quad \forall t : t_i \le t \le t_e \tag{7}$$

$$\bar{x}_r(t_e) = -\bar{x}_c(t_e)m_c/m_r - \bar{x}_p(t_e)m_p/m_r \tag{8}$$

$$\bar{L} = \bar{x}_p(t_e) - \bar{x}_r(t_e) \tag{9}$$

Where: $\bar{x}_r(t_i) = \bar{x}_c(t_i) = \bar{x}_p(t_i) = 0$ *by suitable definition as shown in Fig. 3*

$\bar{L}$ *is the launch stroke of the gun barrel*

m_c *is the propellant (charge) mass*

m_p *is the projectile mass*

t_e *is the time at shot exit*

t_i *is the time at commencement of ignition*

$\bar{x}_c$ *is the position of the center of the propellant (charge) mass*

$\bar{x}_p$ *is the position of the base of the projectile*

$\bar{x}_r$ *is the recoil position of the cannon*

Perspective on the in-bore free recoil stroke may be gained by recognizing that the free recoil displacement of realistic guns is very small relative to the launch stroke. Further, the center of mass of the propellant tends to follow the projectile with about one half the displacement. Thus, at shot-exit the propellant mass has moved about half of the launch stroke. (This approximation neglects the length of the chamber, chambrage ratio, and any density gradient in the propellant gas column.) Thus the free-recoil stroke may be estimated using the above assumptions and (8) as:

$$\bar{x}_r(t_e) \approx -\frac{L}{m_r}\left(m_p + m_c/2\right) \tag{10}$$

For the 105mm M35/M900 the charge mass, projectile mass, launch length, and recoiling mass are approximately 6Kg, 6Kg, 4¾m, and 1,090Kg respectively. Using (10), a distance of -39mm (-1½ inch) is estimated.

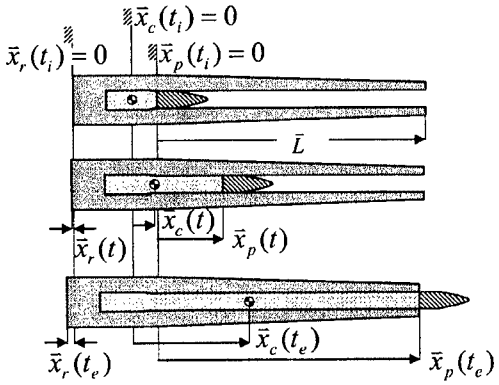


Fig. 2. Depiction of a gun, projectile, and propellant system with center of mass of propellant indicated.

Although blow-down will continue to impart momentum to the gun after shot-exit, and muzzle brake activity occurs in its entirety after shot-exit, it is a

reasonable approximation to endow the recoiling gun with the blow-down momentum as a Dirac delta function at shot exit. (Thus, the time at shot exit will be considered the completion of the event in (6).) Using this assumption:

$$\bar{v}_r(t_i) = 0 \Rightarrow \bar{v}_r(t_e) = \bar{I}_L / m_r \tag{11}$$

$$\bar{v}_r(t_i) = 0 \Rightarrow KE_r(t_e) = \frac{1}{2} m_r \left|\Delta \bar{v}_r(t_e)\right|^2 = \frac{1}{2m_r}\left|\bar{I}_L\right|^2 \tag{12}$$

Computing Recoil Force

Using a flat force profile idealized recoil system to bring the gun to rest (the completion of the recoil event) will require setting the product of the additional recoil stroke by the recoil force to be equal the magnitude of the kinetic energy of recoil at shot exit.

$$\left|\left(\bar{x}_r(t_o) - \bar{x}_r(t_e)\right) \cdot \bar{F}_r\right| = KE_r(t_e) = \frac{1}{2\,m_r}\left|\bar{I}_L\right|^2 \tag{13}$$

If the Dirac delta function approximation to the entire launch momentum is employed and no provision is included for free recoil, the ignition commencement and shot exit times become coincident and the net recoil stroke estimate under these approximations becomes:

$$\left|\Delta \bar{x}_r \cdot \bar{F}_r\right| = \frac{1}{2\,m_r}\left|\bar{I}_L\right|^2 \tag{14}$$

Since FOOB guns inherently do not provide for free-recoil (14) should be used when comparing FOOB to FIB recoil. To do otherwise would lend an unfair advantage to FOOB.

It is worthy to note that since the recoil stroke is negative (backwards recoil) and the force is forwards (decelerating the reward recoiling gun) the recoil cylinders may be considered to extract the kinetic energy of recoil from the gun. Traditionally, this energy is ultimately dissipated as heat from the recoil cylinders.

Computing FOOB Recoil Force

In the case of fire out of battery, half of the momentum may be imparted prior to firing. This is achieved by accelerating the gun forward from the rearward extent of recoil to half the free recoil speed computed in (11). Upon firing, the first half of the launch momentum brings the pre-accelerated cannon to rest while the second half endows it with the second half of the launch momentum, reversing the velocity of the pre-accelerated cannon to half the free recoil velocity (11). This all takes place very quickly during the interior ballistics, and thus may be approximated as a Dirac delta function; accept for the forward intrusion of the cannon during firing.

Using FOOB, the same recoil stroke is traversed twice, once forward and once rearward. Considering either stroke independently of the other:

$$\left|\Delta \bar{x}_r \cdot \bar{F}_r\right| = \frac{1}{2\,m_r}\left|\frac{\bar{I}_L}{2}\right|^2 = \left(\frac{1}{4}\right)\frac{1}{2\,m_r}\left|\bar{I}_L\right|^2 \tag{15}$$

Equation (15) makes it clear that FOOB may theoretically reduce the product of recoil stroke and recoil force by a factor of four relative to (14). If less than half the momentum is imparted to the cannon prior to firing, the recoil velocity and kinetic energy will be higher after firing. Conversely, if more than half the momentum is imparted prior

to firing, the recoil velocity and kinetic energy will be higher prior to firing. Thus, it may be seen that it is ideal to impart half the momentum prior to firing.

IMPLEMENTATION CHALLENGES OF FOOB

There are five basic issues with FOOB: ignition variability, misfire, hang-fire, accuracy, and mechanism complication. The first three issues may be considered the major obstacles to weaponization of a FOOB tank gun and will be elaborated upon. The fourth issue, accuracy, is a concern resulting from the obvious potential for the gun barrel and mount to undergo undesirable flexure immediately prior to firing. This will degrade accuracy. Efforts to improve the stabilization of guns may find application to FOOB to mitigate this undesirable effect. It is also worthy to note that guided ammunition may reduce the reliance upon gun accuracy. The fifth issue is intended to encompass the challenges of loading a gun out of battery, integrating an ignition system that must endure recoil acceleration prior to firing, etc.

Ignition variability

The variation time between when the "trigger is pulled" and the bullet starts to move down the bore is of concern to FOOB recoil. The reason is that when the gun is pre-accelerated forward prior to firing, it reaches its maximum design speed just prior to firing. Thus the cannon may traverse substantial recoil stroke and the kinetic energy will be affected. Application of engineering to address this variability requires that the cannon have extra recoil energy after firing to ensure that it will return to the catch latch. This in turn imposes an impact energy burden on the catch latch while compromising the reduction in peak recoil force. Fortunately, it is anticipated that Electrothermal-chemical (ETC) ignition of tank gun ammunition will dramatically reduce this variability to a small fraction of a millisecond. (Experimental results have indicated less than 50μs variation [9].) Simulation to be presented in Fig 5 will show the cannon to be moving at 7mm/ms and it may be appreciated that a fraction of a millimeter is inconsequential.

Misfire

Misfire occurs when a round does not fire when anticipated. For well-maintained tank cannon this is a rare occurrence, perhaps one in 5,000 rounds. Nevertheless, its potential to occur is substantial enough to warrant engineering consideration. For a FOOB gun, this presents the problem that the cannon has been endowed with considerable momentum during its pre-acceleration forward. If the round does not fire, the cannon must be brought to rest in a controlled fashion using a misfire snubber. The role of the misfire snubber is analogous to a traditional recoil system operating backwards. It must dissipate the kinetic energy of the pre-accelerated cannon, using reasonable forces. Therefore, it must be provided some recoil stroke to enable it to bring the cannon to rest.

Using a very conservative approach, it may be argued that the greatest permissible snubber forces that could be tolerated would have the same magnitude as the greatest permissible recoil forces. Since the cannon would be pre-accelerated using the greatest permissible recoil forces over the intended recoil stroke, it may be seen that extraction of the kinetic energy imparted will require an equal snubber stroke to bring the cannon back to rest. Using this argument, the intended FOOB recoil stroke could only be half of the recoil stroke that would be employed by a FIB gun. The factor of four reduction in recoil force that would be predicted by (15) relative to (14) would therefore be reduced to a factor of two. This still constitutes an impressive achievement in terms of recoil force reduction.

It may be argued that a greater force magnitude may be tolerated of a misfire snubber. Historical limits to recoil force magnitudes may be altered by the reversed application of the load. For example, the gunner's brow-pad will pull away from his forehead during misfire snubbing. Also, destabilization of the vehicle during recoil (e.g., a tendency to flip it over) would actually be righted by the snubber force. For lack of an appreciation for the recoil tolerance limits of potential future combat system vehicles, it will be postulated that misfire snubber loads may employ forces of twice the magnitude of the intended maximum recoil forces. This will allow the misfire snubber to bring the cannon to rest in half the stroke that it took to pre-accelerate it. This will reduce by one third (not half) the recoil stroke available to a FOOB gun (15) relative to a FIB gun (14). Thus, practical recoil force reductions may be estimated to be a factor of three.

Hang-Fire

Hang-fire is a late firing round. Thus, for a hang-fire to occur, it must be immediately preceded by a misfire. As misfires are rare, hang-fires are even more rare. If a hang-fire occurs after the misfire snubber has returned the cannon to rest, it may be seen that it will endow the cannon with the full kinetic energy of (14). Even if an exotic recoil actuation technology (such as magneto-rheological dampers) could be employed to apply a perfect flat force recoil curve to bring the hang-fired cannon to rest, there would be insufficient recoil stroke available to do so without grossly violating the maximum allowed recoil force. For realistic recoil system, the situation is made worse by the challenges that prevent full recoil forces from being applied. There is no known reasonable solution to accommodate hang-fire without catastrophic failure of the gun and the subsequent potential for harm to the remainder of the combat system.

In the absence of a means to accommodate hang-fire, the focus of engineering effort has shifted to a means to eliminate the potential for hang-fire. (A common rule of thumb for acceptable rates for catastrophic failure is one in a million.) ETC ignition of tank gun ammunition has been identified as a potential means to achieve this objective. ETC uses very high-powered electrical ignition to initiate the charge. The electrical flow path may be reliably short-circuited by the mechanics of a misfire. Further, the propellant to be used by ETC is intended to be a low vulnerability propellant. This means that the propellant will be hard to ignite in the absence of the plasma generated by the ETC process. Thus, the potential for prior hang-fire mechanisms such as a burning ember is reduced.

Although there has been no known occurrence of a hang-fire during any the ETC testing to date, this does not ensure that the chances are in the one in a million range. Therefore, a dedicated effort to examine the potential for ETC to eliminate hang-fire is warranted before embarking on a development program that relies upon its performance to enable FOOB recoil.

NUMERICAL SIMULATION OF GUN RECOIL

Clarification of the basic principles of FOOB recoil management is best made by demonstration. The following figures are based upon an M35 105mm tank gun designed to implement FOOB juxtaposed by FIB recoil. The FOOB recoil be essentially be provided for by incorporation three elements:

1) A catch and release latch at a "home" out of battery position.

2) Specialized recuperators designed to provide a softer spring rate with a high pre-load.

3) Variable orifice hydraulic brakes designed to minimize dissipative friction during the intended recoil stroke while providing high braking forces in front of the intended firing position (a misfire snubber) and braking behind the latch (a hang-fire snubber).

Because this test fixture is designed as a retrofit to an existing system using 40 year old ammunition technology, it is considered essential to provide for hang-fire handling. However, because the test gun is only intended to be fired from a hardstand, snubbing forces could be applied that would be unacceptable in a fighting vehicle.

The simulations were conducted using recoil design codes validated for fire in battery recoil on the M35 and XM291 gun programs. The firing impulse with a perforated muzzle brake is 16,780 Ns (3,772 lbf*s) applied to a recoiling mass of 1090Kg (2,400 lbm).

Using fire in battery recoil, the ballistic load is first applied. Subsequently, the motion imparted to the recoiling cannon within the gun mount engages the braking action of the recoil cylinders as shown in Fig 3. (Note, the blow down momentum imparted after shot exit is not shown. This simulation assumes a muzzle brake that essentially eliminates any further momentum after shot exit.)

A peak recoil force of 271 kN is applied despite the peak ballistic force of 4,555 kN. This constitutes a factor of 17 reduction provided by the recoil system. Because of the nearly flat recoil force, the duration of the recoil forces do not follow suite and are only a factor 10 longer than the ballistic event.

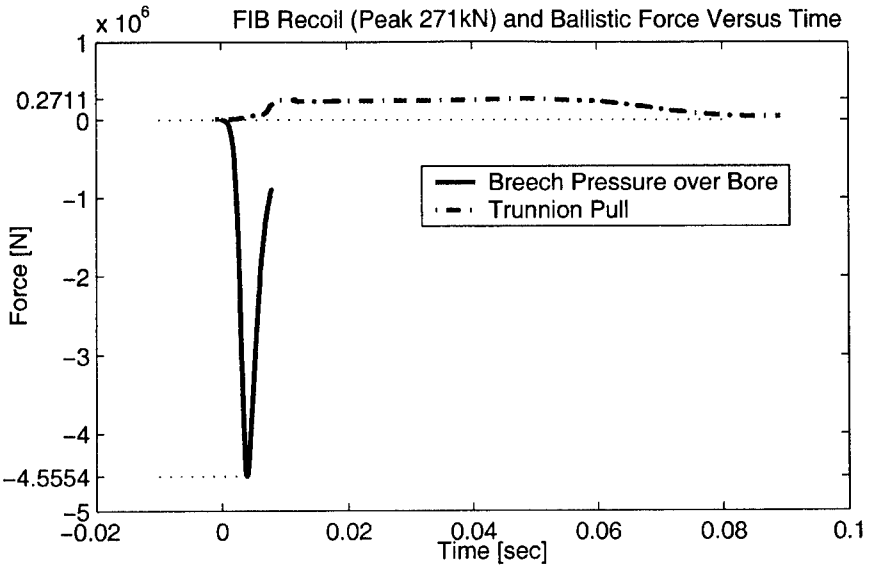


Fig 3. Fire in battery (FIB) ballistic and recoil loads versus time.

For fire out of battery (FOOB) recoil, the recoil forces are applied prior to the firing event in anticipation of the ballistic momentum. This may be seen in Fig 4. This enables the peak recoil load to be reduced to 120kN or 44% of the fire in battery recoil load. We believe this is representative of what may be accomplished in a weapon system that employs ETC ammunition that will not hang-fire and whose variability in ignition timing is a small fraction of a millisecond.

Additional insight may be achieved by comparing the temporal response (momentum) and spatial (energy and phase plane) response of FIB and FOOB system. This is done in the plots of Fig 5.

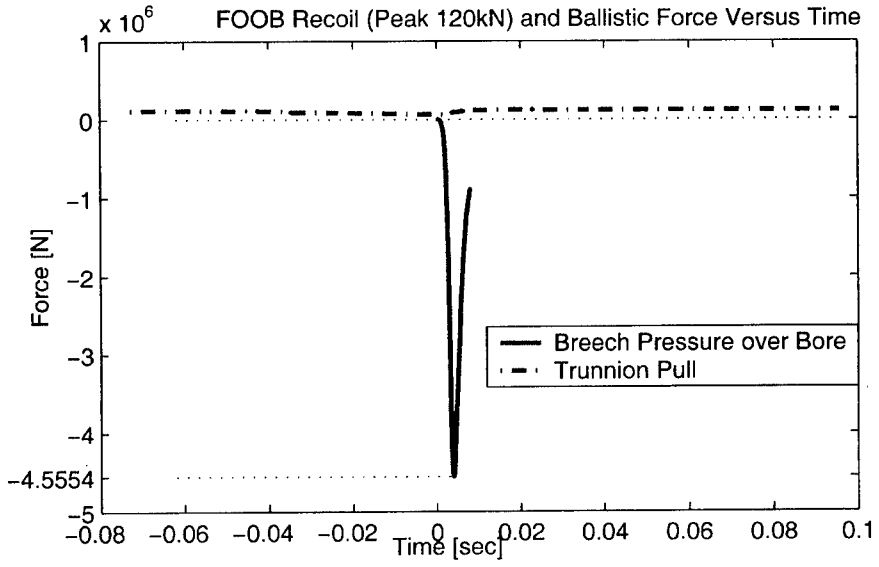


Fig. 4 Fire Out of battery (FOOB) ballistic and recoil loads versus time.

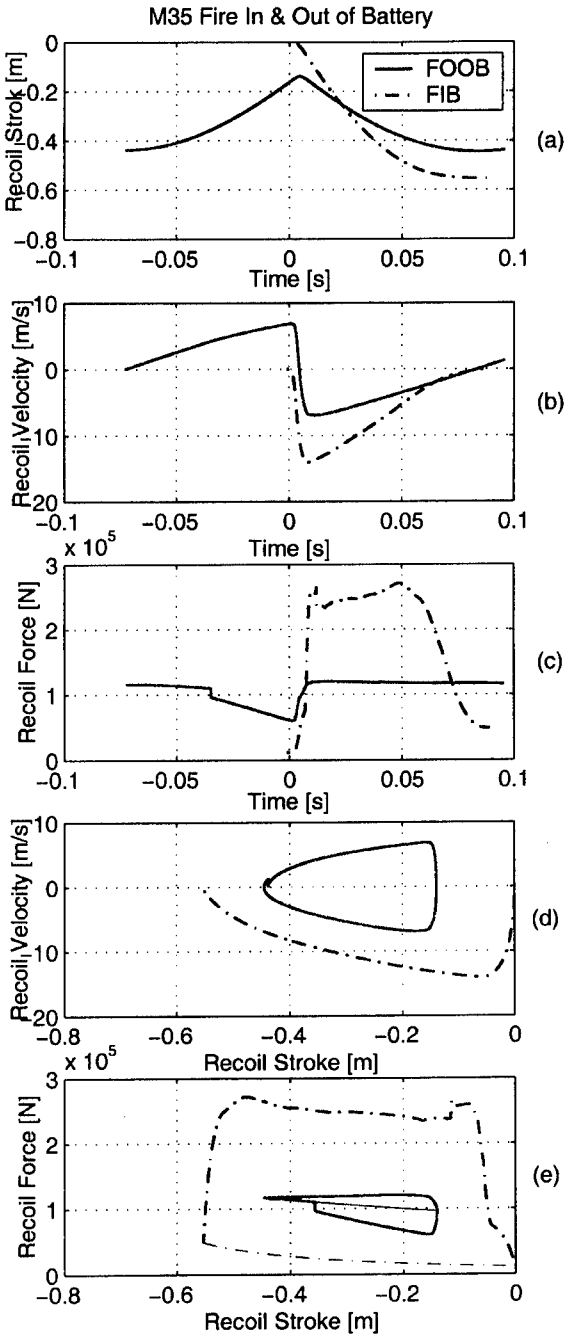


Fig 5. Recoil dynamics.

Fig 5.a shows the FIB system beginning its recoil stroke from the zero –in battery—position and then recoils out to 0.554m (21.8"). The duration of the FIB recoil event is 89 ms. FOOB begins from its latch position at 0.438m (17¼"), then recoils within 0.139m (5½") of battery before its forward motion is reversed by the ballistic force and then surpasses the latch position by 7.6mm (0.3") at 0.446m from battery before its rearward motion is brought to rest. (The recuperators would then accelerate it forward into the latch.) The duration is 167ms.

Fib 5.b shows FIB starting with zero velocity and then quickly being accelerated rearward by the ballistic force to a speed of 14.0 m/s. The recoil system then brings this rearward motion to rest. The FOOB system begins at rest, and is accelerated forward about 73ms prior to firing to reach a peak forward velocity of 6.835 m/s. It is subsequently reversed to a rearward velocity of 6.908m/s by the ballistic forces and is then brought to rest by the recoil system.

Two things are of note here. First, the FOOB cannon is going a bit slow at firing. This is to ensure that the rearward velocity imparted is sufficient to send the cannon beyond the latch position after firing. Second, the change in velocity of the cannon is 13.7m/s. This is 2% lower than for the FIB system. The cause of this is that the FOOB system imparts momentum to the cannon during the ballistic cycle whereas the FIB system does not. Fig 5.c clarifies this.

Fig 5.c reveals the force trajectory with respect to time, the integral of which corresponds to the momentum. For the FIB system, as discussed earlier, the main recoil forces are delayed until the bullet has left the gun for the purposes of accuracy. The variable orifice hydraulic brakes subsequently do an excellent job of maintaining near constant recoil load until the cannon is nearly brought to rest.

Fig 5.c reveals that the FOOB recoil forces diminish prior to firing and then grow. The cause of this is the *undesirable* existence of friction in the system. During the pre-acceleration, friction robs energy from the recuperators that are driving the cannon forward. After reversal of the velocity by the ballistic momentum, the friction and

recuperators conspire to achieve a higher force application than the recuperators alone. (The apparent step change in FOOB recoil force 35 ms prior to firing is the result of the simulated sudden engagement of hydraulic fluids within the brake cylinders.)

Fig 5.d is a phase plane representation for the dynamics of FIB and FOOB recoil. This is an interesting perspective for those familiar with state-space and servo control systems.

Fig 5.e constitutes the energy domain. The total recoil force for both types of recoil is plotted using a thick line. The recuperator forces are included as a thin line. The area under the total FIB recoil force curve constitutes the kinetic energy of recoil extracted by the recoil cylinders (129kJ). The recuperator force extends from a slight preload of 11kN in battery to a maximum load of 49kN at 0.554m out of battery. The area under this wedge constitutes the energy stored in the potential (spring) energy of the recuperators to return the gun to battery for firing the next round. The area between the total force and recuperator force is dissipated as heat by the brakes. The recoil brakes also dissipate the potential energy of the recuperator during the return to battery (not shown).

The total FOOB recoil force traverses its recoil stroke twice, creating a closed hysteretic loop. The FOOB system first begins at its latch position and then moves forward. The aforementioned friction reduces the force, causing the force travel trajectory to have a pronounced negative slope with a magnitude lower than that of the recuperator alone. Upon firing, the friction and recuperator forces conspire to maintain a nearly constant force until the cannon is again brought to rest just past its latch position. The area within the loop constitutes the frictional energy lost during recoil. Examination of the recuperator force line clarifies how a highly preloaded soft spring may approach a flat travel force profile. However, as this is approached, the peak recoil force just after firing would increase due to friction.

The total recoil energy for this system computed using (12) is 129 kJ. FIB recoil force applied over the 0.554m stroke of Fig 5.a is computed as 251 kN using (13) and the free recoil stroke of 39mm computed in (10); it is 233 kN using (14). The simulated value of 271 kN of Figs 3, 5.c, and 5.e is 8% and 16% higher than ideal theory respectively. The FOOB recoil force is computed as 105 kN using (15) over the stroke traversed between –0.438m and –0.139m of Fig 5.a. The simulated value of 120kN of Figs 4, 5.c, and 5.e is 14% higher than the ideal theory.

FOOB RECOIL: A SERVO CONTROL SYSTEM

It is clear from our analysis that modest changes in recoil forces, launch momentum, even gun elevation will have a direct effect on how far the gun must be engineered to overshoot the catch latch to ensure reaching it under a worst case scenario. This overshoot consumes valuable design recoil stroke and imparts greater energy upon the latch during engagement and thus requires a more robust or complicated latch. Therefore methods to control FOOB recoil as a servo control system in analogy to the fire control stabilization of tank guns could be advantageous. In particular, open-loop alteration of the firing time, based upon anticipated momentum, firing angle, and frictional state of the gun may prove effective at rejecting predictable disturbance loads.

Feedback control would prove essential if unpredictable disturbance loads were compromising performance. Until test fixtures mature, and experience is gained, it is very challenging to anticipate the magnitudes of these disturbances and assess their effect. The simplest feedback system could be applied during the pre-acceleration phase and could fine-tune the firing time based on the actual run-up trajectories, but clearly it could not compensate for disturbances incurred after the ignition delay window just prior to firing.

Feedback control of recoil could be achieved through the application of a control actuator run in parallel with the recoil cylinders. (The requirements of such an actuator would bear some similarity to those of an electromagnetic suspension actuator [10].) Force magnitudes perhaps a few percent of the total forces depicted in Fig 5 could achieve substantial disturbance rejection. The ability of these actuators to apply loads with or against velocity could enable them to do more than just disturbance rejection; they could increase performance by encroaching on the optimal flat recoil force profile with zero hysteresis to the degree their force and power can contribute.

The use of low levels of controlled friction (as provided by magneto-rheological fluidic dampers) could also prove of utility, although they inherently reduce performance.

DISCUSSION AND CONCLUSIONS

Fire out of battery recoil may dramatically reduce the recoil forces and/or recoil stroke required relative to traditional fire in battery systems. Reduction of peak recoil forces attenuates the shock environment imposed upon the weapon platform (e.g., the gunner's brow pad) and reduces structural requirements for the mount and turret (e.g. enables reduced weight). It may also find application to mitigate the recoil challenges imposed by lightweight cannon structures (e.g. composites) that are intended to reduce armament weight but increase recoil energy.

This conclusion hinges on the requirements that ammunition for weapon systems that employ FOOB to prove extremely unlikely to hang-fire (fire late). The ammunition should also exhibit very limited variation in the shot start delay, to within a fraction of a millisecond. Electrothermal-chemical propulsion has exhibited ignition properties that may enable such ammunition and thus enable fire out of battery recoil.

Friction during the intended operation stroke of a FOOB recoil system detracts from its overall performance. Its propensity to oppose motion dissipates energy and results in increased maximum recoil forces. This is most pronounced during the rearward recoil stroke of FOOB recoil, immediately following velocity reversal.

It is important to note that fire out of battery does not reduce the recoil momentum imparted to the weapon platform. Therefore issues of vehicle stability during firing are not substantially improved by employing this recoil management technique. A typical vehicle has its first mode upon it suspension near to 1Hz. FIB momentum applied over 89ms essentially has a Dirac delta function "impulse" effect on the vehicle response. FOOB's increased duration to 167ms is also largely impulsive to the vehicle –although some limited enhancement may be anticipated. It is interesting to speculate that an active suspension that increases the vehicles response bandwidth could leverage the increased recoil duration enabled by FOOB to better stabilize the vehicle *during* and after recoil.

ACKNOWLEDGMENTS

The authors would like to acknowledge the contributions to advanced recoil by Larry Burton, the Army Research Laboratory; Steve Floroff of Picatinny Arsenal; and Ken Wynes who recently retired from Rock Island Arsenal.

REFERENCES

1. Kern, LTG Paul J., "Future Combat Systems," The Defense Advanced Research Projects Agency (DARPA) 21st Systems and Technology Symposium, Dallas, TX, 6-8 September 2000.
2. Ogorkiewicz, R. M., *Technology of Tanks: Volumes I and II*, Jane's Information Group, Surrey, UK, 1991.
3. Floroff, S., Private communication, 18 April 2001.
4. Nerdahl, M. C. and Frantz, J. W., "Mathematical Models for Engineering Analysis and Design of Howitzer," Rock Island Arsenal Technical Report R-RRA-S-3-28-73, May 1973.
5. Burton, L., Hoppel, C., and Kaste, R., "Design Tradeoffs for a Very Lightweight 155-mm Howtizer for the U.S. Army Light Forces, Proceedings of the 8th U.S. Army Symposium on Gun Dynamics, Pflegle, G. ed., ARCCB-SP-96032, Benet Laboratories, Watervliet Arsenal, NY, 14-16 May 1996, pp. 15.1-25.
6. Gough, P., "The XNOVAKTC Code," U.S. Army BRL-CR-627, Paul Gough Ass., Portsmouth, NH, 1990.
7. Gast, R., "Modal Analysis of the Dynamic Flexure in Tank Weapons by the Uniform Segment Method," Ph.D. Thesis, Rensselaer Polytechnic Institute, Troy, NY, May 1988.
8. Heron, B. G., "Required Free Travel of 105mm LR Gun," Engineering Study, FMC Ordnance, San Jose, CA, 22 December 1982.
9. Eldredge, N., Private Communication, 6 April 2000.
10. Beno, J. H.; Bresie, D. A., Guenin, A. M., and Weeks, D.A., "The Design of an Electromagnetic Linear Actuator for an Active Suspension," Publication 1999-01-0730, SAE International Congress and Exposition, Detroit, MI, March 1-4, 1999.

ROBUST CONTROL DESIGN FOR THE ELEVATION AXIS STABILIZATION OF THE M256E1 LONG GUN

V. R. Marcopoli, M. S. Ng, and C. R. Wells

General Dynamics Land Systems, 38500 Mound Road, Sterling Heights, MI 48312

A key feature of the Abrams tank is the ability to deliver precision fire during on-the-move vehicle operation. The increased flexibility of a longer gun tube presents a significant additional challenge to stabilization system design. To address the increased difficulties of this problem, an approach to gun stabilization is presented that uses modern robust control techniques to achieve muzzle-pointing accuracy. Such control design methods are model-based, and thus require an accurate mathematical description of the system dynamics. Following a brief description of the model used, the control objectives of performance and robustness are cast in a general framework that precisely quantifies these design goals as optimization objectives. The method of μ-synthesis is then applied, yielding a controller that realizes the objectives. The effectiveness of this control design is illustrated via its implementation in the M256E1 Long Gun demonstration vehicle. Test results of the new controller are compared with a "classically" tuned controller.

1 INTRODUCTION

In order to address future needs for improving the lethality of the M1A2 main battle tank, the army has funded a demonstration program to integrate a longer gun tube. The long tube is based on the German L55 tube, made by Rheinmetall, and is 4.3 feet (1.3 m) longer than the conventional M256 120 mm gun tube. Unfortunately, with the increased length comes increased flexibility, which, if not addressed properly, can introduce significant accuracy degradation when firing on the move.

It is the job of the stabilization system to maintain proper aiming of the gun when the vehicle is moving. In order to address the increased demands made on the stabilization system due to the longer gun tube, a new approach to stabilization design has been investigated. The method is from the area of robust control, called μ-synthesis, and requires an accurate model of the system dynamics. The goal is to use the system dynamics to derive a *design* model that allows control design objectives to be quantified via its inputs and outputs. Once this is accomplished, the μ-synthesis optimization framework can be directly applied to obtain a controller that achieves the design goals. In order to mitigate risk and facilitate evaluation of the new method, a classical stabilization scheme has also been developed. The two approaches are compared in Section 5.3.

The primary goal of this paper is to introduce the general design concepts and summarize how they are applied to the gun stabilization problem. Due to space limitations and program sensitivity, information regarding the modeling details, as well as specific quantitative system properties and performance numbers have been omitted.

2 ELEVATION DYNAMICS

The elevation model framework is shown schematically in Figure 1.

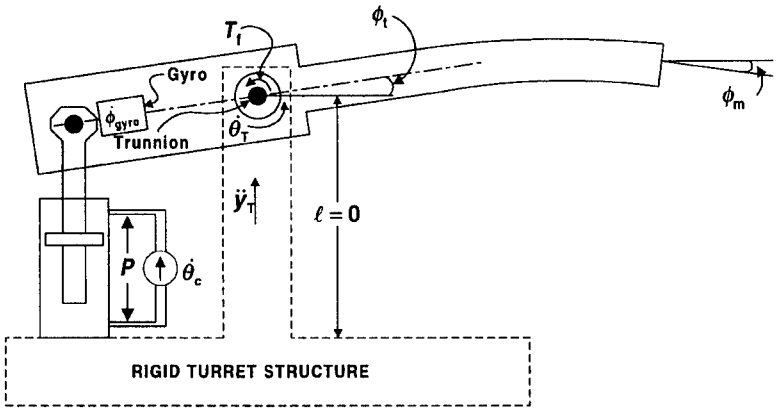


FIGURE 1: ELEVATION SYSTEM MODELING SCENARIO

The "input" quantities are:

T_f = Trunnion friction torque (in-lb)

$\dot{\theta}_T$ = Rotational turret motion (rad/sec)

$\ddot{y}_T$ = Translational turret motion (in/sec^2)

$\dot{\theta}_c$ = Gun rate command (rad/sec)

and the "output" quantities are:

ϕ_m = Muzzle angle (rad)

ϕ_t = Trunnion angle (rad)

$\dot{\phi}_{gyro}$ = Gyro angular rate (rad/sec)

P = Hydraulic pressure (psi)

The gun tube model assumes small angles and point masses. Flexibility is introduced by constraining the motion of the point masses via three bending modes, which are obtained from mass and stiffness distributions, using "pin" constraints at the trunnion and actuator connection points. This yields an 8th order gun tube model. The hydraulic actuator is driven by a flow command, which is equivalent to the gun angular rate command, $\dot{\theta}_c$, that opens a valve to port oil from one side of the piston to the other. Hydraulic leakage and first order oil compressibility dynamics are also accounted for in the actuator model. A pressure difference across the piston is thus generated, resulting in a force applied to accelerate the gun. To account for the unbalance of the longer tube, the elevation mechanism is equilibrated. This is modeled as a simple pressure source that sums with the actuator output to provide the total actuator force on gun. Nonlinear effects considered in the model are trunnion friction and hydraulic loading. This modeling

scenario is described more precisely via the block diagram shown in Figure 2. Detailed development of this model is given in [1]

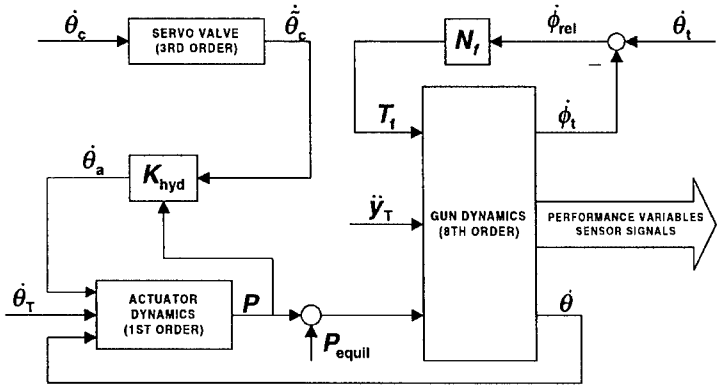
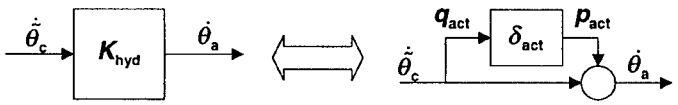


FIGURE 2: BLOCK DIAGRAM MODEL OF ELEVATION SYSTEM

The time varying gain, K_{hyd}, is defined via

$$K_{hyd} = \begin{cases} \sqrt{1-\min\{1,|P/P_S|\}}, & \dot{\theta}_{cmd} P \geq 0 \\ \sqrt{1+|P/P_S|}, & \dot{\theta}_{cmd} P < 0 \end{cases}$$

and models hydraulic loading effects (P_S is the supply pressure). For reasons that are described in Section 3.3, it is convenient to rewrite the hydraulic nonlinearity as an actuator perturbation. The equivalence is shown in Figure 3, where $\delta_{act} = K_{hyd} - 1$, and the perturbation input and output are defined as q_{act} and p_{act}, respectively.



(A) (B)

FIGURE 3: (A) HYDRAULIC NONLINEARITY (B) EQUIVALENT PERTURBATION FORM

The nonlinearity N_f is a simple trunnion bearing coulomb-type friction model, defined as

$$N_f = T_{f,max} \frac{2}{\pi} \tan^{-1} S\dot{\phi}_{rel}$$

where $T_{f,max}$ is the friction magnitude, and S is a "shaping" parameter for adjusting the sharpness of the transition of the friction nonlinearity about zero relative velocity. Combining Figure 2 and Figure 3, the gun system interconnection is redrawn in simpler form in Figure 4, providing a concise input-output view of the plant.

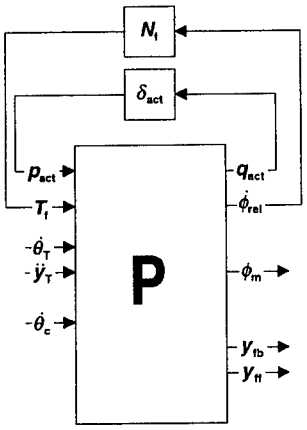


FIGURE 4: ALTERNATIVE BLOCK DIAGRAM VIEW OF ELEVATION SYSTEM (OPEN LOOP)

The vector variables y_{fb} and y_{ff} are introduced to represent the feedback and feedforward sensor signals, respectively, which are sent to the controller. The feedback vector is defined as:

$$y_{fb} = \begin{bmatrix} H_{rslvr}\phi_t \\ H_{gyro}\dot{\phi}_{gyro} \\ H_{AA}P \end{bmatrix} \tag{1}$$

where the variables $H_{()}$ denote relevant filtering dynamics applied to the respective physical quantities. In the case of the trunnion and gyro feedback signals, the sensor dynamic is used, whereas for the pressure feedback, the software anti-alias filter is used because this dynamic dominates the sensor dynamic. The feedforward vector for the long gun system is:

$$y_{ff} = \begin{bmatrix} H_{gyro}\dot{\theta}_T \\ H_{AA}\ddot{y}_T \end{bmatrix} \tag{2}$$

The use of an accelerometer feedforward sensor has been shown to be advantageous when stabilizing out-of-balance armaments [2].

It is important to note that the nominal gun plant, P, is a *linear* system. The nonlinearities are shown explicitly, and enter the system as perturbations. This input-output view of the gun system shown in Figure 4 is a very convenient means of depicting this system, since it puts primary focus on the fundamental linear system behavior while maintaining nonlinear fidelity. More importantly, this framework facilitates the use of modern robust control methodologies, where a linear controller is designed to meet objectives that include nonlinear effects. This is the subject of the next section.

3 ROBUST CONTROL FRAMEWORK

The formulation of a control design problem using tools from robust control theory requires the system to be put into a standard framework. To this end, consider Figure 5, which

depicts the nominal linear plant system, P (from Figure 4), connected to the controller, K, and perturbations δ_{act} and Δ_{fb}.

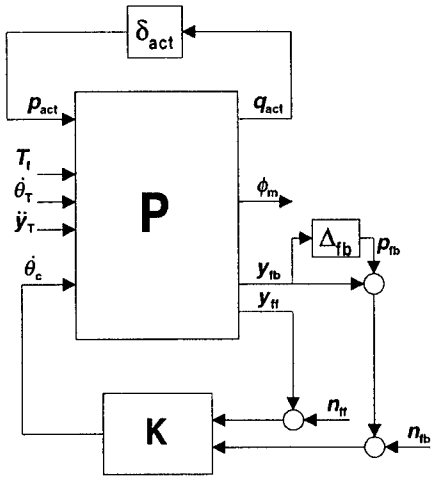


FIGURE 5: CLOSED LOOP SYSTEM

Note the trunnion friction, T_f, is now viewed as an external disturbance, along with the terrain inputs, $\dot{\theta}_T$ and $\ddot{y}_T$. The nonlinear feedback that generates T_f (see Figure 4) is thus neglected. This simplification has proven to be a reasonable assumption, since the trunnion friction is typically small and its effect is primarily in increased errors, and not in any more complicated nonlinear phenomenon such as limit cycling or instability. Finally, the feedback connection is augmented with measurement noise input vectors, n_{fb} and n_{ff}, and a diagonal matrix perturbation, Δ_{fb}. These modifications are necessary when using optimization-based techniques for control design, so the resulting controller is not overly sensitive to measurement noise, and robust to nonlinearities and modeling errors; details are given in the remaining development.

The first step in formulating a robust control design is to group the signals of Figure 5 into three sets of vector input/output signals: 1) Controller variables, u and y, 2) Performance variables, z and w, and 3) Robustness variables, p and q. These standard signals can be defined for any control problem; the task of the design engineer is to choose them wisely so that a meaningful controller optimization problem can be formulated. Once these signal sets are defined, the Figure 5 can be redrawn in the standard robust control block diagram shown in Figure 6(A), where the controller, K, and combined perturbation matrix, Δ, defined in Figure 6 (B), are connected to the so-called "design plant," P_d [3].

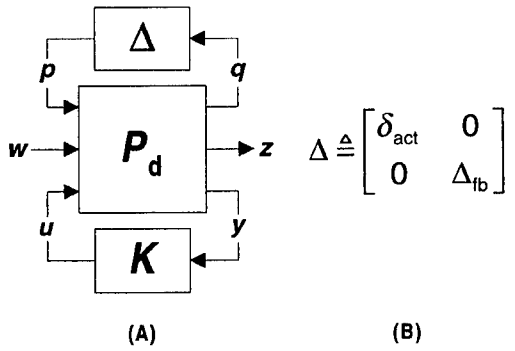


FIGURE 6: (A) STANDARD ROBUST CONTROL BLOCK DIAGRAM (B) DEFINITION OF Δ

Descriptions of the three signal sets are now given, along with the choices made for the current gun stabilization problem. Following these definitions, the robust control design goals will be formulated in terms of this standard framework.

3.1 Control Variables

The control variables, u and y, represent the actuator input and sensor output signals, respectively, and define how the controller, K, connects to the system. In the M1A2 system, u is simply the gun rate command, $\dot{\theta}_c$. The sensor vector, y, consists of all signals available to the controller, and is defined as follows:

$$y = \begin{bmatrix} y_{fb} + n_{fb} + p_{fb} \\ y_{ff} + n_{ff} \end{bmatrix}$$

where y_{fb} and y_{ff} are from (1) and (2), respectively, and n_{fb}, n_{ff}, and p_{fb} are from Figure 5.

3.2 Performance Variables

The performance variables, w and z, represent, respectively, the external system disturbances, and the signals which are required to remain small in the presence of such disturbances. The input vector, w, is a vector of all modeled external influences on the plant. Typical elements of this vector include disturbances, noise, and reference commands. This can be thought of as a vector of "generalized" disturbances, and is often referred to in the literature as the *exogenous inputs* [3]. The performance output vector, z, often called the *regulated variables,* is defined such that all control system performance objectives are captured, where each component in z is chosen such that "smaller is better." For the current stabilization design framework, these variables are chosen as follows:

$$w \triangleq \begin{bmatrix} d \\ \hline n \end{bmatrix} = \begin{bmatrix} T_f \\ \dot{\theta}_T \\ \ddot{y}_T \\ \hline n_{fb} \\ n_{ff} \end{bmatrix}, \quad z \triangleq \begin{bmatrix} e \\ u \end{bmatrix} = \begin{bmatrix} \phi_m \\ \dot{\theta}_c \end{bmatrix} \tag{3}$$

where the notation $\triangleq$ is used to denote a redefinition of the performance variables in a more detailed form. Specifically, the w vector is generically partitioned into *disturbance* and *noise* (vector) components. The reason for such a distinction is primarily in the frequency content of such signals. Disturbances occur typically in lower, operational frequency ranges, whereas noise signals typically have higher frequency content. For the current system, the friction and terrain components are natural choices for the disturbance vector d. The two sensor noise components are grouped into the noise vector, n. The z vector is generally made up of an error component, e, and an actuator command component, u. This reflects the practical control design principle that performance be achieved (e.g. small "errors") without excessive actuator effort, due to physical system limitations. For the current problem of muzzle stabilization, e is simply defined as the muzzle angle, and u is the gun rate command, $\dot{\theta}_c$.

3.3 Robustness Variables

When applying optimization-based design algorithms, it is critical to include robustness considerations to account for system perturbations and modeling errors. The robustness variables can be thought of as a way to introduce conservatism in the design by preventing over-optimization that would occur by assuming that the model is perfect. Alternatively stated from a classical control design viewpoint, designing for robustness is a way to design in stability margins. The goal of this section is simply to establish the "hooks" in the design framework that will later be used to provide for design robustness. The specific manner in which these variables are used to address robustness issues is described in Section 4.2

As alluded to in Figure 5 and the accompanying discussion, robustness issues are addressed by inserting perturbations into the linear closed loop system, in order to account for discrepancies between the linear model and the true physical plant. Recall multiplicative perturbations are inserted into the actuator path via δ_{act} and each sensor path via Δ_{fb}. The combined perturbation matrix, Δ, is thus a 4×4 diagonal matrix containing the individual perturbations. For notational simplicity, the perturbations will be denoted as $\delta_i, i=1\ldots4$, where $\delta_1 = \delta_{act}$ and δ_2, δ_3, and δ_4 represent the sensor perturbations in the position, feedback gyro, and pressure channels. Furthermore, these perturbations are *complex-valued*, and thus account for model discrepancies in both magnitude and phase. Finally, in the remaining development, the perturbations are normalized to unit magnitude, with their sizes specified explicitly via weighting parameters, w_{q_i}. The structure of the individual perturbations is shown in Figure 7.

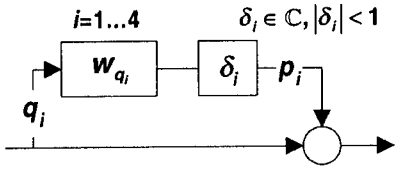


FIGURE 7: MULTIPLICATIVE PERTURBATIONS

It should be noted here that the w_{q_i} parameters can be frequency dependent; this is useful since model uncertainty is typically small at low frequencies and increases in size at high frequencies. Using the notation of Figure 5, this perturbation framework gives rise to the following assignments for the general robustness variables p and q:

$$p = \begin{bmatrix} p_{\text{act}} \\ p_{\text{fb}} \end{bmatrix}, \quad q = \begin{bmatrix} q_{\text{act}} \\ y_{\text{fb}} \end{bmatrix}$$

4 ROBUST CONTROL DESIGN SPECIFICATION

The manner in which the above framework is used to specify control design objectives is now described. The goal of the design is to achieve *robust performance*. Such a design involves optimization criteria that address performance and robustness issues. The method in which performance is specified is described in Section 4.1; Section 4.2 describes the robustness framework. Finally, Section 4.3 describes how both design goals are combined into a single design specification via the concept of μ. See [4] for more details on the concepts presented here.

4.1 The H_∞ Performance Criterion

Using the signals defined in Section 3, performance can be concisely quantified via the linear relationship shown in Figure 6 from w to z, denoted H_{zw}. Since z and w are vectors, H_{zw} is a transfer matrix. Note that this relationship is a function of the controller, K. Therefore, K can be thought of as the optimization variable that must be chosen to make H_{zw} "desirable," in some sense.

The precise specification of performance with H_{zw} requires the performance inputs and outputs to be normalized. This is necessary in order to capture order of magnitude in the vector components that exist because of 1) unit differences, 2) typical sizes of the exogenous inputs, and 3) relative importance, or penalties, of the regulated variables, normalized such that zero represents no importance and 1 represents maximum importance. When considering issue 3) it is typical to frequency weight these penalties, because in practical control problems, performance objectives are often emphasized differently at different frequencies. A typical example is that goals such as disturbance rejection and reference tracking are important at low frequencies, whereas noise rejection and robustness to modeling errors are more important at high frequencies (the latter is due to the fact that models eventually break down at high frequencies).

The above described normalization is accomplished by cascading input and output weightings, W_w and W_z, to the standard block diagram, shown in Figure 8, where it also shows, via dotted lines, the focus of performance specification in the general framework (i.e. p and q are not considered).

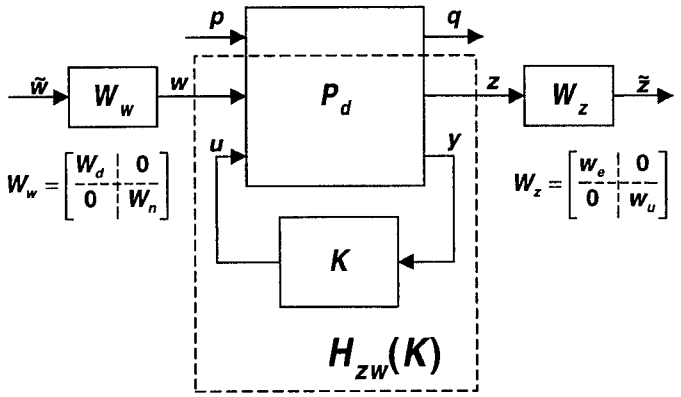


FIGURE 8: PERFORMANCE SPECIFICATION FRAMEWORK

Observe that W_w and W_z are partitioned according to the structure of the input and output performance vectors given in (3). Also, the weighting matrices have a diagonal structure, which has the effect of multiplying the i^{th} component of its input by the $(i,i)^{\text{th}}$ element of the weight matrix, as follows:

$$W_w = \left[\begin{array}{c|c} W_d & 0 \\ \hline 0 & W_n \end{array}\right] = \left[\begin{array}{ccc|cc} w_{T_f} & 0 & 0 & & \\ 0 & w_{\dot{\theta}_T} & 0 & 0 & \\ 0 & 0 & w_{\ddot{y}_T} & & \\ \hline & & & w_{n_{fb}} & 0 \\ & 0 & & 0 & w_{n_{ff}} \end{array}\right], \quad W_z = \left[\begin{array}{c|c} w_e & 0 \\ \hline 0 & w_u \end{array}\right] \tag{4}$$

The method used to choose these parameters is described in the Section 5.1. The transfer matrix providing the desired performance specification can now be written, relating the normalized exogenous input vector, $\tilde{w}$, to the normalized regulated variable vector, $\tilde{z}$:

$$H_{\tilde{z}\tilde{w}} = W_z H_{zw} W_w \tag{5}$$

Since (5) describes a generalized disturbance rejection problem (i.e. smaller is better), a mathematical concept of the "size" of this transfer matrix is needed which will precisely quantify the level of disturbance rejection. To this end, consider the *maximum singular value* of the (complex-valued) matrix $H_{\tilde{z}\tilde{w}}(j\omega)$, denoted $\bar{\sigma}\left(H_{\tilde{z}\tilde{w}}(j\omega)\right)$, defined as:

$$\bar{\sigma}\left(H_{\tilde{z}\tilde{w}}(j\omega)\right) = \max_{\omega \neq 0} \frac{\left\| H_{\tilde{z}\tilde{w}}(j\omega)\tilde{w} \right\|}{\left\| \tilde{w} \right\|}$$

where $\tilde{w}$ is a complex-valued vector, and $\|x\| = x^* x$ is the standard Euclidean norm measure for a complex vector, x. Note for the scalar case, $\bar{\sigma}(h(j\omega)) = |h(j\omega)|$. The maximum singular value can be interpreted as characterizing the maximum amplification of sinusoidal input vectors, as a function of frequency, and is a generalization of the scalar concept of the frequency response of a transfer function. Given this frequency response concept for $H_{\tilde{z}\tilde{w}}$, the desired measure of its size is given by the ∞-*norm*, defined as:

$$\|H_{\tilde{z}\tilde{w}}\|_\infty = \max_\omega \bar{\sigma}(H_{\tilde{z}\tilde{w}}(j\omega))$$

The above criterion provides a single number based on the overall transfer function frequency response, $H_{\tilde{z}\tilde{w}}(j\omega)$, to optimize against. Software to compute the maximum singular value and the ∞-norm is available in many mathematical analysis packages, including Matlab and Xmath.

4.2 The μ Small-Gain Robustness Criterion

Any practical control design must be resilient in the face of uncertainty in its operating environment. Physical reasons for system uncertainty include component tolerances and degradation due to aging. These tolerances give rise to vehicle-to-vehicle variations that must be addressed when designing a single controller for a fleet of vehicles. Uncertainty must also be accounted for when using model-based robust control design approaches, due to the fact that even in the best conditions, the plant model used in the optimization is not perfect. It is thus necessary to account for *unmodeled dynamics*, which are typically small at low frequencies and increase at higher frequencies. In fact, it is this latter aspect of uncertainty that is the focus of the current work, since the goal is to design a controller for a one-of-a-kind demonstration vehicle. The purpose of this section is to establish precisely the properties that the closed loop system must have to ensure stability in the presence of uncertainty.

Recall from Section 3 that perturbations are inserted into the model to address robustness issues. In this work, robustness is quantified via a key result known as the *small-gain* theorem. In its simplest form, the small gain theorem states that for all *single* perturbations, $\delta_i \in \mathbb{C}$, satisfying the magnitude condition $|\delta_i| < 1$ (see Figure 7), the system will remain stable if the following ∞-norm condition holds:

$$\|w_{q_i} H_{q_i p_i}\|_\infty < 1 \tag{6}$$

Alternatively, in terms of a design requirement, since $H_{q_i p_i}$ is a function of the controller, K should be chosen such that

$$|H_{q_i p_i}(j\omega)| < \frac{1}{|w_{q_i}(j\omega)|}, \forall \omega \tag{7}$$

It is seen from (7) that the inverse of the perturbation magnitude serves as an upper bound on the frequency response magnitude function, $|H_{q_i p_i}(j\omega)|$. Therefore, by examining the four bode

magnitude plots $\left|H_{q_i p_i}(j\omega)\right|, i=1\ldots4$, designs can be compared with respect to the relative robustness of each controller path. These four plots will serve as the primary means of arriving at the robustness weightings in the design problem; the details are given in Section 5.2.

Note that the above analysis provides a *loop-by-loop* stability analysis. This is analogous to determining classical gain and phase margins by "breaking the loop" at the actuator and feedback sensors, one at a time. In order to evaluate and design for robust stability in the presence of all perturbations appearing simultaneously, further analysis is needed. To this end, consider Figure 9(A), which explicitly shows the normalized perturbation structure introduced in Section 3.3 (see Figure 7) in the standard framework. The scope of the robust stability problem is also shown via the dashed box (i.e. w and z are not considered).

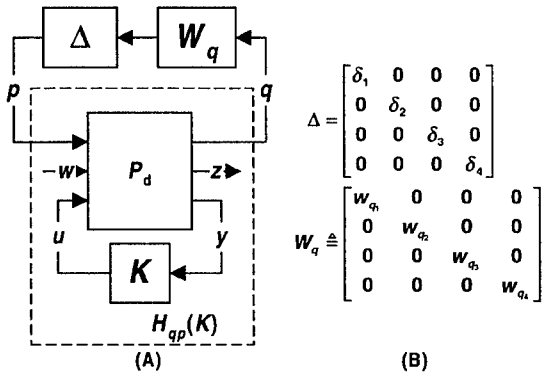


FIGURE 9: (A) NORMALIZED PERTURBATION STRUCTURE (B) DETAILS OF Δ AND W_q

The matrix W_q combines the individual perturbation weights, w_{q_i}, in a diagonal matrix corresponding to the diagonal structure of Δ. These matrices are shown in Figure 9(B). The diagonal matrix structure captures the decoupled nature of the perturbation model, i.e., perturbation δ_i only influences the i^{th} channel

The goal is now to obtain a condition on the matrix transfer function $H_{qp}(K)$ that guarantees stability in the presence of all four perturbations. A direct generalization of the single perturbation condition (6) is the small-gain condition

$$\left\|W_q H_{qp}\right\|_\infty < 1 \tag{8}$$

This stability result does indeed address the case of multiple perturbations, however, the perturbation matrix in this formulation is assumed to have a *full* structure, as opposed to the diagonal structure of Figure 9. Therefore, any stability assessment made using (8) will be unnecessarily conservative. Imposing such a condition on the design will result in severely compromised performance. Because of this issue, it is desirable to have a stability measure which takes into account the diagonal structure of the perturbation matrix.

To address the issue of conservatism when dealing with a system perturbation matrix having an inherent diagonal structure, the concept of μ was developed. Only a basic result from the theory of μ that is relevant to the current problem will be presented here. For more complete details, see [4] and the references therein. The result needed generalizes the small gain condition (8) to accommodate the fact that the perturbation has a diagonal structure, as follows:

$$\left\| W_q H_{qp} \right\|_\mu \triangleq \max_\omega \mu\left(W_q(j\omega) H_{qp}(j\omega)\right) < 1$$

where the function μ is a generalization of the maximum singular value, and is taken with respect to the specific diagonal structure of Δ. Thus μ provides a new notion of matrix size that applies specifically to a complex matrix (e.g. a frequency response matrix) connected in a feedback configuration to a block diagonal matrix. Maximizing μ over frequency provides the desired measure of *system* size, and provides a non-conservative stability criterion for systems with multiple complex uncertainties.

4.3 Combined Performance and Robustness Design Framework

The development of the previous two subsections is summarized in the block diagram of Figure 10.

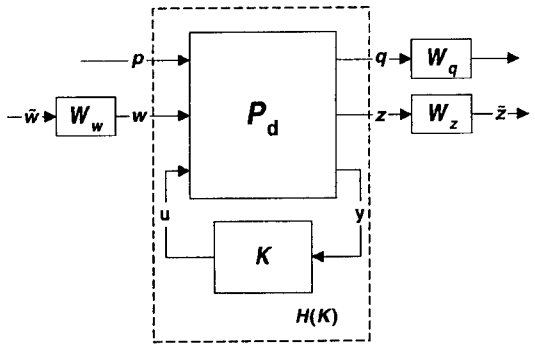


FIGURE 10: SUMMARY OF ROBUST PERFORMANCE DESIGN FRAMEWORK

In this view, all weighting functions are explicitly shown. These parameters represent the designer's "tuning knobs," which allow various control design tradeoffs to be explored. Both performance and robustness objectives introduced in the previous subsections can be combined into a single framework using μ. This is known as the "robust performance" problem, and is obtained by first combining the performance and robustness inputs and outputs:

$$w_{\text{rp}} = \begin{bmatrix} p \\ w \end{bmatrix}, \quad z_{\text{rp}} = \begin{bmatrix} q \\ z \end{bmatrix}$$

The corresponding combined input and output weights are:

$$W_{w_{\text{rp}}} = \begin{bmatrix} I_p & 0 \\ 0 & W_w \end{bmatrix}, \quad W_{z_{\text{rp}}} = \begin{bmatrix} W_q & 0 \\ 0 & W_z \end{bmatrix}$$

where I_p is a $p \times p$ identity matrix. The combined robust performance criteria is:

$$\left\| W_{z_{\text{rp}}} H W_{w_{\text{rp}}} \right\|_\mu < 1 \tag{9}$$

with μ taken with respect to the following augmented uncertainty structure:

$$\Delta_{rp} = \begin{bmatrix} \Delta_{rs} & 0 \\ 0 & \Delta_{perf} \end{bmatrix}$$

where Δ_{rs} is the diagonal uncertainty structure of Section 4.2, and Δ_{perf} is a complex valued matrix having as many rows as elements in w, and as many columns as elements in z.

5 DESIGN RESULTS

The Matlab Mu Analysis and Synthesis Toolbox provides routines to design a controller based on an iterative reduction of the left side of (9). The output of this design algorithm is a *state-space system*, i.e. a system defined by the following equations:

$$\dot{x} = Ax + By$$
$$u = Cx + Dy$$

where x is the state vector, $\dot{x}$ is the time derivative of the state vector, y is the sensor vector, and u is the controller output. The variables A, B, C, and D are appropriately dimensioned matrix parameters that define the controller. The computational complexity of the controller is determined by the size, or *order*, of the state vector, x. Larger state vectors require more computation from the processor. Note the square matrix A dominates the computational burden; since the number of elements in this matrix increase in a manner proportional to the *square* of the number of states. A property of the μ-synthesis design algorithm is that it produces controllers having the same number of states as the design plant, which is the number of states of the plant dynamics plus the number of states in all the design weighting parameters. Because of this, model reduction techniques are commonly applied, which can decrease the number of states quite dramatically. Following this reduction, the controller is converted into a discrete-time system for implementation on the target hardware. This yields a controller of the form:

$$x_{k+1} = A_T x_k + B_T y_k$$
$$u_k = C_T x_k + D_T y_k$$

where k is an integer sample index assuming a sampling time of T, and A_T, B_T, C_T, and D_T are the controller matrices which are implemented in the vehicle processor.

As described in the previous section, a robust control design in the current framework is equivalent to specifying the design weighting parameters W_z, W_w, and W_q. Sections 5.1 and 5.2 describe the choices made for these design parameters. Section 5.3 compares the bump course stabilization performance of the μ-synthesis controller with a classically tuned controller.

5.1 Performance Design Weights

Recall that defining performance is equivalent to defining the weighting matrices, W_w and W_z, defined in (4). Consider first the disturbance component, W_d. Its friction term, w_{T_f}, is chosen as the typical trunnion friction level for an M1A2 vehicle. The terrain disturbance terms, $w_{\dot{\theta}_T}$ and $\ddot{y}_T$, are chosen as the typical rms statistics for a bump course run. It was found that the

design is not particularly sensitive to the choices of these scaling parameters; their main function is to establish general order-of-magnitude differences in the signal values.

The second component of W_w, W_n, represents the approximate contribution of sensor noise to the feedback and feedforward signals. This can be viewed as a specification that the control design should not amplify sensor noise, which can arise from the finite resolution of the sensor, as well as the noise floor of the electronic hardware. This set of parameters can thus be interpreted as containing information regarding the accuracy of each sensor. For the M1A2 system, these parameters are chosen as follows:

$$W_n = \left[\begin{array}{c|c} W_{fb} & 0 \\ \hline 0 & W_{ff} \end{array}\right] = \left[\begin{array}{ccc|cc} \frac{10\times10^{-6}s}{s+2\pi(100)} & 0 & 0 & & \\ 0 & 10^{-3} & 0 & 0 & \\ 0 & 0 & 10 & & \\ \hline & 0 & & 10^{-3} & 0 \\ & & & 0 & 0.02 \end{array}\right]$$

Note that for the resolver feedback of the trunnion position error, it must be assumed that there is no dc noise component (i.e. a position offset) because it would be impossible to reject, due to the fact that positional information is not contained in any other sensor. A first order high-pass filter is therefore used to eliminate such a noise component from consideration.

The performance output weighting matrix, W_z, is now chosen. The weighting functions in W_z provide the means of specifying the performance objectives of the control design. This is in contrast to the input weight W_n, which is used simply to establish general signal magnitudes. A natural starting point for obtaining the muzzle error weighting, w_e, is via the M1A2 rejection ratio specification, $R(\omega)$, which is a stabilization performance bound defined as follows:

$$\frac{\mathrm{PSD}(\phi_t)}{\mathrm{PSD}(\dot{\theta}_T)} < R(\omega)$$

In the context of the design framework of Figure 10, the rejection ratio can be interpreted as a bound on the magnitude of H_{ed} as follows:

$$|H_{ed}(j\omega)| < R(\omega), \forall\omega$$

This expression can alternatively be stated in the form of a robust control performance specification as follows:

$$\max_{\omega}\left[R^{-1}(\omega)H_{ed}(j\omega)\right] = \left\|R^{-1}H_{ed}\right\|_{\infty} < 1 \qquad (10)$$

Therefore, $R^{-1}(\omega)$ can serve as a starting point for determining the performance weight, w_e. Since the rejection ratio specification is conservative from a design standpoint, iterations on w_e are necessary to further refine the performance specification. Specifying higher levels of performance (i.e. smaller muzzle error) requires a larger performance weight, i.e.

$$w_e(j\omega) > R^{-1}(\omega)$$

The final choice for w_e was arrived at via trial-and-error design iterations, and is depicted via a plot of the product $w_e(j\omega)R(\omega)$, shown in Figure 11.

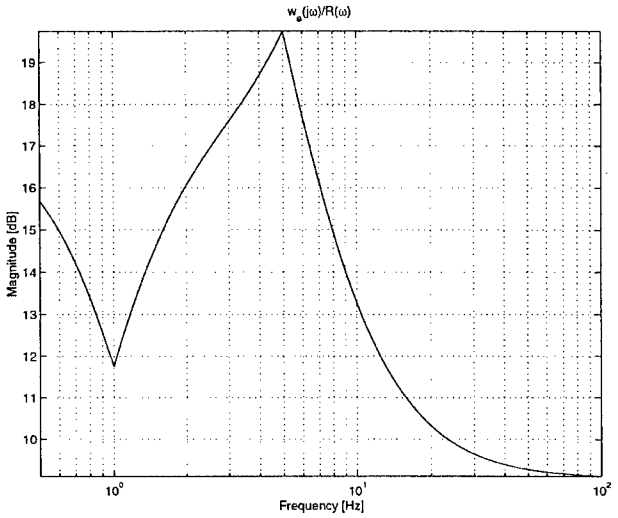


FIGURE 11: NORMALIZED PERFORMANCE SPECIFICATION PLOT

A normalized view of the performance specification is necessary due to the sensitivity of the underlying M1A2 performance requirement. In this plot, 0 dB indicates the performance specification is exactly consistent with the rejection ratio. Larger values represent a more stringent specification.

Finally, the actuator weight, w_u is chosen. This specification is an upper bound on the actuator authority used by the controller, and must be chosen based on the capabilities of the physical system. It is typically chosen so that the controller uses as much of the usable actuator authority as possible, to maximize performance. Furthermore, it should ensure that the controller commands *roll-off* at high frequencies. For the current M1A2 system, this parameter was chosen to be:

$$w_u = 0.56\left[\frac{s/\omega_1 + 1}{s/\omega_2 + 1}\right]^5, \qquad \omega_1 = 2\pi(200), \omega_2 = 2\pi(10^4)$$

Note w_u is a lead-lag filter that ramps up at 200Hz to enforce a roll-off property. The 10 kHz leveling off is due to a technical requirement of the optimization software that all weighting functions be proper.

5.2 Robustness Design Weights

In any control design problem, a fundamental tradeoff exists between performance and robustness. Therefore, a key design goal is to provide the *minimum* robustness required by the system in order to *maximize* system performance. Recall that in the current setting, robustness is addressed via the frequency-dependent weighting parameters, w_{q_i}, which focus the μ-synthesis

optimization on robustness to the i^{th} multiplicative uncertainty. Since an uncertainty is, by definition, not well known, these parameters must be chosen carefully. Ultimate determination of robustness parameters must be made in conjunction with vehicle testing. The purpose of this section is to establish the method used here to guide the selection of the robustness weights.

In addition to their interpretation as a frequency-dependent characterization of the uncertainty magnitude, the robustness weights can alternatively be viewed as frequency-dependent "design knobs" – larger magnitudes increase optimization focus on the robustness objective. Typically this involves trading off performance in that frequency range. As described in Section 4.2, the robustness of the individual feedback loops can be evaluated via the four plots, $\left|H_{q_i p_i}(j\omega)\right|, i=1\ldots4$. Using these plots, the following iterative procedure was used to arrive at the robustness weights:

1) Start with $w_{q_i}=0, i=1\ldots4$.
2) Perform μ-synthesis to generate a controller
3) Compare the resulting closed loop properties to that of a "reference" system, H_{ref}
   a) Plot the robustness plots $\left|H_{q_i p_i}(j\omega)\right|, i=1\ldots4$, for both control systems
   b) Plot the performance plot $\bar{\sigma}\left[W_z(j\omega)H_{zw}(j\omega)W_w(j\omega)\right]$ for both control systems
4) If the plots from 3a and 3b are desirable, then proceed to simulation and implementation; else introduce/modify w_{q_i} according to the general guidelines of Section 4.2
5) If the implementation exhibits problems such as instability or resonance, introduce/modify w_{q_i} as necessary according to the general guidelines of Section 4.2

For this project, the controller used as H_{ref} varied throughout the study. Initially, it was the nominal M1A2 closed loop system, since it is known to have good performance and robustness properties. Once hardware was available, H_{ref} was the most recent controller iteration. Bode magnitude plots for $w_{q_i}, i=1\ldots3$, are shown in Figure 12, while $w_{q_4}=0$. The frequency dependence of the weighting functions has been utilized to tailor robustness around problem frequencies in the system.

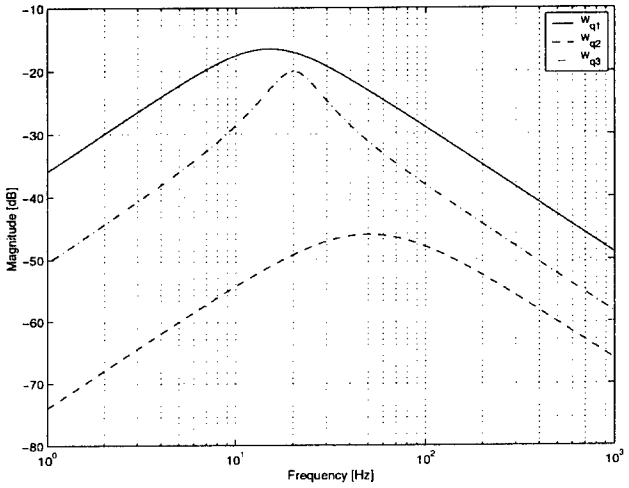


FIGURE 12: ROBUSTNESS DESIGN WEIGHTS

5.3 Bump Course Test Results

Application of the μ-synthesis design routines yielded a 47^{th} order continuous time controller. Subsequent model reduction and discretization resulted in a 22^{nd} order digital controller implemented on the M1A2 system. The stabilization testing shown here was carried out at Aberdeen Proving Grounds, using RRC-9 bumps with a vehicle speed of 10 mph. To evaluate the performance properties of the robust control design and gain the most insight possible, a classically tuned stabilization design was also developed for the long gun system. The details of the classical design will not be given; however, the fundamental difference in philosophy between the two approaches is simply described. Namely, the performance objective of the classical control design is to maintain small trunnion-pointing error, as measured by the gun-trunnion resolver, whereas the performance objective of the robust control design is to maintain small *muzzle*-pointing error. The model-based nature of the robust control design makes it possible to optimize the design goal about a quantity that is not sensed. The key comparison is shown in Table 1, where the terrain disturbance and gun response RMS statistics are compared for each controller.

TABLE 1: ROBUST CONTROLLER BUMP COURSE RMS STATISTICS (RELATIVE TO CLASSICAL DESIGN)

	TERRAIN DISTURBANCE		GUN RESPONSE	
	FF_ACCEL ($\ddot{y}_T$)	FF_GYRO ($\dot{\theta}_T$)	TRUN ERROR (ϕ_t)	MUZZLE ERROR (ϕ_m)
$\Delta\%$	13	9.6	94	-8.1

To convincingly illustrate the muzzle performance of the robust controller, bump course runs were chosen where the terrain disturbances are larger for the robust controller. The most striking difference in the gun response statistics is in the trunnion response. Namely, Table 1 shows that, relative to the classical controller, the robust controller achieves an 8.1% reduction in the muzzle error with a 94% *increase* in the trunnion error. This behavior is somewhat counterintuitive, however, it is consistent with the robust control problem formulation since the performance variable in the μ -synthesis optimization contained the muzzle angle and not the trunnion angle.

Additional insight is obtained by comparing the power spectral densities (PSD's) of the above signals, shown in Figure 13. The small trunnion error of the classical controller is evident across all frequencies. The muzzle behavior, however, is interesting in that the classical controller response exhibits peaking at 10 Hz. The modern controller does not excite this frequency at all. In fact, analysis has shown that muzzle vibration can be excited as a result of a high bandwidth trunnion loop, such as that in the classical controller [5]. Therefore, the robust control design has provided a means of obtaining small muzzle errors without a high bandwidth trunnion loop; such a solution would not have been found using conventional design techniques.

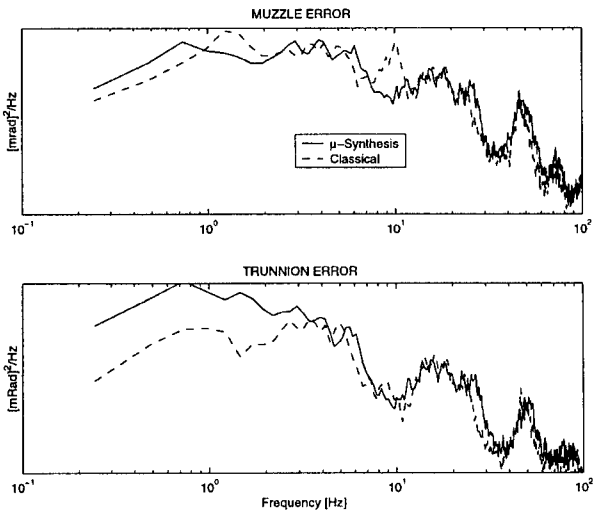


FIGURE 13: POWER SPECTRAL DENSITIES OF GUN RESPONSE

6 CONCLUSIONS

This work has demonstrated the feasibility of using a model-based optimal control design methodology for gun stabilization. This approach is characterized by specifying desired closed-loop performance and robustness objectives. This is an attractive design paradigm, focusing on the higher level issue of *what to do*, instead of *how to do it*. The latter issue is addressed in an automated fashion via the optimization process. However, selection of the frequency weighting parameters is, in general, non-trivial, and must be done with care. Specifically, since the performance and robustness objectives relate to desired closed loop performance, it is possible to specify levels of performance and robustness that are not simultaneously achievable by the system. In such a case, either the design optimization algorithm will not converge, or the resulting design simply will not meet the objectives. Thus the design difficulty lies in gaining experience in understanding how best to translate the physical design objectives into the performance and robustness weighting parameters. This has been achieved here using a combination of simulations and vehicle testing. Once the general principals are established, more design work can be done via computer simulation, which greatly reduces development and testing expense.

REFERENCES

1. V. R. Marcopoli, Independent Research and Development Report, General Dynamics Proprietary Information, 1999.
2. D. J. Purdy, "Comparison of Balanced and Out Of Balance Main Battle Tank Armaments," Proceedings 9th U.S. Army Gun Dynamics Symposium, 1999.
3. S. Boyd and C. Barratt, *Linear Control Design – Limits of Performance*, Prentice-Hall, 1991.
4. G. Balas, J. C. Doyle, K. Glover, A. Packard, R. Smith, *μ-Analysis and Synthesis Toolbox*, The Mathworks, 1995.
5. J. Freudenberg, Independent Research and Development Report, General Dynamics Proprietary Information, 1999.

A CHATTER BOX – INVESTIGATION OF DYNAMIC RESPONSE ACROSS A GAP

10TH U.S. ARMY GUN DYNAMICS SYMPOSIUM

G. Peter O'Hara
Elmhurst Research
60 Loudonville Rd
Albany NY 12204-1513

Virtually all mechanical devices contain several components which are joined or articulated, at joints which must have some clearance. The clearances are required for ease of motion during assembly and/or operation. These clearances produce complex motions when the assembly is subjected to transient motions such as the recoil of a cannon system. This work takes a geometrically simple chatter box system and subjects it to a simple haversine motion using 4 different time frames. The two contact surfaces are given different clearances in an attempt to study one system under a variety of different conditions. The contact stress and the motion of the central slug are shown for all of these 16 cases.

INTRODUCTION

In a previous paper [1] this author reported on the possible catastrophic behavior of a cannon system in response to an adverse (higher speed) loading condition. Further unpublished results tended to support this the early conclusion, for that system. However long experience with cannon systems does not support the notion that this type of problem is common even when very high accelerations are measured on large gun systems. Many modern cannons have rather complex subsystems attached to them such as, muzzle reference devices, firing mechanisms, thermal warnings devices, etc. While the design of these small subsystems is always problematic they never seemed to have, 'show stopping' failures. None the less these small parts occasionally fail and these failures are rarely considered important enough for a detailed failure investigation and frequently go unreported. This author has conjectured that many of these failures are the result of an abnormal and undetected vibration across a gap, that has become a problem due to normal system tolerances combined with everyday wear of the individual components.

In order to gain more insight about this general class of problems, a simple study problem was selected which was small enough to allow a rather large matrix of solutions. The problem selected was the 'Chatter Box' problem which is classically a ball in trapped between two walls. In this case a short cylindrical steel slug was trapped in a one piece case which took the form of a hollow cylinder. This was selected as a first problem which could be extended to a more practical design for an experiment where the hole in the case could allow measurement of the slug motion. A further goal was to produce substantial amplification of the contact stresses similar to the initial practical study.

This is an academic numerical experiment in which the initial design was continued regardless of the result. This design involved the use of four different contact conditions and four different time frames for a total of 16 solutions. These results show the contact conditions and slug motion giving a total of 32 plots of the result. The basic model also includes several elastic body effects that are frequently ignored, such as the distributed mass of the bodies, an array of vibration modes and the non-uniform stress on the contact surfaces. The large number of solutions was intended to form a data base for future reference.

GEOMETRY AND LOADING CONDITION

The problem consists of a solid cylindrical slug with a height and diameter of 25 mm trapped in a case 100 mm long and 100 mm in diameter. This is shown in schematically in Fig. 1 where it can be seen that the slug and case interact at the two ends of the slug and there is a space around the outer diameter of the slug. Because the case is a hollow cylinder, the contact surfaces are in the form rings and the contact conditions at these rings will be one of the primary variables of this report. There are four different contact conditions, the simplest is that the contact surfaces are a perfect fit and are bonded together. This condition simulates a solid structure which permits the contact surfaces to support both tension and compression stress. This condition is not physically realistic but provides a simple reference case. The second condition releases the bonding and provides a surface contact which only supports compression stress, however the initial fit is unrealistically a perfect fit with zero gap. The third condition provides a gap at the top contact surface of 0.00025 mm or 0.001 times the cylinder height. This would be considered a very snug precision fit in any mechanism. The fourth contact condition doubles the gap to 0.0005 mm or about the thickness of a sheet of paper.

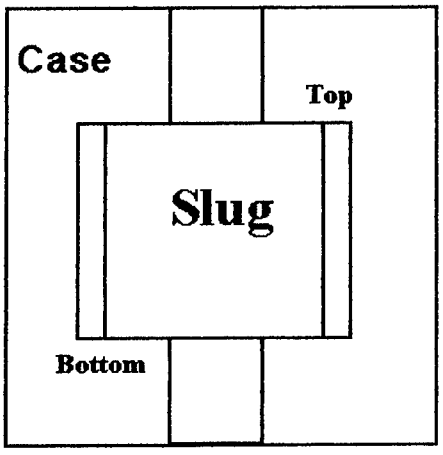


Figure 1 - The geometric arrangement of a short cylindrical slug trapped in a solid case with four different contact conditions.

Again referring to figure 1 the loading input will take the form a controlled displacement at the bottom of the case. The form is a single haversine pulse with a height of 10 mm and four different time durations. The first is a gentile pulse with a total time of 0.002 seconds. The times were then decreased to 0.001, 0.0004 and 0.0002 seconds. The 0.0002 time provides an extremely violent motion with a peak acceleration of 100 times the first.

ANALYSIS

The solutions were carried out using the Direct Integration Dynamic analysis included in ABAQUS/ Standard from Hibbit Karlsson and Sorense Inc. [2]. The slug was modeled with 128 second order quadrilateral elements with three elements interacting at the contact surfaces. The case was modeled with 167 elements. This allowed a rather detailed model of the elastic properties of each body without excessively long computer runs for the individual solutions. The haversine was input as a table with 201 individual data points, which provided a reasonable representation of the function. The minimum time step was set to produce a solution with at least 200 times increments and the error tolerance (HALFTOL) was selected to produce a solution in a maximum of about 350 increments. This allowed a rather detailed solution with some errors which take the form of a few contact stresses which became positive.

At this point it should be pointed out that the numeric integration algorithm requires the use of a small damping factor to produce a stable solution. [3] This damping removes the higher vibration frequencies and is is evident in the solutions with longer time frames (0.002 and 0.001 seconds).

RESULTS

The results of the 16 solutions are shown in two different types of graphs. Figures 2, 4 ,6 and 8, are plots of the average contact stress on the bottom and top contact surfaces. Figures 3, 5, 7 and 9. Are plots of the acceleration and displacement of the center of the slug. Each figure contains four graphs a, b, c, and d, which show the data for the four contact conditions at that particular time interval. This arrangement seemed to be the best for the overall evaluation of the various solutions. The four different time frames in this study produce basic stresses which are very different in magnitude so it was decided to nondimensionalized them by the simple average quasistatc stress. This stress was calculated using the peak acceleration of the haversine, the mass of the slug and the total contact area. Using this method all stresses were plotted using the same range of –3.5 to 2.5 on the Y axis. This produces stress plots which are actually plots of stress amplification factors. This concept was extended to the accelerations data which was nondimensionalized to the maximum acceleration of the haversine function. Then all accelerations could be plotted using a Y axis range of –6.0 to 6.0.

The contact stresses were extracted as axial stress in the three elements, of the slug, which form the contact surface. The most accurate stress in an element is calculated at the nine Gaus integration stations and the three nearest the contact surface were selected to represent the contact stress. With three gaus stations in each of three elements there were nine stresses curves to average for each contact surface. This overall average is the data shown in the plots. The contact stress at the bottom surface is plotted as a solid line and the top surface is shown as a dashed line. Note that with a bonded gap the stress at the top is lower than the stress at the bottom. This is because both surfaces support loads and the top is further from the driven surface.

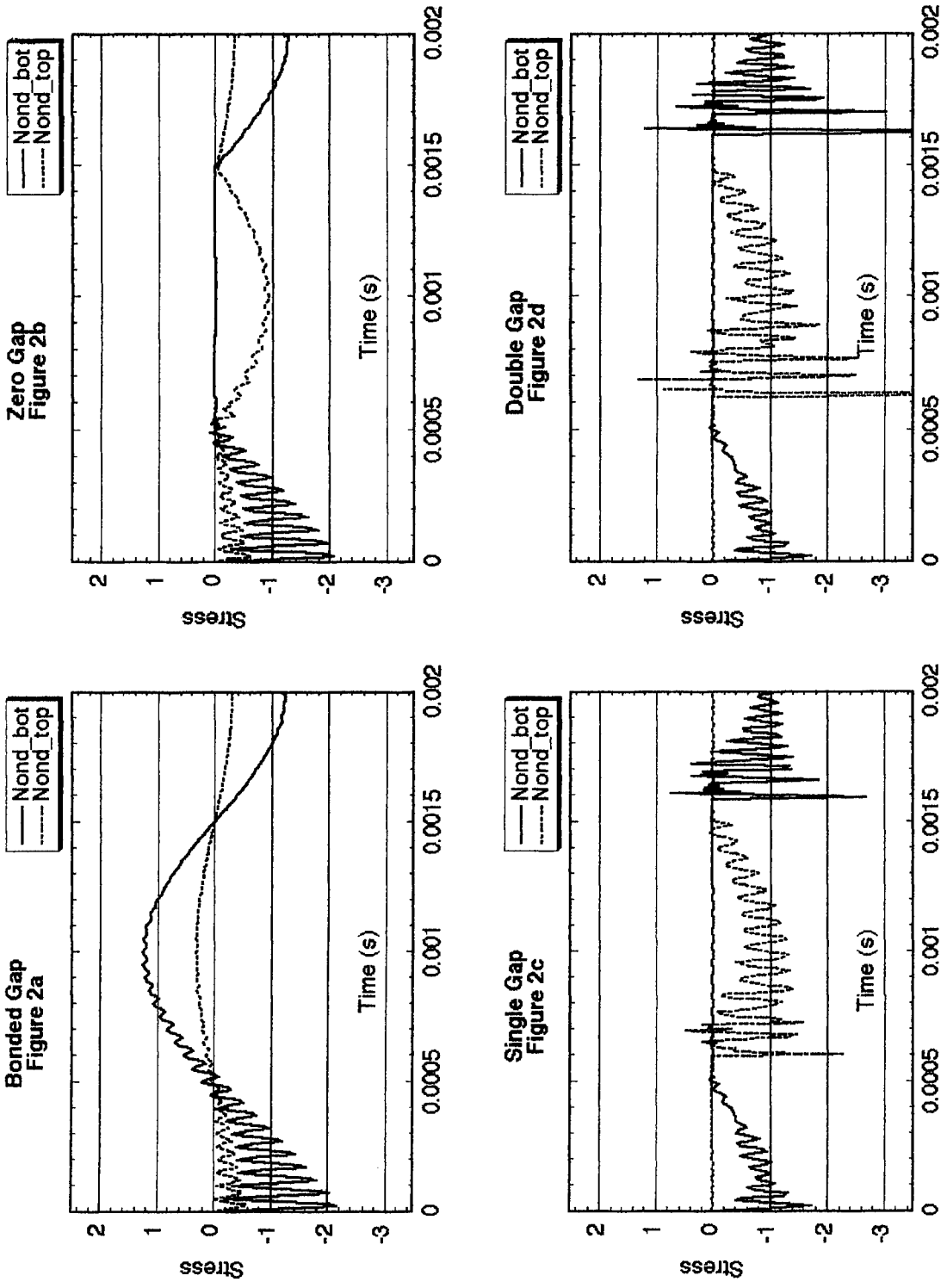


Figure 2 Nondimensional contact stress for four contact conditions and 0.002 seconds total time.

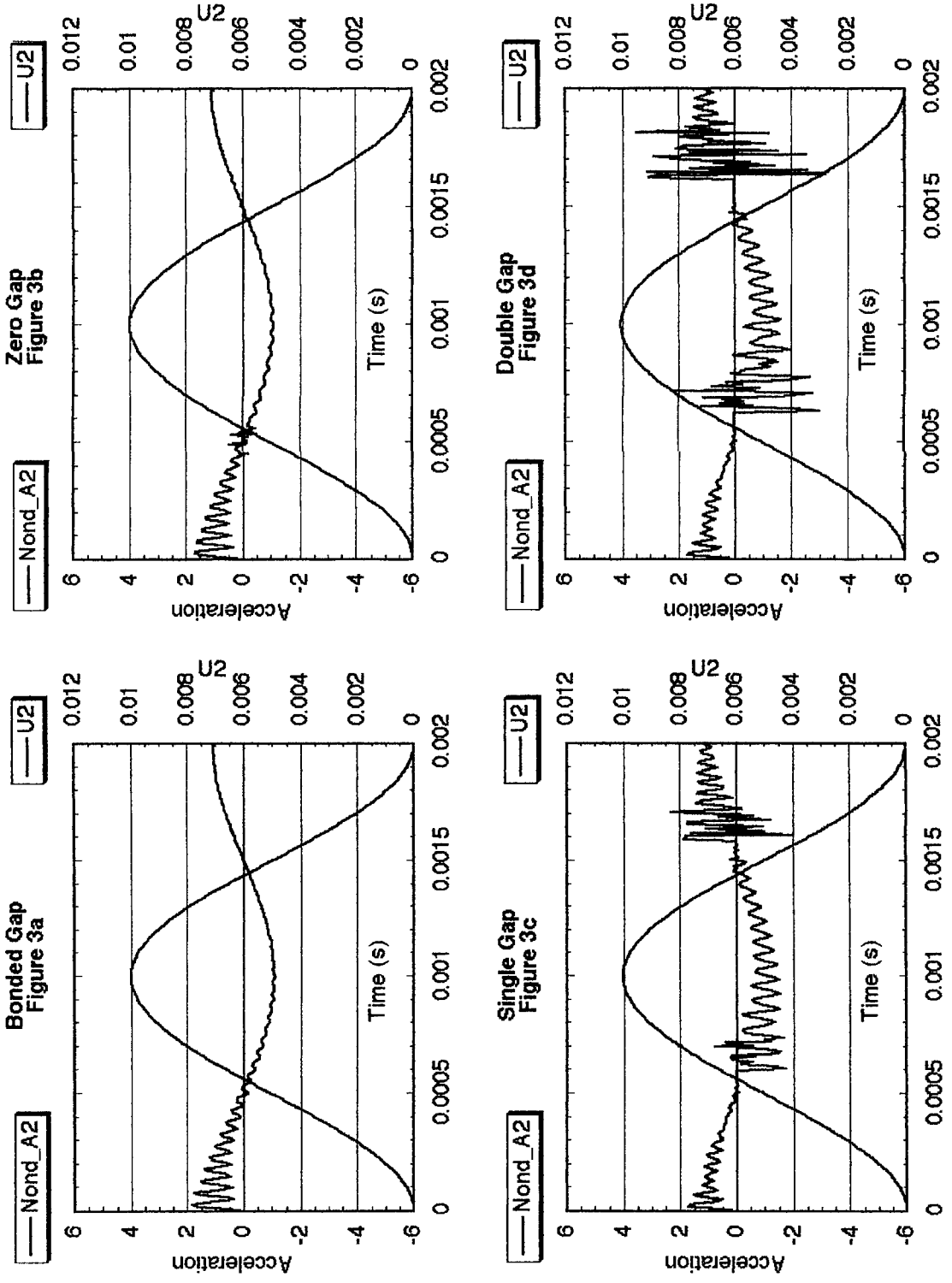


Figure 3 Nondimensional acceleration and displacement for four contact conditions at a total time of 0.002 seconds.

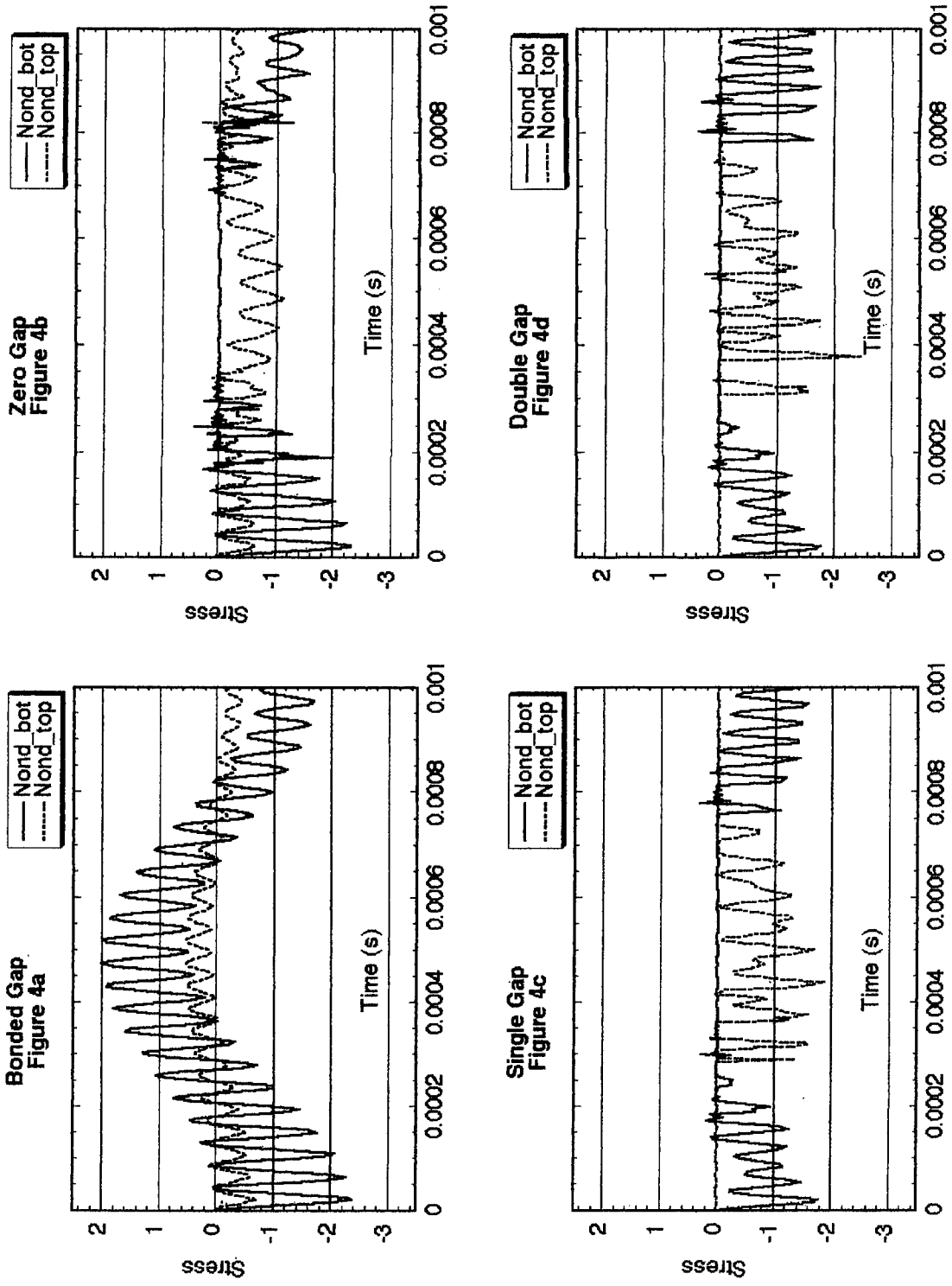


Figure 4 Nondimensional contact stress for four contact conditions and 0.001 seconds total time.

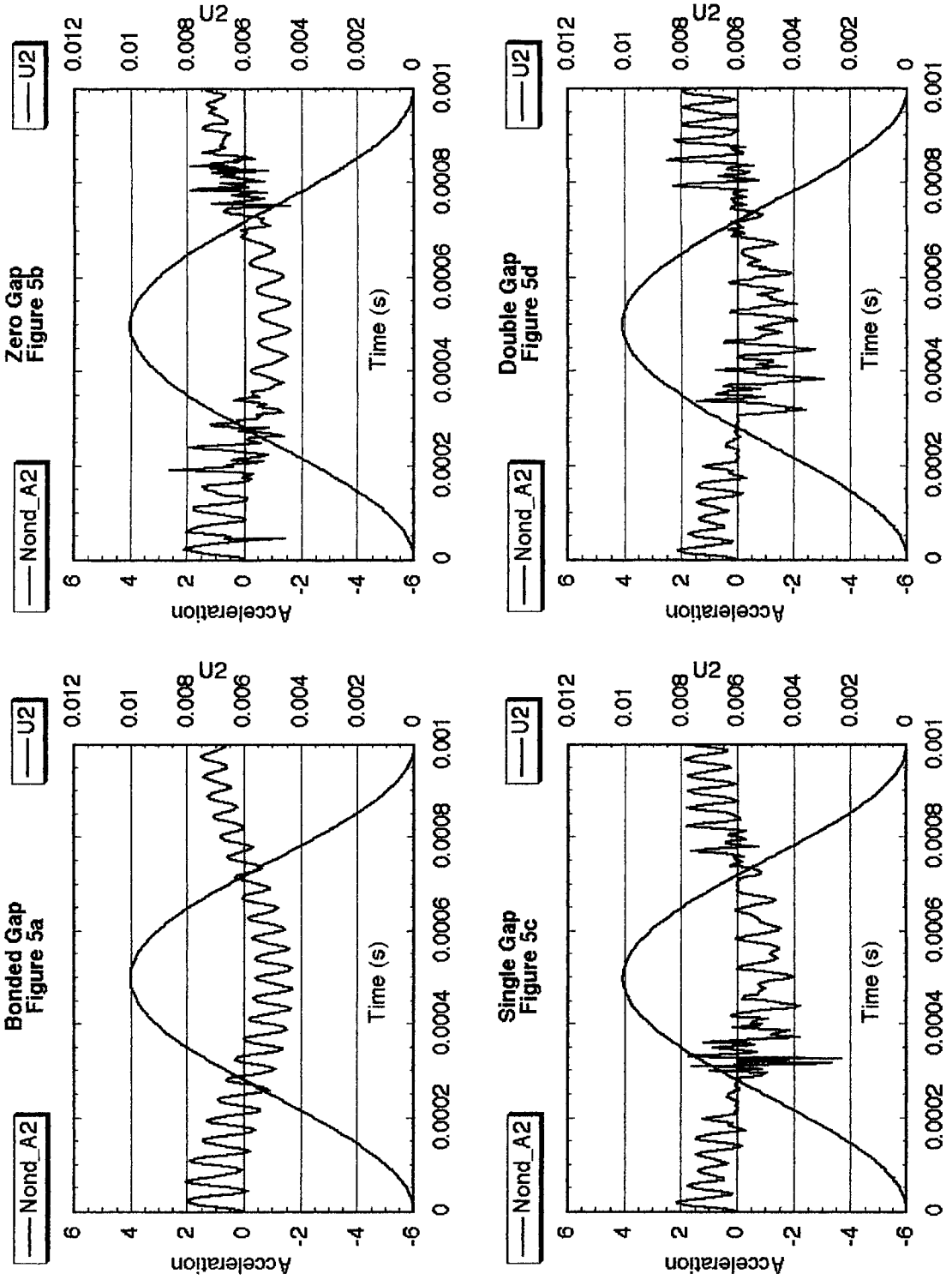


Figure 5 Nondimensional acceleration and displacement for four contact conditions at a total time of 0.001 seconds.

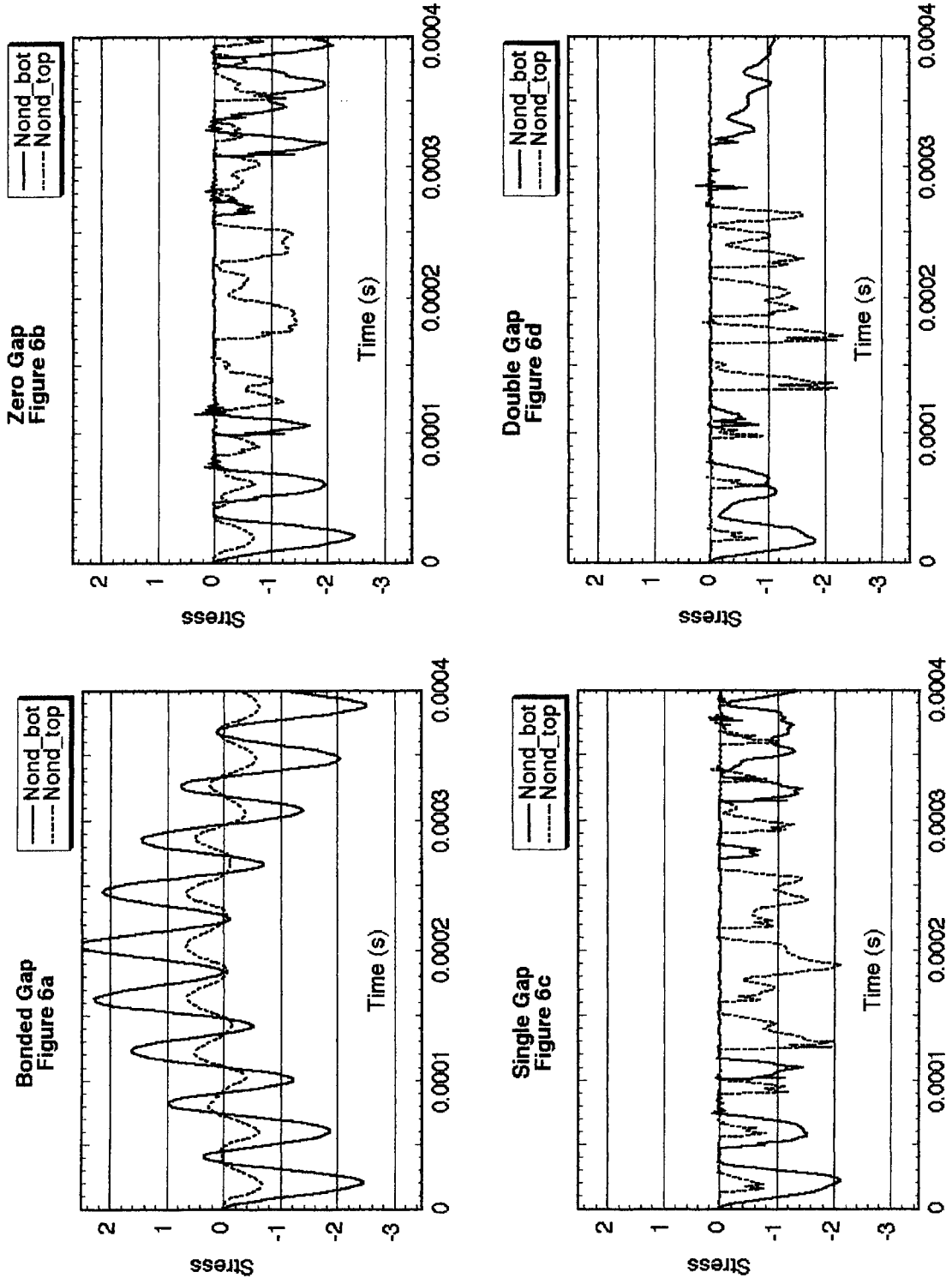


Figure 6 Nondimensional contact stress for four contact conditions and 0.0004 seconds total time.

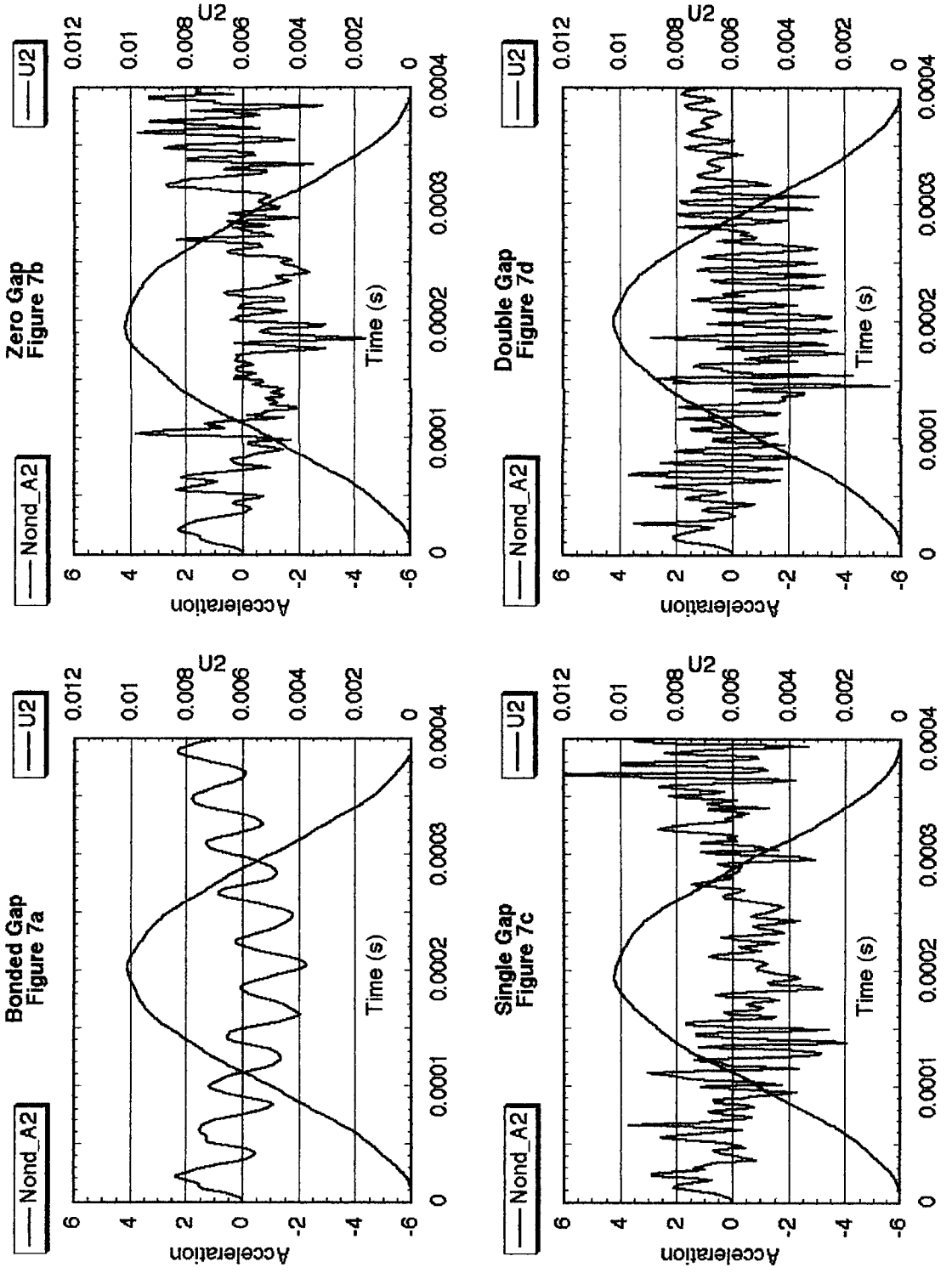


Figure 7 Nondimensional acceleration and displacement for four contact conditions at a total time of 0.0004 seconds.

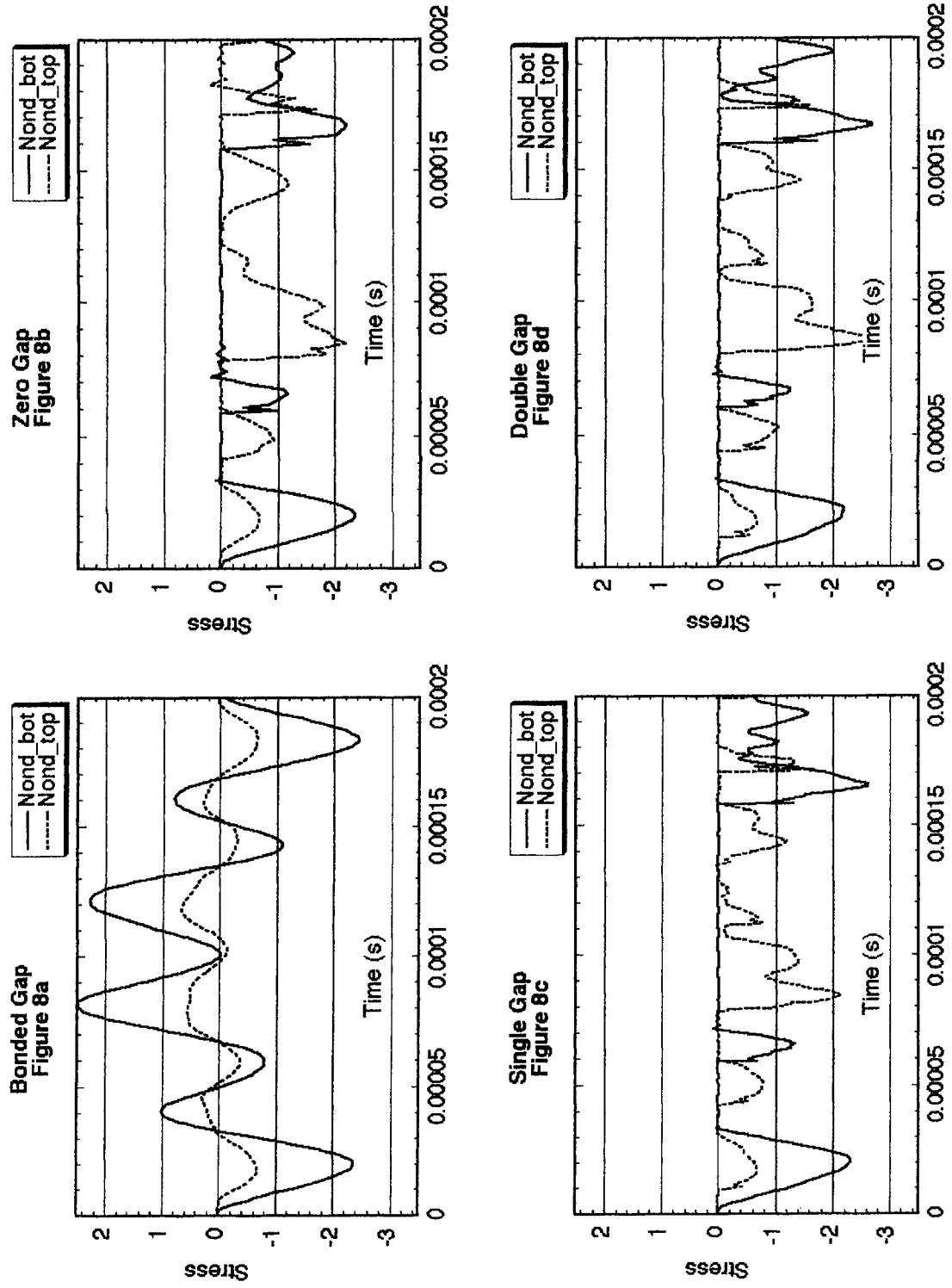


Figure 8 Nondimensional contact stress for four contact conditions and 0.0002 seconds total time.

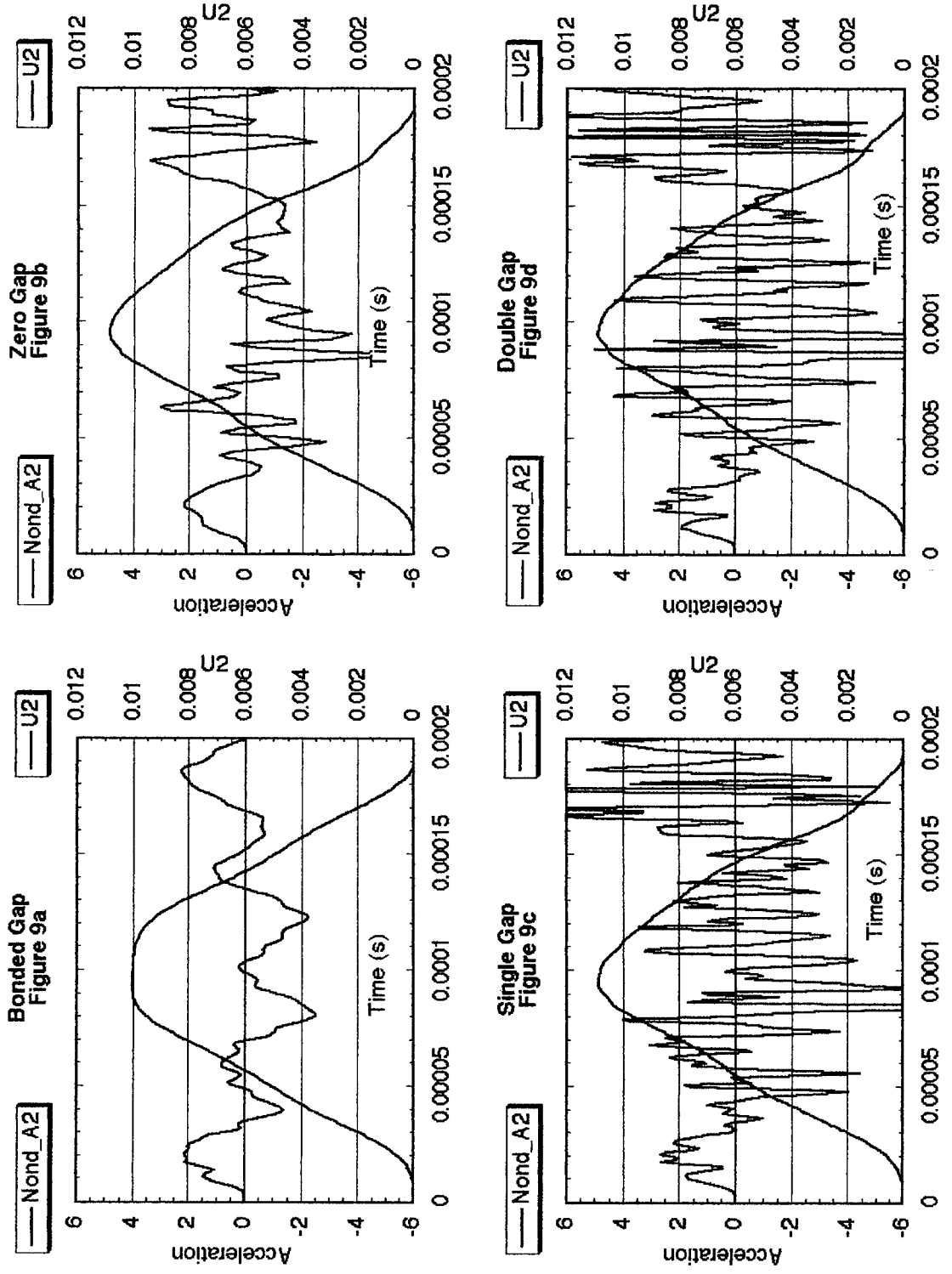


Figure 9 Nondimensional acceleration and displacement for four contact conditions at a total time of 0.0002 seconds.

The plots which show the slug movement each have two curves. First is the displacement of the slug which is nominally has the same maximum value for all cases. The accelerations are nondimensionalized to the maximum acceleration of the Haversine. In this way the acceleration is actually an acceleration amplification factor. Here it should be noted that the displacement curve closely resembles the Haversine at the longer time frames and becomes rather distorted at faster speeds.

DISCUSSON

This study was started as a simple case to explore the behavior of a system that could be set up as a laboratory experiment, However the results are far from simple. The reader can see a variety of behaviors in the 16 solutions, including:

1)The unequal distribution of stress in the bonded cases.

2) The complex multiple impacts of the high speed cases with gaps.

3) The free movement of the slug across the gap.

4) Contact on both surfaces when the gap is zero or small.

5) When the times are long the behavior closely follows the input function.

6) The clear superimposed resonant frequency on the bonded cases.

All of the bonded cases produced the desired result that could be clearly seen and explained. The stresses and movements are a combination of the input haversine plus a small number of resonant frequencies and there is a clear correlation between the slug acceleration and the contact stress. The first resonant frequency is clearly visible in all cases and in the 0.002 second time frame (Fig 2a, and 3a) it is totally damped out by the required numeric damping. In 0.0002 second (Fig 8a and 9a) there are 2 or 3 frequencies visible and damping is not apparent. When the bond is released the behaviors become more complex.

When the bond is released the contact surface no longer supports tension and the slug is free to contact either or both contact surfaces. This adds a strong nonlinear effect to the solution which is apparent at zero gap. First the stress is always compressive and any small tension spikes is the result of numeric error. There also can be contact on both surfaces when the case is in a state of compression. The behaviors are still rather predictable and there remains a good correlation between acceleration and contact stress. The presents of any gap produces two new effects first is the free movement of the slug across the gap and second is the impact of the slug on the new contact surface(Figs 2c and 3c). However the correlation between contact stress and acceleration is present only at the longer time frames and at the shorter time frames the nature of the input function is not apparent from the acceleration or contact stress results. Another effect to note is that the two different gap sizes produce results which are qualitatively similar but strongly different in detail.

The reader should examine the figures closely and draw further information from them and personnel experience. However a review of the mechanics of the basic displacement input function may be useful. The function starts at zero displacement and zero velocity but the acceleration is at the maximum value. The function then forces upward movement to a maximum velocity, at one half of the height and one quarter of the time. The acceleration then reverses in sign and the velocity slows. At one half of the time the displacement is at the maximum, the velocity is zero and the acceleration is again at its maximum value but it has the opposite sign. This process is reversed in the last half of the time as the function returns to its original velocity and position at the full time interval. There is a problem with this approach. At time equal to zero the input function has the acceleration maximum and the two bodies are at rest, This discontinuity is what sets off all initial oscillation in the solutions.

In the description of the applied loads, the 0.002 second haversine is refereed to as a rather gentile input. This is a relative statement, which needs to be clarified. The maximum acceleration is 48,000 meters per second per second or structure, about 5000 g. But in this small size the simple contact stress in only 16.1 mPa which is small when compared to the usual gun steel with a static yield stress of about 1000 mPa. The system also has a first natural frequency, which ranges from 18k to 24k Hz depending on which contact surface is engaged. When the period of the haversine is reduced to 0.0002 seconds the acceleration and simple contact stress increase by a factor of 100 but the natural resonant frequencies do not change and the increase in yield strength is open to question. This brings up the concept that of the importance of size or scale when evaluating the importance of dynamic effects.

The results of this study show that correlation between the contact stress and the acceleration of the slug vary with different time frames. At the longer time frames the correlation is excellent for the bonded and zero gap solutions. However at the shortest interval the correlation is poor in all cases and the single and double gap cases have little correlation at all. With all of this the maximum contact stress usually does not exceed two or three times the simple quasi-static value. This would be within the normal safety factors and would probable only present a failure problem for the most extreme cases. This tend to support the idea that, the presents of the gaps would make the response more complex but may not present sever failure problems.

CONCLUSION

This numeric experiment did not produce the desired result and excessively large contact stresses were not produced. The results show a moderate amplification factor, for contact stress, remarkably close to the 2.0 factor which is given in many undergraduate text books. However the results do become much more complex as the loading speed is increased and the gaps become larger. This tends to support the result which is often seen in the field where the result may be complex but not catastrophic. The acceleration data shows a somewhat different result in which the amplification factor is larger and the signal is also more complex.

ACKNOWLEDGMENTS

The author wishes to thank the management and staff of the U.S. Army Benet Laboratories for the opportunity to complete this investigation and Mr. James Bendick for his support of my work.

REFERENCES

1. G. P. O'Hara, "Dynamic Analysis of a 155 mm Cannon Breech," *Proceedings of the 9 Th. US Army Gun Dynamics Symposium, Mc Lean Vairginia,* , 13-1 – 13-10, Nov. 1998
2. ABAQUS Users Manual Version 5.8, Hibbitt, Karlson & Sorensen Inc. 1080 Main St. Pawtucket RI, 1998
3. ABAQUS Theory Manual Version 5.8, Hibbitt, Karlson & Sorensen Inc. 1080 Main St. Pawtucket RI, 1998, PP 2.4.1-1 – 2.4.1-7

PROPAGATION OF LONGITUDINAL WAVES IN A GUN BARREL

I. Randrianangaly[1], J. Renard[2], B. Campion[1], and E. Petitpas[1]

[1] GIAT Industries,7, route de Guerry, 18 023 BOURGES Cedex, France
[2] Laboratoire Energétique, Explosions, Structures, Université d'Orléans , 63, av de Lattre de Tassigny, 18 020 BOURGES Cedex, France

Very high stresses could occur in long gun barrel wall during firing. The stresses induced are due to the propagation of axisymmetric longitudinal waves along the barrel. To study this propagation, the tube was modelled using medium thickness shell elements. The equations of motion thus obtained were discretised using the centred finite difference method and resolved explicitly using a specifically designed computer programme. The latter outputs the displacements and stresses for all nodal points in the barrel, at any time during the firing cycle. Validation against experimental results gave very good agreement. A parametric study was then contucted to evaluate the influence of certain parameters. Finally, the limits of the model were studied. The study was completed by comparison with finite element modelling.

INTRODUCTION

Currently, the design and analysis of gun barrels are done on the basis of the statics of continuous environments, that is, the barrel is dimensioned in such a way that it withstands a constant pressure in each section of the barrel, corresponding to the maximum firing pressure at that point. Premature wear of the barrels of certain weapons and the existence of high stresses in their wall at the moment of firing have been found.

The technical literature attributes the excessive stresses in the barrel's wall to a longitudinal propagation of axisymmetric waves. This phenomenon is shown and described qualitatively by several documents [1], [2], [3] and [4] and analytical and experimental studies have been published about it.

Since the mid-50s, several analytical formulations have been published about the longitudinal vibrations of a barrel ([5], [6], [7], [8], [9] and [10]).Nevertheless, in these studies, very restrictive hypotheses are made, particularly on the geometry of the barrel and its loading. In particular, most of the studies consider an infinitely long or semi-infinite barrel and do not therefore manage any boundary condition. Moreover, the barrel is more often than not modelled by a thin shell, always of constant thickness whereas, in a weapon barrel, the thickness is never constant. Furthermore, a weapon barrel is very thick by the breech and thin at the muzzle. These geometric hypotheses are therefore not at all realistic in the case of a weapon barrel. Moreover, the velocity of the projectile and the pressure are not constant values : they are functions of time whereas the models reported in the literature assume them to be constant. Finally, contrary to what is represented in these models, the barrel is not free and open at its two ends : it is linked to the breech, whose mass is not inconsiderable and on which a pressure is applied.

From the numerical point of view, all the published studies ([9], [2], [11], [4], [12])are done on the basis of commercial finite element software programs, supplemented in order to be able to model a moving pressure front. In this way, it has been possible for simulations of actual cases to be carried out : this time, the pressure, the geometry of the barrel, the velocity of the projectile and the boundary conditions at the muzzle are realistic. Nevertheless, the munition itself is not taken into account. Only the moving pressure front is modelled on the basis of the actual, calculated or arbitrary curves (square wave). The friction and driving of the munition in the barrel do not seem to be taken into account.

Moreover, as in the analytical models, the breech is not modelled : the barrel is simply locked axially. In this way, neither the inertia due to the mass of the breech nor the pressure which is applied on it is modelled. Moreover, this type of modelling is troublesome to implement : finite element software programs such as ABAQUS require very powerful computers and very considerable computing times. Furthermore, a finite element model is difficult to modify : the slightest change of geometry means that the meshing has to be redone, which is not compatible with a dimensioning procedure or with a parametric study. Finally, several parameters of the computation need to be fixed precisely : for example, the fineness of the meshing or the minimum temporal increment. Indeed, if these two parameters are incorrectly evaluated, the high frequencies cannot be observed ; conversely, if they are too fine, the computing time and the size of the files may well be very considerable. However, in view of the computing times, it is impossible to do a scan of these parameters in order to find their optimum values. Finally, it is impossible to dissociate the forces so as to judge their respective influence.

The only way to overcome these disadvantages is to develop a tool specifically suited to weapon barrels, on the basis of the equations of motion of the barrel dynamically. This tool will make it possible to understand the phenomena, to do the initial simulations and to evaluate thus certain parameters like the fineness of the meshing. These computations could then possibly be supplemented and validated by well chosen finite element simulations.

MODELLING

So as to be able to quantify these phenomena, a model of the barrel was developed. To do this, various hypotheses were advanced.

The first is an axisymmetry hypothesis. Indeed, besides the axisymmetry of geometry, since flexion waves are propagated far more slowly than axisymmetric waves, it is possible to consider that the two motions are decoupled. Moreover, it has been shown numerically [10] that during the internal ballistics phase, the effects of flexion are relatively unimportant for high velocities of the projectile. Finally, Simkins [1] has shown by experiment that the phenomenon studied is perfectly axisymmetric.

Secondly, so as to take account of the internal pressure and of the phenomenon of friction of the munition in the barrel, it is necessary to model it either in shell form or on the basis of the complete three-dimensional theory. Various studies have been published about this, for various theories of shells, and the results have been compared with the three-dimensional theory. In view of the small difference obtained, because the distribution of the stresses in the thickness of the barrel does not interest us here, the Midlin-Reissner theory of shells, or complete theory, was chosen. It takes account of the transverse shear and of the rotational inertia of the straight section of the barrel, so as to model «medium thickness» shells. Moreover, a correction on the radial stress was added to the model, for a more faithful modelling of the thickest barrels.

Thirdly, the barrel is considered to be uniform, and its behaviour is assumed to be elastic.

The lining is not taken into account and the barrel is therefore assumed to be homogeneous.

Finally, American studies including Simkins's in 1978 [13],show that the boundary conditions which exist on a large-calibre weapon before firing are no longer valid during the ballistics phase. The links at the fixing parts seem far from being rigid. In fact, it was found that an excellent agreement between the calculated and experimental self-frequencies can be observed only if the barrel is considered to be free during its ballistics phase. This hypothesis remains valid so long as the displacements of the barrel are less than the plays of the fixing parts.

Various forces are applied on the barrel during the internal ballistics phase.

The friction forces of the projectile on the barrel are represented, in an initial approximation, by a surface distribution of forces which is assumed to be constant depending only on the material of the band, applied on the inner surface of the barrel in contact with the band.

The computation of the pressure forces is carried out on the basis of actual pressure curves at the base and at the breech, a linear interpolation being done at each moment between the two curves.

Furthermore, the breech is taken into account in this model in two ways : by the pressure which is applied on it and by the mass it represents.
In view of the preceeding hypotheses, equations were found for the problem using Hamilton's principle, based on a balance of the system's energy. Mathematical simplifications were carried out, in keeping with the previously formulated geometric hypothesis.
The barrel is assumed to be of length L, of mean radius R, and of thickness h, these two variables being capable of varying with the x-axis in the barrel. Because of the geometry of the problem, any point on the wall of the barrel is identified by its cylindrical co-ordinates r, θ, x. By designating by u and w the axial and radial components of the displacement vector of a point of the neutral axis of the wall of the barrel, and by ψ the angle of rotation of the straight section at the same point, applying Hamilton's principle leads to a system of equations of motion :

$$\rho\cdot\left(R^2\cdot h-\frac{h^3}{12}\right)\cdot\ddot{u}=\frac{E}{1-\nu^2}\cdot\left[\begin{array}{l}\left(R^2-\frac{h^2}{4}\right)\cdot h'\cdot u'+\left(R^2\cdot h-\frac{h^3}{12}\right)\cdot u''+\nu\cdot(R\cdot h'-R'\cdot h)\cdot w\\ +\left(-R^2\cdot R''\cdot h-R^2\cdot R'\cdot h'+R''\cdot\frac{h^3}{12}+R'\cdot\frac{h^2}{4}\cdot h'\right)\cdot\psi\\ +\nu\cdot h\cdot R\cdot w'-R'\cdot\left(R^2\cdot h-\frac{h^3}{12}\right)\cdot\psi'\end{array}\right]$$
$$-\frac{\nu}{1-\nu}\cdot\frac{(2R-h)^2(4R+h)}{64\cdot R^3}\cdot\left(R^2\cdot h-\frac{h^3}{12}\right)\cdot p'$$
$$-\frac{\nu}{1-\nu}\cdot\frac{2R-h}{64\cdot R^4}\cdot\left(\begin{array}{l}6\cdot R^3\cdot R'\cdot h^2-8\cdot R^4\cdot h\cdot h'-6\cdot R^3\cdot h^2\cdot h'\\ +8\cdot R^5\cdot h'+3\cdot R^2\cdot R'\cdot h^3+R^2\cdot h^3\cdot h'\\ +\frac{1}{2}\cdot R\cdot h^4\cdot h'-\frac{1}{2}\cdot R\cdot R'\cdot h^4-\frac{1}{4}\cdot R'\cdot h^5\end{array}\right)\cdot p$$
$$+h\cdot\kappa\cdot G\cdot R\cdot(w'+\psi)+(R+\frac{h}{2})\cdot(R-\frac{h}{2})\cdot q \qquad (1)$$

$$\rho\cdot R\cdot h\cdot\ddot{w}=-\frac{E}{1-\nu^2}\cdot\left[\ln\left(\frac{2R+h}{2R-h}\right)\cdot w+\nu\cdot h\cdot u'-\nu\cdot R'\cdot h\cdot\psi\right]+\cdot\left(R-\frac{h}{2}\right)\cdot p$$
$$+\kappa\cdot G\cdot\left((R'\cdot h+R\cdot h')\cdot w'+R\cdot h\cdot w''+(R'\cdot h+R\cdot h')\cdot\psi+R\cdot h\cdot\psi'\right) \qquad (2)$$
$$+\frac{\nu}{1-\nu}\cdot\frac{(2R-h)^2(4R+h)}{64\cdot R^3}\cdot h\cdot p$$

where E is the Young Modulus of the barrel material, ν its Poisson ratio and G its shear modulus.

$$\rho\cdot\frac{h^3}{12}\cdot\left(\frac{h^3}{12}-R^2\cdot h\right)\cdot\ddot{\psi}=\frac{E}{1-\nu^2}\left[\begin{array}{l}\left(\frac{h^3}{12}\cdot(R'\cdot h+R\cdot h')-R\cdot h^2\cdot\left(\frac{h\cdot h'}{4}+R\cdot R'\right)\right)\cdot u'\\+\nu\cdot\left(h'\cdot\frac{h^3}{12}-R\cdot R'\cdot h^2\right)\cdot w+\nu\cdot h\cdot\frac{h^3}{12}\cdot w'\\+\left(R'\cdot R\cdot h^2\left(R'\cdot R+\frac{h\cdot h'}{4}\right)-\frac{h^3}{12}\left(R'^2\cdot h+R\cdot R'\cdot h'\right)\right)\psi\\\left(\frac{h^2}{4}\cdot\frac{h^3}{12}\cdot h'-2\cdot R\cdot R'\cdot h\cdot\frac{h^3}{12}-R^2\cdot\frac{h^3}{4}\cdot h'\right)\cdot\psi'\\+\frac{h^3}{12}\cdot\left(\frac{h^3}{12}-R^2\cdot h\right)\cdot\psi''\end{array}\right]$$

$$+h^2\cdot\kappa\cdot G\cdot R^2\cdot(w'+\psi)+\left(\frac{h^3}{12}+R\cdot h^2\right)\cdot(R-\frac{h}{2})\cdot q$$

$$-\frac{\nu}{1-\nu}\cdot\frac{2R-h}{64\cdot R^3}\cdot\left[\begin{array}{l}20\cdot R^3\cdot R'\cdot\frac{h^4}{12}-2\cdot R^2\cdot R'\cdot\frac{h^5}{12}+4\cdot R^3\cdot\frac{h^4}{12}\cdot h'\\+2\cdot R^2\cdot\frac{h^5}{12}\cdot h'-16\cdot R^4\cdot\frac{h^3}{12}\cdot h'-R\cdot R'\cdot\frac{h^6}{12}\\-8\cdot R^5\cdot R'\cdot h^2+2\cdot R^4\cdot R'\cdot h^3\end{array}\right]\cdot p \qquad (3)$$

The equations of motion of the problem constitute a system of equations involving hyperbolic second-order linear partial derivatives. Knowing the state of the system at time t therefore makes it possible to predict its changes at time t+dt. The numerical method used here in order to arrive at the resolution of the problem is the centred finite difference method, combined with an explicit resolution, well suited to transient phenomena. After programming, the displacements, deformations and stresses are available at any node, and at any time during firing. The details of this finding of equations and programming are available in [14].

The software thus obtained runs in Windows, which makes for great user-friendliness and ease of use. The computing times were reduced to about twenty minutes on a Pentium 450 as against several weeks on an O_2 type Silicon Graphics work station, for a 6 metre barrel.

NUMERICAL VALIDATION

The numerical validation was done in several stages :

The first phase is a validation phase of the system of equations itself. This system was written in matrix form, and the diagonalisation of the matrix thus obtained supplied the frequencies and self-modes. These were then compared to the results of a modal analysis carried out by finite elements, using the ABAQUS software program. This comparison proved satisfactory. The maximum error on the frequency is only 5% at the 25th mode.

Subsequently, we checked, by programming the equations, that the self-modes and frequencies were indeed retained with time, which confirms the validity of the explicit scheme.
Computations by modal superposition were carried out, for simple cases, and the agreement proved to be good.
Finally, finite element computations made it possible to validate the modelling for more complex configurations. These computations were carried out with the ABAQUS software program. This software program was used with success in the technical literature, with a good correlation between experience and simulation. These results were the subject of an initial publication [15].
Fig 1 shows the changes in the axial displacement in a barrel of constant thickness as a function of time. This barrel is 400 mm long, with an internal radius of 60 and a constant thickness of 40. This mean thickness-to-radius ratio corresponds to the mean ratio of a large-calibre weapon barrel. A pressure front of 1 MPa, moving at a constant velocity of 1000 m/s travels through this barrel. This configuration corresponds to a test case, but permits very reduced computing times and therefore lends itself well to repeated calculations, necessary for validation. On this figure, the computation results for four different computation methods have been entered :
finite element method, using the ABAQUS software program,
finite difference method, with a correction on the radial stress which was nil, constant, or variable in the thickness.

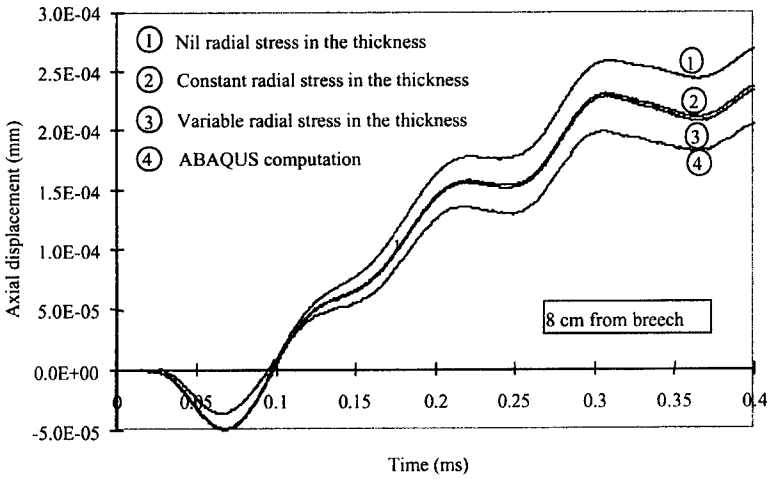


FIG 1 : AXIAL DISPLACEMENT 8 CM FROM THE BREECH OF THE 40 CM THICK BARREL

It is clear that, while the three methods give curves with the same trend, same frequency and same order of magnitude, the introduction of the radial stress permits a clear improvement in the results (the difference compared with the ABAQUS curve is halved). However, the fact of assuming this radial stress to be variable in the thickness does not change much.

Fig 2 shows the changes in the radial displacement with time of a point on the neutral axis of the same barrel. The agreement is clearly better than on the axial displacement, but the same findings can be made on the choice of computation method.

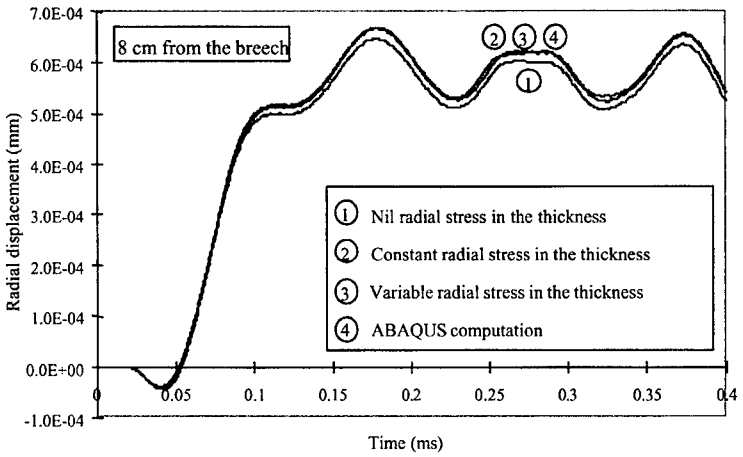


Fig 2 : RADIAL DISPLACEMENT 8 CM FROM THE BREECH OF THE 40 CM THICK BARREL

COMPARISON WITH EXPERIENCE

Once the numerical validation had been carried out, the results were compared with actual experience. To do this, results of firing with a 120 mm gun were used. The firing cycles were simulated for two different types of munitions, with for input data the pressure and kinematics curves of the projectile in the barrel obtained by experiment. The displacements at several points on the external skin of the barrel were obtained experimentally and compared to the numerical results. In the interest of confidentiality, the results in this paragraph will be given without any numerical values. Since the aim is to compare experience and simulation, this precaution does not affect the demonstration.
The curves in Fig 3 show the results obtained. The experimental curves were filtered after analysis, so as to eliminate the noise.

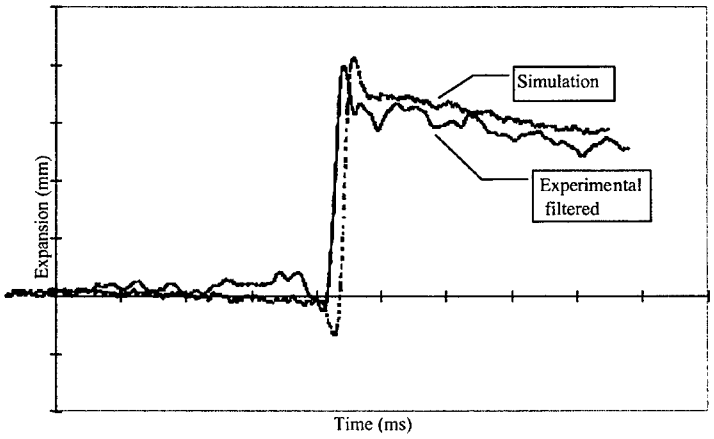


FIG 3 : COMPARISON BETWEEN EXPÉRIENCE AND SIMULATION

It is clear that the pressure rise moment, and the amplitudes and frequencies observed are completely similar numerically and experimentally.
The same agreement was found for all the rounds and for all the gauges, for both types of munitions.
Fig 4 shows the dynamic amplification of the expansion at several places on the barrel

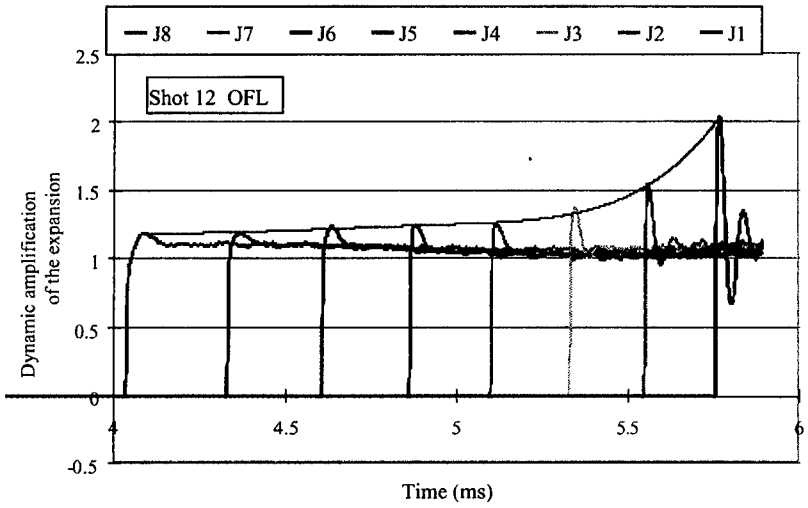


FIG 4 : DYNAMIC AMPLIFICATION OF EXPANSION AT SEVERAL PLACES ON THE BARREL

It can be seen that the closer one gets to the muzzle of the barrel, the greater the amplification.

The swell varies with the thinness of the barrel, the internal pressure and the velocity of the projectile. The first two points play a part in the static component of the swell. Their effects are therefore masked by the computation of the dynamic amplification. The increase in the amplification is therefore due only to the velocity of the projectile.
If one compares at each place the velocity of the projectile with the critical velocity, one notices that the ratio varies between 45 and 75%.

Now that the numerical simulation is validated numerically and experimentally, it can be used to evaluate the influence of certain parameters and to dissociate their effects.

SIMULATIONS AND PARAMETRIC STUDY

Qualitative analysis

So as to properly understand the phenomenon, it is useful to study qualitatively the dynamic response of a barrel in a simplified configuration. The influence of each parameter and each force can thus easily be determined. This analysis was also published in [15].
In the first instance, a barrel of constant thickness, through which a square wave type pressure front, moving at constant velocity, travels, is studied. Only the radial pressure is applied to the barrel: the forces due to the mass of the breech or to the pressure it undergoes are not taken into account ; neither are the forces produced by the interaction between the barrel and the band.

Fig 5 represents, in arbitrary co-ordinates, the changes in the profile of the barrel over its entire length as a function of time. It is clear that :
there is a vibratory phenomenon before and after the pressure front which superimposes itself on the swell of the barrel,
this precursor, with a damped sinusoid trend, is propagated more quickly than the pressure front, is reflected at the muzzle, and disrupts the initial signal,
at the rear of the pressure front, waves with an amplified sinusoid trend are constructed, disrupted on the one hand by the edge effect at the breech and on the other hand by the wave reflected at the muzzle,
the barrel is shortened at its two ends, because of the Poisson effect.

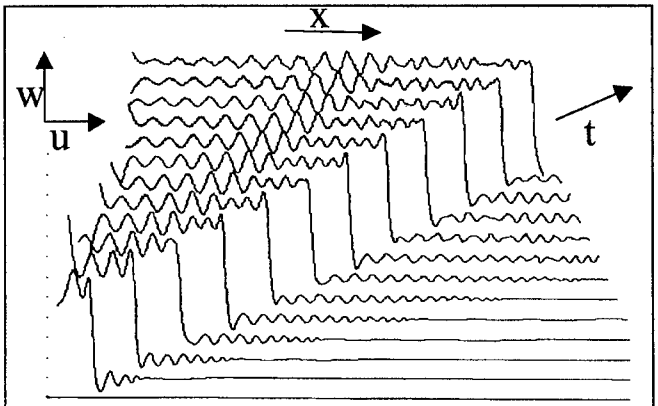


FIG 5 : TREND OF THE DEFORMATION OF BARREL WITH TIME

Fig 6 shows the axial (u) and radial (w) displacements as well as the angle of rotation of the straight section of the barrel (ψ) as a function of the x-axis (horizontal axis) and of time (vertical axis). The position of the pressure front is marked with a line.

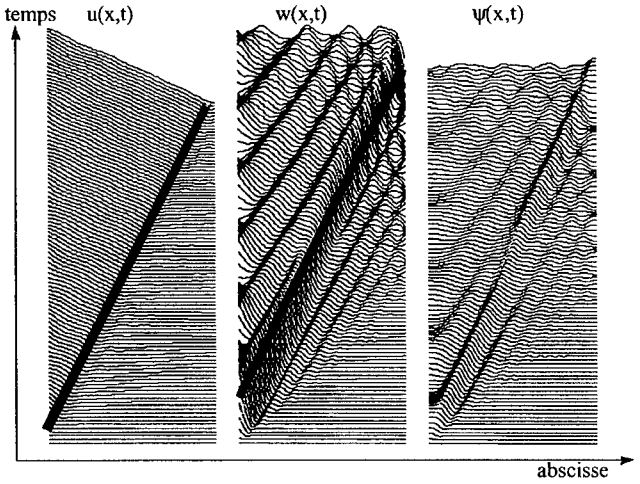


FIG 6 : DISPLACEMENTS AS A FUNCTION OF X-AXIS AND TIME

These graphs make it possible to show clearly the wave which is propagated ahead of the pressure front, as well as its damped sinusoid trend. Similarly, the amplified sinusoid present to the rear of the front is perfectly visible. These findings are present in the three graphs, even though the phenomena are more marked on radial displacement.

Model used for the simulations

In order to study the phenomenon more precisely, and to estimate the influence of the parameters, it is necessary to take realistic orders of magnitude. To do this, a 5 metre barrel with an internal radius of 60 mm and a thickness varying between 90 and 20 mm was chosen (Fig 7).

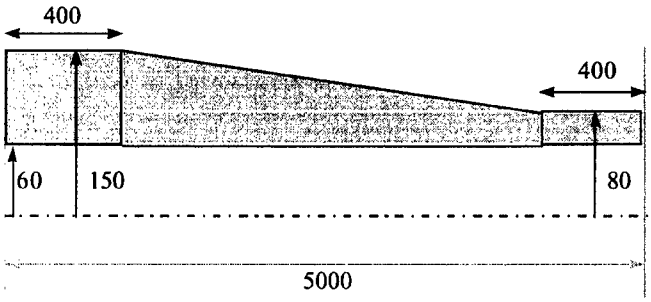


FIG 7 : PROFILE OF THE BARREL USED FOR THE PARAMETRIC STUDY

A square wave type pressure profile is modelled here.
The velocity of the projectile is assumed to vary linearly over the length of the barrel and is chosen in such a way that the muzzle velocity is between 1500 and 2700 m/s.
The friction forces between the projectile's band and the barrel are assumed to be constant and applied on the inner surface of the barrel in contact with the band. In some configurations, a contact pressure was added to the model.
Finally, the forces at the breech are modelled : the pressure and the inertial forces are taken into account.

Influence of the forces

Fig 8 shows the influence of the breech on the Von Mises equivalent stress. All these curves were produced under the same computation conditions. One notes that the most influential parameter is the breech pressure, which disrupts the signal fairly strongly, clearly increasing the amplitude of the oscillations. Mc is breech mass, and Pc represents pressure et breech.

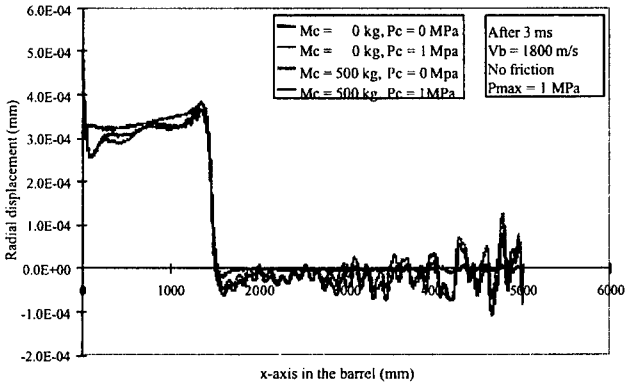


FIG 8 : INFLUENCE OF THE BREECH MASS ON THE RADIAL DISPLACEMENT

The mass of the breech changes only the axial displacement, limiting the rigid body motion associated with the weapon's recoil.

Influence of the velocity

Numerous bibliographical references ([6], [7], [8], [1] and [14]) show, using a quasi-stationary model, the existence of four particular velocities of the projectile in the barrel :

- the propagation velocity of the longitudinal waves in a thin plate,
- the propagation velocity of the longitudinal waves in a bar,
- the propagation velocity of the shear waves,
- a propagation velocity particular to each barrel.

The first three velocities depend only on the barrel's material; the last one depends in addition on its geometry. Of these four particular velocities, the second one and the last one lead to unlimited displacements and can therefore be qualified as critical. A quick calculation shows that the lowest critical velocity is the only one which can be approximated in the case of a weapon barrel. As this velocity depends on the geometry of the barrel, it is necessary to evaluate it at all points on the barrel. To do this, as the expression given by [8] was established in the case of a barrel with constant thickness, it is necessary to consider that the barrel is in fact a series of sections of constant thicknesses.

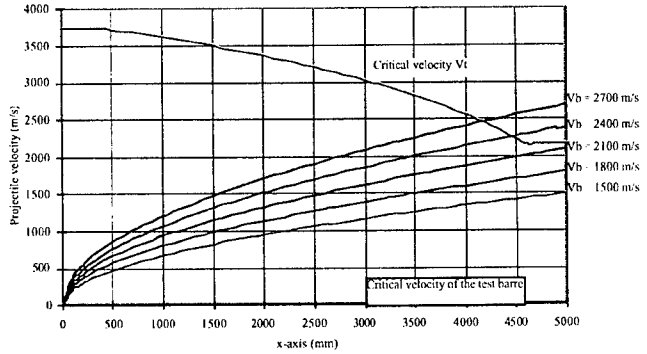


Fig 9 : LOWEST CRITICAL VELOCITY OF THE TEST BARREL

Such a calculation leads to the first curve of Fig 9. On this figure, the trend of the velocity of the munition as a function of the x-axis has been superimposed for several values of the muzzle velocity. The first two velocity values tested are therefore sub-critical throughout the internal ballistics phase. The value of 2100 m/s may well lead to critical conditions, whereas the two largest values of the velocity will be in turn sub-critical, critical and super-critical. The response of the barrel for all these projectile velocities will therefore make it possible to test the three velocity conditions.

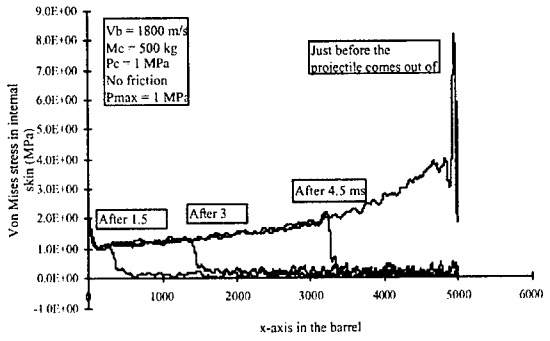


Fig 10 : RADIAL DISPLACEMENT FOR Vb = 1800 m/s

When the muzzle velocity is 1800 m/s, the radial displacement is clearly amplified at the muzzle, just before the projectile comes out of the barrel. The calculation of the dynamic amplifications shows at this point values of about 1.7 in radial displacement, and 2.5 in Von Mises stress. This amplification does not appear as an isolated peak, but indeed as an amplified sinusoidal oscillation. Even though, from Fig. 10, the velocity of 1800 m/s is still clearly sub-critical (about 83% of the critical velocity at the muzzle), the influence of the critical velocity begins to make itself felt, and the dynamic amplification phenomenon is constructing itself.

When the muzzle velocity reaches 2100 m/s (i.e. 96.8 % of the critical muzzle velocity), the dynamic amplification at the muzzle when the projectile comes out of the barrel exceeds 2.5 in radial displacement and 5 in Von Mises stress. This amplification (

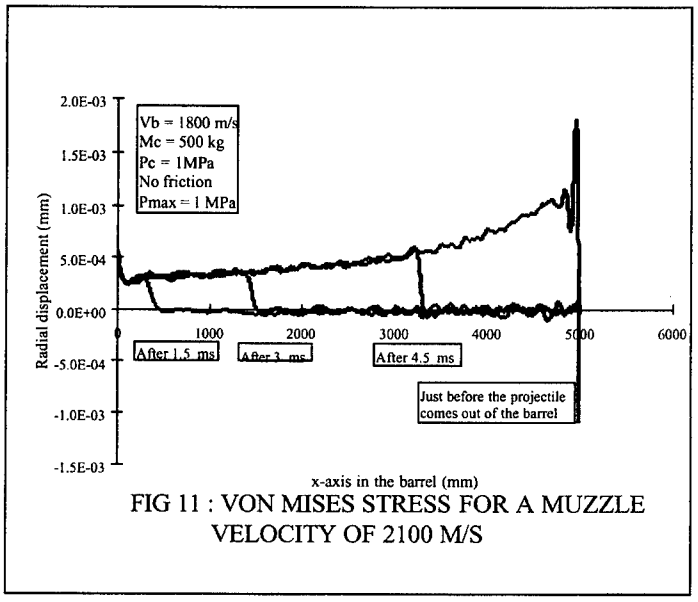


FIG 11 : VON MISES STRESS FOR A MUZZLE VELOCITY OF 2100 M/S

Fig 11) constructs itself in the same way as when the muzzle velocity is 1800 m/s, and always has the trend of an amplified sinusoid. The conditions in this case can be qualified as critical.
For a muzzle velocity of 2400 m/s, Fig 9 shows that the critical velocity is reached, then exceeded.

shows the changes in the radial displacement of the neutral axis of the barrel as a function of the x-axis, at various times. A numerical calculation shows that the critical velocity is reached by the munition at time t=3.94 ms, which means that the munition's band is at about 4470 mm. At 3.75 ms, the munition velocity is therefore still sub-critical, but the amplification is already very clear. The last curve of shows the deformation just before the munition comes out of the barrel. The muzzle velocity is here

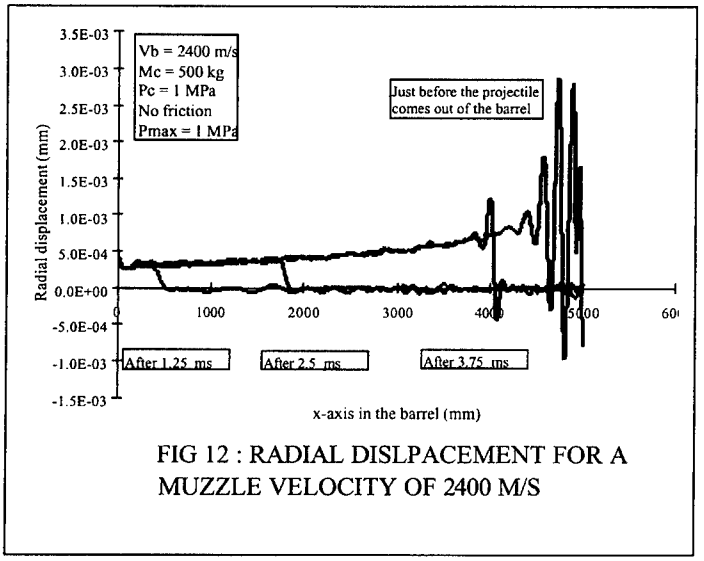


FIG 12 : RADIAL DISLPACEMENT FOR A MUZZLE VELOCITY OF 2400 M/S

super-critical. Just before the munition comes out of the barrel, the dynamic amplification is 3 in radial displacement and 4 in Von Mises equivalent stress.

CONCLUSION

The aim of this study was twofold : on the one hand, to understand and study the longitudinal propagation of waves in a weapon barrel and, on the other hand, to produce a simulation tool suitable for a weapon barrel whose purpose, in time, is to help to dimension barrels dynamically. The results of validation and especially of comparison with actual experience have shown that the modelling implemented is true to reality, both from the points of view of amplitudes and of the frequential content of the barrel's response. The preponderant effects are therefore well represented. The simulation tool developed is therefore validated for studying dynamic amplifications in weapon barrels. Furthermore, this tool has been designed to be user-friendly, easy to use and fast. It is therefore well suited for a parametric study or for a dimensioning procedure.

ACKNOWLEDGEMENTS

This work was carried out in conjunction with the University of Orléans Structures, Explosions and Energy Laboratory, and funded by the DGA. Their assistance is gratefully acknowledged.

REFERENCES

1 **SIMKINS, T.E.** - *Travelling waves resonance in gun tubes.* - Watervliet (N.Y.) : U.S. Army armament research, development and engineering center, Benet Laboratories, 1987, 12 p - Final report N° RPT ARCCB-TR-87028

2 **HASENBEIN, R.G., GABRIELE, A., FINLAYSON, D., ARTUS, B., CUNNINGHAM, C., AND GAST, R.**- Dynamic strain waves : a development perspective.- *In proceedings of the sixth U.S. Army Symposium on gun dynamics*, 1990, p. 286-297

3 **SIMKINS, T.E.** -Dynamic strains in a 60 mm gun tube - an experimental study - *In proceedings of the sixth U.S. Army Symposium on gun dynamics*, 1990, p. 252 - 271

4 **HASENBEIN, R. AND HYLAND, A.** - Dynamic strain waves and bore enlargement.- *Proceedings of the seventh U.S. Army Symposium on Gun Dynamics*, 1993, p. 504-529

5 **HERMANN, G. AND MIRSKY, I.**- Three dimensional and shell theory analysis of axially symetric motions of cylinders - *Journal of Applied Mechanics* - Dec 1956, p.563-568

6 **JONES, J.P. AND BHUTTA, P.G.** - Response of cylindrical shells to moving pressure loads. - *Journal of Applied Mechanics*, 1964, Vol. 86, p. 105-111

7 **TANG, S.C.** - Dynamic response of a tube under moving pressure. - *Journal of the Engineering Mechanics Division*, 1965, Vol. 115, p. 97-122

8 **RENARD, J.** - *Réponse d'un confinement circulaire mince à une onde de pression (Response of a circular confinement to a pressure wave)* – State Thesis : University of Orléans, 1986, 157 p

9 **SIMKINS, T.E.** - *The influence of transient flexural waves on dynamic strains in gun tubes* - Watervliet (N.Y.) : U.S. Army armament research, development and engineering center, Benet Laboratories, 1989, 34 p - Final report N° RPT ARCCB-TR-89020

10 **TADJBAKHSH, I.G. AND YUAN-AN S.** - Transient vibrations and instability in flexible guns - *Proceedings of the sixth U.S. Army Symposium on Gun Dynamics*, 1990, p. 199-229

11 **HOPKINS, D.A..**- *Predicting dynamic strain amplification by coupling a finite element structural analysis code with a gun interior ballistic code* - Aberdeen Proving Ground (M.D.) :. Army armament research and development Command center, Ballistic Research Lab-1991 Final report N° ARBRL-CR-3269, 25 p

12 **SIMKINS, T.E.** - Beating the critical velocity problem - *In proceedings of the eighth U.S. Army Symposium on gun dynamics*, 1996, p. 29-1 - 29-11

13 **SIMKINS, T.E., SCANLON, R., PFLEGL, G**- *Radial and transverse response of gun tubes to travelling ballistic pressure* - Watervliet (N.Y.) : U.S. Army armament research, development and engineering center, Benet Laboratories, 1978, 14 p - Report N° 780609086

14 **RANDRIANANGALY, I.** – *Propagation longitudinale des ondes dans un tube (Propagation of longitudinal waves in a gun barrel)* – Doctoral thesis – University of Orléans – 1999, 166 p

15 **RANDRIANANGALY, I., RENARD, J., CAMPION, B., PETITPAS, E.** – *Apports d'un schéma explicite pour l'étude de la propagation d'ondes dans un tube d'arme (Input of an explanatory sketch to the study of the propagation of waves in a weapon barrel)* – Mécanique industrielle et matériaux - Dec. 1998, Vol. 51, n°4, p173 – 175

MAIN BATTLE TANK FLEXIBLE GUN TUBE DISTURBANCE MODEL THREE SEGMENT MODEL

Dr. Henry J. Sneck[1]

[1]U.S. Army Benet Labs, TACOM-ARDEC, Building #40, Watervliet, NY 12189-4050

A rational approach to disturbance rejection is proposed and applied to a simple three-degree-of-freedom flexible gun tube model using feedforward and feedback compensation. The first two natural frequencies of the pin-free and cantilever tube are matched by adjusting the dimensions of the rigid segments and the stiffness of the torsional springs that join them. It was found that, contrary to the previously analyzed two degree-of-freedom segment model, the muzzle-end segment could be stabilized by the proper choice of transfer functions and elevation driveline response. The analysis serves to establish the requirements for the transfer functions and stabilizing actuator systems.

INTRODUCTION

Modern tank cannon are long, relatively, thin, beam-like hollow cylinders. Their accuracy is, in part, determined by their flexibility, especially under dynamic loading. Very small deflections and rotations of the muzzle end can have a significant influence on the accuracy of the shot at long ranges. Muzzle motions induced by firing are inevitable, and difficult to control because of the time scale of the firing is of the order of milliseconds.

Another source of muzzle motion is the ground-induced motion of the vehicle. These motions, transmitted through the trunnions and gun actuators, can be quite large and have frequencies comparable to the natural frequencies of the tube. The time scales of these disturbances depend on the tank speed and on the nature of the terrain. They are typically of the order of seconds or longer. Sensing and actuation to control the influence of vehicle motion on the muzzle response might be possible, given these relatively long time scales. This raises two questions. First, is it possible to reject some, or all he ground motion disturbance from the muzzle motion? In a previous paper [1] it was suggested that not all of the disturbance could be rejected. Second, if the more comprehensive model used here indicates that all of the disturbance can be rejected, what is the required control strategy?

During a discussion with Dr. Purdy, author of Reference [2], he suggested that the fidelity of his two-segment flexible model, documented in Reference [1], was inadequate. He recommended that the tube should be divided into at least three segments, with intervening

torsional springs and dampers. The author is indebted to Dr. Purdy for this suggestion since this paper is the result of his recommendation.

EQUATIONS OF MOTION

Figure 1 shows the generic model of the tube and the various quantities that determine its dynamic behavior.

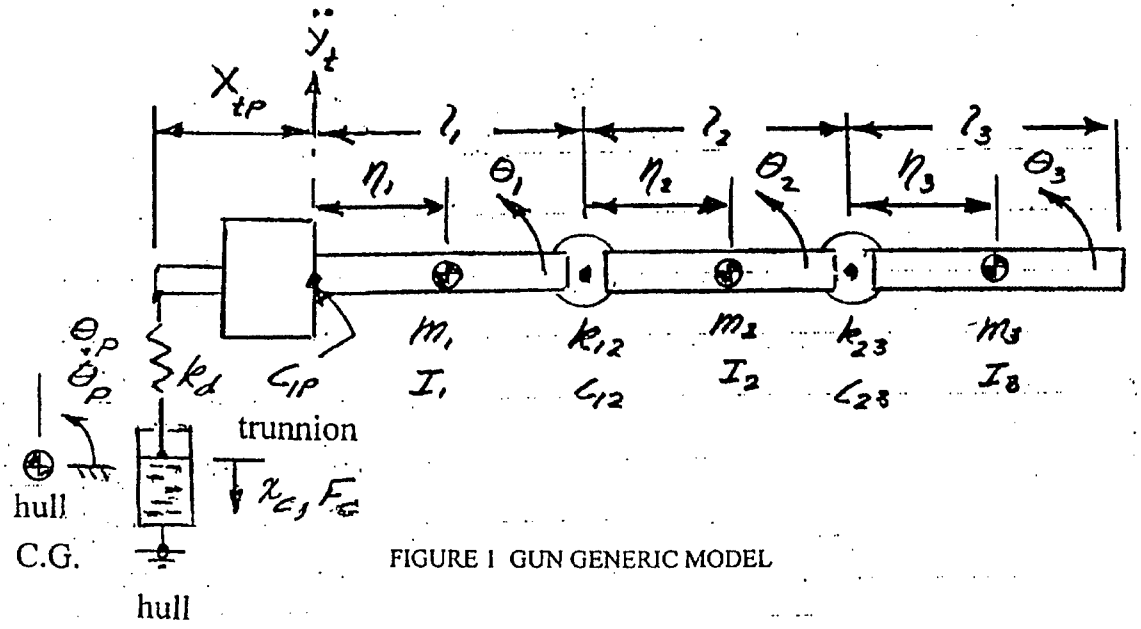


FIGURE 1 GUN GENERIC MODEL

A free body analysis of this model yields the classical dynamic equation,

$$[m]\{\ddot{\theta}\}+[c]\{\dot{\theta}\}+[k]\{\theta\}=\{I\} \qquad (1)$$

The elements of the mass, damping, and stiffness 3 x 3 matrices are shown Appendix A.

Purdy [3] has shown that the tube motion can be adequately modeled if the segmented model matches the pinned-free and cantilever frequencies of the mounted tube. Matching is accomplished by adjusting the size of the rigid segments and the stiffness' of their connecting torsional springs. The 2 x 2 matrices for the cantilever mode are given in Appendix B.

Transformation of Equation (1) into the frequency domain will allow its incorporation into the control strategy. Taking the Laplace transform of Equation (1) yields:

$$[a]\begin{Bmatrix} x_c(s) \\ \theta_1(s) \\ \theta_2(s) \\ \theta_3(s) \end{Bmatrix} = [I]\begin{Bmatrix} F_c(s) \\ s^2 y_t(s) \\ s\theta_p(s) \\ \theta_p(s) \end{Bmatrix} \tag{2}$$

The elements of [a] and [I] are listed in Appendix C. This equation relates the response vector on the left to the disturbance vector on the right. These vectors also contain the actuator force, F_c, and the actuator displacement, x_c, in addition to disturbances ($s^2y_t(s)$, $s\theta_p(s)$, $\theta_p(s)$) and the responses $\theta_1(s)$, $\theta_2(s)$, $\theta_3(s)$.

$$\begin{Bmatrix} x_c(s) \\ \theta_1(s) \\ \theta_2(s) \\ \theta_3(s) \end{Bmatrix} = \frac{1}{\det[a]}[C][I]\begin{Bmatrix} F_c(s) \\ s^2 y_t(s) \\ s\theta_p(s) \\ \theta_p(s) \end{Bmatrix} \tag{3}$$

where [C] is the transpose of the numerators of the cofactors of [a]. The elements of [C] and det [a] are listed in Appendix D.

The final step in the preparation of the dynamic equations is to perform the operation

$$\frac{1}{\det[a]}[C][I] = [B] \tag{4}$$

where the elements of [B] can be found in Appendix E.

The result of these straight forward, but laborious manipulations, is an equation for the response to the disturbance in terms of the properties of the model contained in [B], i.e.,

$$\begin{Bmatrix} x_c(s) \\ \theta_1(s) \\ \theta_2(s) \\ \theta_3(s) \end{Bmatrix} = [B]\begin{Bmatrix} F_c(s) \\ s^2 y_t(s) \\ s\theta_p(s) \\ \theta_p(s) \end{Bmatrix} \tag{5}$$

Of course it was known at the outset that Equation (1) could be put into this form. This section merely provides the details of how this transformation is performed, and documents the intermediate steps and their components.

FEEDBACK AND FEEDFORWARD CONTROL

The portion of the response due to the applied actuating force is

$$\begin{Bmatrix} x_c(s) \\ \theta_1(s) \\ \theta_2(s) \\ \theta_3(s) \end{Bmatrix} = \begin{bmatrix} B_{11} \\ B_{21} \\ B_{31} \\ B_{41} \end{bmatrix} F_c = [G_p] F_c \qquad (6)$$

where $[G_p]$ is the "plant" transfer function.

The portion of the response due to the disturbance is

$$\begin{Bmatrix} \chi_c(s) \\ \theta_1(s) \\ \theta_2(s) \\ \theta_3(s) \end{Bmatrix}_p = \begin{bmatrix} B_{12} & B_{13} & B_{14} \\ B_{22} & B_{23} & B_{24} \\ B_{32} & B_{33} & B_{34} \\ B_{42} & B_{43} & B_{44} \end{bmatrix} \begin{Bmatrix} s^2 y_t(s) \\ s\theta_p(s) \\ \theta_p(s) \end{Bmatrix} = [G_d]\{D\} \qquad (7)$$

where $[G_d]$ is the disturbance transfer function and {D} is the disturbance vector.

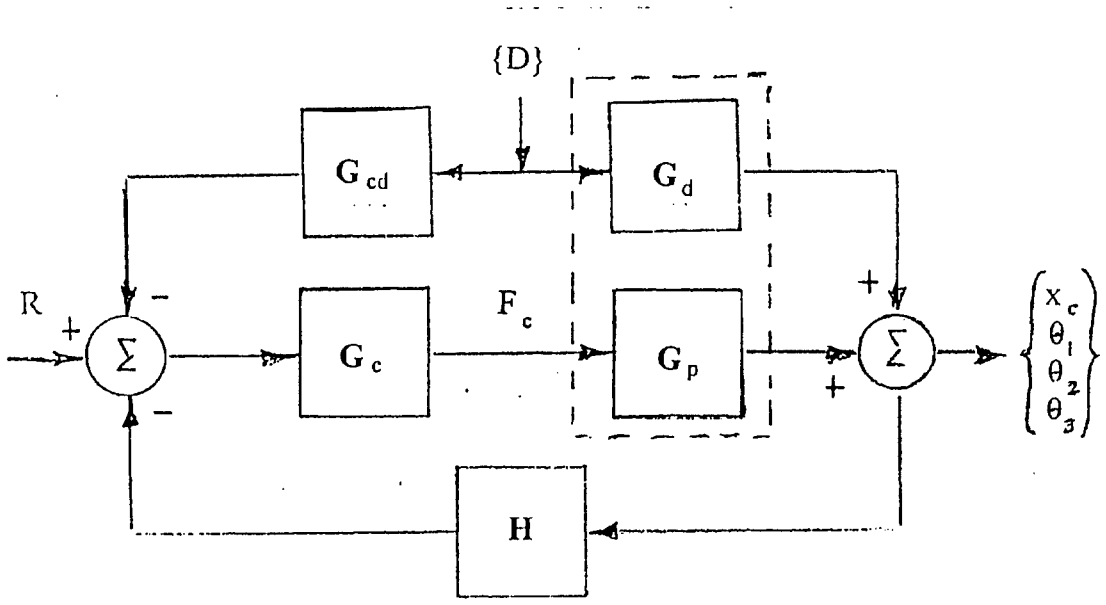


FIGURE 2 BLOCK DIAGRAM OF GUN TUBE SYSTEM

Figure 2 is a block diagram of the gun tube system with a gain G_c, feedback H, feedforward G_{cd}, and reference signal, R. Because R is a scalar the feedforward transfer function is a row vector, i.e.

$$[G_{cd}] = [G_{11}\ G_{12}\ G_{13}] \qquad (8)$$

Assuming that the tube rotations at the trunnions and the muzzle can be sensed, the feedback transfer function is also a row vector, i.e.,

$$[H] = [0 \quad G_{22} \quad 0 \quad G_{24}] \tag{9}$$

Now referring to Figure 2 the response to the disturbance for the controlled system is

$$[[G_d] - [G_p][G_c][G_{cd}]]\{D\} = [[I] + [G_p][G_c][H]]\{\theta_D\} \tag{10a}$$

or in abbreviated notation

$$[d]\{D\} = [q]\{\theta_D\} \tag{10b}$$

The final step in these manipulations is to solve for the response to the disturbance, which is

$$\{\theta_D\} = [q]^{-1}[d]\{D\} = \frac{1}{\det[q]}[r]^T[d]\{D\} \tag{10c}$$

where [r] is the matrix of the cofactors of [q].

The matrices $[r]^T$ and [d] are given in Appendix F. It is interesting to note that [d] contains only the feedforward transfer functions G_{11}, G_{12}, and G_{13}, while [r] and det [q] contain only the feedback transfer functions, G_{22}, and G_{24}.

DISTURBANCE REJECTION

Referring to Appendix F the expanded version of Equation (10c) is

$$\begin{Bmatrix} x_c(s) \\ \theta_1(s) \\ \theta_2(s) \\ \theta_3(s) \end{Bmatrix}_D = \frac{1}{\det[q]} \begin{bmatrix} r_{11} & r_{21} & 0 & r_{41} \\ 0 & r_{22} & 0 & r_{42} \\ 0 & r_{23} & r_{33} & r_{43} \\ 0 & r_{24} & 0 & r_{44} \end{bmatrix} \begin{bmatrix} d_{11} & d_{12} & d_{13} \\ d_{21} & d_{22} & d_{23} \\ d_{31} & d_{32} & d_{33} \\ d_{41} & d_{42} & d_{43} \end{bmatrix} \begin{Bmatrix} s^2 y_t(s) \\ s\theta_p(s) \\ \theta_p(s) \end{Bmatrix} \tag{10d}$$

where

$$\det[q] = 1 + B_{21} G_c G_{22} + B_{41} G_c G_{24} \tag{11}$$

To completely remove the effect of the disturbances on $\theta_3(s)_D$ requires that

$$r_{24}\, d_{21} + r_{44}\, d_{41} = 0, \tag{12a}$$

$$r_{24}\, d_{22} + r_{44}\, d_{42} = 0, \tag{12b}$$

$$r_{24}\, d_{23} + r_{44}\, d_{43} = 0, \tag{12c}$$

and

$$\det[q] \neq 0 \tag{12d}$$

One way to accomplish this is to let $G_{22} = 0$ so that

$$r_{24} = -B_{41}\, G_c\, G_{22} = 0 \tag{13}$$

and then choose

$$d_{41} = B_{42} - B_{41}\, G_c\, G_{11} = 0, \tag{14a}$$

$$d_{42} = B_{43} - B_{41}\, G_c\, G_{12} = 0, \tag{14b}$$

$$d_{43} = B_{44} - B_{41}\, G_c\, G_{13} = 0 \tag{14c}$$

so that

$$\det[q] = 1 + B_{41}\, G_c\, G_{24} = r_{11} = r_{22} = r_{33}, \tag{14d}$$

and

$$r_{44} = 1\,,\; r_{21} = r_{23} = r_{24} = 0 \tag{15}$$

The effect of this choice on the disturbance transfer function is

$$\frac{1}{\det[q]}[r]^T[d] = \frac{1}{r_{11}} \begin{bmatrix} r_{11} & 0 & 0 & r_{41} \\ 0 & r_{22} & 0 & r_{42} \\ 0 & 0 & r_{33} & r_{43} \\ 0 & 0 & 0 & r_{44} \end{bmatrix} \begin{bmatrix} d_{11} & d_{12} & d_{13} \\ d_{21} & d_{22} & d_{23} \\ d_{31} & d_{32} & d_{33} \\ 0 & 0 & 0 \end{bmatrix} \tag{16}$$

An alternative strategy is to let $r_{44} = 1 + B_{21}\, G_c\, G_{22} = 0$, and then choose $d_{21} = d_{22} = d_{23} = 0$ so that $\det[q] = B_{41}\, G_c\, G_{24} = r_{11} = r_{33}$. However, in the end the resulting disturbance transfer function is the same as created by Eq (16).

Since the fourth column of $[r]^T$ is eliminated by the matrix multiplication and det[q] = $r_{11} = r_{22} = r_{33}$, det[q] will be eliminated from the transformation.

IMPLEMENTATION

This analysis of the three-segment model indicates that model muzzle element can be stabilized by properly selecting the feedforward and feedback transfer functions. This is contrary to the finding for the lower order two-segment model [1]. Although the three-segment model only approximates the real tube, the results of this model are encouraging with respect to real tubes.

In order to achieve muzzle stabilization the breech-end of the gun must be actuated. Segments 1 and 2 will also rotate. These motions are determined by Equations (14) and Equation (16). All of the elements of [d] can be written in terms of the elements of [B]. Because $[r]^T$ acts like an identity matrix, the product $[r]^T[d]$ is quite simple. If the process is carried a step further the result can be put in terms of the elements of [C] with startling results, i.e., $d_{22} = d_{23} = d_{32} = d_{33} = 0$, and only $d_{11} = d_{12} = d_{13} = d_{21}$, and d_{31} are non-zero. The surviving elements are

$$d_{11} = \frac{1}{C_{14}\det[a]}\left(\left(C_{14}C_{31} - C_{11}C_{34}\right)I_{32} + \left(C_{14}C_{41} - C_{11}C_{44}\right)I_{42}\right) \quad (17a)$$

$$d_{21} = \frac{1}{C_{14}\det[a]}\left(\left(C_{14}C_{32} - C_{12}C_{34}\right)I_{32} + \left(C_{14}C_{42} - C_{12}C_{44}\right)I_{42}\right) \quad (17b)$$

$$d_{31} = \frac{1}{C_{14}\det[a]}\left(\left(C_{14}C_{33} - C_{13}C_{34}\right)I_{32} + \left(C_{14}C_{43} - C_{12}C_{44}\right)I_{42}\right) \quad (17c)$$

$$d_{12} = \frac{1}{C_{14}\det[a]}\left(C_{14}C_{21} - C_{11}C_{24}\right)I_{23} \quad (17d)$$

$$d_{13} = \frac{1}{C_{14}\det[a]}\left(C_{14}C_{21} - C_{11}C_{24}\right)I_{24} \quad (17e)$$

These transfer functions relate the disturbances to the responses. All of the C's are of order s^4 with the exception of C_{11}, which is of order s^6. Since there is no restraining torsional spring connecting the tube to the mount in the model s = 0 is a root of det[a]. Removing this rigid body factor from det[a] reduces it to order s^5.

TUBE MODEL PARAMETERS

The feedforward transfer functions depend on the length and mass properties of the segments, the torsional stiffness of the joining springs, and the torsional damping coefficients.

These are chosen so that the actual cantilever and pin-free mode shapes and natural frequencies are matched as closely as possible [3]. To simplify the matching process it is assumed that the damping is negligible. The first estimate of the segment lengths can be obtained by "fitting" the straight-line segments to the mode shapes obtained from a finite element model of the tube or other modal analyses. This fitting is best done by graphically overlaying the segments on plots of the mode shapes to estimate the segment lengths. The calculation of the mass properties of the segments can then be performed and these, along with the modal frequencies, inserted into the characteristic equations. The characteristic equations will then contain only the torsional stiffnesses as unknowns. The cantilever and pin-free equations are both quadratic so that the stiffness coefficients can be found directly. The degree of matching is determined by how close the cantilever and pin-free stiffnesses agree.

The characteristic equations for the cantilever and pin-free segments are given in Appendix G. Although the pin-free equation appears to be sixth-order it has a double root that is zero. The calculations for this trial-and-success process are easily implemented on a spreadsheet.

The XM291 tank gun was chosen for modeling because its mode shapes and frequencies were available from an existing, validated analytical model. Matching the stiffnesses proved to be surprisingly easy, requiring only modest adjustments to the first estimates of the segment lengths. Since all their frequencies (cantilever: 97.4 Hz, 40.35 Hz; pin-free: 25.08 Hz, 81.59 Hz) were inserted into the characteristic equations, they are matched exactly. The torsional stiffness for the pinned-free and cantilever modes were matched within 2% using the lengths l_1 = 6.0 ft, l_2 = 5.5 ft and l_3 = 6.0 ft. From this process the model torsional stiffness' $k_{12} = 3.6(10^6)$ lb ft/rad and $k_{23} = 1.69(10^6)$ lb ft/rad. were obtained

Dynamic analyses, [2], [3] have successfully modeled tube response using proportional damping, i.e. [c] = β[k]. In the case of the XM291 β = 0.0015 sec has been found to be reasonable. A reasonable estimate for trunnion damping is c_{1p} = 750 lb ft s/rad.

The first attempt to determine the feedforward transfer function using Equations (12) and (13) failed because the some of the roots of B_{41} were positive. This difficulty was eliminated by using the alternative strategy described above, with the following results.

$$r_{44} = 1 + B_{21} G_c G_{22} = 0 \tag{18}$$

$$G_c G_{11} = \frac{B_{22}}{B_{21}} \tag{19a}$$

$$G_c G_{12} = \frac{B_{23}}{B_{21}} \tag{19b}$$

$$G_c G_{13} = \frac{B_{24}}{B_{21}} \tag{19c}$$

The det [a] plays no role in these functions because it is canceled by ratioing the B's. Figures 3 and 4 show the Bode plots of $G_c G_{11}$ and $G_c G_{12}$. The transfer function $G_c G_{13}$ is zero so that θ_p is not fed forward. The numerators and denominators are all fifth order polynomials, so that the high and low frequency gains are bounded.

The feedback transfer function, $G_c G_{22}$, is shown in Figure 5. The remaining feedback transfer function, $G_c G_{24}$ plays no role in disturbance rejection in this case.

The elements of d_{22}, d_{23}, d_{32}, and d_{33} of [d] were found to be identically zero. The remaining no-zero elements of Equation (10d) and (16) yield the following response equations:

$$x_c = d_{11} s^2 y_t(s) + d_{12} s\theta_p(s) + d_{13}\theta_p(s) \qquad (20a)$$

$$\theta_1 = d_{21} s^2 y_t(s) \qquad (20b)$$

$$\theta_2 = d_{31} s^2 y_t(s) \qquad (20c)$$

Figures 6 through 10 show the transfer functions required by the equations above. Figures 9 and 10 show that affect of the trunnion acceleration on θ_1 and θ_2 is highly attenuated so that large angular displacements of the tube are not required to achieve stabilization.

Figures 6 through 8 are quite similar. It appears that the required x_c will depend largely on the trunnion acceleration and pitch rate at very low frequencies. There is a considerable attenuation of the disturbance inputs up to 100 rad/sec (~15 Hz) with a return to the low frequency levels at 10^3 rad/sec (160 Hz).

CONCLUSIONS

It appears that the results previously obtained with the two-segment model, [1], led to the erroneous conclusion that the effects of the disturbance could not be entirely repeated from the muzzle angular displacement. The analysis of the three-segment model presented suggests that this is possible, at least theoretically. Of course the unanswered question is "what would be revealed by a higher order multi-segmented model, and how many segments are enough."

On the practical side, it is certain that the transfer functions cannot be duplicated precisely. There are four of these that must be implemented with reasonable fidelity to achieve the predicted results of the three-segment model. That number, along with their input signals, indicates the magnitude of the task. While feedforward and feedback control has long been used in fire control it is hoped that this paper provides some guidance in their use when tube flexure is a consideration.

NOMENCLATURE

[a] - dynamic matrix

$[B] = [C]\,[I]$

$[c]$ = damping matrix

c_{12}, c_{23} = damping coefficients

c_{1p} = trunnion viscous friction coefficient

$[C]$ = cofactor matrix of $[a]$

$[d]$ = disturbance input matrix

$\{D\}$ = disturbance vector

F_c = elevation actuating force

G_c = scalar gain

G_{cd} = feedforward transfer function vector

G_d = disturbance transfer function

G_p = plant transfer function

G_{11}, G_{12}, G_{13} = feedforward transfer function vector components

G_{22}, G_{24} = feedback transfer function vector components

H = feedback transfer function vector

$[I]$ = forcing function matrix

$[k]$ = stiffness matrix

k_{12}, k_{23} = stiffness coefficients

k_d = drive line stiffness

l_1, l_2, l_3 = segment lengths

$[m]$ = mass matrix

$[q]$ = disturbance response matrix

x_c = elevation actuator displacement

X_{tp} = distance from trunnions to drive

y_t = vertical displacement of the trunnion

[r] = cofactor matrix of [q]

β = proportional damping coefficient

η_1, η_2, η_3 = center of mass coordinates

REFERENCES

1. Sneck, H.J., "An Assessment of Main Battle Tank Flexible Gun Tube Disturbance Rejection", Proc. 9th U.S. Army Symposium on Gun Dynamics, ARCCB-SP-99015, image No. 009, November 1998.

2. Purdy, D.J., "Modeling and Simulation of a Weapon Control System for a Main Battle Tank", Proc. 8th U.S. Army Symposium on Gun Dynamics, ARCCB-SP-96032, pgs 20-1 to 20-19, May 1996.

3. Purdy, D.J., "An Investigation into Modeling and Control Flexible Bodies", Ph.D. Thesis, Cranfield University, England, 1994.

APPENDIX A

$$[\mathrm{m}] = \begin{bmatrix} m_{11} & m_{12} & m_{13} \\ m_{21} & m_{22} & m_{23} \\ m_{31} & m_{32} & m_{33} \end{bmatrix}$$

$$m_{11} = I_1 + m_1\eta_1^2 + l_1^2(m_2 + m_3)$$
$$m_{22} = I_2 + m_2\eta_2^2 + m_3 l_2^2$$
$$m_{33} = I_3 + m_3\eta_3^2$$
$$m_{12} = m_{21} = m_2 l_1\eta_2 + m_3 l_1 l_2$$
$$m_{13} = m_{31} = m_3 l_1\eta_3$$
$$m_{23} = m_{32} = m_3 l_2\eta_3$$

$$[\mathrm{c}] = \begin{bmatrix} c_{12} & -c_{12} & 0 \\ -c_{12} & c_{12} + c_{23} & -c_{23} \\ 0 & -c_{23} & c_{23} \end{bmatrix}$$

$$[\mathrm{k}] = \begin{bmatrix} k_{12} & -k_{12} & 0 \\ -k_{12} & k_{12} + k_{23} & -k_{23} \\ o & -k_{23} & k_{23} \end{bmatrix}$$

APPENDIX B

$$[m_c] = \begin{bmatrix} m_{22} & m_{23} \\ m_{32} & m_{33} \end{bmatrix}; \quad [c_c] = \begin{bmatrix} c_{12} + c_{23} & -c_{23} \\ -c_{23} & c_{23} \end{bmatrix}; \quad [k_c] = \begin{bmatrix} k_{12} + k_{23} & -k_{23} \\ -k_{23} & k_{23} \end{bmatrix}$$

APPENDIX C

$$[a] = \begin{bmatrix} a_{11} & a_{12} & 0 & 0 \\ a_{21} & a_{22} & a_{23} & a_{24} \\ 0 & a_{32} & a_{33} & a_{34} \\ 0 & a_{42} & a_{43} & a_{44} \end{bmatrix}$$

$$a_{11} = k_d$$
$$a_{12} = a_{21} = -k_d X_{tp}$$
$$a_{24} = a_{42} = m_{13}s^2$$

$$a_{22} = m_{11}s^2 + (c_{12} + c_{1p})s + (k_d X_{tp}^{\ 2} + k_{12})$$
$$a_{23} = a_{32} = m_{12}s^2 - c_{12}s - k_{12}$$
$$a_{33} = m_{22}s^2 + (c_{12} + c_{23})s + (k_{12} + k_{23})$$
$$a_{34} = a_{43} = m_{23}s^2 - c_{23}s - k_{23}$$
$$a_{44} = m_{33}s^2 + c_{23}s + k_{23}$$

$$[I]=\begin{bmatrix} I_{11} & 0 & 0 & I_{14} \\ 0 & I_{22} & I_{23} & I_{24} \\ 0 & I_{32} & 0 & 0 \\ 0 & I_{42} & 0 & 0 \end{bmatrix}$$

$$I_{11}=1.0 \qquad I_{14}=-k_d X_{tp}$$

$$I_{22}=-(\eta_1 m_1 + l_1 m_2 + l_1 m_3)$$
$$I_{23}=c_{1p}$$
$$I_{24}=k_d {X_{tp}}^2$$
$$I_{32}=-(\eta_2 m_2 + l_2 m_3)$$
$$I_{42}=-\eta_3 m_3$$

APPENDIX D

$$[C]=\begin{bmatrix} C_{11} & C_{12} & C_{13} & C_{14} \\ C_{21} & C_{22} & C_{23} & C_{24} \\ C_{31} & C_{32} & C_{33} & C_{34} \\ C_{41} & C_{42} & C_{43} & C_{44} \end{bmatrix}$$

$$C_{11}=a_{22}a_{33}a_{44}+2a_{23}a_{34}a_{24}-(a_{24}a_{33}a_{42}+a_{43}a_{34}a_{22}+a_{23}a_{32}a_{44})$$
$$C_{22}=a_{11}(a_{33}a_{44}-a_{34}a_{43})$$
$$C_{33}=a_{11}(a_{22}a_{44}-a_{24}a_{42})$$
$$C_{44}=a_{11}(a_{22}a_{33}-a_{23}a_{32})-a_{12}a_{21}a_{33}$$
$$C_{12}=C_{21}=-a_{21}(a_{33}a_{44}-a_{34}a_{43})$$
$$C_{13}=C_{31}=a_{21}(a_{33}a_{44}-a_{34}a_{42})$$
$$C_{14}=C_{41}=-a_{21}(a_{32}a_{43}-a_{33}a_{42})$$
$$C_{23}=C_{32}=-a_{11}(a_{32}a_{44}-a_{34}a_{42})$$

$$C_{24}=C_{42}=a_{11}(a_{32}a_{43}-a_{33}a_{42})$$
$$C_{34}=C_{43}=-a_{11}(a_{22}a_{43}-a_{23}a_{42})+a_{12}a_{21}a_{43}$$

$$\det[a]=a_{11}(a_{22}a_{33}a_{44}+a_{23}a_{34}a_{42}+a_{32}a_{43}a_{24})$$
$$-a_{11}(a_{24}a_{33}a_{42}+a_{34}a_{43}a_{22}+a_{23}a_{32}a_{44})-a_{12}a_{21}(a_{33}a_{44}-a_{34}a_{43})$$

APPENDIX E

$$[B]=\begin{bmatrix} B_{11} & B_{12} & B_{13} & B_{14} \\ B_{21} & B_{22} & B_{23} & B_{24} \\ B_{31} & B_{32} & B_{33} & B_{34} \\ B_{41} & B_{42} & B_{43} & B_{44} \end{bmatrix}$$

$$B_{11} = C_{11}I_{11}/\det[a]$$
$$B_{12} = (C_{21}I_{22} + C_{31}I_{32} + C_{41}I_{42})/\det[a]$$
$$B_{13} = (C_{21}I_{23})/\det[a]$$
$$B_{14} = (C_{11}I_{14} + C_{21}I_{24})/\det[a]$$
$$B_{21} + (C_{12}I_{11})/\det[a]$$
$$B_{22} = (C_{22}I_{22} + C_{32}I_{32} + C_{42}I_{42})/\det[a]$$
$$B_{23} = (C_{22}I_{23})/\det[a]$$
$$B_{24} = (C_{12}I_{14} + C_{22}I_{24})/\det[a]$$
$$B_{31} = (C_{13}I_{11})/\det[a]$$
$$B_{32} = (C_{23}I_{22} + C_{33}I_{32} + C_{43}I_{42})/\det[a]$$
$$B_{33} = (C_{23}I_{23})/\det[a]$$
$$B_{34} = (C_{13}I_{14} + C_{23}I_{24})/\det[a]$$
$$B_{41} = (C_{14}I_{11})/\det[a]$$
$$B_{42} = (C_{24}I_{22} + C_{34}I_{32} + C_{44}I_{42})/\det[a]$$
$$B_{43} = (C_{24}I_{23})/\det[a]$$
$$B_{44} = (C_{14}I_{14} + C_{24}I_{24})/\det[a]$$

APPENDIX F

$$[r]^T = \begin{bmatrix} r_{11} & r_{21} & 0 & r_{41} \\ 0 & r_{22} & 0 & r_{42} \\ 0 & r_{23} & r_{33} & r_{43} \\ 0 & r_{24} & 0 & r_{44} \end{bmatrix}$$

$$r_{11} = \det[a] = 1 + B_{21}G_cG_{22} + B_{41}G_cG_{24} \qquad r_{33} = r_{11}$$
$$r_{21} = -B_{11}G_cG_{22} \qquad r_{41} = -B_{11}G_cG_{24}$$
$$r_{22} = 1 + B_{41}G_cG_{24} \qquad r_{42} = -B_{21}G_cG_{24}$$
$$r_{23} = -B_{31}G_cG_{22} \qquad r_{43} = -B_{31}G_cG_{24}$$
$$r_{24} = -B_{41}G_cG_{22} \qquad r_{44} = 1 + B_{21}G_cG_{22}$$

$$[d]=\begin{bmatrix} d_{11} & d_{12} & d_{13} \\ d_{21} & d_{22} & d_{23} \\ d_{31} & d_{32} & d_{33} \\ d_{41} & d_{42} & d_{43} \end{bmatrix}$$

$$d_{12} = B_{13} - B_{11}G_cG_{12}$$
$$d_{22} = B_{23} - B_{21}G_cG_{12}$$
$$d_{32} = B_{33} - B_{31}G_cG_{12}$$
$$d_{42} = B_{43} - B_{41}G_cG_{12}$$

$$d_{11} = B_{12} - B_{11}G_cG_{11}$$
$$d_{21} = B_{22} - B_{21}G_cG_{11}$$
$$d_{31} = B_{32} - B_{31}G_cG_{11}$$
$$d_{41} = B_{42} - B_{41}G_cG_{11}$$
$$d_{13} = B_{14} - B_{11}G_cG_{13}$$
$$d_{23} = B_{24} - B_{21}G_cG_{13}$$
$$d_{33} = B_{34} - B_{31}G_cG_{13}$$
$$d_{43} = B_{44} - B_{41}G_cG_{13}$$

APPENDIX G

$\varpi_1 = \varpi_2 =$ *first two natural frequencies*

$$k_{23}^2 - \left[\left(\varpi_1^2 + \varpi_2^2\right)\left(m_{22}m_{33} - m_{23}m_{32}\right)/\left(m_{33} + 2m_{23} + m_{22}\right)\right]k_{23}$$
$$+ m_{33}\left(\varpi_1^2\varpi_2^2\right)\left(m_{22}m_{33} - m_{23}m_{32}\right)/\left(m_{33} + 2m_{23} + m_{22}\right) = 0$$
$$k_{12} = \left(\varpi_1^2 + \varpi_2^2\right)\left(m_{22}m_{33} - m_{23}m_{32}\right)/m_{33} - \left(m_{33} + 2m_{23} + m_{22}\right)k_{23}/m_{33}$$

DISCUSSION OF FIRE OUT OF BATTERY TEST RESULTS

Matthew Tedesche [1] , Robert Durocher [1] , Michael Gully [1]

(1) Benet Laboratories
AMSTA-AR-CCB-DE
Watervliet, NY 12189-4050

Abstract:

The U.S. Army's vision of it's future is a lighter faster more lethal fighting force. The U.S. Army's Future Combat Systems Multi-Role Fighting Vehicle is an example of the application of this vision. In order to combine a lighter faster vehicle with a more lethal weapon system, non-conventional recoil methods will need to be considered. Currently a recoil system called FOOB or fire out of battery is being experimented with. This report will include an explanation of how this recoil system works and results attained from a series of testes performed with a FOOB system. Lessons learned from these tests and how they apply to the design of a FCS Multi-Role Vehicle weapon system will be discussed.

Introduction

The vision of the future U.S. army involves a lighter faster more lethal combat system. In harmony with this vision, a combat vehicle that will meet these requirements is currently in development. This "multi-role" combat vehicle will weigh less than 20 tons and be able to fit in the cargo bay of the Army's C130 transport aircraft. The lightweight and compact design will give this vehicle the advantage of rapid deploy ability compared to the Army's current main battle tank. Although this vehicle will not have the same level of armor as the Abrams, it's lethality will come from its speed, and the range and accuracy of it's main weapon system. With the ability to fire a variety of guided and unguided ammo, this vehicle will be capable of both direct and indirect target engagement. The ability to fire ammo that is up to 30% greater impulse than what is currently be fired from the Abrams main battle tank will give this vehicle the ability to engage and defeat heavily armored vehicles with lethality. However it is this same ability that will present the greatest design challenge in the development of this vehicle, and perhaps one of the greatest challenges in the development of any armored vehicle in modern warfare.

Ogorkiewicz Ratio [1], Round Impulse/Vehicle Mass, is often used when analyzing recoil effects on fighting vehicles, a ratio of 900 N*sec/M. ton is recommended as an upper design limit. The following table, (table #1) is a comparison of Ogorkiewicz Ratio for a number of armored vehicles designed in the later half of the twentieth century compared to the FSC vehicle design concept.

Table#1 [2]

Vehicle	Mass (metric Tons)	Main Weapon	Round	Impulse, Lbf*sec / N*sec	Ogorkiewicz Ratio N*sec/ M.t
FCS Vehicle	18.15	105 mm	FCS Case Telescoping	8200 / 36,475	2010 N*s/M.ton
M8 AGS L.T. (1995)	18	105 mm	M-490 KE Tactical	4700 / 20,906	1161 N*s/M.ton
LAV-105 (1988)	13.86	105 mm	M-490 KE Tactical	4700 / 20,906	1500 N*s/M.ton
M1A1(1988)	57.15	120 mm	M-829 KE Tactical	6100 / 27,134	475 N*sec/M.ton
M1 (1984)	54.54	105 mm	M-490 KE Tactical	4700 / 20,906	384 N*sec/M.ton
M 60 (1960)	52.167	105 mm	M-490 KE Tactical	4701 / 20,906	400 N*sec/M.ton
M551 (Sheridan)	15.85	152 MM		3700 / 16650	1050 N*sec/M.ton

Although the LAV-105 has an Ogorkiewicz Ratio of 1500, it was never fully tested or type classified. The M8 armored gun system was fully tested and type classified. This vehicle (although not in production) is probably the closest in design to the FCS vehicle concept and its Ogorkiewicz Ratio is only half of what the FSC vehicle will be.

So we are challenged with the question of how to mount a cannon that fires an 8200 Lb*Sec round on a vehicle with out exceeding the total vehicle weight of 20 tons, while maintaining vehicle stability and relative crew comfort when the weapon is fired. In order to do this we are forced to look at non-traditional recoil systems for the solution.

Currently Benet' Laboratories is investigating and experimenting with a recoil concept called fire out of battery, or FOOB. In a FOOB system the recoiling mass is accelerated over some fixed length to a speed equal to half the maximum of what it would be if fired from a stationary position with a given round impulse. Then at the desired position the gun is fired and it recoils back at half the speed it would during conventional firing. Therefore the net change in momentum is the same for both conventional and Fire out of Battery, as it should be due to the same impulse being imparted to each system for a given round. However the recoil velocity in a Fire out of Battery system never gets above half the conventional firing velocity. The recoil force is a function of the recoil velocity squared, (equations 1-3). This means for any given recoil length and mass, a FOOB system will require one quarter the force required by a conventional system in order to start and stop the recoiling mass.

Equation # 1

$$\int_0^L F dx = \int_0^V mv dv$$

Equation # 2

$$FL = \frac{1}{2} mV^2$$

Equation # 3

$$F = \frac{1}{2} MV^2 / L$$

- M=Recoiling Mass
- L= Recoil Length
- V = Recoil Velocity imparted by round impulse

Testing Goals

A series of two FOOB tests were performed. One test was conducted in October of 2000 at the Write Malta Corporation's test facilities in Malta NY. Another test was conducted in February 2001, in cooperation with United Defense L.P. at the Aberdeen Testing Center, Aberdeen Proving Grounds, Aberdeen Maryland.

Showing recoil force reduction via Fire Out of Battery and acquiring data that could be analyzed to gain insight into the dynamics of a FOOB recoil system was the major goal of the first series of test. The effects of round ignition delay time variation on FOOB, which has been identified as one of the most influential variables, was to be studied during both series of tests and will be discussed subsequently. During the second series of tests, a new and much more precise ignition technology, provided by United Defense L.P., was introduced and studied. The effects of this technology will subsequently be discussed also.

Hardware

A 105 mm M-35 cannon was modified in order enable it to fire out of battery. The original gas springs that are used to recover after standard recoil, with a compression ratio of about 2.25, were used as actuators. A basic mechanical latch that could catch and release the gun was fixed to the gun mount structure and actuated pneumatically. A position sensor was used to determine and record the gun position during operation in real time. A sensor with a very fast response time would need to be used, as the accelerations of the gun during recoil would be as high as 40 to 50 gees. It was determined that a sensor called a Tempo-Sonic device would meet the requirement. This device uses a permanent magnet fixed to the gun and a guide rail on the mount structure. The position of the magnet is calculated by circuitry in the device. This signal is then sent to a comparator circuit, which would send a firing signal to the gun when the gun was in the predetermined position. The gun would then recoil back and if possible be caught and latched back to its original position by the latching mechanism. Although the actual hardware used in the test was not optimal in many ways, it was felt that there would be valuable lessons learned in the process of making the system function even at a sub optimal level.

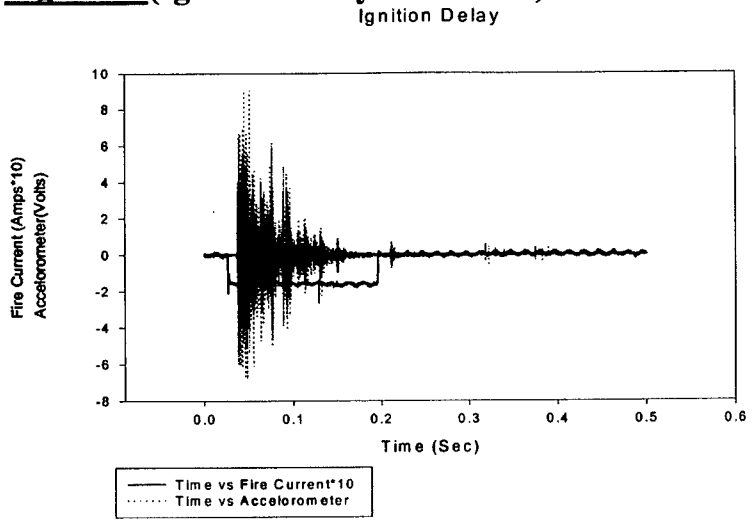
Test Results

Determining Average Ignition Delay Times

The timing of round ignition may be the most crucial factor in the successful operation of a FOOB system. In all ammunition there is a delay between the time when current is sent to the primer and round ignition. This delay is caused by the thermal-chemical reaction time of the primer and propellant. This delay time will vary with round type, batch, and lot. During testing these times were observed to be on the order of 10 to 30 milliseconds. While these times may be virtually undetectable to the eye, and were certainly acceptable for conventional systems, they can make a difference of inches in the position of a gun being accelerated in a FOOB recoil system. This is not acceptable considering control of the ignition position should ideally be a quarter-inch at most. If the average delay time is known it can be factored in to the firing circuit, however the ignition delay time variation will have a significant effect on the performance of FOOB.

During the testing conducted in Malta, NY the M-724 105 mm round was used. By fixing an accelerometer to the breech and comparing its output to the fire current signal during conventional firing, we were able to determine the ignition delay time for each round fired. Figure#1 shows the fire current, (show as the negative rectangular signal) and accelerometer output compared on the same time reference. Table #2 shows statistical data for the M-724 round, based on six of these tests.

Figure#1 (Ignition Delay Time-Test)



Table#2

Round	Ignition Delay Time	Average=9.33 ms
1	11ms	St. Dev. =1.65 ms
2	7.25 ms	
3	8.875 ms	
4	8.875 ms	
5	8 ms	
6	12 ms	

Using this method we calculated an average delay time of 9.3 milliseconds with a standard deviation of 1.65 milliseconds. It is note worthy however that all the ammunition we used came from the same lot which could mean that the consistency in ignition delay time from round to round was better than what a tank crew may see in their ammo store.

During the testing conducted at Aberdeen Test Center the M-490 105mm round was used. United Defense L.P provided a study of the ignition delay time of this round using both conventional primers and their ETC (electro thermal chemical) ignition system. ETC uses a controlled high current pulse to form and inject plasma into the propellant. Table #3 shows statistical data for the M-490 round. T2 times are synonymous for ignition delay time.

Table #3

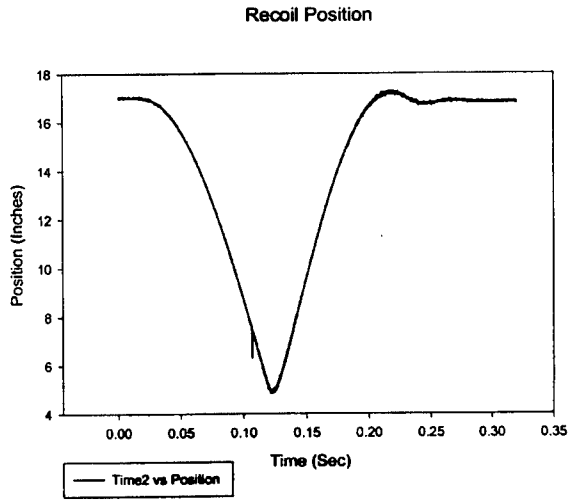
Ignition Type	Convention	ETC
Number of shots	10	7
Velocity	1192 m/s	1208 m/s
T2 Time	31.4 ms	4.69 ms
T2 Sigma	4.85 ms	0.170 ms

As seen in table 3, ETC ignition produces a much quicker ignition and even more importantly, a significant reduction in ignition delay time variation. The effects of this technology will be discussed later in this paper.

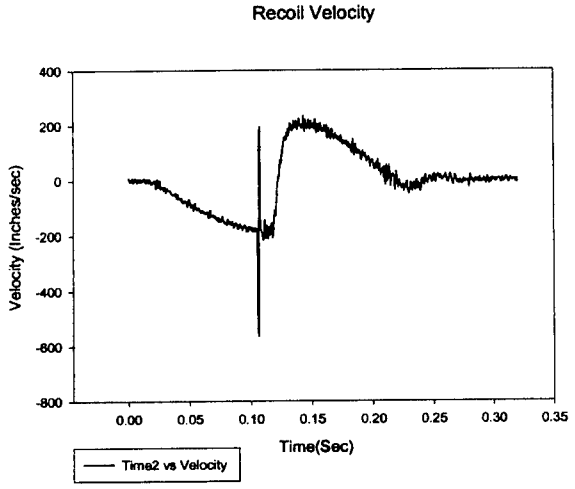
The following figures, figure 2, figure 3 and figure 4 show typical examples of some of the results attained from these tests. In figure 2 we see a characteristic Fire Out of Battery motion profile. The gun starts at about 17 inches out of battery and goes forward to about four and a half inches out of battery before it starts to recoil back. It is then successfully capture by the latching mechanism. The entire cycle takes under 200 milliseconds.

Figure 3 is a velocity profile for the same cycle. Note that the velocity before ignition and after ignition is the same, about 190 inches per second, giving a symmetric curve about the halfway point of the cycle. The spike seen in both plots at about 10 milliseconds is the EM interference of the firing current.

Figure #2 (Recoil Position)



Figure#3(Recoil Velocity)



Figure#4(Recoil Force)

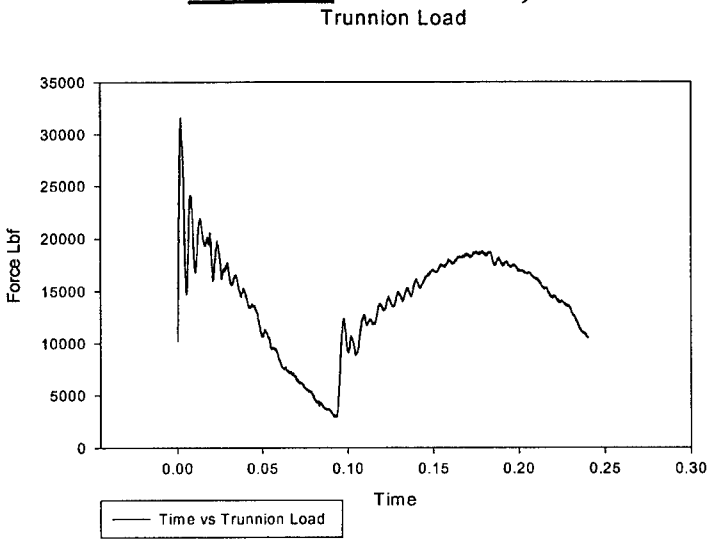
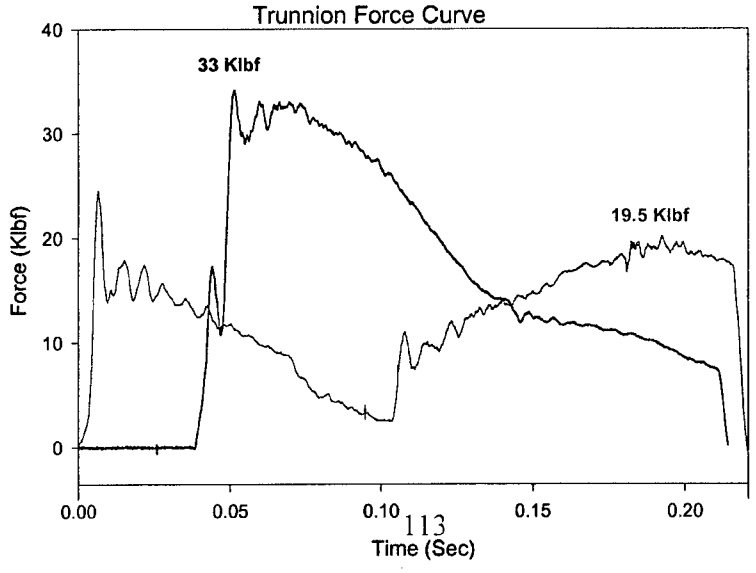


Figure 4 is recoil force time cure for a FOOB cycle. The high frequency oscillations seen in the beginning of the force curve are a result of the dynamic step response of the relatively elastic load cell that connects the gun to the mount and would not be present if the gun were attached directly to the mount. This can be easily understood if we think of this system as a spring, mass, damper system. Compared to the load cells the gun mount will be much more rigid and will have much higher damping properties. Because of the higher damping properties in the gun mount these oscillations will tend to be damped out causing the force curve to lie on the mean value of these oscillations, about 20,000 lbf for this curve.

The theoretical maximum reduction of recoil forces is 75%. In figure 5 we see a comparison of a FOOB firing vs. conventional firing with the same round (M-724). The FOOB force curve has a maximum of about 19.5 thousand lbs force (ignoring the oscillations), and the conventional curve peaks at about 33 thousand lbs force, a 40 % reduction.

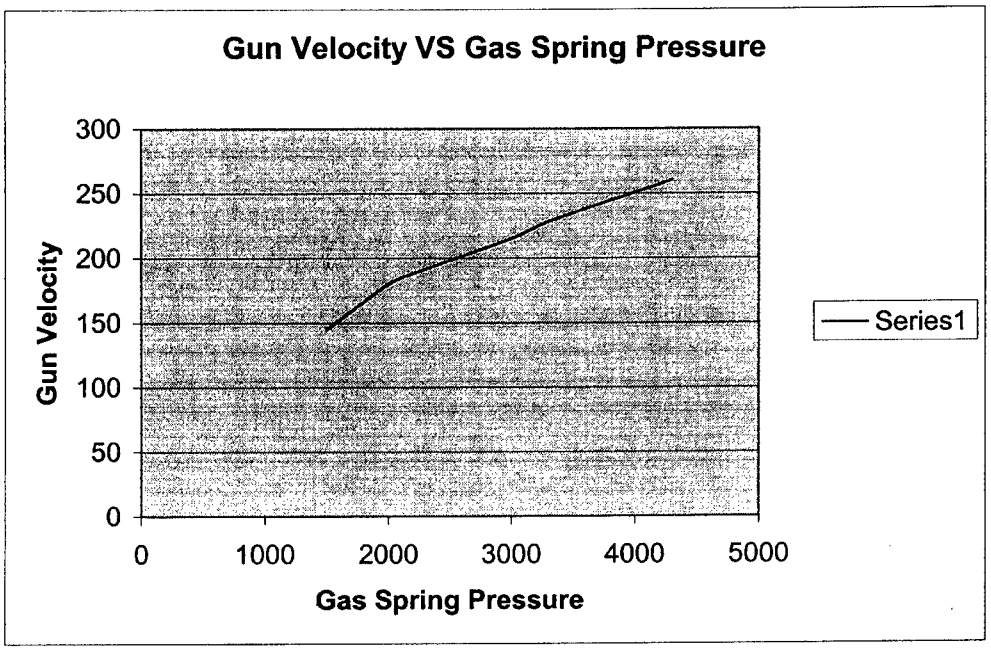
Figure#5



The first question to address is why we see only a 40% reduction, much less than the theoretical maximum reduction. We know the integral of the force time curve is the impulse imparted to the gun by the round. For a constant round impulse or area under the force time curve, we realize that a perfectly rectangular shape will give the lowest peak force for that given area. This assumption is what the maximum theoretical 75% reduction based on, and this is what we would strive for in a final FOOB design. However the gun system that was tested was not optimized and we should not expect this kind of performance from a proof of principal test system.

As we can see in figures 3 and 4 the force curve is far from rectangular due primarily to the high compression ratio of our gas springs. Another factor that contributed to the loss of performance was high levels of system damping. Although it was not possible to exclusively isolate one variable at a time, such as damping, one of the tests we performed did give some indication as to the effects of damping in the system. While performing tests to determine what velocity the gun would achieve under different gas spring pressures we noted significant damping effects. These tests were performed by charging the pneumatic actuators to a specific pressure, and then releasing the gun from its latched position and allowed to travel forward into battery. The velocity achieved after 12 inches of travel was compared for different gas spring pressures. In figure #6 we see a plot of the gun velocity (after 12 inches of travel) vs. initial gas spring pressure, for a number of tests.

Figure#6



As we can see the relation ship is not linear. The shape of the cure indicates that the system is significantly damped. This is not surprising considering this gun system was not original designed for a Fire Out Of Battery recoil configuration. The conventional design of the 105 mm M-35 cannon allows the recoiling mass to slide on a set of greased rails after the gun is fired. While this method is acceptable for conventional recoil, it presents a great deal of inefficiency for FOOB. While system damping helps during the recoiling portion a cycle it will cause system disturbances and variations that will interfere with system repeatability and predictability, which are two essential characteristics for this type of recoil system. Higher levels of uncontrolled damping will also create an unsymmetrical recoil force curve as the direction of damping forces will change to oppose the direction of gun velocity, but the direction of actuator forces will not change. This deviation from the ideal rectangular force curve will reduce efficiency, drive up recoil forces and limit the effectiveness of FOOB.

Although the recoil force reduction was much less than ideal, the reduction achieved was significant considering the system was highly unoptimized. The first goal of testing was to show reduced recoil forces, and that goal was achieved. These tests indicate that a system designed specifically for FOOB will achieve much higher reductions in recoil force. A system that incorporates even a few important design improvements such as actuators that produces a force that is closer to a constant and a reduction of system damping, perhaps through the use of bearing, will achieve reduction much closer to 75%.

Ignition Delay

Analysis of the effects on performance of ignition delay time variation was the second major goal of these tests. The way this analysis was conducted was to tune the system properly and conduct a repeatability series. By analyzing the result of these tests we established a correlation between variations in system performance and ignition delay time variation.

The first tests, conducted in Malta, were based on conventional round ignition methods with the M-724 round. The converted M-35 system used for these tests, had maximum recoil of 13 inches, after which the gun would enter a braking zone, therefore the proper gun speed needed to be achieved around 12 to 12.5 inches of travel. When the accelerating gun passed the specified position the comparator circuit would then send the firing signal. Due to ignition delay this position was somewhere before the 12 inches of maximum travel. Using a computer simulation we found the necessary gun speed, the necessary gas spring pressure to achieve that speed at the correct position, and considering average ignition delay time, the best trigger position. Using these values and about four test firings for fine-tuning, the system was properly tuned. A velocity of about 190 inches per second, a gas spring pressure of about 2,250 psi, and a trigger position of 9.5 inches gave the best performance.

Table#4 shows data collected from Malta test rounds 5 through 10. For these tests the average recoil travel was 12.263 inches, with a standard deviation of .23 inches. The average final recoil position was .346 inches past the latching or starting position, with a standard deviation of .214 inches. The average ignition delay time was 9.758 milliseconds, with a standard deviation of .956 milliseconds.

Table#4 Malta Repeatability Test ResultsM-724 Conventional Primers

Test Round	Ignition Position	Ignition Delay Time	Maximum Travel (Inches)	Final Recoil Position (Inches)	Max. Recoil Fo
#5	9.5 inches	9.25 milliseconds	12.32 inches	.05 inches	19,300 Lbf
#6	9.5 inches	8.9 milliseconds	12.05 inches	-.4 inches	19,400 Lbf
#7	9.5 inches	8.4 milliseconds	11.95 inches	-.6 inches	19,400 Lbf
#8	9.5 inches	10.5 milliseconds	12.17 inches	-.43 inches	19,400 Lbf
#9	9.5 inches	11 milliseconds	12.59 inches	-.5 inches	19,300 Lbf
#10	9.5 inches	10.5 milliseconds	12.5 inches	-.2 inches	19,065 Lbf
Average		**9.758**	**12.263**	**-0.346**	**19310**
St. Deviation		**0.956**	**0.23**	**0.214**	**118**

The second series of tests, conducted in Aberdeen, was based on conventional round ignition methods with the M-490 round. These tests used the same converted M-35 gun system with an additional muzzle brake. Using our dynamic computer simulation and a number of real test rounds to fine tune we found a gas spring charge pressure of about 3350 psi, a gun speed of 230 inches per second and an ignition position 5 inches from release position or 12 inches from battery, gave the best results. Table#5 shows results from 5 FOOB M-490 rounds fired with conventional primers.

Table#5 ATC Repeatability Test Results M-490 Conventional Primers

FOOB Firing Test Data
Test data record for live fire testing

Test date: 3/15/01 Temperature: 55° F Location: Aberdeen Proving Grounds, Barricade 3

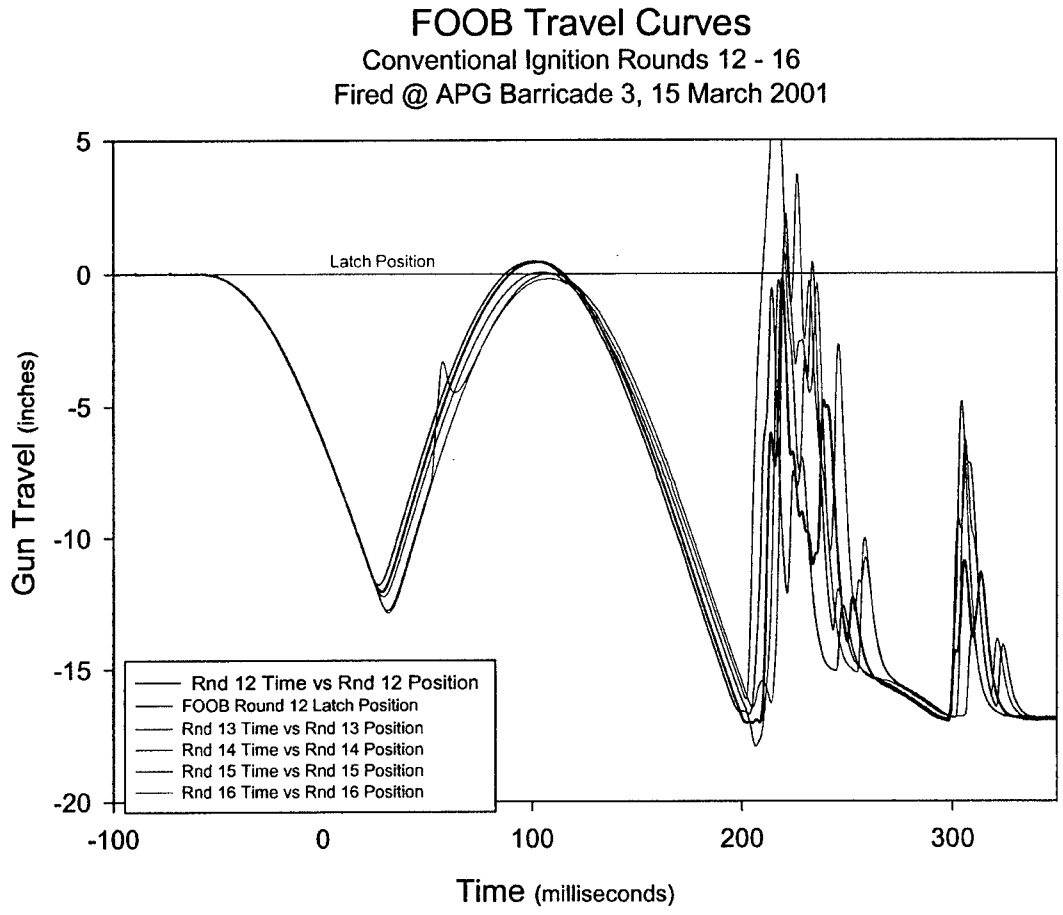
PFN Calibration	Charge Volts:	3.7 KV
	Voltage Offset:	
	Adjusted Firing Charge Volts:	

* Indicates data taken from Benet's Tektronix equipment

Shot # / Description	Nitrogen Pressures PSI (after pressurizing system)			Latch Position (" from battery)	Max Recoil (" from battery)	Turn Around Position (" from battery)	Gun Velocity @ 5"	Notes
	Tank		Gun					
	System	Pump	Recoup					
Dry Run			500					Dry Run to verify instrumentation
Conventional FOOB Shot 1	2700	2700	3370	16.85	17.27*	4.91*	218*	1st conventional FOOB shot; Ignition-10.54"; T2=20.22mS
Conventional FOOB Shot 2	2500	2500	3370	16.77	16.75*	4.03*	225*	T2 = 23.97mS
Conventional FOOB Shot 3	2200	2250	3360	16.77	16.80*	4.66*	224*	T2 = 21.43mS
Conventional FOOB Shot 4	1950	1900	3370	16.87	17.30*	5.18*	212*	T2 = 19.09mS
Conventional FOOB Shot 5	1700	1400	3380	16.87	16.59*	4.18*	224*	T2 = 23.25mS

Due to the slower ignition delay of the M-490 we needed to send the fire signal to the gun at a position about 2.5 inches closer to the release point of the gun than we did with the M-724 rounds. For the M-490 with conventional primers the average maximum travel was about 12.25 inches or 4.592 inches from battery, with a standard deviation of .484 inches. The average ignition delay time was 21.54 milliseconds with a standard deviation of 2.034 milliseconds. Figure #7 is a superposition of five recoil travel curves, using M-490 conventional primer rounds. The travel cures in figure 7 and 8 represent a FOOB firing were the gun was not latched back to its initial position due to mechanical issues. In a final FOOB design the gun will always be captured at its release position, as seen in figure 2. Both Figures 7 and 8 contain noise introduced by the sensor if shock levels exceeded a threshold.

Figure # 7 Recoil Position VS. Time ATC M-490 Conventional Primers



The third series of tests, which was conducted in Aberdeen, used the M-490 round, and the ETC ignition methods provided by United Defense L.P.. Tuning the system for these tests involved adjusting only the ignition position, as our system was previously tuned for the M-490 round. The ignition position was moved forward to 11 inches, or 6 inches from battery due to the very short ignition delay time achieved by ETC ignition. Table#6 shows results from 5 FOOB rounds fired with ETC primers.

Table#6 ATC Repeatability Test Results M-490 ETC Primers

FOOB Firing Test Data
Test data record for live fire testing

Test date: 3/14/01 Temperature: 55° F Location: Aberdeen Proving Grounds, Barricade 3

PFN Calibration	Charge Volts:	3.7 KV
	Voltage Offset:	570 V
	Adjusted Firing Charge Volts:	

* Indicates data taken from Benet's Tektronix equipment

Shot # / Description	Nitrogen Pressures PSI (after pressurizing system)			Latch Position (" from battery)	Max Recoil (" from battery)	Turn Around Position (" from battery)	Gun Velocity @ 5"	Notes
	Tank		Gun					
	System	Pump	Recoup					
Dry Run 1	2200	1400	500	17.25				Low pressure dry run t verify elec. sys. & instrumentation
Dry Run 2			500	17.28				ETC dump to calibrate
FOOB / ETC Shot 1	1900	1100	3380	16.95	17.58*	3.89*	227*	FOOB/ETC w/relatch, sticking, possible ben
FOOB / ETC Shot 2	2500	2800	3380	16.71	??	3.91*	227.1*	Broken fins, incompl data (timing issue), h velocity
FOOB / ETC Shot 3	2300	2600	3380	16.77	17.39*	3.91*	227.4*	Broken fins, 530 Mpa, M/s velocity
FOOB / ETC Shot 4	2000	2300	3380	16.77	17.46*	3.90*	235.4*	Good shot with good
FOOB / ETC Shot 5	1800	1950	3380	16.77	17.48*	3.88*	227.9*	
FOOB / ETC Shot 6	1500	1400	3380	16.77	17.33*	3.88*	224.9*	
FOOB / ETC Shot 7	1400	900	3380	16.82	17.55*	3.88*	229.2*	
			3380					

For the M-490 with ETC primers the average maximum travel was about 12.9 inches or 3.89 inches from battery, with a standard deviation of .014 inches. The average ignition delay time was 4.417 milliseconds with a standard deviation of .0822 milliseconds. Figure #8 is a superposition of five recoil travel curves, using M-490 ETC primer rounds.

Figure # 8 Recoil Position VS. Time ATC M-490 ETC Primers

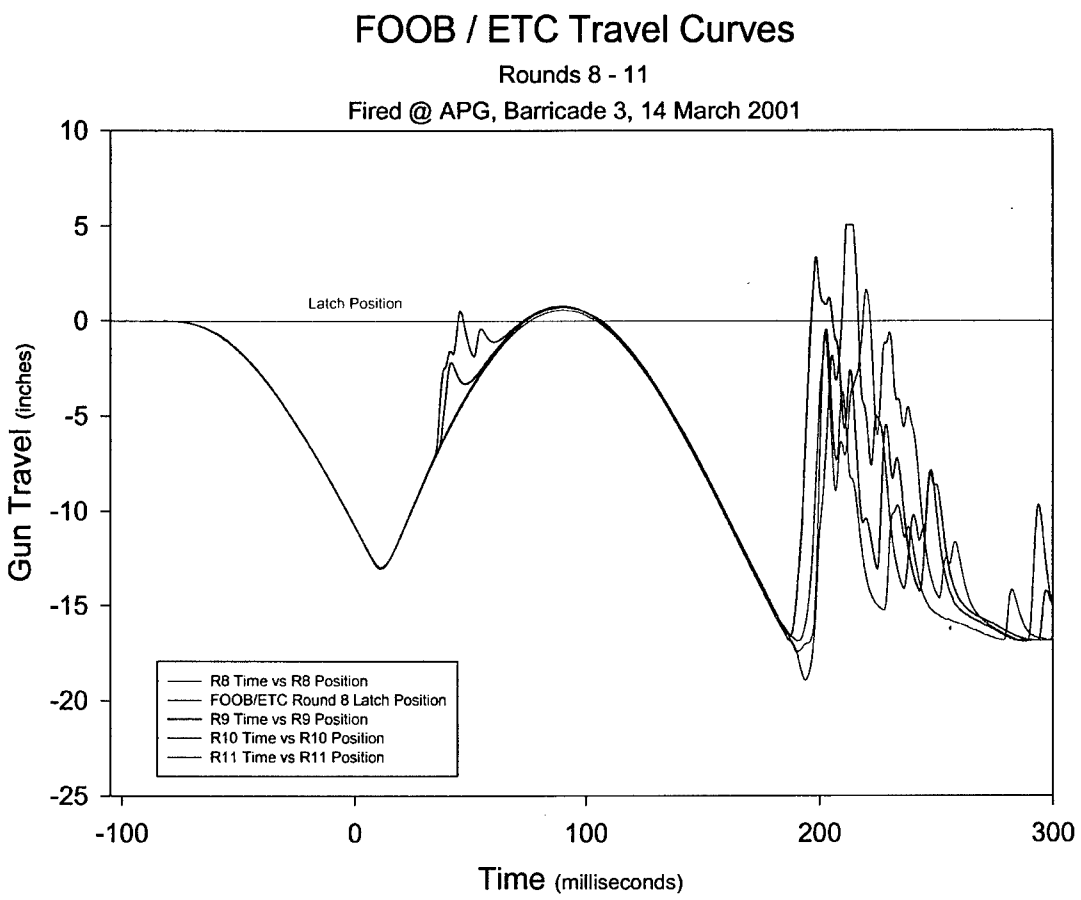


Table 7 compares results from all the tests performed. If a linear regression is performed we can see a correlation of .9274 between ignition time variation and travel length variation. This clearly shows that ignition delay variation has a direct and significant effect on system repeatability and predictability, as would be expected. These results indicate a need for precise ignition timing if a FOOB gun is to be successfully weponized.

Table#7 Test Result Summary

Test	Round	Ignition Method	Maximum Travel	St. Deviation	Ignition Delay	St. Deviation
Malta	M-724	Conventional	12.263	0.23	9.75 ms	.956 ms
ATC	M-490	Conventional	12.25	0.484	21.54	2.034
ATC	M-490	ETC	12.9	0.014	4.417	0.0822
Linear Regression	a=2.0697	b=.4853	Correlation =.92737			

Conclusion

Although the system used in these tests does not represent a design optimized for FOOB, its performance was satisfactory relative to the goals set out before testing. A recoil force reduction of 40% with an inefficient system seems to indicate that force reduction on the order of 55% to 65% should be achievable with a more careful design. The importance of a low a friction system and optimal actuators were indicated by these tests as well. A direct correlation between precise ignition timing and precise system performance was established. All of these lessons will be very useful in the effort to design a weponized FOOB system.

References

1. **Ogorkiewicz, R.M., *Technology of Tanks* Volumes I and II, Jane's Information Group, Surry, UK, 1991.**

2. **Jane's, "Armor and Artillery", Blair Catton Defense Products, Foss, 19th Edition 1998-99.**

3. **Burton "Design Tradeoffs " pp15. 1-25, 8th Gun Dynamics Symposium**

SMART ISOLATION MOUNT FOR AIRBORNE GUNS

Daryoush Allaei[1], David J. Tarnowski[1], Michael S. Mattice[2], Robert Testa[2]

[1] QRDC, Inc., 125 Columbia Court North, Chaska, MN 55318-2348
[2] *Advanced Drives and Weapon Stabilization Lab, Fire Control Division, Building 92 North, Picatinny Arsenal, NJ 07806-5000*

Structural deformations at the turret interface points in an airborne-helicopter system need improvement. Such deformations occur due to large firing reaction forces. The deformation of the helicopter body and propagation of vibrations result in reduced accuracy and cause reoccurring failure of hydraulics and onboard electronics. Smart Isolation Mount for Airborne Guns addresses the vibration issues in the weapon stabilization and fire control systems. SIMAG^{TM} is composed of the optimum integration of vibration control by confinement and a smart control system. It reconfigures the distribution and propagation of excess vibration energy; and therefore, confines vibrations within its own structural elements. SIMAG^{TM} makes significant progress towards solving the firing control problems with acceptable weight and power penalties by compensating for all errors at the turret-aircraft interface. Concentrated smart damping elements or cancellation techniques effectively dissipate the trapped vibrations. The insertion of SIMAG^{TM} in an onboard gun system reduces the fluctuating loads and deformations by up to 50%.

INTRODUCTION

There exists a need for the development of a low-cost, high-performance weapon stabilization and fire control system for the U.S. Army. These developments may include optimal sensor fusion algorithms and fire control implementation prototypes. Applications consist of platforms such as attack helicopters and ground vehicles.

Currently, there are several major error sources influencing turreted weapon accuracy on a helicopter. Among the major sources of error are non-linearity and uncertainties in hydraulic elevation and azimuth drivers, deformations of the supporting structure in the vicinity of the turret attachment points, turret dynamics excited by firing action, and non-observable motions that include deformations of the gun barrel. For example, helicopter structural deformations, local to the turret interface points, can exceed 15 mrad, depending on the location of the interface point. Such deformations occur due to large firing reaction forces that can be as high as 8000 lbs at 10 Hz. The firing accuracy of the gun is significantly affected by the deformation of the helicopter body (also referred to as body bending) and bending of the gun barrel. Both of these deformations influence the vertical exit angle of the fired round.

The exit angle is one of the most significant parameters affecting the trajectory of the round as demonstrated in the following example. A small vertical displacement, h, will result in a small error at a distant target. On the other hand, a small rotational displacement, θ, may result in a large error at a distant target. For instance, for a shot fired downrange 1500 ft, a

0.25 ft vertical displacement at the barrel tip produces only a 0.25 ft error. An angular deviation of 0.002 radians produces an 8.5 ft error.

Presence and propagation of such relatively large vibration levels not only result in reduced probability of kill but also cause reoccurring failure of hydraulics and onboard electronics (i.e., fuses) in an attack helicopter. The attack helicopter PMO and manufacturers [1] been identified aircraft structural deformation and vibration issues as well documented, long-term, and unresolved problems.

The Advanced Drives and Weapons Stabilization (ADAWS) laboratory in ARDEC has focused on the development of the Advanced Electric Turret (AET) based on a gearless electronic drive, digital control technologies, and smart barrel actuators. The AET program addresses only two of the error sources, non-linearity in hydraulic elevation and azimuth drivers and turret dynamics. Improvement in these two error sources may result only in reduction of operating and support (O&S) cost of hydraulics.

The ***S***mart ***I***solation ***M***ount for ***A***irborne ***G***uns (SIMAG^{TM}) addresses the other two error sources, deformations of the helicopter structure near the turret attachment points and non-observable motions such as deformations of the gun barrel. The main weapon O&S cost drivers for these improvements will be the failure reduction of onboard electronics and enhanced probability of kill. The latter benefit will result in reduction of onboard ammunition and thus, an increase in fuel storage and payload capabilities. Additional benefits of reducing excess vibration propagating to the body of the helicopter include: decreased wear to the helicopter structural components, reduced whole-body vibrations on crew, increased effectiveness of maintenance procedures, enhanced man-machine interface, and reduced crew fatigue.

In this paper, the feasibility of developing the SIMAG system is presented. SIMAG is based on the Vibration Control by Confinement^{TM} (or VCC^{TM}) approach [2,13-16]. It is shown that SIMAG reduces the transmission of excess vibratory loads to the helicopter structure and improves the pointing accuracy of the gun. The former will result in damage reduction in the helicopter structure and onboard electronics.

AN OVERVIEW ON VIBRATION CONTROL BY CONFINEMENT ^{TM}

Researchers have explored the applicability of the mode localization phenomenon and vibration energy confinement to engineering problems, such as vibration suppression, isolation, absorption, and control. Recently an overview of these works and the impact they may have on vibration control was presented [2]. One of the main questions raised in these studies was whether passive and/or active vibration control by confinement has the potential to become an alternative or complementary approach to the current noise and vibration control schemes. A review of the current literature [2-16] indicates that the Vibration Control by Confinement approach is an effective means for managing the vibration energy associated with a structure.

The patented VCC approach [13,14] is comprised of four primary steps. First, certain design parameters of the structure are modified within allowable limits to induce a desired vibration energy confinement. This confinement causes a significant portion of the vibration energy to be directed to non-critical sub-structures, thereby isolating and quieting critical areas. Second, should a stronger confinement, and thus greater suppression, be required, specially designed add-on components can be used to strengthen the degree of confinement. Third, passive and/or active damping elements concentrated in the regions of trapped vibration energy are applied to remove the confined energy. Fourth, a set of discrete or

distributed feedback forces may be employed to transform the original system-wide vibration response into spatially decaying (regionally confined) or vortex power flow responses. This four-step process results in simultaneous decay of vibrations in the time and spatial domains. Therefore, excess vibration energy may be trapped near its source, dissipated, and prevented from propagating to other parts of a structure.

The energy diversion and confinement features in spatial domain is analogous to the effect that damping has on the vibration response in time domain. Whereas damping decays vibration in the time domain, VCC decays vibration in the spatial domain. Confinement may also be used to control the vibration power flow throughout the structure. VCC also differs fundamentally from conventional controls in that conventional controls are reactive, acting on incoming vibration energy to reduce its levels. VCC is proactive; prohibiting vibration energy from entering selected regions of a system. It is used to tailor the final energy distribution and resultant vibration levels to meet the specified vibration and damage control requirements.

The VCC technique is an integral part of SIMAG concept that has enormous applications in aircraft, spacecraft, ground vehicles, surface ships, submarines, and commercial systems. Our first attempt will be to fulfill the described Army requirements for airborne guns. However, the larger market is in the commercial segments including automotive, manufacturing, and space systems. Other applications will be pursues at the end of this work.

SIMAG CONCEPT

In this work, the issue of controlling the gun-generated vibrations is address by an energy flow control approach. Managing the propagation of vibration and shock energy within a smaller structural space (i.e., SIMAG) that interfaces the gun and an air vehicle (i.e. helicopter) will be an effective technique to protect the onboard electronic and optical systems, and interrupt the random flow of this destructive and often dangerous propagation of energy throughout the airborne vehicle. It is dangerous because not only can it damage interior systems but it also can cause excess vibration and noise that can distract and fatigue the crew. Steering and confining the excess vibration energy to less critical sections or less-radiating modes of the continuous isolation unit allows for the application of concentrated passive or active control efforts. The SIMAG system has both passive and active energy managing elements. The energy-managing approach reduces effectively the propagation of vibration or shock energy to a helicopter shell and frame structures. SIMAG approach is implemented without compromising the performance of the equipment or vehicle while keeping the structural weight and cost of the isolation units at their minimum.

The development of SIMAG whose continuous structural elements can **manage** (i.e., **confine, divert, convert, absorb, steer, and dissipate**) excess vibration and shock energies has a profound impact on the general area of vibration isolation and shock mitigation technologies. In particular, our ultimate isolation system will be a high pay-off product with direct benefits to U.S. Army, other DOD components, and commercial markets.

SIMAG utilizes the isolating capabilities of VCC to suppress vibration levels across the helicopter body by performing five functions. (1) It redirects the vibration energy away from its interface to the helicopter body. (2) It redirects the vibration energy away from its interface to the gun turret. (3) It traps vibration energy within itself at non-interface locations. (4) It converts elastic energy to kinetic, and vice versa. (5) It dissipates the energy before it can propagate to the helicopter shell. The SIMAG insert is shown in Figure 1. First, the helicopter body is separated from the gun turret components. Second, the energy

diverting SIMAG insert is positioned between the helicopter body and the turret. Third, the components are reassembled with both the helicopter body and the gun turret interfacing the SIMAG insert. Positioned in this manner, SIMAG is capable of performing its five functions. SIMAG may be used to retrofit the current gun-turret systems or may also be integrated into a new design of turret structures. It is anticipated that when SIMAG is an integral part of a turret, it will have the highest performance and payoff.

SIMAG is composed of optimum integration of two innovative technologies, namely Vibration Control by Confinement and an active control system. In the current project, these two complementary approaches are combined to solve the firing problem at the gun mount and turret interface location. SIMAG is designed to first passively reconfigure the distribution and propagation of excess vibration energy and confine vibrations to certain pre-defined non-critical regions of the helicopter-turret-gun system. Concentrated damping elements (CDE), in passive or active forms, are then applied to effectively dissipate or cancel the trapped vibrations and to prevent an energy build up in the assembly. Should a more robust confinement be required, closed-loop control forces may be applied to further redirect and confine the vibratory energy. The application of SIMAG results in a significant reduction in fluctuating loads and deformations. SIMAG makes significant progress towards solving the firing control problems. It accomplishes these goals with very small weight and power penalties. The application of the SIMAG approach to the gun barrel is also under investigation and will be reported in subsequent papers.

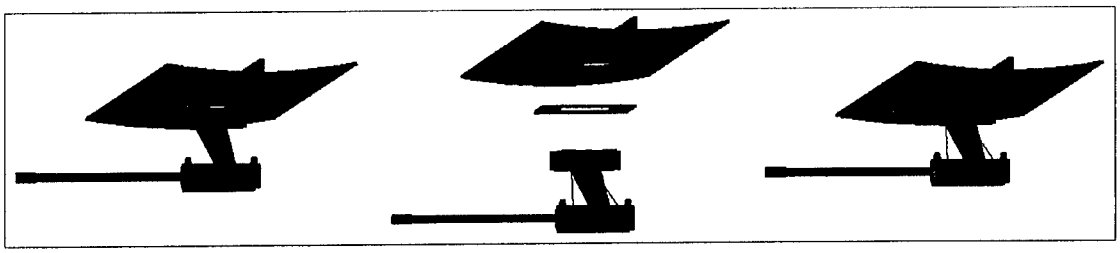


Figure 1 SIMAG system approach (a) baseline system, (b) SIMAG inserted between helicopter body and gun system, (c) SIMAG-inserted system

ANALYSIS AND RESULTS

The free vibration analysis of the baseline helicopter-gun structure and SIMAG-helicopter-gun system were modeled using standard ANSYS-based finite element package. The forced vibration and active control parts of the analysis were conducted using in-house developed software, VECAS (Vibration Energy Confinement Analysis Software), that is based on the commercially available MATLAB package. The baseline model was calibrated against measured vibration characteristics of an attack helicopter in ground and non-operating conditions.

Details significant to the dynamic characteristics of the system components were modeled. The baseline and SIMAG-inserted system models are displayed in Figures 1(a) and 1(c), respectively. The baseline model consists of the following components: the bottom section of a helicopter body, turret, gun-supporting forks and cradle, gun, barrel, and end suppressor. The SIMAG-inserted model consisted of the above gun and helicopter components plus SIMAG inserted between the helicopter body and turret.

For this study, all the components of the models were comprised of steel. Table 1 shows the material properties used in this study.

Table 1 Material properties and geometry of the modeled components

Property		Value
Elastic Modulus		30.023×10^6 psi
Density		7.3463×10^{-2} lb-s^2/in^4
Poisson Ratio		0.29
Helicopter Shell: Single Curved Plate	Dimensions	240 in. × 48.8 in. × 0.5 in
	Curvature	Radius: 148 in, Arc: 18.9°
	Rectangular Hole	21 in. × 14 in.
Passive SIMAG	Footprint	24 in. × 26 in.
	Center Hole	21 in. × 14 in.
	Weight	61 lb
Finite Element Model	No. of Nodes	1,897
	No. of DoF	11,382
	Active DoF	10,378
	No. of Elements (solid, shell, discrete)	846

The helicopter body was modeled as a singly curved plate with the axis of curvature lying along the length of the plate whose dimensions and curvature are given in the above table. The curvature of the plate was a circular arc having a radius of 148 in. subtending an angle of 18.9°. The actual helicopter body must have the capability to transport ammunition to the gun. The computer model accommodated this need with a hole placed toward the front of the plate. To mimic the dynamic behavior of the actual helicopter body, a stiffening keel was added to the model along the length of the helicopter body. The geometric requirements for SIMAG limited the insert footprint as shown in Table 1. To accommodate the transport of ammunition to the gun, a hole was also required in the SIMAG insert.

In this preliminary study, passive confining elements were employed to induce the required energy distribution within SIMAG. Even though the passive version of SIMAG has limited flexibility, it can be used to demonstrate the effectiveness of the concept. Several configurations of passive energy-diverting components were considered for this study.

Stiffening ribs have been used for decades for static and dynamic strengthening of structures. It has been shown [2-16] that the addition of confining ribs and patches may also be used effectively for energy redistribution and confinement. For example, rib geometry, material properties, and placement may significantly alter, in a predictable manner, the flow of vibration energy within a structure. In the work presented here, component (patch) thickness and location were used to induce confinement. The passive SIMAG insert adopted for this demonstration had a total weight of 61 lb. By retrofitting existing Apache systems with SIMAG, the normal take-off weight of the helicopter is increased by a nominal 0.37%.

The ANSYS-based, SIMAG-inserted model contained 846 solid, shell, and discrete spring elements. The number of nodes, total degrees-of-freedom (DoF), and total active DoF are given in Table 1. The helicopter body was simply supported at its edges. The models were designed to capture the dynamic behavior of a typical helicopter-turret-gun system. Not only the models were developed and correlated with measured vibration characteristics of the helicopter-turret-gun system, but also existing lumped-mass fire-control models [17] of the 30mm gun were used during the calibration process.

The input firing load was simulated using the digitized version of the measured firing force for the 30mm gun. The actual measured and digitized forces are shown in Figures 2(a) and 2(b), respectively. As shown in Figure 3, the input forces (firing loads) were applied at the gun surface interfacing the barrel. Also shown in Figure 3 are the output locations (nodes). Six nodes selected on the helicopter body component and labeled with 500- and 600-series numbers are shown in the figure. These six nodes were used for quantifying the reduction of vibratory energy propagating to the helicopter bottom shell. Also of interest for this study are the interface nodes between the helicopter body and turret (baseline model) or SIMAG insert (SIMAG-inserted model). These nodes are located at the helicopter interface points.

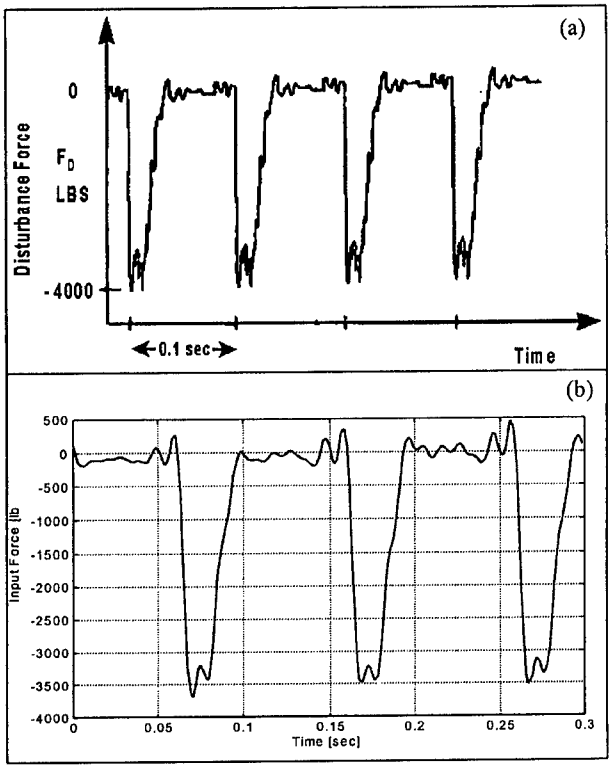


Figure 2 Gun firing force (a) measured, (b) digitized for computer models

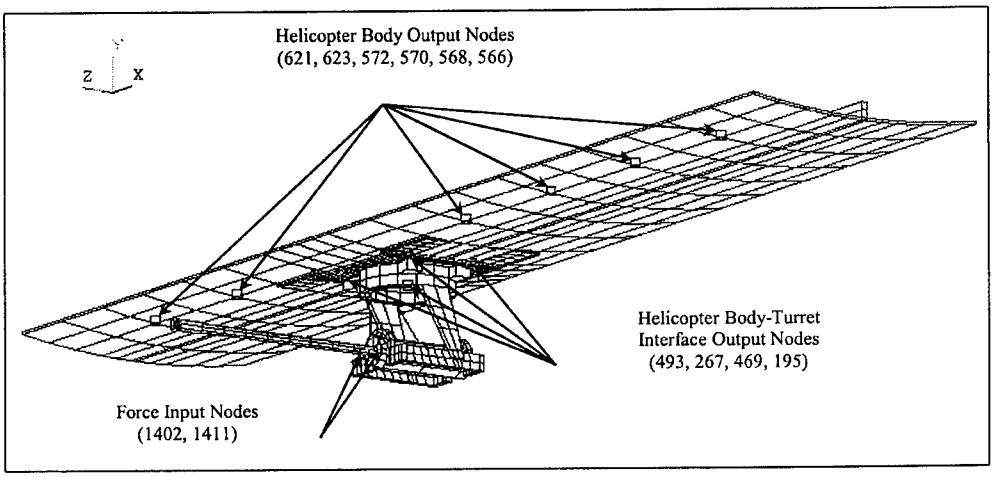


Figure 3 Input and output nodes for baseline and SIMAG-inserted models

The free vibration characteristics of the systems were determined from the FEA model. The vibration characteristics (natural frequencies and mode shapes) were exported to an in-house developed analytical software, namely VECAS (Vibration Energy Confinement Analysis Software). VECAS has the capability to perform forced-response analyses once given a system's vibration characteristics. It also has the capacity to simulate active control

loops. The active control strategies investigated in this study include direct velocity feedback control (DVFC) and the implementation of active vibration confinement via the method of Spatial Decay-Causing Actuators (SDCA) [7,9,12]. VECAS has been verified previously for accuracy against accepted closed-form and numerical analysis routines [15]. Sample verification results for this project, however, are shown in Figures 4 and 5. Figures 4(a) and 4(b) show the dynamic response of the models calculated with the ANSYS transient analysis routines and with VECAS, respectively. The output locations for this verification study were the helicopter body nodes shown in Figure 3. Figure 5 shows a similar plot of dynamic response for the helicopter gun-system interface points. It is observed from these figures that the two analysis procedures produce results in acceptable agreement.

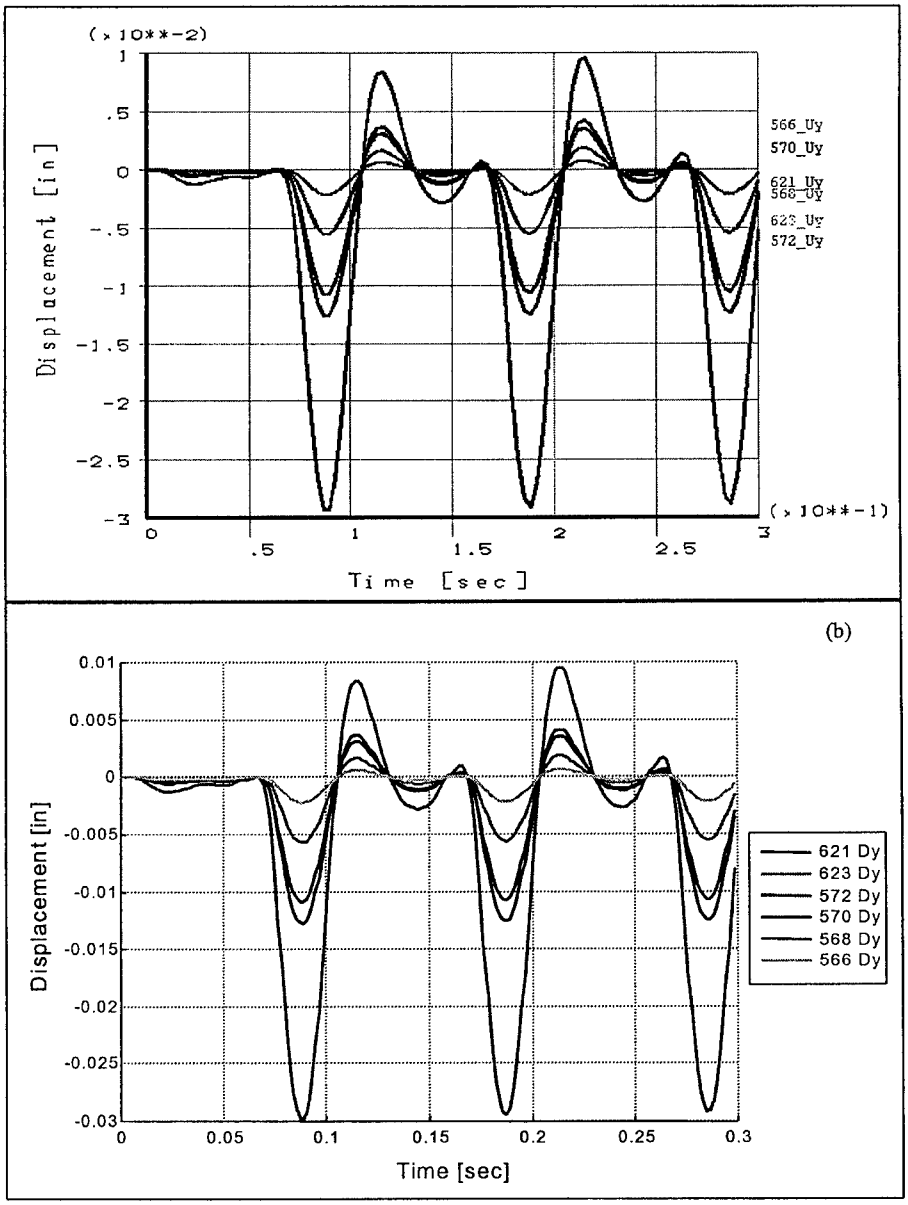


Figure 4 Validation of ***VECAS*** analysis codes for helicopter shell output nodes (a) ANSYS transient response results, (b) ***VECAS*** transient response results

For both the baseline and SIMAG-inserted models, the dynamic response of the system due to the simulated gunfire was calculated. The method of modal superposition was used to calculate the response. Twenty-five modes, covering a frequency range of 15 Hz to 180 Hz were used in the analysis. A constant damping factor of 35% was used for all modes. Time histories for the aforementioned output nodes were stored and plotted. For comparison, the maximum absolute displacement magnitudes were determined for all relevant points on the helicopter model.

Forced response analyses were conducted to demonstrate the effectiveness of several passive confinement configurations for the SIMAG Insert. Results indicate that SIMAG significantly reduces the firing-induced vibratory energy transmitted to the helicopter body.

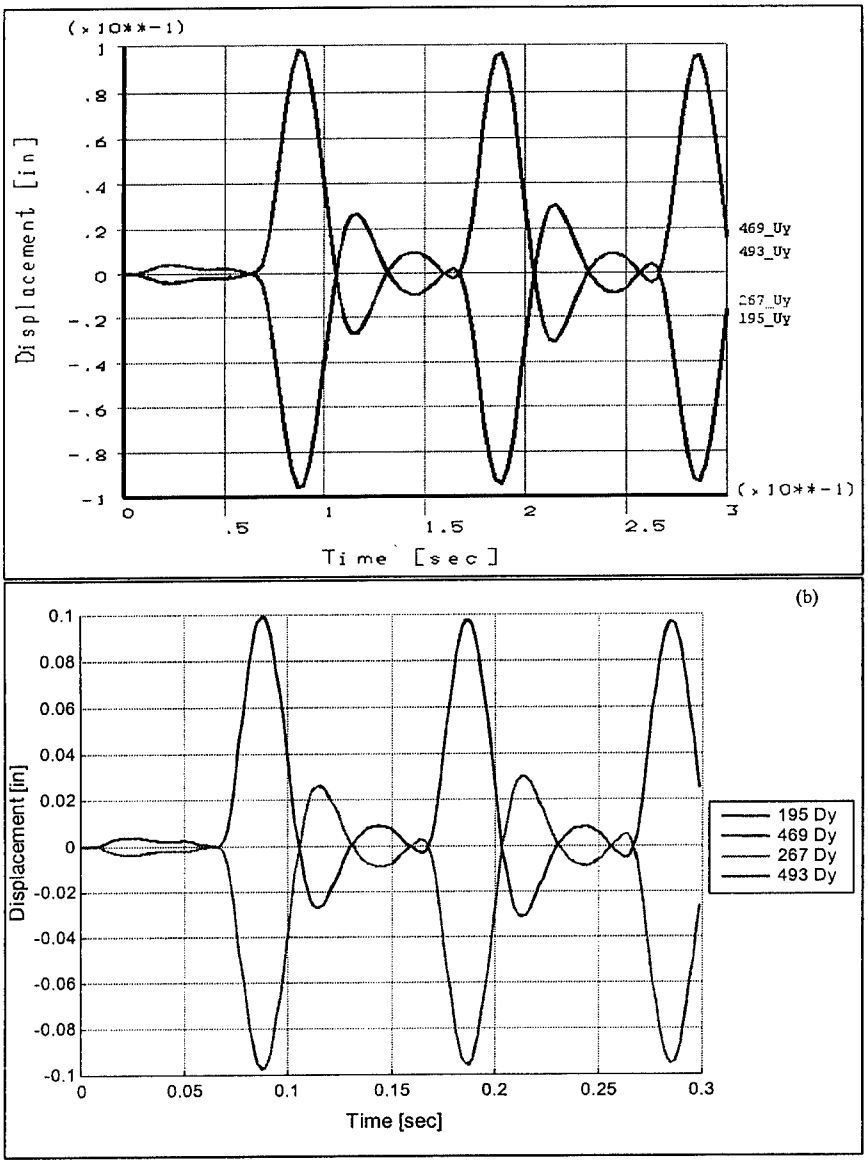


Figure 5 Validation of ***VECAS*** analysis codes for helicopter shell-gun system interface nodes (a) ANSYS transient response results, (b) ***VECAS*** transient response results

Figure 6 shows the results in tabulated; charted; and time history format. Figures 6(a-c) show the influence of the passive SIMAG on reducing the energy transmitted to the helicopter body over its length. Figures 6(d-f) show the similar results as calculated at the helicopter-gun system interface locations. Figures 6(g-i) illustrate the reduction in gross-body rotations of the gun turret once the passive SIMAG insert is in place. As mentioned in the introductory section, the gross rotation of the gun system due to helicopter body bending has a critical impact on the accuracy of gun firing. It may be seen from Figure 6(a) that the maximum absolute transverse displacements of the helicopter body is reduced by as much as 40% at all points along its length. This is an extremely good indication of the effectiveness of the passive SIMAG system.

It is pointed out that SIMAG is most effective at reducing the displacements at nodes 623 and 572, which had the highest baseline displacements. The bar graph in Figure 6(b) shows a comparison of the two systems for displacement reductions at the helicopter body. Figure 6(c) traces the time response of node 572 for both the baseline and SIMAG-inserted systems. Figures 6(a-c) show the passive SIMAG is effective at isolating the helicopter body from the firing-induced disturbances. It is observed that SIMAG does not adversely influence the modal characteristics of the system in that the participating modes, which dominate the transient response of the system, have not changed. The latter may be a requirement when considering the integration of SIMAG, as a retrofit solution, into the current fire-control systems.

Figures 6(d-f) relate the significant reduction in displacements transmitted to the helicopter-turret interfaces. The transverse displacements at these interfaces indicate the effectiveness of the SIMAG system at reducing energy propagation to the helicopter shell. These displacements are also related to the gross rotation of the turret, and subsequently the rotation of the gun-barrel system. Effectively reducing the interface displacements may directly and significantly impact the firing accuracy of the gun system. It may be seen from the table and bar graph that SIMAG operates equally on all interface locations and reduces the transverse displacements by over 50%. Figure 6(f) shows a representative interface time response at node 267. It is observed that SIMAG brings the turret to a near-rest state more quickly than does the baseline system. This is significant for firing accuracy and repeatability, as a more stable gun mount will behave more predictably.

Figures 6(g-i) show that the insertion of SIMAG reduces the gross rotations of the turret. In these figures, the relative displacements at the four interface locations were determined and the maximum angular deviations produced by these displacements were calculated and tabulated in Figure 6(g). The rotations are defined as follows. The x-axis runs along the length of the helicopter, directed from the front to the back. The z-axis runs along the width of the helicopter, directed from the left to right when facing the helicopter.

	Maximum Shell Displacements [in.]		
Node #	Baseline	Passive SIMAG	Percent Change
621	1.09E-02	7.03E-03	-35.3%
623	*2.99E-02*	*1.79E-02*	*-40.2%*
572	*2.98E-02*	*1.78E-02*	*-40.4%*
570	1.27E-02	8.19E-03	-35.6%
568	5.64E-03	3.58E-03	-36.4%
566	2.17E-03	1.34E-03	-37.9%

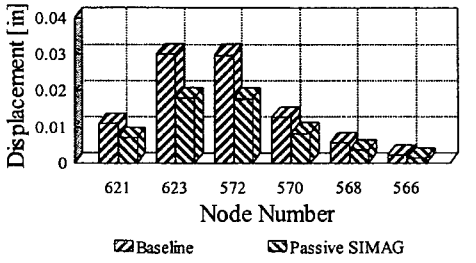
(a)

	Maximum Turret Displacements [in.]		
Node #	Baseline	Passive SIMAG	Percent Change
195	*9.75E-02*	*4.60E-02*	*-52.8%*
469	*9.92E-02*	*4.69E-02*	*-52.7%*
267	*9.77E-02*	*4.60E-02*	*-52.9%*
493	*9.93E-02*	*4.69E-02*	*-52.8%*

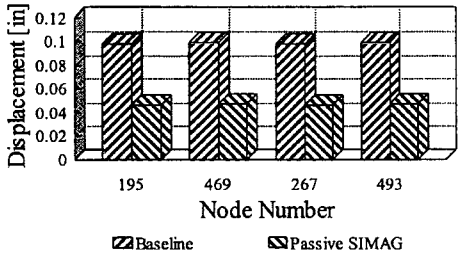
(d)

	Maximum Turret Rotation [rad]			
Rotational Axis	Edge	Baseline	Passive SIMAG	Percent Change
X	*Front*	*1.41E-02*	*6.64E-03*	*-52.8%*
X	*Rear*	*1.41E-02*	*6.64E-03*	*-52.8%*
Z	Right	9.07E-06	2.31E-06	-74.5%
Z	Left	1.03E-05	2.83E-06	-72.6%

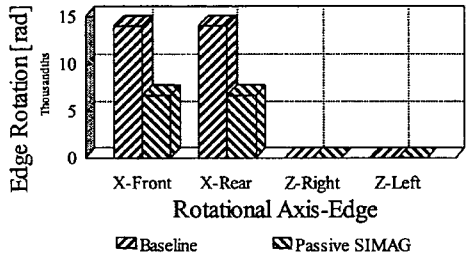
(g)



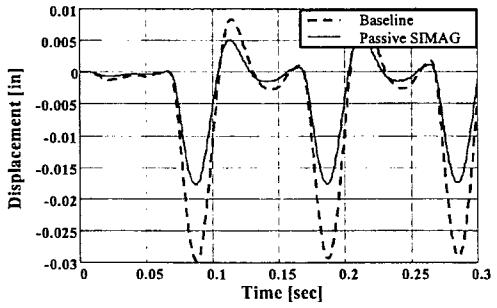
(b)



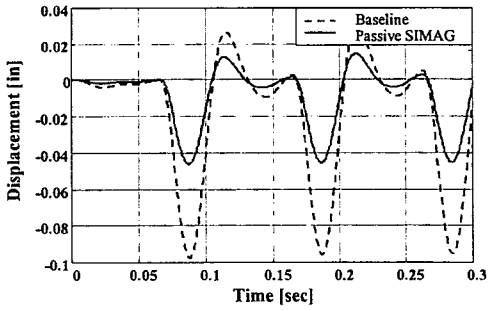
(e)



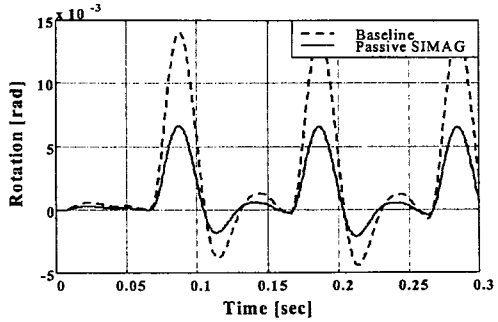
(h)



(c)



(f)



(i)

Figure 6 Analytical results for baseline and SIMAG-inserted models (a)-(c) helicopter shell output nodes, (d)-(f) helicopter shell-gun system interface output nodes, (g)-(i) turret gross rotation

Rotations about the x-axis are critical for the pointing accuracy of the side-pointing gun as they affect the vertical displacement of the gun barrel. The less-critical rotations about the z-axis affect gun canting. SIMAG reduces (see Figures 6(g) and 6(h)) the critical x-axis rotations by over 50% along lines connecting both the front interface points and the rear interface points. Figure 6(i) shows the time response of the angular measurement at the turret interface about the critical x-axis at the front of the interface locations. It is observed that SIMAG operates effectively to reduce rotations at both the maximum and minimum values.

CONCLUSIONS

The presented results indicate that the passive SIMAG effectively isolates the helicopter body from the gun firing-induced vibrations. The passive SIMAG reduces the transverse displacements propagating to the helicopter shell by as much as 40% while reducing the displacements at the turret interfaces by over 50%. Therefore, SIMAG is capable of effectively isolating mission-critical electronic components within the helicopter. The latter was accomplished while improving an attack helicopter as a stable platform for mounting the 30-mm gun. The performance of SIMAG was demonstrated through the reduced gross rotations of the gun turret with the passive SIMAG in place. The passive SIMAG approach thus provides an effective and relatively light-weight isolation system, capable of maintaining or improving the gun system objectives and reducing operating and support costs, while providing the additional benefits by reducing exposure to whole-body vibrations and fatigue for the crew. The passive SIMAG used in this work had a total weight of 61 lb that increased the normal take-off weight of the helicopter only by 0.37%. Our goal is to reduce the SIMAG weight by 14% resulting in a 47 lb insert.

SUMMARY AND FUTURE DIRECTIONS

In this paper, two of the opportunities for improving the performance of Army airborne guns were identified and resolved via SIMAG. The positive impacts that ***S***mart ***I***solation ***M***ount for Airborne Guns (SIMAG) may have on the deficiencies of the current system were reviewed. Baseline and SIMAG-inserted finite element models were developed and analyzed. A forced response of the two systems under simulated gun firing loads was analyzed. Numerical simulations indicated that a completely passive SIMAG system has a strong potential for significantly reducing the vibratory energy propagating from the gun system to the helicopter shell. It was demonstrated that SIMAG has the capability to redirect the vibratory energy present in the system away from the interfaces between the helicopter shell and turret. The subsequent reduction in adverse excess energy may have numerous benefits to the operating and support cost for an attack helicopter and its subsystems. Additionally, SIMAG provides these benefits while enhancing the capabilities of attack helicopters as a viable mounting platform for the gun.

In the future phases of this work, conventional closed-loop active control capability will be added to the passive SIMAG system. These active control layers will target the vibratory energy remaining after the insertion of the passive SIMAG layer. Further studies will investigate the effectiveness of an active energy confinement system based on Spatial Decay-Causing Actuators (SDCA). It is anticipated that the addition of the SDCA layer will make SIMAG a smart system. With the realization of the full SIMAG system, the distribution of vibratory energy will be optimized and conventional active controls will be seamlessly incorporated into the control algorithm.

In addition to an attack helicopter, both passive and active versions of SIMAG have strong potentials for other Army systems. The SIMAG technology may be transitioned in ground vehicles such as various HMMWV and the Light Scout Vehicle.

ACKNOWLEDGEMENTS

The Small Business Innovation Research (SBIR) program, under Army contract numbers DAAE30-99-C-1014 for Phase I and DAAE30-00-C-1007 for Phase II, supported this work. The authors acknowledge the strong support of the technical and administrative personnel at the Picatinny Arsenal, NJ. Their valued assistance to this project is greatly appreciated and has aided us in producing a highly successful outcome.

REFERENCES

1. M. Mattice, "Plenary presentation: Improving Combat Vehicle Lethality with Innovative Applications of Smart Materials," *Symposium of Smart Structures and Materials*, San Diego, 1998.
2. D. Allaei, "Vibration Control by Confinement: An Overview," *Proceedings of the Fourth International Congress on Sound and Vibration*, M. Crocker and N. Ivanov, St. Petersburg, Russia, 1996.
3. M. B. Levine-West and M.A. Salama, "Mode Localization Experiments on a Ribbed Antenna," *AIAA Journal*, 31(10), 1993.
4. F. J. Shelley and W. W. Clark, "Active Mode Localization in Distributed Parameter Systems with Consideration of Limited Actuator Placement," *15th ASME Biennial Conference on Vibration & Noise*, 1995.
5. A. Yigit and S. Choura, "Vibration Confinement in Flexible Structures via Alternation of Mode Shapes by Using Feedback," Journal of Sound and Vibration, 179(4), pp. 553-568, 1995.
6. A. F. Vakakis, M. E. King, and A. J. Pearlstein, "Free and Forced Localization in a Nonlinear Periodic Lattice," *ASME Journal*, 59, 1993.
7. D. Allaei, "Application of Localized Vibration and Smart Materials in Controlling the Dynamic Response of Structures, Part I-VI," delivered to DARPA-SBIR, 1992-97.
8. M. Labadi and D. Allaei, "Loci Veering and Mode Localization in Elastic Linkages and Frames," *Southeastern Conference on Theoretical and Applied Mechanics (SECTAM XVI)*, The Univ. of Tennessee Space Institute, 1992.
9. D. Allaei, "Application of Localized Modes in Vibration Control," *2nd International Congress on Recent Developments on Air and Structure Borne Sound and Vibration*, 1992.
10. D. Allaei, Y. T. Shih, and D. J. Tarnowski, "A Comparison between Passive Vibration Control by Confinement and Current Passive Techniques," SAE paper 97NV61, 1997.
11. D. Allaei and Y. T. Shih, "Influence of Confined Vibration on Sensor and Actuator Optimization," SAE 97NV48, 1997.
12. D. Allaei, "Smart Isolation Mount for Army Guns," Final Phase I report, Army-SBIR, ARDEC, 1999.
13. D. Allaei, "Vibration Control by Confinement of Vibration Energy," U.S. Patent 6,032,552, March 7, 2000.
14. D. Allaei, "Apparatus and Method for Confinement and Damping of Vibration Energy," U.S. Patent 6,116,389 dated September 12, 2000.
15. D. Allaei, "Vibration Energy Confinement Analysis Software (VECAS)," Report, NSF-SBIR, June 1998.
16. D. Allaei, D. J. Tarnowski, M. S. Mattice, and R. Testa, "Smart Isolation Mount for Army Gunds – part I: Preliminary Results," Proceedings of SPIE, Vol 3990, Paper No. 3990-08, March 2000.
17. Phase I Final report, Integrated Systems, Inc., Cont. No. DAAA21-87-C-0276, 1988.

THE DYNAMIC MODELLING OF A NOVEL DESIGN OF 120mm APFSDS TRAINING ROUND

D N Bulman[1] and J G Ferries[2]

[1]*Danby Engineering Ltd., High Gill House, Low Row, Richmond, North Yorkshire, DL11 6NE, UK.* Tel: +44 (0) 1748 886345 Fax: +44 (0) 1748 886014 e-mail: dnbulman@cs.com
[2]*On behalf of the design team:* BAE SYSTEMS, *RO Defence, Birtley, Chester-le-Street, Co. Durham, UK* Tel: +44(0) 191 411 2040 Fax: +44(0) 191 411 2022 e-mail: jamie.ferries@baesystems.co.uk

A novel design for a low cost, high volume production, APFSDS training round has been proposed for use in 120mm tank gun systems. The design of this round is unusual because of the method of support between the penetrator and the sabot, and also in the way in which the forces are transmitted to the penetrator in order to accelerate it up the bore. This has meant that the standard gun dynamics model has required modifying in order to produce meaningful simulations. This paper describes the design concept and the way in which an existing gun dynamics simulation package has been used to model the round in order to optimise its design parameters. The results from these simulations have been successfully used to assist the design iterations during development, and achieve the project requirements.

INTRODUCTION

It is now accepted that the design or modification of new or existing gun systems will benefit considerably from a full dynamic analysis of the firing and launch process. This analysis should include the behaviour of the barrel, the mounting, and the shot as it travels up the bore. Over the last 25 years studies in this subject area have provided guidance in the development of mathematical models [1 to 11] which describe the interaction between the various components and can finally predict the weapon performance. Comprehensive simulations now include flexible and recoiling barrels, effects of bore wear, non-linear supports, flexible cradles, rigid or flexible shots, and the supporting vehicle. However it is almost impossible to develop a single simulation program which can cover, with basic data entry, all the possible configurations and modifications which the designer may want to introduce. For this reason, user defined programming areas are provided for development of special cases. The proposed APFSDS (Armour Piercing, Fin Stabilised, Discarding Sabot) training round, for use in a 120mm tank gun system, is an unusual design and required the use of this facility to ensure that accurate and comprehensive simulations could be made.

THE TRAINING ROUND

The design of most APFSDS rounds is centred on the principal that, to improve penetration, the actual projectile is required to be relatively long and thin, with high mass and maximum possible kinetic energy. To achieve high kinetic energy, the velocity needs to be

high, and this therefore requires high forces to accelerate it in the bore. For a certain pressure, the projectile therefore needs to have a large diameter to achieve the require acceleration. This conflicts with the smaller diameter required to increase penetration.

The solution to this problem has been to support the penetrator in a light weight structure (the sabot) which has a larger diameter than the penetrator. The pressure force from the propellant acts on the base of the sabot, which then accelerates and carries the penetrator with it. At shot exit, the sabot, which is normally in three parts, falls away and leaves the penetrator to continue to the target.

Because of the relatively high mass of the penetrator combined with the very high accelerations, the longitudinal forces between the penetrator and the sabot are very large. The sabot must also prevent bending of the penetrator, due to severe lateral motion, and the possibility of buckling deformation [12]. The interface between the sabot and penetrator, which carries these forces, is often in the form of a screw thread. This therefore requires careful design in order to prevent failure.

A large part of the cost in developing a round is concerned with trials and evaluation. Once a round has been successfully designed and tested to provide good accuracy and consistency, combined with high penetration, the costs are basically concerned with production. In this case the material costs of the high density penetrator are normally high, and the accurate machining of the interface between the penetrator and the sabot add significantly to the final total.

A training round needs to have the same overall characteristics as the service round. It must have similar overall dimensions so that ergonomically, handling the round feels no different. It must also fire in a similar way with equivalent accuracy and consistency, although penetration is not important. It is preferable if its maximum range can be reduced so that it can be fired on ranges where overshoot could be a problem. This must then be achieved at minimum cost.

This has been accomplished by RO Defence with the design shown in Fig 1.

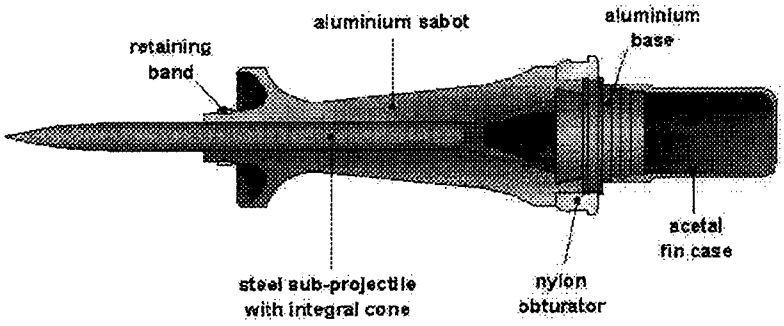


FIGURE 1. THE 120MM TRAINING ROUND.

It should be noted that this round is part of a separate three piece ammunition system consisting of the round, the charge and a detonation cartridge. The round shown in Fig 1 is therefore handled separately from the charge.

The basic construction of the round consists of three main components, the penetrator (sub projectile), the sabot, and the aluminium base block. The penetrator is considerably shorter than that of the service round. It is made of steel and, instead of stabilising fins, it has

a cone at its base which modifies the aerodynamic characteristics. This ensures that its operating range is reduced, which enables it to be fired on ranges where over shoot may be a problem.

The internal shape of the sabot is considerably different from that of the service round and the cone of the penetrator fits within it. The sabot is in three parts, split radially, so that discard can be achieved in the same way as normal.

The significant difference between this round and the service round is the interface between the penetrator and the sabot. There is no screw thread to transmit the longitudinal forces between the two parts, therefore an aluminium base block has been added which takes the base pressure and then acts on the back of the penetrator. Although this effectively adds an extra component, the reduction in manufacturing costs, in not having to produce an interfacing thread between the penetrator and the sabot, is very significant. The major components are then held together with the nylon obturator at the rear of the sabot and a simple retaining band at the front.

A further point to note is that the service round has a much longer penetrator than the training round and protrudes well behind the back of the sabot with its stabilising fins. It then has a combustible protective cover, which fits over the fins. The training round has a similar dummy component, the acetal fin case, so that the overall dimensions and appearance remain the same as the service round. When fired, this case is designed to disintegrate immediately at shot start so that the propelling gases act directly on the aluminium base and the nylon obturator.

THE MODEL

The Main Considerations

The modelling of the training round was based on the gun dynamics simulation package SIMBAD [13,14]. The round is fired from a rifled barrel, so although spin is reduced by a slipping driving band, the spinning two piece flexible shot model was used. This assumes the standard configuration which is found in the service round. It was therefore modified to meet the requirements of the training round by using the 'User Defined Routines' of the program [14].

The first and most obvious difference is the aluminium base block, which takes the majority of the base pressure and rests squarely against the rear of the penetrator. It is held together with the sabot by the nylon obturator (the driving band), and the taper ensures that it cannot easily be detached once it is assembled. There is a gap between the base block and the sabot at each perpendicular face.

The transverse stiffness of the driving band is a significant parameter in the simulation, and the force from this normally acts directly on the sabot. In this design the force must be split between the sabot and the base block. Similarly, the torque produced by the rifling through the driving band must also be split between the sabot and the base block.

The standard model assumes that this rifling torque is imparted to the sabot, and hence to the penetrator by the threaded interface. In the training round the transmission of torque must be from the base block to the penetrator at the rear interface, and/or from the sabot to the penetrator through contact at the top edge of the cone. (It may be noted that the tapered

section at the rear of the penetrator is such that contact with the sabot is only around its greatest diameter.)

It has already been stated that the pressure acts on the base block, which pushes against the rear of the penetrator. Pressure will also act on the driving band, and the force generated will act on the sabot. If the exposed rear area of the band was large compared with the exposed rear area of the base block, it may be possible that the acceleration of the sabot may try to exceed that of the base block and move forward relative to the penetrator. This would also depend on the relative masses of the components. However, the design is such that the penetrator should always act to push against the sabot, but even so, both cases should be considered in the model.

In this new concept, the support which the sabot gives to the penetrator is only in the transverse direction. With a threaded interface, as used in the service round, any transverse clearance is normally reduced as the threads engage when the shot starts to accelerate. With the proposed design this support may not be consistent from shot to shot, and may even vary while the shot travels up the barrel. This is because manufacturing tolerances may produce varying clearance between the sabot and the penetrator, and this clearance may increase during firing. This could occur because the three petals of the sabot may be forced apart by either the gas forces on the front of the sabot, or by the penetrator at the tapered rear interface. The effect of this could be to allow the penetrator to move transversely within the sabot, and possibly increase shot transverse motion (linear and angular).

Application to the Model

The penetrator and base block were modelled directly using the penetrator model in SIMBAD. The modulus and density factors for the base block were set to give the correct properties for aluminium. It was assumed that contact was maintained on the complete interface between the two parts. This was considered justified following initial calculations, which showed that, once shot motion commenced, the reaction between the two parts should not drop below 100kN. The interface was therefore modelled as a perfect joint.

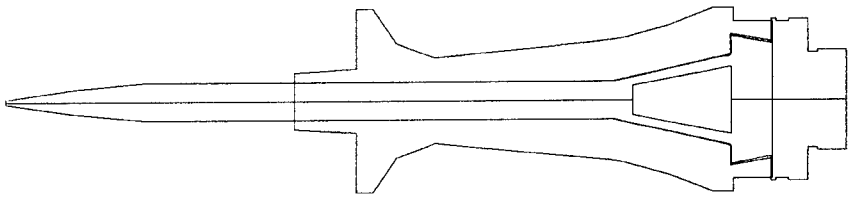


FIGURE 2. THE COMBINED PROFILES AS ENTERED FOR THE SIMULATION.

Later analysis of the results confirmed that any resultant moments due to flexing of the penetrator were unlikely to cause separation at any part of the interface. Furthermore, recovered components from actual firings confirmed that no slip or movement occurred between the two parts.

The sabot was modelled in the normal way. Fig 2 shows a plot, directly from the program, of the combined profiles for the two basic parts of one of the early designs. It may be noted that the program automatically reduces each profile into the individual elements, and following this the modulus and density factors for the base block were changed.

The interface between the sabot and the penetrator normally assumes a stiffness between each corresponding node of the sabot and penetrator. There are separate stiffnesses for the longitudinal and transverse directions, and also for the spin. In each case this stiffness can be non-linear with or without clearance. To model this unusual design, the longitudinal and spin stiffnesses were set to zero, and the transverse stiffness was modelled with clearance. Separate stiffnesses were then introduced to act between the sabot and the penetrator at the nodes which corresponded with the rear of the cone on the penetrator. These stiffnesses acted in the longitudinal and spin directions. By monitoring the resultant forces from these stiffnesses it was possible to determine the torque and the longitudinal force transmission between the sabot and the penetrator.

The distribution of the transverse forces and spin torques from the driving band to the sabot and the base block is difficult to define. SIMBAD allows for non-linear compression of the driving band, and will also allow for the initial compression of the band as it enters the bore. The calculation of the forces uses the relative displacements between the sabot and the barrel, plus the initial diameter of the band and the bore profile. The calculated forces are then applied to the sabot. The program does not model the force distribution along the band so, in order to split the forces and torques between the sabot and base block, it was assumed that the driving band stiffnesses could effectively be factored between the sabot and the base block. This factor was based on the contact areas between the band and the sabot and/or the base block. Two independent calculations were then made using the relative displacements between the sabot and the barrel, and the base block and the barrel.

[It may be considered that a simpler solution was to apply the existing single calculation of the band forces using the relative displacements between the sabot and the barrel. These could then be factored between the sabot and the base block. However it must be noted that there is relative movement between the sabot and the base block. Even though this may be very small, application of a force on the base block, which is dependent upon the sabot deflection, can result in an unstable solution.]

The slipping driving band was modelled by setting the rifling stiffness of the driving band to a very low value, and setting the viscous torsional damping coefficient to a value which gave the correct spin rate at shot exit. In practice the actual process is much more complicated, but this model of a viscous coupling gave very close correlation to the accepted behaviour.

The acetal fin case on the rear block was ignored because it is assumed that the design is such that it will disintegrate quickly in the bore at shot start, and will not affect the remainder of shot travel.

SIMULATION PROCESS

Once the model had been completed, various tests were applied to validate the modifications to the basic model. These included changing the diameter of the base block, and changing the factor used to distribute the driving band forces between the sabot and the base block. In this way it was possible to demonstrate how the direction of the longitudinal force between the sabot and the base block would change as the diameter of the base block was reduced. It was also possible to show how the torque transfer between the sabot and the penetrator would vary with the driving band force distribution factor.

It is not the intention of this paper to give a detailed description of all the simulations which were made to optimise the design of the training round, but the few results below are designed to show how the simulations can be used to influence the design decisions.

The table shows the change in penetrator pitch velocity at shot exit for changes in the driving band force distribution factor. A factor of 1 indicates that all of the driving band sits on the sabot. A factor of 0 indicates that all of the driving band sits on the base block. The indication is that as the force distribution from the driving band is increased towards the base block, a reduction in pitch velocity at shot exit should occur. Previous experience has shown that this will normally result in a reduction in dispersion.

Factor	Pitch Velocity rads/s.
1.00	-2.70
0.75	-1.93
0.50	-1.13
0.25	-0.806
0.00	-0.425

It must be emphasised that this set of results is achieved with all other parameters fixed. The situation may change if, for example, the length of the sabot was changed or the clearance between the penetrator and the sabot was different. There are many other possibilities, and it is for this reason that many simulations need to be made with different barrel profiles, different pressure time curves, and many shot design possibilities. An optimised solution can then be achieved.

In this particular case the main variables chosen for investigation on the shot are shown in Fig 3. The temperatures indicate the use of different pressure time profiles, which would be expected at those temperatures.

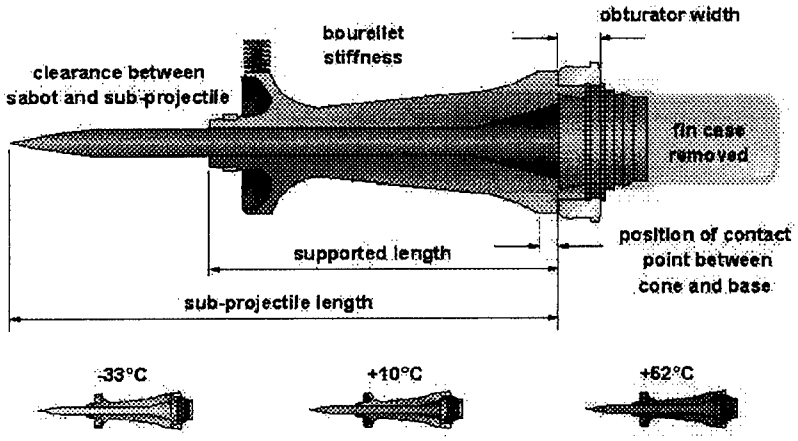


FIGURE 3. CHOSEN VARIABLES FOR ANALYSIS WITH SIMBAD.

The time for each simulation was approximately 5 minutes on a 733MHz Pentium 3 PC. The simulations were made using the multiple run facility which also enables the parameter analysis function of the program to be used. Many simulations were made to cover a wide range of the chosen variables.

APPLICATION OF RESULTS

The results from the analysis have been used together with experimental firings to assist in the optimisation of the design of the new training round. The aim has been to achieve

the same accuracy and consistency of the service round, and also give the same handling characteristics.

At the stage of writing this paper, over 600 rounds of various designs have been fired. This has helped in understanding the interaction between the main physical parameters of the shot. Supported by the theoretical analysis and the trials data, significant improvements to the design of the projectile have been accomplished. All the parameters shown on Fig 3 have been optimised, and the required objectives of the project have been met.

ACKNOWLEDGMENTS

The authors would like to acknowledge the help and assistance of RO Defence (Birtley). The training round described in this paper is part of a development program designed to meet the future training requirements of the British Army with Challenger 2.

REFERENCES

1. T E Simkins, Parametric Resonance in Gun Tubes. *First Conference on Dynamics of Precision Gun Weapons.* R-TR-77-008, US Army Armament Research and Development Command, Dover, New Jersey, January 1977.
2. T E Simkins, Transverse Response of Gun Tubes to Curvature Induced Loads. *Second US Army Symposium on Gun Dynamics,* 19-22 September 1978.
3. B A Taylor and P G Thomasson, A Consistent R and D Assessment Technique for the Modelling of Gun System Dynamics. *Third US Army Symposium on Gun Dynamics,* 11-14 May 1982.
4. M T Soifer and R S Becker, Gun Dynamics Simulation Model of the 75mm ADMAG Gun System. *3rd US Army Symposium on Gun Dynamics,* 11-14 May 1982.
5. D N Bulman, The Effect of Bearing Clearance and Barrel Expansion on Barrel Response. *4th US Army Symposium on Gun Dynamics,* 7-9 May 1985.
6. H J Sneck and R Gast, Normal Mode Analysis of Gun Tube Dynamics. *4th US Army Symposium on Gun Dynamics,* 7-9 May 1985.
7. E M Schmidt, Analysis of Sources of Firing Error. *9th International Symposium on Ballistics, UK,* 29 April to 1 May 1986.
8. T E Simkins, Resonance of Flexural Waves in Gun Tubes. *5th US Army Symposium on Gun Dynamics,* 23-25 September 1987.
9. T F Erline and M D Kregel, Modelling Gun Dynamics with Dominant Loads. *5th US Army Symposium on Gun Dynamics,* 23-25 September 1987.
10. D A Raburn and K A Bannister, Finite Element Models to Predict the Structural Response of 120mm Sabot/Rods during Launch. *6th US Army Symposium on Gun Dynamics,* 15-17 May 1990.
11. D. N. Bulman, Simulation of Gun Dynamics to Improve Accuracy and Consistency. *15th International Symposium on Ballistics, Israel,* 21-24 May 1995.
12. D N Bulman, The Introduction of Spin to an Existing Flexible Shot Model within a Gun Dynamics Simulation. *9th US Symposium on Gun Dynamics,* 17-19 November 1998.
13. SIMBAD (Simulation of Barrel Dynamics) User Manual (November 2000), Danby Engineering Ltd, High Gill House, Low Row, Richmond, N. Yorks, DL11 6NE, UK. Tel/Fax +44 (0) 1 748 886345/886014.
14. SIMVED (Simulation of Vehicle Dynamics) User Manual (November 2000), Danby Engineering Ltd, High Gill House, Low Row, Richmond, N. Yorks, DL11 6NE, UK. Tel/Fax +44 (0) 1 748 886345/886014.

ADAPTIVE GUN BARREL VIBRATION ABSORBER

Andrew Littlefield and Eric Kathe[1]

[1]*US Army, TACOM-ARDEC Benét Laboratories, Watervliet Arsenal, NY 12189-4050*

Gun barrel vibrations lead to dispersion in the shot patterns. Thus, reducing these vibrations should lead to increased accuracy. Since the muzzle is the anti-node for all vibration modes and its vibrations have the greatest effect on shot dispersion, it is the obvious location to attempt to dampen the vibrations. A model of the gun barrel was created in MATLAB® and verified by modal impact testing. Modal impact testing was done for the barrel alone and for three different muzzle brake vibration absorber configurations. Significant reductions in muzzle vibrations were achieved using the vibration absorber. Methods of making the vibration absorber adaptive and models of such a system are presented.

INTRODUCTION

Vibration of the gun barrel in rapid-fire systems leads to dispersion in the shot patterns. The wider the dispersion the more rounds required to effect the desired damage on the enemy. An intuitive way to reduce this shot dispersion is to reduce the vibrations of the barrel. The end of the barrel is the anti-node for all vibration modes and its vibrations have the greatest affect on shot dispersion, so it is the obvious location to attempt to dampen the vibrations. This work focuses on doing just that.

The system under study in this work is the 25mm M242 Bushmaster chain gun. It is part of the M2A3 and M3A3 Bradley Fighting Vehicle Systems and is designed to engage and defeat armored vehicles as well as provide suppression fire. When engaging armored enemy assets, such as armored personnel carriers, accuracy is extremely important. The M242 fires five different rounds, M791, M792, M793, M910, and M919, though only the M793 training round was used in the tests.

A gun barrel vibration absorber has been previously designed [1] and tested [2] for use on the 120mm XM291 tank gun [3]. This design had the absorber as part of the gun's thermal shroud. The present effort differs in its unique location, application to rapid-fire gun systems and its possible dual use as part of a fuse setting system.

The vibration absorber being considered is of the proof mass actuator type and is mounted unto the muzzle brake. This allows for the absorber to be easily mounted and removed with the muzzle brake while still acting at the barrel location of greatest vibration activity. Addition of the absorber reshapes the frequency response by moving the resonant modes and zeros. This shifting effectively rejects the vibrational energy. Also the motion of the absorber enhances the dissipation of this energy.

First, the barrel is modeled in MATLAB® using a finite element approach [4]. The Euler-Bernoulli finite element technique is used to generate second order equations of motion of the barrel as a non-uniform beam. These are then converted to the first-order state space domain and transformed into the frequency domain. Predictions for the mode shapes and resonant

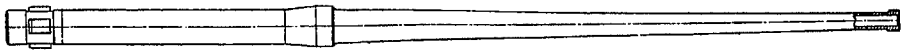


FIGURE 1. M242 BARREL

frequencies are generated. After completing the model, it is verified by performing modal impact testing on the barrel. These results are then used to fine-tune the model.

Testing of the barrel with different vibration absorbers is then conducted. Three different versions are used, the differences being the number of rods connecting the mass to the barrel. By varying the number of connecting rods the stiffness, and thus the frequency, of the vibration absorber can be tuned.

For the vibration absorber to be adaptive, this tuning of its frequency should be accomplished without physically changing the rods. Ideally this should be done autonomously or at worst, by selecting a setting from a list. As a first step, a MATLAB® model for an absorber with adjustable stiffness will be presented. Possible ways of making the absorber truly adaptive will be presented.

MATLAB® MODEL

A finite element model of the barrel minus the vibration absorber was created in MATLAB®. Euler-Bernoulli beam approximations and Hermite-cubic interpolation functions are used to form the mass and stiffness matrices for the undamped second order equations of motion by approximating the barrel, a continuous non-uniform beam, as a series of discrete elements. Continuity of lateral displacement and slope are imposed at the element boundaries. When assembled these elements closely approximate the dynamics of the barrel [4].

The geometry of the barrel is entered in 1 mm increments and any non-circular cross sections are smeared together to become circular. This smearing was done to the lugs near the breech end and to the rifling. The mass of the beam is calculated by adding the mass of each of these slices. The actual shape of the beam can be seen in Figure 1. The model's version of this can be seen in Figure 2.

The barrel is just over 2 m long. The muzzle brake was approximated as two hollow cylinders with different interior diameters followed by a hollow cone. The diameters of the cylinders and cones were selected so that both mass and location of the center of gravity matched those of the muzzle brake. A Pro/Engineer® solid model of the muzzle break was used to verify the mass properties.

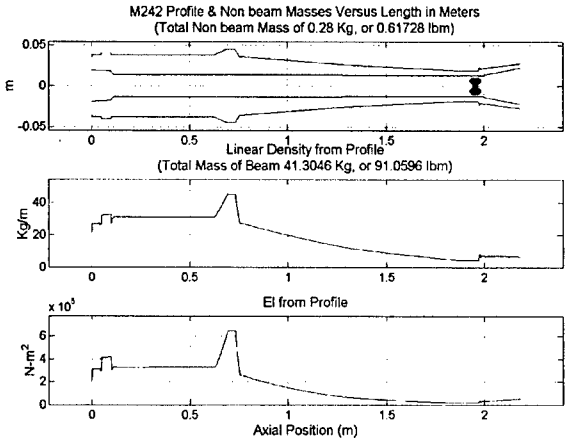


FIGURE 2. BARREL GEOMETRY

After the geometry has been entered the barrel is automatically broken into a user defined number of elements. Nodes are forced to exist at both ends of the barrel and anyplace where constraints are specified. The springs used to hang the barrel during modal testing were entered as constraints in this fashion. The spring constant for the springs was found by hanging weights on them and measuring the deflection.

The other enforced node was at the location of the response accelerometer. This was to allow easy comparison between

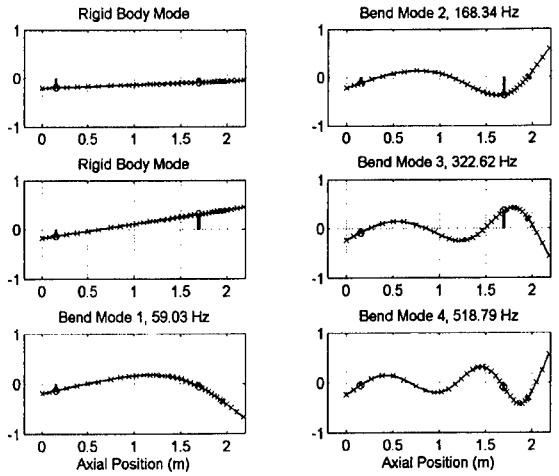


FIGURE 3. DAMPED MODE SHAPES AND NATURAL FREQUENCIES

model and experiment. The mass of the accelerometer was also included and shows up as the dark circles in Figure 2.

Rayleigh proportional damping is used in the model. The values entered were determined in a previous report using this software for analyzing an XM291 gun barrel [1]. After performing an experimental modal analysis on the barrel, experimentally found values were used and the model was rerun. Only minor differences in the resonant frequencies were found.

After the required data was entered the model was run and output generated. The software generates undamped and damped mode shapes and natural frequencies, a pole zero plot of the eigenvalues, time response of the muzzle to a breech impulse, and a bode plot of the muzzle response, plus additional plots about the quality of the FEA analysis. In this case we are interested in the damped mode shapes and natural frequencies. These can be found in Figure 3.

MODAL IMPACT TESTING

After completion of the MATLAB® model, an experimental modal analysis was performed to validate the model. The barrel was hung from two springs to simulate a free-free condition. These springs were contained in the model as mentioned above. This did not present a perfect free-free situation but there is more than an order of magnitude between the highest rigid body mode (1.27 Hz) and the lowest flexible mode (59.03 Hz) so this was deemed satisfactory. Additionally the springs are explicitly represented in the model.

The goal of the modal analysis was to generate a frequency response plot between a force at the breech and the response of the muzzle. For this study an impact was used as the force and the acceleration of the muzzle was the response. An HP 3566A PC Spectrum / Network Analyzer was used to calculate the frequency response. A PCB Impact Hammer with a Delrin tip delivered the impact. The 6 dB roll off point of the tip was found to be 1.605 kHz. A PCB ICP Accelerometer measured the response. The ICP power supply and signal conditioning for both of these was provided by a PCB 12 Channel Rack Mounted Power Unit with a variable gain of 0 to 100 per channel. This set up can be seen in Figure 4.

The HP 3566A was setup with a bandwidth of 800 Hz, 3200 frequency lines and force / exponential windowing. Uniform averaging was performed with a total of 16 averages being used per run. The gain was set to provide good signal strength. After each

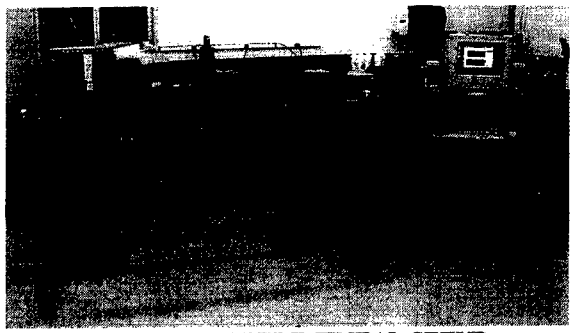


FIGURE 4. EXPERIMENTAL SETUP

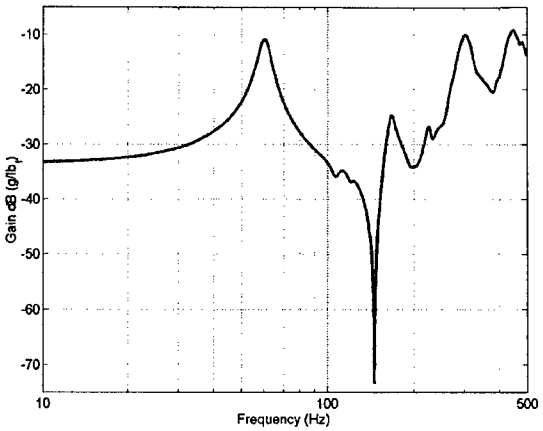


FIGURE 5. PLAIN BARREL – FREQUENCY RESPONSE

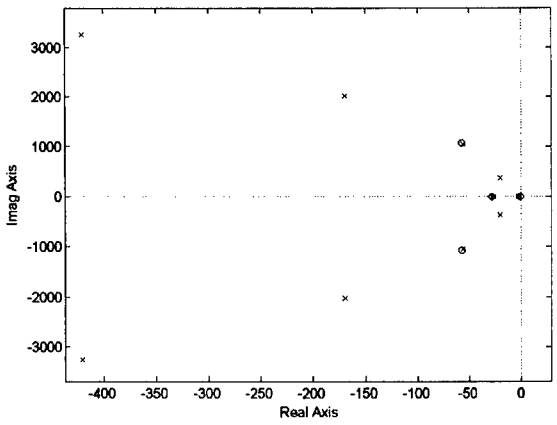


FIGURE 6. POLE-ZERP MAP FOR PLAIN BARREL

impact the data was checked for double hits and overloading of the accelerometer.

The frequency response for barrel can be seen in Figure 5. The first four modes are plainly visible. A collocated pole–zero pair, causes the strange behavior of the second mode. Examination of a pole-zero plot from MATLAB® shows this same behavior. Figure 6 shows this plot for the first four modes and how there is a zero collocated with the second mode.

The Peak Amplitude Method [5] was used to extract the necessary modal parameters from this data. To determine the damping ratio of a peak, equations (1) and (2) were used.

$$\zeta = \frac{1}{2}\eta \tag{1}$$

$$\eta = \frac{1}{2}\frac{\omega_a^2 - \omega_b^2}{\omega_r^2} \tag{2}$$

Where ζ is the viscous damping ratio, η the structural damping loss factor, ω_r is the natural frequency of the peak, and ω_a and ω_b are the half power points. These quantities can be seen in Figure 7.

Once ζ has been found for at least two peaks the proportional damping coefficients, α and β can be found from the following formulas:

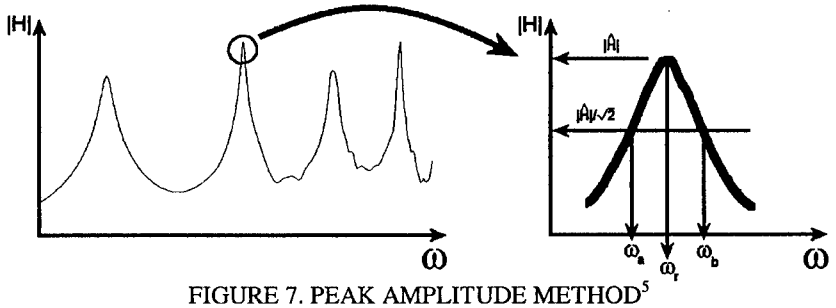


FIGURE 7. PEAK AMPLITUDE METHOD[5]

$$\alpha = -2\frac{\omega_1\omega_2(\omega_1\zeta_2\sqrt{1-\zeta_2^2} - \omega_2\zeta_1\sqrt{1-\zeta_1^2})}{-\omega_1^2 + \omega_1^2\zeta_2^2 - \omega_2^2\zeta_1^2 + \omega_2^2} \quad (3)$$

$$\beta = \frac{-\alpha + \alpha\zeta_2^2 + 2\zeta_2\sqrt{1-\zeta_2^2}\omega_2}{\omega_2^2} \quad (4)$$

Using these formulas the following data was found for the three tests shown in Figure 5.

TABLE 1. FREQUENCY RESPONSE PARAMETERS

Plain Barrel with Muzzle Brake				
Peak	**Magnitude**	**Frequency**	**Coherence**	**ζ**
	dB (g/lbf)	Hz		
1	-10.870	60.25	0.9990	0.0456
2	-24.710	167.25	0.9543	0.0361
3	-10.008	304.50	0.9306	
4	-9.117	448.25	0.9314	
α (s-1)	28.428			
β (s)	4.293E-05			

Comparison of this data with Figure 3 shows that the model predicted a stiffer system than was experimentally found. The higher in frequency one goes the more divergent the model and reality become. We are concerned with low frequencies though and the match between the model and experiment is very good for the first two modes. It is only off by about 1 HZ for these modes. This small amount of error is within what was seen from different runs and could be due to the accelerometer mounting and cabling and or the non-ideal connections of the support springs. The measured α and β were put back into the model to see if it would improve results but no appreciable difference was found.

MATLAB® MODEL WITH VIBRATION ABSORBER

Now that the model has been validated for plain barrel it must be modified to include the vibration absorber. The vibration absorber is a proof mass actuator that mounts to the muzzle brake. It consists of a 4.037 lb (1.831 kg) mass, suspended from spring rods, which are attached to a collar, which is in turn press fitted onto the standard muzzle break. The rods are ¼" in (6.35 mm) diameter and extend 5.8" (147.32 mm) from the collar to the mass.

There are three configurations of the vibration absorber: one with eight rods; another with four, two middle one removed top and bottom; and the last with

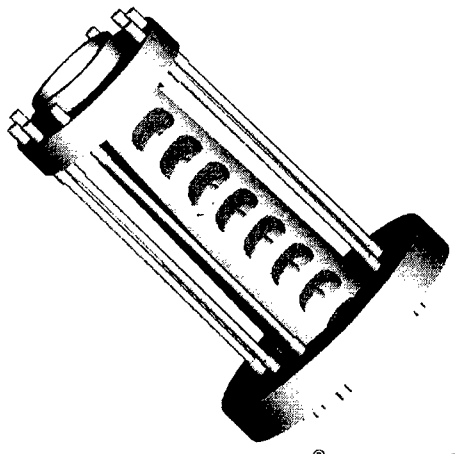


FIGURE 8. PRO/ENGINEER® MODEL OF THE VIBRATION ABSORBER

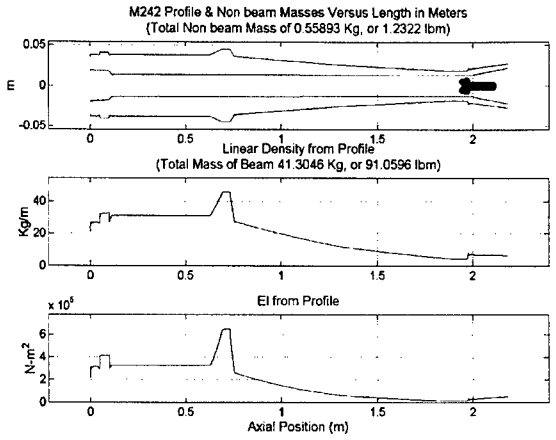


FIGURE 9. BARREL GEOMETRY WITH EIGHT-ROD VIBRATION ABSORBER

two rods oriented diagonally. Only the eight and four rod versions were modeled, using the same number of nodes and enforced node locations as the plain barrel. . The absorber's mounting collar was included by increasing the barrel's outer diameter in that area until the correct mass was added. Since the vibration absorber mounts to the muzzle brake, as before a Pro/Engineer® model was used to ensure that mass and center of gravity location were correct for the entire assembly. Figure 8 shows the model.

The connecting rods were treated as springs and thus by the standard approximation for a spring with mass, 1/3 of their mass was added to the absorber mass and 2/3 was added to the barrel as a lumped mass. The location of the lumped mass was adjusted so as that the center of gravity of the rods and absorber mass together was positioned as in the actual assembly.

The MATLAB® model allows for a mass and stiffness to be entered for a vibration absorber. The mass was a combination of the absorber mass and 1/3 of the rod mass. The stiffness of the absorber was found experimentally by assuming a cantilevered condition between the rods and the mounting collar and then performing a beam bending test. The natural frequencies were found to be 41 Hz and 29 Hz for the eight and four rod versions respectively.

The geometry used by the model for the eight-rod absorber can be seen in Figure 9. The dark area near the muzzle brake is the mass of the accelerometer as before plus the distributed mass of one third of the connecting rods. The only difference between the eight-rod and four-rod versions of the model is the mass of the rods. For the four-rod version the non-beam mass drops to 0.41947 Kg.

As with the plain barrel, the models were run once all required data was entered. Damped mode shapes and natural frequencies were recovered along with bode plots and pole-

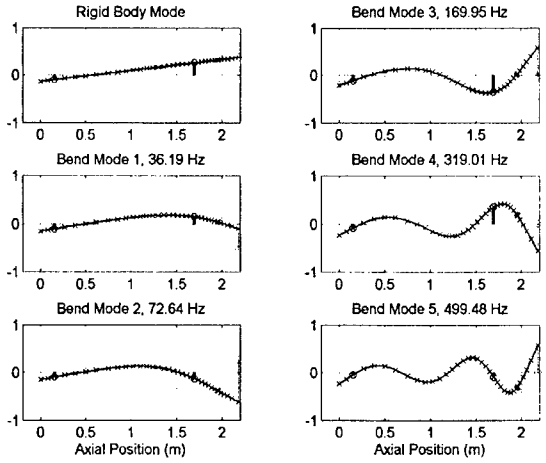


FIGURE 10. DAMPED MODE SHAPES AND NATURAL FREQUENCIES FOR EIGHT-ROD ABSORBER

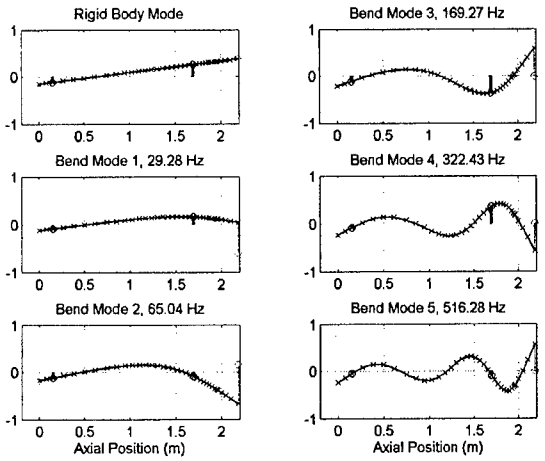


FIGURE 11. DAMPED MODE SHAPES AND NATURAL FREQUENCIES FOR FOUR-ROD ABSORBER

zero maps. The damped mode shapes and natural frequencies can be seen in Figure 10 and Figure 11. The circle at the end of the barrel represents the vibration absorber.

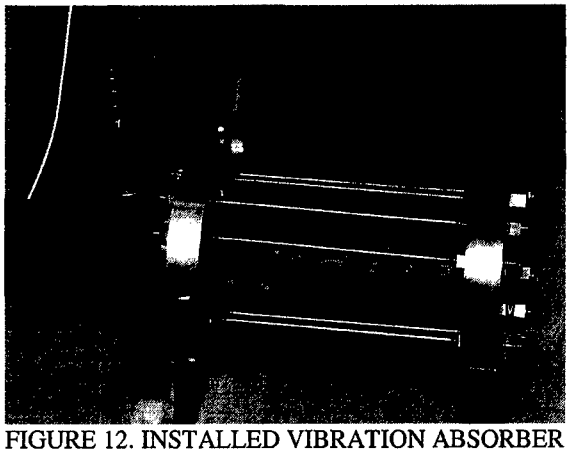


FIGURE 12. INSTALLED VIBRATION ABSORBER

VIBRATION ABSORBER

Now that we have a model including the vibration absorber, modal analyses were done on the different vibration absorber configurations. The barrel orientation and accelerometer placement was kept the same as the last plain barrel test. This ensured that any changes in the frequency response should be directly attributable to the vibration absorber and not changes in test setup.

Three configurations of the vibration absorber were tested, one with eight rods; another with four, two middle one removed top and bottom; and the last with two rods oriented diagonally. The four and eight rod versions were modeled in the previous section. The installed 8-rod absorber can be seen in Figure 12.

The same testing procedure outlined above was used. The rods were removed with the absorber in place so as to minimize any test setup changes between the runs. The absorber was aligned such that the flats of the muzzle brake were parallel to the floor. This is the normal firing position for the cannon. The results of the testing can be seen in Figure 13.

A couple of points are obvious from the plot. First, the major difference between the different configurations is the amount the first peak of the plain barrel is shifted. As fewer rods are installed in the absorber, and thus the absorber stiffness decreases, the first peak moves to progressively lower frequencies. Not only the amount of shift but also the magnitude of the first peak appears to vary with absorber stiffness. At first glance it appears that the eight and four rod vibration absorbers have the same magnitude, with the two rod having a lower magnitude. This will be discussed more when numbers are culled from the data. Lastly, the higher frequency peaks appear to have been largely unchanged.

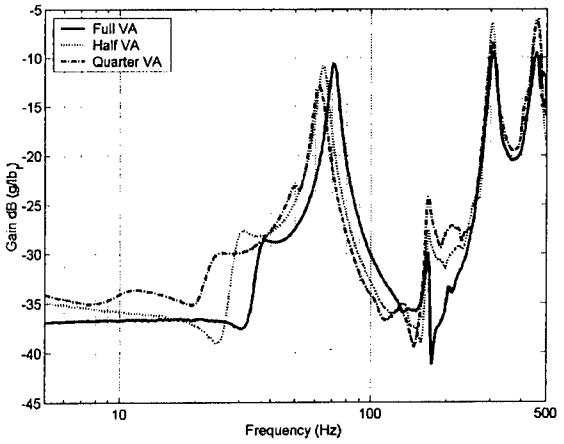


FIGURE 13. VIBRATION ABSORBER – FREQUENCY RESPONSE

If the absorber's frequency coincided with the first peak exactly the peak would have been removed and its energy shifted into the new peaks on either side of it [6]. However we do not have this case so the absorber pushes the peak to a higher frequency. Had the absorber's frequency been above that of the barrel's first mode then it would have pushed the peak to a lower frequency. The additional pole / zero added by the absorber can be seen in the small resonance before the first peak. As stated earlier the strange response at the barrel's second mode is due to a collocated pole-zero pair.

TABLE 2 FREQUENCY RESPONSE PARAMETERS

Full Vibration Absorber			
Peak	**Magnitude**	**Frequency**	**Coherence**
	dB (g/lbf)	Hz	
0	-28.642	38.50	0.9937
1	-10.614	71.25	0.9991
2	-29.886	168.50	0.9887
3	-9.323	307.00	0.9139
4	-9.513	456.25	0.8915
Half Vibration Absorber			
Peak	**Magnitude**	**Frequency**	**Coherence**
	dB (g/lbf)	Hz	
0	-27.683	31.25	0.9998
1	-10.793	64.50	1.0000
2	-27.711	169.75	0.9993
3	-6.541	304.00	0.8724
4	-6.054	460.75	0.8821
Quarter Vibration Absorber			
Peak	**Magnitude**	**Frequency**	**Coherence**
	dB (g/lbf)	Hz	
0	-29.940	25.50	0.9996
1	-13.033	62.50	0.9995
2	-24.251	169.50	0.9777
3	-8.395	304.75	0.8640
4	-6.412	458.50	0.8528

In order to draw more detailed conclusions and to compare to the non-vibration absorber results actual numbers must be removed from the results. The same peak amplitude method was used to pull out this data. The results of this analysis can be seen below in Table 2. The peaks are numbered to coincide with the ones in Table 2, with Peak 0 being the absorbers own peak.

From these numbers it is apparent that the less stiff, i.e. less rods, the vibration absorber is the lower it shifts the first frequency of the barrel. For the higher frequency peaks it appears that the differences seen are due to errors in the data. As far as magnitude goes there appears to be some contradictory data. It appears that the half-absorber produce large magnitude gains than the full but that the quarter absorber produces smaller ones. This could be due to the fact that the quarter absorber no longer has the same cantilever boundary conditions as the other two.

Comparison of this data with Figure 10 and Figure 11 shows that the model overall predicted a stiffer system than was experimentally found. Though the mode of the vibration absorber itself was found to be higher than predicted. This may be due to the way its stiffness was found. The higher in frequency one goes the more divergent the model and reality become. We are primarily concerned with low frequencies though and the match between the model and experiment is very good for the first three modes. It is only off by about 1 HZ for these modes. This small amount of error is within what was seen from different runs and could be due to the accelerometer mounting and cabling and/or the non-ideal connections of the support springs.

COMPARISON

Now that we have looked at the barrel by itself and with a vibration absorber separately it is time to compare the two directly. Figure 14 shows the frequency response of the plain barrel and the three vibration absorber configurations. Figure 15 shows a close up view of the first mode of the barrel.

Examining Figure 14 the two most obvious changes are the shifting of the first mode and the lessening of the zero around 150

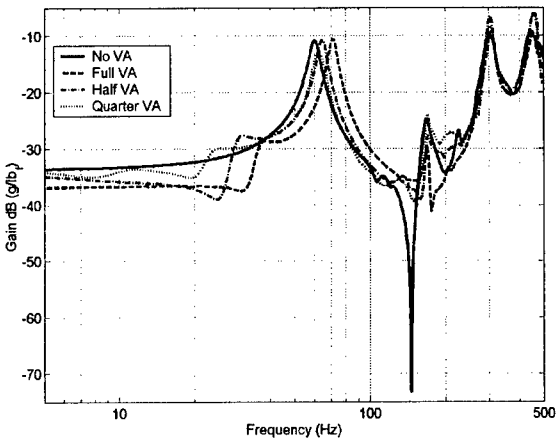


FIGURE 14. FREQUENCY RESPONSE – COMPARISON

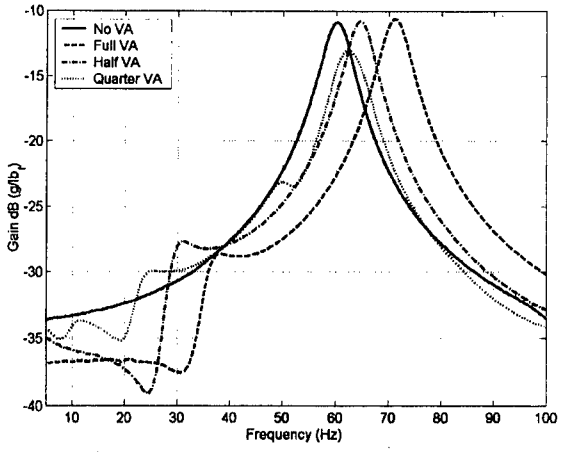


FIGURE 15. FREQUENCY RESPONSE COMPARISON 0 TO 100 HZ

Hz. The higher modes do not appear changed at all. Figure 15 shows the shifting of the first mode more clearly and how the two-rod version is able to reduce the magnitude of the first mode.

Comparing Table 1 and Table 2 one can see that these observations are born out. The second and higher modes are hardly shifted, if at all, while the first one is shifted by as much as 11 Hz. This shifting is what allows the absorber to dampen the system's vibrations. If the system resonance can be shifted away from the disturbance then the vibrations will be reduced.

As stated previously the inclusion of a vibration absorber shifts the modes around it away from its own mode. This accounts for the shifts seen in the barrel's first mode. As part of this shift the absorber can also take energy from the peak it shifts. If the absorber's mode is coincident with one of the system resonances then it would have split the mode and its energy into two smaller resonances.

The two-rod absorber is the only that has an appreciable effect on the magnitude of the barrel's first mode. It reduces the magnitude by almost 3 dB. Due to its different boundary conditions though this may not be as beneficial as it first seems. It could be that it is shifting energy from the vertical plane to the horizontal. Without further testing, it cannot be determined if this drop in the magnitude of the vertical response is beneficial or detrimental to system performance. An increase in horizontal motion would not be beneficial.

MATLAB® MODEL – VARIABLE STIFFNESS ABSORBER

As a first step towards an adaptive absorber it must be determined if any advantages can be achieved by adjusting the stiffness of the vibration absorber. If the same level of performance gains are achievable with a fixed stiffness vibration absorber than there is no need undertake making the absorber adaptive. To undertake this study the absorber models created earlier are rerun with different values used for the absorber's stiffness. Being able to change the stiffness while leaving the other properties the same would allow for the absorber to be tuned for various operating conditions.

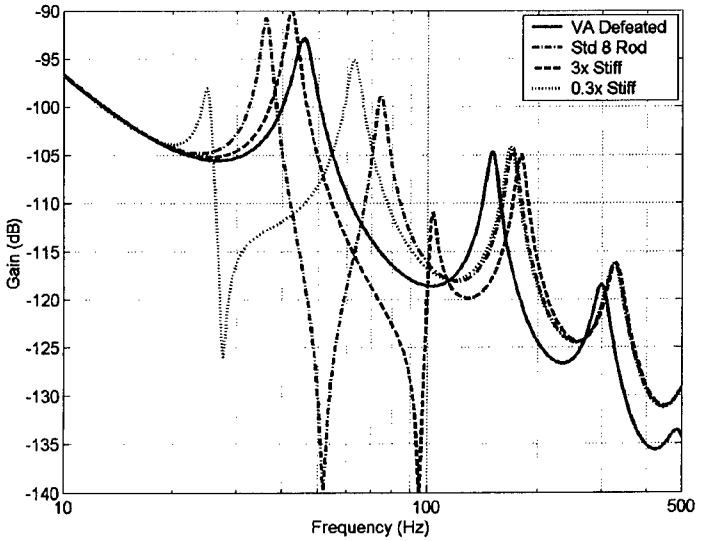


FIGURE 16. POINTING ANGLE FREQUENCY RESPONSE FOR DIFFERENT STIFFNESS 8 – ROD ABOSORBERS

Frequency response functions for the pointing angles of the muzzle were calculated for different configurations. The configurations included the absorbers as tested, with their stiffness increased by a factor of 3, and with their stiffness decreased by a factor of 3. Additionally a defeated version of the eight-rod absorber was modeled. The defeated absorber models the absorber as simply a mass on the end of the barrel. This allows us to see whether the changes in the frequency response are simply due to the additional mass.

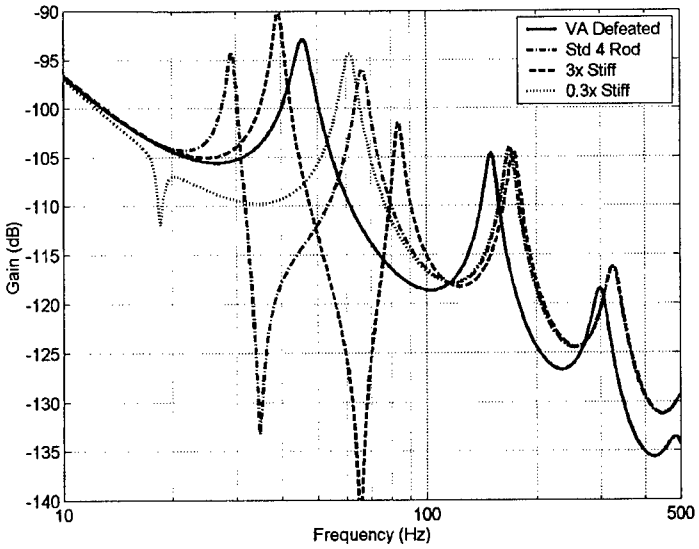


FIGURE 17. POINTING ANGLE FREQUENCY RESPONSE FOR DIFFERENT STIFFNESS 4 – ROD ABSORBERS

Figure 16 shows the results for the eight-rod absorber variant and Figure 17 does the same for the four rod ones. It is apparent from these figures that the ability to change the stiffness can greatly affect the response of the system. By increasing the stiffness of the four-rod we can make it perform similar to the eight rod. Conversely, by decreasing the stiffness of the eight-rod we can make it perform like the four rod one. All of these changes though only effect the response greatly below 100 Hz. Above there they all perform similarly and are appear as versions of the defeated absorber shifted to higher frequencies.

Which version of the absorber is best depends upon the operating conditions. Careful inspection of the figures shows that each has a range of frequencies over which they offer significantly reduced response compared to the defeated absorber. The eight-rod version of the absorber has been fired and shown to cut shot dispersion in half [7]. However this was under only one set of operating conditions. Looking at the responses, it is apparent that there are areas where the other absorbers outperform the eight rod one. Thus if the operating conditions change to an area where an eight rod absorber with a different stiffness is superior being able to change this stiffness would yield an increase in performance.

MAKING THE ABSORBER ADAPTIVE

Now that we have seen that performance gains can be achieved by making the absorber adaptive how can this actually be accomplished? In the previous section we changed the stiffness of the absorber to effect the desired change in frequency. In the laboratory experiments we changed the stiffness by removing rods. Obviously this is not a satisfactory way to make the absorber adaptive. For the absorber to be adaptive the stiffness change should be accomplished rapidly and without need for gross mechanical modifications like removing rods.

This type of application lends itself to active materials. Materials such as shape memory alloys, piezoceramics, or other induced strain actuators are designed for such applications. If only a few natural frequencies and large changes in stiffness are desired then shape memory

alloys are a natural choice. If a range of natural frequencies is desired then piezoceramics may be a better choice. Piezoelectrics also may be useful for eliminating high frequency modes.

Which type of actuator to utilize would depend upon the desired change. The perfect solution may actually contain different types of actuators all working together. The previous section showed the types of changes that could be achieved by increasing or decreasing the stiffness by a factor of three. The changes were concentrated in the low frequency (below 100 Hz) regime. If these types of changes are desired then shape memory alloys (SMA) become a logical choice as their Young's modulus can change by a factor of three when going from martensite to austenite [8].

There are a couple of different ways in which SMAs can be used to make the absorber adaptive. The most direct way would be to replace the existing spring rods with hybrid SMA rods. The core of the rods would be stainless and would be just large enough to withstand the axial loads. The rest of the rod would be SMA and would take care of the bending loads. Thus when activated an immediate factor of three in the modulus of the rods could be achieved. Since the stiffness of the rods is directly proportional to its Young's modulus, this would translate directly into an increase in stiffness.

Another possible way of using SMA to achieve a stiffness change would be in the connections between the spring rods and the collar. If SMA inserts were used as part of the connection, they could be used to loosen or tighten the connection. If the connection was loosened then the rods would able to deflect more for a given applied force. Conversely if the connection was tightened the rods would deflect less. Since the stiffness of the absorber can be viewed as how far the rods will deflect under a given load, a change in the connection would manifest itself as a change in the apparent stiffness of the absorber.

SMAs are bistable so they are most useful when there are only two desired operating points, the base one being when the SMA is in its martensite phase and the second when it is in its austentite phase. For the M242 there are two operating speeds so this does not appear to pose a problem. However if more than two operating points were desired then it might be possible to achieve them by only operating some of the SMA actuators. This is something that would have to be considered during the design of the absorber.

CONCLUSIONS

This paper has shown the effect of mounting a vibration absorber to the muzzle brake of an M242 Bushmaster. A MATLAB® model of the barrel was developed and then verified by performing modal impact testing upon the actual barrel. Good agreement was found between the model and experimental data.

After modeling and testing the plain barrel a vibration absorber was modeled and tested to find its effects upon the barrels frequency response. Two different configurations were modeled, while three were tested. As with the plain barrel good agreement was found between the model and reality. It was found that the absorber shifted the first resonant frequency of the barrel higher in frequency and that the two-rod version of the absorber reduced the magnitude of the response by 3 dB.

It was shown that changing the absorber's stiffness could change its frequency response. Which version of the absorber is best would depend upon the operating conditions. Through the

use of active materials the absorber could be made adaptive and thus able to handle different operating conditions with out physically changing the absorbers configuration.

Overall it was shown that by mounting a proof mass type actuator on the muzzle brake, the performance of the gun system could be increased. Since this is a part of the barrel meant to be screwed on and off, this allows for very easy mounting without affecting the rest of the gun system.

An additional advantage of mounting the absorber to the muzzle is that its mass ring may be combined with a muzzle fuse set device [9]. Previously a drawback of such devices was that they increased the weight affixed to the muzzle brake. Combining it with the absorber allows for its additional mass to be used to improve the gun's accuracy

REFERENCES

1 Kathe, E., "Design and Validation of a Gun Barrel Vibration Absorber Proceedings of the 67th Shock and Vibration Symposium: Volume 1, Published by SAVIAC, Monterey, CA, 18-22 November 1996, pp. 447-456.

2 Kathe, E., "A Gun Barrel Vibration Absorber for Weapon Platforms Subject to Environmental Vibrations," *AIAA Paper No. 98-1846, A Collection of Technical Papers – 39th AIAA/ASME/ASCHE/AHS/ASC Structures, Structural Dynamics, and Materials Conference and Exhibit and AIAA/ASME/AHS Adaptive Structures Forum*, 1998, pp.1284-1294.

3 Kathe, E., "Gun Barrel Vibration Absorber," US Patent 6167794, January 2001.

4 Kathe, E., "MATLAB® Modeling of Non-Uniform Beams Using the Finite Element Method for Dynamics Design and Analysis," U.S. Army ARDEC Report, ARCCB-TR-96010, Benét Laboratories, Watervliet, NY, April 1996.

5 Ewins, D. J., "Modal Testing: Theory, Practice and Application," Research Studies Press, Ltd., Baldock, England, 2000.

6 Den Hartog, J. P., "Mechanical Vibrations," McGraw-Hill Book Company, Inc., New York, 1956.

7 Kathe, E., "Lessons Learned on the Application of Vibration Absorbers for Enhanced Cannon Stabilization," Proceedings of the Eighth U.S. Army Symposium on Gun Dynamics, Eric Kathe Ed., ARDEC, CCAC, Benét Technical Report ARCCB-SP-99015, Mc Lean, VA, 17-19 Nov 1998, pp10-1 – 10-15.

8 NASA Technical Memorandum 107861, "A State of the Art Assessment of Active Structures," Sept 1992.

9 Freymond, P. H., and Buckley, A., "Programmable Fuzing for Tube Launched Ammunition," NDIA 35th Annual Gun & Ammunition Symposium, Williamsburg, VA, May 2000.

A SHOT ACCURACY MODEL FOR PREDICTING THE FIRING PERFORMANCE OF A DIRECT FIRE WEAPON SYSTEM

D.W. Lodge[1], and A.M. Dilkes[1]

[1] *Defence Evaluation & Research Agency, Chobham Lane, Cherstey, Surrey, KT16 0EE, UK.*

DERA performs research into the accuracy of various weapon systems for the UK MoD and has developed a Shot Accuracy Model (SAM) to simulate the complete 'breech-to-target' motion of the projectile. The suite is used to gain a greater understanding into the performance of current and future ammunition and gun system combinations. Knowledge gained from the models is used to influence gun and ammunition design and to reduce the dependency on costly firing trials.
The main areas that are modelled are: internal ballistics, in-bore gun dynamics, sabot separation, free flight dynamics and vehicle platform motion. Modification of these individual programs has also been undertaken to incorporate a stochastic ('Monte Carlo') simulation phase to better predict accuracy and dispersion effects of the projectiles at the target.
The SAM is designed within a Microsoft Access® database running within the Windows NT® operating system. Its structure allows for the introduction of further modules, e.g. barrel wear, 2D internal ballistics etc. It also has links into other commercially available software, namely Graphics Server®, Matlab® and visualNastran Motion®, which are used as pre- and post-processing tools.

INTRODUCTION

The Defence Evaluation and Research Agency (DERA) has conducted applied research for the UK Ministry of Defence over many years into the accuracy and consistency of conventional gun systems and projectiles. One strand of this work investigates the in-bore dynamics of the system using the gun dynamics codes such as SIMBAD [1]. Work over the last 10 to 15 years [2-4] has shown that the prediction of accuracy and consistency of a gun-fired projectile is dependent on all aspects of its journey to the target. A complete 'breech-to-target' simulation was recommended as far back as 1992 [5].

Work within Key Technical Area (KTA) 2-11 of Weapons Technical Panel (WTP) 2 of 'The Technical Co-operation Programme' was completed in 1995. This took the key stages of the projectile dynamics of a 105mm APFSDS projectile and simulated them separately, using data from one simulation to feed into that of the other [6]. Comparisons were made with experimental results, which showed some good correspondence.
It was felt by DERA, that the concept was worth taking further and funding from the UK MoD was used to develop a 'breech-to-target' model for use with the Challenger 2 gun system. This was named the Shot Accuracy Model' (SAM). The SAM is a gun accuracy simulation tool

which attempts to predict the motion of projectiles from propellant ignition to terminal strike on target.

INITIAL INVESTIGATIONS

Preparatory work was initially undertaken to look at currently available software. Funding was not available to allow for the development of code completely from scratch. It was therefore necessary to chose existing code, which had already been validated in some fashion.

Some necessary requirements were laid down prior to choosing these codes. The main criterion was that the SAM should run on a PC with x86 processor using the Windows NT4 operating system. This meant that the chosen codes would also have to run on this system without the need for extensive rewriting. Another requirement was that the code should be non-system specific, i.e. as far as possible, models of various gun systems and projectiles could be created with relative ease without the need for time consuming set-up.

Finally, the overall solution time was required to be relatively low, i.e. less than one hour per run for a standard model, as it was envisaged that the use of a stochastic element to the models using multiple runs would be required. The packages that were finally used for the SAM are as follows:

- SIMBIB (internal ballistics) [1]
- SIMBAD (internal gun dynamics) [1]
- AVCO/SACT (sabot separation) [7]
- SIXES (free flight dynamics) [8]
- SIMVED (vehicle dynamics) [9]

SAM DESIGN

The SAM was developed under a contract for DERA by the firms of Simatics Ltd. and Danby Engineering Ltd [10]. The initial design interfaced with the first four codes listed above and was later extended to the last. To ensure that the SAM could be upgraded easily and independently of the proprietary software packages, it was decided to make it a 'stand-alone' package. The SAM interfaces with the packages through there own individual input and output (results) data files. Only if the structure of these files changed would the SAM need to be modified.

An overall structure of the SAM is shown in the Figure 1. The core of the SAM was developed in Microsoft Access 97 using two databases. The first database was for the user interface and the second for storing input data. Input data for each of the external proprietary software packages is stored in the SAM database for recall at a later date. Each data set has its own unique user defined name. This input data can be edited or deleted.

The SAM contains its own graphics routines using the Graphics Server software that the user can modify as required. The internal graphing routines will allow the SAM to plot graphs to a set format. This format can be changed by the user interactively to set such parameters as the axes scale and text, the graphs labels and the curves properties, for example smoothed lines, point markers etc. The individual proprietary software packages generate their own output files in their native formats. This allows the individual packages to be used

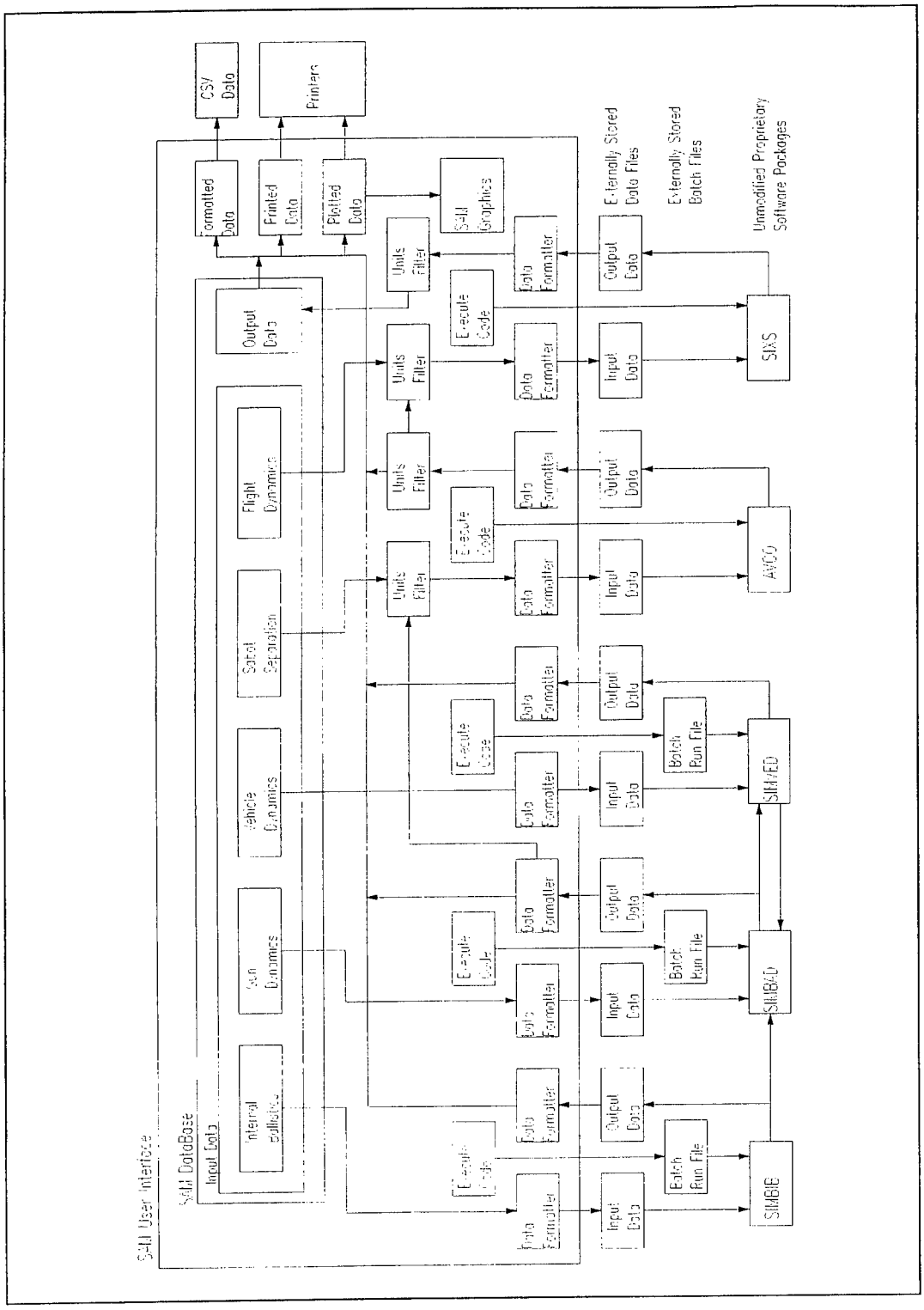


FIGURE 1. Overall structure of Shot Accuracy Model.

to post-process their own results external to the SAM if required. The SAM can also read these output files, by reformatting them and converting the respective units into those used by the SAM.

SIMBAD and SIMBIB both use Standard International (SI) units, which were used as default in the SAM. However, the data structure for the input files still needs to be defined, so the SAM formats the data to produce compatible data files for both SIMBAD and SIMBIB. When the user wishes to run SIMBAD or SIMBIB, the input data stored in the SAM database is formatted into the required format and a data file is generated and stored on disk. A batch run file is also generated and stored on disk. SAM issues an execute command that loads the required program (SIMBAD or SIMBIB) and informs the program which batch file to run. The batch file includes the information as to which data files to use for the analysis. The program runs normally and generates a results file (output file) that has been defined in the batch file. Once the program has completed the analysis and results storage, control is passed back to SAM. To post-process the results from SIMBAD or SIMBIB in the SAM, the output data files from SIMBAD or SIMBIB have to be read and formatted. The SAM contains the data formatter to do this and offers the user a variety of output options.

The SAM user interface to AVCO/SACT is similar to that of SIMBAD/SIMBIB. The differences are that the input data has to be converted into the units required by AVCO prior to SAM formatting its data to be compatible with AVCO/SACT, since AVCO/SACT uses mainly imperial units. Also when reading the output files from AVCO/SACT, after SAM has formatted them, they are passed through a units filter to convert the results into the units (metric) used by the SAM (See Figure 2). AVCO/SACT can be run directly without the need of a run batch file. The "Execute" command is sent directly to AVCO/SACT from the SAM. The SAM user interface to SIXS is identical to that between the SAM and AVCO/SACT.

SAM - Units Specification

Delete Record | Main Menu

Find parameter: Mass — Description: pounds

	Description	Acronym	Multiply by	Divide by	then Add
Standard	kilogrammes	kg			
Non-Standard	pounds	lb	0.4535924	1	0

Example: 1 lb = 0.4535924 kg

Units library

Description	Acronym	Multiply	Divide	Add
grammes	g	1	1000	0
Hundredweight	cwt	50.8023	1	0
kilogrammes	kg	1	1	0
pounds	lb	0.4535924	1	0

FIGURE 2. Example of the Units specification form for the 'mass' parameter.

The SAM user interface consists of a number of different input and utility forms. A main menu form controls the access to subsequent forms (See Figure 3), making the system logical to use and follow.

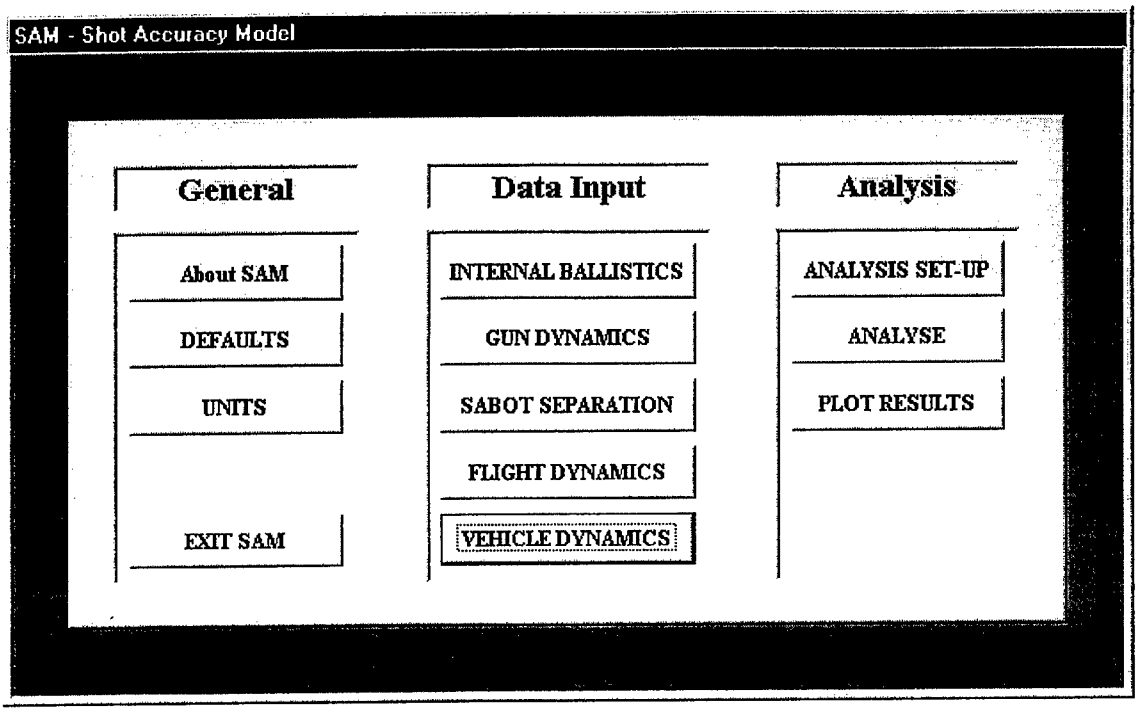


FIGURE 3. Main form of the Shot Accuracy Model.

The graphics output from the SAM has been developed using Graphics Server. The reason for this is that Graphics Server is much faster than Microsoft's Graph 5 and is more flexible. Graphics Server allows for a high degree of user modification of the final graphic presentation, without the need to change the graphs at a developers level.

The User Defined Routines of SIMBAD are not directly accessible through the SAM. It is however possible to modify the SIMBAD User Defined Routines, compile them external to the SAM and then run this modified version of SIMBAD from the SAM. It should also be noted that if user defined outputs are defined in SIMBAD User Defined Routines, then these currently would also not be automatically picked up by the SAM.

ANALYSIS CONTROL

The SAM presents the user with an analysis selection form (See Figure 4). All types of analysis are offered to the user, internal ballistics, gun dynamics, sabot separation and flight dynamics. If the user selects one of these analysis types, a selection box becomes visible that offers the user a choice of proprietary software for that analysis. Another selection box also becomes visible, where the user can then select the input data set required for that analysis.

If internal ballistics was chosen, then the sabot separation and flight dynamics options is 'greyed' out and not be selectable by the user. This is because the output from an internal ballistics analysis would not present the correct or sufficient information for these other two types of analysis. Deselecting internal ballistics in this instance would then automatically allow the user to select any one of the four analysis types.

Having selected internal ballistics analysis type, if the user then selects gun dynamics, the other three options automatically become selectable as flight dynamics is an allowable selection without sabot separation and vice versa. Once the analysis selection has been made, the analyse button is clicked and the SAM will control the whole process, running the selected analyses in the required order and passing the relevant data from the SAM database and any output from a previous analysis. For example, pressure time curve and shot acceleration data from SIMBIB into SIMBAD.

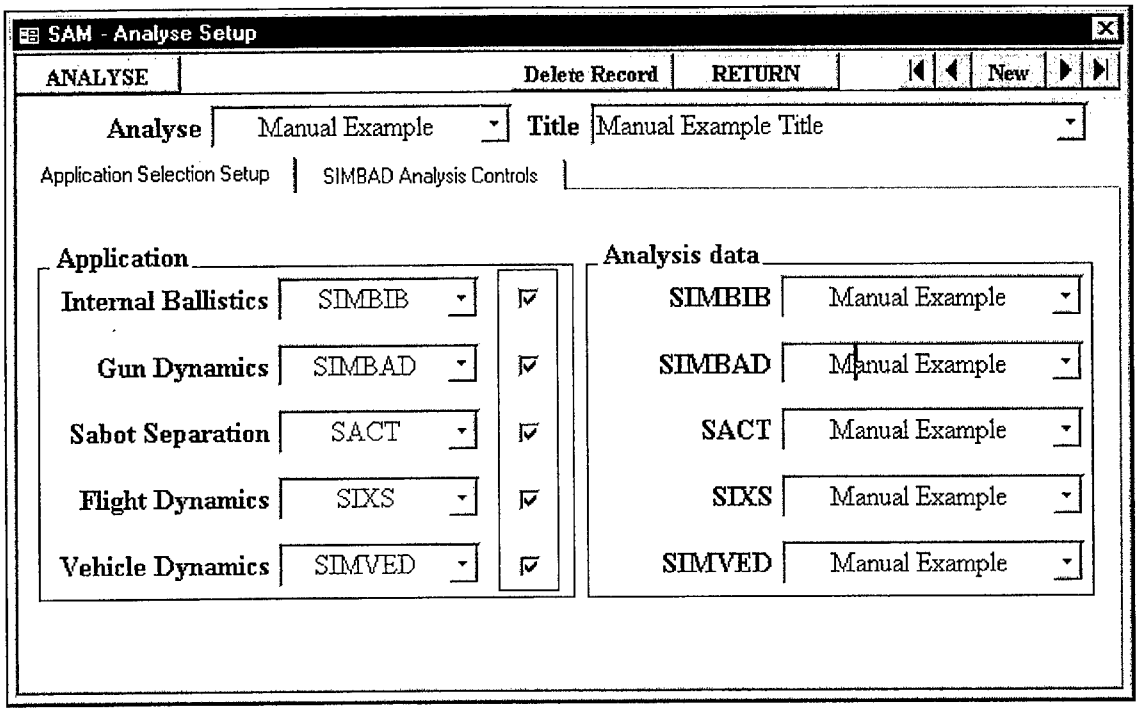


FIGURE 4. Analysis selection form.

RESULTS OUTPUT

The SAM calculates the mean point of impact (MPI) for a particular weapon system from the output of SIXS. This is displayed graphically and indicate numerically to an accuracy of two decimal places the MPI.

The SAM includes a graphics form that enables one selected variable from a drop down list of variables to be plotted against one or more variables selected from another drop down list of the same variables. This method offers the greatest flexibility in that there is no limitation on the variables selected to plot against each other. It is then up to the user to select what plots are most meaningful to them.

FURTHER ENHANCEMENTS

To obtain predicted values of MPI and dispersion from a model such as the SAM requires that a stochastic component be included in the calculations. This solution has been partly attained by the inclusion of a 'Monte-Carlo' type simulation within SIMBAD using the 'user defined routines' and the writing of additional code.

For a given gun system, each input parameter within SIMBAD is assigned a Standard Deviation (SD) about the baseline value that appears in the input file. Standard SIMBAD multiple run files are used to run the data through SIMBAD numerous times. Prior to each run, a pseudo-random routine regenerates the input data based on the SDs and baseline values. An example of the output from such a study is given in Figure 5 below. An extension of these principles to the other components in the SAM suite has yet to be achieved.

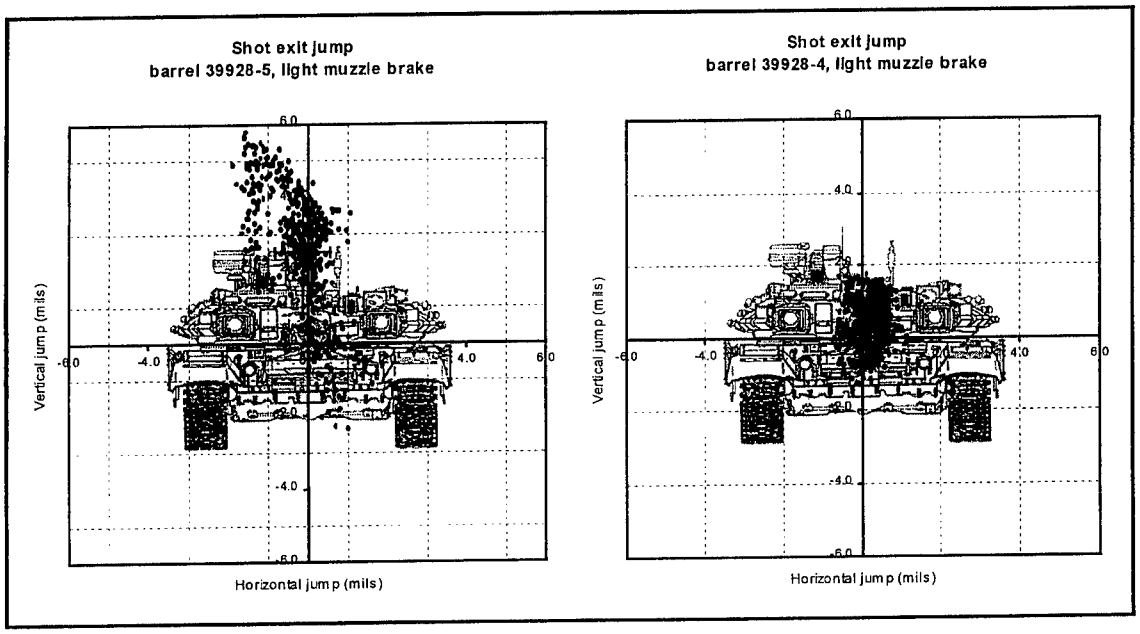


FIGURE 5. Example of predicted shot jump using 'Monte-Carlo' techniques within SIMBAD.

LINKS TO OTHER PACKAGES

No direct links exist with other packages at this moment in time. However, some initial steps have been taken to investigate linking both the input and output to the following:

- *Matlab*: mainly for use in converting results to obtain frequency response.
- *Solid Edge CAD*: used to automatically generate SIMBAD input files for the barrel, cradle, penetrator and sabot from solid model equivalents.
- *Algor FEA*: import SIMBAD input files for the barrel, cradle, penetrator and sabot. Automatically generate FEA models for obtaining natural frequencies and mode shapes. Import SIMBAD results files for stress analysis of projectile designs.

visualNastran Motion: automatically import relevant Solid Edge projectile model and SIMBAD results for visual post-processing purposes.

ACKNOWLEDGMENTS

The authors wish to acknowledge the work of Mr D.N Bulman of Danby Engineering Ltd., Mr S.F. Storey of Simatics Ltd. for their contribution to the work contained within this presentation.

REFERENCES

1. *SIMBAD Manual (Version 28).* Danby Engineering Ltd. May 2000.

2. WARWICK, HD, PENNY, PHG et al. *120 mm APFSDS accuracy investigation phase 1.* RARDE memorandum 87020, December 1988, UK RESTRICTED.

3. LODGE, DW. *Barrel bore straightness effects on the MPI of direct fire weapons and the prediction of barrel-to-barrel MPI's in MBT guns.* DRA customer report DRA/FV&S4/CR9503/draft, April 1995. UK RESTRICTED - COMMERCIAL.

4. LODGE, DW. *The RAMA gun dynamics program using improved barrel profile data.* Proceedings of the KTA 2-11 Workshop (TTCP), DREV Canada, September 1993, UNCLASSIFIED.

5. POWELL, SE. *The need for an integrated mathematical model of shot motion, from breech to target, for tank guns.* 13th international symposium on ballistics, Stockholm, Sweden, 1992.

6. LODGE, DW. *A comparison of the RAMA, SIMBAD and RASCAL gun dynamics programs using leopard 1 MBT and C76 105mm APFSDS experimental data.* DRA customer report No. DRA/LS(LSF1)/CR9586/1.0, January 1996. UNCLASSIFIED.

7. JARVIS, JM. *Capability of 'AVCO' sabot separation code.* Report by GDA associates for DRA under contract FHD/B/0243E, September 1994. UNCLASSIFIED.

8. JARVIS, JM. *A six degree-of-freedom trajectory model (SIXS) for axis-symmetric spin-stabilised projectiles.* RARDE divisional working paper 1/88(GS2), 1988. UNCLASSIFIED.

9. *SIMVED Manual (Version 3).* Danby Engineering Ltd. May 1999.

10. *The Shot Accuracy Model (SAM).* Report by Simatics Ltd. under contract LSF/E30007, December 1998. UK RESTRICTED - COMMERCIAL.

© British Crown copyright 2000. Published with the permission of the Defence Evaluation and Research Agency on behalf of the Controller of HMSO.

COMPARISON BETWEEN THE M256 120-MM TANK CANNON JUMP TEST EXPERIMENTS AND ARL'S GUN DYNAMICS SIMULATION CODES FOR PROTOTYPE KE

J. F. Newill,[1] B. J. Guidos,[1] and C. D. Livecchia[2]

[1] *U.S. Army Research Laboratory, AMSRL-WM-BC, Aberdeen Proving Ground, MD 21005*
[2] *U.S. Army Armament Research Development and Engineering Center,* AMSTA-AR-FSF-T, *Picatinny Arsenal, NJ 07806*

The interaction between the gun system and projectile cannot be directly measured during the launch event, leaving the interaction to be inferred from the exit state conditions of the projectile through various recording devices. The only direct means of studying the in-bore motion of the projectile and projectile-gun system interaction is through numerical simulation. The best approach for validation of the Army Research Laboratory's (ARL) gun-projectile dynamic simulation codes is comparison with projectile motion data obtained from ARL ballistic jump test experiments. In such tests, four or more sets of orthogonal radiograph images (x-rays) are typically used to characterize the state of the projectile at muzzle exit. The results from the x-rays can be directly compared to the predictions made by the gun-projectile dynamic simulations. This paper describes the methodology used to compare recent jump test data to gun-projectile dynamic simulations and presents comparisons for seven 120-mm prototype kinetic (KE) energy projectiles. The projectiles contain significant differences in their charge, subprojectile, and sabot designs that span the design parameters encountered in cartridge development.

Improving accuracy for both direct- and indirect-fire weapons is a major challenge to the ballistician during gun and projectile development. The ability to control the interior and exterior ballistic processes to minimize adverse dynamic perturbations to the projectile during the launch represents a major step toward "designing in" accuracy. Recently, emphasis has been placed on the direct-fire accuracy of tank main armament systems to enhance the lethality of this class of weapon and to improve accuracy of supersonic kinetic energy (KE) projectiles. Fundamental understanding of gun system and projectile interaction is paramount to meeting this goal. In addition to the direct effects launch has on accuracy, the interior ballistic motion sets the dynamic state of the projectile during the transitional and exterior ballistics phases of flight to a target. Experimentally, the interaction between the gun system and projectile cannot be determined during the launch event, leaving the interaction to be inferred from the exit state conditions of the projectile through various recording devices. The only direct means of studying the in-bore motion of the project and projectile-gun system interaction is through numerical simulation. The best approach for validation of the U.S. Army Research Laboratory's (ARL) gun-projectile dynamic simulation codes is comparison with projectile motion data obtained from ARL ballistic jump test experiments.

1. JUMP MODEL

The complete set of jump test data provides a range of information concerning the launch and flight behavior of the rounds. A substantial portion of the data is used to construct a jump diagram for each shot. The jump diagrams are based upon a jump closure model that characterizes the launch and flight aspects of the rounds, as well as providing a basis for statistical analysis of the entire set of rounds. The jump model has been presented along with the techniques in reports by Bornstein et al. (1988), Bornstein et al. (1989); and Plostins et al. (1990) and is briefly reviewed here.

The total jump of a particular shot can be defined as the vector angle between projectile target impact and the pre-trigger line of fire, with gravity drop removed. The jump vector is defined using the nomenclature introduced in Figure 1.

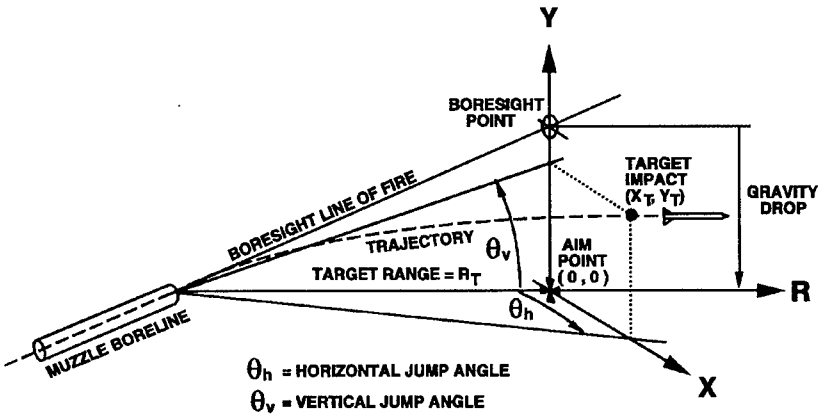


FIGURE 1. ILLUSTRATION OF JUMP ANGLES.

The boresight line of fire is established as the line connecting the center of the muzzle and boresight point obtained by the muzzle borescope. The gravity drop can be extracted separately from various data sources, including the radar track, and is considered known. The line of fire and gravity drop together establish a target aim point from which the target impact point is measured. The resulting vector is denoted as (X_T, Y_T), with the subscript "T" representing the values at the target impact point. For the KE projectiles of interest here, the magnitude of this vector is small enough compared to the target range, R_T, such that the vector is converted directly into an angle, in radians, when divided by the range to form the total jump, $\bar{\theta}$, (small angle assumption), i.e.,

$$\bar{\theta} = \theta_h \hat{i} + \theta_v \hat{j} \cong {}^{X_T}\!/_{R_T}\, \hat{i} + {}^{Y_T}\!/_{R_T}\, \hat{j} \qquad (1)$$

In the above expression, θ_h and θ_v are the horizontal and vertical components, respectively, of the total jump. The unit vector $\hat{i}$ is oriented to the gunner's right (positive X in Figure 1) and the unit vector $\hat{j}$ is oriented up (positive Y in Figure 1), and these orientations represent jump coordinates as used in this paper.

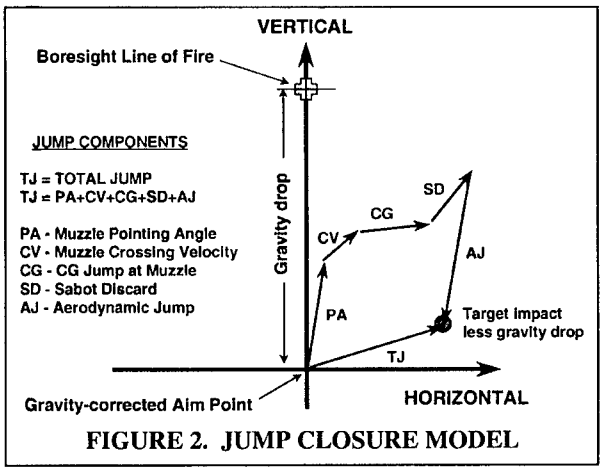


FIGURE 2. JUMP CLOSURE MODEL

The jump closure model, shown in Figure 2, follows that which has been presented in previous jump tests (Bornstein et al. 1988; Plostins et al. 1990). The origin is defined as the intersection of the horizontal and vertical axes (labeled H and V) and represents the aim point. The aim point is determined by subtracting the gravity drop from the boresight line of fire. The target impact point is denoted as a solid circle. A set of five vectors is defined whose summation is equal to the vector whose tail is located at the aim point and whose head is located at the target impact point. These vectors are jump component vectors, each having a horizontal and vertical component, and are defined as follows:

Muzzle Pointing Angle (*PA*) - The muzzle pointing angle at the time of shot exit relative to the aim point.

Muzzle Crossing Velocity Jump (*CV*) - The angular deviation corresponding to muzzle lateral motion, obtained by dividing the muzzle lateral velocity at shot exit by the projectile launch velocity.

Center-of-Gravity Jump (*CG*) - The angular deviation of the subprojectile center of gravity (c.g.) at the muzzle relative to the instantaneous bore centerline at shot exit. Also referred to in previous jump tests as the jump due to mechanical disengagement of the projectile from the gun tube. The vector arises from the c.g. motion caused by the balloting interaction between the projectile and the gun tube.

Sabot Discard Jump (*SD*) - The angular deviation of the projectile c.g. attributable to the transverse disturbance arising from the sabot discard process.

Aerodynamic Jump (*AJ*) - The angular deviation of the projectile c.g. attributable to aerodynamic lift forces associated with the free-flight projectile yawing motion. The source of the angular deviation is the angular rate at muzzle exit combined with the angular impulse caused by sabot discard.

In addition, the Total Center-of-Gravity Jump (CG_{TOT}) is defined as the sum of the *PA*, *CV*, and *CG* jump vectors. The CG_{TOT} jump represents the angular deviation of the center-of-gravity at muzzle exit, relative to the pre-trigger line-of-fire.

2. INSTRUMENTATION AND TEST APPARATUS

Figure 4 is an illustration of the primary instrumentation situated around the tank and the line of fire. The measurement techniques follow the general set up and procedures described in reports of previous tests conducted at Aberdeen Proving Ground (APG) (Schmidt et al. 1984; Bornstein et al. 1988; Plostins et al. 1990). Table 1 lists the approximate ranges of the instrumentation.

A muzzle pressure probe, used to provide an electronic trigger to the various recording devices, is positioned a few centimeters from the muzzle and supported by a cantilever that rotates away from the muzzle when impacted by the initial blast. Four sets of orthogonal x-ray stations are situated at four non-overlapping axial stations within 10 m from the muzzle, Figure 3.

Each station consists of a pair of orthogonal 150 kV flash x-ray units and associated film with screen intensifiers enclosed and protected in wooden cartridge cases constructed prior to the test. The x-ray units are mounted onto a steel x-ray rig, shown in Figure 2, and the loaded cartridges secured onto the rig prior to each shot.

TABLE 1 DISTANCES FOR INSTRUMENTATION POSITIONS AS MEASURED FROM MUZZLE.

Instrumentation	Range (m)
Eddy Probe Station #1	-0.495
Eddy Probe Station #2	-0.343
X-Ray #1	0.5
X-Ray #2	2.5
X-Ray #3	4.5
X-Ray #4	7.5
Orthogonal Smear Camera	10
High Speed Video Camera	30
Yaw Cards #1	37
Yaw Cards #2 thru #15	7.0 m spacing
Yaw Card #16	142
Target	963

A set of eight proximity gauges (eddy probes) are mounted onto a specially constructed self-supporting aluminum rig slid over the gun tube to a location approximately 50 cm from the muzzle, as shown in Figure 5. The eddy probe rig is designed to secure two groups of four eddy probes each at two axial locations approximately 15 cm apart. Each eddy probe returns a voltage signal that corresponds to the distance between the probe tip and the gun. Prior to each shot, the eddy probes are adjusted within the rig to be positioned approximately 0.04 inches from the tube surface, where a highly linear voltage

signal exists. A temporary sunscreen, visible in Figure 3, is constructed from wood, cloth, and rope to shield the gun tube from direct sunlight and to minimize gun tube movement induced by disparate heating (Bundy et al. 1993).



FIGURE 3. X-RAY RIG.

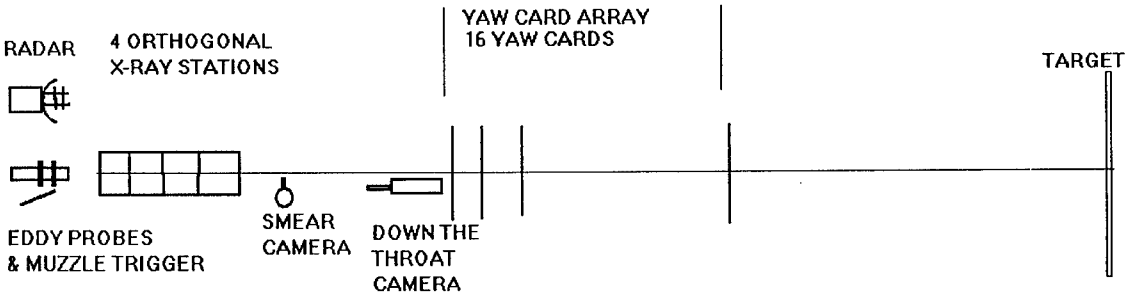


FIGURE 4. INSTRUMENTATION SET-UP

The complete set of eddy probe data is reduced in the post-test analysis into the form of muzzle pointing angle and lateral displacement as a functions of time using the procedure reported by Bornstein and Haug (1988). From this data, the *PA* and *CV* jump vector components can be obtained as part of the jump analysis. This data could also be used to compare with numerical simulations if the muzzle motion itself was simulated and stored during the numerical procedure. However, such is not the case for the numerical simulation approach used here, where projectile motion parameters, rather than muzzle motion parameters, are compared.

The jump test setup also consists of yaw card stations equally spaced along the line of fire at axial locations between 37 and 142 m forward of the muzzle. The cloth target is located 963 m downrange of the muzzle. Two orthogonal color smear camera images are collected at 10 m from the muzzle. The smear images are obtained by exposing highly sensitive film that is spooled at a high rate of speed as the projectile passes through the image domain. A "down-the-throat" high-speed video camera records each launch event using a line of sight acquired by a mirror positioned 30 m from the muzzle and approximately 0.6 m below the line of fire. Weibel radar data is collected for each firing. With accompanying electronics and equipment, the instrumentation provided the data and visual records necessary to calculate the set of jump components sought for the particular shot.

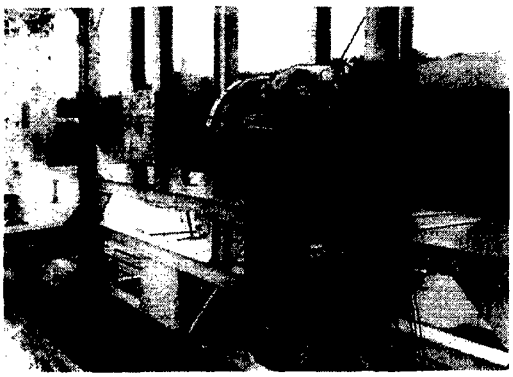


FIGURE 5. EDDY PROBE RIG.

The general test procedure for each shot is as follows: The muzzle is aimed at a pre-determined point on the target using a collimated borescope. This boresight point, typically the lower right corner of the square formed by the intersection of the horizontal and vertical cross, is then surveyed. The cardboard yaw cards are mounted to the wooden support frames and marked with horizontal and vertical reference lines using the boresight. The loaded x-ray cassettes are secured into the rig. A fiducial cable is a steel cable containing two reference beads at each x-ray station is hung along the line of fire, as shown in Figure 6.

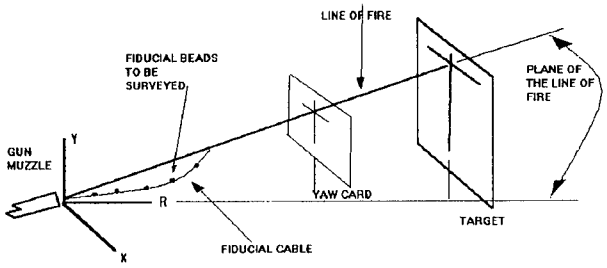


FIGURE 6. TEST SET-UP

The steel fiducial cable is supported at the downrange end of the rig by a laterally adjustable pulley sighted to be near the line of fire, and at the breech by a metal plate. Mass of approximately 60 kg is hung from the downrange end of the cable, reducing the droop of the cable to a few millimeters. The applied mass forces the metal plate to abut tightly against the breech housing. The plate is laterally adjusted such that the cable is centered at the muzzle. The cable contains fiducial beads at each x-ray station to provide orientation and magnification references. Survey is conducted of the cable position at the muzzle, the pulley, and the fiducial beads. The x-ray film is exposed at a low power level to mark the bead locations, the cable is removed, and the pulley is lowered via a hinged platform attached to the x-ray rig. The eddy probes are adjusted, all instrumentation is set to initiate at pulse trigger, and firing commences.

3. MEASURED PROJECTILE MUZZLE EXIT STATE AND JUMP COMPONENTS

A single x-ray station is drawn schematically in Figure 7. After the fiducial cable and beads are exposed onto the x-ray film prior to the shot, the shot is fired and x-rays are taken of the projectile in flight. In each x-ray image, the position and orientation of the projectile are measured and can be related to the boresighted line of fire determined from the cable image. Linear fits are made to the projectile lateral position and angular orientation, thus providing measured values of projectile angular and translational rates at muzzle exit. Projectile angular rate and projectile lateral translation rate at muzzle exit are the two quantities that are compared in the validation of numerical

simulation with experimental measurement. The values are extracted from the data at a time that corresponds to shot exit, defined here as the instant in time when the rear bourrelet (also called the rear bore rider or bulkhead) mechanically disengages from the gun tube. At this time, the obturator undergoes a process of disintegration and the main blast uncorks.

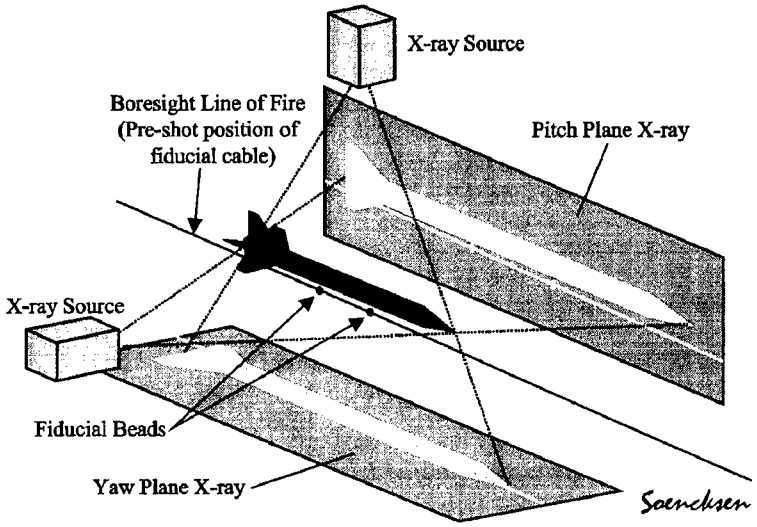


FIGURE 7. ORTHOGONAL X-RAY SETUP.

The CG_{TOT} jump vector is directly related to the lateral translation rate at muzzle exit. The CG_{TOT} jump is obtained by dividing the projectile lateral translation rate (a two component vector, plane transverse to the line of fire) by the projectile launch velocity. The AJ vector is closely related to the projectile angular rate at muzzle exit. Guidos and Cooper (1999) used a linear impulse model to generalize the expression given by Murphy (1963) that relates projectile angular rate at the muzzle and aerodynamic jump. For application to a KE projectile with sabot discard, the expression can be approximated and written in complex coordinates (the transformation between complex coordinates and range coordinates, consistent with that used by Guidos and Cooper (1999) is not an issue of concern here) as:

$$AJ = -k_t^2 \frac{C_{L\alpha}}{C_{M\alpha}} \left(\tilde{\xi}_0' + \tilde{\vartheta}_l^* \right) \tag{3}$$

where, k_t^2 = subprojectile non-dimensional radius of gyration,

$C_{L\alpha}$ = subprojectile aerodynamic lift force coefficient derivative,

$C_{M\alpha}$ = subprojectile aerodynamic pitching moment coefficient derivative,

$\tilde{\xi}_0'$ = subprojectile angular rate at muzzle exit (rad/caliber)

$\tilde{\vartheta}_l^*$ = change in subprojectile angular rate attributable to sabot discard (rad/caliber)

$\tilde{\xi} = \alpha + i\beta$ = subprojectile angle of attack in complex coordinates

α = pitch angle (positive up)

β = yaw angle (positive nose left)

In the above equation, the subprojectile angular rate at muzzle exit, $\tilde{\xi}_0'$, is a measure of the total angular impulse applied to the projectile by the gun. The change in subprojectile angular rate attributable to sabot discard, $\tilde{\vartheta}_l^*$, is a measure of the total angular impulse applied to the

subprojectile during the sabot discard process. Further discussion of the quantity $\tilde{\gamma}_l^*$ is made by Guidos and Cooper (1999).

To complete the discussion of jump components, it is noted that the *SD* jump vector is typically obtained through closure, where the aerodynamic jump vector is placed on the jump diagram such that its tip is coincident with the actual recorded projectile impact point. The *SD* vector is constructed such that closure is achieved between the tip of the *CG* vector and the base of the *AJ* vector, as shown in Figure 2. As stated, this vector is actually a combination of the *SD* vector and the sum of all measurement errors, which are typically on the order of 0.2 mrad or less (Lyon et al, 1991).

4. NUMERICAL SIMULATION OF TANK GUN PROJECTILES

Gun/projectile dynamic simulations utilize three-dimensional (3-D) Finite Element (FE) models of the M256 120-mm tank cannon launching projectiles (Figure 8. The method is described in Rabern 1991; Wilkerson and Hopkins 1994; Burns, Newill, and Wilkerson (1998); Newill, Burns, Wilkerson (1998); Newill et al. (1998a, 1998b, 1998c, 1999a, 1999b, 2000); Guidos et al. (1999). The hydrocode finite element formulation was chosen to allow investigation of stress wave propagation due to elements of launch. The models are 3-D to capture the asymmetric response of the projectile and gun system resulting from the nonlinear path of the projectile during launch, asymmetric boundary conditions, general lack of symmetry in the centerline profiles of the gun tube, and asymmetric gun motion.

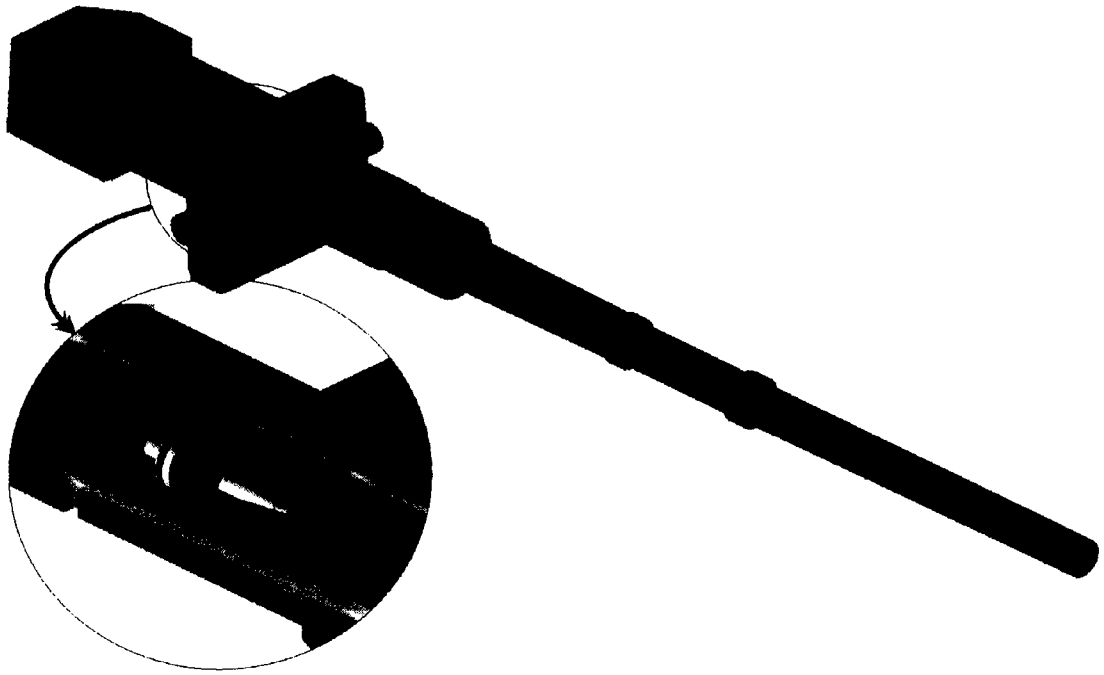


FIGURE 8 M1'S M256 GUN SYSTEM WITH KE PROJECTILE SHOWN IN-BORE.

The projectiles and gun systems are both built in similar manners. Models are developed for the components and then integrated. Relative motion is obtained by defining the proper physics to allow interaction between the parts. Since this projectile is relatively simple, the nose, body, stabilizer and obturator are welded together, and sliding interfaces are defined between the nose, body, stabilizer, between the sabot petals, and the gun bore. One of the purposes of these types of studies, is to estimate tank fleet performance. In order to do this, the projectile model is integrated

into (and fired from) a number of gun models each of which have unique tube centerlines (the centerlines are covered later in this paper). The propellant pressure loading for the gun system and projectile is generated from IBHVG2 (Anderson and Fickie, 1987) which provides good quality interior ballistic prediction for production charges.

The gun dynamic simulation codes predict the transverse rates (velocity and angular rate) during the launch cycle (Figure 9). Three types of information are used from these predictions, the dynamic path, variability in jump, and the average jump. The dynamic path gives qualitative information on the rate history of the projectile during the launch cycle. The variability and average jump predicted by the codes are related to accuracy errors where reduction in variability or error represents improved performance of the system.

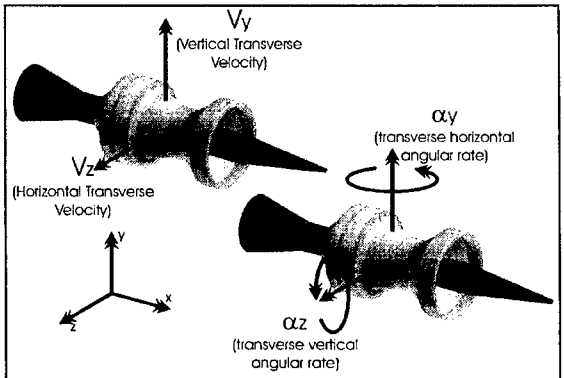


FIGURE 9. DEFINITION OF TRANSVERSE RATES

To intentionally induce the variability into the dynamic path which results in variability the muzzle exit rates, a series of initial conditions are used. The initial condition that has the strongest influence is the initial cocking angle of the projectile in the forcing cone/bore. Since the diameter of the projectile's bourrelets is less than the interior bore and forcing cone diameter, there exists a clearance between the projectile and the gun tube. The angle the centerline of the projectile can make with these confines is defined as the cocking angle. Therefore, the cocking angle is relative to how the gun bore/forcing cone and chamber are manufactured, the projectile and cartridge's manufacturing dimensions along with total run-out of the cartridge (how straight the cartridge is made). There are an infinite number of ways that the projectile can be cocked in tube, but typically, the cocking angles used in simulations are up, down, left, right, and straight since they encompass the maximum variability. The cocking angles are calculated on a model by model basis using the specific dimension of the particular projectile/gun geometry. The straight projectile has the forward and rear bourrelet centered relative to the initial location of the projectile in the gun.

In order to validate the gun codes, some type of methodology is required in order to compare various projectiles performance. Since the phenomena being predicted is nonlinear and stochastic in nature and the initial conditions are not known precisely on a shot-by-shot basis, the gun dynamic codes are used to predict an envelope of performance. This is consistent with the experimental methodology. Typically a series of projectiles shots are simulated to predict both the center of impact (COI) and variability. Essentially, in the gun codes to induce the variability, the initial conditions are varied, typically projectile initial cocking angles up, down, left, right, and straight; then a series of simulations is accomplished (Newill 1998a). Using these simulations, the range of angular rates and range of transverse velocities are predicted.

On a smaller scale, this is consistent with the how the gun codes are used to predict performance. To define projectile "tank fleet" performance the same type of data is predicted, but it is combined with multiple gun systems at a range of temperatures. When comparing to experimental data only one gun tube and propellant temperature combination is used. Figure 10 shows how the envelope predicted from the simulations and measured in the experiment at compared. In Figure 10, there are four items of interest: the experimental data, predictions from the simulation, the envelope (variability) of performance from the simulation, and 95% confidence level for the experimental data. The comparison between the experiment and simulation is made through the relative sizes of the variability and the averages of predicted and measured data.

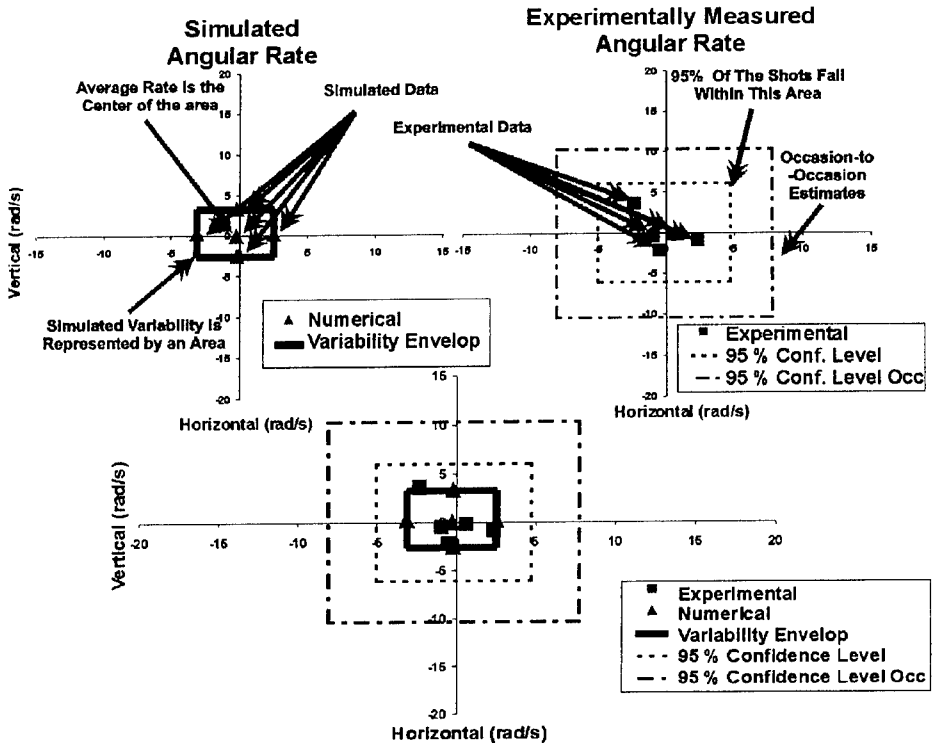


FIGURE 10. SIMULATION COMPARISON WITH EXPERIMENTAL RESULTS.

It is very important to note that the experiment is a ballistic phenomenon that is not entirely predictable. Even with production ammunition, with as many factors as possible controlled, there can be significant deviation of the shooting performance. For this reason, there can never be absolute comparison between the simulated data and the experimental data.

Figure 11 shows an extrapolation of the experimental data to help understand and define the 95 % confidence level and occasion to occasion envelope. The figure uses the experimental data to predict the shot patterns directly from the experiment and using the empirical knockdown factor applied to the experimental results. The figure shows that the two boxes essentially define the two different groups. These two boxes are used to define the performance of the experimental data.

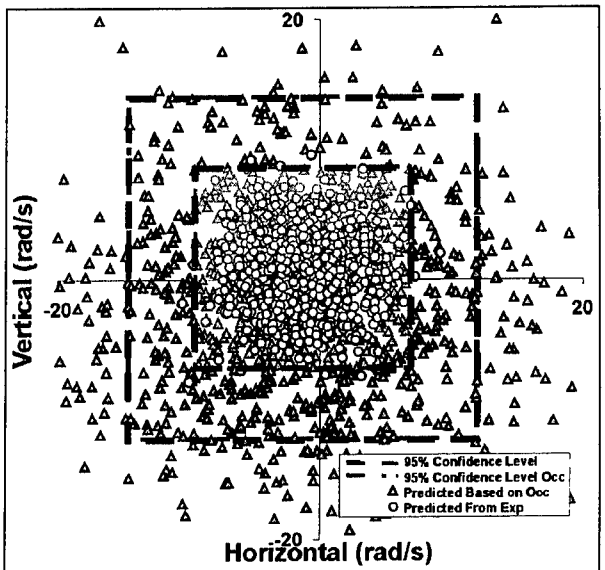


FIGURE 11. EXPLANATION OF THE 95 % ENVELOPE AND OCCASION TO OCCASION ENVELOPE.

The variability predicted should typically be smaller than the variability (95% confidence level) in the experiment, although working with prototype projectiles complicates the situation. Prototype projectiles are made in small numbers with custom-designed propellant charges. Both the small numbers and custom charge induce variability that would not be seen in a well-made production projectile. Other reasons for the variability in the experimental data to be larger than the simulation data is related to ambiguity

in shot start (fracture of the case adapter), variability due to the propellant burning,* and the fracture problem at muzzle exit associated with the breaking of the obturator. Each of these is significant and is attacked through other means as separate problems to reduce variability and improved projectile performance.

There are two ways that the average is compared to the experimental data. The first level compares the simulation data to the experimental data, the average should lie within the 95% confidence level of the experimentally measured values. Unfortunately, due to the nature of tank firing, a second envelope needs to be used. The issue is related to what is typically called occasion-to-occasion error. It basically accounts for differences in the experimental data seen when firing the same tank at two different times while still controlling the other factors of the experiment. The second box represents the uncertainty from this source is determined using empirical methods based on a history of shooting results. The average of the simulation data should lie within the occasion to occasion estimate for a good comparison.

In spite of this ambiguity, the resulting model is quite capable of accomplishing numerical sensitivity studies (given that appropriate computer assets are available). Several ballistic issues have been studied, including the following:

- The effect of projectile initial condition on shot exit kinematics.
- The effect of subtle projectile geometry variations on both shot fall dispersion and mean jump.
- The effect of gun tube centerline profile on both shot fall dispersion and mean jump.
- The comparison of projectile design to assess the accuracy attributes of different designs.
- Studies to ascertain the means to reduce the dynamic motion of the gun barrel.

For many of the projectile modifications accomplished using this tool, the results have been confirmed through large numbers of projectile firings.

5. COMPARISONS BETWEEN EXPERIMENT AND SIMULATION

The predictions from the projectile/gun dynamics simulation codes can be very useful if it can be related to the physical system. In this section, several examples are shown to show the range of comparison between experiment and simulation. The ballistic data was obtained in jump tests conducted by ARL at Army Test Center (ATC).

Seen in Figure 12 through Figure 18, the experimental and simulated data compare well in both variability and average to the experimental data.

Only in the last two figures are the average rates significantly different from the experiments, although the variability data is fine. In Figure 19, the rates of the horizontal and horizontal angular velocity can be seen to be changing rapidly near muzzle exit. The horizontal component is seen to change much faster especially during the last 0.4 ms of travel. Also, if there is a time error in muzzle exit and the projectile actually exited earlier than predicted, then both horizontal components move toward zero, which is what was seen in the experiment. There are several aspects of the simulation that can cause variability in muzzle exit times relative to the experiment. The first is differences in muzzle exit time. While these differences are small in magnitude, it implies that the projectile exited early. Other problems with these predictions have to do with shot start and propellant variability. The shot start has to do with the projectile not moving until the propellant has developed enough pressure to break the case-base adapter. The propellant issue deals with variability due to development of the flame and the symmetry of the burning. In any of these cases, the exit time can vary.

---

* The propellant can burn asymmetrically and generate large transverse pressure waves. Either effect can severely degrade the performance of the projectile or destroy it.

For the projectile design in Figure 20, examining the same quantities shows that the accelerations near muzzle are relatively low and that the change in rates is also very low. In each case, the simulation and experiment show a very good correlation and provides insight into how sensitive the performance is to small changes in muzzle exit time. Figure 21 and Figure 22 show what happens to the experimental/simulation comparisons when these small time differences are considered. Figure 21 clearly shows that the transverse velocity matches well at the earlier time whereas the angular rate data is not affected as much. Figure 22 shows the same type of comparison for a well behaved projectile. Here the comparisons are almost identical regardless of the exact exit time.

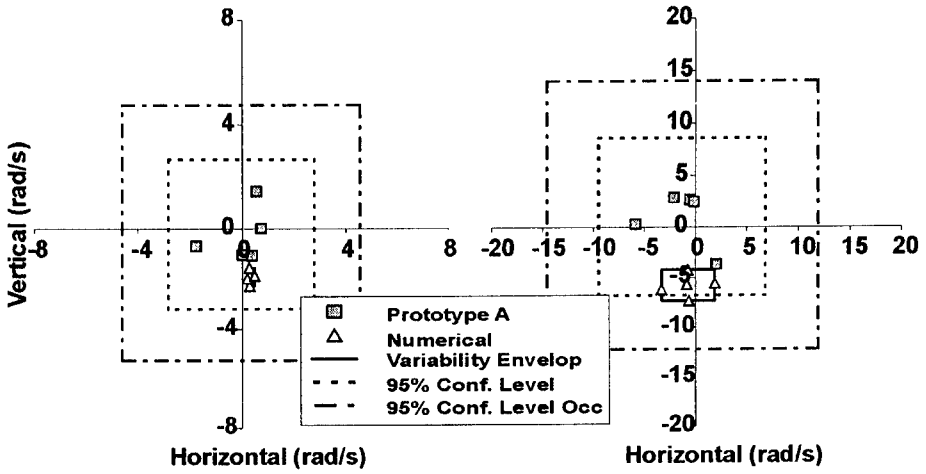


FIGURE 12. TRANSVERSE VELOCITY AND ANGULAR RATE COMPARISONS, RESPECTIVELY FOR PROJECTILE A.

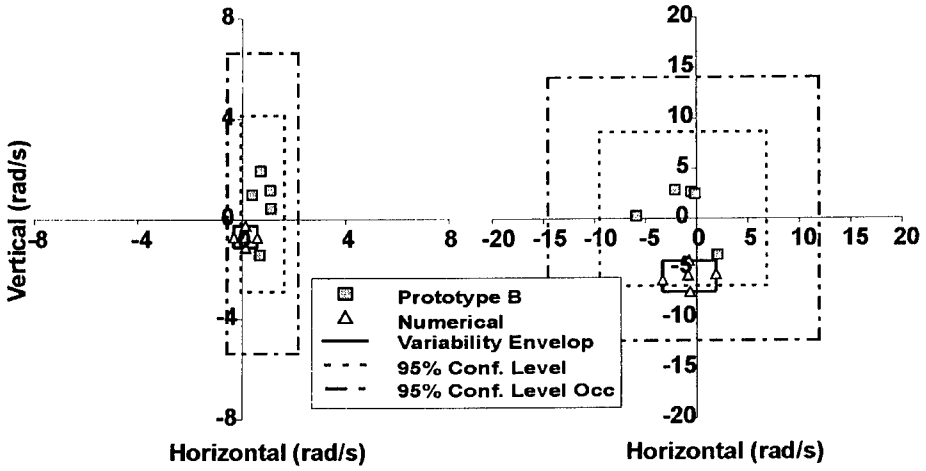


FIGURE 13. TRANSVERSE VELOCITY AND ANGULAR RATE COMPARISONS, RESPECTIVELY FOR PROJECTILE B.

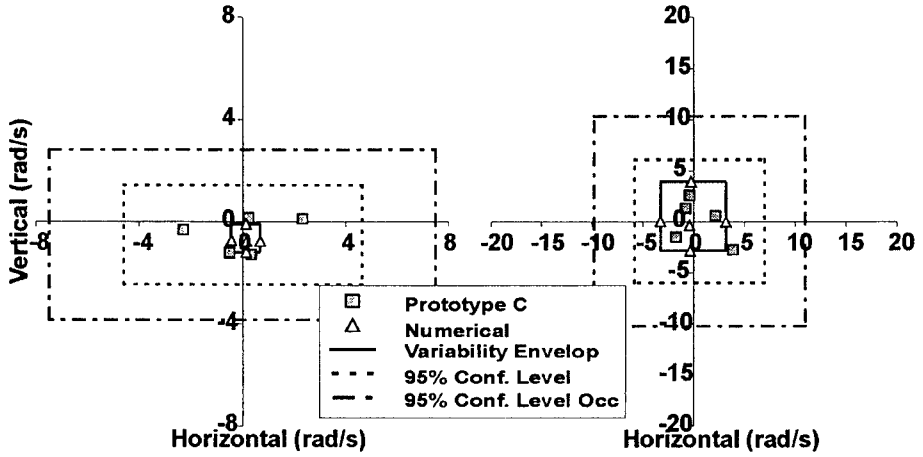


FIGURE 14. TRANSVERSE VELOCITY AND ANGULAR RATE COMPARISONS, RESPECTIVELY FOR PROJECTILE C.

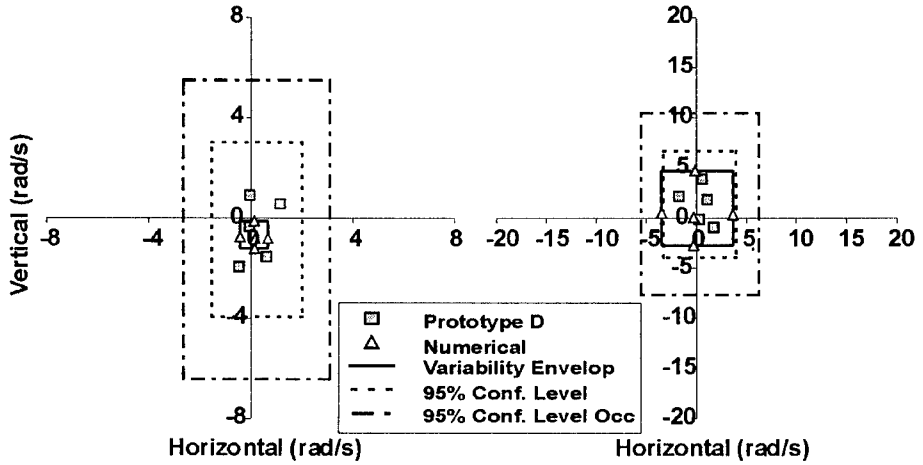


FIGURE 15. TRANSVERSE VELOCITY AND ANGULAR RATE COMPARISONS, RESPECTIVELY FOR PROJECTILE D.

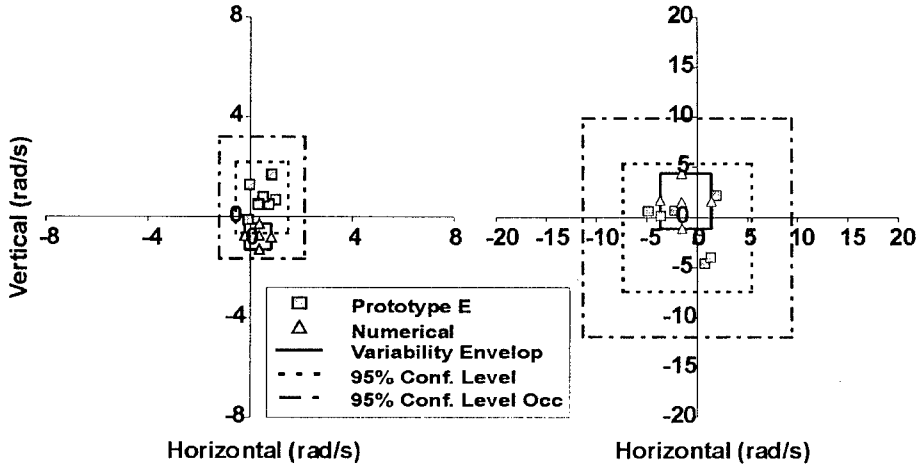


FIGURE 16. TRANSVERSE VELOCITY AND ANGULAR RATE COMPARISONS, RESPECTIVELY FOR PROJECTILE E.

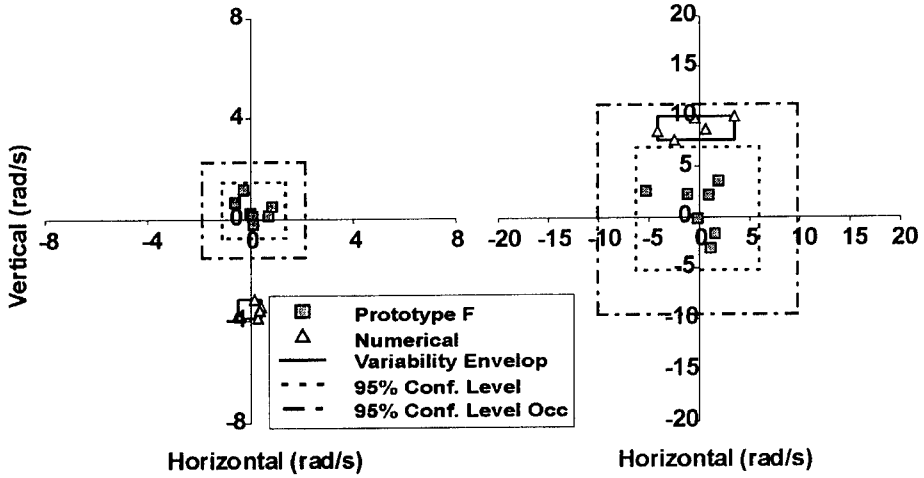


FIGURE 17. TRANSVERSE VELOCITY AND ANGULAR RATE COMPARISONS, RESPECTIVELY FOR PROJECTILE F.

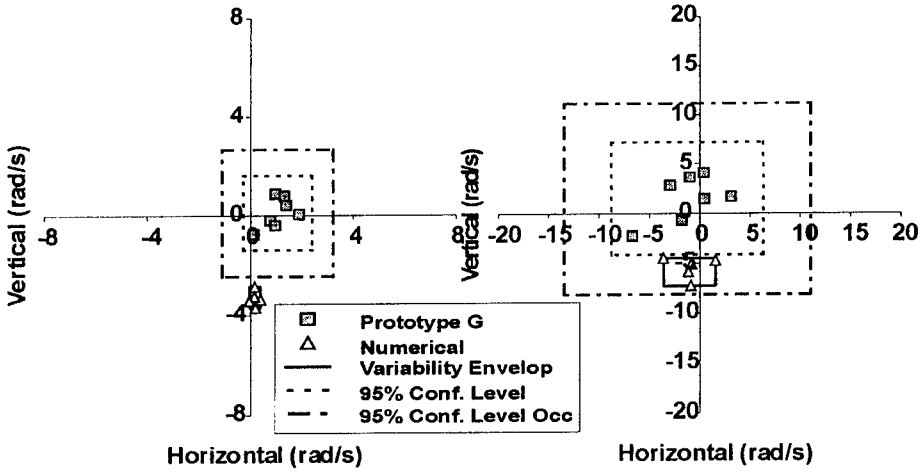


FIGURE 18. TRANSVERSE VELOCITY AND ANGULAR RATE COMPARISONS, RESPECTIVELY FOR PROJECTILE G.

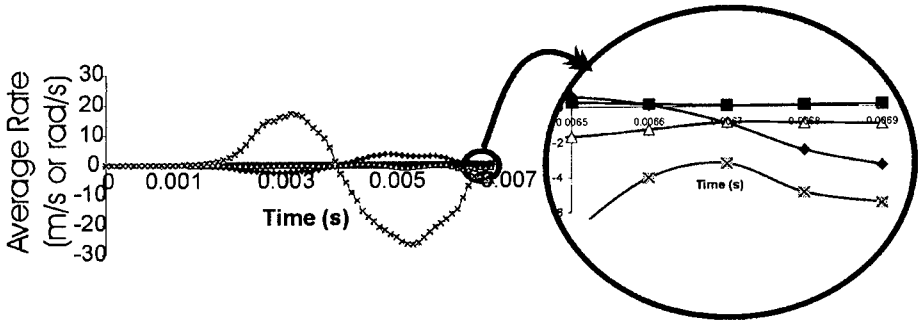


FIGURE 19. AVERAGE TRANSVERSE RATES AND ACCELERATIONS DURING LAUNCH FOR PROTOTYPE G

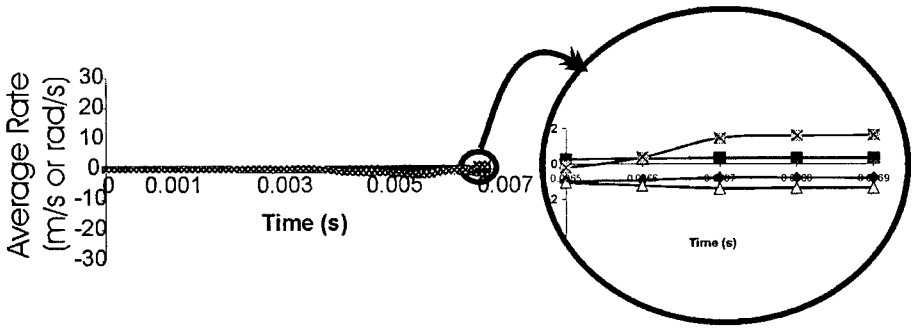


FIGURE 20. AVERAGE TRANSVERSE RATES AND ACCELERATIONS DURING LAUNCH FOR PROTOTYPE E.

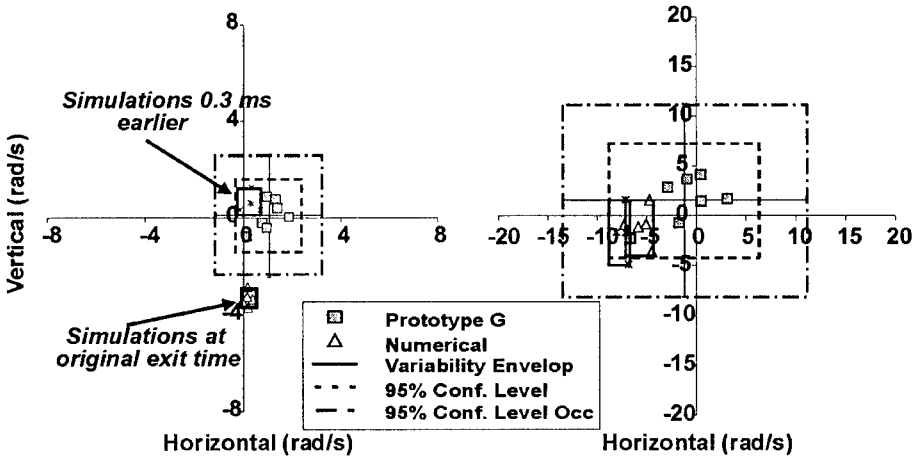


FIGURE 21. MULTIPLE TIME COMPARISONS FOR PROTOTYPE G.

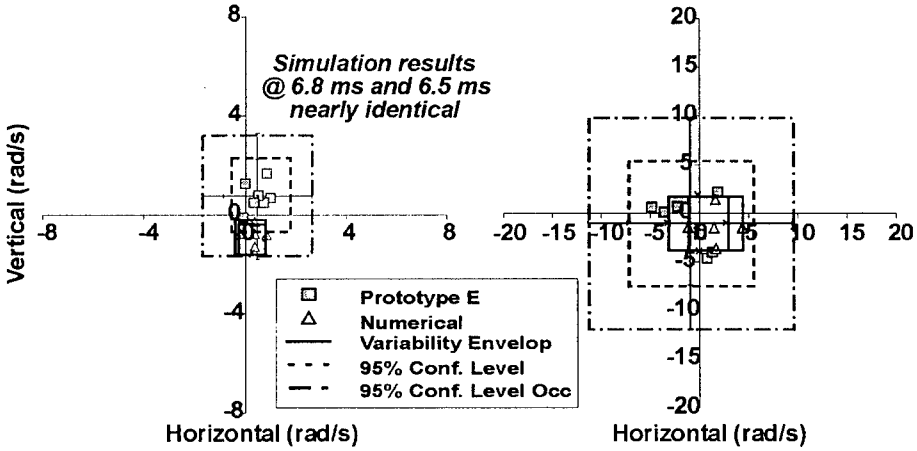


FIGURE 22. MULTIPLE TIME COMPARISONS FOR PROTOTYPE E.

6. CONCLUSION

It is quite clear that the computational capabilities to study the details of in-bore projectile motion are in hand. Predictions of the flight mechanics of the subprojectile are also tractable so that realistic predictions of fall of shot for complicated direct-fire projectiles are now feasible. We have started to couple this advanced modeling capability to the design of future generations of systems. From this we expect significant economic advantages to emerge along with reduced time

expenditures for development coupled with a direct method of reducing gun system and projectile contributions to accuracy.

The numerical methodology also permits new insight into the dynamical behavior of the projectile while undergoing in-bore acceleration. The derivation of dynamic performance envelopes should now allow the definition of realistic specifications for electronic modules, sensors, and sensitive mechanisms associated with advanced submunitions and maneuvering (smart) projectiles. With the maturation of these high-performance technologies, the projectile designer now finally has very powerful tools to rely on the design process; the challenge is to make them assessable and timely.

7. ACKNOWLEDGEMENTS

A study of this magnitude requires a coordinated effort and support from many people. The principal organizations are Project Manager for Tank and Medium-caliber Armament Systems (TMAS) program office, U.S. Tank Automotive and Armament Command (TACOM) Armament Research, Development, and Engineering Center (TACOM-ARDEC), Alliant Techsystem Inc, and General Dynamics Ordnance and Tactical Systems. Their leadership expertise and experience are invaluable. This study relied heavily on supercomputers supplied by DOD's High Performance Computing initiative (specifically by the Major Shared Resource Center at ARL).

8. REFERENCES

Anderson, R. D., and K. D. Fickie. "IBHVG2 - A User's Guide." BRL-TR-2829, U.S. Army Ballistic Research Laboratory, Aberdeen Proving Ground, MD, July 87.

Bornstein, J., and B. Haug, "Gun Dynamics Measurements for Tank Gun Systems." BRL-MR-3688, U.S. Army Ballistic Research Laboratory, Aberdeen Proving Ground, Maryland, May 88 .

Bornstein, J., I. Celmins, and P. Plostins, "Launch Dynamics of Fin-Stabilized Projectiles." AIAA Paper No. 89-3395, August 89.

Bornstein, J., D.S. Savick, D.H. Lyon, E.M. Schmidt, J. Kietzman, and D. Deaver, "Simulation of Tank Cannon Launch Dynamics." Proceedings of The Seventh U.S. Army Gun Dynamics Symposium, May 93 .

Bornstein, J., I. Celmins, P. Plostins, E. M. Schmidt, "Techniques for the Measurement of Tank Cannon Jump." BRL-MR-3715, US Army Ballistic Research Laboratory, Aberdeen Proving Ground, Maryland, December 88.

Bundy, M.L., "Thermal Distortion Protection by Candidate Metal and Composite Thermal Shrouds for 120-mm Tank Cannon." BRL-TR-2807, U. S. Army Ballistic Research Laboratory, Aberdeen Proving Ground, Maryland, June 87 .

Bundy, M.L., N. Gerber, and J.W. Bradley, "Thermal Distortion Due to Wall Thickness Variation and Uneven Cooling in an M256 120-mm Gun Barrel, U.S. Army Research Laboratory, Aberdeen Proving Ground, Maryland, September 93 .

Guidos, B. J. and G. R. Cooper. "The Effect of a Simple Lateral Impulse on Kinetic Energy Projectile in Flight." ARL-TR-2076, U.S. Army Research Laboratory, Aberdeen Proving Ground, Maryland, Dec 99.

Lyon, D.H., D.S. Savick, and E.M. Schmidt, "Comp. of Computed and Measured Jump of 120mm Cannon." AIAA Paper 91-2898, Jul 91.

Murphy, C.H., "Free Flight Motion of Symmetric Missiles." BRL-R-1216, U.S. Army Ballistic Research Laboratories, aberdeen Proving Ground, Maryland, July 63 .

Newill J.F., B.P. Burns, and S.A. Wilkerson, "Overview of Gun Dynamics Numerical Simulations." Technical Report in work, US Army Research Laboratory, Aberdeen Proving Ground, Maryland, July 98a.

Newill J.F., C. P. R. Hoppel, and W. H. Drysdale, "Comparison of Launch Mechanics and Dynamics from the M1A1 M256 Gun System for the M829A2 Kinetic Energy Long Rod Fin Stabilized Projectile Containing Different Penetrator Materials." Technical Report 1671, US Army Research Laboratory, Aberdeen Proving Ground, Maryland, April 98b.

Newill J.F., D. Webb, B. Guidos, C.P.R. Hoppel, and W.A. Drysdale, "Methodology for Formal Comparison of Experimental Ballistic Firing of Kinetic Energy Projectiles with Numerical Simulation." Technical Report in work, US Army Research Laboratory, Aberdeen Proving Ground, MD.

Newill J.F., S.A. Wilkerson, C.P.R. Hoppel, and W.H. Drysdale, "Numerical Simulation of Launch Interaction of Kinetic Energy Long Rod Fin-Stabilized Projectiles and M1A1 Abrams M256 Gun System with Comparison to Experimental Results." Classified Ballistics Symposium, Elgin Air Force Base, FL, May 11-14, 98c.

Newill, J.F., C.P.R. Hoppel, and W.H. Drysdale, "Comparison of Launch Mechanics and Dynamics from the M1A1 M256 Gun System for the M829A2 Kinetic Energy Long Rod Fin Stabilized Projectile Containing Different Penetrator Materials." ARL-TR-1671, U.S. Army Research Laboratory, Aberdeen Proving Ground, Maryland, April 98d.

Plostins, P., I. Celmins, and J. Bornstein, "The Effect of Sabot Front Borerider Stiffness on the Launch Dynamics of Fin-Stabilized Kinetic Energy Ammunition." AIAA Paper No. 90-0066, January 90.

Rabern D. A., "Axially Accelerated Saboted Rods Subjected to Lateral Forces." Contractor Report No. 671, US Army Ballistic Research Laboratory, Aberdeen Proving Ground, Maryland, August 91.

Rabern, D.A., "Axially Accelarated Saboted Rods Subjected to Lateral Forces." LA-11494-MS, Los Alamos National Laboratory, Los Alamos, New Mexico, March 89 .

Webb, D.W., "Optimal Partitioning of M829A1 Cartridges for the TGAD Jump Test." ARL-TR-55, U.S. Army Research Laboratory, Aberdeen Proving Ground, Maryland, June 99 .

Wilkerson S. A. and D. Hopkins, "Analysis of a Balanced Breech System for the M1A1 Main Gun System Using Finite Element Techniques." Technical Report 608, US Army Research Laboratory, Aberdeen Proving Ground, Maryland, November 94.

9. BIBLOGRAPHY

Burns B. P., "MC-AAAC In-Bore Projectile Technology." Technical Report ARBRL-TR-02364, US Ballistic Research Laboratory, Aberdeen Proving Ground, Maryland, September 81.

Burns B.P., D. L. Henry, C. D. McCall, and J. F. Newill, "Flexural Characteristic of the M829 Projectile Family." Technical Report 1201, US Army Research Laboratory, Aberdeen Proving Ground, Maryland, September 96

Held, B.J., and D.W. Webb, "Tank Cannon Accuracy Error Due to Inaccurate Measurement of Ammunition Temperature." ARL-MR-128, U.S. Army Research Laboratory, Aberdeen Proving Ground, Maryland, February 94 .

Held, B.J., and T.F. Erline, "Dynamics of the Balanced Breech System for the 120mm Tank Main Gun." BRL-TR-3186, U.S. Army Ballistic Research Laboratory, Aberdeen Proving Ground, Maryland, January 91 .

Held, B.J., D.W. Webb, and E.M. Schmidt "Temperture Dependent Jump of the 120 mm M256 Tank Cannon." BRL-MR-3927, U.S. Army Ballistic Research Laboratory, Aberdeen Proving Ground, Maryland, December 91 .

Hopkins D. A., "Predicting Dynamic Strain Amplification by Coupling a Finite Element Structural Analysis Code with and Interior Ballistic Code." Technical Report No. 3269, US Ballistic Research Laboratory, Aberdeen Proving Ground, MD, September 91.

Hoppel C.P.R., J.F. Newill, and W.H. Drysdale, "Design Optimization of Composite Sabots for Kinetic Energy Projectiles." Classified Ballistics Symposium, Eglin Air Force Base, FL, May 11-14, 98.

Kirkendall, R.D., "Physical Measurements of M829A1 Cartridges for an Accuracy Test." ARL-CR-243, U.S. Army Research Laboratory, Aberdeen Proving Ground, Maryland, September 95 .

Plostins, P., "Launch Dynamics of APFSDS Ammunition." BRL-TR-2595, U.S. Army Ballistic Research Laboratory, Aberdeen Proving Ground, Maryland, October 84 .

Schmidt, E. M., P. Plostins, and M. Bundy, "Flash Radiographic Diagnostics of Projectile Launch from Cannon." Proceedings of 84 Flash Radiography Symposium, E.A. Webster, Jr. And A.M. Kennedy, Eds., The American Society for Nondestructive Testing, 84.

Schmidt, E.M., and D. D. Shear, "Aerodynamic Interference during Sabot Discard." USABRL Report R-20, U.S. Army Ballistic Research Laboratory, Aberdeen Proving Ground, Maryland, September 77. (AD A50308)

Schmidt, E.M., J.A. Bornstein, P. Plostins, B. Haug, and T.L. Brousseau, "Jump from M1A1 Tank." BRL-TR-3144, U.S. Army Ballistic Research Laboratory, Aberdeen Proving Ground, Maryland, September 90 (CONFIDENTIAL).

Schmidt, E.M., P. Plostins, and M. Bundy, "Flash Radiographic Diagnostics of Projectile Launch from Cannon." Proc. of 84 Flash Radiography Symposium, E.A. Webster, Jr. And A.M. Kennedy, Eds., The American Society for Nondestructive Testing, 84 .

Siegleman, D., J. Wang, and P. Crimi, "Computation of Sabot Discard." U.S. Army Ballistic Research Laboratory, Aberdeen Proving Ground, Maryland, BRL Contract Report ARBRL-CR-505, February 83 .

Tzeng J. T. and D. A. Hopkins, "Dynamic Response of Composite Gun Tubes Subjected to a Moving Internal Pressure." Technical Report No. 889, US Ballistic Research Laboratory, Aberdeen Proving Ground, Maryland, October 95.

Wilkerson S. A., M. Berman, and M TingLi, "A Modal Survey of the M1A1 Main Weapon System." Proceedings of the 7th U.S. Army Symposium on Gun Dynamics, New Port RI, May 93.

Zucrow, M.J., and D. Hoffman, Gas Dynamics, John Wiley and Sons, Inc. 76 .

LAUNCH DYNAMICS OF THE 120-MM M831A1 HEAT TRAINING PROJECTILE

J. F. Newill,[1] J. Garner, [1] K. Soencksen, [1] and C. P. R. Hoppel[2]

[1] *U.S. Army Research Laboratory, AMSRL-WM-BC, Aberdeen Proving Ground, MD 21005*
[2] *U.S. Army Research Laboratory, AMSRL-WM-MB, Aberdeen Proving Ground, MD 21005*

The M831A1 is the high explosive anti-tank (HEAT) training round used in the 120-mm M256 gun system of the M1 tank. This projectile has been in production for several years and while it typically performs very well, anomalies are occasionally observed. Since this is a training projectile, large numbers are fired each year. As a result, there is constant pressure to reduce the cost of procurement.

In order to understand and improve the performance of the 120-mm M831A1 projectile, a gun-projectile dynamics study was undertaken using the U.S. Army Research Laboratory's (ARL) gun-projectile dynamics simulation codes. The goals of the study were to determine the baseline launch dynamics of the projectile, investigate the performance effects of projectile position in the forcing cone, examine the sealing abilities of the obturator and sealing ring, and examine the effects of worn tubes.

The results show the M831A1's dynamic path differs from its kinetic energy counterpart, the M865, and the general launch state of the projectile. The results also show the projectile's variability at muzzle-exit can be affected by the projectile's initial location in the forcing cone and that the projectile is sensitive to erosion in the M256 gun tube. The sealing ability of the obturator and rubber seal are presented to show that while there are differences in the initial seal, the primary seal is obtained. Finally, an explanation is given for erratic discard of the obturator band.

1.0 INTRODUCTION AND PURPOSE OF THE STUDY

The M831A1 is the high-explosive, anti-tank (HEAT) training round used in the 120-mm M256 gun system of the M1 tank shown in Figure 1. This projectile has been in production for several years and while it typically performs very well, anomalies are occasionally observed. As with all training ammunition, a large number of projectiles are fired, resulting in a constant pressure to minimize projectile procurement costs. Understanding the interactions of the projectile with the gun system and their effect on the subsequent flight provides insight into methods of meeting the goals while maintaining performance.

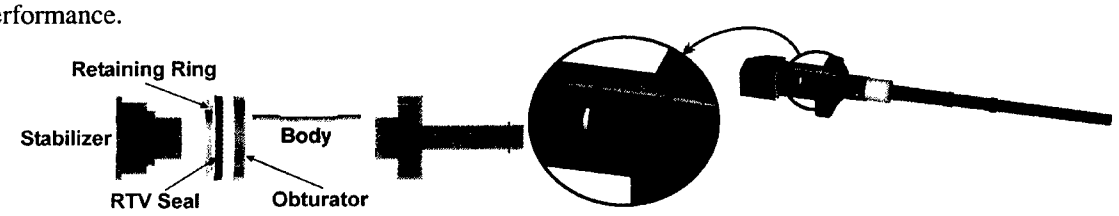


FIGURE 1. PRIMARY COMPONENTS AND A CUT-AWAY VIEWS OF THE M831A1.

The study was initiated by the U.S. Army Armament Research Development and Engineering Center (ARDEC), the Operations Support Command (formerly the Industrial Operations Command), the U.S. Army Research Laboratory (ARL), General Dynamics Ordnance and Tactical Systems (formerly Primex Technologies Inc.) and Alliant Techsystems Inc. The purpose of the study was to describe the in-bore performance of the M831A1 and to show the projectile's sensitivity to system parameters. This paper briefly describes the projectile, along with the modeling techniques, and methods for assessing performance. These descriptions form the groundwork for presenting the basic attributes of launch dynamics, and the effects of launch on the projectile. Focus is then turned to system level performance data to explain the basic behavior along with the factors that influence behavior. Simulation data is compared to ballistic data, with recovered hardware to substantiate the results where possible. The

projectile's obturation system coupled with effects of gun tube erosion are also be presented with hypotheses for the infrequently observed erratic launch. In all over 3,000 simulations were performed

2.0 DESCRIPTION OF THE PROJECTILE AND GUN SYSTEM

The projectile is relatively simple and comprised of six main parts. The nose section is made of steel, while the stabilizer, seal retaining ring, and projectile body are made of aluminum. The seal ring is made of rubber and the obturator is made of Nylon 6. The projectile is full bore in diameter (~119.70 mm [4.712 in]), 476.5 mm (18.76 in) long and weighs is 119.1 N (26.76 lbf).

3.0 SIMULATION TECHNIQUE AND DESCRIPTION OF PERFORMANCE

Gun/projectile dynamic simulations utilize three-dimensional (3-D) Finite Element (FE) models of the M256 120-mm tank cannon launching projectiles. The method is described in Rabern 1991; Wilkerson and Hopkins 1994; Burns, Newill, and Wilkerson (1998); Newill, Burns, Wilkerson (1998); Newill et al. (1998a, 1998b, 1998c, 1999a, 1999b, 2000); Guidos et al. (1999). The hydrocode finite element formulation was chosen to allow investigation of stress wave propagation due to elements of launch. The models are 3-D to capture the asymmetric response of the projectile and gun system resulting from the nonlinear path of the projectile during launch, asymmetric boundary conditions, general lack of symmetry in the centerline profiles of the gun tube, and asymmetric gun motion.

The projectiles and gun systems models are both built in similar manners. Models are developed for the components and then integrated. Relative motion is obtained by defining the proper physics to allow interaction between the parts. Since the M831A1 is relatively simple, the nose, body, stabilizer and obturator are welded together, and sliding interfaces are defined between the nose, body, stabilizer, and the gun bore. One of the purposes of the study is to estimate tank fleet performance. In order to do this, the projectile model is integrated into (and fired from) a number of gun models each of which have unique tube centerlines (the centerlines are covered later in this paper). The propellant pressure loading for the gun system and projectile is generated from IBHVG2 (Anderson and Fickie, 1987).

Projectile performance is often defined in terms of jump, where jump is fully defined in Bornstein et al., 1988; Bornstein, Clemins and Plostins, 1989; Guidos et al. 1999; Soencksen et al. 1999; Soecksen, Newill, and Plostins, 2000 and is also detailed in the previous references to gun dynamic simulations, along with how the jump models have been adapted to the gun dynamic simulations. The gun dynamic simulation codes predict the transverse rates (velocity and angular rate) during the launch cycle. Three types of information are used from these predictions: the dynamic path, variability in jump, and the average jump. The dynamic path gives qualitative information on the rate history of the projectile during the launch cycle. The variability and average jump predicted by the codes are related to accuracy errors where reduction in variability or error represents improved performance of the system. Accuracy error is composed of contributions from many sources, although there are two main contributions from the projectile perspective; dispersion errors, (target impact dispersion TID) and occasion-occasion (occ-occ) error. These concepts are loosely followed in the gun codes i.e., both dispersion and average (center of impact [COI]) are calculated for each group fired, but overall accuracy is not computed in the same manner as in the error budget. The average of a group also has meaning when assessing projectile modifications. If a resulting modification changes the average performance for the projectile, this results in degraded system performance or a potential re-zeroing (new computer correction factor [CCF]) for the projectile.

To intentionally induce the variability into the dynamic path which results in variability the muzzle-exit rates, a series of initial conditions are used, typically the initial cocking angle of the projectile in the forcing cone/bore. Since the diameter of the projectile's bourrelets is less than the interior bore and forcing cone diameter, a clearance exists between the projectile and the gun tube. The angle that the centerline of the projectile can make with these confines is defined as the "cocking angle". There are an infinite number of ways that the projectile can be cocked in tube, but typically, the cocking angles used in

simulations are up, down, left, right, and straight since they encompass the maximum variability. The cocking angles are calculated on a model-by-model basis using the specific dimension of the particular projectile/gun geometry. The straight projectile has the forward and rear bourrelet centered relative to the initial location of the projectile in the gun. Figure 2 defines how the performance envelope is obtained for one projectile, in one gun system, and at one temperature. For a given projectile, when this data is combined with multiple gun systems at a range of temperatures for which tank fleet performance can be defined and then a relative change in performance can be ascertained (Newill et al. to be published).

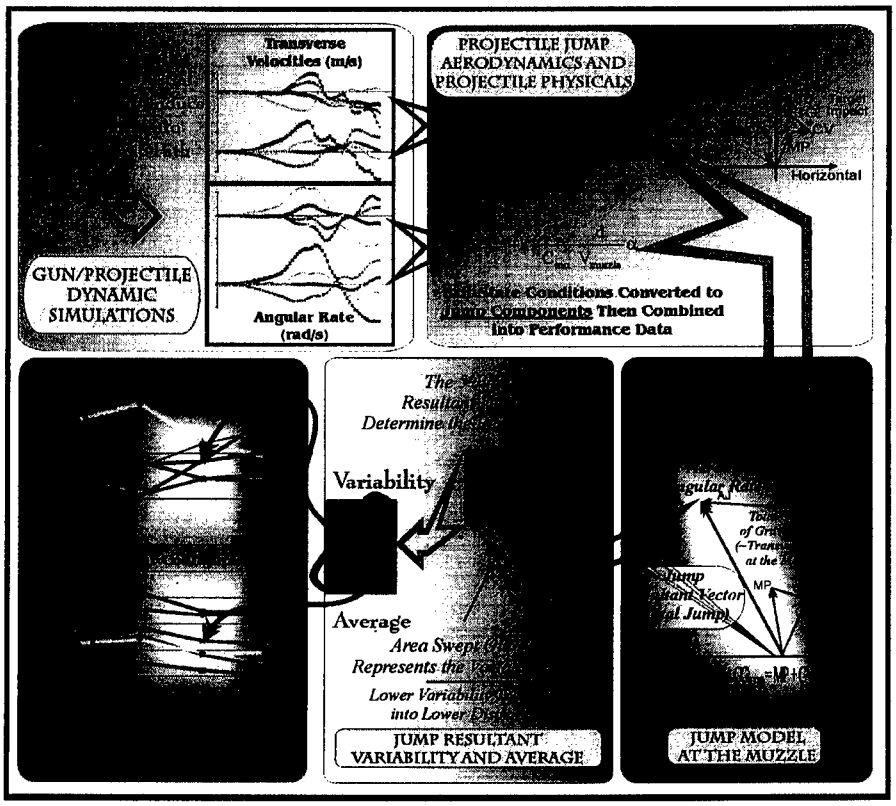


FIGURE 2. DATA ANALYSIS METHODOLOGY.

4.0 LAUNCH DYNAMICS

To understand the launch behavior of the M831A1, the interior ballistic (IB) data is presented first. This data provides an overview of the launch cycle, which pedagogically translates into developing the dynamic path of the M831A1. The dynamic path is compared to that of other ammunition types during the launch cycle. From this basis, system performance of the projectile is addressed.

4.1 Description of the launch event

This study used IBHVG2 (Anderson and Fickie 1987) to approximate the IB loading. The data shows that due to the projectile's relatively heavy mass, it takes approximately 3 ms, or about one third of the launch cycle, to move the projectile the first 0.3 m (12 in) down the gun tube. The projectile travels the remaining 4.32 m (170 in) in approximately 6 ms reaching a nominal velocity of 1,100 m/s and experiencing a peak acceleration of 30 kgees during launch. Figure 3 shows simulation data at several different times, (approximately every 2 ms during launch). Depicted is the effective stress state of the gun along with relative projectile location.

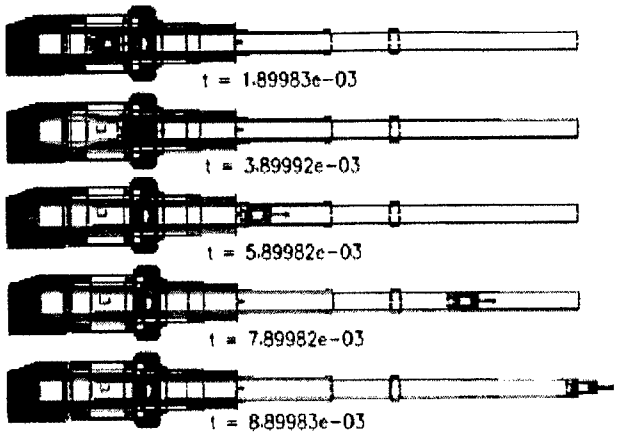


FIGURE 3. EFFECTIVE STRESS STATE AT SEVERAL TIMES.

4.2 Dynamic Path with comparison to other ammunition types

The M831A1 has a relatively long in-bore time, approximately 9 ms, when compared to kinetic energy (KE) projectiles, which are typically approximately about 6 ms. Since the projectile is relatively heavy and stiff, the dynamic path of the projectile would be expected to be very different from its KE counterparts. Figure 4 though Figure 6 shows a comparison in dynamic paths for the M831A1 and a prototype long rod KE projectile, and the M865, a relatively stiff, short wheelbase projectile.

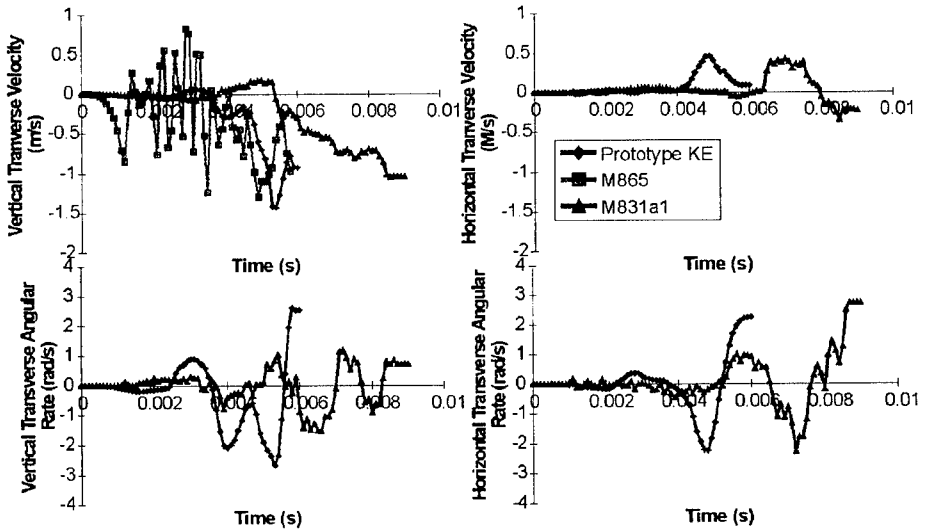


FIGURE 4. COMPARISON OF DYNAMIC PATH WITH PROTOTYPE KE AND THE M865.

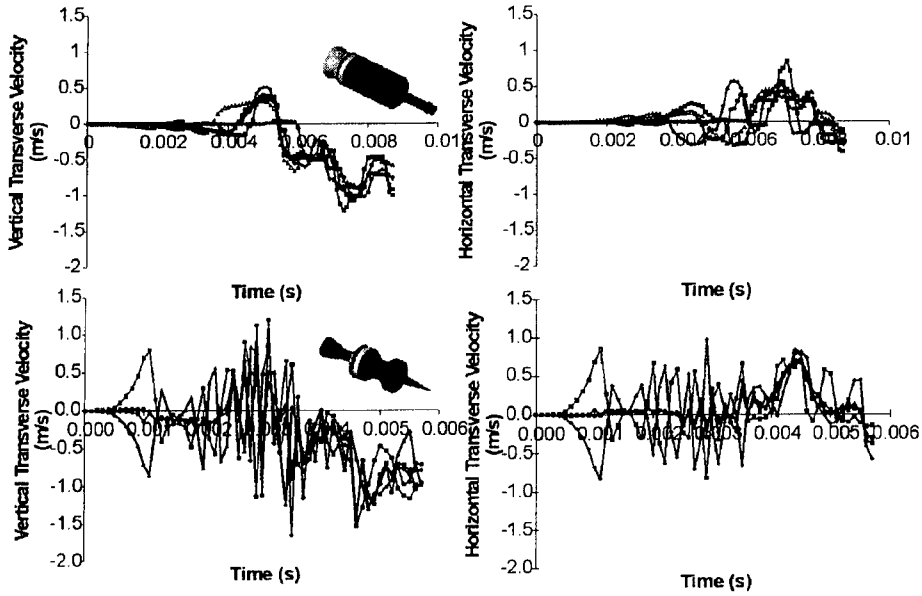


FIGURE 5. COMPARISON OF TRANSVERSE VELOCITY FOR DIFFERENT INITIAL CONDITIONS.

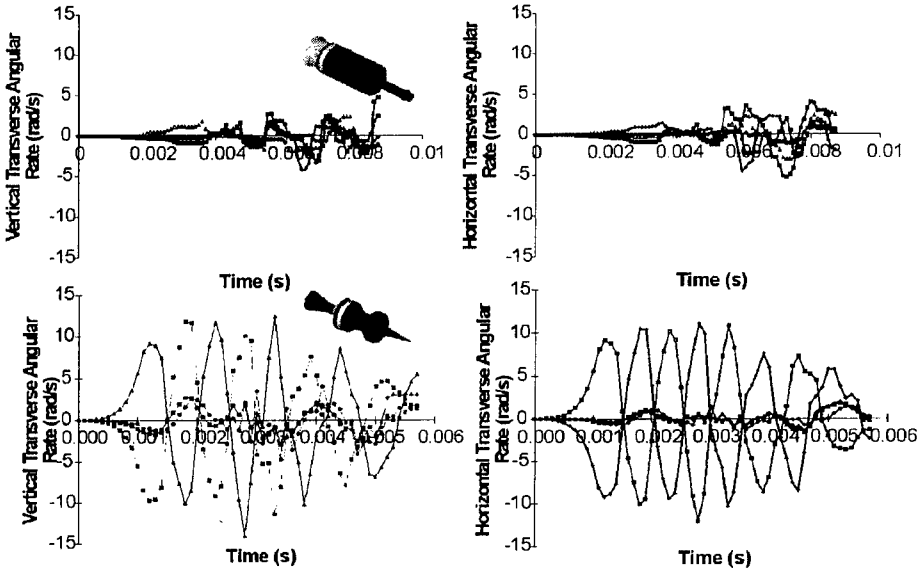


FIGURE 6. COMPARISON OF ANGULAR RATES FOR DIFFERENT INITIAL CONDITIONS.

From the first frame, it is clear that the M865 exhibits a more violent dynamic path than either of the other two projectiles. In the remaining frames, even though the two projectiles (M831A1 and the prototype KE projectile) have very different physical attributes, their in-bore behavior is very similar from a frequency and order of magnitude perspective. While the times are offset due to the velocity differences, the projectile basis response to the system is similar. The reason that the dynamic path for the long rod KE projectile and the M831A1 are probably similar is the relatively low level of balloting experienced during launch. In comparison, the M865's behavior is dominated by balloting probably due to its short wheelbase and small transverse moment of inertia. Again, looking at Figure 4, if the M865 balloting behavior is averaged out, then the projectile follows a path that is similar to the other projectiles.

Figure 5 shows a comparison between transverse velocities and Figure 6 shows a comparison of transverse angular rates velocities of the M865 and the M831A1 for a range of initial conditions. These plots differ from Figure 6 in that the initial conditions have been varied to estimate the relative portion of the total dispersion that will be caused by projectile-gun interaction. From the figures, it is seen that intense balloting behavior does not insure poor performance. It does place more demands on the sealing system of the M865, but the variability is low at muzzle-exit. The M831A1 does not experience the same extreme balloting behavior in-bore, but its variability at muzzle-exit is also relatively low.

These figures illustrate two opposite extremes for a well-designed projectile. Again, if the avg. performance of the M865 is examined instead of the envelope created by the different initial conditions (i.e., removal of balloting), the basic response to the gun system is similar to that of the M831A1.

4.3 Dynamic Effects on the Projectile

The gun system exerts asymmetric loads on the projectile during launch. While the initial conditions of the projectile (cocking angles) are asymmetric with respect to the gun centerline, the initial loading of the projectile is relatively symmetric. Figure 7 shows the effective stress near muzzle-exit as well as several earlier times. The stress state in the projectile is clearly asymmetric at this point

The figure shows that the stress state is relatively uniform early in the launch cycle (i.e., 2 ms), but that asymmetries appear by as early as 5 ms, as the projectile starts moving. As the projectile approaches full velocity the stress state is asymmetric.

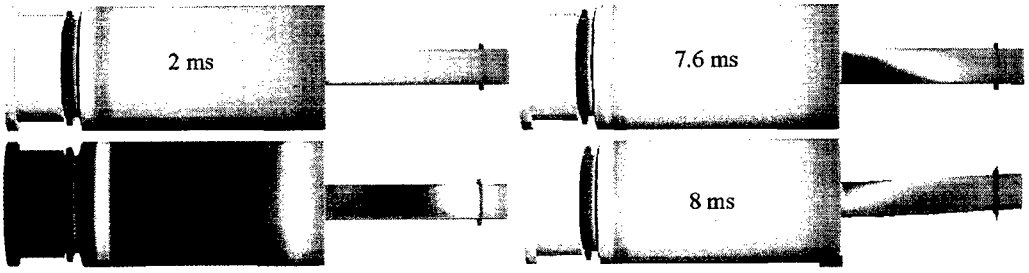


FIGURE 7. EFFECTIVE STRESS STATES AT FOUR TIMES DURING LAUNCH.

4.4 Effect of Initial Projectile Location in the Forcing Cone

Figure 8 shows muzzle-exit jump variability as a function of projectile initial location in the forcing cone. The distance plotted on the x-axis shows the location of the aft point on the rear bourrelet with respect to the rear face of the tube (RFT). The two vertical lines on the graph are significant locations. The first, located at 555 mm (21.85 in), is the furthest aft location of the point on the rear bourrelet that is possible from the tolerance stack up from the drawings. The second line, 565 mm (22.4 in), is the designed, or ideal location of the projectile in the chamber and represents a location at which the obturator is properly engaged. Locations further aft of the 555 mm position represent the point where the back of the rear bourrelet sits outside of the forcing cone although the obturator is still engaged. While these locations lie outside of the total drawing package (TDP), short cartridges in this range have been produced.

Figure 8 shows that the muzzle jump variability is reasonably constant, if the projectile is within the designed tolerances. However, when the initial location of the rear bourrelet starts moving aft of the forcing cone, the variability increases substantially.

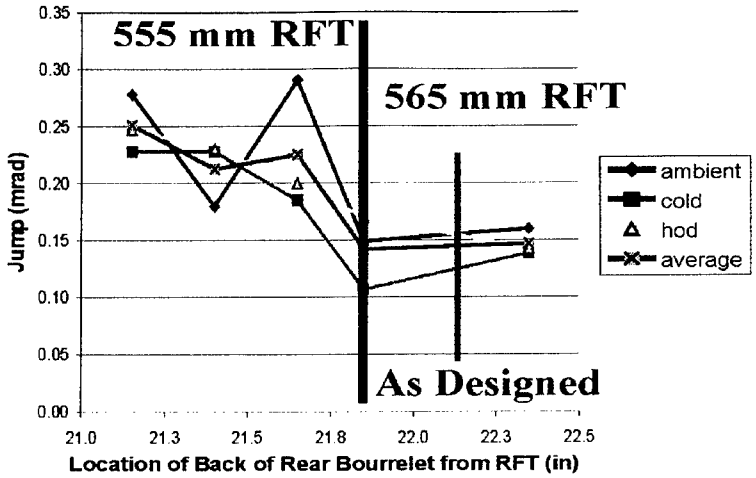


FIGURE 8. MUZZLE JUMP VARIABILITY VS LOCATION OF THE REAR BOURRELET.

There are several other important results from Figure 8. The first is that the source of variability is related to the initial conditions. As the projectile initial location moves aft, the clearance between the forcing cone and the projectile bourrelet increases. The results show that when the projectile is reasonably constrained by the forcing cone, the muzzle variability does not change. Likewise, as the cocking angle is allowed to grow, muzzle variability increases. Therefore, another way to view this figure is the sensitivity of muzzle jump variability to cocking angle. The figure shows that the jump variability grows with increasing cocking angle.

4.5 Centerline Effects and Projectile Jump

Numerous experiments show that the gun tube centerline has a substantial influence on projectile accuracy. Another goal of the present study was to expand the number of gun tube centerlines used to describe tank fleet performance in order to better represent tank fleet performance. Typically, these types of studies have used a "good" tube and a "bad" tube, where the "good" tube conforms to the Held-Wilkerson profile* (uniform profile, tube e). The bad tube's shape is defined as being outside of this profile. Figure 9 shows the centerlines of the ten tubes used in this study.

The gun tube centerline shapes where chosen to represent a range of shapes observed in the tank fleet. The ten shapes encompass the original "good" and "bad" tubes used in the methodology to date. The figures show the tube in the traditional method of supporting the ends of the tubes with gravity removed.

Figure 9 shows the average projectile jump from each of the tubes in the study for three propellant temperatures. In these results, there is a significant deviation in center of impact (COI) with respect to gun tube centerline whereas the temperature effects are less significant. Tube "d" and "e" represent the previous "bad" and "good" centerline tubes, respectively.

* The uniform profile gun tube shape is named after B. Held (formally part of PM-TMAS and current at Rand Corp.) and S. Wilkerson (ARL) for accomplishing the research that identified the importance of this shape.

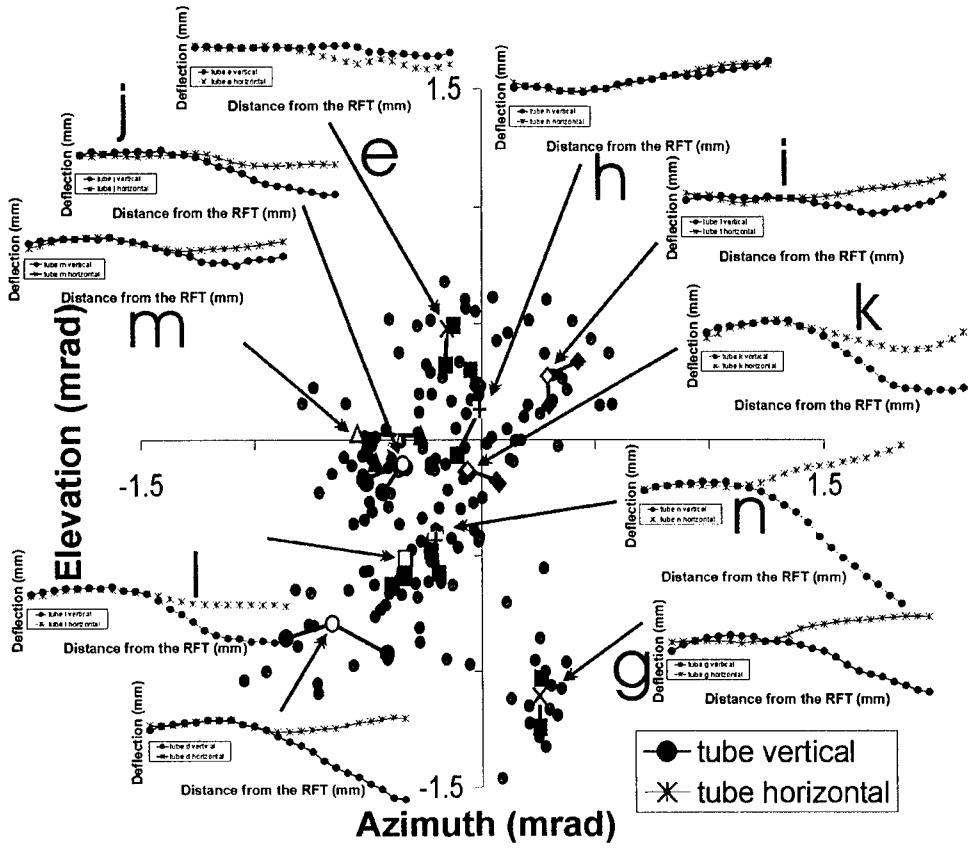


FIGURE 9. AVERAGE JUMP (COI) VERSUS GUN TUBE CENTERLINE.

5.0 COMPARISON WITH EXPERIMENTAL DATA

An experiment was conducted at the Transonic Experimental Facility (TEF) in the Fall of 1998 (Soencksen, Newill, Plostins, 2000, Soencksen et al. 2001) to measure first maximum yaw. The gun tube centerline used in the simulations was that of the actual gun tube used in the TEF experiment. Comparing data to the predicted ranges of first maximum yaw (Soencksen et al. 2001), it is seen that the range and variability are a good match with the exception of one shot. This shot had a first maximum yaw in excess of 9 degrees. Since this very large motion was present immediately in the first yaw cycle, it was necessarily caused by launch disturbances. Inspection of the gun tube at the time of the test showed that the tube had some bore erosion damage . It is confidently hypothesized that the high first maximum yaw for this shot was due to this gun tube damage and would not have been part of the normal population launch from this tube when it was in pristine condition.

In (Soencksen et al. 2001) simulations are used to predict first maximum yaw from a gun tube with bore damage. The envelopes predicted span all the results. It is important to note that simulation of tube damage is extremely difficult due to the complexity of the phenomenon, and no attempt was made to match the exact type of damage seen in the TEF gun tube (beyond the modeling capability). These types of simulations, combined with the experimental data, are used to provide some insight into the sensitivity and the level of performance degradation possible from tube damage.

6.0 OBTURATION

As part of the study, the obturation system of the projectile was examined to help assess its ability to seal the projectile from the propellant gases during launch. It should be noted that the M831A1 discards its obturator band at muzzle-exit in about half of all firings (Manole 1998). Since this behavior represents variability in launch performance, one of the goals of the study was to explain the cause and offer solutions. Table 1 lists the materials properties for Nylon 6 under a range of environmental conditions. The table demonstrates the large range of variability in material that exists in production obturators. This means that the obturator has to function properly almost regardless of its properties.

TABLE 1. NYLON 6 MATERIAL PROPERTIES (DOHRN, 1998).

Condition	# Specimens	Max. Tensile Strength (psi)	Elastic Modulus (ksi)	Elongation to Failure (%)
Brittle	23	11057.9	576	7.75
Tough	12	9569.9	380.87	39.65
Tough-Wet	15	5907.7	23.4	71.62
Variability		2X	25X	9X

Figure 10 shows the configuration of the production projectile. Obturation is achieved through an RTV sealing ring along with a Nylon 6 obturator. One of the first questions addressed was the effectiveness of the sealing ring. Recovered hardware showed areas under the seal containing soot, which indicates gas leakage. The soot deposits were very irregular (asymmetric) with large differences found on each of the recovered projectiles (Demitroff, 1998). There were also signs of soot forward of the sealing ring on the projectile body.

With this information the first step in the modeling was to assess the mechanism of seal gas leakage and to determine if it could prevent the seal from providing adequate protection. Three cases were modeled which are shown in Figure 10.

Even though the three cases represent only an approximation of what is happening to the projectile, in each case the sealing ring offer some level of sealing at relatively early times in the cycle. The reason for this is that the amount of surface area exposed to the gas pressure that contributes positively to the seal is greater than that which contributes negatively.

In these scenarios, it is possible to initially leak gas around the rubber seal and then seal. This is consistent with the recovered hardware. There is no experimental data available on the seal since it does not survive after muzzle-exit , but this is also consistent with gas wash observed on recovered the projectiles.

A similar series of simulations was performed on the nylon obturator, Figure 11. The Nylon 6 was modeled using Bamman plasticity model with constant developed at ARL (Gazonas, 2000). These simulations indicate that the initial sealing pressure is highly dependent on seating locations of the projectile. But even with these initial seating issues, the constriction of the bore forcing cone creates an adequate seal during the ballistic cycle. The figure also shows that the high-compressive-radial stresses occur in the obturator. This correlates well with recovered hardware (Dimitroff, 1998). Relative to the uncertainty of the initial seal, the current obturator design (depending on dimensional factors of the obturator, the body, and location in the forcing cone) can leak propellant gas underneath the band.

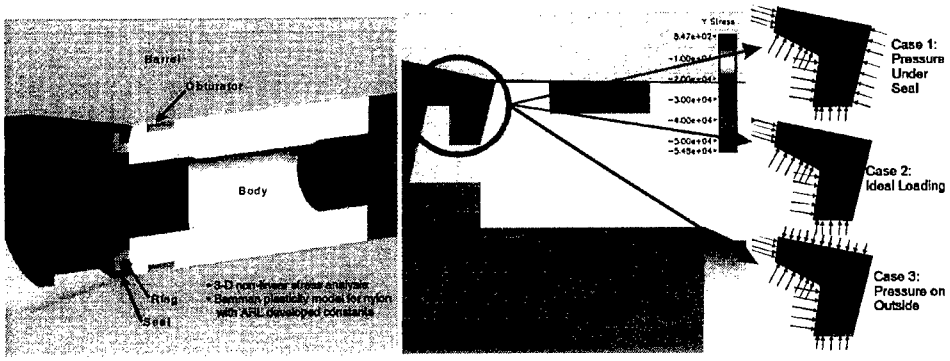


FIGURE 10. CONFIGURATION OF THE SEALS AND BOUNDARY CONDITIONS OF THE MODELS.

Gas leakage underneath the obturator does not degrade the obturator sealing performance, in fact, it increases the sealing efficiency in-bore. The problem occurs at muzzle-exit, where the obturator loses tube support, and the gas either vents or blows the obturator off the projectile body. The sporadic leakage of gas underneath the obturator is believed to be responsible for the intermittent loss of the obturator band at muzzle-exit.

To ensure the bands remain in place, the obturator design was modified to the configuration seen in Figure 12. Figure 13 shows the pressure at the interface of the M831A1 obturator seat. The plot shows the radial sealing pressure at the aft underneath section of the obturator and the sealing pressure under the front of the undercut. For comparison, the negative of the base pressure is plotted. An adequate seal is defined as the absolute value of the obturator-body interface pressure being greater than the absolute value of the base pressure.

The main conclusions from Figure 13 are that a gas seal is present from the beginning of the pressure cycle, and that it continues to increase as peak pressure is approached. The figure also shows that the section underneath the front of the undercut also seals well. Figure 14 also shows a plot at the interface pressure between the obturator and the tube. The graph shows that an adequate seal is created, but not until the projectile moves further into the forcing cone/bore. There actually could be a seal from shot start depending on the initial conditions. If there is an interference fit between the obturator and bore when the cartridge is loaded the initial stress would increase, which could seal the projectile at early times. In either case, the obturator seal the gun gases during launch once the initial seal is formed, it increases at a rate that is faster than the increase in the base pressure. This increasing differential pressure along with the ramp in the obturator seat helps feed the obturator against the bore, and helps maintain sealing as the projectile passes bore damage.

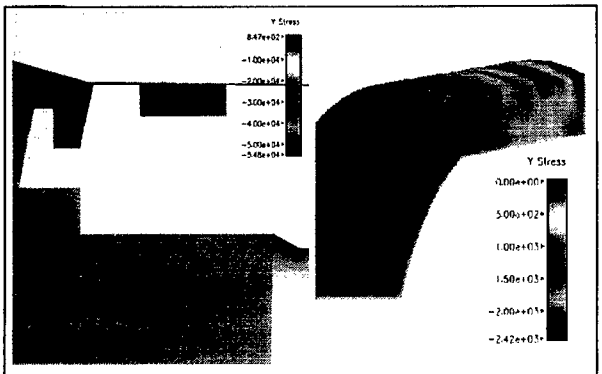


FIGURE 11. OBTURATOR SIMULATION.

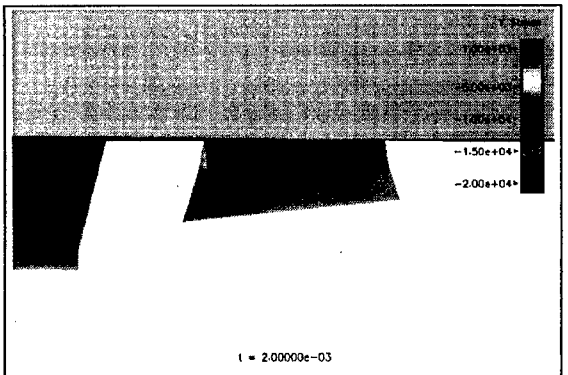


FIGURE 12. RAMP STYLE OBTURATOR.

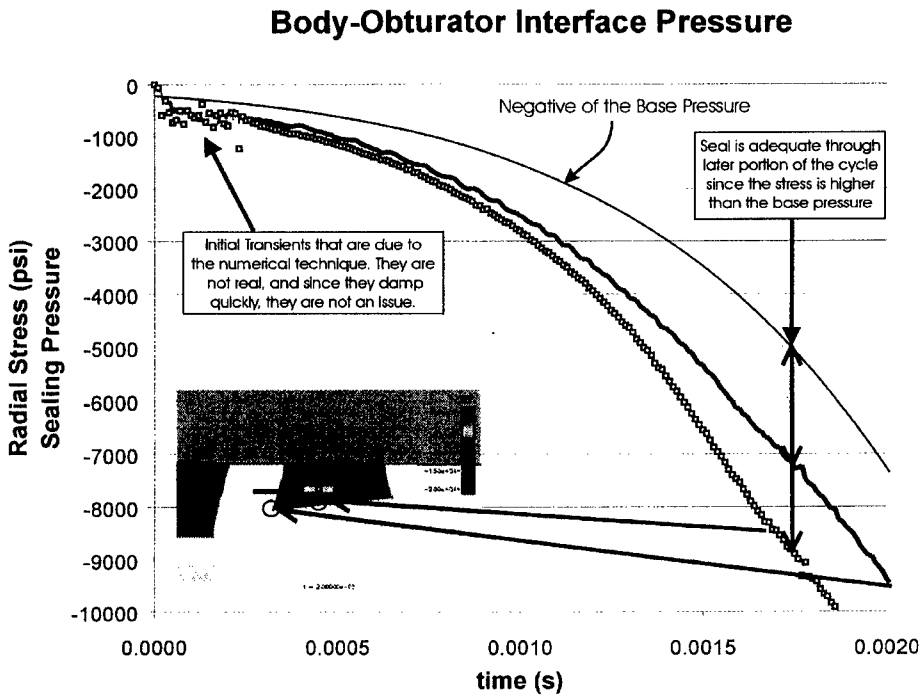


FIGURE 13. M831A1 BODY – OBTURATOR SEAT SEALING.

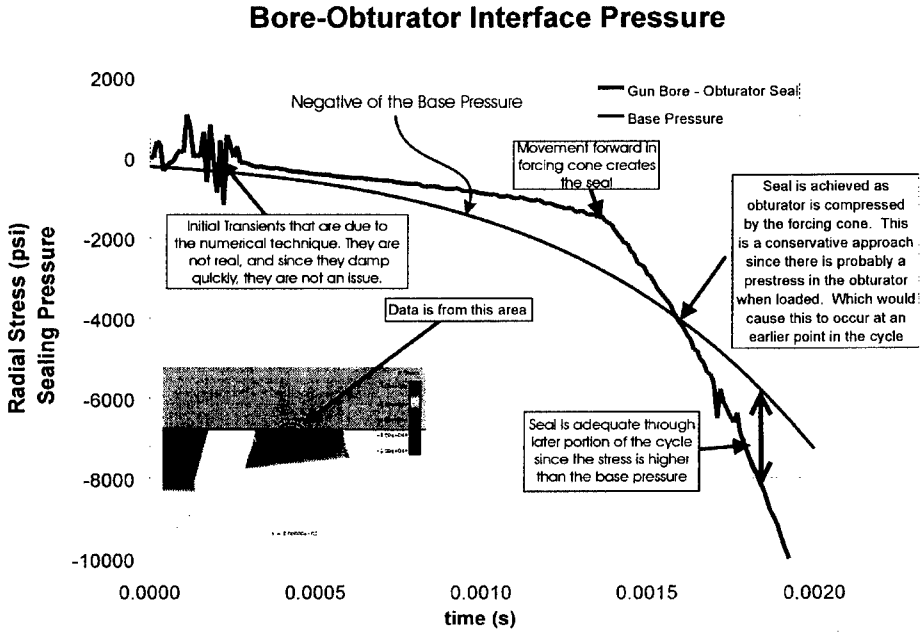


FIGURE 14. M831A1 BODY – BORE SEALING.

7.0 EFFECTS OF GUN TUBE EROSION ON PERFORMANCE

The effect of in-bore damage on projectile performance is very difficult to quantify. It is generally known that as damage to the bore becomes significant it affects system performance through increased projectile dispersion. Even with this knowledge, there is very little research that directly quantifies the phenomenon, since experimental programs rarely use a gun tube with significant bore damage. In general , if control rounds exhibit performance problems and the tube condition is determined to be questionable, the tube is changed. It is also important to note that the type of bore damage of interest here occurs while the gun tube is still considered serviceable, i.e., it is still safe to fire and does not meet condemnation criterion. Since it is likely that tank projectiles will be fired from a gun with some bore damage, this study attempts to address the M831A1 sensitivity to observed types of damage. The remainder of this section briefly quantifies the types of damage of interest and then shows that in some regions of the tube it can affect performance. There are two types of damage that are of primary interest: erosion and chrome stripping. Erosion is typically caused by initial manufacturing defects in the chromed surface of the gun bore that, through repeated firing cycles, cause local damage to the bore surface that continues to erode through the life of the tube (Cote 2000). Figure 15 is a picture of a cast made of the gun tube bore surface with bore erosion damage.

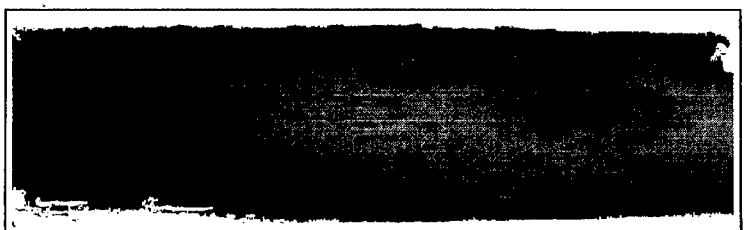


FIGURE 15. TUBE "Y" AFTER 1275 FIRINGS.

The damage seen in Figure 15 consists of long thin (approximately 3 mm wide furrows) regions. These regions are between 50 and 200 mm long, with many that are connect together. Chrome stripping damage is located further down the gun tube and consists of thin strips of chrome removed by the violent mechanical interaction with the projectile. This study takes the approach of trying to assess what types and location of damage affect projectile performance the most.

In order to model this type of damage, many assumptions are made since the interaction between the projectile, obturator, propellant gas, and the damage is extremely complicated. Both the stripping and erosion damage are modeled with respect to leaking gas, but do not include effects caused by the mechanical interaction between the projectile and gun bore. A primary assumption made is that as the projectile and obturator pass gun tube bore damage, local gas jets are opened and closed as the projectile passes the damage (catastrophic failure did not occur). This work does not attempt to quantify the damage to the projectile caused by the jetting, which is recognized in severe cases to cause catastrophic failure. The jet is assumed to cause a localized pressure load on the portion of the projectile forward of the obturator, and this is assumed to ramp up to the base pressure of the projectile for the time it is subjected to the damage, and then drop back down to zero as the projectile passes the damage area. The rise and fall times are assumed approximated to be 0.05 ms.

The duration or size of the modeled damage approximates the types of damage actually seen in the gun tubes. The remainder of this section will first show how the pulses are constructed, then show how size and location could potentially affects the projectile performance.

Figure 16 shows base pressure of the projectile. It also shows that as the projectile passes a particular location with bore damage, the pressure ramps to the base pressure then continues to rise to a pressure between the projectile base pressure and the chamber pressure. Figure 16 also shows the pressure pulses associated with a 1 inch pit at various locations in the gun tube. The reason that the pulses sizes are different is that the projectile's velocity is continually increasing, therefore the dwell time that the pulse has to act on the projectile decreases. At the early times, the length (approximately time of application) of the pulse is relatively long whereas near the muzzle, where the projectile is near full velocity, the pulses' application time are relatively short.

Figure 17 shows a second set of pulses associated with a eight in erosion pit. This figures provides insight into the question of what type of pressure pulse has the greatest influence on the dynamic path of the projectile. Figure 18 shows the pressure impulse (the pressure times the amount of time it is applied. The figure shows that the pressure pulses that impart the most significant energy to the projectile are caused by damage located near the forcing cone of the gun tube. While such early damage has the best chance to impart energy, there is a significant dependence with damage size at locations near the forcing cone.

Both of these effects are related to projectile velocity. If the projectile is moving slowly, then gas leakage has a good chance of significantly impacting the projectile dynamic path. As the velocity increases to a significant level, the projectile passes damage fast enough that the effects of the damage are minimized. Unfortunately the majority of the erosion damage occurs between the chamber and the location of the projectile at peak pressure, which is typically less than 2 m from the RFT.

The first frame of Figure 20 shows the effect of having a 25 to 225 mm erosion pit located 1 m from the RFT and the second frame shows the effect of a 75 mm erosion pit from 0.5 to 4.8 m from the RFT. In both frames, there are three straight horizontal lines near the bottom of the figure. These three lines represent the baseline performance of the projectile at hot (120 F), ambient (70 F), and cold (-20 F) propellant temperatures without any tube damage. The first frame shows results that are chaotic with no

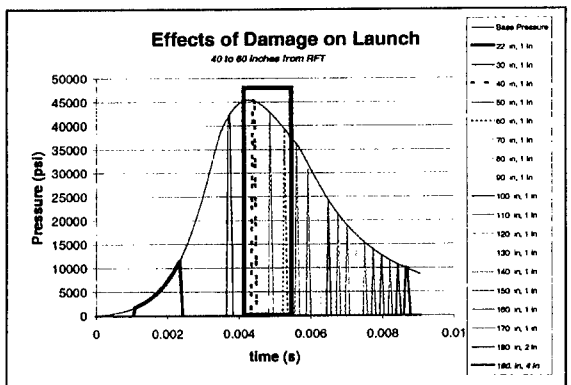


FIGURE 16. PRESSURE PULSES FOR A 1 INCH PITS.

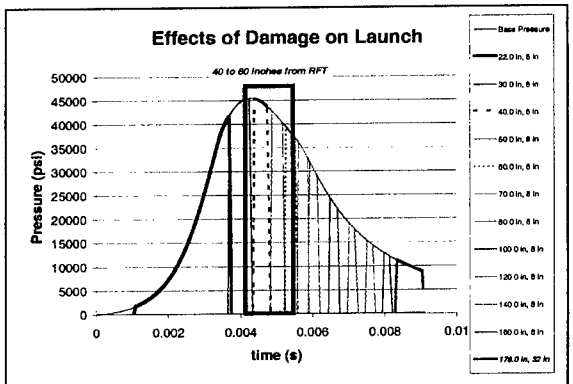


FIGURE 17. PRESSURE PULSES FOR AN 8 INCH PITS.

clear trend with damage size. The figure also shows that in most cases the damage increases the jump variability , but not in all cases although clearly the potential range of exit state conditions has increased. In the second frame the results have a definite trend. As the location of the damage is moved toward the muzzle the damage has less and less effect on the exit state variability.

While in some cases the variability even dropped below the baseline variability, this should not be interpreted as potential method to improve performance, because the overall state is more chaotic which will lead to poorer performance. This study can only give some idea of the sensitivity since it is only examining a single erosion pit or chrome strip that conforms to the assumptions in the study. Figure 20 gives some insight into the effect that more extensive gun damage has on the dynamic path of the projectile. In the case described in the figure random pits were used in gun tube between 0.53 and 2.03 m at various circumferential locations. The figure shows that the dynamic paths were altered significantly and looking at muzzle-exit, the dispersion in the muzzle angular rates has increased substantially. This backs the premise that severe enough damage will substantially alter the launch cycle and degrade the system performance.

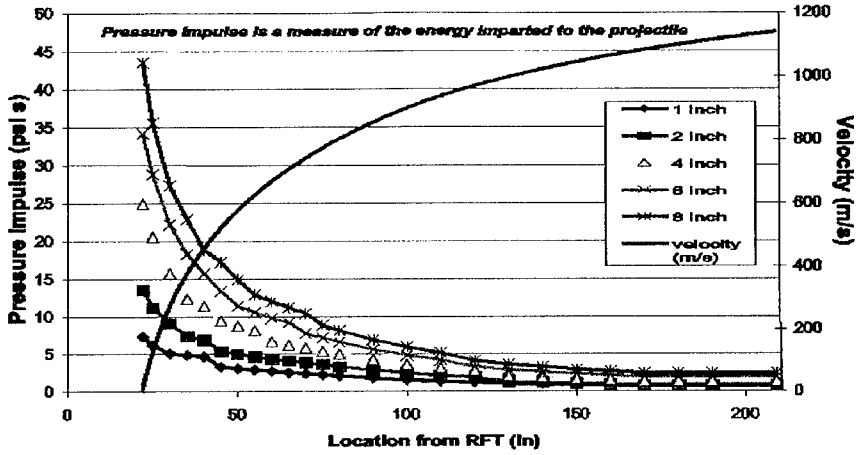


FIGURE 18. PRESSURE IMPULSE VS. DAMAGE SIZE AND LOCATION.

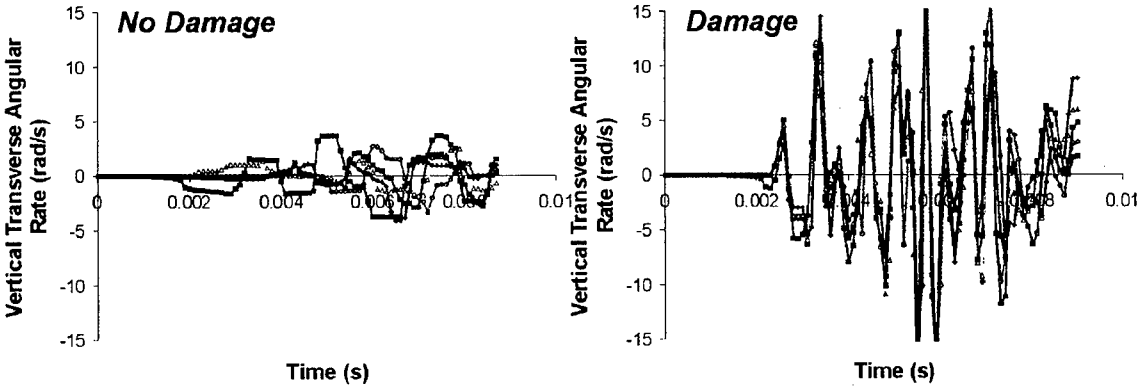


FIGURE 19. VARIABILITY VS. PRESSURE PULSE SIZE AND LOCATION.

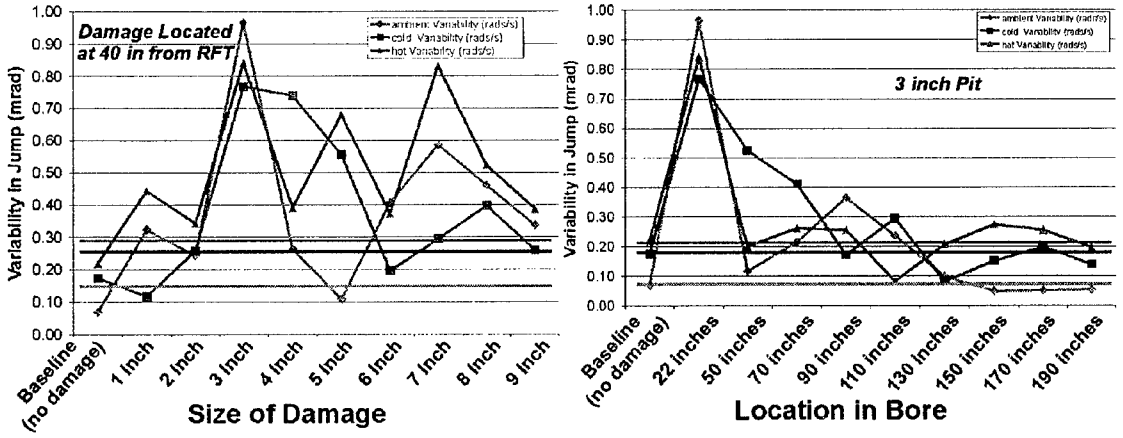
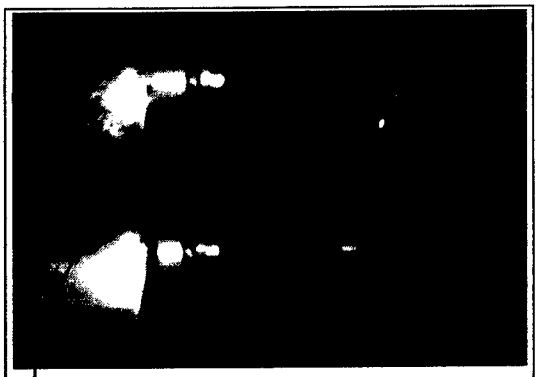


FIGURE 20. MUZZLE JUMP VARIABILITY VERSUS PRESSURE PULSE SIZE AND LOCATION.

8.0 HYPOTHESIS FOR OCCASIONAL ERRATIC BEHAVIOR

Occasionally, erratic flight behavior of the M831A1 has been observed. The behavior typically manifests itself as a target impact that is significantly out of pattern or by a ground impact short of the target. There are currently at least five theories that provide potential explanations for this behavior: (1) poor launch dynamics, (2) roll-yaw lock-in, (3) aerodynamic trim-induced trajectory bias (4) discarding obturator, and (5) sealing ring interference with the stabilizer. The occurrence of occasional high yaw rates was demonstrated at TEF (Soencksen, Newill, Plostins, 2000). While these theories are documented here, the source of the theories is referenced.

The first hypothesis is the result of the study presented in this paper. If a gun tube has bore damage , and if the obturator system is not able to prevent local jetting, then the dynamic path of the projectile can be altered. The second theory is that roll-yaw lock-in, (Arrowtech Associates Inc and Alliant, 1999) is related to the very slow roll-up of the projectile observed in experiments. Since the projectile is full-bore and heavy, it has a large axial moment of inertia. These attributes, coupled with the fact that the stabilizer diameter is smaller than the body diameter, and implies that the stabilizer is not wetted by the free stream sufficiently. This limits available roll torque. The low torque available combined with the high axial moment of inertia results in the very slow projectile roll up . This was shown experimentally by Soencksen, et al. (2001). Since the projectile is slowly rolling, as the roll frequency approaches the yaw frequency, resonance can occasionally cause catastrophic yaw amplification, which leads to drastically increased drag, and thus a potential short ground impact. The slow roll characteristics may also be responsible for trajectory bias in the event that aerodynamic trims are present. Such trims were shown in TEF experimental data (Soencksen, et. al, 2000), and a detailed description of their effect on the trajectory is found in that work. The forth theory is related to discard of the obturator band, which occurs approximately 50% of the time. Occasionally, as the band attempts to discard, it either gets temporarily caught on the obturator seat or becomes stuck in the seat (Manole, 1998). If this occurs such that the band stays partially attached to the projectile throughout the flight, this could adversely affect the flight in two ways. First, the hanging band will create an asymmetry that will lead to a trim and potentially a trim-induced trajectory bias. Secondly, drag could also be affected. The final theory was also observed during ballistic testing by Alliant Techsystems (Demitroff 2000). During the test, Hadland digital photographs show a projectile where the sealing ring did not break or discard at muzzle-exit as is normally the case. In this case, the ring slipped over the retaining ring, moving aft and seating at the end of the stabilizer (Figure 21), partially masking the slots used to generate roll torque.



Launch with Sealing Ring on Back of Stabilizer

FIGURE 21. NORMAL LAUNCH AND SEALING RING ON THE STABILIZER.

Its final observed position during flight was on the back of the stabilizer covering the slots used to generate spin-up torque. If the ring stays in this position throughout the flight, it could adversely affect roll torque generation, possibly causing changes in the jump.

9.0 CONCLUSION

This paper analyzes the launch dynamics of the M831A1 using computer simulation technology, and validating the simulations with experimental data. The launch cycle and its effects on the M831A1 are described showing that the projectile spends a relatively long period of time in the bore of the gun. Even

with the long dwell times, the launch dynamics of the projectile are similar to those of a typical prototype kinetic energy (KE) projectile. This does not imply that the launch of the projectile occurs without disturbance. While the initial effects on the projectile are symmetric, as the launch cycle proceeds, the projectile exhibits balloting behavior leading to asymmetric effects. While not as severe as the balloting seen for the M865, the balloting is still violent enough to cause flexing in the steel nose spike during launch. While the balloting behavior contributes some of the variability at muzzle-exit, the gun tube shape remains one of the dominant influences. Overall, the projectile performance is good provided it is manufactured within specified tolerances and is not subjected to large lateral forces from bore erosion. When bore erosion is present, it has the largest influence in the early portion of the launch cycle since it has a longer action time due to the projectile's relatively low velocity here. Bore erosion affects obturation of the propellant gases. Simulations show that while the current obturation system appears adequate, there are some questionable aspects of its behavior. Simulations suggest a remedy to address the issue and is scheduled for ballistic testing. Finally, the simulations have been compared to experimental data obtained at TEF with good agreement. The ultimate result of this work has been a better understanding of the launch dynamic effects on the projectile, and to offer explanations for the occasional erratic ballistic behavior.

10.0 ACKNOWLEDGEMENT

A study of this magnitude requires a coordinated effort and support from many people. The principal organizations are ARL, ARDEC's AMSTA-AR-CCH-B, Rock Island Operations Support Command, Alliant Techsystem Inc, General Dynamics Ordnance and Tactical Systems, and the people at ARL. Their leadership expertise and experience are invaluable. This study relied heavily on supercomputers supplied by DOD's High Performance Computing initiative (specifically by the Major Shared Resource Center at ARL).

11.0 REFERENCES

Anderson, R. D., and K. D. Fickie. "IBHVG2 - A User's Guide." BRL-TR-2829, APG, MD, Jul 1987.

Bornstein, J., I. Celmins, and P. Plostins, "Launch Dynamics of Fin-Stabilized Projectiles." AIAA Paper No. 89-3395, Aug 1989.

Bornstein, J., I. Celmins, P. Plostins, E. M. Schmidt. "Techniques for the Measurement of Tank Cannon Jump." BRL-MR-3715, U.S. Army Ballistic Research Laboratory, Aberdeen Proving Ground, MD, Dec 1988.

Bundy M. L., J. F. Newill, and C. P. R. Hoppel, "A Notional Redesign of the M865E3 Obt." ARL-TR-2325, Sep 00.

Bundy M., J. Newill, V. Marcopoli, M. Ng, C. Wells, "A Meth. for Char. Barrel Flex. Due to Tank Motion." ARL-MR-479, Jun 00

Burns B. P. , D. L. Henry, C. D. McCall, J. F. Newill, "Flex. Char. of the M829 Proj. Family." ARL-TR-1201, Sep 96.

Burns B. P. , J. F. Newill, and S. A. Wilkerson, "In-Bore Projectile Gun Dynamics." *Proceedings of the 17th International Ballistics Symposium*, Midran, South Africa, 26 Mar 98.

Cote, P.J., Rickard, C., " Gas Metal Reaction Prod. in the Erosion of Chromium Pltd Gun Bores" Wear, Vol. 241, Is. 1 pp 17-25, Jun 00.

Demitroff, D., Personal communication with J. Newill. Alliant Techsystems, Hopkins, MN, 1998-2000.

Dohrn, R. Personal communication J. Newill. Alliant Techsystems, Hopkins, MN, 1998-2000.

Guidos B. , P. Plostins, D. Webb, J. F. Newill, "120-mm Tank Gun Acc. Demonstrator (TGAD) Jump Test." ARL-TR-29, Dec 99.

Gazonas, G.A., "Impl. Of A Finite Strain Plasticity Model For Nylon 6/6 Into DYNA3D", in: *Structures Under Shock and Impact VI*: N. Jones, C.A. Brebbia, and A.J. Watson [Editors], Comp. Mech. Pub., Ashurst Lodge, Ashurst, Southhampton, UK, Jul 00.

Hoppel C.P.R., J. F. Newill, and K. P. Soencksen, "Evaluation of Obturator and Sealing Cuff Properties for the M865 Training Projectile with Comparison to Ballistic Testing." ARL-TR-2039, APG, MD, Sep 99.

Lyon, D. H. "Radial Stiffness Measurements of 120-mm Tank Projectiles." ARL-TR-392, U.S. Army Research Laboratory, Aberdeen Proving Ground, MD, Apr 94.

Lyon, D. H. and K. P. Soencksen. "Radial Stiffness and In-Bore Balloting Analysis for the M900 Projectile." ARL-TR-593, U.S. Army Research Laboratory, Aberdeen Proving Ground, MD, Oct 94.

Manole L., Personal communication with J. Newill. ARDEC, Picatinny Arsenal NJ, 1998-2000.

Newill J. F., B. P. Burns, and S. A. Wilkerson, "Overview of Gun Dynamics Numerical Sim." ARL-TR-1760, APG, MD, Sep 98a.

Newill J. F., C. P. R. Hoppel, D. Kamdar, B. Guidos, and B. Drysdale, C. Livecchia, and M. Luciano, "Geometric and Material Changes to the Forward Bourrelet to Optimize Performance of KE Ammunition." ARL-TR-2328, Sept 00.

Newill J. F., C. P. R. Hoppel, K. P. Soencksen, and P. Plostins, "Simulation of the M865 Kinetic Energy Projectile with Experimental Validation." Proceedings of the 18th International Ballistics Symposium, San Antonio, TX, Nov 99a.

Newill J. F., C. P. R. Hoppel, W. H. Drysdale, and D. S. Kamdar, "Effects of Bourrelet Stiffness on the Interior Ballistic Performance of Kinetic Energy Ammunition." ARL-TR-02, APG, MD, Jun 99b.

Newill J. F., C. P. R. Hoppel, W. H. Drysdale, and S. A. Wilkerson "Numerical Simulation of Launch Interaction of Kinetic Energy Long Rod Fin-Stabilized Projectiles and M1A1 Abrams M256 Gun System with Comparison to Experimental Results." National Def. Industrial Assoc. 48th Annual Bomb & Warhead Technical Symp., Eglin Air Force Base, FL. May 11-14, 98b.

Newill J. F., C. P. R. Hoppel, and W. H. Drysdale, "Comp. of Launch Mechanics and Dynamics from the M1A1 M256 Gun System for the M829A2 Kinetic Energy Long Rod Fin Stabilized Projectile Containing Diff. Penetrator Materials." ARL-TR- 1671, . Apr 98c.

Newill J. F., S. A. Wilkerson, C. P. R. Hoppel, and W. H. Drysdale. "Numerical Simulation of Composite Kinetic Energy Projectiles Launched by an M1A1 Abrams M256 Gun System." Proc. of the 30th SAMPE Technical Conference, San Antonio, TX, 23 Oct 98d

Newill, J. F., D. Webb, B. Guidos, C. P. R. Hoppel, and W. H. Drysdale. "Meth.. for Formal Comp. of Exp. Ballistic Firing of Kinetic Energy Projectiles With Num. Sim." Technical Report, U.S. Army Research Laboratory, APG, MD, in progress.

Plostins, P., I. Celmins, and J. Bornstein. "The Effect of Sabot Front Borerider Stiffness on the Launch Dynamics of Fin-Stabilized Kinetic Energy Ammunition." AIAA Paper No. 90-0066, Jan 90.

Rabern D.A., "Axially Acc. Saboted Rods Subjected to Lateral Forces." BRL Contractor Report No. 671, Aug 91.

Schmidt, E. M., P. Plostins, and M. Bundy. "Flash Radiographic Diagnostics of Proj. Launch from Cannon." Proc. of Flash Radiography Symposium, E.A. Webster, Jr. and A.M. Kennedy, editors., The American Society for Nondestructive Testing, 84.

Soencksen K.P., J. F. Newill, P. Plostins, "Aerodynamics of the 120-mm M831A1 Projectile: Analysis of Free-Flight Experimental Data." Proceedings of AIAA Atmospheric Flight Mechanics Conference & Exhibit, Denver, AIAA-00-4198, CO, 14-17 Aug, 00

Soencksen, K. P., J. F. Newill, J. M. Garner, and P. Plostins, "Comp. of the 120-mm M831A1 Projectile's Exp. Launch Dynamic Data with Hydrocode Gun-Projectile Dynamic Simulations." 10th Army Gun Dynamics Symposium, Austin, TX, 23 – 26 Apr 01

Soencksen, K.P., J.F. Newill, P. Plostins, "Roll Characteristics of the 120-mm M831A1 Projectile." *Proceedings of the 39th AIAA Aerospace Sciences Meeting & Exhibit,* 8-11 January 2001, Reno, NV.

Whirley R. G, D. E. Englemann, and J. O. Hallquist. "DYNA3D; A Nonlinear, Explicit, 3-D Finite Element Code for Solid and Structural Mechanics - User's Manual" Lawrence Livermore's National Laboratory, UCRL-MA-107254 Rev 1, Nov 93.

Wilkerson S. A. and D. Hopkins, "Analysis of a Balanced Breech System for the M1A1 Main Gun System Using Finite Element Techniques." Army Research Laboratory Technical Report 608, Nov 94.

The Influence of Projectile Mass upon Precision

E. Schmidt and H. Edge

U.S. Army Research Laboratory, Aberdeen Proving Ground, MD 21005-5066, USA

Precision, or round-to-round dispersion is an important parameter contributing to the accuracy of tank fire. It is typically a lot acceptance specification for ammunition, both war and target practice rounds. A kinetic energy war round is fabricated from a dense metal such as tungsten alloy while the practice round is made from steel. In an attempt to improve training round performance and lower cost, a series of designs using aluminum was examined. The test results showed a considerable degradation in precision. This paper examines the firing data for a set of rounds having widely different inertial characteristics and attempts to explain the results.

INTRODUCTION

In training, it is desirable to have a round that closely resembles the actual war round in terms of visual appearance, size, weight, and, up to a point, ballistic performance. To remain within the boundaries of military reservations, it is required that the maximum range of the training round be considerably less than that of the war round. Also, penetration should be limited in the event of an accidental impact on another vehicle in training. For the 120mm cannon, the training round is a flare-stabilized projectile made of steel. The round is launched at 1700 m/s and provides satisfactory simulation of the war round out to 3 km; however, beyond that range, the high drag of the flare provides rapid deceleration and limits the maximum range. At the high muzzle velocity, a steel core round has appreciable penetration capability. Kennedy, et al[1], attempted to provide an alternative with greatly reduced penetration. By employing a hollow aluminum flight body, they succeeded in matching the trajectory of the existing trainer, while reducing the penetration by about a factor of ten. However, precision testing showed that round-to-round dispersion grew by a factor of more than three.

In examining the possible sources of launch and flight disturbances[2], it was determined that the aerodynamic jump coefficient[3] of the aluminum round was significantly greater than that of the steel core design. One obvious way to improve the jump sensitivity was to increase the static margin. This suggested the use of higher density counter weights in the nose region. Lead, copper, and steel were all tested. Significant improvements in precision were observed; however, levels equivalent to the steel round were not achieved. The present paper examines this body of data and correlates inertial properties of the projectiles with both overall precision and the components of flight disturbance. Four fin-stabilized round types are considered: tungsten alloy, steel, aluminum, and aluminum with a steel counterweight.

EXPERIMENTS

Data is taken from three separate experiments. The tungsten alloy and steel rounds were fired in a fully instrumented[2] accuracy test conducted at the ARL Transonic Range. This experiment made use of eddy probes and strain gages to measure gun tube motion as the shot moved down the bore. External to the gun, a set of six orthogonal x-rays captured the disengagement and sabot discard dynamics while the Transonic Range recorded the projectile free flight. An impact target was placed at 1 km. All components were careful surveyed into common temporal and spatial references. The aluminum round was fired at Yuma Proving Ground[4]. Instrumentation consisted of yaw cards near the first maximum of yaw, smear cameras, and targets at 1 and 2.5 km. The final set of data was taken at Transonic Range as part of the present tests. Instrumentation consisted of three orthogonal x-rays located at 0.5, 2.5, and 4.5 m from the muzzle. Transonic Range measured the projectile flight motion and a target was located at 1 km. For all three experiments, the gun was laid using a muzzle boresight. The inertial and aerodynamic properties of the four rounds are presented in Table 1.

	m (kg)	D (m)	I_t (kg-m^2)	V_m (m/s)	C_D	$C_{L\alpha}$	$C_{M\alpha}$
Tungsten	4.43	0.038	0.048	1650	0.322	7.58	-16.9
Steel	2.73	0.038	0.034	1680	0.314	7.20	-14.2
Aluminum	0.94	0.038	0.0074	1700	0.269	8.02	-7.00
Al-Steel	0.86	0.028	0.011	1690	0.508	8.00	-41.9

Table 1. Properties of Fin-Stabilized Projectiles

The aerodynamic properties of the tungsten, steel, and Al-steel rounds were measured at the Transonic Range, while those of the aluminum round were computed using PRODAS[5]. The aluminum round with the steel counterweight is of a different family than the others. This is because this round is based on the M829 projectile while the other three are based on the M865 technology, Fig. 1. When the M829 cartridges were scheduled for demilitarization, it was of interest to determine if the heavy metal core could be removed and replaced by an aluminum core. This would serve to recover most of the components thus providing a low cost training round. For this reason, the M829 envelope was selected to extend the earlier tests of the all aluminum training round.

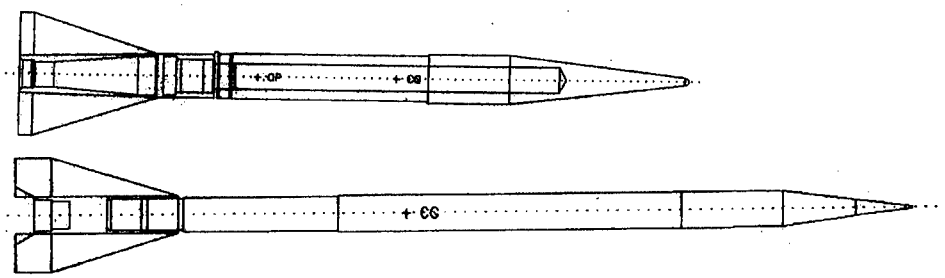


Figure 1. Test projectiles

The rounds were fired from different gun tubes, at different sites, and at different times. While these factors influence accuracy, it is hypothesized that the influence on precision is not great. Simply stated, the tank firing error budget is treated as arising from three, independent sources: tank-to-tank bias, occasion-to-occasion bias, and round-to-round dispersion. The differences in the test conditions would affect the bias, but have limited influence on the final factor that is of interest in the present study. The fact that two different families of ammunition, M865-like and M829-like, were tested does provide a potential source of variability in precision. This needs to be kept in mind as comparisons are made between experimental results; however, the program was not resourced to include heavy core results for the M829 case.

Lyon, et al[2], describe the launch disturbances as being comprised of a set of components related to the gun and projectile dynamics and aerodynamics. The gun tube pointing angle and crossing velocity at shot exit are measured and used to capture the changes in the gun attitude from its rest state. X-ray data taken over the first fifteen feet following exit provide a measurement of the projectile velocity vector which when compared to the gun data shows the influences of disengagement dynamics. A second set of x-rays another fifteen feet downrange capture the linear and angular velocity of the round after sabot separation. The measured angular velocity is used to extrapolate the trajectory downrange onto the target plane. This requires use of the expression for aerodynamic jump

$$\Theta = (I_t/mD^2)(C_{L\alpha}/C_{M\alpha})\xi_o' \qquad (1)$$

where ξ_o' is the complex yawing velocity expressed in radians per caliber of projectile travel. The methodology of dissecting the launch disturbances and extrapolating downrange to the target produces good agreement between with measured impacts, i.e., closure.

The experiments on the aluminum and Al-steel rounds could not provide such a complete evaluation of launch disturbances. An abbreviated version was employed to capture the influence of aerodynamic jump and initial projectile velocity. From the known boresight point on the target an expected impact point is computed by taking into account the known gravity drop. The difference between the expected and actual impact points gives the total jump for that individual shot. In all cases, data were taken on the angular motion of the round in sufficient detail to provide an estimate of ξ_o', providing an estimate of the aerodynamic jump, Eq. (1). Subtracting this from the total jump yields the initial projectile velocity vector:

$$(u + iv)/V_m = (x_t + iy_t)/L - (I_t/mD^2)(C_{L\alpha}/C_{M\alpha})(\beta_o' + i\alpha_o') \qquad (2)$$

where x_t, y_t and L are the horizontal and vertical components of on-target jump and the range to the target, respectively.

DATA ANALYSIS

Firings of all rounds showed structural integrity and produced first maximum yaw levels of less than two degrees, Fig. 2. To examine the statistics of the launch and impacts, the circular probable error[6] is used as defined by Mirabelle[7] for cases with unequal horizontal and vertical components

$$CPE = 1.18[(\sigma_h + \sigma_v)/2] \quad (3)$$

where CPE is the radius of the circle containing one-half of the data set and σ_h, σ_v are the horizontal and vertical standard deviations of the component of interest. For ease of comparison, all values are normalized to those of the tungsten round. Test results are summarized in Table 2.

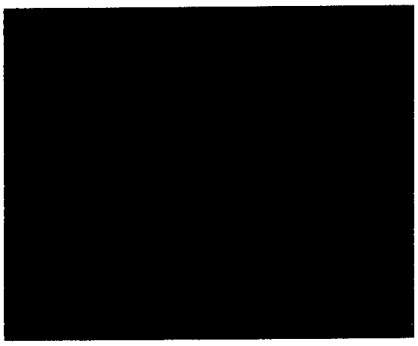


Figure 2. Smear photograph of Aluminum/Steel Counterweight Round

	CEP on Target (mr)	CEP u,v/V_m (mr)	CEP Angular Velocity (rad/s)	**Aero. Jump Coef. (Θ/ξ_∞')**
Tungsten	1	1	1	3.35
Steel	1.29	2.50	2.58	4.38
Aluminum	3.53	5.67	4.19	6.18
Al-Steel	2.35	5.75	3.24	5.5

Table 2. Circular Probable Errors for Various Rounds

The decay in CEP from the tungsten to the aluminum-based rounds is apparent. A number of factors are responsible. The linear and angular velocities both take on a progressively more random nature. In addition, the aerodynamic jump coefficient is roughly twice as large for the aluminum round as for the tungsten round. This serves to amplify the effects of initial angular velocity disturbances. The fact that the CEP on Target does not grow to the same extent as the CEPs in Linear and Angular Velocities, reflects the fact that the latter two can interact in a fashion to partially cancel each other. Some interesting correlations are possible between the dynamic results and the inertial properties of the rounds, Fig. 3 and 4. The CEP in initial lateral velocity decreases with increasing projectile mass. Even the data for the M829-like, Al-Steel projectile seems to follow this behavior. Similarly, the CEP in initial angular rate correlates reasonably well

with the transverse moment of inertia. Reversing the variables, i.e., correlating linear velocity with moment of inertia produces a less satisfying result.

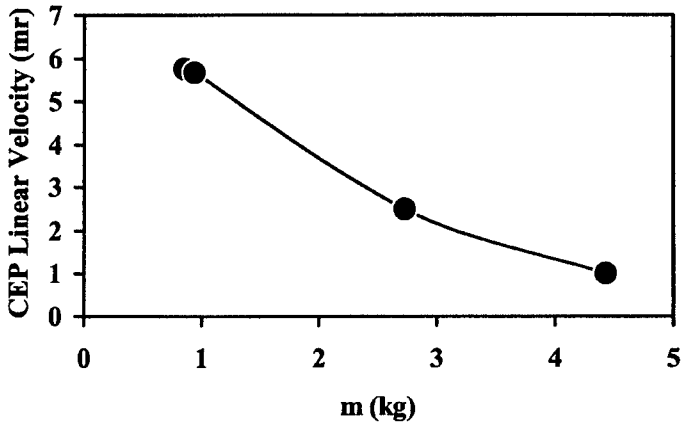


Figure 3. Correlation of flight mass with CEP in initial linear velocity

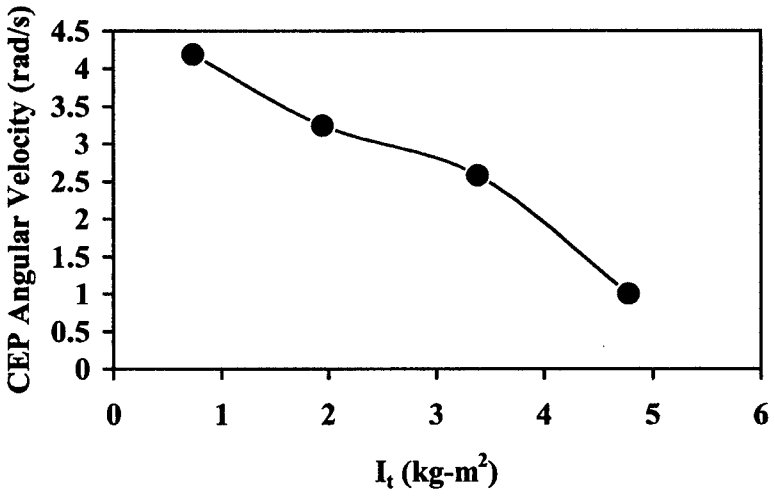


Figure 4. Correlation of transverse moment of inertia with CEP of angular velocity

Perhaps it should not be surprising that the linear and angular velocities correlate with their respective multipliers of the inertia tensor. A simple model of a spring-mass system helps to illustrate these correlations. The solution for a simple undamped oscillator responding to an initial displacement is

$$z = z_o \cos(k/m)^{1/2} t \quad (4)$$

with derivatives

$$dz/dt = -z_o (k/m)^{1/2} \sin(k/m)^{1/2} t \quad (5)$$

$$d^2z/dt^2 = -z_o\,(k/m)\cos(k/m)^{1/2}\,t \qquad (6)$$

The argument is made that since the CEP in lateral velocity represents the variability of this term, it should be directly related to the derivative of this term, Eq. (6), times some perturbation parameter, e.g., a variation in exit time, t_o. Thus, from Eq. (6),

$$\text{CEP}\,(u/V_m,\, v/V_m) \sim 1/m \qquad (7)$$

The 1/m function is plotted in Fig. 5, where it is normalized to the value of tungsten mass. It is seen that the measured variation and that conjectured by Eq. (7) are similar. This may be fortuitous or indicative of the nature of the in-bore and separation dynamics. Consideration of Eq. (6) suggests that reduction in the stiffness (parameter, k) of the sabot could have improved the CEP of the lower mass rounds. This approach was not considered at the time. Both the M865-like and M829-like rounds were fired with existing sabots that were compatible with the high mass projectiles.

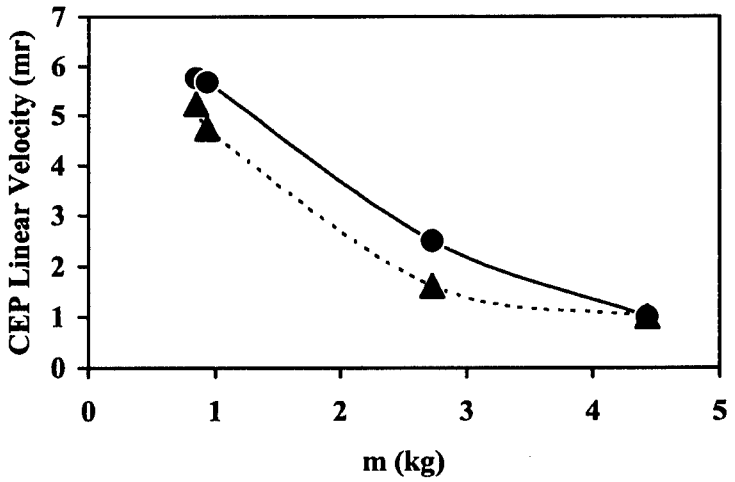


Figure 5. Comparison of measured CEP dependence (solid circles) with the parameter m_{WA}/m (solid triangles)

CONCLUSIONS

In the process of attempting to develop improved and/or low cost training rounds, accuracy firings were performed. It was found that lower mass projectiles had significantly greater round-to-round dispersion than tungsten or steel core designs. This was ascribed to larger values of the aerodynamic jump coefficient, Θ/ξ_o'. While undoubtedly a factor, careful analysis of the data indicates that variability in initial dynamics dominates. A simple dynamics argument suggests that when the inertial properties of the round are changed, it is necessary to match the sabot properties, e.g., stiffness. To better understand this behavior, higher fidelity simulations of the in-bore vibration and disengagement dynamics are required.

ACKNOWLEDGEMENT

Mr. E. Fennell and B. Wong of ARDEC are recognized for their support and inputs as are F. Brandon and M. Hollis who defined many of the designs tested.

REFERENCES

1. E. Kennedy, M. Hollis, F. Brandon, E. Schmidt, J. Zukas, and F. Robbins, "Evaluation of a Hollow Aluminum Training Round," *Proceedings 14th International Symposium on Ballistics, Quebec,Canada,* Sep 1993.
2. D. Lyon, D. Savick, and E. Schmidt, "Comparison of Computed and Measured Jump of 120mm Cannon," *Proceedings 12th International Symposium on Ballistics, San Antonio, TX,* Oct 1990.
3. C. Murphy, "Free Flight Motion of Symmetric Missiles," R1216, *Ballistic Research Laboratory, APG, MD,* Jul 1963.
4. J. Castleton, "M865E2 Test Data Summary," *Yuma Proving Ground, Yuma, AZ,* Mar 1994.
5. Arrowtech Associates, "User's Manual, PC PRODAS," *South Burlington, VT,* 1991.
6. F. Grubbs, "Statistical Measures of Accuracy for Riflemen and Missile Engineers," *Privately Published, Havre de Grace, MD,* Nov 1964.
7. F. Mirabelle, Private Communication, *BRL, APG, MD,* 1984.

COMPARISON OF THE 120-MM M831A1 PROJECTILE'S EXPERIMENTAL LAUNCH DYNAMIC DATA WITH HYDROCODE GUN-PROJECTILE DYNAMIC SIMULATIONS

K. P. Soencksen,[1] J. F. Newill,[1] J. M. Garner,[1] and P. Plostins[1]

[1] *U.S. Army Research Laboratory, AMSRL-WM-BC, Aberdeen Proving Ground, MD 21005*

This paper documents experimental validation for numerical simulations using the U.S. Army Research Laboratory's (ARL) gun-projectile dynamic simulation codes. The experimental program was conducted at ARL's Transonic Range Experimental Facility on the M831A1 high-explosive antitank (HEAT) training projectile for the M256 gun system. The experimental program consisted of the M831A1 HEAT training projectile fired for the measurement of aerodynamic characteristics. Measured first maximum yaw levels are compared to simulated data for the same system. The effect of damage tubes to help explain occasional launch anomalies is also shown.

1. INTRODUCTION

The 120-mm M831A1 projectile is a low-cost training projectile used by U.S. armor troops. The M831A1 training ammunition program is managed by the Operations Support Command (OSC) at Rock Island, IL, which is supported by the U.S. Army Armament Research, Development, and Engineering Center (ARDEC) at Picatinny Arsenal, NJ. The M831A1 is used as a surrogate training round for high-explosive antitank (HEAT) M830 and M830A1 service rounds. In 1994, the M831A1 replaced the M831 projectile. The M831A1 resulted in significant cost savings to the government since the boom and fins of the M831 were replaced with a simple slotted stabilizer. Today the round is produced by two government contractors, each producing approximately 50% of the rounds purchased by the Army. A photograph of the M831A1 is shown in Figure 1.

The M831A1, a full-bore projectile, provides a unique analytical opportunity for an analysis of the type examined here since it is not a saboted projectile. This means that the projectile enters free flight very near the muzzle, and the muzzle rates are not modified by sabot discard. Since the muzzle rates are the same as the rates entering free flight, direct comparison between the muzzle rates predicted by the gun codes and those measured in experiments is straight forward.

The M831A1 is fired from the M1A1 tank in large numbers annually by training armor crews. As with all projectile types, a computer correction factor (CCF) or fleet zero is used in the tank's fire control system to account for average fleet projectile jump. For the last several years, the OSC (formerly the Industrial Operations Command, IOC) has received feedback from the user that, in some cases, M831A1 impact performance did not appear consistent with the current M831A1 CCF. Based on this information, the OSC and ARDEC sought a low-scale but in-depth experimental analysis of the round to assess its aeroballistic qualities and to hopefully identify any potential issues that could affect accuracy. The five-shot experiment was conducted at the Transonic Experimental Facility (TEF) operated by the Aerodynamics Branch of the U.S. Army Research Laboratory (ARL), Aberdeen Proving Ground, MD.

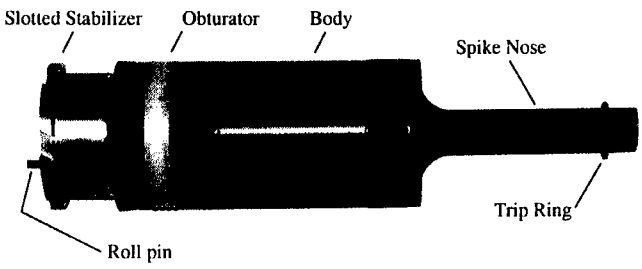


FIGURE 1. 120-MM M831A1 TRAINING PROJECTILE.

Concurrently, funding was provided to initiate in-depth computer simulation analyses of the interior ballistic characteristics of the M831A1.

Specifically, the effects of bore erosion and bore centerline were examined as to their potential effect on projectile dynamic path and angular rates at muzzle exit. This paper first presents the experimental methodology and data leading to the indirect measurement of projectile first maximum yaw. The first maximum yaw is central in this study since it is a proportional indicator of angular rates at the muzzle for a nonsaboted projectile like the M831A1. Next, a direct comparison is made between the performance predictions obtained from the simulation study and the experimental data obtained from the range.

2. TEST SETUP AND METHODOLOGY

The test was fired from an M1A1 main battle tank equipped with a 120-mm M256 gun system, tube serial number 3700. This tube did display some damage, which is key to the findings of this paper, and will be discussed later. All five rounds were fired through the TEF's spark range facility containing 25 orthogonal shadowgraph stations. An interior view of the range is shown in Figure 2. From the figure, camera positions are noted along the left-hand wall of the range facility and in pits along the range floor. The camera stations are arranged in five groups of five stations each along a trajectory length of approximately 183 m. Opposite each camera is a large reflective screen, as seen on the right-hand wall and ceiling in the figure. As the flight projectile approaches a station, an infrared sensor detects the projectile just uprange of the station and sends a signal to the station camera with a preset delay time based on the expected projectile velocity. After the delay time has elapsed, a high-intensity spark source is initiated. Each camera is carefully focused on the screen, and thus the shadow of the projectile is captured in flight.

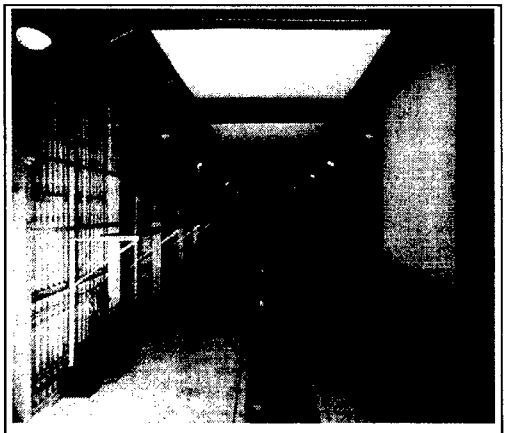


FIGURE 2. INTERIOR VIEW, TRANSONIC EXPERIMENTAL FACILITY.

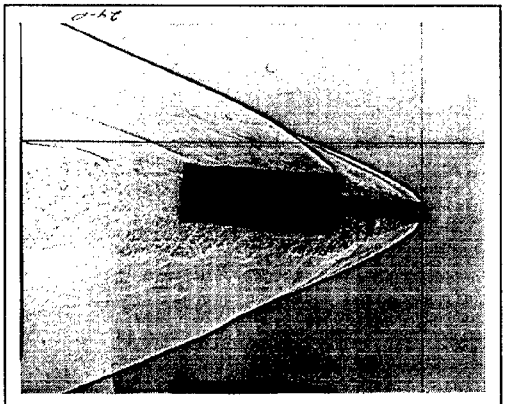


FIGURE 3. SHADOWGRAPH, SHOT 2, 102 M, M=3.1, ANGLE=4.4 DEG.

Figure 3 shows a shadowgraph of the M831A1, which is representative of those recorded from the test. The image shows the M831A1 at a moderate angle-of-attack, 4.4 deg. From this, we see the basic flowfield encountered by the projectile, including the shock pattern and boundary layer. Note the thin vertical line just to the right of the projectile nose. This is the image of the fiducial cable which is tightly suspended in a surveyed position about 25-mm from the surface of each station screen. Attached to the cable are fiducial beads, two of which are evident in the figure just above the nose tip. The surveyed locations of the cable and beads are used to determine the exact position and orientation of the projectile in each plane, at each shadowgraph station. Careful examination of Figure 3 in the vicinity of the projectile base reveals the shadow of a roll pin. This is a small pin inserted in the base of the projectile (see Figure 1) that is used to measure roll orientation. Measurements of the position of the roll pin in each shadowgraph are used to derive the roll history, allowing for the calculation of roll-related aerodynamics, as described further below.

As stated, first maximum yaw is central to the study presented here since it is a proportional indicator of angular rates present at the muzzle. However, first maximum yaw is not directly measured experimentally. This is because the range shadowgraph stations begin approximately 38 m downrange of the gun muzzle. Thus, once the six-degree-of-freedom (6-DOF) fit to the data is computed, the fit is extrapolated uprange to the muzzle providing the approximate first maximum yaw magnitude and orientation. Accuracy of these values depends on accuracy of the fit, which, in turn, depends on accuracy of the position and orientation measurements.

Since the range facility generally yields highly accurate position and orientation measurements, the first maximum yaw is typically accurate to within 0.1 deg.

3. EXPERIMENTAL DATA REDUCTION AND RESULTS

This section describes the important aerodynamic coefficients of a projectile and presents details of how they were calculated. Accurate calculation of the pertinent coefficients is a prerequisite to determining the actual flight dynamics (position and orientation) anywhere along the trajectory.

Aeroballistic flight qualities are described by the set of aerodynamic coefficients. These are calculated using the Aeroballistic Research Facility Data Analysis System (ARFDAS) code written and supported by Arrowtech Associates (Whyte and Hathaway 1981). This code uses an inverse routine that fits the measured projectile angle and position data first to the linearized equations of motion and then to the full 6-DOF equations of motion and computes the aerodynamic forces and moments required to have produced the measured flight. Integral to this routine is the input of roll orientation, which allows calculation of the static roll moment coefficient, C_{l_0}, and roll damping moment coefficient, C_{l_p}. These coefficients are then used in the 6-DOF motion analysis to improve the accuracy in determining other aerodynamic coefficients.

The ARFDAS code also supports a multiple-fit capability that allows the computation of a single set of aerodynamic parameters using the data from multiple shots. This allows the estimation of aerodynamic coefficients with higher confidence levels.

In addition to the obvious advantage of obtaining more accurate coefficients, the multiple-fit capability has another powerful benefit. Frequently, a projectile flight occurs with low level motion in terms of both angle of attack (AOA) and center of gravity (CG) motion (swerve). While such a trajectory is highly desirable in a tactical engagement, low-levels of motion result in the measurement errors being similar in magnitude to the actual motion. Hence, less accurate aerodynamic coefficients are computed. Thus, in the experimental environment, ballisticians desire at least moderate AOA and CG motions. When such motions are not present for a particular shot, aerodynamic coefficients usually cannot be accurately derived from the data set. However, as in the case of the current study, there is usually a need to reasonably determine the projectile yaw and swerve history. This can be obtained, in turn, by utilizing the accurate aerodynamic coefficients that have been computed from multiple fits of the data of other shots containing larger motions. Usually, this procedure improves the relative knowledge about the yaw and CG motion history of a low-yaw shot, providing at least an order of magnitude assessment of some important trajectory characteristics such as first maximum yaw.

Moreover, occasionally in range experiments, instrumentation malfunction or flight anomalies yield only sparse shadowgraph data for a particular shot. As in the case previously described, the coefficients obtained from multiple fits of the data of other shots containing more complete data often allow a user to determine approximate trajectory characteristics much more accurately than with the sparse data of a particular shot.

4. AERODYNAMIC COEFFICIENTS

A comprehensive analysis was performed on the data from all five shots using the ARFDAS code as previously described. First, a best fit was obtained to the measured position and angle data using the linearized equations of motion. From this, a "first cut" group of aerodynamic coefficients was obtained. Next, this data was used as initial input for the 6-DOF computations. Here, the aerodynamic coefficients were adjusted to provide the best data fit to the full 6-DOF equations of motion. The aerodynamic coefficient data resulting from the analysis for zero-yaw drag, pitching moment, normal force, and pitch damping moment are presented next.

First, zero-yaw drag is plotted in Figure 4. Since drag is easily and accurately measured, all five individual data points fall on a line with minimal scatter. All shots were fired without tracers; thus, the drag coefficients determined would likely be a few percent higher than those obtained from any other testing in which traced rounds were fired. The solid circle data points represent multiple fits in which the reduction routine is constrained to compute a single value of drag coefficient for the data of multiple shots. In the case of zero-yaw drag, C_{x_0}, the coefficient value is not enhanced by the multiple-fit capability, since the coefficients obtained from the individual shots are so accurate to begin with. The data are in excellent agreement with predicted values computed by the PRODAS design code. Two wind tunnel data points are also shown for

comparison (Farina 1998). Although not plotted, the first and second nonlinear drag components are obtained with greater-than-anticipated accuracy. This was possible because of several shots that exhibited moderate-to-high yaw levels. The average value determined for $C_{X_{\alpha 2}}$ is 29.8, with a probable error of just 2.1%; and that for $C_{X_{\alpha 4}}$ is –530, with a probable error of 6.2%. These values, previously unknown, are somewhat different from predicted values.

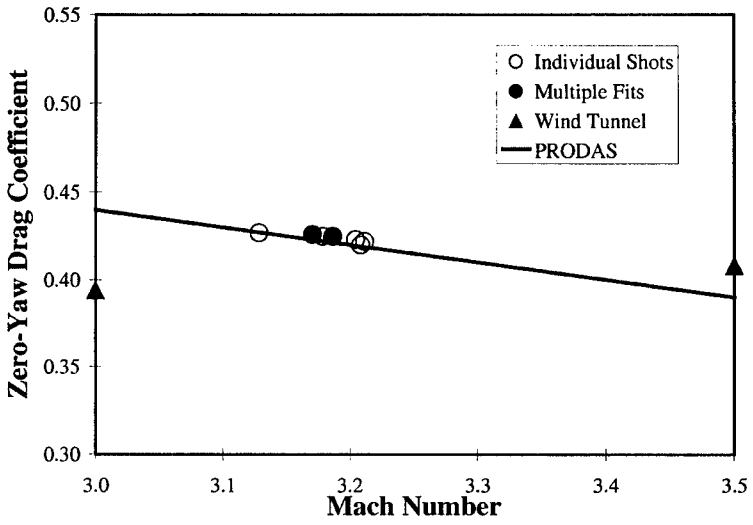


FIGURE 4. ZERO-YAW DRAG VS. MACH NUMBER.

Pitching moment coefficient, C_{m_α} , is plotted in Figure 5.

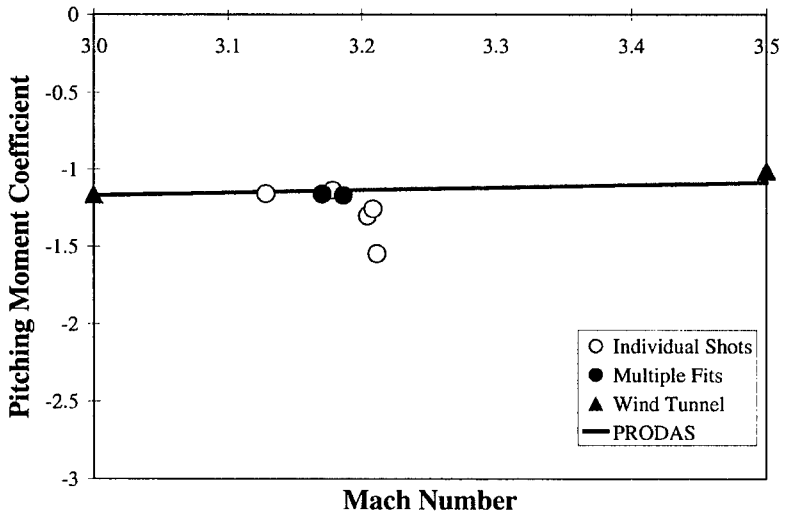


FIGURE 5. PITCHING MOMENT COEFFICIENT VS. MACH NUMBER.

As in the case of drag, the individual data points show little scatter, and both the PRODAS predicted values and wind tunnel data match very well with the experimental data. The value of C_{m_α} for Shot 3 is –1.54, the most different from the multiple-fit values. This can be attributed to the low yaw on this shot, resulting in a less accurate determination of C_{m_α}. Note that the pitching moment coefficient values are much smaller

than what is typical for a statically stable projectile due to its relatively lower static margin. The cubic pitching moment coefficient, $C_{m_{\alpha 3}}$, is determined to be –5.2, with a 10% probable error.

The normal force coefficient, C_{N_α}, is plotted in Figure 6. Only multiple-fit values of the coefficient are plotted, since individual shot data produced fairly significant scatter. This is because accurately calculating the coefficient is a function of the amount of projectile swerve (cg motion). Three shots in particular result in poor C_{N_α} values; these all have swerve arm magnitudes that are significantly smaller than those of the other two shots, thus leading to more error in these values. The analysis of C_{N_α} offers validation of the value of the multiple-fit reductions. Again, both wind tunnel data and PRODAS predictions match well with the experimental free-flight numbers.

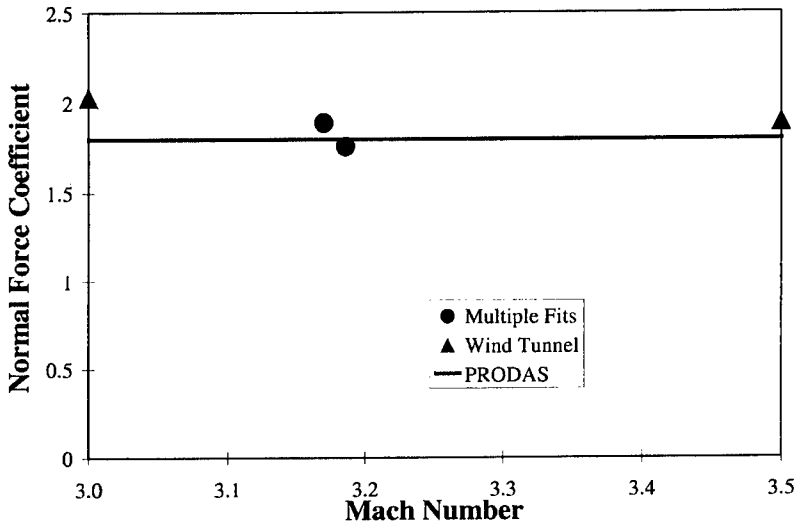


FIGURE 6. NORMAL FORCE COEFFICIENT VS. MACH NUMBER.

Finally, Figure 7 plots multiple-fit values of the pitch damping moment coefficient, C_{mq}. Accurately computing C_{mq} depends on the yaw magnitude, the amount of change in the yaw magnitude, the number of complete yaw cycles measured. In general, the greater the yaw magnitude and the more cycles that are measured, the more accurate the pitch damping coefficient will be. However, even for high yaw shots in which several complete yaw cycles are measured, if the overall *change* in yaw level with range is small, then damping characteristics are very difficult to accurately extract. This was the case with Shot 2 of the current experiment, which exhibits very high yaw levels. Despite high yaw and approximately 3.5 yaw periods of measured flight, the yaw level stays nearly constant with range. In other words, damping is neutral; hence, an accurate pitch damping moment coefficient is indeterminate. The same type of phenomenon is observed in three other shots that display marginal pitch damping characteristics. In all three cases, a low yaw level, a minimal *change* in yaw with range (marginal damping), or a combination of both result in C_{mq} values with high probable errors. One shot produces a calculated C_{mq} of –12.4 with low yaw, but the amount of damping present allows a somewhat reasonable probable error of 25%. This data point is not plotted, but this value is consistent with the PRODAS prediction. Even the multiple-fit values of C_{mq} result in very high probable errors, again because the relative amount of damping is very small. This fact provides further confirmation that an accurate value for pitch damping moment coefficient is not possible from the current data set. However, the experimental data analysis clearly indicates that marginal pitch damping exists; therefore, the PRODAS-predicted value might be optimistic.

Table 1 presents a summary of aerodynamic coefficient values (determined from multiple-fit data analysis) with their associated probable errors. In addition to the coefficients listed in the table, a complex analysis is conducted in an attempt to determine the roll-related coefficients: static roll moment coefficient, $C_{\ell 0}$, and roll damping moment coefficient, $C_{\ell p}$. Details of this analysis, beyond the scope of this work, are presented by Soencksen et al. (2001).

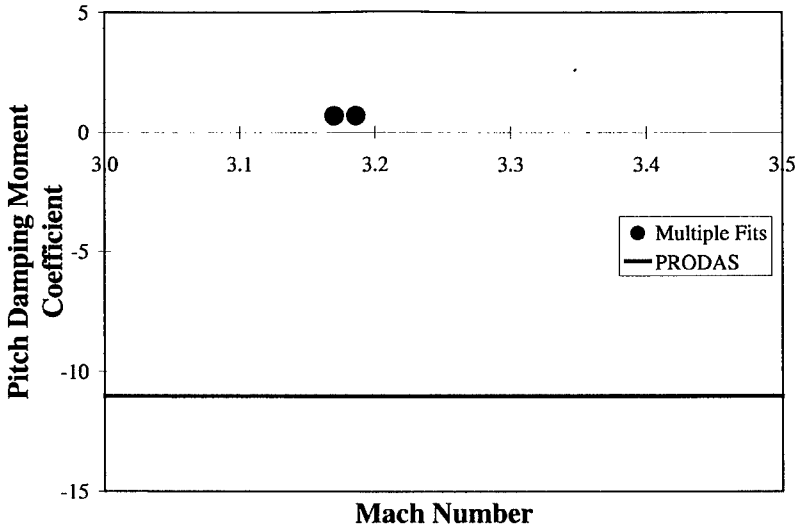


FIGURE 7. PITCH DAMPING MOMENT COEFFICIENT VS. MACH NUMBER.

TABLE 1. AERODYNAMIC COEFFICIENTS.

Coefficient	Value	Probable Error (%)
Drag		
Zero-Yaw (CX0)	0.425	0.1
Squared Component (CXa2)	29.8	2.1
Quad Component (CXa4)	-530	6.2
Pitching Moment		
Linear (Cma)	-1.17	0.9
Cubic Component (Cma3)	-5.2	9.9
Normal Force	1.8	3.8
Pitch Damping Moment	1	**

** Probable error too high for reliable value.

Several interesting observations are gleaned from plots of the projectile yawing motion, as produced by the 6-DOF fits to the position and orientation data. The yawing motion in orthogonal planes is plotted in Figure 8 for Shot 1.

In this and subsequent yaw plots, the gun muzzle is located 38 m uprange of the first spark station (marked by a vertical line near the left-hand edge of the plot), and the sign convention is positive up and left. This plot shows the experimental data points in each plane, together with the computed best fits from the 6-DOF solution to the equations of motion. Notice that the pitch angle peaks grow slightly with range, while the yaw angle peaks appear to be approximately constant. When this angular data is combined into total AOA, the plot shown in Figure 9 results.

Here, all yaw maxima and minima are evident to about 220 m. Note that the first maximum yaw (about 1.65 deg) is greater than the second maximum yaw, as expected. The third maximum yaw, however, is greater than both the first and second maxima. In general, a slightly growing step-like pattern is displayed. A similar step-like pattern is seen when examining the yaw minima. This is indicative of an aerodynamic trim angle, as described by Soencksen et al. (2000). The magnitude of the stepping motion is possibly slightly less than that indicated by the total yaw fit. This is hypothesized because of the fit error inherent in any data-fitting procedure and is based on the fact that some data points are underpredicted by the fit curve. Despite the uncertainty in its exact magnitude, the stepping phenomenon of the yawing motion is definitely present and significant enough to be measurable. More importantly, identification of the presence of aerodynamic trim is critical to the accurate extrapolation of the fit to determine first maximum yaw. Had the trim not been isolated, the first maximum yaw would probably have been slightly underpredicted in this case.

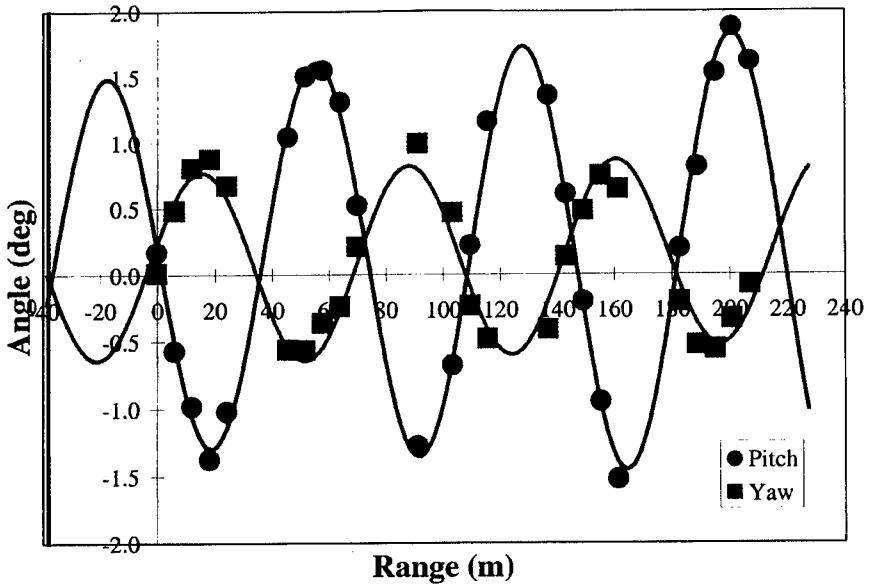


FIGURE 8. PITCH AND YAW VS. RANGE, SHOT 1.

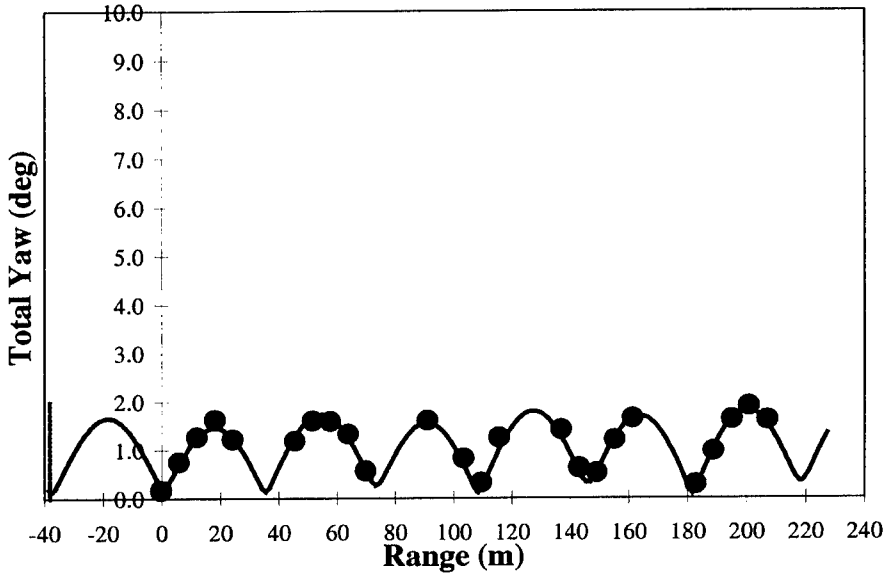


FIGURE 9. TOTAL YAW VS. RANGE, SHOT 1.

The total AOA did not display any visible stepping motion on Shot 2, as shown in Figure 10, but evidence of aerodynamic trim is again found in Shots 3 – 5. The total AOA is plotted for these shots in Figure 10 and Figure 11. The yawing motion for Shot 3 is so small that a good quality fit to the data is not obtained, even using multiple-fit aerodynamic coefficients. The first maximum yaw for this shot is almost certainly less than 0.5 deg.

A fair amount of variability in the yaw levels from shot to shot is noted. The first maximum yaw varies from less than 1 deg to over 9 deg for these shots.

Analysis of yaw data shows evidence of the presence of a trim vector of varying magnitude for four out of the five shots. Computed trim angle values for all shots are presented in Table 2. Agreement is good between the independent calculations of linear theory and 6-DOF. Inclusion of the computed trims in the angular fits results in improved fit errors, and thus more accurate first maximum yaw values, in all cases except Shot 2, where trim is not a significant factor.

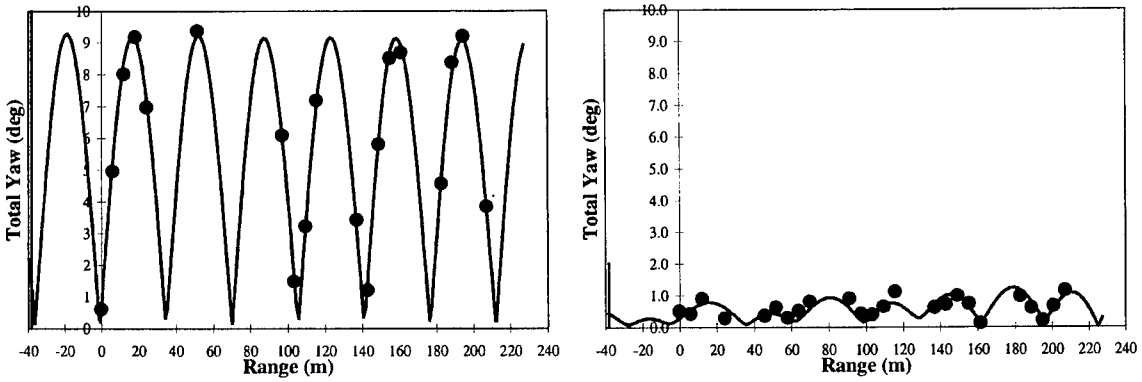


FIGURE 10. TOTAL YAW VS. RANGE, SHOT 2 AND 3.

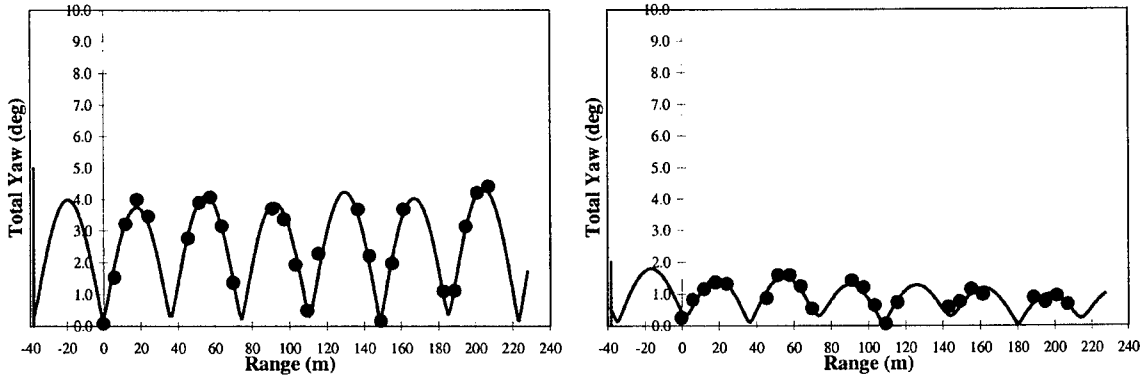


FIGURE 11. TOTAL YAW VS. RANGE, SHOT 4 AND SHOT 5.

TABLE 2. CALCULATED TRIM ANGLES.

Shot	Linear Theory Trim (deg)	6-DOF Trim (deg)
1	0.114	0.136
2	0.001	0.038
3	0.257	0.264
4	0.108	0.171
5	0.162	0.149

5. NUMERICAL SIMULATION OF TANK GUN PROJECTILES

Gun/projectile dynamic simulations utilize three-dimensional (3-D) finite element (FE) models of the M256 120-mm tank cannon launching projectiles. The method is described in Rabern 1991; Wilkerson and Hopkins 1994; Burns et al. (1998); Newill et al. (1998a); Newill et al. (1998b, 1998c, 1998d, 1999a, 1999b, 2000); Guidos et al. (1999). The hydrocode finite element formulation was chosen to allow investigation of

stress wave propagation due to elements of launch. The models are 3-D to capture the asymmetric response of the projectile and gun system resulting from the nonlinear path of the projectile during launch, asymmetric boundary conditions, general lack of symmetry in the centerline profiles of the gun tube, and asymmetric gun motion. Figure 12 shows the solid models used to simulate the M831A1.

The projectiles and gun systems are both built in similar manners. Models are developed for the components and then integrated. Relative motion is obtained by defining the proper physics to allow interaction between the parts. Since this projectile is relatively simple, the nose, body, stabilizer, and obturator are welded together, and sliding interfaces are defined between the nose, body, stabilizer, and the gun bore. The propellant pressure loading for the gun system and projectile is generated from IBHVG2 (Anderson and Fickie 1987), which provides good quality interior ballistic prediction for production charges.

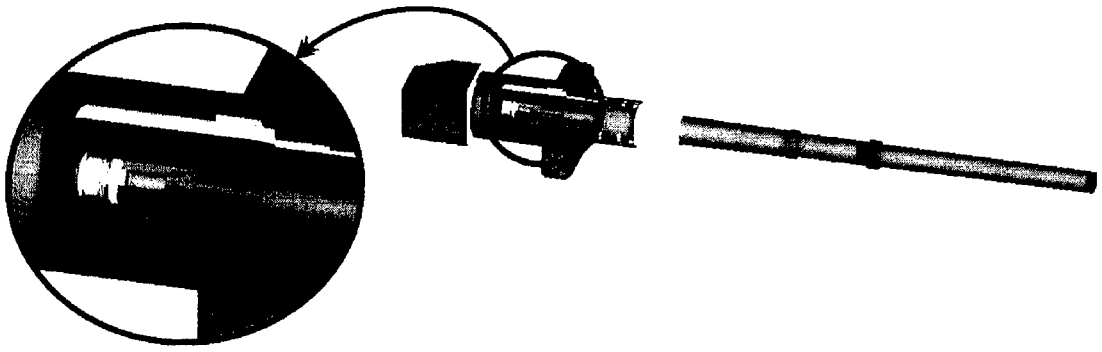


FIGURE 12 M1'S M256 GUN SYSTEM WITH KE PROJECTILE SHOWN IN-BORE.

The gun dynamic simulation codes predict the transverse rates (linear and angular, see Figure 13) during the launch cycle. Three types of information are used from these predictions: the dynamic path, variability in jump, and the average jump. These are illustrated in Figure 14. The dynamic path gives qualitative information on the rate history of the projectile during the launch cycle. The variability and average jump predicted by the codes are related to accuracy errors where reduction in variability or error represents improved performance of the system. It should be noted that the simulations used the same gun tube profiles as the experiments at TEF.

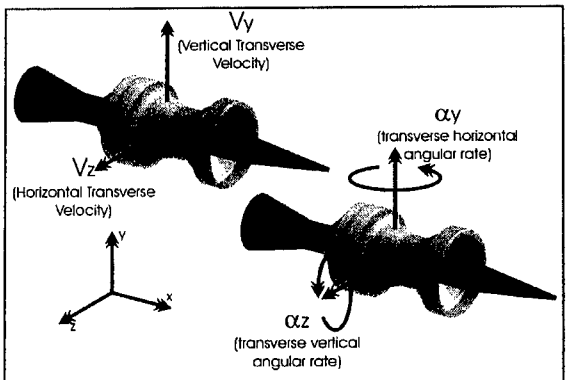


FIGURE 13. DEFINITION OF TRANSVERSE RATES

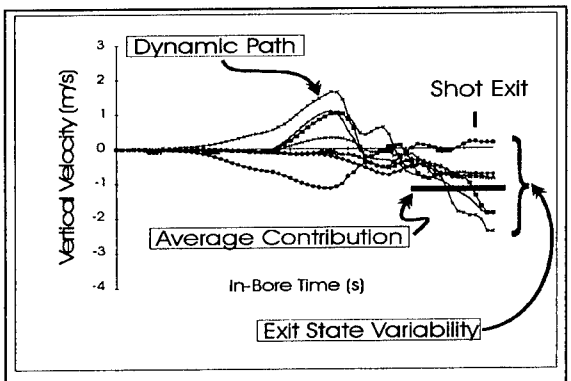


FIGURE 14. DEFINITION OF DYNAMIC PATH.

In order to validate the gun codes, some type of methodology is required in order to compare simulation results to experiments. Since the phenomena being predicted are nonlinear and stochastic in nature and the initial conditions are not known precisely on a shot-by-shot basis, the gun dynamic codes are used to predict an envelope of performance, which is comparable to the groups fired during the experiment.

It is very important to note that a firing experiment is a ballistic phenomenon that is not entirely predictable. Even with production ammunition, and with as many factors as possible controlled, there can be significant deviation of the shooting performance. For this reason, a direct comparison between the simulated data and the experimental data is very difficult.

Figure 15 and Figure 16 show the dynamic paths from the simulations. The dynamic paths show that the projectile motion is relatively low transverse motion for approximately the first one third of the in-bore cycle. When the projectile begins reacting to the gun system, it exhibits moderate balloting behavior. The projectile exits the gun bore at approximately 8.8 ms (ambient conditioned propellant).

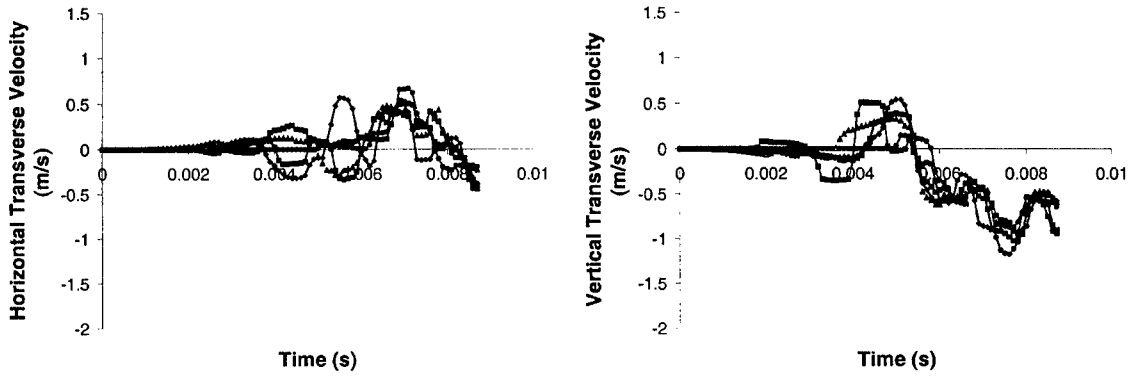


FIGURE 15. TRANSVERSE VELOCITY VS TIME.

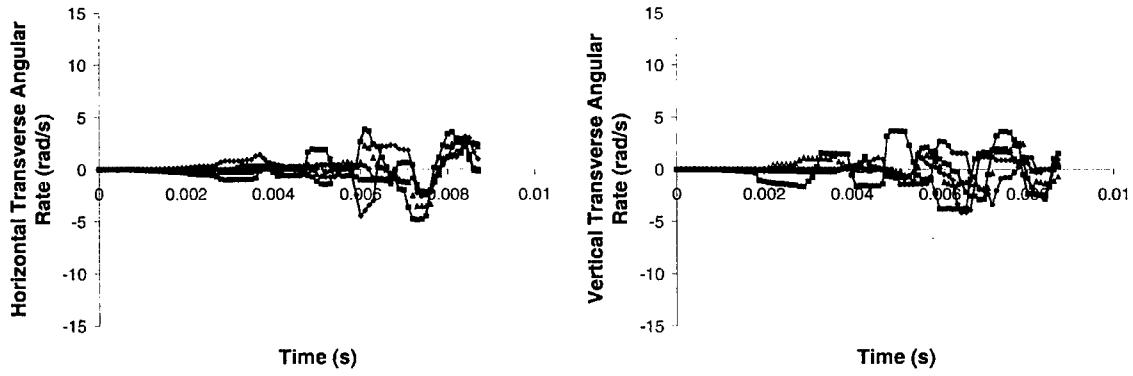


FIGURE 16. ANGULAR RATE VS TIME.

The simulation data is compared to the experimental data by predicting the first maximum yaw from the angular rate data at the muzzle seen in the dynamic path plots. The rates are converted using equation (1) with the constants provided as determined from the experiment.

$$\alpha_{1^{st}\,max} = \frac{|\alpha_{muzzle}|}{\omega}, \quad \omega = \frac{V_{muzzle}}{d\sqrt{-\frac{c_{m\alpha}\pi\rho d^5}{8I_{transverse}}}} \tag{1}$$

$$d = 0.11968\ m,\ \ \rho = 1.225\,kg/m^3,\ c_{m\alpha} = -1.2\ ,$$

$$I_{transverse} = 0.1427\,kg\,m^2,\ V_{muzzle} = 1165\,m/s$$

The values of the first maximum yaw predicted by the gun codes are up to 1.7 deg. The comparison between the simulation data and the experimental data is given in Figure 17. The figure shows the first maximum yaw measured during the TEF test, along with two ranges of simulation data, represented by two shaded regions. The first region is a grey rectangular box near the bottom of the figure. This is the range of first maximum yaw values predicted by the codes for a pristine gun tube. The upper patterned region shows the degradation of these results when the simulations incorporate some effects of bore erosion damage (Newill et al. 2001).

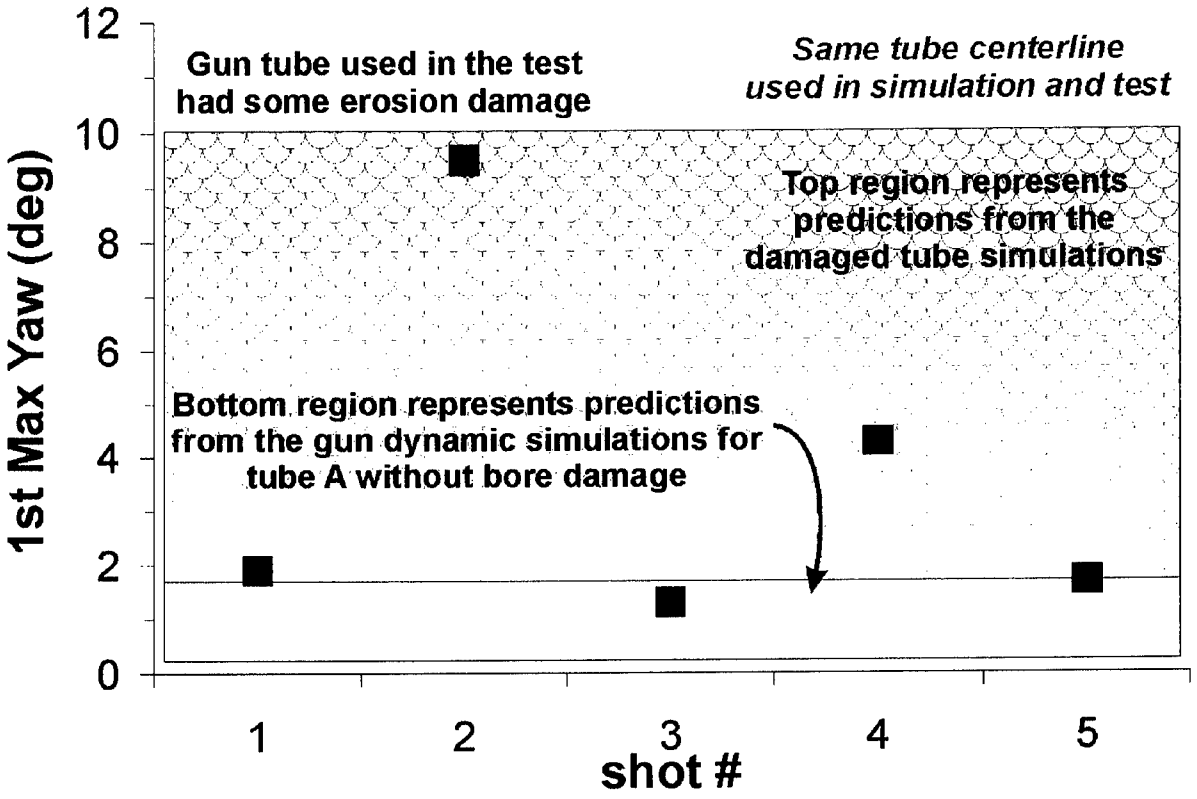


FIGURE 17. SIMULATION COMPARISON WITH EXPERIMENTAL RESULTS.

The predictions were modified to include damage because the experiment was fired using a gun tube with some bore damage. This test was conducted concurrently with another experimental program, and consequently, the other program drove the choice of the gun tube. No attempt was made to map the bore or simulate the exact damage in the gun tube as this is beyond the capability of the codes utilized.

The data showed reasonable agreement between the experiment and the simulations. The use of a gun tube with erosion in the experiment introduced some ambiguity when compared to the simulations. One of the shots, # 2, experienced a large launch disturbance out of the normal distribution of launch rates of the projectile. This shot showed that something abnormal occurred during the in-bore portion of the launch, implying that all the shots in the experiment may have been disturbed to some extent.

6. CONCLUSIONS

The data and analysis presented in this report are the result of the first free-flight, highly instrumented and analyzed experiment conducted on the M831A1 training projectile, combined with a detailed assessment

of numerous computer simulations. This work was a significant step toward a more comprehensive understanding of the complex aerodynamic phenomena affecting the performance characteristics of the M831A1.

Experimental yawing motion was determined accurately in most cases. First maximum yaw displayed significant variability from shot to shot, with the first maximum yaw of one shot reaching over 9 deg. Another shot displayed moderate yaw levels, while the remaining three exhibited relatively low levels. For a nonsaboted projectile, launch dynamics alone were the source of the yaw that grew immediately from the muzzle, eventually peaking at the first maximum yaw. These were a direct combined result of all in-bore phenomena affecting the projectile and giving it both angular and cg rates at the muzzle.

Detailed computer simulation analyses yielded predictions of first maximum yaw based on computed muzzle angular rates. Agreement with the experimental data was good, although comparison had to be made both with and without damage. The results of the simulation provided a high degree of confidence that the models were performing correctly.

Erratic launch dynamics as observed experimentally (and predicted in simulation) provided a potential explanation for the occasional anomalous rounds observed by the user in training.

7. ACKNOWLEDGEMENTS

The magnitude of this study required a coordinated effort and support from many people. The principal organizations involved were ARL, ARDEC, OSC, Alliant Techsystems Inc, General Dynamics Ordnance and Tactical Systems. Their leadership, expertise and experience were invaluable. This study relied heavily on supercomputers supplied by the Department of Defense's High Performance Computing initiative (specifically by the Major Shared Resource Center at the ARL).

8. REFERENCES

Anderson, R. D., and K. D. Fickie. "IBHVG2 - A User's Guide." BRL-TR-2829, U.S. Army Ballistic Research Laboratory, Aberdeen Proving Ground, MD, Jul 1987.

Bornstein, J., I. Celmins, and P. Plostins, "Launch Dynamics of Fin-Stabilized Projectiles." AIAA Paper No. 89-3395, Aug 1989.

Bornstein, J., I. Celmins, P. Plostins, E. M. Schmidt. "Techniques for the Measurement of Tank Cannon Jump." BRL-MR-3715, U.S. Army Ballistic Research Laboratory, Aberdeen Proving Ground, MD, Dec 1988.

Bundy M. L., J. F. Newill, and C. P. R. Hoppel, "A Notional Redesign of the M865E3 Obturator." M. L. Bundy, J. F. Newill, and C. P. R. Hoppel, ARL-TR-2325, Sep 00.

Bundy M., J. Newill, V. Marcopoli, M. Ng, C. Wells, "A Methodology for Characterizing Barrel Flexure Due to Tank Motion." ARL-MR-479, Jun 00

Burns B. P. , D. L. Henry, C. D. McCall, and J. F. Newill, "Flexural Characteristic of the M829 Projectile Familmily." ARL-TR-1201, APG, MD, Sep 96.

Burns B. P. , J. F. Newill, and S. A. Wilkerson, "In-Bore Projectile Gun Dynamics." Proceedings of the 17th International Ballistics Symposium, Midran, South Africa, 26 Mar 98.

Demitroff, D. Personal communication first two authors. Alliant Techsystems, Hopkins, MN December 1999-2000.

Dohrn, R. Personal communication first two authors. Alliant Techsystems, Hopkins, MN December 1999-2000.

Durkin, P. Personal communication first two authors. Aberdeen Test Center, Aberdeen Proving Ground, MD December 1999.

Guidos B. , P. Plostins, D. Webb, J. F. Newill, "120-mm Tank Gun Accuracy Demonstrator (TGAD) Jump Test," ARL-TR-29, Dec 99.

Hathaway, W. Personal communication. Arrowtech Associates, South Burlington, VT December 1999.

Hoppel C.P.R., J. F. Newill, and K. P. Soencksen, "Evaluation of Obturator and Sealing Cuff Properties for the M865 Training Projectile with Comparison to Ballistic Testing," ARL-TR-2039, APG, MD, Sep 99.

Lyon, D. H. "Radial Stiffness Measurements of 120-mm Tank Projectiles." ARL-TR-392, U.S. Army Research Laboratory, Aberdeen Proving Ground, MD, Apr 94.

Lyon, D. H. and K. P. Soencksen. "Radial Stiffness and In-Bore Balloting Analysis for the M900 Projectile." ARL-TR-593, U.S. Army Research Laboratory, Aberdeen Proving Ground, MD, Oct 94.

Manole, L. Personal communication. U.S. Army Research Development and Engineering Center, Picatinny Arsenal, NJ December 1999.

Murphy, C.H. "Free Flight Motion of Symmetric Missiles." BRL-MR-1216, U.S. Army Ballistic Research Laboratory Technical Report, Aberdeen Proving Ground, MD July 1963.

Newill J. F., B. P. Burns, and S. A. Wilkerson, "Overview of Gun Dynamics Numerical Simulations," ARL-TR-1760, APG, MD, Sep 98a.

Newill J. F., C. P. R. Hoppel, D. Kamdar, B. Guidos, and B. Drysdale, C. Livecchia, and M. Luciano, "Geometric and Material Changes to the Forward Bourrelet to Optimize Performance of KE Ammunition," ARL-TR-2328, Sept 00.

Newill J. F., C. P. R. Hoppel, K. P. Soencksen, and P. Plostins, "Simulation of the M865 Kinetic Energy Projectile with Experimental Validation." Proceedings of the 18th International Ballistics Symposium, San Antonio, TX, Nov 99a.

Newill J. F., C. P. R. Hoppel, W. H. Drysdale, and D. S. Kamdar, "Effects of Bourrelet Stiffness on the Interior Ballistic Performance of Kinetic Energy Ammunition." ARL-TR-02, APG, MD, Jun 99b.

Newill J. F., C. P. R. Hoppel, W. H. Drysdale, and S. A. Wilkerson "Numerical Simulation of Launch Interaction of Kinetic Energy Long Rod Fin-Stabilized Projectiles and M1A1 Abrams M256 Gun System with Comparison to Experimental Results." National Def. Industrial Assoc. 48th Annual Bomb & Warhead Technical Symp., Eglin Air Force Base, FL. May 11-14, 98b.

Newill J. F., C. P. R. Hoppel, and W. H. Drysdale, "Comparison of Launch Mechanics and Dynamics from the M1A1 M256 Gun System for the M829A2 Kinetic Energy Long Rod Fin Stabilized Projectile Containing Different Penetrator Materials." ARL-TR-1671, APG, MD, Apr 98c.

Newill J. F., S. A. Wilkerson, C. P. R. Hoppel, and W. H. Drysdale. "Numerical Simulation of Composite Kinetic Energy Projectiles Launched by an M1A1 Abrams M256 Gun System." Proceedings of the 30th SAMPE Technical Conference, San Antonio, TX, 23 Oct 98b.

Newill, J. F., D. Webb, B. Guidos, C. P. R. Hoppel, and W. H. Drysdale. "Methodology for Formal Comparison of Experimental Ballistic Firing of Kinetic Energy Projectiles With Numerical Simulation." Technical Report, U.S. Army Research Laboratory, Aberdeen Proving Ground, MD, in progress.

Plostins, P., I. Celmins, and J. Bornstein. "The Effect of Sabot Front Borerider Stiffness on the Launch Dynamics of Fin-Stabilized Kinetic Energy Ammunition." AIAA Paper No. 90-0066, Jan 90.

Rabern D.A., "Axially Accelerated Saboted Rods Subjected to Lateral Forces," Ballistic Research Laboratory Contractor Report No. 671, Aug 91.

Schmidt, E. M., P. Plostins, and M. Bundy. "Flash Radiographic Diagnostics of Projectile Launch from Cannon." Proceedings of Flash Radiography Symposium, E.A. Webster, Jr. and A.M. Kennedy, editors., The American Society for Nondestructive Testing, 1984.

Soencksen K., J. F. Newill, P. Plostins, "Aerodynamics of the 120-mm M831A1 Projectile: Analysis of Free-Flight Experimental Data," Proceedings of AIAA Atmospheric Flight Mechanics Conference & Exhibit, Denver, AIAA-00-4198, CO, 14-17 Aug, 00

Soencksen, K. P., J. F. Newill, J. M. Garner, and P. Plostins, "Comparison of the 120-mm M831A1 Projectile's Experimental Launch Dynamic Data with Hydrocode Gun-Projectile Dynamic Simulations." 10th U. S. Army Gun Dynamics Symposium, Austin, TX, 23 – 26 Apr 01

Soencksen, K.P., J.F. Newill, P. Plostins, "Aerodynamics of the 120-mm M831A1 Projectile: Analysis of Free-Flight Experimental Data," Proceedings of the AIAA Atmospheric Flight Mechanics Conference & Exhibit, 14-17 August, 2000, Denver, CO.

Soencksen, K.P., J.F. Newill, P. Plostins, "Roll Characteristics of the 120-mm M831A1 Projectile," Proceedings of the 39th AIAA Aerospace Sciences Meeting & Exhibit, 8-11 January 2001, Reno, NV.

Whirley R. G, D. E. Englemann, and J. O. Hallquist. "DYNA3D; A Nonlinear, Explicit, Three-Dimensional Finite Element Code for Solid and Structural Mechanics - User's Manual" Lawrence Livermore's National Laboratory, UCRL-MA-107254 Rev 1, Nov 93.

Whyte, R., Hathaway, W., "Free Flight Range Data Reduction – ARFDAS User's Manual," General Electric Co., Armament & Electrical Systems Department, Burlington, VT, March 1981.

Whyte, R., W. Hathaway, and J. Groth. "Aeroballistic Characteristics of the M831A1 Determined from Doppler Radar Data." Arrowtech Associates Technical Report, South Burlington, VT August 1994.

Wilkerson S. A. and D. Hopkins, "Analysis of a Balanced Breech System for the M1A1 Main Gun System Using Finite Element Techniques," Army Research Laboratory Technical Report 608, Nov 94.

MODELING OF BARREL/PROJECTILE INTERACTION IN A ROTATING BAND

P. C.T. Chen and M. Leach

U.S. Army Benet Labs TACOM-ARDEC, Watervliet, NY 12189

The ABAQUS program was used and a refined finite element mesh was chosen to complete the modeling of the barrel/projectile interaction in a rotating band. The calculations for the engraving processes proceeded until the projectile has passed completely through the forcing cone in the land and groove. The axially symmetric cases were considered and the elasticity of the tube and projectile was neglected. Sliding friction was considered and the copper band was either elastic-plastic or ideally plastic. The magnitude and distribution of the contact pressure between the band and the tube were obtained during and after engraving. For the first time we have observed the opening of a gap between the band and the bore after engraving was completed even when we observed full contact in the forcing cone.

INTRODUCTION

Earlier research has indicated that most cases of rotating band failure can be attributed to excessive wear (deformation) in the initial portion of the projectile's travel even when the failure does not occur until well down the tube [1]. When the projectile enters the barrel of the gun, the rotating band passes through a forcing cone which places it under compressive interference stresses and large plastic deformation occurs along the driving edges of the forcing cone. The radial pressure between the projectile band and bore produces friction and an abrasive action on the bore surface. Approximate theoretical estimates of radial band pressure have been obtained by using the rigid-plastic flow theory and assuming uniform distribution [2,3]. A satisfactory stress analysis of the engraving process and wear has never been reported. In an earlier paper [4], a two-dimensional elastic-plastic analysis of the engraving process in a projectile rotating band was obtained by using the finite element program – ABAQUS. The modeling for the engraving through the groove was completed but not for the engraving through the land. The later calculations ended before the projectile passed through the forcing cone.

In this paper, we have completed the modeling for the engraving process through the land and groove. A refined finite element mesh was chosen and the new version of the ABAQUS program [5] was used. The calculations proceeded until the projectile has

passed completely through the forcing cone. The axially symmetric cases such as smooth bores were considered and the elasticity of the tube and projectile was neglected. The copper band was considered as elastic-plastic or ideally plastic. An appropriate coefficient of sliding friction was also chosen. The magnitude and distribution of the contact pressure between the band and the tube were obtained as the projectile traveled through the forcing cone and further down the tube. The magnitude of the band pressure was very large and the plastic deformation in the band was very severe. For the first time we have observed the opening of a gap between the band and the bore after engraving was completed even when we observed full contact in the forcing cone. A theoretical estimate for the average band pressure of an ideal plastic material was also obtained for comparing with our numerical results of band pressure.

FINITE ELEMENT MODELING

Geometry : Figure 1 shows a schematic diagram of the tube/projectile interaction in a forcing cone. The geometry of the gun system XM297m549 was chosen in this study. The rotating band is of axial length L_o=37.084 mm and radial thickness B_o =2.3114 mm. The radius of the projectile is R_p =76.581 mm and the band is attached to the projectile. The radius of the bore behind the forcing cone is R_o=79.38 mm and the length of the forcing cone is L_c = 40.54 mm. The radii of the bore after the forcing cone through the groove and land are R_g =78.74 mm and R_l=77.485 mm, respectively. Therefore the reduction in thickness through the groove and land are 6.6% and 60.9%, respectively. A simple mesh of the band was constructed of 281 nodes and 250 4-node bilinear elements [4]. Figure 1 also shows the old mesh #1 and new mesh #2 for the band. The new finite element mesh consists of 510 nodes, 400 CAX4H elements and 100 CAX3H elements.

Material : The tube and projectile are assumed to be rigid and the copper band is considered as either elastic-plastic or ideally plastic. The values of Young's modulus and Poisson's ratio for the copper are 110 GPa and 0.33, respectively [6]. The initial yield stresses in compression and shear are 314 MPa and 181 MPa, respectively. For an elastic-plastic hard copper band, the dependence of the yield stress upon the plastic strain in the plastic range are piece-wisely defined by the data points (314MPa, 0.0), (620MPa, 0.126) and (620MPa, 10.0) and the flow stress is 620 MPa. For an ideally-plastic soft copper band, the flow stress is 314 MPa.

Boundary Conditions : We assume no separation between the band and the projectile because the band was welded to the projectile. In addition to sliding contact between the band and the tube in the forcing cone, the band may be deformed to slide axially in either direction against the projectile faces. The coefficient of sliding friction was assumed to be 0.01 for the band/tube pair.

Force/Displacement : Initially the back face of the band is assumed to be only 40.0mm behind the entrance of the forcing cone whose length is 40.54mm. Therefore when the projectile travels 80.54mm, the band will have passed the forcing cone and the engraving

process is considered as completed. The prescribed displacement used in this nonlinear analysis is 100mm for the groove engraving and 150mm for land engraving.

ENGRAVING THROUGH GROOVE

The initial thickness of the band is B_o=2.3114mm and the final thickness of band after passing through the groove will be $B_g=R_g-R_p$=78.74mm-76.581mm=2.159mm. Therefore the reduction in areas through the groove is

$$A_g=[1- B_g*B_g /(B_o* B_o)]x100\%= 12.8\%. \quad (1)$$

Using the mesh #1, it takes 81 increments to complete the ideally-plastic analysis but it takes only 49 increments to complete the elastic-plastic analysis. Figure 2 shows the contact pressure and the deformed mesh after the elastic-plastic band has traveled 100mm. Larger plastic deformation occurs at the front and back ends near the band/projectile interface. The maximum equivalent plastic strain is 2.233 at the back end close to the band/projectile interface. The distributions of the contact pressure between the tube and the band at different stages of traveling through the groove are shown in Figures 3 and 4, respectively, for the ideally-plastic and the elastic-plastic cases. The maximum value of contact pressure is 1849 MPa in the ideally-plastic band and 3548 MPa in the elastic-plastic band. It is interesting to point out that the maximum value of contact pressure/flow stress is 5.89 and 5.72, respectively, for the ideally-plastic and elastic-plastic cases.

ENGRAVING THROUGH LAND

The initial thickness of the band is B_o =2.3114 mm and the final thickness of band after passing through the land will be $B_l = R_l - R_p$ =(77.485 - 76.581) mm= 0.904 mm. Therefore the reduction in area through the land is

$$A_l=[1- B_l* B_l /(B_o* B_o)]x100\% = 84.7\%. \quad (2)$$

Using the old mesh #1, it takes 268 increments to travel 49.4mm for the ideally-plastic band but it takes 227 increments to travel 49.7mm for the elastic-plastic band. The computation ends because the time increment required is less than the minimum (0.001mm) specified. Plastic deformations are very large and severe distortions have occurred especially at the front and back ends near the band/projectile interface. The distortions are so severe that computation stops. The maximum equivalent plastic strain is 57.58 at the front end. This value of plastic strain is so large that some failure criterion has to be introduced. The distributions of the contact pressure between the tube and the band at different stages of traveling through land in the forcing cone are shown in Figure 5 and 6, respectively, for the ideally-plastic and elastic-plastic cases. The maximum value of contact pressure is 3505 MPa in the ideally-plastic band and, 6991 MPa in the elastic-plastic band as shown in the figures. It is interesting to point out that the maximum value

of contact pressure/flow stress is 11.16 and 11.28, respectively, for the ideally-plastic and elastic-plastic cases.

Using the new mesh #2, we have carried out the computations for the projectile to travel 150mm. It takes 3636 increments to complete for the ideally-plastic band and 4643 increments for the elastic-plastic band. The maximum value of contact pressure/flow stress is 11.66 and 11.29, respectively, for the ideally-plastic and elastic-plastic cases. It occurs during engraving. When the projectile travels 80.54mm, the band will have passed the forcing cone and the engraving process is considered as completed. The numerical results for the elastic-plastic case are shown in Figures 7 to 12. Before the band has passed the forcing cone, the contact pressure and deformation in the band during engraving are shown in Figures 7 and 8, respectively, for 61.17mm and 76.74mm travel. The band is in complete contact with the tube and two points on the band/projectile interface (C and D) represent the front and back ends of the band. Plastic deformations are very large and severe distortions have occurred especially at the front and back ends near the band/projectile interface. When the projectile travels 80.54mm, the band will have passed the forcing cone. The contact pressure and deformation in the band are shown in Figures 9 and 10, respectively, for 115.89mm and 150.00mm travel. Now the distortions are more severe and the values of contact pressure become smaller but the distributions are quite different from earlier stages. For the first time we have observed the opening of a gap between the band and the bore after the band has passed the forcing cone. The magnitudes and locations of the gap are shown in Figures 11 and 12, respectively, for 115.89mm and 150.00mm travel. When the band has traveled 150.00mm , the maximum value of contact pressure/flow stress is 7.58 and 7.24, respectively, for the ideally-plastic and elastic-plastic cases.

THEORETICAL ESTIMATE OF BAND PRESSURE

All theoretical estimates were trying to obtain the average band pressure for an ideal plastic material. An approximate formula for the average band pressure at the instant of complete engraving [7] is

$$P/Y=2.97\ [W_l / (W_l+W_g)] \ + 0.29\ W/T \qquad (3)$$

where Y, W_l , W_g , W and T are yield (flow) stress, land width, groove width, final band width and band thickness, respectively. The value of 2.97 corresponds to the indentation pressure on the tops of the lands, assuming the rifling is a rigid material pressing into an ideal plastic band [8]. The bracketed factor, $W_l/(W_l+W_g)$, averages the pressure acting on the lands over the entire bore surface. The additional term corresponds to the average pressure exerted by two rigid plates squeezing an ideal plastic material [9].
If we assume $W_l = W_g$, W=5.2mm and $T=(B_g + B_l)/2$= 1.532mm, then P/Y=2.47.

DISCUSSION AND CONCLUSION

The contact pressure between the band and tube has been obtained as the projectile travels through the forcing cone and further down the tube. The distribution is non-uniform and the magnitude of the band pressure is very large. Although the magnitudes for the elastic-plastic band are quite different from those for the ideally plastic band, the maximum value of contact pressure/flow stress (P/Y) are about the same according to our numerical results. The maximum P/Y is about 5.8 for engraving through groove and about 11.5 for engraving through land. When the engraving is completed, the maximum P/Y reduces to about 7.5 in the land. The average values of P/Y during engraving are estimated to be 50% of the maximum, i.e. 2.9 through groove and 5.8 through land. It is reasonable that these average values based on calculations are larger than the theoretical estimate 2.47. The calculated values which were based on sliding through the forcing cone should be larger than the theoretical estimate which was based on indentation because more deformation energy required for sliding.

Based on the comparison with theoretical estimate for the band pressure, we conclude that the calculated finite element results are reasonably accurate. The two dimensional modeling could be used for discussing the effects of geometry, material properties and friction on the band. We can determine the maximum contact pressure and also observe the deformation in the band. The 3-D simulations are still very difficult now.

REFERENCES

1. Montgomery, R.S., 1985, "Wear of Projectile Rotating Bands," ARLCB-TR-85008, US Army Benet Lab, Watervliet, NY.
2. DARCOM, "Design for Projection," Engineering Design Handbook, AMC Pamphlet No. 706-247, July 1964.
3. Tirosh, J., and Dayan, A., "On the Impact Engraving of Metal Bands," Proceedings of the 15th NAMRC, Vol 2, pp.358-363, May 1987.
4. Chen, P.C.T., "Analysis of engraving and wear in a projectile rotating band", *Proceedings of the Ninth US Army Symposium on Gun Dynamics*, McLean, VA, November 1998, ARCCB-SP-99015, Benet Labs, Watervliet, NY, pp 2-1 to 2-12.
5. Hibbitt,Karlsson & Sorensen,Inc, "ABAQUS/Standard User's Manual," and "ABAQUS/Explicit User's Manual," version 5.8, 2000.
6. Boyer, H.E.(editor), "Atlas of Stress-Strain Curves," 1987 ASM International, Metals Park, Ohio.
7. Watertown Arsenal, "Rifling and Rotating Band Design", Report No. WAL 760/410, 1951.
8. Lee, E.H., and Schaffer, B.W.,"Some Problems of Plastic Flow Arising in the Operation of Engraving Bands on Projectiles", Report No. WAL 893/81-84, 1949.
9. Nadai,A., "Plasticity", McGraw-Hill, pp.221-225, 1931.

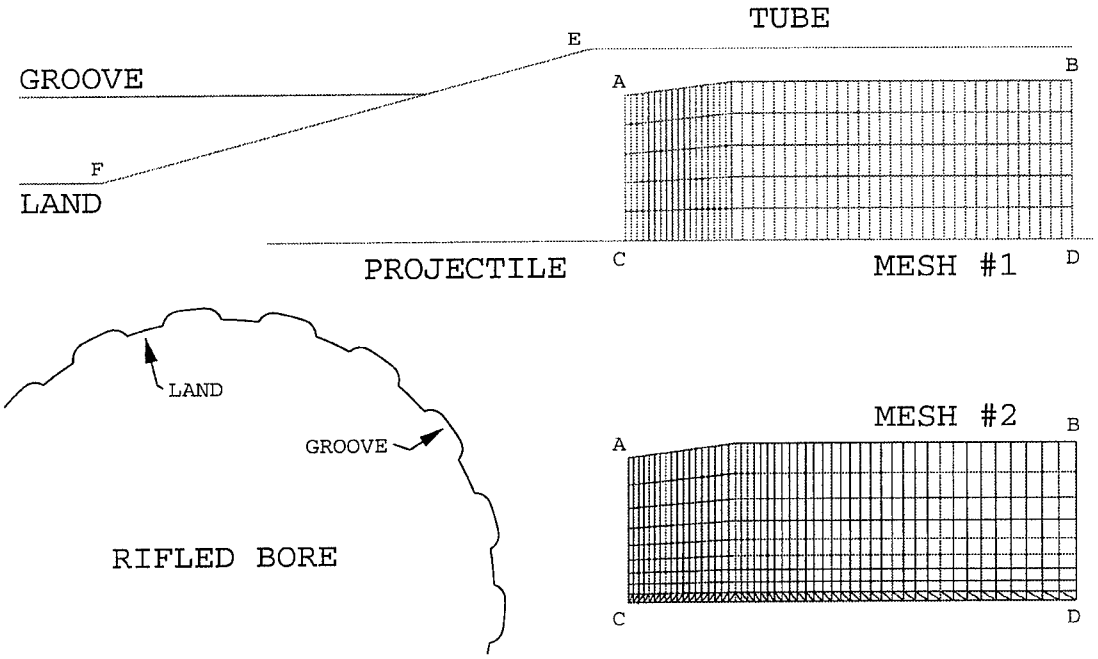


Figure 1 Schematic diagram of tube/projectile interaction in a forcing cone and finite element meshes for the band

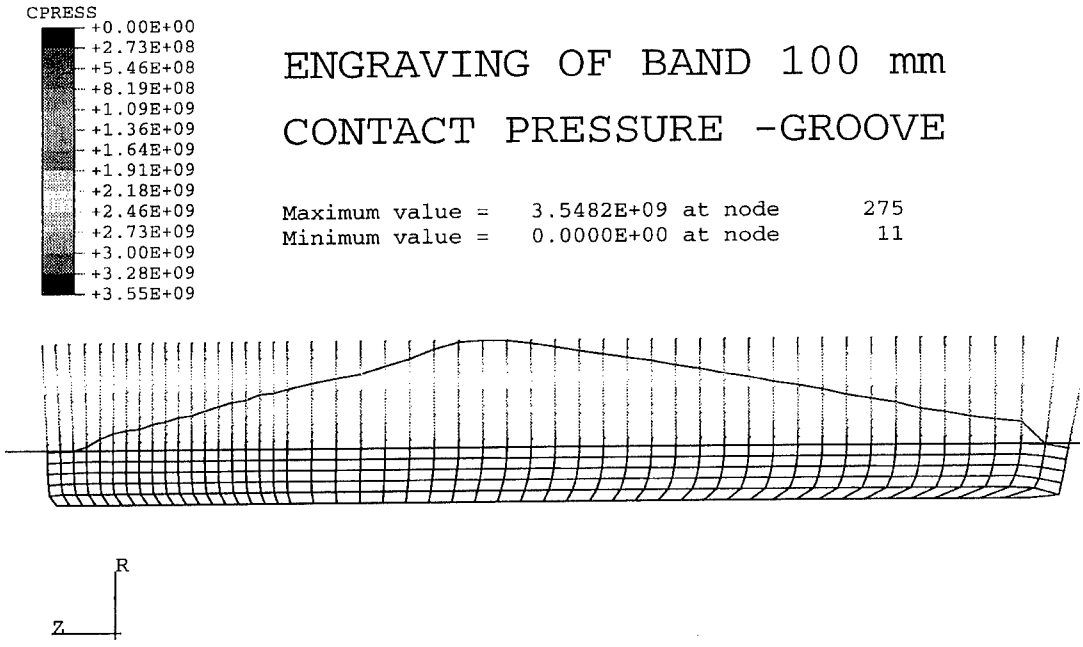


Figure 2 Contact pressure between tube and band after traveling 100mm through groove

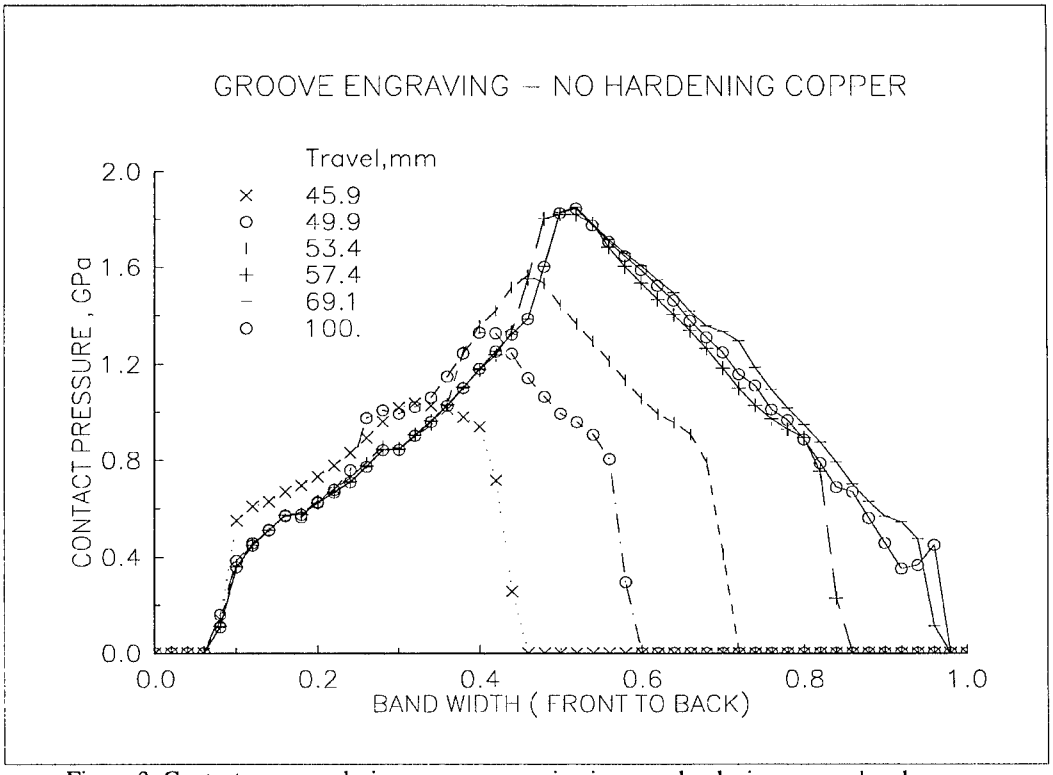


Figure 3 Contact pressure during groove engraving in a non-hardening copper band

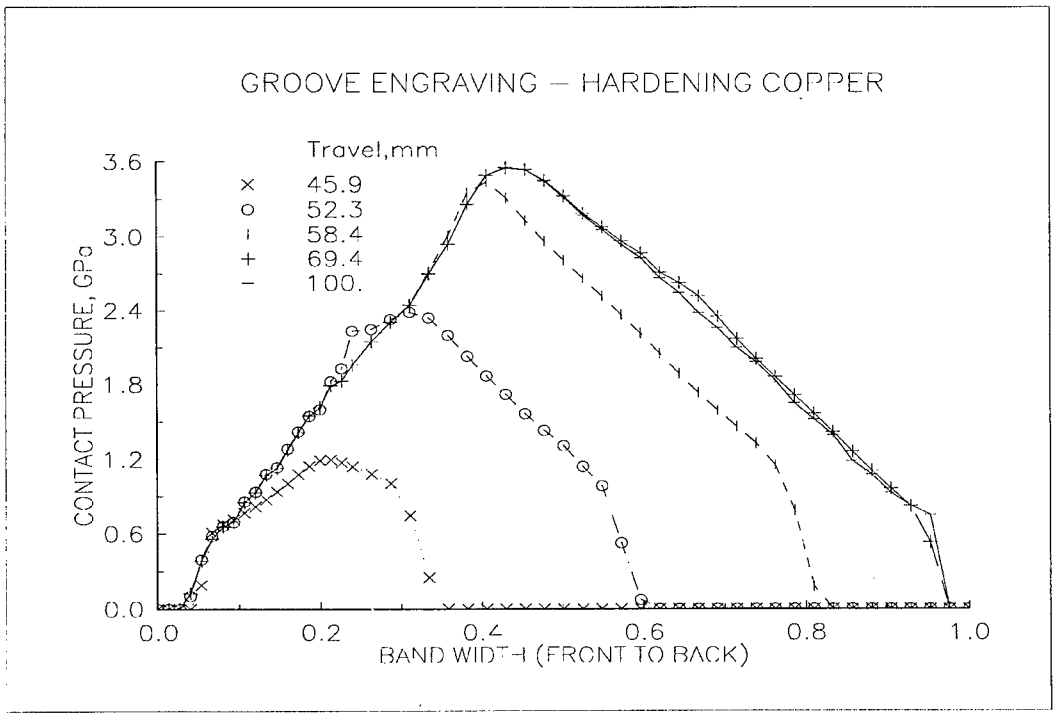


Figure 4 Contact pressure during groove engraving in a hardening copper band

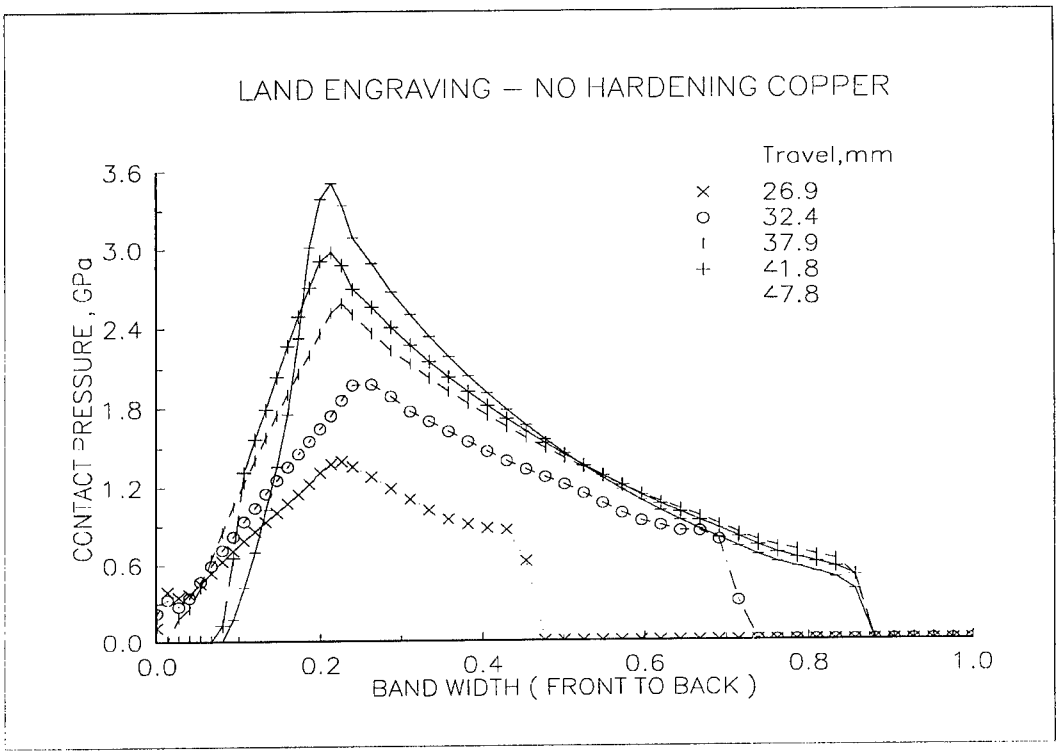


Figure 5 Contact pressure during land engraving in a non-hardening copper band

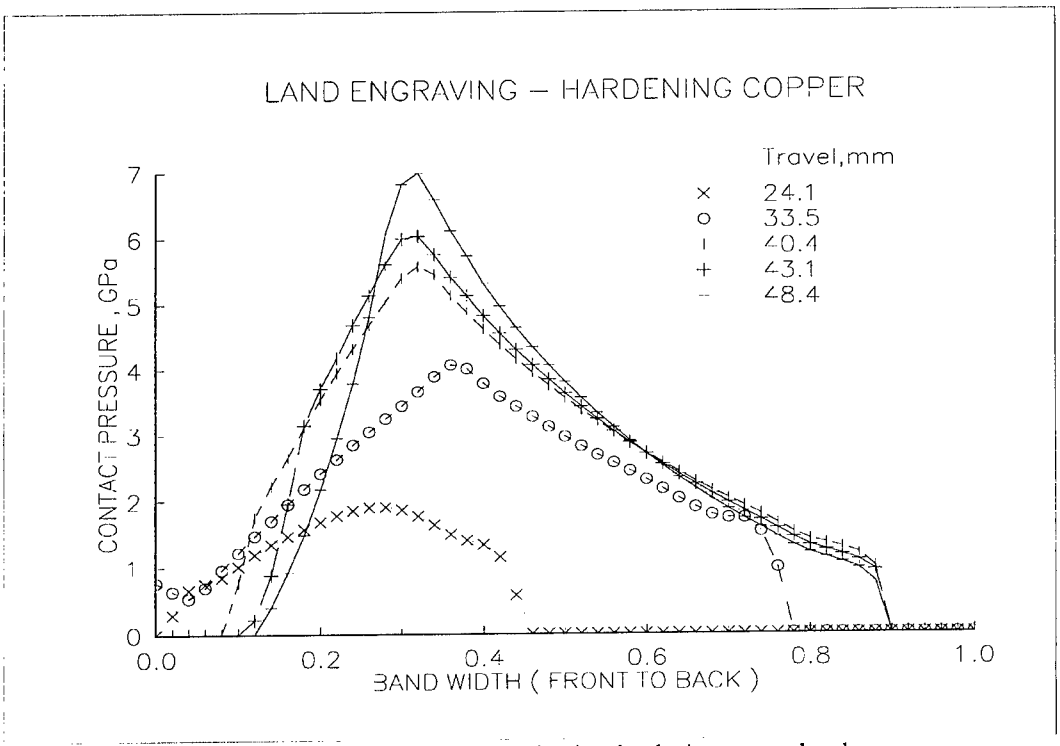


Figure 6 Contact pressure during land engraving in a hardening copper band

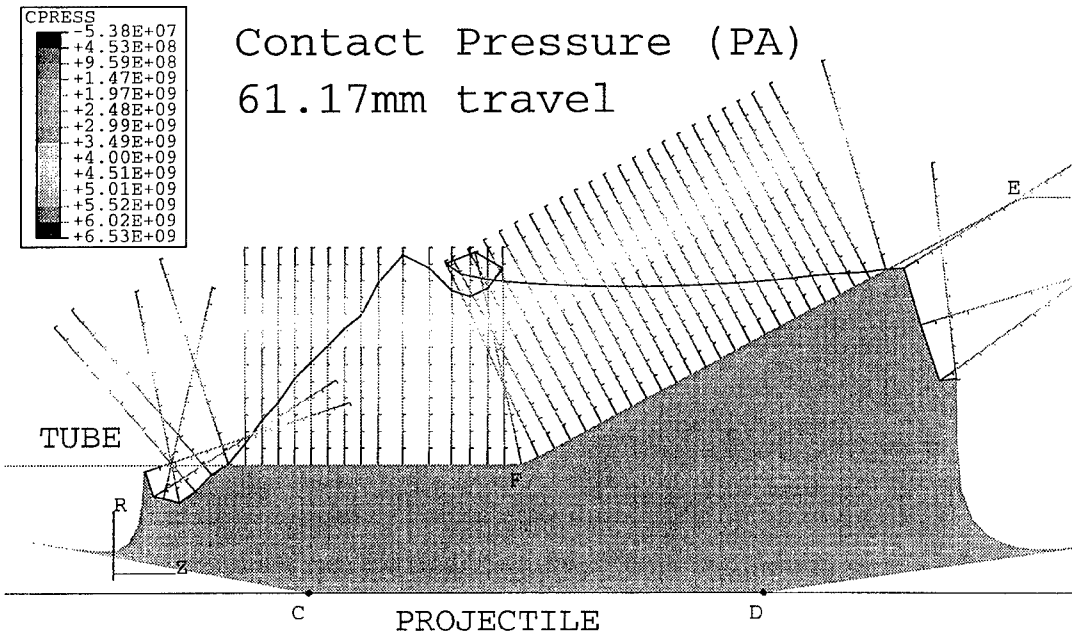


Figure 7 Contact pressure and deformed band after traveling 61.17mm through land

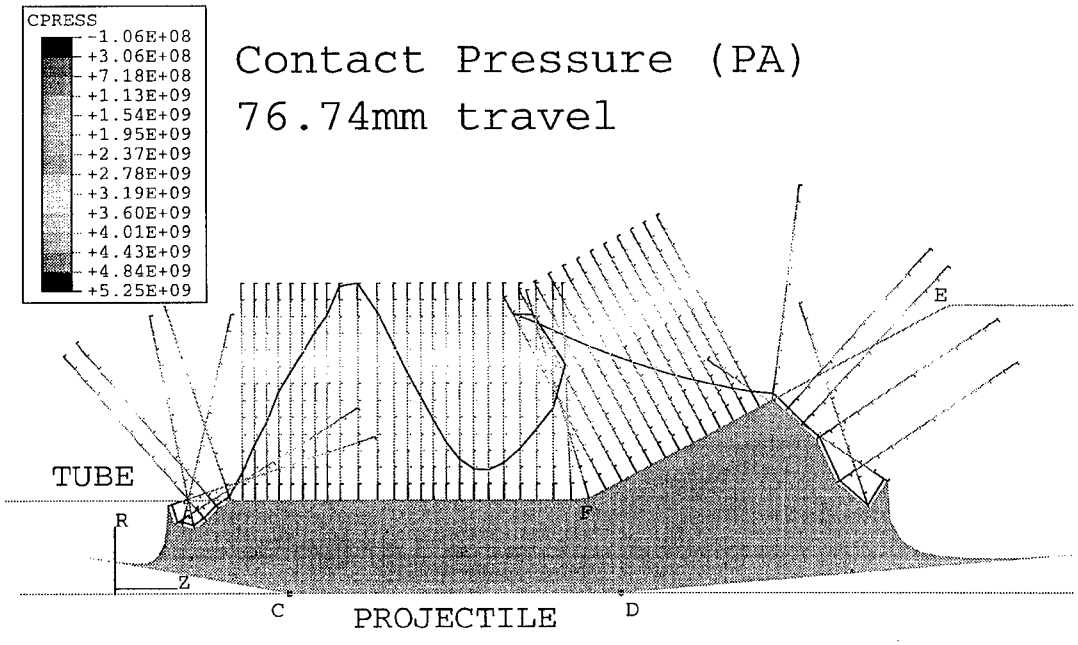


Figure 8 Contact pressure and deformed band after traveling 76.74mm through land

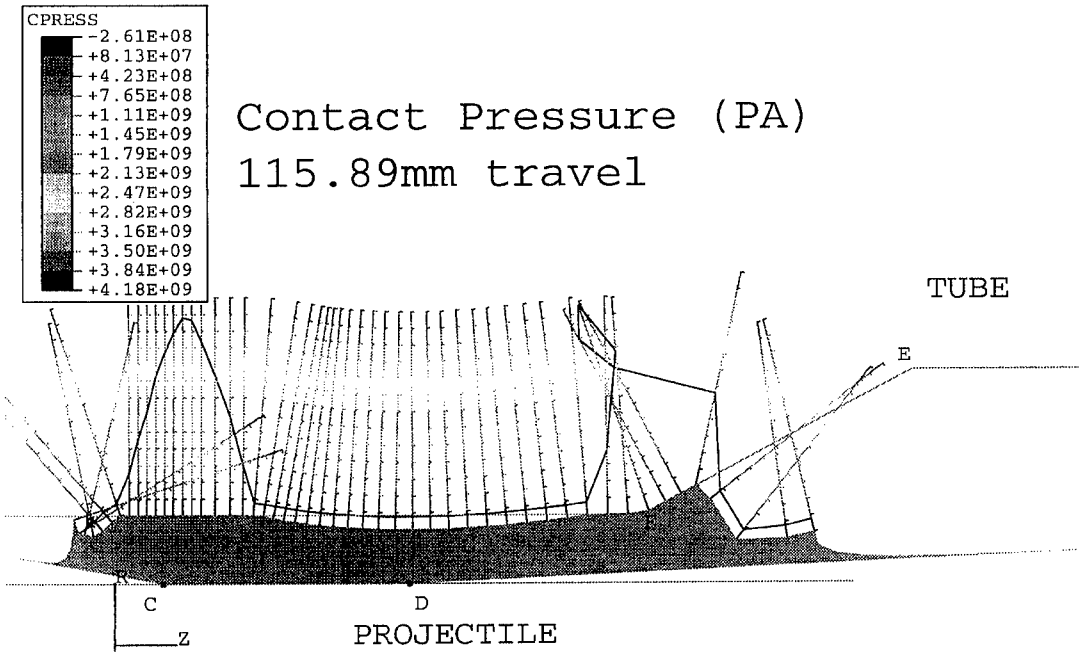


Figure 9 Contact pressure and deformed band after traveling 115.89mm through land

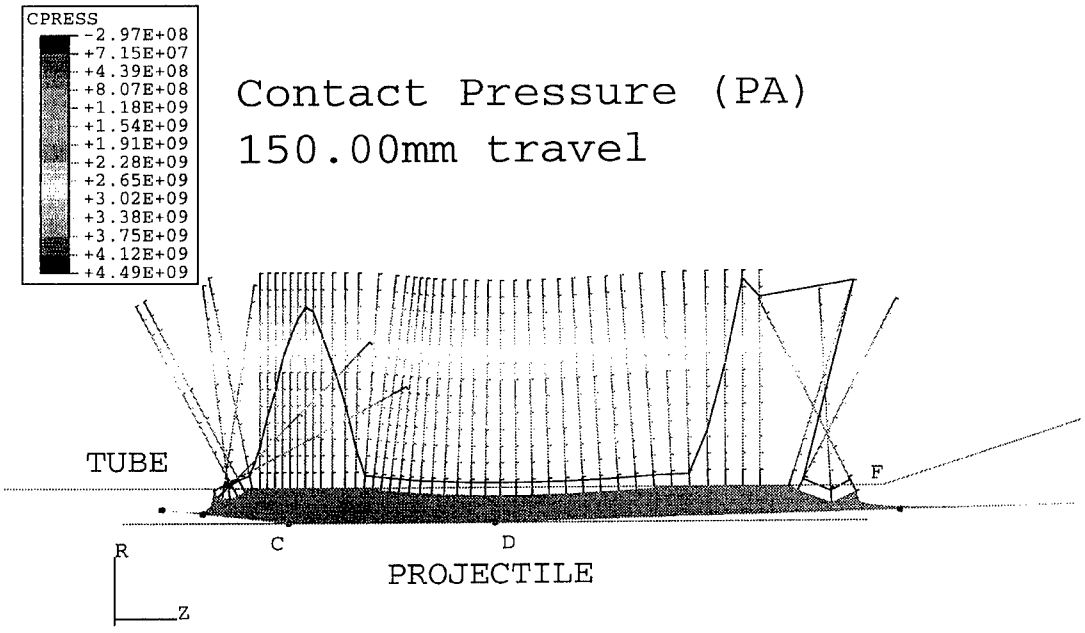


Figure 10 Contact pressure and deformed band after traveling 150mm through land

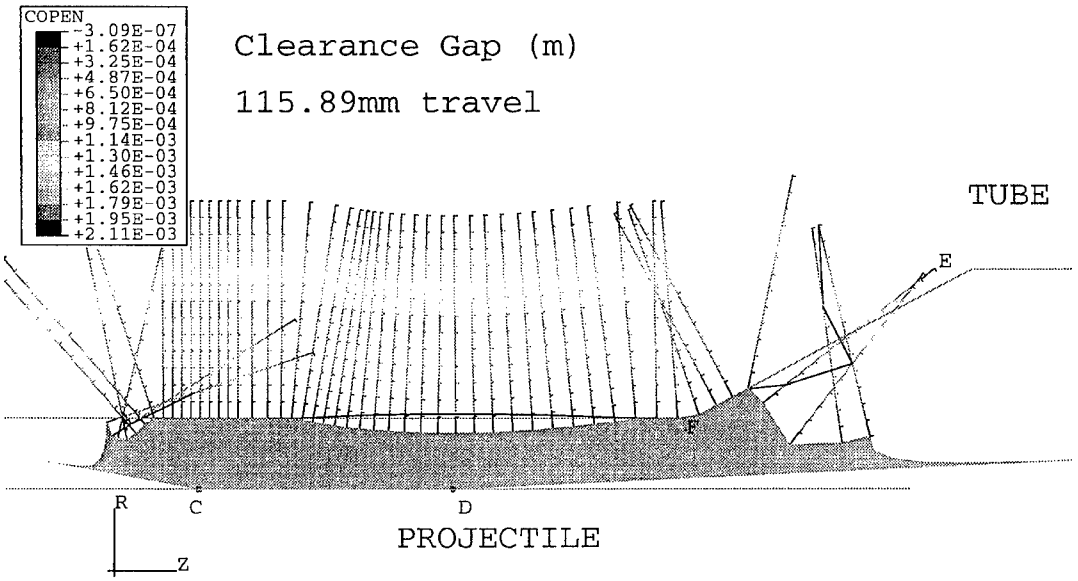


Figure 11 Gap between band and barrel after traveling 115.89mm through land

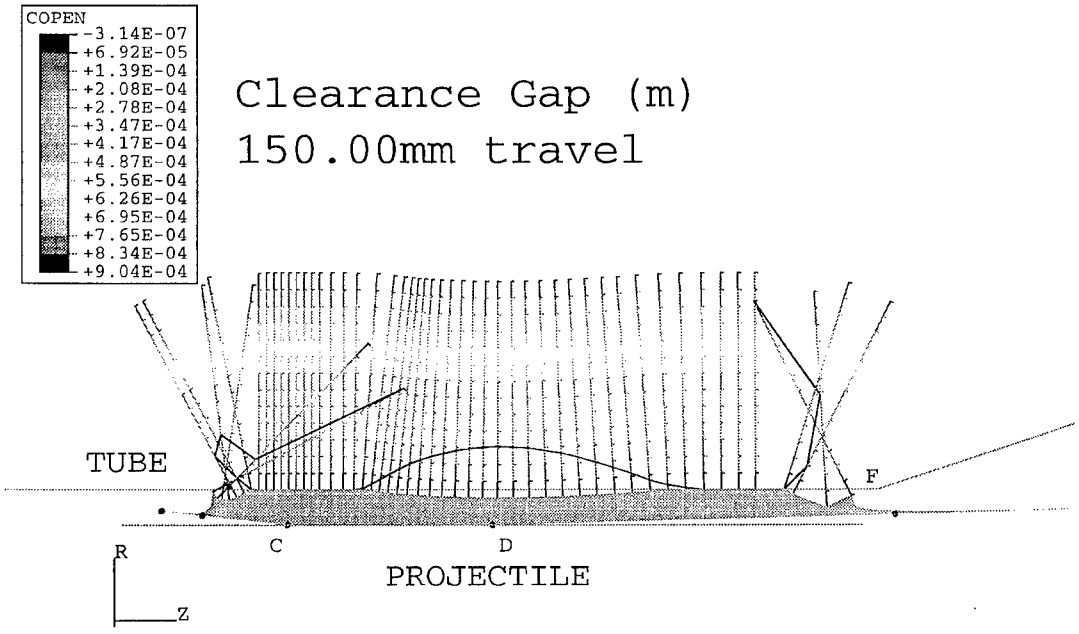


Figure 12 Gap between band and barrel after traveling 150mm through land

GUN TUBE SURFACE KINETICS AND IMPLICATIONS

Paul J. Conroy[1], Michael J. Nusca[1], Cary Chabalowski[1], William Anderson[1]

[1]U.S. Army Research Laboratory, Aberdeen Proving Ground, MD 21005-5066

Current theories concerning gun tube erosion consider that erosion can occur under various conditions. Propellant product gases are known to react with the surface resulting in an altered surface material which may melt or pyrolyze due to a lower melting temperature than that of the gun steel and or weakened mechanical properties. Previous surface reaction studies by the authors used a generalized equilibrium scheme with a control volume analysis to represent surface reactions occurring during a cannon firing. This led to a post reaction treatment at the interface which incorporated the subsurface diffusion of species to limit the surface reaction. In this study, the surface reactions and rates are specified explicitly with published rates and guidance from fundamental molecular modeling results. The results demonstrate the utility of the employed surface reaction mechanism as well as the incorporation of finite rate surface kinetics.

INTRODUCTION

In consideration to the development of the Future Combat System, it is necessary to understand the physics and chemistry of the interior ballistic erosion problem in order to focus mitigation efforts. This current study focuses upon the incorporation/application of generalized finite rate kinetics to the gun tube erosion problem. Previously, there has been documented a melt wipe model by Weinacht, Conroy, [1], and Conroy, Weinacht, Nusca [2], followed by the inclusion of generalized equilibrium of Conroy, Weinacht, Nusca, [3], [4], and [5]. The melt-wipe description enabled very severely eroding systems to be modeled. However, it did not account for the erosion in systems which apparently did not reach the melting temperature of the gun steel. These systems at the time were thought to have some form of augmented heat transfer due to projectile blowby [6], or heat release at the surface due to chemical reactions. It was initially thought that the oxidation of the surface was releasing sufficient energy to melt the oxidized material. This material along with its energy was subsequently blown out of the gun tube in the product gases. Thus the tube effectively did not experience any additional heating as might be evidenced experimentally. Chemical phenomena were investigated initially due to unusual behavior of RDX containing propellants. The adiabatic flame temperature of M43, which contains RDX, is lower than that of M30,which does not contain RDX, while the erosivity was typically higher [7]. This behavior conflicts with previously held beliefs and correlations which used the flame temperature to identify erosivity [8], [9], and [10]. Possible causes for this behavior were hypothesized after the inclusion and application of equilibrium chemistry to the erosion problem [5]. The equilibrium chemistry required the definition of a specific control volume for the reaction which was defined by the diffusion depth of carbon into the surface. The

premise was that no more steel could react with carbon or oxygen than that in physical contact with the gaseous atomics. Therefore the limiting factor was diffusion.

Although equilibrium chemistry continues to be applied for reaction of materials which diffuse into the substrate in the present work, the inclusion of finite rate kinetics at the surface has resulted in an elimination of many of the assumptions from the equilibrium calculations. Finite rate kinetics also allows the inclusion of many erosion reaction inhibition concepts which can lead or direct investigations of mitigating additives or chemical surface alterations.

PHYSICAL DESCRIPTION

Figure 1 describes the physical result of gun firings on a coated gun tube. The cracks inherent in the chromium plating, produced by either residual stresses from the manufacturing process or from thermo-mechanical cycling during gun firings, enable gases to reach the substrate where they react with the surface altering it from virgin gun steel. This altered surface is much easier to remove either through pyrolysis or melting. A critical description of the loss of surface coatings was pointed out by Conroy, Weinacht, and Nusca, [5], namely in that the erosion preferentially traverses laterally under the coating following the conductive energy transported through the coating to the substrate. Thus the interface between the substrate and the surface material is the hottest location at the bottom of the pit or crack and therefore the most reactive. This causes coating undermining and subsequent removal by high pressure gas in this region after the passage of the rarefaction wave during gun tube blowdown.

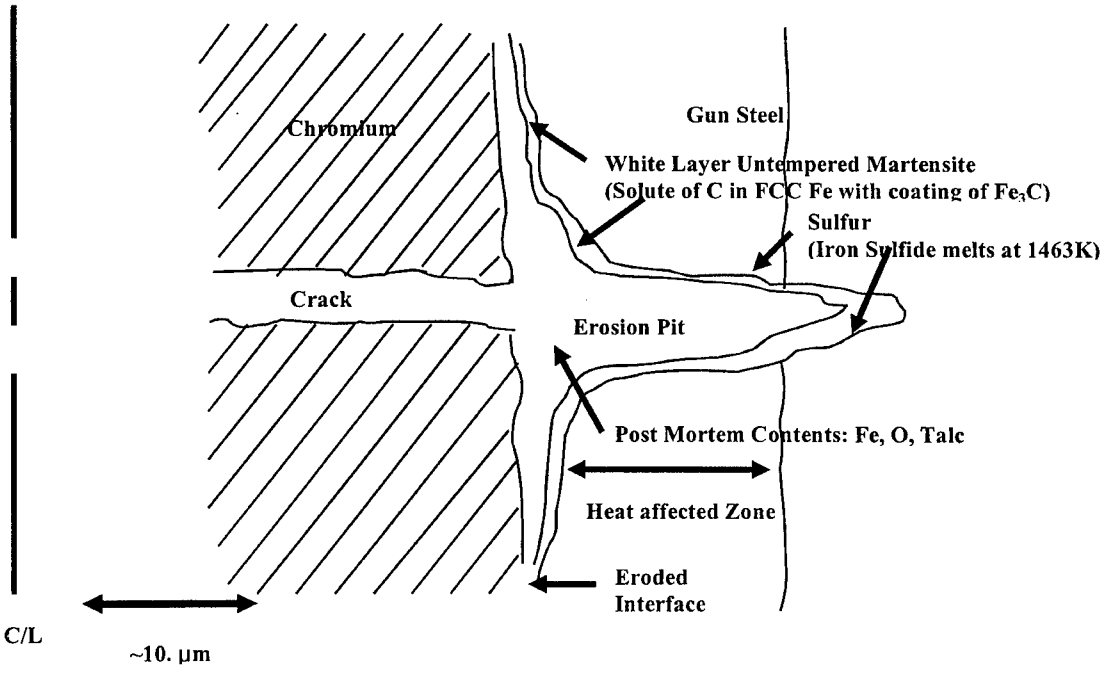


Figure 1. Description of Post Mortem Erosion Pit [19].

Figure 2 describes the physical representation that has been incorporated into the erosion model. Included in the figure and representation are the core flow species which supply both heat and mass transfer to the surface. Stresses are considered in both the coating as well as the substrate. This stress results from both the surface boundary condition of pressure as well as the mismatch in coefficients of thermal expansion between the coating and substrate. When the stress in the coating exceeds the ultimate strength a crack is assumed to form. This produces a crack distribution within the coating. Excessive interfacial shear stress would cause the coating to delaminate and subsequently be removed. Convective heat transfer imparts energy to the surface of the coating as well as in the crack where it is augmented. Energy is transported through both the coating and substrate material. Further details are described in previous reports [3], and [5].

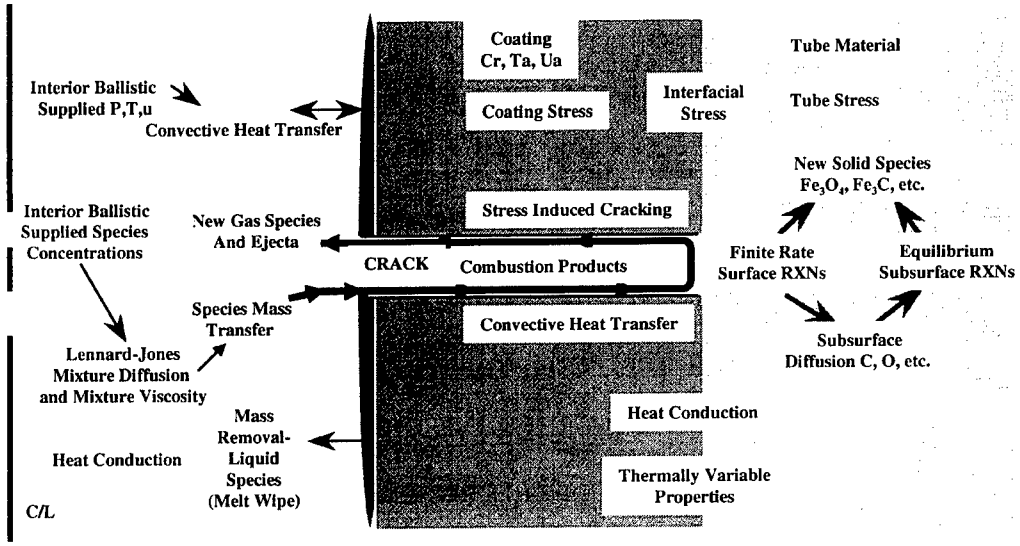


Figure 2. Analytical Description Including Kinetics and Coatings.

Surface kinetics have been included in the following manner. The species transported down into the crack are determined through multi-component diffusion with Wilke's [11] mixing rule to account for interactions. The quantity of surface iron available for reaction remains determined from the thermally variable diffusion depth for carbon over the computational time step at the crack base surface temperature where alpha is the diffusivity and dt is the time-step. The reaction mixture temperature is determined through a weighting function between the gas and solid phase materials. Given the specific heats, average molecular weight, identity and quantity of reactants along with user supplied reactions such as provided in Table 3, the nonequilibrium kinetic subroutine models the reaction of the species through the macroscopic hydrodynamic time-step. By specifying the maximum kinetic time-step, which is much smaller than the hydrodynamic time-step, to at least 1/25 but no more than 1/500 iterations per hydrodynamic time step enables the product species from one kinetic computational sweep through the reaction mechanism to interact as reactants for all the other reactions in the mechanism.

When the kinetics routine calculation is completed for the hydrodynamic time-step the integrated quantity of carbon and oxygen which diffused into the steel from the dissociation of CO is subsequently reacted with the substrate through equilibrium chemistry as guided from previous work with the model. In the current model binary diffusion of species into the solid phase is assumed. This approach does not account for cross terms of additional species. Inclusion of full multi-component subsurface diffusion is planned as a future effort. The quantity of material diffused appears to be small in comparison to the surface reacting material, although during the cooling portion of the ballistic cycle the diffusion continues for quite some time after the surface passes the melting temperature of Fe_3C. The period of time between the time when the interface temperature decreases below the melting temperature of Fe_3C and the time when the temperature at which diffusion stops is reached is what potentially makes diffusion important. During this time material is being inserted through diffusion into the steel and the following shot will encounter a loaded substrate which will be removed.

Once both the surface and subsurface systems have reacted the post reacted products are prepared for carry over to the next time-step. This step allows for the determination of energy released positive or negative as well as the surface material lost or gained. This energy is incorporated as a surface source term.

NONEQUILIBRIUM CHEMICAL KINETICS

The nonequilibrium (or finite-rate) chemical kinetics subroutine has been adapted from the NSRG computational fluid dynamics code written at ARL [12], and recently applied to propulsive reacting flow systems [13] as well as an open-air, high-speed chemically reacting jet [14]. In the NSRG code, this subroutine is used to compute the chemical source term that appears on the right-hand side of each species conservation equation in the Navier-Stokes equation set. For use in the present effort, this subroutine has been adapted so that it is patterned after the equilibrium subroutine, documented previously [5]. As a result, the Army Research Laboratory Erosion Code, (ATEC) determines the local flow conditions (density, temperature, and species mass fractions) and numerical conditions (time step or interval) while the nonequilibrium subroutine (using an appropriately smaller chemical time step) returns the new chemical constituency based on a predetermined set of chemical reactions and rates (i.e., the chemical mechanism). In this section a general review of the nonequilibrium routine is given.

Chemical reactions can be expressed in a general fashion (where X_i represents the symbol for species i, for example H_2O) with stoichiometric coefficients, ν, for each species in these reactions.

$$\sum_{i=1}^{N} \nu_i' X_i \Leftrightarrow_{k_b}^{k_f} \sum_{i=1}^{N} \nu_i'' X_i \tag{1}$$

A chemical kinetics mechanism will consist of L such reactions. For each reaction a general reaction rate equation is written.

$$\frac{dC_i}{dt} = \sum_{i=1}^{L} (\nu_i'' - \nu_i') \left(k_f \prod_i^N C_i^{\nu_i'} - k_b \prod_i^N C_i^{\nu_i''} \right) \tag{2}$$

where the C_i above represents the concentration of species i. This equation relates the time rate of change of this concentration for a particular species (the left-hand side) to the current values of concentrations for all N species, raised to powers of either the reactant coefficient (ν-prime) or product coefficient (ν-double-prime). In Equation 2, the reaction rates (k) and the stoichiometric coefficients for the reaction (ν) multiply the product sums. In order to compute the total change in C_i this equation represents a sum over every reaction (total of L) in the reaction mechanism. The nonequilibrium routine determines the largest physical time step (dt in Equation 2) which is also smaller than the fluid time step from ATEC and computes the new species concentrations (using dC_i/dt) for all N species. Concentrations can be converted to mass fractions for convenience. In general, tens or hundreds of chemical time steps will have to be taken per one fluid time step (see [11], for more details).

The forward reaction rate is usually defined using the Arrhenius form,

$$k_f = A\,T^n \exp(-E_a / kT) \tag{3}$$

where the rate data: A, E_a and n are determined from physical chemistry (k is Boltzmann's constant and is used to express E_a/k in temperature units). The backward rate can either be specified in the same form as the forward rate (above) or can be computed using the equilibrium constant for each reaction,

$$k_b = k_f / K_c \;\; ; \;\; K_c = \exp\left(-\Delta G / RT\right) \tag{4}$$

where K_c is the equilibrium constant for a particular reaction computed from the change in Gibbs energy (ΔG) for that reaction (see [12] for details). Gibbs energy for each species is computed using the NASA-Lewis database [15].

There are many situations for which reaction rates are of the additive type (wherein two rates are computed and added together for the final rate) or the pressure dependant "falloff" type (wherein the final rate is the product from three factors; two separate rates and a function based on the local flowfield temperature, pressure and mixture). The nonequilibrium routine will accept special coding for these cases. In other situations, certain reactions involve a "third-body" or a "collision partner" (often denoted M). The species M can stand for any of the N species being considered in the mechanism; thus a single reaction involving M-type species is actually N reactions with the same reaction rate. For these N reactions, there is usually specified a third-body collision efficiency for a particular collider species. These efficiency factors are multiplied by the concentration of the collider species in the product-summation terms of Equation 2. The nonequilibrium routine is setup to automatically handle third-body reactions. For an example of these situations (i.e., non-Arrhenius reaction rates and third-body reactions) the reader is directed to [14].

CHEMICAL KINETICS MECHANISM

A finite rate chemical reaction module has been incorporated into the erosion package as described. Before proceeding to use the package a series of numerical experiments were made to insure that the correct information was passed to and returned from the module. One the numerical validating experiments involves a simple set of reactions to test various areas

of kinetics involving both temperature sensitivity as well as possible third body reactions, presented in Table 1.

Table 1. Example Kinetics Validation Reaction Set.

Reaction		A (cm^3/mole s) or (cm^6/$mole^2$-s)	n (-)	E_a/k (K)	3rd Body
1	H_2 (g) + O_2 (g) ⇒ 2OH (g)	1.7e13	0.0	24169.	no
2	OH (g) + H_2 (g) ⇒ H_2O (g) + H	2.2e13	0.0	2593.	no
3	OH (g) + H (g) ⇒ H_2O (g)	2.2e22	-2.0	0.0	Yes

Table 2 describes the results for the validation kinetic reaction calculation, presented in Table 1, using the module as a stand alone package which has been extensively tested (Nusca 1998) and the integrated version of the module in the erosion package. Both the stand alone and integrated versions produce identical results without the reverse reactions. However, if the reverse reactions are enabled then the integrated package depends upon the older version of the NASA Lewis database which is automatically read in, while the stand alone package uses a newer NASA Lewis database. The differences observed with the reverse calculations implemented is due to versions of the thermochemical database. If this ultimately causes large discrepancies, the older database could be updated, however, the effect appears to be orders of magnitude smaller than what would be considered an issue.

Table 2. Mass Fraction Production Rates for Kinetics Validation Reaction Set.

Integrated Kinetics (With and without backward reactions)			Stand Alone Kinetics Module (With and without backward reactions)		
SPECIES	g/cm^3-s		SPECIES	g/cm^3-s	
1	-0.16962E+05	H	1	-0.16962E+05	H
2	0.00000E+00	H_2	2	0.00000E+00	H_2
3	0.00000E+00	O_2 Without	3	0.00000E+00	O_2 Without
4	-0.28622E+06	OH Backward	4	-0.28622E+06	OH Backward
5	0.30318E+06	H_2O Rate	5	0.30318E+06	H_2O Rate
1	-0.16962E+05	H	1	-0.16962E+05	H
2	0.18858E+00	H_2	2	0.19973E+00	H_2
3	0.29935E+01	O_2 With	3	0.31805E+01	O_2 With
4	-0.28623E+06	OH Backward	4	-0.28623E+06	OH Backward
5	0.30318E+06	H_2O Rate	5	0.30318E+06	H_2O Rate

A proposed set of reactions between the primary propellant combustion products (H_2, CO, CO_2, H_2O) with the surface of the gun tube BCC, FCC iron is presented in Table 3. Although the reverse reactions could have been included at this time only the forward reactions are considered. The coefficients and exponents in Table 3 are literature values except for the coefficient of reaction number 2 which was not available from the literature. Fortunately the exponent for reaction number 2 was available. This provided a starting point from which to develop some estimates for the coefficient. A parametric study involving

many calculations was performed on the coefficient, a few of which are presented in Figure 3. As the coefficient A_2 is increased from 3.8e14 to 6.0e14 what is immediately clear is the effect of reaction temperature and duration on pit growth. This modification affects the quantity of material removed in the forcing cone region. Farther down-bore there is a gradual asymptote to a common amount of material removed.

Table 3. Proposed Reaction Mechanism

	Reaction	A (cm^3/mole-s) or (cm^6/$mole^2$-s)	n (-)	Ea/k (K)	3rd Body
1	$CO(g) + O(ads) + (Surface) \Rightarrow CO_2(g) + (Surface)$ [16]	6.17e14	0.0	1510.0	Yes
2	$CO(g) + (Surface) \Rightarrow C(ads) + O(ads) + (Surface)$ [17] (Collider)	5.2e14 (Estimate)	0.0	23903.0	No
3	$O(ads) + O(ads) + (Surface) \Rightarrow O_2(g) + (Surface)$ [16]	1.89e13	0.0	-900.0	Yes
4	$H(g) + OH(ads) + (Surface) \Rightarrow H_2O(g) + (Surface)$ [16]	8.35e21	-2.0	0.0	Yes
5	$H_2(g) + (Surface) \Rightarrow 2H(g) + (Surface)$ [16]	4.57e19	-1.4	52530.0	No
6	$H(g) + O(ads) + (Surface) \Rightarrow OH(ads) + (Surface)$ [16]	4.71e18	-1.0	0.0	Yes
7	$CO(g) + O_2(ads) + (Surface) \Rightarrow CO_2(g) + O(ads) + (Surface)$ [16]	5.06e13	0.0	31800.0	No

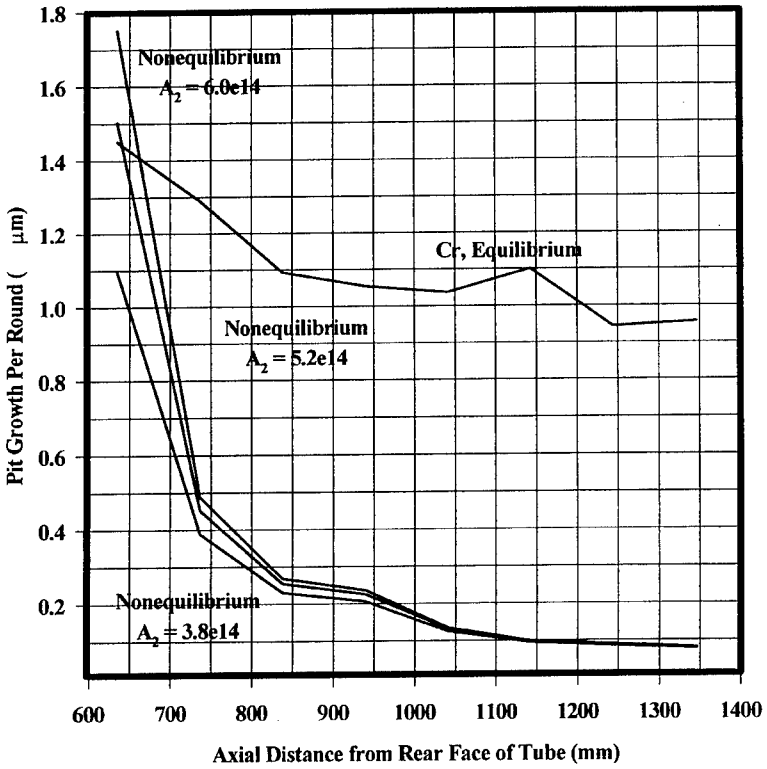


Figure 3. Pit Growth Rate for Chrome Coated Steel 120mm, M256 Canon Firing and APFSDS Round with Various Reaction Rate Coefficients.

A substantial difference exists between the previous calculation using infinite rate (equilibrium) chemistry and the finite rate chemistry results. The previous results do not take reaction rates into account and therefore the pit growth rate results are much higher down-bore than they apparently should be. The chemical reaction rates control the amount of product formed as well as the supply of potential reactants for intermediate reactions. The depth of material typically removed from the base of a pit is between 0.7μ and 1.5μ per shot for this particular APFSDS round [19]. This magnitude is verified by micrographs [20], such as shown in Figure 4. This leads to assignment of 5.2e14 to the coefficient value A_2. Whether this assigned value is correct or not is purely speculation at this time. One item which the equilibrium calculations provided is the resultant chemical constituency involving iron carbide. Therefore, the resultant carbon, from reaction number 2 in Table 3, was enabled to react with the iron at the surface to produce iron carbide.

RESULTS

Figure 5 compares the previous equilibrium assumption to the present nonequilibrium assumption for a 0.010" chromium plated M256 120mm tank canon firing an APFSDS round.. Also presented is data from a M68 non chromed tank cannon firing a similar round but reduced by a factor of ten (Ward, 1980). The difference in predictions between the equilibrium and nonequilibrium assumptions is striking. The equilibrium assumption produces more erosion down-bore than the nonequilibrium assumption. Closer to the forcing cone for the M68 data as well as the nonequilibrium calculation we see that the higher temperatures guide the reaction rate. Although the nonequilibrium resultant eroded depth should be less than that of the equilibrium this is not necessarily the case since the computational scheme is somewhat different between the two. The equilibrium scheme was based on a fixed control volume with a finite amount of iron, while the nonequilibrium scheme enables iron to be consumed as needed by the surface reaction.

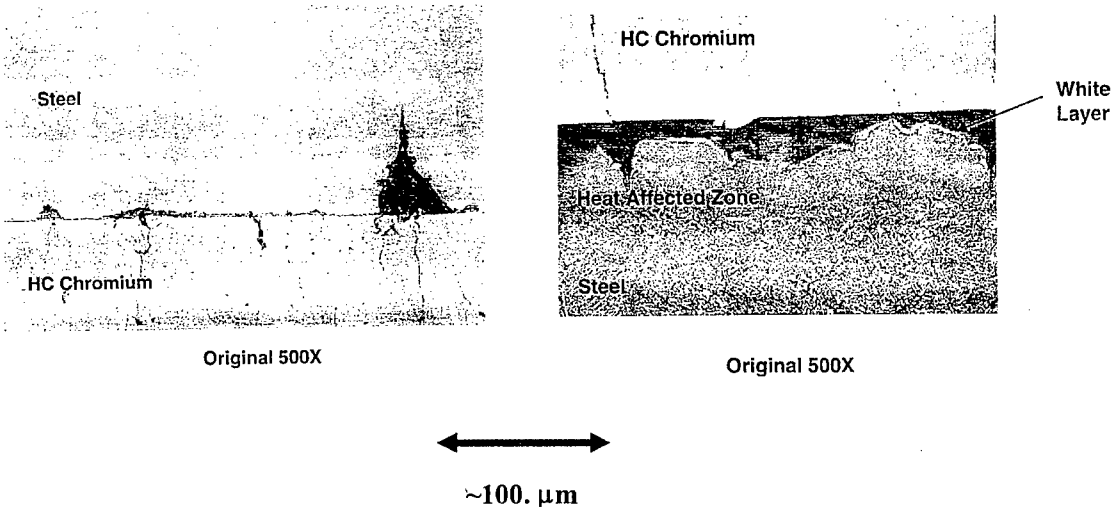


Figure 4. Substrate Erosion Beneath Cracks Showing Lateral Erosion Distribution [20].

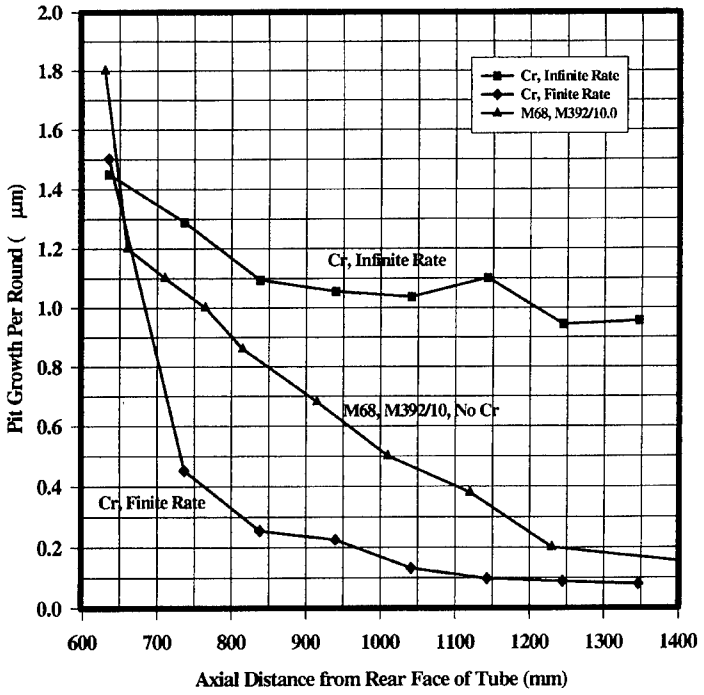


Figure 5. Single Firing Pit Growth Rate for 0.010" Chrome Plated Steel Compared to M68 Non-Chromed Gun Firing an M392/10. APSFDS Round.

Using the previously determined value for A_2, calculations for a similar tantalum coating were made and presented in Figure 6. The only modifications were to the physical properties of tantalum. Figure 6 also compares equilibrium as well as non equilibrium results for both chromium as well as tantalum coated tubes. The large difference in the potential pit growth rate at the forcing cone, between Cr and Ta, is due to the inherent higher temperature experienced with the tantalum coating as seen in Figure 7. The peak temperature experienced by the pit interface is almost 200K higher for the tantalum than that for the chromium. This drives the exponent in the Arrhenius reaction rates as well as the substrate diffusion of the species. This may imply that if there was a crack or other type of pit form given a tantalum coating of equal thickness as chromium then perhaps the tantalum coating would not tend to have the longevity of the chromium coating in similar circumstances.

NITROGEN HYPOTHESIS

Considering that the primary driving reaction of the chemical mechanism is the dissociation of the carbon monoxide, ways to possibly mitigate erosion would include methods to suppress this dissociation or suppress the production of carbon monoxide in the first place. Interestingly, Ponec and Barneveld, [21] suggest that the surface dissociation of CO on an iron surface is spoiled by nitrogen intrusion or nitriding the surface. They do not state specifically why this occurs. This leads to the possibility that increasing the nitrogen content of the propellant products may diminish the CO dissociation and thereby the erosion. Leveritt, Conroy, and Johnson [22] have discovered that some advanced propellants, with similar flame temperatures as older propellants such as JA2, do not erode as much as the older double base propellant. Complicating matters is the fact that these advanced propellants have a much higher CO/CO_2 ratio than that of the double base propellants. One

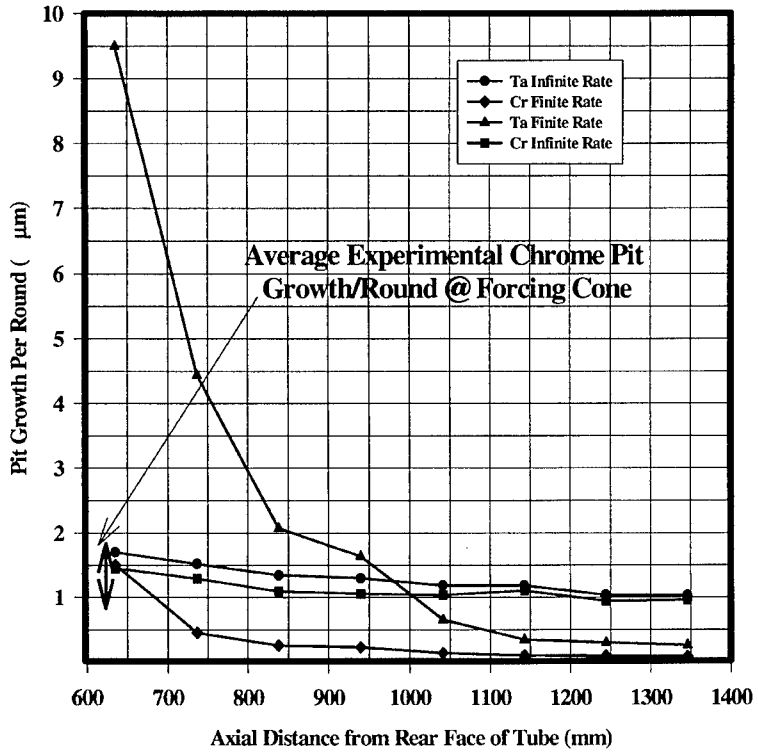


Figure 6. Single Firing Pit Growth Rates for 120mm, M256, Cr and Ta Lined, Firing an APFSDS Round.

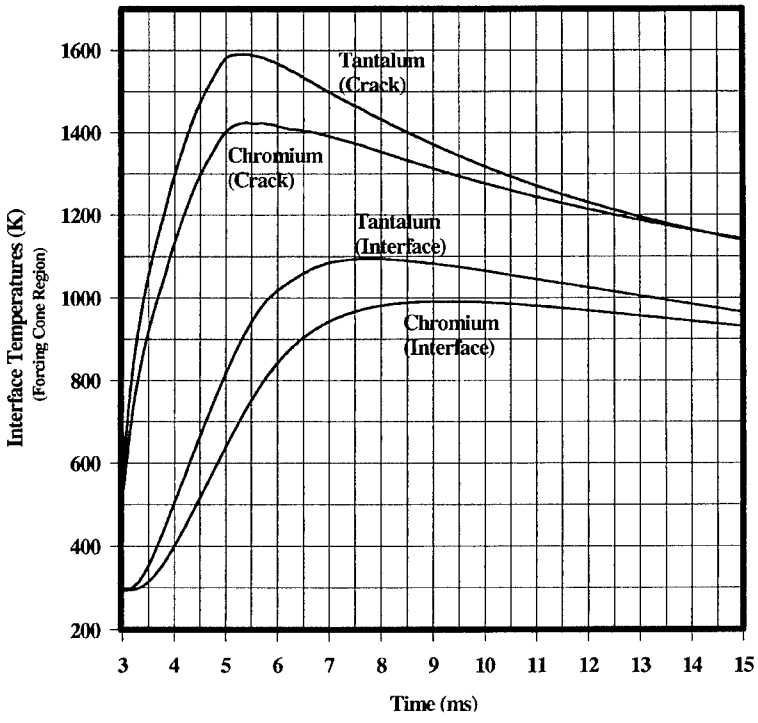


Figure 7. Computed Interfacial Crack Base Temperatures for 0.010" Chromium Coating Compared to 0.010" Tantalum Coated M256 Canon Firing an APFSDS Round.

would expect these higher ratios to exacerbate the carburization mechanism. Fortunately, Ponec's explanation may be applied to these new propellants because their nitrogen content is approximately three times that of conventional propellants.

The M242 Bushmaster barrel has the option of nitriding or chrome plating. If it is chrome plated, access for erosion is through the cracks to the substrate [5]. Considering Ponec's and Barneveld's hypotheses, investigation into nitriding surfaces before they are chrome plated or even afterward may lead to technological breakthroughs to increase the service life by mitigating the erosion at the base of the cracks. It is not believed by the authors at this time that the nitrided chemical process involved for nitriding to mitigate erosion was previously understood, other than that it increased the surface hardness. We now have a possible chemical rationale for nitriding gun barrels in that the nitrogen appears to either interfere with the dissociation of the carbon monoxide on the surface, or perhaps interfere with the diffusion of carbon into the substrate steel.

DISCUSSION

Nonequilibrium chemical kinetics have been incorporated in the erosion calculations. The user may input externally the reaction mechanism desired with standard kinetic rate parameters. For the iron-gas system a potential mechanism was investigated. One reaction coefficient was unknown for the mechanism and was estimated through a parametric study. Fortunately Grabke [17] investigated the specific dissociation of CO on the iron surface and reported the activation barrier. This enabled the inclusion of the reaction while an estimate of the reaction coefficient was made through a parametric study.

Nonequilibrium and equilibrium chemistry erosion computational results were presented. The differences are striking in that the equilibrium calculation shows much more down bore erosion than the nonequilibrium calculation and also is limited near the forcing cone by the control volume description. The nonequilibrium calculations show a larger influence of the reaction temperature than the equilibrium results when comparing tantalum to chromium. Tantalum may have more erosion than chromium under similar circumstances due to its physical properties.

The dissociation of CO is important and ways to mitigate it were investigated through a review of the literature. Ponec and Barneveld, [21] provided a clue that nitrogen or nitriding the surface may inhibit this dissociation. Experimentally this inhibition of CO dissociation may have been observed by Leveritt, Conroy, and Johnson [22] in new high energetic propellants.

REFERENCES

1. Weinacht, P., and Conroy, P. J., "A Numerical Method for Predicting Thermal Erosion in Gun Tubes," ARL-TR-1156, APG, MD, July 1996.
2. Conroy, P. J., Weinacht, P., and Nusca, M.J., "120-mm Gun Tube Erosion Including Surface Chemistry Effects," US ARL-TR-1526, ARL, APG, MD, 6 October 1997.
3. Conroy, P.J., Weinacht, P., Nusca, M. J., Rice, K., " Analytical Thermal and Erosion Investigation of the Extended Range 5" Navy Gun," Proceedings of 35th JANNAF Combustion Subcommittee Meeting, Tucson, AZ, December 1998.
4. Conroy, P.J., Weinacht, P., Nusca, M. J., "Erosion: A Parametric Study - Flame Temperature," US ARL-TR-1954, June 1999.
5. Conroy, P.J., Weinacht, P., Nusca, M. J., "Gun Tube Coatings in Distress," Proceedings of 36th JANNAF Combustion Subcommittee Meeting, Cocoa Beach, FL, October 1999.
6. Gerber, N., Bundy, M. L., "A Gun Barrel Heating Model that Includes Heat Input During Projectile Passage," ARL-TR-439, APG, MD, June 1994.
7. Ward, J.R., Brosseau, T. L., Kaste, R. P., Stobie, I. C., Bensinger, B., "Erosivity of LOVA Propellants," ARBRL-TR-02368, APG, MD, September 1981.
8. Jones, R.N., Breitbart, S., "A Thermal Theory for Erosion of Guns by Powder Gases," U.S. Army Ballistic Research Laboratories Report No. 747, Aberdeen Proving Ground, MD, January 1959.
9. Frankle, J.M., Kruse, L.R., "A Method for Estimating the Service Life of a Gun or Howitzer," U.S. Army Ballistic Research Laboratories Memorandum Report No. 1852, Aberdeen Proving Ground, MD, June 1967.
10. Lawton, B., "thermal and Chemical Effects on Gun Barrel Erosion," Proceedings of the 10th International Symposium on Ballistics, Orlando FL, October 1984.
11. Anderson, J.D., Hypersonic + High Temperature Gas Dynamics, McGraw Hill, NY, NY, 1989.
12. Nusca, M.J., "Numerical Simulation of Electromagnetic Wave Attenuation in Nonequilibrium chemically Reacting Flows," *Computers and Fluids*, Vol. 27, No. 2, pp.217-238, 1998.
13. Nusca, M.J., Dinavahi, S.P.G., and Soni, B., "Grid Adaptation Studies for Reactive Flow Modeling of Propulsion Systems," AIAA Paper 99-0970, Jan. 1999.
14. Nusca, M.J., McQuaid, M.J., and Anderson, W.R., "Numerical Simulation of an Open-Air Plasma Jet Using a Multi-Species Reacting Flow CFD Code," AIAA 2000-2675, June 2000.
15. Gordon, S., and McBride, B.J., "Computer Program for Calculation of Complex Chemical Equilibrium Compositions, Rocket Performance, Incident and Reflected Shocks, and Chapman-Jouget Detonations," NASA SP-273, NASA Lewis, Cleveland, OH, 1971.
16. Tsang, W., Hampson, R. F., "Chemical Kinetic Database for Combustion Chemistry Part 1. Methane and Related Compounds," Journal of Physical Chemistry Reference Data 15 , 1087, 1986.
17. Grabke, H. J., "Kinetics of the Oxygen Transfer from Carbon Dioxide to the Surface of Iron," Proceedings of the Third International Congress on Catalysis, Vol 2, pp. 928-938, Amsterdam, July 1964.
18. Baulch, D.L., Cobos, C. J., Cox, C. A., Esser, C., Frank, P., Just, Th., Kerr, J. A., Pilling, M. J., Troe, J., Walker, R. W., Warnatz, J., " Evaluated Kinetic Data for Combustion Modeling," Journal of Physical Chemistry Reference Data 21 , pp. 411-429, 1992.
19. Hubbard, C., Gilley, R., Bore Scope Records, Aberdeen Test Center, 1998.
    Ward, J.R., Brosseau, T.L., "Role of the Insulating Layer from TiO_2-Wax Liner in Reducing Gun Tube Wear,"ARBRL-TR-02238, Ballistic Research Laboratory, APG, MD, April, 1980.
20. Cote, P.J., Rickard, C., "Gas Metal Reaction Products in the Erosion of Chromium Plated Gun Bores," Wear, Volume 241, Issue 1, pp. 17-25, June 2000.
21. Ponec, V., van Barneveld, W. A., "The Role of Chemisorption in Fischer-Tropsch Synthesis," Journal of Industrial Engineering Chemical Product Research and Development, Vol. 18, No. 4, 1979.
22. Leveritt, C. S., Johnson, A. J., Conroy, P.J., "Characterization of the Erosivity of Advanced Solid Gun Propellants," Proceedings of 37th JANNAF Combustion Subcommittee Meeting, Monterey, CA, November 2000.

INTERNAL BALLISTICS ANALYSIS FOR THE RAVEN PROPULSION SYSTEM

S. Dunn, J. French, and D. Coats*
E. Kathe, R. Dillon, S. Sopok, and M. Witherell†

* *Software and Engineering Associates, Inc., 1802 N. Carson Street, Suite 200, Carson City, NV, 89701-1230, www.seainc.com.*
† *US Army, TACOM-ARDEC, Benét Laboratories, Watervliet Arsenal, NY 12189-4050*

ABSTRACT

The recently proposed light Future Combat System (FCS) vehicles require a highly lethal cannon with greatly reduced recoil momentum. A novel approach to this problem was proposed by Kathe[1], which utilizes a **RA**refaction wa**VE** gu**N** (**RAVEN**) propulsion system to significantly reduce the recoil momentum and barrel heating. To accurately assess the effectiveness of this approach, a Navier-Stokes flow solver was developed to calculate the internal ballistics of this unconventional hybrid propulsion system. The results of the internal ballistics analysis for the current 120mm M256 firing an M829A2 Kinetic energy round indicated that the proposed system could theoretically reduce the recoil momentum by 75% and reduce the barrel heating by 50%[1].

INTRODUCTION

The **RAVEN** propulsion system may be considered a hybrid technology with features common to both closed-breech cannons and recoilless rifles. The basic principal behind this concept is derived from the fluid dynamic laws which state that a disturbance can not travel faster than the speed of sound in addition to the local velocity of the gases through which it propagates. Therefore, if the gases at the breech plate are allowed to vent to the atmosphere at the time when the projectile is approximately one-forth the way down the barrel, the resulting rarefaction wave will not reach the projectile until it exits. The resulting recoil forces will be significantly reduced due to both the elimination of the high-pressure acting on the breech plate and the momentum of the venting gases.

The validity of the concept was initially supported by simple one-dimensional calculations and approximations, which subsequently required more rigorous verification. Unfortunately, the tools required to validate the **RAVEN** concept did not exist, although there was an existing internal ballistics computer code which had most of the required capabilities. The **G**un **T**ube **B**oundary **L**ayer (**GTBL**) code was developed for Benét Laboratory in support of calculating thermochemical erosion in gun tubes. The **GTBL** code is a time accurate Navier-Stokes analysis used to calculate the fluid flow and heat transfer in gun barrels including the effects of a moving boundary, spatial mass addition, chemistry, and spatial compressibility. The code incorporates a feature that allows adjustable boundary conditions for each boundary node, which may vary with time, pressure, or any other defined variable.

DISCUSSION

The **G**un **T**ube **B**oundary **L**ayer (**GTBL**) Code was developed as a collaborative effort between Software and Engineering Associates Inc. and ROYA Inc in support of Benét Laboratories[2]. **GTBL** is an adaptation of an earlier **L**iquid **T**hrust **C**hamber **P**erformance (**LTCP**) code that implements a multispecies/multiphase Navier-Stokes flow solver using a fully implicit discretization scheme[3]. The left and right states of the inviscid fluxes for both phases are based on the Total Variation Diminishing (TVD) method. The Lax-Friedrichs and Van-Leer methods are implemented for the gaseous phase to calculate the total inviscid fluxes by combining the left and right states. Both schemes are second order accurate in space.

The **GTBL** code required the extension of the **LTCP** code to include time and position dependent mass addition to model the burning of the propellant grains, and the moving boundary condition of the base of the projectile. Due to the extremely high pressures and gas densities, local compressibility effects were included. The code also had to be time accurate. The analysis incorporated the mass addition and moving boundary conditions provided by the **NOVA**[4] interior ballistics code. This enabled the leveraging of this existing and well-calibrated interior ballistic code to effectively drive the **GTBL** code. This approach effectively de-couples the two-dimensional flow challenges associated with burning rates, propellant grain form functions, bore friction, projectile motion, etc. Also, integration of the detailed interior ballistics model into the **GTBL** code would result in extensive challenges that would require almost all-available resources, and thus was not undertaken. Therefore, the **GTBL** development was concentrated on the higher fidelity interior ballistic flow characteristics associated with the **RAVEN** analysis.

Although the **GTBL** code has the capability to evaluate fully kinetic chemistry, the following analysis employed equilibrium chemistry. This is justified because of the extremely high-pressure levels and the relatively long characteristic times. This assumption reduced computer run time by a factor of more than ten-fold, without appreciably changing the validity of the solution. The **C**ompressible **C**hemical **E**quilibrium and **T**ransport Property Program (**CCET 1.5**™)[5] was used to generate a Mollier Chart of equilibrium gas properties, including the compressibility term. These tables were subsequently used by the **GTBL** code to evaluate the fluid dynamic properties and their derivatives. The baseline **GTBL** code was validated by comparison to **NOVA** and associated data. Although there are several unresolved discrepancies (for example, the temperature at the base of the projectile for **NOVA** is approximately 1000° higher than the adiabatic flame temperature, while the corresponding temperature for **GTBL** is near the adiabatic flame temperature), the overall comparison was favorable.

Adding the capability for the gases to exhaust to the atmosphere at the breech plate at a prescribed time required a significant program modification. Although the ultimate goal is to model a complete nozzle attached to the breech plate, the scope of the study required a scaled down approach. It was decided to uncouple the solution, with the subsonic portion included within the **GTBL** code, and the supersonic nozzle portion as a subsequent stand-alone analysis. Thus, the boundary conditions at the breech plate were modified to allow subsonic flow exiting the chamber at a prescribed time. This approach approximated the subsonic entrance portion of a converging-diverging nozzle section. The opening process was simulated by continuously changing the subsonic area ratio from a very large area ratio to the final value of approximately 1.05. The resulting subsonic Mach Number boundary condition went from near zero to 0.70. Both a *fast (opening time of 0.1 ms)* and *slow (opening time of 1.0 ms)* opening scenario were analyzed, which simulate a burst disk and an inertial system, respectively.

ANALYSIS: 120mm M256/M829A2 GUN SYSTEM

A **CCET 1.5™** analysis was performed for the M829A2 propellant to generate a Mollier Chart, which was subsequently used as input to the **GTBL** code. This table provides gas and transport properties over a large range of temperatures and pressures. Dr. S. Sopok of Benét Laboratory performed a **NOVA** analysis for an ambient temperature firing of the 120mm M256/M829A2 gun system. The results of the **NOVA** run, which were used as input to the **GTBL** code, included geometry and gas production rates. The **GTBL** analysis was run with 25 radial nodes and 151 axial nodes, which was determined to yield the minimum acceptable accuracy. The grid structures at the initial and final times are shown in Figures 1 and 2, respectively. All computations assumed an adiabatic wall boundary condition, since a cold wall boundary condition requires a much finer radial node spacing resulting in significantly longer run times.

The nominal baseline case without venting was run from the start of ignition until 0.0180 seconds, which accounted for virtually all of the recoil momentum. At the time the projectile reached the muzzle exit plane, the moving boundary condition was changed to a non-moving extrapolative boundary condition, allowing flow to exit the barrel. In order to maintain acceptable accuracy, approximately 45,000 time steps were taken. Typical internal ballistic pressure and temperature contours are shown in Figures 3 and 4.

The earliest time at which the chamber of a gun could be vented without compromise can be computed from the output of the above non-venting case. The speed of sound including the effects of compressibility can be calculated using the **CCET 1.5™** code. This value can then be added to the local gas speed to determine the speed at which a rarefaction wave would travel. The rarefaction wave may be assumed at the muzzle exit plane, with the base of the projectile at shot exit. The wave front may then be back propagated through time using Euler's method. The results for the above case (ambient temperature firing of an M829A2 out of an M256) are shown in Figure 5. Based on the above analysis, a venting time of 0.0038 seconds was chosen.

The fast opening scenario, which simulates a burst disk, assumed that at 0.0038 seconds the vent was closed, while at 0.0039 seconds the vent was fully opened. The opening process was approximated by a cubic 'S' function, whereby the subsonic area ratio was 10,000 at the start of opening and 1.05 when fully opened. For purposes of comparison, the same grid structure was used for all cases, with approximately 10,000 more time steps than the non-venting case. Corresponding internal ballistic pressure and temperature contours for the fast venting scenario are shown in Figures 6 and 7.

The slow opening scenario, which simulates an inertial system, assumed that at 0.0038 seconds the vent was closed, while at 0.0048 seconds the vent was fully opened. The opening process employed the same function as the fast opening scenario. As with the fast venting scenario, the same grid structure was used, with approximately 12,000 more time steps than the non-venting case. Resulting internal ballistic pressure and temperature contours for the slow venting scenario are shown in Figures 8 and 9.

RESULTS: 120mm M256/M829A2 GUN SYSTEM

Since the gas production term was taken from **NOVA**, the results of the baseline scenario were compared with **NOVA** output as a merit of consistency. It should be noted that **NOVA** is a

one-dimensional Euler analysis, while **GTBL** is an axially symmetric Navier-Stokes analysis. Therefore, the following comparison is for the **GTBL** centerline solution. Figure 10 shows the comparison of the pressures at the breech plane and projectile base, and Figure 11 shows the comparison of the temperatures at the same locations. Both solutions show remarkable agreement for the breech pressure, while the projectile base pressures show some divergence. This could be attributed to the fact that at each time **NOVA** uses a global compressibility term, while **GTBL** utilizes a local compressibility function. The compressibility variation for the Breech plane and projectile base is shown in Figure 12. The temperature comparisons show a basic inconsistency, whereby the **NOVA** temperature at the projectile base is almost 1000°R higher than the adiabatic flame temperature of the propellant. Also, the **NOVA** temperature at the breech plane is almost 1000°R lower than the adiabatic flame temperature. The **GTBL** temperature solution appears to be consistent with the adiabatic flame temperature (approximately 6300°R), and no further attempt has been made to resolve these differences.

Figures 13 through 16 show the pressure and temperature histories at the centerline for the breech plane and projectile base for the baseline, slow, and fast venting scenarios. Figure 17 shows the projectile velocity for the baseline, slow, and fast venting scenarios, which indicates that the velocity degradation is minimal. The above analysis has verified that the breech plane can be vented while the projectile has traveled a short distance in the barrel without a loss in muzzle exit velocity.

SUMMARY: 120mm M256/M829A2 GUN SYSTEM

The reduction of the recoil impulse is due to three effects: 1) lower pressure in the chamber, 2) elimination of pressure force acting on the breech plate, and 3) anti-recoil force from the momentum of the exiting gas out a converging-diverging nozzle. The impact of the first two effects is calculated by the **GTBL** code. The net force resulting from the flow out a converging-diverging nozzle was calculated by an auxiliary code, which used the **GTBL** boundary outflow conditions as nozzle entrance conditions. From basic nozzle flow analysis, it can be shown that the most efficient configuration incorporates a very small subsonic entrance area ratio, and as large as possible exit area ratio. Therefore, the following analysis assumed that the fully opened subsonic entrance area ratio was 1.05, with exit area ratios of 5 and 50.

Figure 18 shows the recoil force and impulse for the baseline scenario. Figure 19 shows the mass outflow history for the fast opening scenario. Figures 20 and 21 show the fast opening recoil force and impulse for exit area ratios of 5 and 50, respectively. Figure 22 shows the mass outflow history for the slow opening scenario. Figures 23 and 24 show the slow opening recoil force and impulse for exit area ratios of 5 and 50, respectively. Figure 25 shows a comparison of the recoil impulse for the baseline, fast and slow opening scenarios. It can be seen that the fast opening scenario with an exit area ratio of 50 reduces the total recoil impulse by approximately 75 percent.

For purposes of comparison, the heat transfer in the barrel was calculated from the **GTBL** boundary layer edge conditions, using the analysis incorporated in **NOVA**. Figure 26 shows a comparison of the cumulative heat input into the barrel for the **NOVA** analysis, and the **GTBL** baseline, fast, and slow venting analysis. The fast opening scenario reduces the total heat load by approximately 50 percent.

CONCLUSIONS: 120mm M256/M829A2 GUN SYSTEM

The above Navier-Stokes internal ballistic analysis verified that the basic **RAVEN** propulsion system significantly reduces the recoil momentum and barrel heating. The reduction was greatest for a fast opening scenario, which simulates a burst disk. The slow opening scenario, which simulates an inertial system, is shown to be less efficient, but is still quite effective. Although the feasibility of the **RAVEN** propulsion system has been shown to be sound, implementation has not been completed to date, and could pose a formidable task.

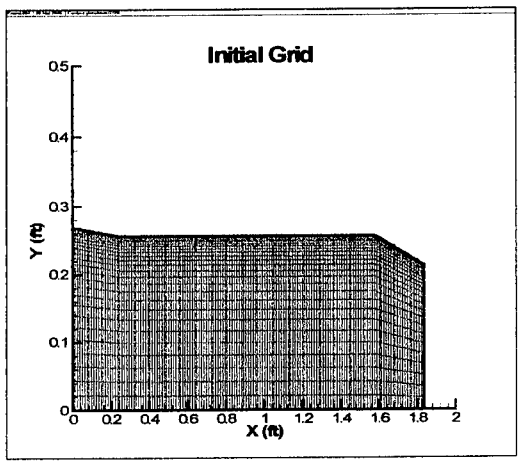


Figure 1. Initial Grid Structure

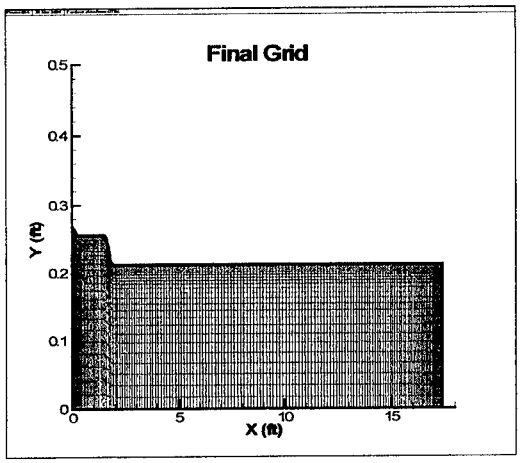


Figure 2. Final Grid Structure

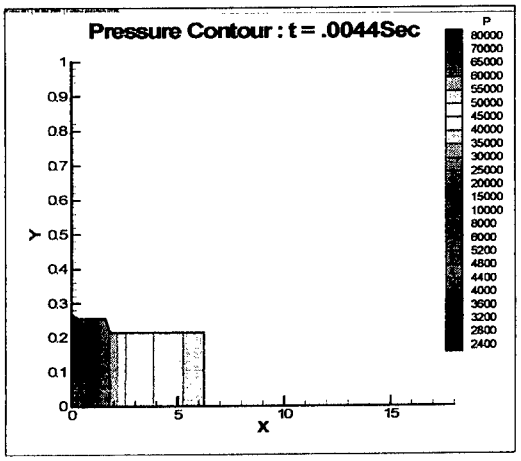


Figure 3. Pressure Contour for Baseline Scenario at t = .0044 Sec

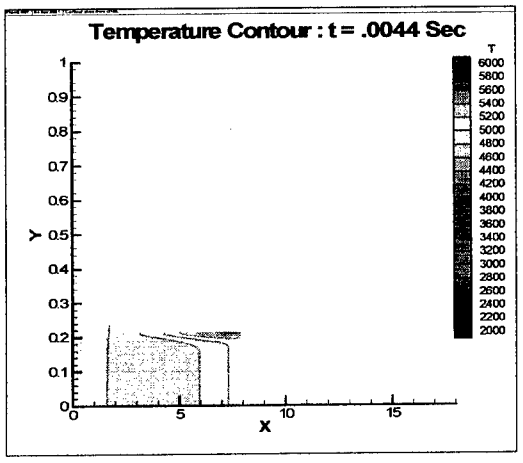


Figure 4. Temperature Contour for Baseline Scenario at t = .0044 Sec

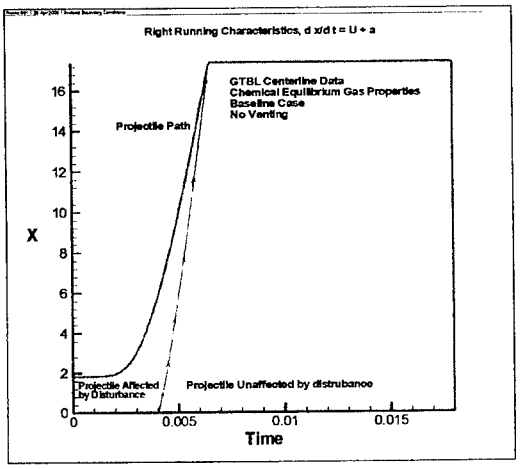


Figure 5. Propagation of Rarefaction Wave

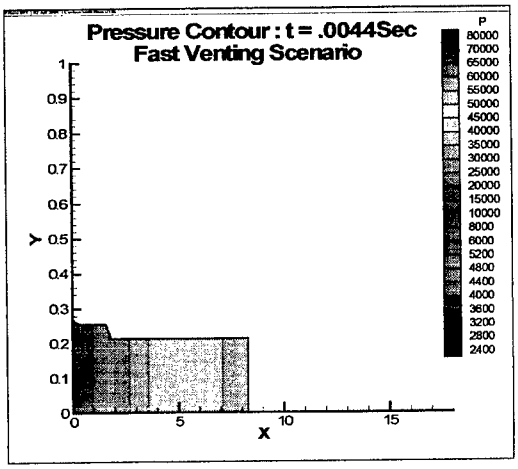


Figure 6. Pressure Contour for Fast Scenario at t = .0044 Sec

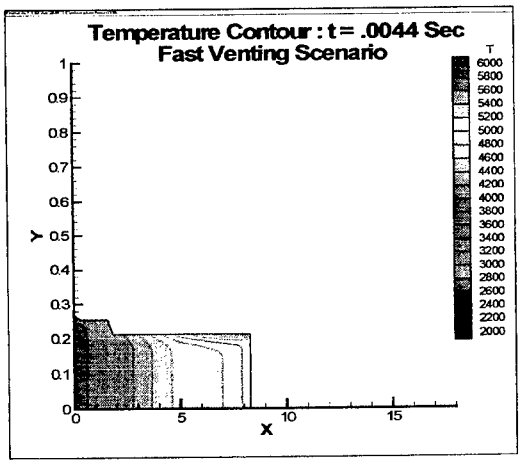


Figure 7. Temperature Contour for Fast Scenario at t = .0044 Sec

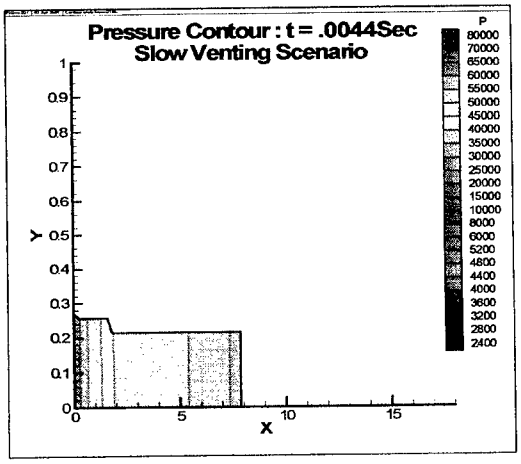


Figure 8. Pressure Contour for Slow Scenario at t = .0044 Sec

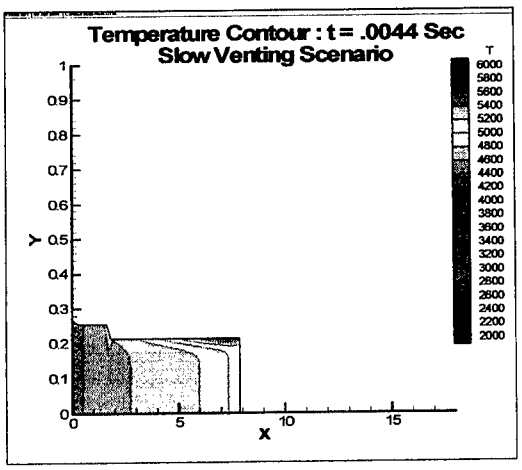


Figure 9. Temperature Contour for Slow Scenario at t = .0044 Sec

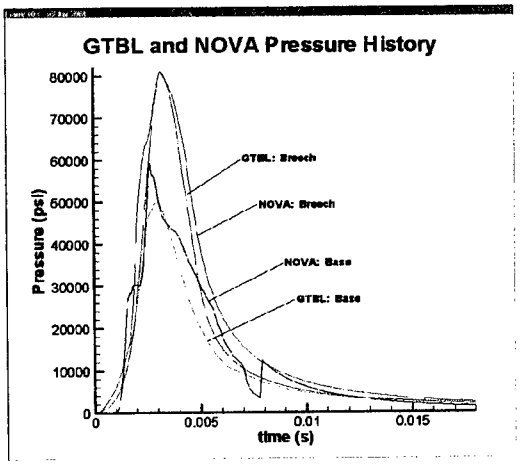


Figure 10. Comparison of GTBL and NOVA Pressure History at Breech and Projectile Base

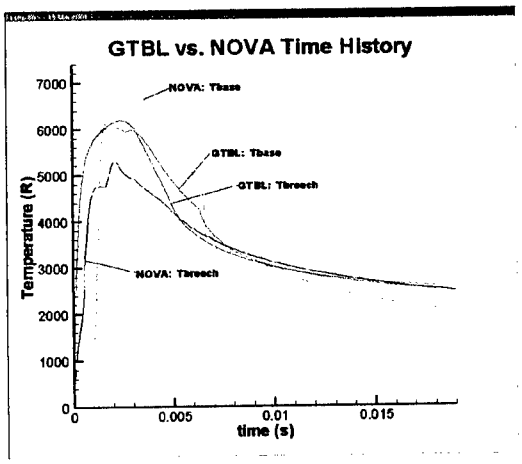


Figure 11. Comparison of GTBL and NOVA Temperature History at Breech and Projectile Base

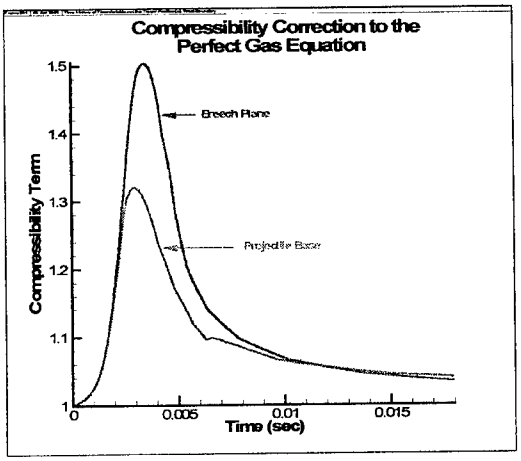


Figure 12. Compressibility Correction to the Perfect Gas Equation

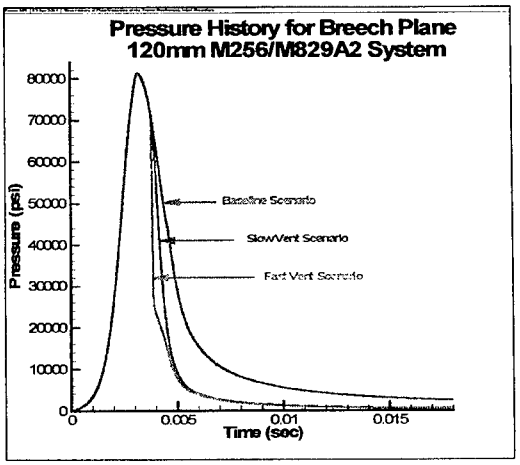


Figure 13. Pressure History for Breech Plane Centerline

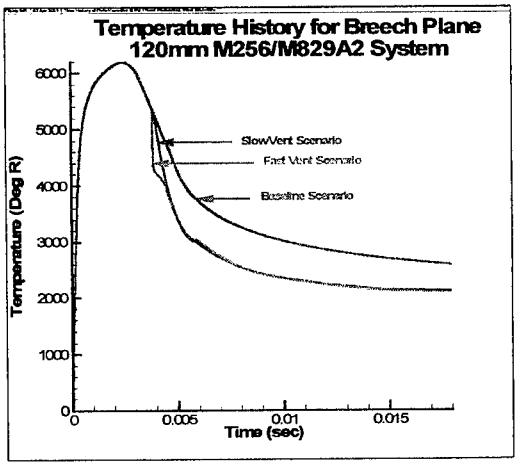


Figure 14. Temperature History for Breech Plane Centerline

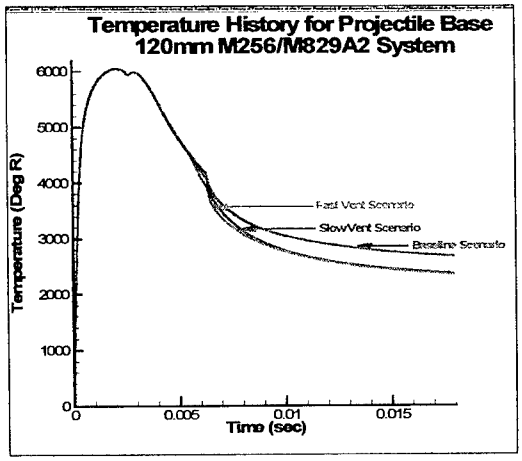


Figure 15. Pressure History for Projectile Base Centerline

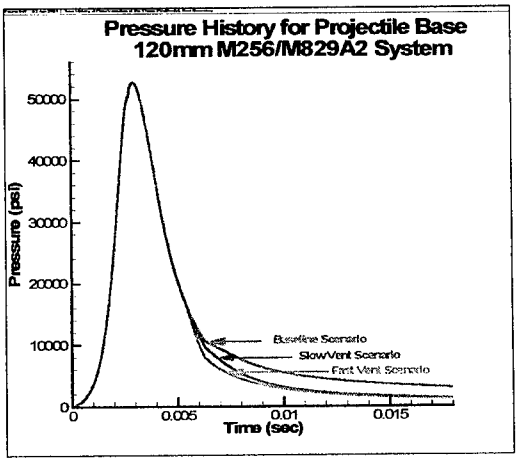


Figure 16. Temperature History for Projectile Base Centerline

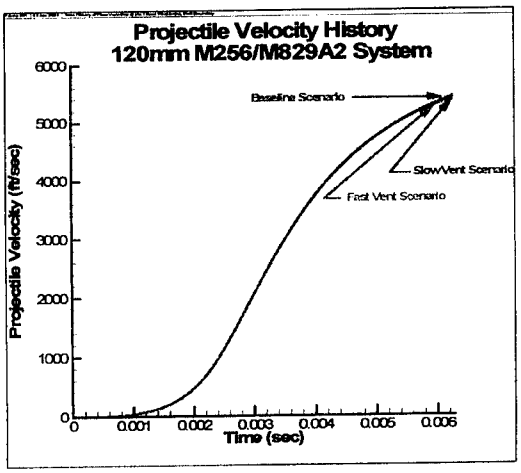


Figure 17. Projectile Velocity History

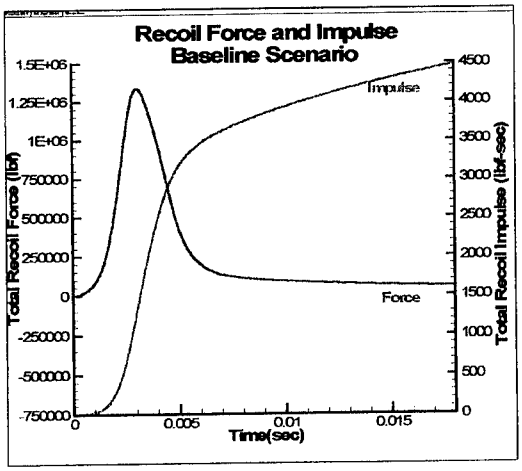


Figure 18. Recoil Force and Impulse for Baseline Scenario

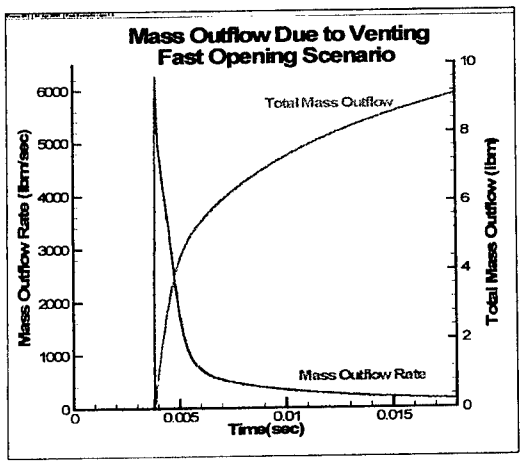


Figure 19. Mass Outflow Due to Venting for Fast Scenario

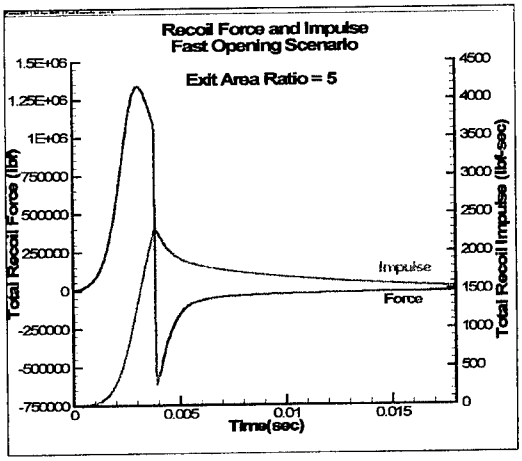


Figure 20. Recoil Force and Impulse for Fast Scenario, Eps=5

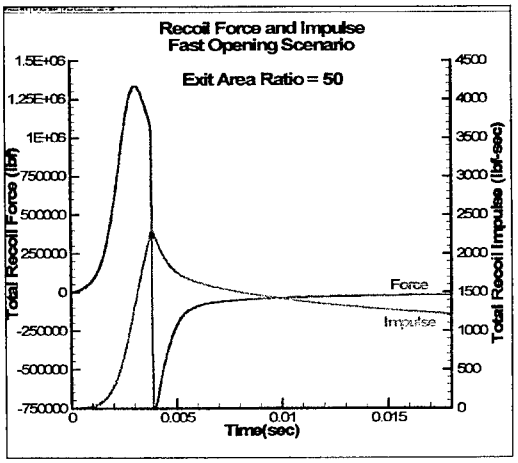


Figure 21. Recoil Force and Impulse for Fast Scenario, Eps=50

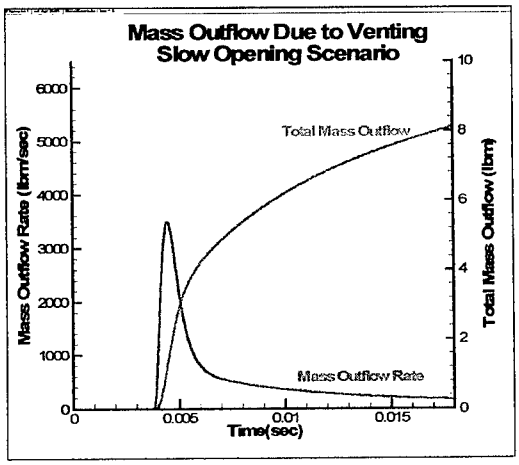


Figure 22. Mass Outflow Due to Venting for Slow Scenario

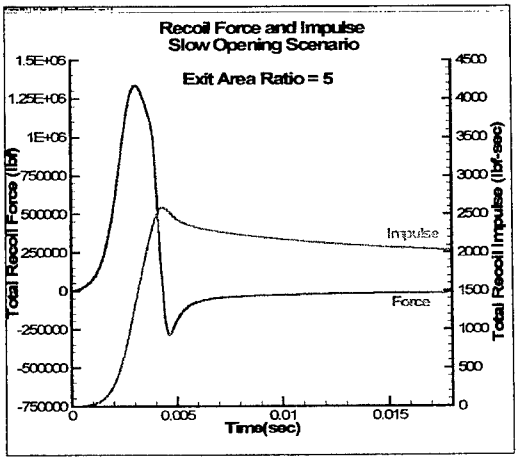


Figure 23. Recoil Force and Impulse for Slow Scenario, Eps=5

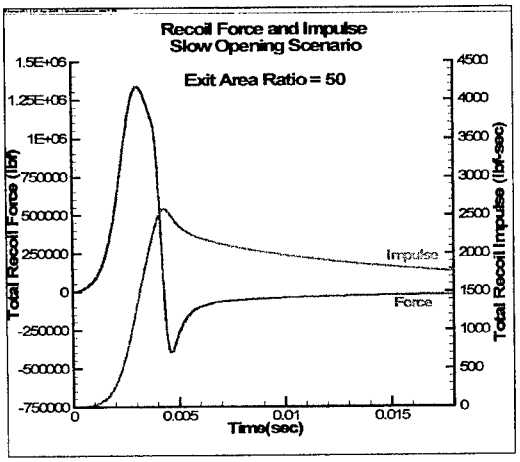


Figure 24. Recoil Force and Impulse for Slow Scenario, Eps=50

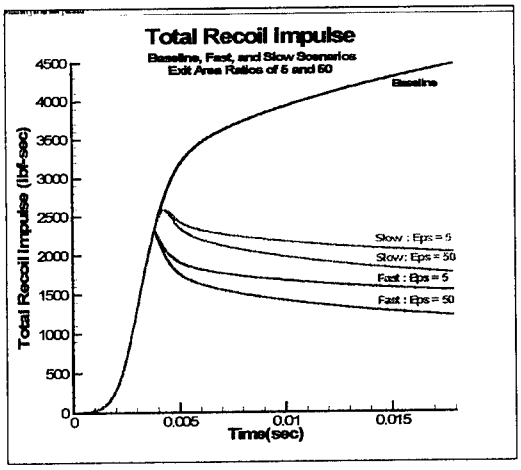


Figure 25. Total Recoil for Baseline, Slow, and Fast Scenarios

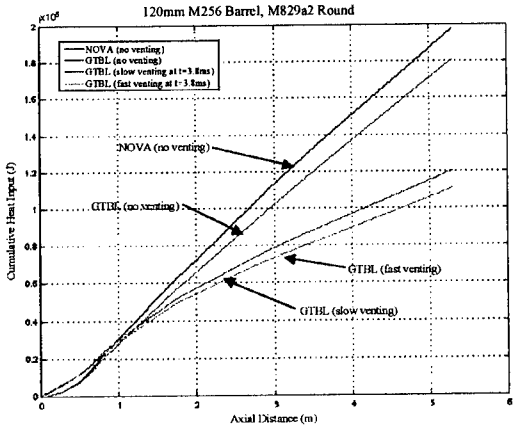


Figure 26. Effects of Venting on Barrel Heat Transfer

REFERENCES

1 Kathe, E., Dillon, R., Sopok, S., and Witherell, M., "Sonic Rarefaction Wave Low Recoil Gun," AIAA Paper Number AIAA-2001-0743, presented in Reno, NV, January 2001.

2 Navaz and Dunn, "A Computer Model for Gun Barrel Flow Analysis: The Gun Tube Boundary Layer Code (GTBL)," Final Report, Software and Engineering Associates, Inc., Carson City, NV, September, 1999

3 Navaz and Dang, "LTCP: Liquid Thrust Chamber Performance Computer Code," NASA Contract NAS 8-38798, Physical Research, Inc. Irvine CA, November, 1992

4 Gough, P., "The XNOVAKTC Code," U.S. Army BRL-CR-627, Paul Gough Associates, Portsmouth, NH, 1990.

5 Dunn, S., Coats, D., and Sopok, S., "A New Chemical Equilibrium Code with Compressibility Effects," Proceedings of the 33rd JANNAF Combustion Meeting, Monterey, CA, October 1996.

Recoil Reduction Using Propellant Gas

E. Kathe[1]

[1] *U.S. Army Benét Labs TACOM-ARDEC, Building 115, Watervliet, NY 12189*

Rarefaction wave gun (RAVEN) propulsion has renewed interest in the fundamental limits of recoil reduction attainable by redirecting propellant gases rearward from a gun without compromising the projectile propulsion. Traditionally, this has only been achievable through the use of muzzle brakes. RAVEN's unique ability tap into the internal energy of propellant gases that are not gainfully employed to propel the projectile may be considered analogous to efforts to mechanically close the muzzle of a gun at shot exit to drive all of the propellant gases through a muzzle brake. The recoil reduction potential for RAVEN and current technology muzzle brakes will be extrapolated across viable gas gun velocities using simple empirical relationships. The quantitative findings of this parametric study must be considered to provide perspective as opposed to true predictions because of the extrapolated nature of the study; particularly at higher muzzle velocities.

INTRODUCTION

RAVEN propulsion has been proposed as a radical departure from current closed breech guns to dramatically reduce recoil momentum and heat transfer to future guns [1, 2]. It is based on the simple premise that a rarefaction wave can travel no faster than the combined gas and sonic velocities through which it propagates. Thus, a gun system designed to vent the breech end of the chamber after the bullet has begun its travel down the bore would release a forward traveling rarefaction wave. Compromise of the projectile propulsion could only occur after the rarefaction wave front was able to reach the base of the bullet. Surprisingly, it has been shown that the rarefaction wave released by venting the back of the chamber of a current 120mm tank gun firing an M829A2 will not reach the bullet prior to shot exit if the release occurs after the bullet has traversed only one fourth of the launcher travel [2]. The time delay between venting and the rarefaction wave front reaching the base of the bullet and muzzle simultaneously is estimated to be 2.5 ms. During this period of concurrent venting and projectile propulsion, half of the propellant gas may be exhausted rearward out an expansion nozzle to negate some portion of the recoil momentum initially imparted to the gun. The hastened blow down of such a launcher will be rearwards, drawing fresh air into the muzzle upon its completion. It has been estimated that such a launcher will eliminate three quarters of the closed breech recoil momentum and reduce the heat transfer to the bore substantially [2].

SPECIFIC IMPULSE OF GUN PROPELLANT GASES AFTER PROPELLING A PROJECTILE

In the following analysis it will be assumed that the gas constant is specific to the propellant gas. Thus:

Eq. (1) $R = R_u / mm$

Using SI units, R_u is equal to 8,314 J/kmol/K. The molecular mass, *mm*, of common propellants is near 25 kg/kmol.

It is worth noting the specific heat for constant pressure minus the specific heat for constant volume is equal to the gas constant. [3, Eq. (5.27)] Thus, the specific heats may be related to the gas constant and ratio of specific heats as [3, Eq.s (7.30-31)]:

Eq. (2) $\gamma = C_p / C_v$

Eq. (3) $C_v = R/(\gamma - 1)$

Eq. (4) $C_p = \gamma R/(\gamma - 1)$

This application of perfect gas theory to interior ballistics must be considered an approximation whose validity often falls into question but never the less is employed in interior ballistic analysis. [4, pp. 1.2, 1.15] Until experimentally validated, analysis based on these assumptions should be considered an estimate that provides perspective; however, that traditional interior ballistics has employed these assumptions lends a strong precedent.

The internal energy of the propellant after the burn is commonly computed via the gas constant multiplied by the adiabatic flame temperature divided by the ratio of specific heats minus one. The terms in the numerator are typically known as the propellant "force" [3, Eq. (1-6)] while the energy release per mass unit of propellant is termed the specific energy or propellant potential [3, pp. 1.15] or the heat of explosion [6, pp. 84].

Eq. (5) $$U_o = m_c C_v T_o = m_c \frac{RT_o}{(\gamma - 1)}$$

Regardless of the ultimate motion of the gases, internal energy of the gas will be expended on kinetic energy imparted to the projectile and heat transfer to the cannon walls and base of the projectile. Corner has argued that heat transfer to the gun may be reasonably assumed proportional to the muzzle energy with heat transfer rarely more than 30% of the muzzle energy [5, pp. 141]. It has been estimated that RAVEN will reduce net heat transfer by one third [2]. Assuming heat transfer to be about 20% of the muzzle energy, these combined energies (six fifths of the muzzle energy) may be removed from the heat of explosion.

Eq. (6) $$U_1 = m_c \frac{RT_o}{(\gamma - 1)} - \frac{3}{5} m_p v_p^2 = m_c C_v T_1 = m_c \frac{R}{(\gamma - 1)} T_1$$

One may consider the remaining energy in Eq. (6) to be the energy of the propellant gases following shot exit if the muzzle of the gun were corked behind the bullet and all of the gases were to come to rest adiabatically. The temperature of these gases, T_1, is of interest and may be computed as:

Eq. (7) $$T_1 = T_o - \left(\frac{3}{5} m_p v_p^2\right) \Big/ \left(m_c C_v\right) = T_o - \frac{3(\gamma - 1)}{5R}\left(\frac{m_p}{m_c}\right) v_p^2$$

This temperature will be used as an approximation to compute the reservoir gas energy and enthalpy available to drive the gases through a de Laval nozzle.

The relationship between gas flow through a nozzle is based on the first law of thermodynamics as expressed via the Bernoulli equation. Neglecting gravitational forces as small, the change in kinetic energy of the gases may be directly related to the change in enthalpy [3, Eq. (14.21)]. The enthalpy, like the internal energy, is a function only of temperature. Using ideal gas assumptions [3, Eq. (5.29)] we arrive at:

Eq. (8) $$H_1 = m_c C_p T_1 = m_c \frac{\gamma R}{(\gamma - 1)}\left(T_o - \frac{3(\gamma - 1)}{5R}\left(\frac{m_p}{m_c}\right) v_p^2\right) = m_c\left(\frac{\gamma R}{\gamma - 1}\right) T_o - \frac{3}{5}\gamma m_p v_p^2$$

Using Bernoulli's equation, the kinetic energy of the propellant gases exhausted from the gun system will decrement the enthalpy [3, Eq. 14.21].

Eq. (9) $$H_2 + \frac{1}{2} m_c v_c^2 = H_1$$

The temperature of the gases as they depart the nozzle, T_2, is related to the magnitude of the exhaust velocity and is of interest:

Eq. (10) $$v_c = \sqrt{\frac{2}{m_c} m_c C_p (T_1 - T_2)} = \sqrt{2\left(\frac{\gamma R}{\gamma - 1}\right)(T_1 - T_2)}$$

If the gun were to discharge into a vacuum through an arbitrarily large nozzle, the gases would theoretically cool to absolute zero if elements of reality such as condensation of the gas into a liquid would not occur. Setting T_2 to zero constitutes an upper bound on the exhaust velocity magnitude. Doing this in Eq. (10) results in the accepted value for this thought exercise [7, Eq. (6.10)].

Exactly how much the gas cools and is accelerated is a function of the nozzle design. It is well known that guns have ample gas energy and pressure to meet the requirements for de Laval nozzle design to reach the sonic velocity at the throat through the vast majority of the gas discharge event [3, pp. 2.48]. (For common propellants, the ratio of atmospheric (discharge) pressure to chamber pressure need only be 0.55 [5, pp. 248].)

Heat conduction and other loss factors within the nozzle are also assumed negligible. [3, pp. 2.48] Empirical evidence supports that nozzle inefficiencies only detract from the theoretical values by a few percent [5, pp. 248]. Further, the effect of co-volume on thrust is considered small and is also neglected [3, pp. 2.49]. Corner has quantified an upper bound for the co-volume effect to be 6.5% for reasonable guns [5, pp. 251].

What remains is the geometric expansion ratio of the nozzle from the throat to the exit plane. The relationship between expansion ratio and Mach number is provided below [3, Eq. (14.46)]:

$$\text{Eq. (11)} \quad \frac{A}{A^*} = \frac{1}{M}\left[\left(\frac{2}{\gamma+1}\right)\left(1+\frac{\gamma-1}{2}M^2\right)\right]^{(\gamma+1)/2(\gamma-1)}$$

The resulting relationship between Mach number at exit and the expansion ratio from the throat is shown in Fig 1 for two different ratios of specific heat that are common for gun propellants.

Perspective on reasonable area ratios for large caliber guns may be gained by looking at the cross-sectional area of current breech rings as compared to the bore area. This ratio is approximately 15.5 and 18.5 for the 105mm M35 and 120mm XM291 guns respectively. If one were to incorporate a modestly larger expansion nozzle, say 50% larger in diameter than the breech ring, while venting through a throat of bore area, the expansion ratio would be 40, and result in an exit Mach number of nearly four. The later analysis is not particularly sensitive to this number, so four will be used.

The temperature of the gases exhausting out the reservoir may be related to the Mach number as below [3, Eq. 14.37d]:

$$\text{Eq. (12)} \quad \frac{T_1}{T_2} = 1+\frac{(\gamma-1)}{2}M^2$$

Recalling the derivation of the reservoir temperature in Eq. (7), the temperature of the gases as the exit the expansion nozzle may be computed as follows:

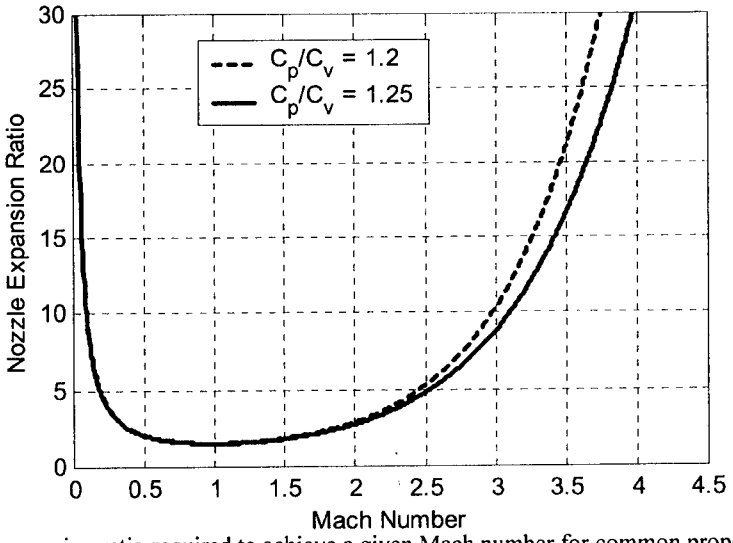


Fig 1. Nozzle expansion ratio required to achieve a given Mach number for common propellant gases.

Eq. (13) $$T_2 = \left[T_o - \frac{3(\gamma-1)}{5R}\left(\frac{m_p}{m_c}\right)v_p^2 \right] \Big/ \left[1 + \frac{(\gamma-1)}{2}M^2 \right]$$

More directly, Eq. (12) may be used to compute the temperature difference within Eq. (10):

Eq. (14) $$T_1 - T_2 = \left(\frac{(\gamma-1)}{2}M^2\right)T_2 = \left(\frac{(\gamma-1)}{2}M^2\right)\frac{\left[T_o - \frac{3(\gamma-1)}{5R}\left(\frac{m_p}{m_c}\right)v_p^2 \right]}{\left[1 + \frac{(\gamma-1)}{2}M^2 \right]}$$

The magnitude of the exhaust velocity may be computed by inserting the results of Eq. (14) into Eq. (10) and simplifying:

Eq. (15) $$v_c = \sqrt{\frac{\left(\gamma R M^2\right)\left[T_o - \frac{3(\gamma-1)}{5R}\left(\frac{m_p}{m_c}\right)v_p^2 \right]}{\left[1 + \frac{(\gamma-1)}{2}M^2 \right]}}$$

It may be seen that the effect of the energy imparted to the projectile and the approximation for heat transfer to the gun and projectile may be interpreted as a decrement on the adiabatic flame temperature.

To lend perspective on this it is known that the projectile velocity may be estimated as 1,500 m/s multiplied by the root of the ratio of charge to projectile mass where this ratio is nearly unity. (This relationship will be employed later and referenced in Eq. (17).) Using this approximate relationship the projectile to charge mass ratio of Eq. (15) and the ratio of charge to projectile mass used to estimate the square of the velocity cancel. Assuming representative gas properties similar to JA2 with a molecular weight of 25 Kg/kmol and a ratio of specific heats of 1.225 the temperature decrement may be estimated to be 913 K. For the representative case at hand, using a propellant with an adiabatic flame temperature of 3,400K and a Mach four nozzle, the velocity is 2.4 km/s. This is about 400m/s slower than it would be without the energy lost to the projectile propulsion and heat transfer, which indicates a lack of strong sensitivity to the energy lost to gun propulsion. (For those who prefer specific impulse expressed as momentum per unit weight, 2.4 km/s = 2.4 kN*s/Kg => 245 lb*s/lb = 245 s.)

The result of Eq. (15) constitutes the purpose of this derivation. It represents a realistic upper bound on the specific impulse that could possibly be attained from the propellant gases used to propel a bullet out a gun with out regard to the mechanism used to achieve it. This upper bound is relevant for any RAVEN launcher as well as any clever muzzle

brake devices that would obstruct the bore at the muzzle following shot exit. It is also a valid upper bound for recoil amplifiers (nozzle's at the muzzle used to increase recoil momentum imparted to the gun, occasionally used for recoil operated automatic weapons.) We may now say with confidence using Eq. (15) that the net rearward recoil imparted to any gun will be bracketed as follows:

$$\text{Eq. (16)} \quad m_p v_p + m_c v_c < net\ rearward\ recoil < m_p v_p - m_c v_c$$

The left side corresponds to a recoil amplifier ejecting gases forward and the right side to recoil abatement that ejects gases rearward. The left side corresponds to the greatest rearward momentum that could be imparted to the gun. The right side corresponds to the least rearward momentum. For current high performance kinetic energy rounds, there exists sufficient specific impulse in the propellant gases to completely negate the rearward momentum imparted by the projectile and generate a net forward momentum. Accessing the specific impulse of the propellant gas to encroach upon recoillessness with little if any compromise in projectile propulsion is the intent behind RAVEN.

A PARAMETRIC STUDY

To lend perspective on recoil momentum, a parametric study will consider the momentum imparted to a gun as a function of the muzzle velocity. It will be assumed that virtually no degradation in projectile propulsion will be tolerated. Therefore, schemes such as prior recoilless rifles [7] or achieving recoil reduction through large muzzle brakes employed by guns of low expansion ratio with large charge to propellant mass ratio rounds [5, pp. 391] will not be considered.

A simple and reasonably accurate empirical relationship to determine muzzle velocity as a function of the charge to projectile mass ratio for fielded guns has been published by Ogorkiewicz. [8, Eq. 4.8]

$$\text{Eq. (17)} \quad v_p = (1{,}500 m/s)\left(\frac{m_c}{m_p}\right)^{0.45}$$

The approximation is depicted in Fig 2 for various charge to projectile mass ratios. Included are real performance points largely drawn from Stiefel [9] with the inclusion of a current 120mm M829A2 round. A similar relationship has been made by Schmidt [10] that is within 5% agreement over most of the ratios and within 2% for high-speed rounds.

Although enhancement of this empirical relationship could be made, it's unaltered fidelity is more than adequate for the current purposes. Although Eq. (17) may appear purely empirical, the square root of the charge to projectile mass ratio can be interpreted as a simple energy balance between the chemical energy of the charge mass and the kinetic energy of the projectile. The difference between the 0.5 and 0.45 power that remains may be considered a velocity dependent efficiency factor that penalizes higher velocities more so than lower ones.

The momentum of closed-breech launch may be broken down into three components corresponding to the projectile momentum, momentum imparted to the gases up to shot exit, and the momentum imparted during the blow-down of the gases after shot exit. The momentum is often termed the impulse of the round and will be denoted by I. Assuming constant gas density along the length of the gas column and a linear propellant gas velocity gradient along the length of bore from rest at the breech to projectile velocity at the base of the projectile at shot exit, the center of mass of the propellant gas may be approximated as traveling at one half the projectile velocity. There exists no simple and accurate formula for the blow-down or post-ejection momentum, I_{BD}, although an approximation will later be made.

Eq. (18) $$I = m_p v_p + m_c\left(v_p/2\right) + I_{BD}$$

Maintaining a separation between the gas momentum prior to and after shot exit will facilitate the use of formulae for the momentum reductions afforded by muzzle brakes.

A simple empirical rule for the estimation of the average outflow velocity of all the propellant gases relates the velocity to the sonic velocity of the gases at the muzzle and the projectile velocity. Such empirical estimations cannot be held in high regard, but for the purpose of providing reproducible and easily understood results they are of value. The sonic velocity may be estimated as 1,000 m/s and the resulting velocity computed as below [6, Eq. 64]:

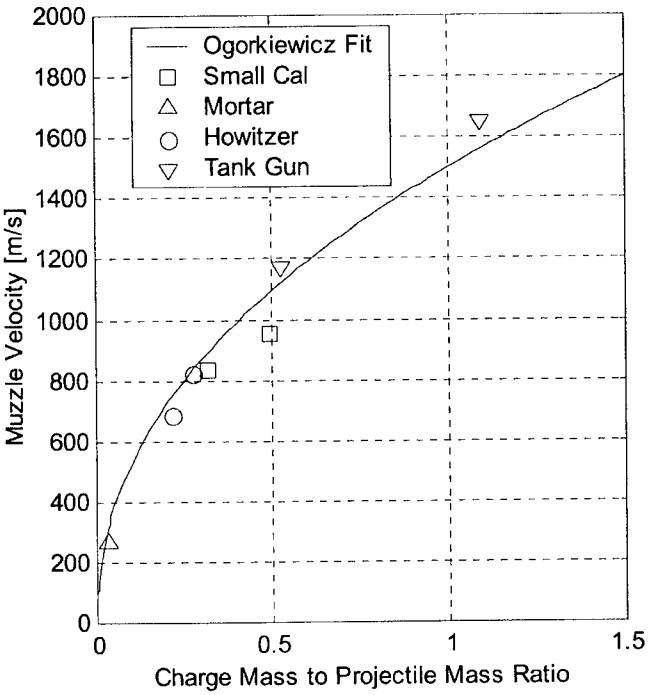


Fig 2. Empirical relationship between charge to projectile mass ratio and muzzle velocity.

Eq. (19) $$v_m = m_c\sqrt{(1{,}000m/s)^2 + v_p^2}$$

Thus the blow down momentum may be computed as:

Eq. (20) $$I_{BD} = m_c\left(\sqrt{(1{,}000m/s)^2 + v_p^2} - \frac{v_p}{2}\right)$$

There is particular reason to be concerned about the fidelity of Eq. (19) as historically, when such empirically supported relationships were generated, terms of the order of the charge to projectile mass ratio squared were considered small and ignored [5, pp. 365]. For current tank ammo this ratio is near unity and may call into question the results. However, no mention of this historical assumption that would not be valid is included in reference 6.

There are currently two different methods used to predict the performance of muzzle brakes based upon the recoil momentum imparted to guns. Unfortunately, both are termed beta, β. The first method attributed to Oswatitsch relates the recoil reduction to the entire gas momentum imparted during normal launch ($m_c v_m$ using Eq. (19)) [11]. The second method championed by Corner and used here relates the momentum reduction as a ratio of the blow-down momentum. [12, Eq.s 3.37-39] Thus:

Eq. (21) $$I = m_p v_p + m_c(v_p/2) + (1-\beta)I_{BD}$$

Although strictly incorrect, it is often assumed that a physical limit of muzzle brakes is that their performance could not exceed a complete reversal of the entire gas momentum relative to a gun with out a muzzle brake. (This would be an Oswatitsch beta of two.) This belief is analogous to the actual performance limit of impulse bucket design for hydraulic turbines, where the working fluid is incompressible. The potential to expand the gases from the muzzle pressure to atmospheric pressure within a nozzle is what is missing in this limit. Despite the lack of validity to this upper performance limit, design considerations have kept the muzzle brakes of practical weapons substantially below this perceived limit.

Using the theoretical limit of rearward gas velocity attainable from Eq. (15), a theoretical lower bound on the impulse may be derived as below:

Eq. (22) $$I_{LB} = m_p v_p - m_c v_c$$

It is postulated that the performance of RAVEN will be very closely related to the percentage of the charge mass that is ejected out the rear expansion nozzle. This will be termed alpha, α. The utility of a muzzle brake for a RAVEN may be substantial. For lack of a better model, the specific forward impulse imparted to that portion of the propellant gases ejected out the muzzle will be assumed equivalent to the close breech case using Eq. (19). The specific impulse of the portion of the gases ejected out a rearward facing Mach 4 nozzle will be assumed to be that computed using Eq. (15). The use of an aggressive muzzle brake may be anticipated to reduce the specific impulse of the muzzle

gases to zero. (Loosely speaking this could be considered a beta of unity.) Actual RAVEN performance may be anticipated to occur between these two limits.

Eq. (23) $$m_p v_p - \alpha m_c v_c < I_{RAVEN} < m_p v_p + (1-\alpha) m_c v_m - \alpha m_c v_c$$

In a manner analogous to the RAVEN impulse, the momentum imparted to a closed breech gun (α = 0%) that may incorporate a muzzle brake may be considered practically limited by a brake that eliminates all gas momentum. Thus:

Eq. (24) $$m_p v_p < I_{Closed\ Breech} < m_p v_p + m_c v_m$$

These results are plotted in Fig 3 for α equal 0%, 50%, 75%, 90%, and 100%. The example used JA2 with a ratio of specific heats of 1.225, a molecular mass of 24.865 Kg/kmol, and an adiabatic flame temperature of 3410K. The dotted lines passing through the close breech field are the impulses for a gun employing a perforated (β = 0.700) brake, single baffle brake (β = 0.910), and a double baffle brake (β = 1.351). The performance of the first is based on the Benet designs for the 105mm EX35 and 155mm XM297 while the later two are found in the literature [12, Table 3-3]. It is worthy to note that the back blast directed at the turret by the perforated muzzle brake on the EX35 tank gun was too aggressive for fielding where the crew was required to be allowed to fire with hatches open and double ear protection. It was therefore removed prior to type classification as the M35. It must also be reiterated, that the empirical relationships employed here must be considered extrapolations, and therefore are meant only to provide perspective.

Independent evaluations of RAVEN firing an M829A1 or M829A2 round from and M256 based gun system indicate that about two thirds of the charge mass will be ejected out the back [2]. This would place the anticipated RAVEN performance between the 50% and 75% regions. The recoil reduction estimates for the analyses is between 66% and 75% for a 1650m/s or so round velocity and no muzzle brake [2]. Examination of the plot confirms that reduction in momentum. Validation of this mix of analytical and empirical analysis by comparison to unvalidated computational fluid dynamic models provides optimism that it is reasonable. However, without experimental validation, this form of validation between models may be considered unsound.

CONCLUSIONS

A reasonably well-founded upper limit on the specific impulse remaining in propellant gases that have been employed to fire a bullet out of the gun has been identified. This limit may be used in a manner analogous to the Carnot cycle limit for heat engines to determine the viability of later RAVEN impulse reductions predictions arrived at through computational fluid dynamics (CFD) analysis efforts.

Perspective has been shed on the limits of current technology muzzle brakes to reduce recoil momentum. It was pointed out that the use a moderate performance perforated muzzle brake was considered too aggressive for a tank gun where the crew was to maintain the ability to fire with hatches open and double ear protection.

Prior simulations of RAVEN have indicated that it may vent two thirds of the propellant gas rearward through an expansion nozzle, thus eliminating three fourths of the recoil momentum. This earlier result was placed into a context where it could be considered reasonable, and within the thermodynamic feasibility of interior ballistics.

Estimations of performance of future RAVEN configurations and muzzle brakes may be drawn from simple relationships developed in this work. However, discretion is advised to the extrapolated nature of the predictions. The intent has been to provide perspective.

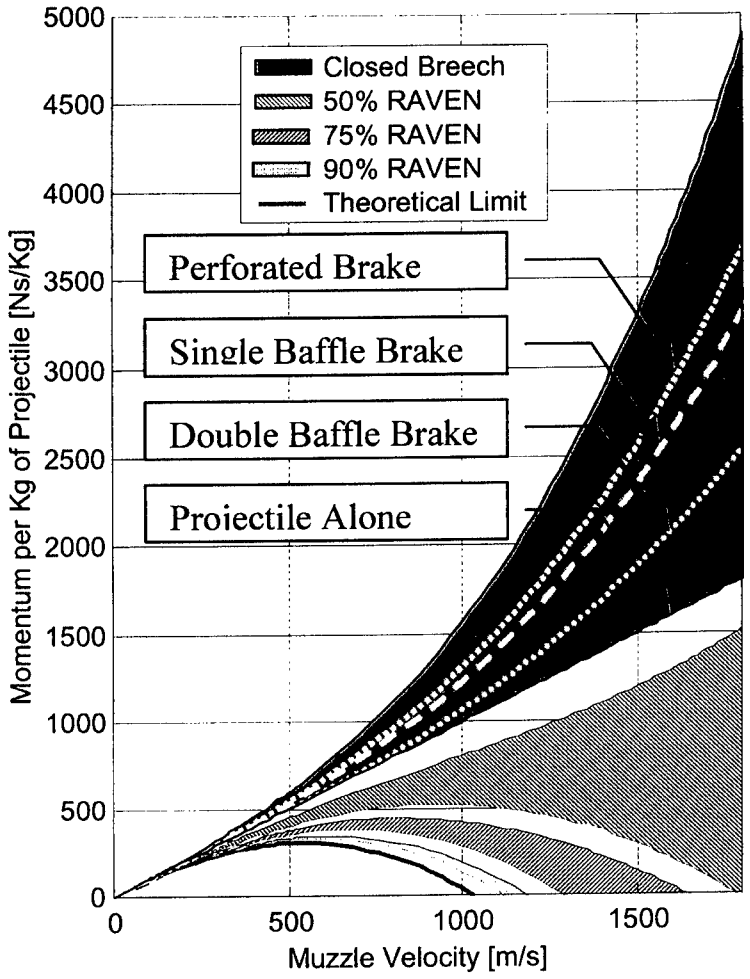


Fig 3. Specific impulse as a function of muzzle velocity up to 1,800 m/s.

REFFERENCES

1. Kathe, E., "Sonic Rarefaction Wave Recoilless Gun System," US Patent Application Serial Number 09/631142, 2 August 2000.
2. Kathe, Dillon, Sopok, Witherell, Dunn, and Coats, "Rarefaction Wave Gun Propulsion," JANNAF Interagency Propulsion Committee, Joint Meeting, 13-17 November 2000, Monterey, CA.
3. Van Wylen, G. J. and Sonntag, R. E., *Fundamentals of Classical Thermodynamics*, 3rd Edition, SI Version, Wiley, New York, 1985.
4. Jones, R. N., Hitchcock, H. P., and Villegas, D. R., *Engineering Design Handbook: Ballistics Series: Interior Ballistics of Guns*, AMC Pamphlet AMCP 706-150, US Army Material Command, Alexandria, VA, February, 1965.
5. Corner, J., *Interior Ballistics of Guns*, Wiley, New York, 1950.
6. Germershausen, R. and Melchior, E., "Internal Ballistics," in *Handbook on Weaponry*, First English Edition, Rheinmetall GmbH, Düsseldorf, Germany, 1982.
7. Olcer, N. Y., and Levin, S., *Engineering Design Handbook: Recoilless Rifle Weapon Systems*, AMC Pamphlet AMCP 706-238, US Army Material Command, Alexandria, VA, January 1976.
8. Ogorkiewicz, R. M., *Technology of Tanks: Volumes I and II*, Jane's Information Group, Surrey, UK, 1991.
9. Stiefel, L., "Pressure-Time-Velocity-Travel Relationship in Typical Gun Systems," in *Gun Propulsion Technology*, Stiefel, L. (ed), AIAA, Washington, 1988.
10. Schmidt, E. M., "Recoil Characteristics of Electromagnetic Cannon," in *Proceedings of the Ninth U.S. Army Symposium on Gun Dynamics*, Kathe, E. (Ed.), TACOM-ARDEC Benet Laboratories Report ARCCB-SP-99015, November 1998, pp. 22.1-5.
11. Schmidt, E. M., "Muzzle Flow Gasdynamics," in *Gun Propulsion Technology*, Stiefel, L. (ed), AIAA, Washington, 1988.
12. Franklin Institute, Philadelphia, PA, *Engineering Design Handbook: Guns Series: Muzzle Devices*, AMC Pamphlet AMCP 706-251, US Army Material Command, Alexandria, VA, May, 1968.

RELATIVE EROSIVITY OF NITRAMINE GUN PROPELLANTS WITH THERMOPLASTIC/ELASTOMER BINDER SYSTEMS

Charles S. Leveritt, Paul J. Conroy, and Andrew W. Johnson

U.S. Army Research Laboratory, Aberdeen Proving Ground, MD 21005

Current and future gun propellant development programs are necessarily moving toward compositions possessing ever-higher impetus and flame temperature. A common goal is impetus above 1250 J/g, resulting in flame temperature above 3400 K. Propellants showing the most promise are composite in nature, consisting of an energetic solid in an energetic thermoplastic elastomer (ETPE). Oxidizers are typically CL-20 or RDX. Normally, such systems could be expected to provide some gun tube erosion problems. Erosivity characterizations have been conducted in a blowout chamber, which has been fabricated from the breech and chamber of a 37-mm gun. Relative erosivity is determined by observing the mean mass loss from a contoured nozzle resulting from a series of test firings. In general, the RDX/ETPE and CL-20/ETPE propellants that have been evaluated in this program are considerably less erosive than conventional propellants of similar flame temperature.

INTRODUCTION

In the quest for ever-increasing muzzle energy, propellants showing the most promise are composite in nature, consisting of an energetic solid in an energetic thermoplastic elastomer (ETPE). Oxidizers are typically RDX or CL-20. The ETPE's are most commonly selected from a family of oxytane polymers. The polymers can be tailored for nitrate ester, azido, or nitratoamine functionality. Systems in common use are BAMO-AMMO, BAMO/BAMO-AMMO, and BAMO-NMMO. Coolants such as NQ, TEX, or TATB are sometimes incorporated, but are limited so as not to degrade impetus.

Prior to this study, no wear and erosion data existed for propellants of this type. In addition to the more energetic thermochemistry, charge designs possess uncommonly high loading density and high mass generation rates, contributing to the potential wear and erosion problem. The propellant thermochemistry coupled with the high performance charge design was expected to provide severe tube wear and erosion problems.

RDX and CL-20 based propellants with oxetane ETPE binder systems have been characterized and compared to triple-base (M30), double-base (M8 & JA-2), and a more recent nitramine composite propellant (M43). Comparison propellants were initially chosen on the basis of similarity in gun chamber flame temperature. The compositions of the

comparison propellants are shown in Table 1; compositions of the oxetane propellants are presented in Table 2.

The propellants identified as TGD-002 and TGD-009 were formulated to meet the requirements of the Electrothermal Chemical (ETC) Gun firing demonstration program that was completed some time ago [1,2]. The charge design for this program utilized traditional "fast-core" propellant increments consisting of an inner layer of a relatively fast burning propellant, TGD-002, to which was bonded two outside layers of TGD-009 [3]. This design provided an increased loading density as well as high progressivity, since the inner layer burns at about three times the rate of the outer layers. The TGD-019 propellant was developed more recently as a possible replacement for JA-2, has a slightly more energetic binder system than TGD-009, and is not cooled with TEX [4].

Table 1. **COMPOSITION OF STANDARD PROPELLANTS**

	M8	**M30**	**JA-2**	**M43**
Nitrocellulose	52.15	28.0	59.02	4.00
(% Nitrogen)	(13.25)	(12.60)	(12.98)	(12.60)
Nitroglycerine	43.00	22.5	14.78	
Nitroguanidine		47.7		
Ethyl centralite	0.60	1.50		0.40
Potassium nitrate	1.25			
Diethylphthalate	3.00			
Cryolite		0.30		
RDX				76.00
Cellulose acetate/butyrate				12.00
Bis (dinitropropyl) acetal				3.80
Bis (dinitropropyl) formal				3.80
Diethyleneglycol dinitrate			24.60	
Akardite 2			0.70	
Barium oxide			0.05	
Graphite			0.05	

Table 2. **COMPOSITION OF OXETANE PROPELLANTS**

	TGD-002	**TGD-009**	**TGD-019**
CL-20	78.0		
RDX		58.0	76.0
TEX		18.0	
BAMO	14.3	6.0	6.0
AMMO	7.7	18.0	
GAP			18.0

The RDX/ETPE and CL-20/ETPE propellants that have been characterized provide thermochemistry that is considerably more fuel-rich than any of the comparison propellants. In Table 3, the calculated thermochemistry of the propellants is displayed. For the test chamber conditions, properties have been calculated using the BLAKE code [5]. For the test apparatus described in the experimental method below, these conditions apply up until the time that the shear disk fails and are calculated at a standard reference loading density of 0.2 g/cc. When the shear disk fails and flow through the nozzle is established, the NASA-Lewis code, Chemical Equilibrium with Applications (CEA), is used [6,7]. Conditions in the nozzle are calculated for each propellant test series using the actual pressure at which the shear disk failed. The propellant identified as TGD-9/2/9 is the complete "fast-core" propellant assembly consisting of a two mm thick layer of TGD-002, to which has been bonded two outer layers of 0.3 mm thick TGD-009. Since the available TGD-9/2/9 propellant had been designed to meet the ballistic requirements of a 120-mm gun, action time is slow when fired in a 37-mm gun chamber, leading to some heat loss in the experiment. Since the intent of this program is to fairly evaluate propellant thermochemistry, charges identified as Propellant 009+002 were prepared. The Propellant 009+002 charges possess separate weights of TGD-002 and TGD-009 identical to those of the TGD-9/2/9 assemblies; the TGD-002 and TGD-009 are not bonded in the 009+002 propellant so that combustion is simultaneous and action time is reduced acceptably.

Table 3. **SUMMARY OF THERMOCHEMICAL PROPERTIES**

	CHAMBER			**NOZZLE**			
	Temp(K)	**F(J/g)**		**Temp(K)**	**CO/CO_2**	**H_2/H_2O**	**N_2**
M30	3022	1078		2176	3.14	0.61	0.28
TGD-009	2570	1070		1886	21.31	5.16	0.26
M43	3004	1155		2129	7.70	1.54	0.24
M8	3746	1169		2898	1.51	0.21	0.14
TGD-002	3722	1356		2645	14.98	2.31	0.32
JA-2	3390	1139		2520	2.53	0.41	0.12
TGD-019	3262	1294		2293	15.34	2.77	0.29
TGD-9/2/9	3413	1292		2395	19.22	3.30	0.30
009+002	3413	1292		2395	19.22	3.30	0.30

EXPERIMENTAL METHODS AND RESULTS

A classic method to determine relative propellant erosivity is to measure the mass loss from a nozzle exposed to flow from the combustion gases of the propellant. The erosivity experiments described in this program were conducted in a blowout chamber, which has been fabricated from the breech and chamber of a 37-mm gun. A schematic of the fixture is shown in Figure 1. The gun tube has been shortened considerably and has been provided with a

bored cavity on the muzzle end to accept a nozzle and shear disk assembly. The nozzle is made of AISI 4340 gun steel and is located approximately 30 millimeters downstream from the mouth of the cartridge case. Mild-steel shear disks are placed downstream of the nozzle. The shear disks are held against the back of the nozzle by a "short barrel" tailpipe insert having an internal diameter of 12.7 millimeters. This erosivity apparatus has been in use at the US Army Ballistic Research Laboratory (BRL) and subsequently the US Army Research Laboratory (ARL) since the Second World War [8,9].

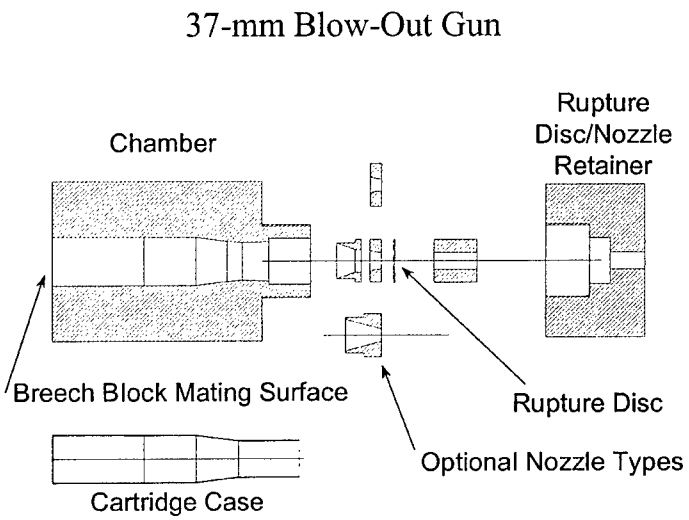


Figure 1. Test Fixture Schematic

In this fixture, the throat diameter of the nozzle is chosen to be 12.5 millimeters so that choked flow is established at the nozzle in preference to the tailpipe. With these nozzle and tailpipe dimensions, two 1.6 millimeter thick shear disks provide a rupture pressure in the nominal range of 260-270 MPa. Shear disk performance can be a study in classical shear dynamics, with relatively quick propellants providing a somewhat higher failure pressure and slow propellants the opposite. Propellant charge masses were adjusted to give a closed bomb pressure of 306 MPa to insure shear disk rupture.

Wear for each propellant was determined by conducting a repetitive series of five to six tests and then averaging the results. Following each shot, the steel nozzle was cleaned with soap and water, dried, and weighed on a balance with a sensitivity of 0.1 milligram. Pressure versus time in the chamber was measured as a record of shear disk failure pressure and to assure that no anomalous ballistic behavior had occurred. In all cases the propellants were ignited with the standard M1B1A2 percussion primer/igniter containing 6.5 grams of black powder. Averages and one standard deviation for shear disk failure pressures and nozzle mass loss (wear) are presented in Table 4.

Table 4. **SUMMARY OF EROSIVITY DATA**

	NOZZLE CONDITIONS			DISK BURST (MPA)	WEAR (mg)
	Temp(K)	**CO/CO_2**	**N_2**		
M30	2176	3.14	0.28	274 +/- 0.8	21.1 +/- 5.5
TGD-009	1886	21.31	0.24	251 +/- 6.2	21.4 +/- 2.6
M43	2129	7.70	0.24	274 +/- 5.5	26.8 +/- 7.8
M8	2898	1.51	0.14	---	240.5 +/-5.0(*)
TGD-002	2645	14.98	0.32	261 +/- 3.2	193.3 +/-3.2
JA-2	2529	2.53	0.12	254 +/- 9.1	250.6 +/-8.4
TGD-019	2293	15.34	0.29	269 +/- 11.3	40.0 +/- 6.0
TGD-9/2/9	2395	19.22	0.30	260 +/- 8.0	79.9 +/- 5.1
009+002	2395	19.22	0.30	261 +/- 4.0	104.3 +/-7.1

Note: (*) signifies data for **M8** obtained from [10]; not repeated in this program.

DISCUSSION

The RDX/ETPE and CL-20/ETPE propellants that have been characterized and compared to more traditional propellants in this evaluation provide thermochemistry that is considerably more fuel-rich than any of the comparison propellants. The propellant TGD-009 possesses the lowest chamber and nozzle temperatures of all propellants studied; yet the erosivity is equivalent to the comparison propellants, M30 and M43. In a previous investigation, it had been predicted that, due to the production of much more CO and H_2, M43 would be about 25% more erosive than M30 despite the equivalent flame temperature [11]. The predominant erosion mechanism proposed at that time stated that carburization leading to iron carbide formation would be an important contributing factor for much of the material lost from the gun steel. The M43 erosivity increase has finally been experimentally confirmed in this program. Given the benign chamber and nozzle temperature of TGD-009, the unexpected erosivity equivalency to M30 in the more fuel rich TGD-009 experiment appears to be a more extreme case of the carburization erosion mechanism.

The higher temperature TGD-002 and TGD-019 propellants are similarly high in CO and H_2, but are strikingly different from their respective comparison propellants, M8 and JA-2, in nitrogen content. Ponec suggests that the surface disassociation of CO on an iron surface is spoiled by nitrogen intrusion that produces a nitriding of the surface [12]. This leads to the possibility that increasing the nitrogen content of the propellant products may diminish the CO disassociation and thereby the erosivity. We have discovered in this program that for TGD-002 and TGD-019, with similar flame temperatures to the conventional relatively clean burning double-base comparison propellants, erosivity has in fact been greatly reduced. Complicating matters is the fact that these advanced propellants

have a much higher CO/CO_2 ratio than that of the double-base propellants which should exacerbate the carburization mechanism. Fortunately, Ponec's explanation may be applied to these new propellants because their nitrogen content is approximately three times that of the conventional propellants. Diatomic nitrogen as a product is probably preferred over carbon monoxide, if lower molecular weight is desired for increased impetus, even though the molecular weight of each is the same.

The M242 Bushmaster barrel has the option of nitriding or chrome plating. If it is chrome plated, access for erosion is through the cracks to the substrate [13]. Considering Ponec's hypothesis, nitriding barrels before they are chrome plated may increase the service life by mitigating the erosion at the base of the cracks. It is not believed that the nitrided material chemical process for erosion mitigation was previously understood, other than that it increased the surface hardness.

The strong reducing environment presented to the combustion chamber and nozzle in our erosivity test fixture can apparently be beneficial, at least over the range studied. In general, the RDX/ETPE and CL-20/ETPE propellants that possess a large excess of nitrogen in the products are considerably less erosive than conventional propellants of similar flame temperature.

REFERENCES

1. P. Braithwaite, G. Dixon, I. Wallace, R. Wardle, J. Northrup, W. Waesche, "Development of Fast and Slow Burning Rate TPE Propellants for ETC Gun Systems", 49th JANNAF Propulsion Meeting, Tucson, Arizona, December 1999.

2. P. Braithwaite, R. Stuart, J. Northrup, "Closed Bomb Characterization of TGD-002 and TGD-009 Propellants", 36th JANNAF Combustion Subcommittee and Propulsion Systems Hazards Subcommittee and Airbreathing Propulsion Subcommittee Joint Meeting, Cocoa Beach, Florida, October 1999.

3. F. W. Robbins, B. F. Raley, A. A. Koszoru, J. R. Hewitt, "High Loading Density Gun Charge Configurations of Slab Propellant – Loading and Gun Firing Experiments", 30th JANNAF Combustion Subcommittee Meeting, Monterey, CA, November 1993.

4. P. C. Braithwaite, "Development of an Improved Thermoplastic Elastomer (TPE) Gun Propellant," Contract Final Report, TR12255, February 2001, Thiokol Propulsion, Brigham City, UT.

5. E. Freedman, "BLAKE - A Thermodynamics Code Based on TIGER: Users' Guide to the Revised Program", ARL-CR-422, July 1998, US Army Research Laboratory, Aberdeen Proving Ground, MD.

6. Gordon, S., and McBride, B.J., 1976, Computer Program for Calculating Complex Chemical Equilibria, Rocket Performance, Incident and Reflected Shocks, and Chapman-Jouguet Detonations, NASA SP—273.

7. Gordon, S., and McBride, B.J., 1994, Computer Program for Calculation of Complex Chemical Equilibrium Compositions and Applications, Part I: Analysis, NASA RP—1311.

8. J. R. Ward, R. W. Geene, "Erosivity of a Nitramine Propellant with a Flame Temperature Comparable to M30 Propellant", ARBRL-MR-02926, June 1979, US Army Ballistic Research Laboratory, Aberdeen Proving Ground, MD.

9. R. P. Kaste, I. C. Stobie, J. R. Ward, B. D. Bensinger, "Relative Erosivity of Nitramine, Triple-Base, and Double-Base Propellants", ARBRL-MR-02339, July 1981, US Army Ballistic Research Laboratory, Aberdeen Proving Ground, MD.

10. J. R. Ward, R. P. Kaste, I. C. Stobie, B. D. Bensinger, "Role of Surface Oxide on Gun Barrel Wear", ARBRL-TR-02437, November 1982, US Army Ballistic Research Laboratory, Aberdeen Proving Ground, MD.

11. P.J. Conroy, P. Weinacht, M. J. Nusca, "Extended Range 5" Navy Gun, Theoretical Thermal and Erosion Investigations", Proceedings of 35th JANNAF Combustion Subcommittee Meeting, Tucson, AZ, December 1998.

12. Ponec, V., van Barneveld, W. A., "The Role of Chemisorption in Fischer-Tropsch Synthesis," Journal of Industrial Engineering Chemical Product Research and Development, Vol. 18, No. 4, 1979.

13. Conroy, P.J., Weinacht, P., Nusca, M. J., "Gun Tube Coatings in Distress," Proceedings of 36th JANNAF Combustion Subcommittee Meeting, Cocoa Beach, FL, October 1999.

(10th U.S. Army Gun Dynamics Symposium, Austin, April 2001)

CANNON COATING EROSION MODELING ACHIEVEMENTS

S. Sopok [1], S. Dunn [2], P. O'Hara [1], D. Coats [2], G. Pflegl [1], C. Rickard [1]

[1] *U.S. Army TACOM-ARDEC Benet Labs, Watervliet NY 12189*
[2] *Software & Engineering Associates, Carson City NV 89701*

Our repeatedly verified erosion theories are derived from many years of conducting the Army's mission of characterizing a broad spectrum of fired and eroded cannons. Based on these characterizations, we chronicle the establishment, development, achievement, and advancement of the first practical cannon and cannon coating/ablative erosion models for large and medium caliber gun systems. ARL's subsequent confirmation and adoption of our cannon and cannon coating/ablative erosion theories and models is also chronicled. This new method, in conjunction with limited scale firings, has greatly increased the Army's technical capability and provides a reliable and cost effective means of comprehensively studying the erosion of coated cannon bores that previously required costly full scale firings. Our comprehensive cannon erosion theories, models, and predictions have been widely embraced by Army and Navy Program Managers, saving them millions of dollars, and having a far reaching impact on gun system design, optimization, and testing.

Initially we discuss our early erosion theories and limited erosion models. Then we continue in chronological order with a discussion of our first practical cannon erosion model with an advanced artillery gun system example. Next, we discuss the extension of this initial model to our first practical cannon coating/ablative erosion model with an advanced medium caliber gun system example. We then discuss the adaptation of our cannon coating/ablative erosion model to advanced tank gun systems. Finally, we conclude with a description of our recent erosion modeling efforts. The following is a description of the methodology that has been established, developed and applied to address the current Army problem of cannon bore erosion on advanced gun systems.

EARLY EROSION THEORIES AND LIMITED MODELS

During the 1980's, we gained significant experience examining and characterizing eroded cannons to determine their erosion mechanisms which set the stage for developing our current cannon and cannon coating erosion models. In 1990, we acquired the XKTC interior ballistics [1] and BLAKE thermochemistry [2] gun codes from ARL which provided the initial building blocks necessary to develop our cannon/cannon coating erosion models based on our cannon erosion theories. We also acquired the CET thermochemistry [3], IBHVG2 interior ballistics [4], and CHEMKIN chemical kinetics [5] codes that year which further enhanced our capabilities.

In 1991 we were given two opportunities on crisis teams to determine erosive-ablative mechanisms and model these mechanisms with our limited thermal-thermochemical modeling capabilities. Over a three year period, these crisis teams investigated unexpected severe cannon erosion in the experimental chromium plated 155 mm AFAS RLPG, nitrided steel 25 mm M242/M919, and chromium plated 25 mm M242/M919 gun systems. Their respective baseline 155 mm AFAS (solid propellant bag and Unicharge) and 25 mm M242/M791 gun systems had normal erosion. We examined and characterized associated eroded cannons to determine their erosion and ablative mechanisms. The results of these microscopic, metallurgical, and chemical examinations/characterizations allowed us to formulate erosion theories that are widely accepted today. Using our limited erosion modeling capabilities, we conducted interior ballistic and thermochemical calculations to predict erosion for these gun systems [6,7].

Etched and unetched cross-sectional samples of these baseline and experimental eroded cannons were microscopically and metallurgically characterized as new and after firing. The chromium plated cannons had significant mechanical wear of the chromium plate, heat checking, chromium plate cracking-pitting, and gun steel gas wash in the exposed pits at and near the bore origin. These unfired chromium plated cannons had a very fine radial crack network at all positions due to manufacturing. This crack network extends to the interface upon firing. Its radial crack density stayed essentially constant to cannon condemnation but these cracks widened due to combustion gas heating from firing. The nitrided cannons had significant gun steel mechanical wear, gun steel heat cracking, and gun steel gas wash for the first six inches of bore travel.

We chemically and metallurgically examined unetched cross-sectional samples and residues of these fired cannons by elemental (SEM/EDS, DRES, ICP), molecular (Auger, ESCA), and thermal (TGA-FTIR, DSC-FTIR, TMA) techniques. Turbulent combustion gas induced thermal-chemical-metallurgical degradation of the chromium plate/exposed gun steel, their degradation thresholds, and their molecular decomposition products were determined.

With sufficient turbulent heating, the main contributors to the degradation of gun steel in chromium plated cannons are combustion gas induced thermal heating (transformations, stresses, heat check cracking), diffusional-thermochemical damage (interstitials, reactions, reaction product melting), and pure mechanical effects. Gun steel gas-wall reaction products form a brittle scale that easily spalls and also melts at a lower temperature than gun steel metal.

We found that all degraded bore surface, radial crack-pit wall and interfacial wall locations of the fired chromium plate exposed to combustion gases universally had subsurface grain growth/recrystallization, a thin passivated semi-metallic oxide surface layer and a non-metallic surface residue that included iron oxide, iron sulfide, and other minor combustion products. The chromium plate is fairly inert to reactions.

We also found that all degraded bore surface, crack-pit wall and interfacial wall locations of the fired gun steel exposed (directly or exposed through the chromium plate) to combustion gases universally had a subsurface heat affected zone of untempered martensite, a near surface carburized white layer, and a surface thin flaking semi-metallic oxide scale layer of the same iron oxide, iron sulfide, and other minor combustion products. Its non-metallic surface residue also had these same chemical combustion products. Interfacial gun steel exposed to combustion gases is preferentially degraded due to its higher energy state compared to adjacent gun steel.

Carburization of gun steel (and chromium) involves the diffusion of carbon into its matrix at peak gun temperatures and pressures thus forming a solid solution. As the system returns to room temperature, the matrix cannot physically retain the free carbon and precipitates

it as iron carbide (Fe_3C). This rapid cooling causes thermal contractions between the surface austenite and the carburized subsurface tempered martensite that produces stress cracks called heat checking. Carburization degrades the gun steel by significantly lowering its melting point and inducing cracks.

Oxidation of gun steel (and chromium) involves the diffusion of oxygen and sulfur into the metal surface at peak gun temperatures and pressures forming a distinct brittle oxide scale layer that is susceptible to cracking. This oxidation occurs despite the reducing solid propellant combustion environment. As the system returns to room temperature, this metal oxide scale layer retains the same high temperature chemical structure. Oxidation degrades the gun steel by significantly lowering its melting point.

Rifled large caliber artillery and medium caliber cannons have a much lower erosion condemnation depth and tolerate erosion less than smooth bore large caliber tank cannon. Degradation of their bore surfaces, radial crack-pit walls and interfacial walls was worst in the peak eroded locations of these fired cannons. In these peak eroded areas, chromium crack tip extension into the gun steel is slowed/blunted by erosion of these gun steel crack tips which is less prevalent in lesser eroded areas. The sulfur compound erosion products are universally from black powder igniters and flash suppressants. The other minor combustion products typically included condensed phase products of additives, fillers, ablatives, and soot.

Our many and varied characterizations of fired cannons directly confirm our theories that high temperature combustion gas products that include oxygen, carbon, and sulfur are chemically reacting with/degrading the gun steel at exposed bore surfaces, crack-pit walls, and if coated then the interfacial walls by way of cracks-pits.

We theorize that the coating cracks are initially very narrow allowing modest amounts of combustion gases to reach-degrade the gun steel interface by high pressure filling. As the coating is repeatedly heated by subsequent firings, we theorize that it progressively shrinks-contracts leading to progressive crack widening. This allows significant combustion gases to reach-degrade the gun steel interface and thereby accelerate platelet spallation and pitting. Different coating materials vary in the: degree of shrinkage/contraction, distributions of crack-pit frequencies and distributions of crack-pit widths. Linking up of this interfacial gun steel degradation at coating crack tips leads to abrupt spallation forming pits. Mechanical interaction between the projectile and loosened platelets assists in this pit formation. Without the coating as protection, the gun steel in these pits readily gas washes and erodes to condemnation by the same degradation mechanisms that degraded its interface. This accelerates the loss of adjacent coating platelets forming larger pits.

Coating shrinkage is due to non-metallic out-gassing/repacking from heating and yielding at the coating crack walls. Low contractile chromium plate has less shrinkage-contraction producing a lower crack-pit density and narrower crack-pit widths compared to high contractile chromium plate. These two chromium coating types are non-equilibrium materials that tend to evolve back to equilibrium when heated or fired.

FIRST PRACTICAL CANNON EROSION MODEL

Although our customers were pleased with our previous accomplishments, we realized that we needed a more comprehensive cannon erosion modeling capability. In 1991, we searched

the military, national, and international literature for a year hoping to find a more comprehensive cannon erosion code. There was an unsuccessful cannon erosion code called TBLIMP by Aerotherm from 1984 that was funded by US Navy-Indian Head [8]. Upon further investigation we found that poor quality BLIMP rocket calculations nearly bankrupted Aerotherm in the 1970's and 1980's. TBLIMP was based on BLIMP, and we determined that this model could not do coated cannon bores and its melt-wipe progressive ablation model lacked the thermochemical component necessary to do non-coated cannon bores.

By 1992, we had convinced ourselves that what we sought for cannons did not exist. We set our sights in a different direction looking for viable analogous rocket erosion codes. We interviewed people associated with a half dozen of the most promising potential rocket erosion code sources. It quickly became clear that only one source had the analogous rocket erosion code that we sought. By mid-1992 we realized that our co-authors at Software and Engineering Associates (SEA) had what we were seeking. After more than a half year of discussions, we teamed with them to develop their rocket erosion codes [9-10] into a cannon erosion code. SEA's standardized rocket codes were the necessary missing models that we needed. These codes are used throughout the industry for rocket nozzle and nose tip erosion.

It took until March 1995 to develop our progressively ablating-eroding cannon thermal-chemical-mechanical erosion code [11]. This initial modeling effort featured the previously examined/characterized baseline 155 mm AFAS Unicharge solid propellant gun system as an example [6]. Our updated erosion theories, models, and predictions are guided and calibrated by substantial gun system firing data and laboratory analysis of fired specimens. This data is derived from firing tests, laboratory tests, and nondestructive/destructive cannon characterizations.

Our erosion model made comparisons of different round types for the same bore material or different bore materials for the same round type. This complex computer analysis is based on rigorous scientific thermochemical erosion considerations that have been validated in the reentry nose-tip and rocket nozzle community over the last forty years. It consists of five main modules. The first two modules include the gun community's XKTC interior ballistics code [1] and their non-ideal gas BLAKE thermochemical equilibrium code [2]. The last three modules, significantly modified for gun systems, include three rocket community codes. These are the mass addition boundary layer MABL code [9], gas-wall thermochemical CET code [3], and the wall material ablation conduction erosion MACE code [10]. This analysis provided wall temperature, ablation, and erosion profiles for each material as a function of time, axial position, and rounds/round types fired. Experimental data showed that thermomechanical effects alone did not fully explain the extent of erosion in cannon tubes thus implying a thermochemical effect.

Figure 1 shows a flow chart of our cannon coating erosion model. The various codes, their inputs, and their outputs have respective boxes with solid borders, fine dashed borders, and coarse dashed borders.

Although our erosion model could only show calculations for non-cracked coatings and gun steel, it was still a remarkable landmark achievement. We predicted low rate of fire erosion results for the 155 mm AFAS Unicharge gun system with non-cracked chromium and bare gun steel. The exposed bare gun steel took about 8000 rounds to achieve erosion condemnation while the non-cracked chromium plate essentially did not erode at all by 8000 rounds. Both results agreed well with firing data. In both cases the peak eroded position was at the bore origin. It is important to note here and for the rest of the paper that distributions exist around these cannon erosion predictions.

Our cannon erosion modeling efforts have the most value to our customers when they are used in conjunction with a new gun system propellant, projectile and/or cannon with limited firings. Field and laboratory examinations of these cannons with limited firings helps calibrate our models. These calibrated erosion models can then be used to predict what has not been measured yet and what is not measurable. When we have very few measured inputs, we make many assumptions, and produce less reliable predictions. When we have many measured inputs, we make few assumptions, and produce good predictions.

The thermochemical equilibrium products are confirmed by experimental thermal gas-wall Arrhenius testing, experimental combustion gas analysis for metal products (gas chromatography, mass spectrometry, x-ray diffraction), experimental surface-subsurface bore analysis for metal products (Auger, ESCA), and previous experimental data for combustion product species. A key point is that gun steel's oxide products melt and ablate well below that of gun steel, thus cooling the surface and somewhat inhibiting the melting of gun steel. Chemical equilibrium is a practical approximation for cannon erosion modeling since high pressures and temperatures generate lots of collisions, activation energy achievement, and fast reaction rates.

Due to the lack of gas-wall kinetic reaction rate data, we invented, developed and/or applied various kinetic rate characterization techniques (TGA-FTIR, DSC-FTIR, and others) to study the reactions of combustion gases with bore materials. These included gas-wall degradation thresholds and reaction rates as a function of temperature, pressure and time. Reaction rate is a weak function of pressure. Low pressure flow of propellant gases is compensated by the extreme sensitivity of these instruments. These Arrhenius gas-wall techniques determine degradation thresholds of bore coating and substrate materials for their transformation, carburization, oxidation-scale, other reactions, oxide melting, and metal melting thresholds. Figure 2 shows typical normalized gas-wall coating and substrate steel oxidation rate data as a function of wall temperature for an advanced tank gun system.

Previously, ARL provided us with copies of their BLAKE and XKTC codes. We provided ARL presentations and descriptions of our cannon erosion theories, mechanisms, and models on multiple occasions in 1995. In March 1995, we first presented our cannon erosion theories, mechanisms, and models to Keller, Montgomery and Conroy of ARL at a small ARDEC-ARL gun erosion workshop [11]. In June 1995, we again presented and Army-wide published this same information at the annual ARDEC-ARL Gun Propulsion Review Meeting [12] that included Keller, Conroy, and many other ARL modeling personnel. In July 1995, we further presented and internationally published a detailed description of our practical cannon erosion theories, mechanisms, and models at an AIAA Joint Propulsion Conference [13]. Prior to our July 1995 AIAA presentation and paper, no other organization within or outside the U.S. Army had a practical gun erosion model or code. This is supported by ARL's lack of an erosion model or code in their March – July 1995 presentations and papers [14,15].

Based on Conroy and his co-authors first presentation and paper on ARL's gun tube erosion model at the JANNAF Combustion Meeting in October 1995 [16], it appears that our cannon erosion theories, mechanisms, and models were subsequently confirmed and adopted by them by modifying analogous codes available at ARL. They used XKTC and IBHVG2 codes for core flow, the Blake and CET codes for thermochemistry, and the XBR-2D code for convective/ conductive heat transfer, surface binary diffusion, surface reactions, melt-wipe ablation, and multi-round gun tube erosion.

From the M256/M829A1 gun system example in their initial erosion modeling paper, it appears that they were not fully able to implement our cannon erosion model in about a dozen key areas. Variable values instead of constant values are required for the density-specific heat-conductivity material inputs. Chromium plate protection must be included despite its cracking and eventual spalling. The exposed gun steel substrate must be eroded by a full gas-wall thermochemical model instead of a lesser melt-wipe model. Their erosion model needs to include combustion gas-exposed gun steel reactions at threshold temperature onsets, reaction product melting at higher threshold temperature onsets, and exposed gun steel melting at still higher threshold temperature onsets. The model needs to include a turbulent reacting boundary layer with mass addition and a gas-wall kinetic rate functions to supplement gas-wall chemical equilibrium. In addition, their model must allow reaction energy to provide all the energy for future reactions and melting. Their erosion model is film coefficient driven for energy when it should be enthalpy driven and highly dependent on all species and reactions chosen. They need an exposed gun steel ablation and erosion gas-wall products model. This model should include the reacting/melting of the gas-wall iron oxidation products (particularly FeO and FeS) and of the gas-wall iron carburization products (particularly Fe_3C).

In December 1995 and June 1996, we further presented and published these same practical cannon erosion theories, mechanisms, and models [17-18].

FIRST PRACTICAL CANNON COATING/ABLATIVE EROSION MODELS

Although our customers were further pleased with our accomplishments, we realized that we needed a more comprehensive cannon erosion modeling capability that better addressed our erosion theories and mechanisms for chromium plated gun steel. It took us until May 1996 to develop our cannon coating erosion model. In May 1996, we presented and published results of our non-ablative and ablative cannon coating erosion models [19] using the previously examined/characterized 25 mm M242 gun systems as examples [7]. Although we applied our models to the M242 chromium plated cannon, we did not publish the specific details of these models until the 1999 after gaining significant confidence. Our modeling efforts provide a means for evaluating the erosive nature of candidate charges, protective nature of candidate cannon bore coatings, and protective nature of ablatives.

Destructive micrographic examination-characterization techniques historically gave only one important snapshot of erosion as a function of axial position at the end of a cannon's life. As a result of this deficiency, in 1996 we invented, developed, and applied a nondestructive magnifying borescope characterization technique to monitor the cannon bore substrate exposure and erosion as a function of axial position and rounds/round types fired. Figure 3 shows typical substrate exposure data from a magnifying borescope as a function of axial position at various stages of an advanced tank gun system's life. Our monitoring of substrate exposure and erosion through a cannon's life is due to the lack of a thermal-mechanical crack-pit model. Substrate exposure is based on crack-pit frequency, coating shrinkage-contraction, and crack-pit widths. Our magnifying borescope technique was chronologically used on the PM-Bradley M242/M919 (ARDEC-Benet Labs, 1996), PM-TMAS M256/ M829E3 (TECOM-APG, 1997), and PM Crusader XM297/ MACS (TECOM-Yuma, 2001) programs. Even in the absence of erosion

modeling, periodic magnifying borescope monitoring throughout a cannon's life says volumes about its erosion progression.

We have further discovered that magnifying borescope subsurface exposure measurements allows us to calculate conductive and convective exposed gun steel interface temperatures at the base of coating crack-pits as a function of axial position and rounds/round types fired. Figure 4 shows typical exposed substrate interface temperatures as a function of coating crack-pit width for selected advanced tank gun system axial positions. Based on these exposed gun steel interface temperatures, we thermally, metallurgically, and thermochemically use the model to degrade the exposed gun steel substrate interface through these coating cracks-pits producing coating platelet spallation and subsequent exposed gun steel gas wash to condemnation.

Benet Laboratories also employs a complementary evaluation technique call the LOTIS system. Typical LOTIS system resolution is about 0.0100" (typically ranges from 0.0070" to 0.0150") and it cannot measure typical crack-pit widths, crack-pit frequencies, and pit initiation that ranges from 0.0001" to 0.0010". Even though it fails to measure crack-pit initiation-development, the LOTIS system is a valuable tool that can measure erosion depths of much smaller pits than the standard Benet Laboratories erosion gage.

These M242 cannon coating modeling efforts predicted erosion for exposed bare gun steel, nitrided gun steel, and most importantly, chromium plated gun steel which was a remarkable achievement. Figure 5 shows typical rounds to erosion condemnation for various round type/bore type configurations associated with the M242/M919 Program using the Cycle A firing scenario at the 6" RFT peak eroded position. The round type-wall material combinations shown are M919 (HES9053)-nitrided gun steel, M919 (HES9053)-0.002" chromium plated gun steel, M791-nitrided gun steel, and M919 (type-classified)-0.002" chromium plated gun steel. It took about 400, 800, 4000, and 5000 rounds to achieve erosion condemnation for these four respective round type-wall material combinations which agreed well with firing data.

Based on Conroy and his co-authors next presentations and papers on ARL's gun tube erosion model from May 1996 – July 1996 [20-23], it appears that our cannon coating erosion theories, mechanisms, and models were subsequently confirmed and adopted by them in the latter two papers by additionally modifying analogous codes available at ARL. They used enhanced XKTC and IBHVG2 codes for core flow, enhanced Blake and CET codes for thermochemistry, and the enhanced XBR-2D code for convective/conductive heat transfer, surface binary diffusion, surface reactions, melt-wipe ablation, and multi-round gun tube erosion. They supplemented these calculations by including Janke's ETC extension to IBHVG2 code called the IBBLAKE code [24] and by adding a pyrolysis model where the reaction products can now be solids, liquids, and gases.

From the M829A1 and M829E3 tank round examples in their last four papers, it appears that they were still not fully able to implement our cannon/cannon coating erosion models in the same key areas mentioned above with the following exceptions. They adopted a variant of our gas-solid phase conceptual diagram. The exposed gun steel substrate still needs to be eroded by a gas-wall thermochemical model instead of their lesser melt-wipe (stated as ~99%) and pyrolysis (stated as ~1%) model. They added a lesser iron oxide gas-wall product (incorrectly Fe_3O_4 instead of FeO) model but failed to include an iron carbide gas-wall product (Fe_3C) model.

In October 1996 – July 1997, we presented and published further results of our non-ablative and ablative cannon coating erosion models [25-26] using the same previously

examined/characterized 25 mm M242 gun system examples [7]. We assisted in the type classification of the M919 round by modeling its erosion life for the various configurations compared to the baseline configuration. Our M919 erosion modeling efforts made it possible to reject many configurations without firing tests resulting in significant Army savings. The final type classified configuration increased erosion life by an order of magnitude over the initial experimental M919 (HES9053) round and equaled the baseline M791 round. This final configuration included a HES9053/HC33 propellant mix, an ablative, and chromium plating.

In July 1996, we presented and published our erosion related theories and mechanisms on environmental assisted cracking of cannon bore materials [27]. This RLPG environmental assisted cracking modeling effort contributed to the demise of this gun system resulting in significant Army savings. In October 1996, we presented and published two more erosion modeling related papers. The first [28] was the transformation of the NASA-Lewis ideal gas CET thermochemical equilibrium code [3] into the robust-compressible CCET code by combining it with BLAKE and TIGER [2]. The second [29] was the Navy 5"-54/EX99 gun system analysis versus its Navy 5"-54/NACO gun system baseline. This Navy 5"-54/EX99 gun system erosion modeling effort made it possible to reject numerous design configurations without firing tests resulting in significant Navy savings.

FIRST PRACTICAL TANK CANNON COATING/ABLATIVE EROSION MODELS

In 1996, our M256 cannon erosion characterizations, theories and modeling efforts for various M829E3 propellants detailed how their associated M256 cannons failed dramatically premature. These erosion related efforts became the cornerstone justification and then guide for the TACOM-ARDEC Wear and Erosion Program which focuses on refractory metal sputtered coatings. This guidance played a significant role in determining refractory metal sputtered coating types and properties which resulted in significant Army savings. Our efforts on every important artillery, tank and medium caliber gun system since 1992 contributes to this guidance.

Although customers continued to be pleased with our accomplishments, we realized that we needed a cannon coating erosion model for large caliber chromium plated smooth bore tank gun systems. It took us until the Spring of 1997 to develop this enhanced cannon coating erosion model which calculated large caliber chromium plated smooth bore tank cannon erosion in a similar manner that we used for rifled medium caliber chromium plated cannons.

From April 1997 – November 2000, we presented and published cannon coating erosion modeling and erosion EFC factor predictions [30-39]. These predictions were for a variety of rounds (M865, M829, M829A1, M829A2, various HEAT, and various M829E3 type rounds) used in the chromium plated M256 tank cannon. These erosion EFC factors allow the Army to better manage their M256 tank cannon inventory resulting in significant Army savings. These predictions were supported by developing erosion mechanism theories for newly examined and characterized 120 mm M256 gun systems that have fired these rounds. These nondestructive and destructive thermal, metallurgical, and chemical examinations/characterizations were based on techniques used for previous artillery and medium caliber gun systems [6-7]. We used our non-ablative and ablative cannon coating models for predicting erosion of these M256 round types. In 1999, we publish the specific details of these models after gaining significant confidence. The ablative-like components of this analysis are the initial bore protecting 1600 K combustible case

gases and the further bore protecting paste ablative. They each protect the beginning of the bore from extreme heating and each move the peak heating position farther down bore where the heating is less extreme. We also determined that the muzzle wear was purely mechanical erosion.

Our M256 cannon coating erosion modeling efforts for chromium plated gun steel in smooth bore tank cannons which was a further landmark achievement and included the evaluation of hot, ambient and cold round conditioning temperatures (RCT). Our erosion predictions for the M256/M829A2 gun system include about 350 (120 °F RCT), 500 (70 °F RCT), and 775 (-25 °F RCT) rounds to achieve erosion condemnation at the 85" RFT peak eroded position. Our erosion predictions for the M256/M829 gun system include about 500 (120 °F RCT), 750 (70 °F RCT), and 1200 (-25 °F RCT) rounds to achieve erosion condemnation at the 95" RFT peak eroded position. The M829A2 and M829 erosion predictions agreed well with firing data for this 0.005" chromium plated M256 cannon.

We assisted in the optimization of the various experimental M82E3 rounds used in the M256 cannon including propellant, case and ablative configurations. Our M829E3 erosion modeling efforts made it possible to reject many design configurations without firing tests resulting in significant Army savings. We determined that M829E3 cannon erosion was much more severe than its M829A2 counterpart, that M829E3 peak erosion moved up-bore a half meter more than its M829A2 counterpart, and that HEAT rounds in combination with M829E3 rounds moved the M829E3 peak eroded position further up-bore to the origin. We predicted the effects of an ablative on erosion. This was supported by paste decomposition and paste viscosity degradation measurements as a function of increasing temperature. We extensively detailed our model for determining the exposed substrate interface temperature for a give crack-pit width which combines conductive and convective elements. We determined degradation thresholds of materials for transformation, oxidation, reactions, carburization, oxide melting, and material melting. We also used diffusion controlled transformation codes for multi-component gun steel transformation calculations. Finally, we observed that tank, artillery and medium caliber cannon erosion positionally correlates with maximum interface degradation and maximum substrate exposure but not necessarily with maximum crack-pit depth or maximum transformation depth.

Figure 6 shows typical predicted rounds to erosion condemnation for various round conditioning temperatures associated with the non-ablative M256/M829E3 gun system at the 60" RFT peak eroded position. Our erosion predictions indicate that it takes about 130 (120 °F RCT), 210 (70 °F RCT), 190 (-25 °F RCT), and 170 (equal distribution of RCTs) M829E3 rounds to achieve erosion condemnation. We also predicted erosion results for the M256 cannon firing a non-ablative mixture of M829E3 and HEAT rounds Our erosion predictions indicate that it takes about 120 (120 °F RCT), 200 (70 °F RCT), 180 (-25 °F RCT), and 160 (equal distribution of RCTs) M829E3 rounds to achieve erosion condemnation at the 25" RFT peak eroded position. Similarly, Figure 7 shows typical predicted rounds to erosion condemnation for various round conditioning temperatures associated with the ablative M256/M829E3 gun system at the 60" RFT peak eroded position. Our erosion predictions indicate that it takes about 240 (120 °F RCT), 390 (70 °F RCT), 350 (-25 °F RCT), and 315 (equal distribution of RCTs) M829E3 rounds to achieve erosion condemnation. All these erosion predictions agreed well with firing data.

Based on work by Cote and co-authors, it appears that our cannon/cannon coating theories and mechanisms (thermal, metallurgical, thermochemical and mechanical) mentioned earlier were completely confirmed by them in their first presentations and papers on gun erosion

theories and mechanisms in 1999 [40-43]. Dr. Cote and his associates did a remarkable and comprehensive investigation of tank cannon, artillery cannon, and medium caliber cannon erosion mechanisms. They confirmed our theories and mechanisms of cannon erosion including theories detailing thermal, metallurgical, and thermochemical damage to the exposed chromium plated gun steel at surfaces layers, crack-pit walls layers, and interfacial walls layers.

Cote and his co-workers used similar characterizations techniques (microscopy, SEM-EDS, and atomic electron microprobe analysis) to find what they called "heat affected zones, gray layers and white layers" (our heat affected zones, wall layers and white layers) which formed with sufficient heating and consisted of the same iron oxides, sulfides and carbides compounds. They also found as we did earlier that the initiation of chemical attack of the exposed gun steel substrate interface begins at the tips of the narrow chromium cracks by combustion gas-gun steel wall oxidation reactions. These reactions form semi-metallic layers on the exposed gun steel walls consisting of iron oxide and iron sulfide. They also confirmed our findings that as the coating progressively shrinks/contracts, the radial cracks progressively widen, and accelerate the linking up of substrate interfacial damage at crack tips. This lead to coating platelet spalling/pitting and subsequent substrate gas wash of these pits.

Based on Conroy and his co-authors next presentations and papers on ARL's gun tube erosion model from October 1997 – November 2000 [44-48], it appears that our cannon coating erosion theories, mechanisms, and models were further confirmed and adopted by them by additionally modifying analogous codes available at ARL. They further enhanced their XKTC, IBHVG2, IBBLAKE, BLAKE, CET, and XBR-2D codes.

From the M829A1, M829A2, M829E3, M791, 616W, Navy 5"-62/NACO, Navy 5"-62/M30A1, and Navy 5"-62/EX99 round examples in their last five papers, it appears that they were still not fully able to implement our cannon/cannon coating erosion models in the same key areas mentioned above with the following exceptions. They adopted a variant of our gas-solid phase conceptual diagram. They also added variable temperature dependent materials input values for density, specific heat, and conductivity. They added a surface roughness model to address chromed plated gun steel pitting but still ignored lesser subsurface exposure such as progressive radial cracks widening of the chromium plate. They improved their pyrolysis model to include a higher percentage of ablation-related gas-wall chemical reaction products. This now makes it a more balance melt-wipe and pyrolysis model. They added a subsurface-interfacial multi-component diffusion and reactions model now realizing that gun steel degradation is important at the chromium crack tips and exposed gun steel interfaces. They further updated a lesser iron oxide gas-wall products model (incorrectly Fe_3O_4 instead of FeO) and correctly included a iron carbide gas-wall product model (Fe_3C). They need to calculate the effect on erosion of the Navy 5"-62/EX99 and Army M829E3 gun system ablatives that were deposited on the bore surface of these cannons. They added a finite rate thermochemistry model which we also have but do not use due to the lack of available input data.

RECENT EROSION MODELING EFFORTS AND CONCLUSIONS

In 1999, we developed a robust time dependent gun tube boundary layer (GTBL) code [49] to complement and eventually replace our current steady state gun tube mass addition boundary layer (MABL) code [9]. In that same year, when conventional interior ballistic models

failed us, we successfully began using the GTBL code for Future Combat System rarefaction wave gun (RAVEN) systems. In these RAVEN systems, high velocity combustion gases exit both a breech venting nozzle for recoil reduction as well as the conventional muzzle venting after projectile exit [50-53]. From 1999-2000, we conducted an extensive erosion modeling effort for the U.S. Navy Advanced Gun System, the results are proprietary, and are only published in very limited distribution. These RAVEN and AGS modeling efforts made it possible to reject design configurations without firing tests resulting in significant savings for these respective programs.

In the last ten years, the Army and Navy's quest for increased performance resulted in significant cannon erosion on their advanced gun systems. We have assisted or are currently assisting in the design, optimization, testing, characterization, and/or type classification of the advanced: M242/M919, M256/M829A2, M256/M829E3, Navy 5"/EX99, Navy AGS, XM297/MACS, and FCS-RAVEN gun systems. Applications of this method have led to: identifying erosive gun system design configurations prior to testing or with limited testing, optimizing gun system design configurations to minimize erosion and increase life, comparing competing gun system design configurations, guiding-justifying coating and charge design programs, predicting round type specific erosion EFC factors for inventory management, and predicting what otherwise has not been or can't be measured in gun systems.

REFERENCES

1. P. Gough, "The XNOVAKTC Code," Paul Gough Associates, Portsmouth NH, *U.S. Army BRL-CR-627*, February 1990.
2. Freedman E., "BLAKE - A Thermodynamic Code Based on Tiger: User's Guide and Manual," *U.S. Army BRL TR-02411*, Aberdeen MD, 1982.
3. S. Gordon, and B. McBride, "Computer Program for Calculation of Complex Chemical Equilibrium Compositions, Rocket Performance, Incident and Reflected Shocks, and Chapman-Jouguet Detonations (CET)," *NASA Lewis SP-273*, Cleveland OH, 1971.
4. R. Anderson, K. Fickie, "IBHVG2 – A User's Guide", *U.S. Army BRL TR-2829*, Aberdeen MD, 1987.
5. "CHEMKIN User's Guide Code", *U.S. DOE-SNL Manual*, Sandia NM, 1990 & 1997.
6. P. Thornton, J. Senick, J. Underwood, S. Sopok, J. Cox, "LP Gun No.2 Materials/ Failure Analysis", *U.S. Army ARDEC Special Publication SP92-1*, Watervliet NY, 1992.
7. G. Capsimallis, J. Cox, P. O'Hara, M. Witherell, S. Sopok, J. Underwood, G. Pflegl, P. Cote, "M242/ M919 Multi-Disciplinary Analyses", *U.S. Army ARDEC Special Publication SP92-2*, Watervliet NY, 1992.
8. M. Evans, "User's Guide for Transient Boundary Layer Integral Matrix Procedure TBLIMP", *Aerotherm UM-74-55*, Prepared for U.S. Navy Indian Head, Mountain View CA, October 1984.
9. J. Levine, "Transpiration and Film Cooling Boundary Layer Computer Program (MABL) - Numerical Solution of the Turbulent Boundary Layer Equations with Equilibrium Chemistry", *NASA Marshall N72-19312*, Huntsville AL, June 1971.
10. S. Dunn, "Materials Ablation Conduction Erosion Program (MACE)," *Software and Engineering Associates User's Guide*, Carson City NV, June 1989.
11. Sopok, S., "First Gun Erosion Modeling Code", *Proceedings ARDEC/ARL Gun Erosion Workshop*, Stanhope NJ, March 1995.
12. S. Sopok, "First Gun Erosion Modeling Code", *Proceedings 8th ARDEC/ARL Gun Propulsion Review Meeting*, Pocono Manor PA, June 1995.
13. S. Dunn, S. Sopok, D. Coats, P. O'Hara, G. Nickerson, G. Pflegl, "Unified Computer Model For Predicting Thermochemical Erosion In Gun Barrels", *Proceedings 31st AIAA Joint Propulsion Conference*, San Diego, July 1995; Also: S. Sopok, S. Dunn, D. Coats, P. O'Hara, G. Pflegl, "Unified Computer Model For Predicting Thermochemical Erosion In Gun Barrels", *J. of Propulsion. and Power V15, N4*, July 1999.

14. G. Keller, P. Conroy, "Gun Tube Erosion", *Proceedings ARDEC/ARL Gun Erosion Workshop*, Stanhope NJ, March 1995.
15. G. Keller, P. Conroy, "Gun Tube Erosion", *Proceedings 8th ARDEC/ARL Gun Propulsion Review Meeting*, Pocono Manor PA, June 1995.
16. P. Conroy, P. Weinacht, M. Nusca, "ARL Tube Erosion Code", *Proceedings 32nd JANNAF Combustion Meeting*, Huntsville AL, October 1995.
17. S. Sopok, S. Dunn, P. O'Hara, D. Coats, G. Pflegl, "First Computer Model for Predicting Thermochemical Erosion in Gun Barrels", *Proceedings JANNAF Propulsion Meeting*, Tampa, December 1995.
18. S. Sopok, S. Dunn, P. O'Hara, D. Coats, G. Pflegl, "First Computer Code for Predicting Thermochemical Erosion in Gun Barrels", *Proceedings 20th Army Science Conference*, Norfolk, June 1996.
19. S. Sopok, P. O'Hara, G. Pflegl, S. Dunn, D. Coats, "Thermochemical Erosion Modeling of M242 Gun Systems", *Proceedings 8th Army Symposium on Gun Dynamics*, Newport RI, May 1996.
20. G. Keller, P. Conroy, "ARL White Paper on Gun Barrel Erosion", *U.S. Army ARL Report*, Aberdeen MD, May 1996.
21. P. Conroy, P. Weinacht, M. Nusca, "Surface Chemistry Effects on High Performance Tank Ammunition", *Proceedings 8th Army Symposium on Gun Dynamics*, Newport RI, May 1996.
22. P. Conroy, P. Weinacht, M. Nusca, "Direct Fire Gun Tube Erosion Calculations", *Proceedings 20th Army Science Conference*, Norfolk VA, June 1996.
23. P. Weinacht, P. Conroy, "A Numerical Method for Predicting Thermal Erosion in Gun Tubes", *U.S. Army ARL TR-1156*, Aberdeen MD, July 1996.
24. P. Janke, J. Dyvik, C. Marksberry, "Electrothermo-Chemical Propellant Extension to IBHVG2 Interior Ballistic Simulation: Model Development and Validation", *Proceedings JANNAF Combustion Meeting*, Monterey, October 1994.
25. S. Sopok, P. O'Hara, G. Pflegl, S. Dunn, D. Coats, "Thermochemical Erosion Modeling of the Original M242/M919 Gun System", *Proceedings 33rd JANNAF Combustion Meeting, Monterey*, October 1996.
26. S. Sopok, P. O'Hara, G. Pflegl, S. Dunn, D. Coats, "Thermochemical Erosion Modeling of the 25mm M242/M791 Gun System", *Proceedings 33rd AIAA Joint Propulsion Conference*, Seattle, July 1997.
27. S. Sopok, P. O'Hara, "Chemical Factors Associated with Environmental Assisted Cracking of Generic Gun Systems - RLPGs, Tanks, & Howitzers", *Proceedings 32nd AIAA Joint Propulsion Conference*, Lake Buena Vista FL, July 1996.
28. D. Coats, S. Dunn, S. Sopok, P. O'Hara, G. Pflegl, "A New Chemical Equilibrium Code with Compressibility Effects", *Proceedings 33rd JANNAF Combustion Meeting*, Monterey, October 1996.
29. S. Dunn, D. Coats, S. Sopok, P. O'Hara, G. Pflegl, "Thermochemical Erosion in the Navy 5-inch 54 Caliber Gun", *Proceedings 33rd JANNAF Combustion Meeting*, Monterey, October 1996; Also *U.S. Navy Indian Head CR 99-71*, Indian Head MD, 1999.
30. S. Sopok, P. O'Hara, P. Vottis, G. Pflegl, C. Rickard, and R. Loomis, "Erosion Modeling of the 120mm M256/M829A2 Gun System", *Proc. 32nd ADPA Gun and Ammunition Meeting*, San Diego, April 1997.
31. S. Sopok, P. O'Hara, "Modeling of Erosive Combustion Products Affecting The 120mm M256/M829A2 Gun System", *Proceedings 34th JANNAF Combustion Meeting*, West Palm Beach, October 1997.
32. S. Sopok, P. Vottis, P. O'Hara, G. Pflegl, C. Rickard, "Comprehensive Erosion Model for the 120mm M256/M829A2 Gun System", *Proceedings 29th CH/GE/NL/US 120mm Joint Configuration Board Meeting*, Hampton VA, April 1998.
33. S. Sopok, P. Vottis, P. O'Hara, G. Pflegl, C. Rickard, "Shot-By-Shot Erosion Modeling of Retired 120mm M256 Tube #1988", *Proceedings 34th AIAA Joint Propulsion Conference*, Cleveland, July 1998.
34. S. Sopok, P. Vottis, P. O'Hara, G. Pflegl, C. Rickard, "Comprehensive Erosion Model for the 120mm M256/M829 Gun System", *Proceedings JANNAF Propulsion Meeting*, Cleveland, July 1998.
35. S. Sopok, P. Vottis, G. Pflegl, C. Rickard, "Erosion Modeling of Fielded 120mm M256/M829A2 Gun Systems", *Proceedings CH/FR/GE/NL/US High Performance Tank & Artillery Gun Erosion Conference*, Bundesamt Fur Wehrtechnik Und Beschaffung, Koblenz, Germany, October 1998.
36. S. Sopok, R. Billington, "Erosion EFC Factors for Kinetic Energy Rounds Used in the 120mm M256 Tank Cannon", *Proceedings 35th AIAA Joint Propulsion Conference*, Los Angeles, June 1999.
37. S. Sopok, R. Loomis, G. Pflegl, C. Rickard, "Preliminary Erosion Analysis for the Experimental M829E3 Kinetic Energy Round", *Proc. 36th JANNAF Combustion Meeting*, NASA-Kennedy FL, October 1999.

38. S. Sopok "Cannon Coating Erosion Model With Updated M829E3 Example", *Proceedings 36th AIAA Joint Propulsion Conference*, Huntsville, June 2000.
39. S. Sopok, M. Fleszar, "Ablative Erosion Model for the M256/M829E3 Gun System", *Proceedings 37th JANNAF Combustion Meeting*, Monterey CA, November 2000.
40. P. Cote, "Fools Gold, Soot, Wurtzite and Talc in the Degradation of Gun Bore Surfaces", *Benet Laboratories Technology Seminar*, Watervliet NY, April 1999.
41. P. Cote, "Initiation of Chrome Loss on Gun Bore Surfaces", *Benet Laboratories Technology Seminar*, Watervliet NY, September 1999.
42. P. Cote, C. Rickard, "Gas-Metal Reaction Products in the Erosion of Chromium Plated Gun Bores", *Journal Wear N241 120*, September 1999.
43. P. Cote, C. Rickard, "Gray Layers and the Erosion of Chromium Plated Gun Bore Surfaces, *U.S. Army ARDEC TR 99016*, Watervliet NY, September 1999.
44. P. Conroy, P. Weinacht, M. Nusca, "A Parametric Erosion Investigation", *Proceedings 34th JANNAF Combustion Meeting*, West Palm Beach, October 1997; U.S. Army ARL TR-1954, APG MD, June 1999.
45. P. Conroy, P. Weinacht, M. Nusca, K. Rice, "Extended Range 5" Navy Gun, Theoretical Thermal and Erosion Investigations", *Proceedings 24th TTCP WPN/TP4 Meeting*, Indian Head MD, April 1999.
46. P. Conroy, P. Weinacht, M. Nusca, "An Investigation of the Erosion Physics/Mechanisms of Current Army Systems (Point Studies)", *U.S. Army ARL TR 2054*, Aberdeen MD, September 1999.
47. P. Conroy, P. Weinacht, M. Nusca, "Gun Tube Coatings in Distress", *Proceedings JANNAF Combustion Meeting*, Cocoa Beach FL, October 1999.
48. P. Conroy, M. Nusca, C. Chabalowski, W. Anderson "Gun Tube Erosion Macroscopic Surface Kinetics (Initial Study)", *Proceedings JANNAF Combustion Meeting*, Monterey CA, November 2000.
49. S. Dunn, D. Coats, S. Sopok, "Gun Tube Boundary Layer Code (GTBL)", *Software and Engineering Associates User's Guide*, Carson City NV, 1999.
50. E. Kathe, Dillon, "RArefaction waVE guN (RAVEN)," *Proceedings NDIA Guns and Ammunition Meeting*, Williamsburg VA, May 2000.
51. E. Kathe, R. Dillon, S. Sopok, M. Witherell, S. Dunn and D. Coats, "Rarefaction Wave Gun Propulsion,", *Proceedings 37th JANNAF Combustion Meeting*, Monterey, November 2000.
52. E. Kathe, R. Dillon, S. Sopok, M. Witherell, S. Dunn and D. Coats, "Rarefaction Wave Gun Propulsion," *Proceedings 22nd Army Science Conference*, Baltimore, December 2000.
53. E. Kathe, R. Dillon, "Sonic Rarefaction Wave Low Recoil Gun," *Proceedings 39th AIAA Aerospace Sciences Meeting*, Reno, January 2001.

Fig. 1 – Flow Chart Of Cannon Coating Erosion Model

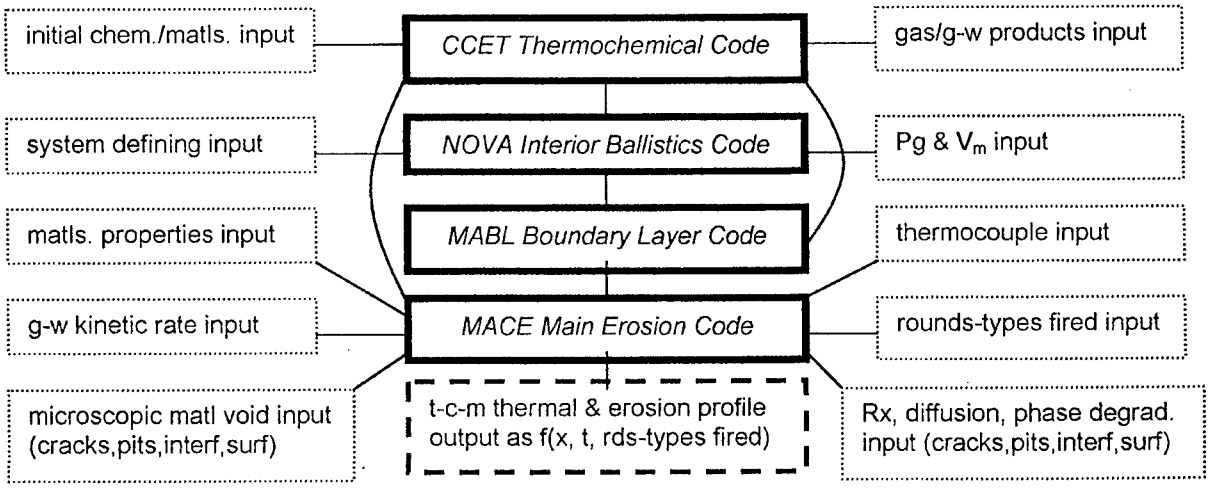


Fig. 2 - Typical Gas-Wall Oxidation Rate

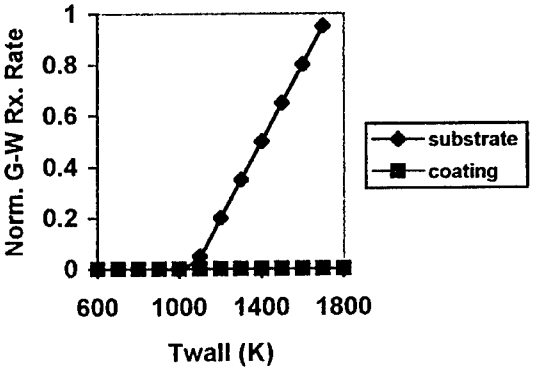


Fig. 3 - Typical Magnifying Borescope Data

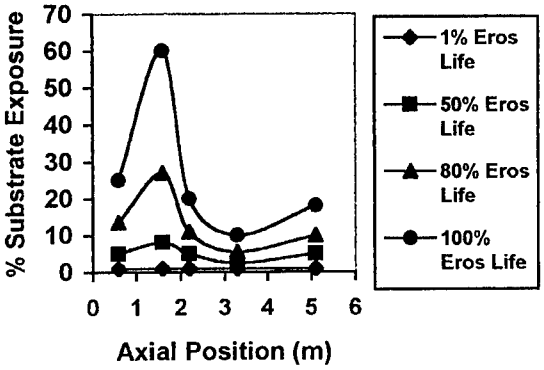


Fig. 4 - Typical Exposed Substrate Interface Temperature

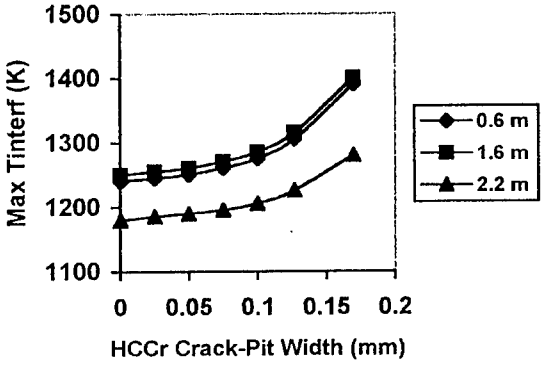


Fig. 5 - M242 Erosion For Cycle A Scenario At 6" RFT

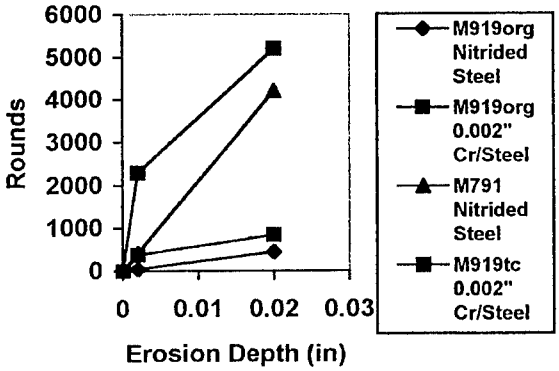


Fig. 6 - Non-Ablative M256/M829E3 Erosion At 60" RFT

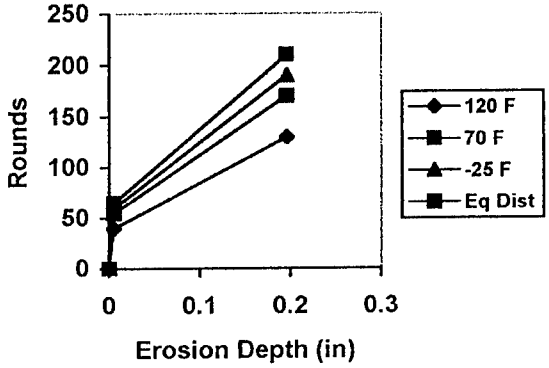
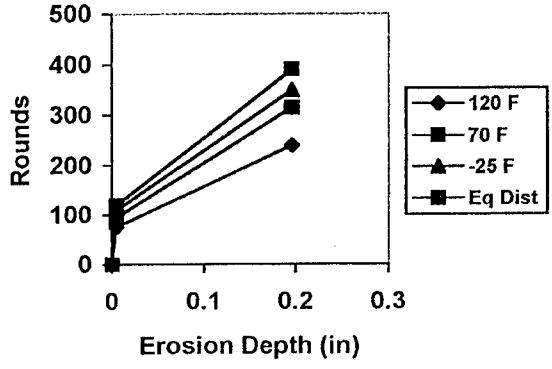


Fig. 7 - Ablative M256/M829E3 Erosion At 60" RFT



INDUCTIVELESS RAIL LAUNCHERS FOR LONG PROJECTILES

Yuri Dreizin
Independent researcher, Minneapolis, yurid@protomold.com

The paper presents rail launchers having substantially higher efficiency than railguns and much lower mechanical stresses in projectiles and launch tubes.

Based on novel – inductiveless – architecture, which is especially effective for long projectiles, these launchers promise a number of weighty advantages such as:

- Order of magnitude lower rail-to-rail repulsion, resulting in lightweight launch tubes
- No sabots, armature mass share only 25 – 35%
- Suppressed velocity and transient skin effects
- Low stress acceleration of launch packages by forces spread over long armatures
- Negligible parasitic inductive energy – no muzzle flash, no need for energy recovery
- Launch efficiency – ratio of launch package muzzle energy to supplied energy – up to 70%
- Net launch efficiency – similar ratio for in-flight projectile only – up to 50%
- No need for forced cooling of launch tubes due to significantly reduced energy losses

INTRODUCTION

The days of cannon balls are long over. Most in-flight projectiles have large length-to-diameter ratio. For heavy metal rod penetrators, for example, this ratio reaches 20-30. Long projectiles with small cross sections have better ballistic properties, increased range and armor penetration. However, such projectiles are hard to accelerate in powder or other gas guns without sabots adjusting them to larger caliber bores, as the driving force exerted by gas pressure is proportional to the bore cross-section area. Sabots also distribute the driving force (applied to the rear surface of the launch package) over the length of the projectile, thus reducing axial stress in slender projectiles to an allowable level. The downside of the use of sabots is significant parasitic mass they introduce into launch packages – a portion of the launch package muzzle energy associated with it is wasted when the sabot is discarded.

When railguns drive projectiles with metal armatures, magnetic pressure works quite similar to gas pressure. Two key factors – the velocity skin effect and transient skin effect – are responsible for this similarity, because they tend to localize the current and the driving force at the trailing end of the armature. Unsurprisingly, railguns accelerate slender projectiles by using the same subcaliber technique as gas guns – inserting them in larger diameter integrated sabots/armatures to increase their cross section and distribute the force.

In principle, EM launchers could accelerate such projectiles in a quite different mode – without sabots and, nevertheless, with low axial stress – if $\mathbf{j}\times\mathbf{B}$ forces could be well spread lengthwise over thin and long armatures, potentially as long as the projectiles (see Fig.1).

So far this remarkable potential of electromagnetic acceleration has remained unrealized. While long armatures could be readily designed for most projectiles, railguns cannot use them to advantage because of the factors mentioned above.

The inductiveless rail launchers presented here enable this highly desirable mode of acceleration. They also provide two additional benefits – radical reduction of repulsion force between the opposite rails in the launch tube, and substantial – 2-2.5 times – increase in the net launch efficiency as compared to the state-of-the-art railguns.

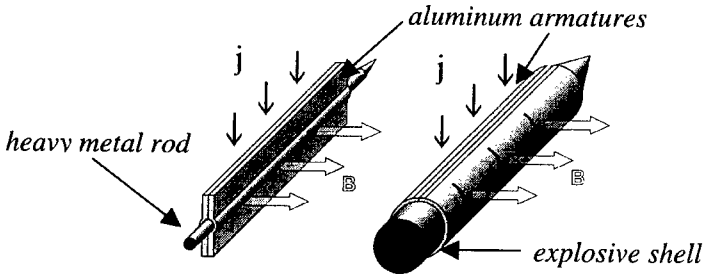


Fig.1. Long projectiles in long but thin armatures can be accelerated at low internal mechanical stress provided that magnetic induction **B** and current density **j** are spread sufficiently evenly over the armature length.

It is convenient to start discussion with the latter issue. Major causes leading to low efficiency of railguns are well known. In addition to losses due to parasitic mass of sabots and resistive losses in the rails and other conductors, a large portion of supplied energy (50% for a rectangular current pulse) is accumulated during the launch in the inductive (magnetic) energy of the rail circuit behind the projectile. On exit, this accumulated energy is wasted dissipating in the muzzle flash or in the ballast resistors used to suppress the muzzle flash.

Two concepts have been proposed to improve the efficiency of railguns by getting rid of this parasitic energy – railgun with nested rails and distributed energy store (DES) by Marshall [1], and muzzle-fed railgun with nested rails and single energy source by Bauer [2]. Marshall's DES railgun is shown in Fig.2. A large number of segmented and nested mini-rails assembled in a chevron-like pattern form two compound rails supplying the current to the armature. Each pair of opposite mini-rails in the assembly receives a short current pulse from a separate energy source (distributed storage capacitors are usually considered for this purpose). The pulse occurs when the armature closes the circuit between the two mini-rails.

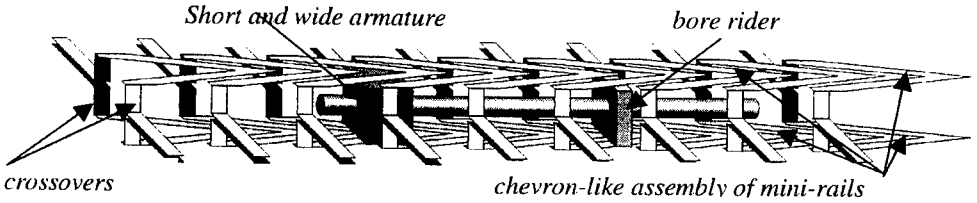


Fig.2. Schematic illustration of the DES railgun. Each pair of mini-rails is connected to a separate pulse power source (not shown). A short and wide armature with large cross-section area simultaneously contacts with several nested mini-rails.

The DES railgun concept eliminates the need to transmit the current along the launch tube, reducing resistive losses in the rails. Also, at any given moment the segment of the launch tube filled with inductive energy is limited by the span of a mini-rail. However, this reduction of accumulated inductive energy does not necessarily mean that the energy lost in a sequence of mini-arcs flashing when the armature breaks contacts with mini-rails is smaller than in conventional railguns. For example, multi-stage railguns with stages arranged in series (i.e., without nesting) loose the same energy in series of smaller arcs occurring on exit from each stage as conventional railguns do in one large muzzle flash. What actually reduces losses in Marshall's concept is increased magnetic (inductive) coupling between nested mini-rails. It improves switching of the current from the mini-rail breaking the contact with the armature to the neighboring mini-rails, because such switching disturbs magnetic fields less.

The DES railgun concept is not readily applicable to tactical guns because it is hard to integrate sizable storage capacitors into the barrel. To circumvent this difficulty, pulse power

sources could be situated near the breech and connected to their respective loads by high current cables laid along the barrel. However, the total weight of such numerous cables (each transmitting only a very short pulse of the full high current) appears to be prohibitive.

The launcher illustrating Bauer's concept (dubbed "HYPE" by its author) is shown schematically in Fig.3. HYPE borrows from Marshall's DES railgun the idea of mini-rails' nesting, but instead of multiple pulse power sources uses a single source connected to the muzzle terminals. Two additional continuous rails carry the current from the muzzle terminals to a few mini-rails contacting with the moving armature at the moment.

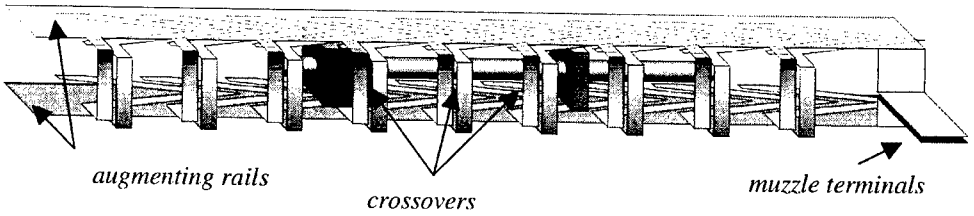


Fig.3. Schematic illustration of a muzzle fed railgun with nested rails and single power source. It can use the same nested rails and armatures as Marshall's DES railgun, but the current is supplied from the muzzle terminals via augmenting rails. To avoid clutter, crossovers on the far side of the launch tube are not shown.

Importantly, each of the two continuous rails is connected to the mini-rails situated on the opposite side of the launch tube. Due to such cross-strap connection, the continuous rails augment the flux created by the mini-rails in and behind the armature (hence the name augmenting rails). The augmenting rails also create magnetic flux in front of the armature, all the way up to the muzzle terminals. Inductive energy associated with this flux has to be supplied by the power source at the beginning of the launch. Contrary to conventional railguns, the portion of the launch tube containing inductive energy shortens as the projectile moves towards the muzzle, until it finally disappears when the projectile exits.

While this concept indeed completely eliminates the residual inductive energy, losses of inductive energy on contact breaks between the armature and mini-rails are about the same as in Marshall's DES railgun. They are lower than in conventional railguns for the same reason – due to increased magnetic coupling of nested mini-rails. As to the ordinary resistive losses in the rails, they are higher in HYPE than in conventional railguns, in particular because the current is delivered to the armature over a longer path (on average), especially if the pulse power sources have in fact to be located near the breech. For this reason, the efficiency improvement over conventional railguns promised by this concept is moderate.

It appears that for both advanced concepts discussed above there was not as much experimental development (especially at higher currents) as their underlying idea – the use of inductively coupled mini-rails – deserved. In addition to restraining factors noted above, there is probably one more reason for that. Launch tubes with segmented rails are difficult to design because of multiple crossovers – conductors carrying current to segmented rails across high magnetic field. The recoil forces acting on crossovers are equal to or even exceed, as in HYPE, the driving force applied to the projectile. It appears that no compelling design solution for high current launch tubes with multiple crossovers has been found so far. Finding a robust design is necessary for any high current experiments involving segmented rails.

The inductiveless architecture presented in the next section continues the line of thought expressed in Marshall's and Bauer's concepts. It adds two new ideas – the use of long armatures and low inductance busses for current transport along the launch tubes. These synergistic ideas bring new merits to launchers with nested segmented rails.

INDUCTIVELESS LAUNCH TUBES

Fig.4 illustrates the inductiveless architecture in a manner highlighting its similarities to and differences from the concepts discussed above. Magnetic flux in a long armature is created by compound rails formed by slanted, densely stacked tongue-like mini-rails, or railettes, as they will be called here. At the interfaces railettes are electrically insulated from each other, while at the tips they pass the current to the armature either via sliding metal-to-metal contact or, preferably, via a thin discharge gap (a plasma brush).

The current in such compound rails can only flow at an angle with respect to the launch direction, and, hence, cannot be transmitted by the rails over the launch tube length. This function is performed in the inductiveless launch tube by a low inductance bus (or several busses) laid along the tube to feed the railettes. The bus receives the current from a supply line connecting a pulse power source to input terminals of the bus; these terminals are located, preferably, between the breech and the muzzle. To reduce the inductance of the supply line and to lower mechanical loads in it, a large number of parallel cables can be used, each carrying a small portion of the total current during the entire launch event.

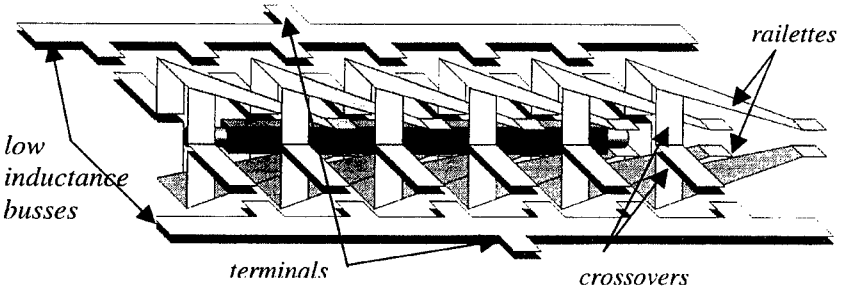


Fig. 4. Skeletal diagram of the inductiveless rail launcher. Densely stacked slanted railettes (to avoid clutter, they are shown rarified) receive current from low inductance busses connected to a single power source. A long armature simultaneously contacts with a large number of railettes. The current flowing in the railettes creates the transverse component of magnetic field in the armature.

Multilayer busses are especially suitable for inductiveless launch tubes because they can have very low inductance and resistance (the latter not only due to larger total cross section area of the bus but also because thin interleaved bus conductors, or busbars, are practically free from the skin effect). Another useful property of multilayer busses is their ability to carry high currents at relatively low mechanical loads.

Due to extremely low inductance attainable with multilayer busses, this architecture is virtually free from accumulation of inductive energy throughout the launch. Yet it can be used with a single power source. Thus it combines the merits of the DES railgun and HYPE.

The conceptual design presented below implements the inductiveless architecture in a different, more robust form. The launch tube in this design consists of stacked metal plates and railettes of alternating electrical polarity. This core assembly is surrounded by a multilayer bus consisting of radially oriented busbars.

Fig. 5 shows the main building block of inductiveless launch tubes - a pair of consecutive plates and railettes (which can be detachable as shown). Fig.6 presents two views of a section of the core assembly along with a pair of busbars carrying direct and return currents.

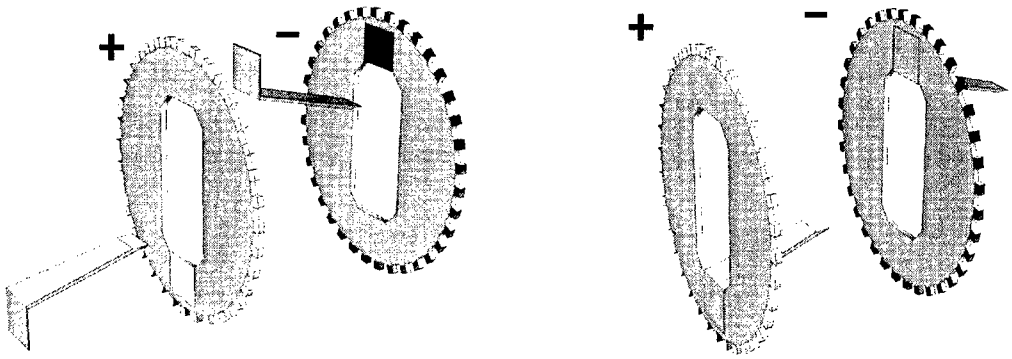


Fig. 5. A pair of plates and railettes of opposite polarity. Positive and negative contacts are shown in white and black.

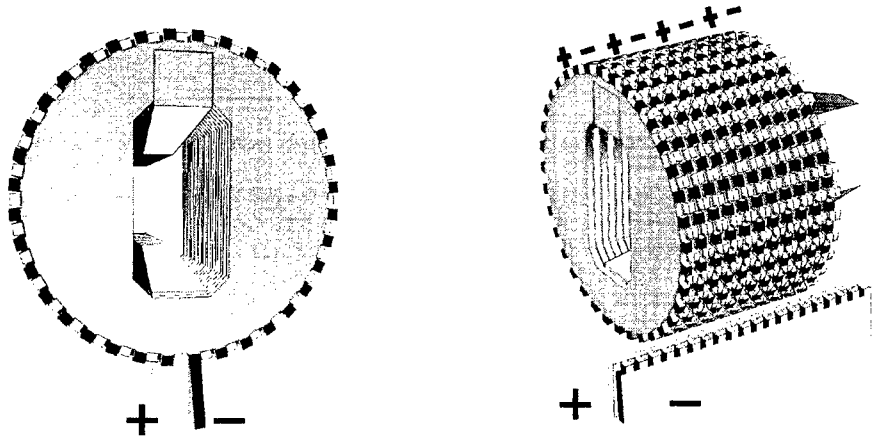


Fig. 6. Short section of launch tube assembled from plates of alternating polarity. Two busbars of opposite polarity belonging to the multilayer bus are also shown. Toothing at the edges (rectangular as shown or of some other shape) helps organize contact interface between plates and busbars.

The plates' geometry – in particular the shape of the bore – depends on the launch packages to be accomodated, and thus may differ from that shown here. Note that positive and negative plates may have exactly the same shape, differing only in orientation. The plates may be not quite flat – in particular, they can be slightly corrugated or conical. It is essential, however, that the plates and railettes are densely stacked forming robust, quasi-monololithic structures of the launch tube and compound rails.This implies that slanted railettes are thinner than plates. Dense stacking of thin railettes results in strong inductive coupling between the current loops containing them. As was discussed above, this reduces losses resulting from the current switching upon breaking of contacts between the armature and railettes.

Candidate materials for plates and busbars are high strength aluminum alloys, and for railettes highly conductive copper alloys because of higher current density near the tips of railettes. The tips can be coated with materials improving contact properties. Insulation between adjacent plates, for example with epoxy or teflon coating, must be thick enough to withstand the maximum voltage applied to the launch tube (which, however, is significantly lower than in railguns). Note that the stacked plates in this design are bifunctional: they serve as electric crossovers passing the current from the busbars to the railettes, and as structural elements supporting the compound rails against repulsion forces. In optimized designs, parameters of the plates, railettes and busbars may vary along the launch tube.

The multilayer bus surrounding the core assembly is shown in Fig.7. In addition to carrying high current to the plates, its busbars tie together the core assembly in the axial direction with the help of radial projections at their ends. Moreover, busbars can prestress the core assembly to keep it quasi-monolithic in the presence of strong recoil forces acting on the plates during the launch (i.e., to preclude occurrence of even instantaneous gaps between the plates). Thus the busbars also perform two functions, electrical and mechanical.

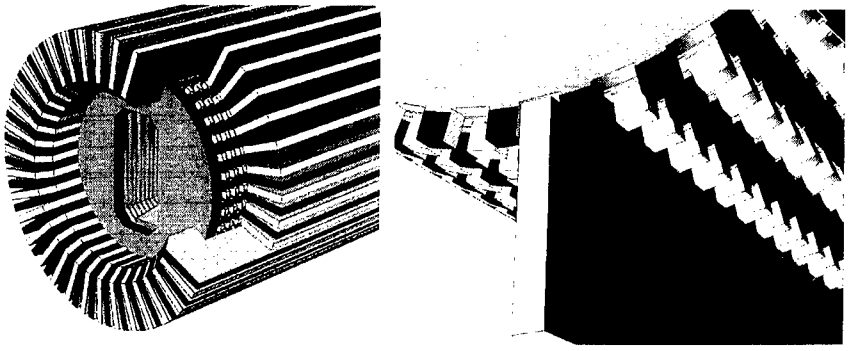


Fig. 7. Cut-out view of busbars near the breech (left), and zoomed view of the checkered pattern of electrical contacts between the plates and busbars (right). Positive and negative busbars and insulating layers between them are shown with white, black and gray edges respectively.

To avoid rail gouging and reduce wear, launch packages in inductiveless launch tubes can be guided not by the rails but by more easily replaceable wall inserts (shown in Fig. 8) made of an insulator with low friction coefficient.

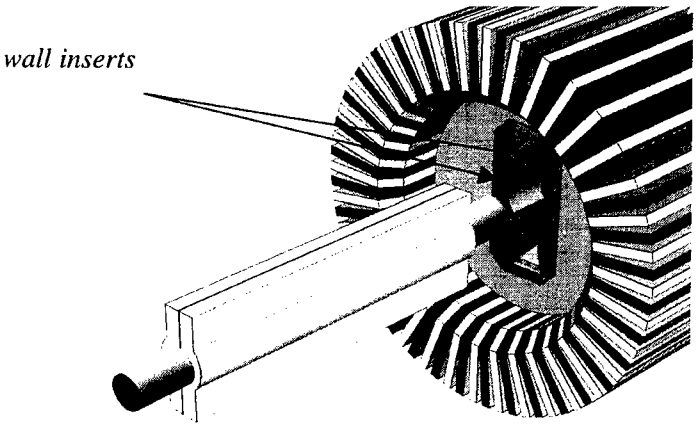


Fig.8. Heavy metal rod in a long armature being inserted in the bore of inductiveless launch tube.

As Figs.5 – 8 show, the launch tube is built with laminated metal structures carrying finely interleaved direct and return currents. Inductances of such structures can be far lower than those of rail circuits in railguns. As was already noted, this greatly reduces the accumulation of parasitic inductive energy as well as mechanical loads accompanying the transmission of high current. As to the thin lamination of compound rails, it enables strong magnetic coupling between neighboring railettes, which reduces current switching losses.

Completing the description of inductiveless launch tubes, Fig. 9 depicts a steel tubular shell, or barrel. Its function is to house the entire launch tube structure, increase its flexural stiffness and provide armor protection. The barrel, however, may have virtually no role in the containment of mechanical loads caused by magnetic pressure – as shown below, rail-to-rail repulsion is reduced so much that it can be contained by the aluminum plates only, while radial forces due to mutual repulsion of the busbars are quite low.

Note that in the barrel shown in Fig.9 the input terminals via which the current is supplied to the launch tube are positioned between the breech and the muzzle. This diminishes the average length over which the current is delivered to the moving armature, further lowering resistive losses. This also facilitates gun designs with an intermediate pivoting point (helping balance the barrel and reduce its forward projecting length).

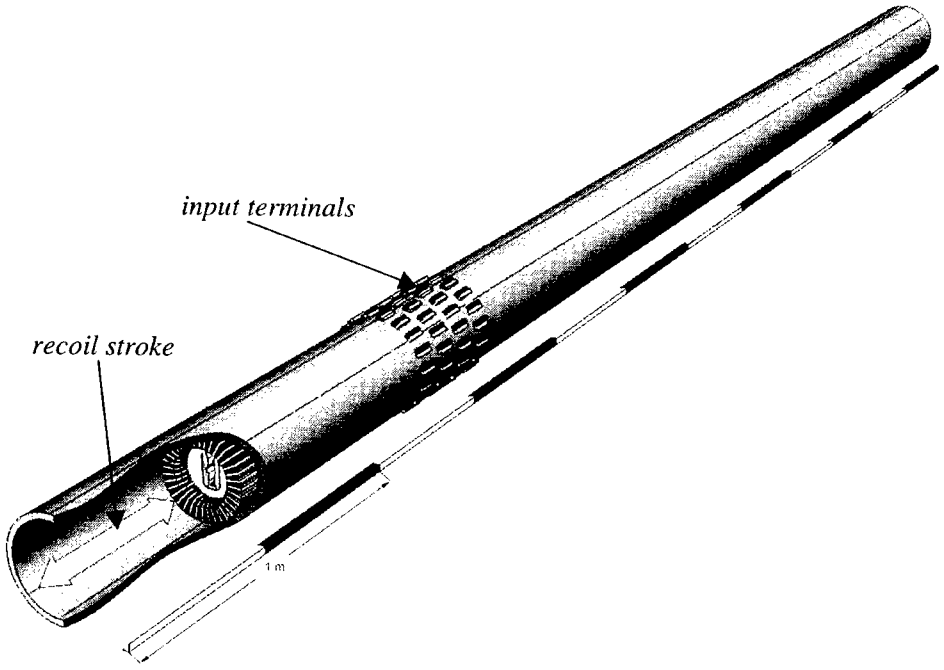


Fig. 9. Launch tube structure in a steel barrel. With sliding contacts between the terminals and busbars inside the barrel, the recoil of the launch tube structure can be absorbed within the barrel, possibly using friction between the structure and barrel (the barrel must have an insulating lining to avoid short-circuiting busbars).

The conceptual design presented here for inductiveless launch tubes has a short list of basic parts – railettes, plates, busbars and wall inserts – that can be readily manufactured and assembled with good precision to provide a highly symmetrical launch environment.

The only essential component missing in Figs. 5 - 9 is the system of distributed ballast resistors connected in series with each plate/railette. As shown in the next section, ballast resistors suppress generation of eddy currents in the launch tube circuitry and help distribute the current from the busbars quasi-uniformly over the length of the armature. Note that the energy lost in ballast resistors would otherwise (i.e., if they were absent) be lost in arcing and contribute to erosion of the contact surfaces. Design consideration for ballast resistors will be discussed below after the basic electromechanical characteristics of inductiveless launchers are presented.

BALLAST RESISTORS AND CURRENT DISTRIBUTION IN LONG ARMATURES

As will be shown shortly, electric current in a long armature can be spread approximately evenly along its length. The corresponding magnetic field created by the current in and around the armature is visualized in Fig.10 as a superposition of two simpler field patterns – the field shown by thin black lines mostly parallel to the armature, and the transverse field shown by gray lines passing through the armature and around the railettes.

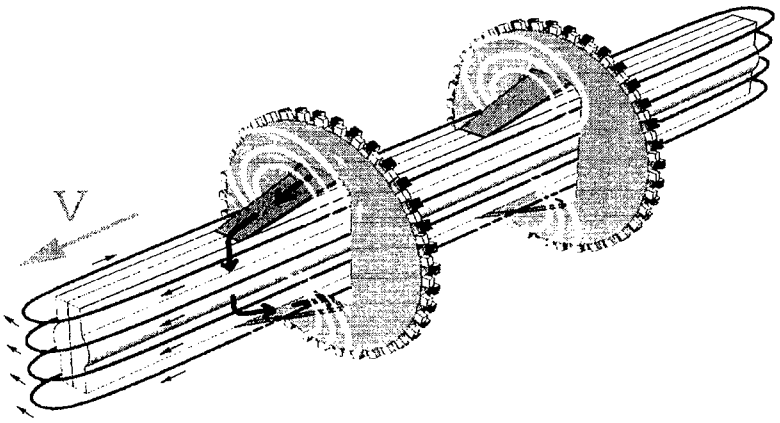


Fig.10. Magnetic field patterns in the inductiveless launch tube. For clarity, only two pairs of plates/railettes are left visible.

It is well known that quasi-static Maxwell equations in their differential form can be difficult to solve numerically in the presence of fast moving metal conductors because of very high magnetic Reynolds numbers. In the case of inductiveless rail launchers the problem is further aggravated because thin lamination of conductors comprising the launch tube necessitates a very fine mesh. Fortunately, lamination makes effective another approach based on circuit equations. In the form appropriate for circuits with sliding elements they are briefly discussed in the Appendix; these equations have been used to find currents in railettes.

The essence of this approach is simple: each pair of plates/railettes together with the adjacent portion of the armature short-circuiting the railettes can be viewed as a current loop. The loops are connected to the common bus feeding them with current, and the current distribution in the loops is controlled, along with their resistances and self and mutual inductances, by the Lorentz electromotive force $\mathbf{v}\times\mathbf{B}$ in their sliding elements.

Two typical current distributions in railettes in contact with the armature are plotted in Fig.11 (model parameters for these graphs will be discussed in the next section). The left-hand graphs correspond to the case when the only resistances in the current loops are those of plates and railettes, which are very low. This results in high internal (eddy) currents having opposite directions in the neighboring railettes. As was already noted above, introduction of ballast resistors in the plate/railette loops helps suppress the eddy currents. With sufficient ballast resistors, the current distribution smoothes out as shown by the right-hand graphs. Of course, ballast resistors reduce the launch tube efficiency, but, as also was already noted, some of the energy dissipated in them would be lost anyway in more intensive arcing contributing to erosion of the rails. As follows from the numeric modeling, with sufficient resistances of ballast resistors and good inductive coupling of railettes, the efficiency of inductiveless launchers can be substantially higher than that of conventional railguns.

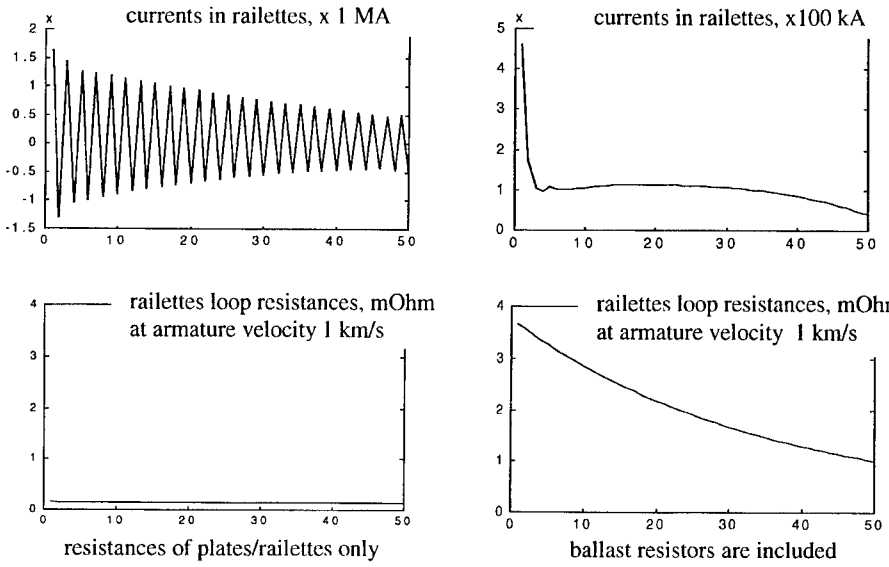


Fig.11. Examples of current distributions for two distributions of circuit resistances. Numbers on horizontal axis increasing from the trailing end to the front end of the armature refer to railettes contacting with the armature at the moment.

With eddies suppressed, the current distribution is nearly constant along the armature, except for a current peak at the trailing end and a reduced current density zone at the front end. As shown in the Appendix, the current distribution remains steady during the launch provided that local ballast resistances increase with the travel proportionally to the expected projectile velocity.

The current peak at the trailing end can locally melt the armature. To avoid that, the armature cross section near the trailing end should be increased, while the current peak amplitude should be lowered to an acceptable level by further increase of ballast resistances. As this would increase energy losses in ballast resistors and hence lower launch efficiency, it is preferable to shape the ballast resistances so that they ramp up towards the trailing end of the armature (as shown on the right lower graph in Fig.11) where they suppress the current peak most effectively.

Note that the ballast resistors belong to the launch tube and move with respect to the armature. For this reason, the increase of resistances at the trailing end (in the frame of reference associated with the armature) means that the resistance of each ballast resistor increases with time as the armature passes by. Such behavior can be achieved, for example, if resistors are made of pure metals and heated red hot by the current pulse, because resistivity of many pure metals increase several times before they melt.

The volume of red hot metal needed to accommodate the required energy loss in the resistors proves to be much smaller than the volume of the aluminum plates. For this reason, ballast resistors can be implemented as metal foils sandwiched between thin ceramic or oxide insulating films and sealed into the aluminum plates (thus resembling heat tapes in ordinary cookers). In another solution, small ceramic chips filled with metal wires or tapes can be integrated into the busbars or plates so that instead of being in direct electrical contact the busbars and plates are connected via such resistor chips.

DESIGN EXAMPLE FOR FTP CLASS INDUCTIVELESS LAUNCHER

To get a better feel of electromechanical properties of inductiveless launchers, a design example with performance parameters set forth by the Focused Technology Program may be useful. Such an example supported by numeric modeling of the current distribution in railettes is presented here, and its characteristics are compared with state-of-the-art railgun technology. For convenience, numeric values quoted below are rounded, and a simple rectangular current pulse is considered.

In this example, a heavy metal rod (diameter 20 mm, length 500 mm, mass 3 kg) inserted in aluminum armature of the same length (like the one shown in Fig.1, with average thickness 8 mm, contact-to-contact distance 80 mm, mass 1 kg – so that the total mass of this launch package is 4 kg, with armature mass share 25%) is launched to 2.8 km/s (16 MJ total launch package muzzle energy, of which 12 MJ is in the rod) by constant driving force 320 ton with acceleration 80 kgees in a launch tube 5 m long. The launch duration is 3.6 ms.

The conceptual launch tube design for this example has already been depicted in Figs.5 – 8, so only dimensions and other numerical details remain to be specified. The core assembly consists of 1000 plates, each 5 mm thick (4.5 mm aluminum and 0.5 mm insulation), with diameter 220 mm and size of the central hole 120 mm by 50 mm. The bus consists of 120 busbars 30 mm wide in the radial direction with average thickness 6.5 mm (6 mm aluminum and 0.5 mm insulation). Inductance gradient of the bus is only 1.8 nH/m – far smaller than 0.4-0.6 μH/m typical for rails in a railgun. The outer diameter of the launch tube structure (without the encasing steel barrel) is 280 mm. Properties of aluminum alloy 7075 T6 were used to estimate mechanical and electrical parameters of plates and busbars.

Copper railettes are 2 mm thick and span 100 mm in the direction of the launch. They form compound rails of trapezoidal cross section (40 mm wide at the base supported by the plates assembly, 20 mm wide at the opposite base interfacing with the armature, and 20 mm high). The armature simultaneously contacts with 50 pairs of railettes. Properties of copper alloy C16200 were used for estimates concerning railettes.

The weight of this mostly aluminum structure is 160 kg/m. A steel barrel with the inner diameter 280 mm and outer diameter 320 mm adds 150 kg/m, raising the weight per unit length to 310 kg/m. The total weight of 5 m long launch tube is thus only 1550 kg.

The graphs in Fig.11 are taken from numerical modeling of this launch tube. The modeling has determined the current and voltage needed to create 320 tons of driving force: 5.2 MA current at voltage rising linearly from zero to 2.7 kV at exit. The total energy supplied to the launch tube is 25 MJ, of which 16 MJ is the launch package kinetic energy, and 9 MJ is lost (7.5 MJ in the ballast resistors and 1.5 MJ in the busbars). It is interesting to note that after the temperature levels out over the cross-section of the launch tube, which takes about 30 s, the average temperature rise resulting from 9 MJ energy loss is ~10° C.

Assuming that ballast resistors are implemented as metal foils sealed in the aluminum plates comprising the launch tube, each of 1000 ballast resistors has to accommodate 7.5 kJ. Assuming also that the allowed metal foil temperature at the end of the pulse is 800° C, the required volume of metal foil is just ~3 cm^3 per plate. For the foil occupying 200 cm^2, or ~80% of the plate area, this translates to 0.15 mm thickness (without insulation, and ~0.5 mm with thin ceramic/oxide insulation). The resistivity of the foil metal and its length-to-width ratio should be chosen from the required ballast resistances varying (in the initial cold state) from ~0.3 mOhm at the breech to ~1.5 mOhm at the muzzle.

To realistically compare the inductiveless launcher characterized by the parameters specified above with state-of-the-art conventional railguns, one should take into account that launch packages designed for railguns are substantially heavier than those for inductiveless launchers. In carefully designed launch packages for railguns parasitic mass ratio of the integrated armature/sabot exceeds 50%, as compared to only 25% for the armature considered here (with parameters also carefully chosen with action and stress limitations in mind).

At parasitic mass ratio 50%, the muzzle energy of the launch package in a comparable railgun must be 24 MJ in order to have the same 12 MJ in the in-flight projectile. This is 1.5 times greater than 16 MJ in the inductiveless launcher. Accordingly, the driving force in the comparable railgun must be 480 tons instead of 320 tons. With this in mind, the current and voltage at exit in a comparable railgun with 0.5 μH/m inductance gradient are estimated as 4.4 MA and 7.0 kV. This corresponds to 43% launch efficiency for the rectangular current pulse considered here, which is a pretty decent allowance given lower launch efficiencies routinely observed in railguns with current pulses shaped more favorably in terms of efficiency (with the current drooping towards the end) than the rectangular pulse.

Thus the inductiveless launcher in our example requires 2.6 times lower voltage and only 1.2 times higher current than a comparable railgun. While a railgun with 43% efficiency would take 55 MJ to launch heavy metal rod with 12 MJ muzzle energy, the inductiveless launcher produces the same result with only 25 MJ, or 2.2 times more efficiently.

Comparing mechanical stresses in inductiveless launchers and railguns, one can easily estimate that repulsion between railgun rails carrying 4.4 MA current and separated by 100 - 120 mm distance would be practically impossible to contain with a structure made of an aluminum alloy. The current supplied to the inductiveless launcher is higher, while its rail-to-rail distance smaller. Why then it is possible to contain rail-to-rail repulsion with aluminum plates in inductiveless launchers? To answer this question, one should take into consideration that in inductiveless launchers the current in any cross section of the compound rail is substantially smaller than the full current supplied to the armature, their ratio being roughly proportional to the ratio of the railette span to the armature length.

As follows from the distribution of current in railettes shown by right-hand graph on Fig. 11, the current in the compound rails at the central region of the armature does not exceed 1.2 MA, which is nearly 4 times lower than the current in a comparable railgun. Recalling that the rail-to-rail repulsion is proportional to the square of the current, it is about ten times lower in the inductiveless launcher after taking into account geometric factors. With such drastically reduced repulsion, the average stress in the most stressed cross section of aluminum plates is, by estimate, just ~40 MPa, which is about one order of magnitude lower than the yield stress, and leaves enough room for stress concentration factor and safety margin. If needed, the barrel encasing the core launch tube structure can provide an additional containment capability.To tap into this reserve, slightly corrugated plates can be used instead of flat ones to transfer the repulsion load to the barrel before being irreversibly deformed.

The rectangular current pulse considered here is not typical for available pulse power sources. With more realistic pulses in which the current droops towards the end of the launch, either the length of the launch tube and duration of the pulse or the maximum driving current may be increased to compensate for the droop. As was mentioned above, such current pulses increase somewhat the launch efficiency of railguns (at the price of lower piezometric quality of the railgun barrels), but these relatively minor corrections can hardly mitigate the significant advantages of inductiveless rail launchers.

APPENDIX :

CIRCUIT EQUATIONS FOR CIRCUITS WITH SLIDING CONTACTS

In structures composed of wire-like conductors in which geometry of current loops can be derived from conductors' geometry, circuit equations can be very effective. For circuits involving sliding contacts these equations must account for Lorentz emf $\mathbf{V}_{rel}\mathrm{x}\mathbf{B}$ due to the relative motion of conductors with respect to the current loop. Retaining this usually omitted term, following the standard derivation of circuit equations and Faraday's law (see, for example, [3]) and taking into account that the magnetic induction linearly depends on the currents, the equations for circuits with sliding elements can be written as:

$$d/dt(Li) + Ri = e + Si$$

in which $i = \{ i_n \}$ is the vector of currents in the loops, e is the vector of external voltages (emf) applied to the loops, L and R – the usual matrices of inductances and resistances. Matrix S with elements given by

$$S_{mn}(t) = \int \mathbf{j}_m(\mathbf{r},t)\,[\mathbf{V}_{rel}(\mathbf{r},t)\mathrm{x}\mathbf{B}_n(\mathbf{r},t)]\,d\mathbf{r}$$

links Lorentz emf acting in a loop to the currents in the same and other loops. In this formula $\mathbf{B}_n$ – vector of magnetic induction created by $\mathbf{j}_n$ – is given by Ampere's law,

$$4\pi\mathbf{B}_n(\mathbf{r},t) = \mu_0 \int (|\mathbf{r} - \mathbf{r}'|^{-3})\,[\mathbf{j}_n(\mathbf{r}',t)\mathrm{x}(\mathbf{r} - \mathbf{r}')]\,d\mathbf{r}'$$

To apply these equations to inductiveless launchers, current loops are defined as consisting of pairs of opposite railettes, crossovers connecting them to the bus, and adjacent segments of the armature short-circuiting the railettes. It is convenient to choose the frame of reference associated with the armature, in which the railettes and crossovers are the sliding conductors, because this choice allows for a steady solution for the currents in the armature.

If a steady solution exists, it can be found from the abridged equation

$$(R - S)\,i = e$$

A steady solution exists, in particular, for the case of constant acceleration. As matrix S is proportional to the armature velocity with respect to the launch tube, it varies in this case linearly with time. If the resistances R in the loops adjacent to the armature as well as voltages e applied to the loops also vary linearly with time, the time dependence can be factored out from the abridged equation. Numerical solution of thus derived system of time-independent linear equations yielded the data used in preparation of this paper.

The increase of resistances of ballast resistors adjacent to the moving armature means they increase along the launch tube proportionally to the expected armature velocity at a given position, varying as the square root of the travel in the case of constant acceleration.

ACKNOWLEDGMENTS

The author would like to thank Prof. R. Marshall for his kind interest and review of the paper.

REFERENCES

1. R.A.Marshall, "The use of Nested Chevron Rails in a Distributed Energy Store Railgun", IEEE Trans. on Mag. Vol.20, No.2, March 1984, pp 389-390
2. D.P.Bauer, "A Novel Railgun Launcher Design", IEEE Trans. on Mag. Vol.31, No.1, January 1995, pp.267-272; see also D.P.Bauer, patent US5375504, Augmented hypervelocity railgun with single energy source and rail segmentation, December 1994
3. L.D.Landau, E.M.Lifshitz and L.P.Pitaevskii, Electrodynamics of Continuous Media, 2nd edition, ISBN 0-7506-2634-8, §§ 33, 61, 63

ON THE PARASITIC MASS OF LAUNCH PACKAGES FOR ELECTROMAGNETIC GUNS

M. J. Hinton[1], N. R. Cooper[2], D. Haugh[3], and M. A. Firth[4]

[1] *Future Systems Technology Division (FST), DERA, Fort Halstead, UK*
[2] *Structures and Materials Centre, FST Division, DERA, Farnborough, UK*
[3] *Security Division, DSTL, Fort Halstead, UK*
[4] *Centre for Defence Technology, FST Division, DERA, Fort Halstead, UK*

Point of Contact: *Professor M. J. Hinton, Director of Technology (Operations),*
FST Division, DERA, Fort Halstead, Sevenoaks, Kent, TN14 7BP, UK
Telephone: 44 (0) 1959 514946
Fax: 44 (0) 1959 516059
e-mail: mjhinton@dera.gov.uk

© British Crown Copyright 2001. Published with the permission of the Defence Evaluation and Research Agency on behalf of the Controller of HMSO. This work was carried out as part of Technology Group 01 of the UK MoD Corporate Research Programme.

Conventional gun and projectile design methodology has evolved over the last 50 years to a state where computer generated models can safely predict shot behaviour, from loading into the gun through to target impact. Long rod kinetic energy (KE) projectile packages with parasitic mass ratios (PMR) below 0.3 are becoming the norm for the conventional gun launched environment. In contrast, electromagnetic (EM) gun and projectile design methodology is far from mature, given the relative youth of the technology (<15 years), the increased complexity of the governing physics and the scarcity of major programmes addressing the area. The Defence Evaluation and Research Agency (DERA) is investigating EM gun technology on behalf of the United Kingdom Ministry of Defence, as a possible contender for the direct fire role in a future armoured land vehicle. One of many key issues is to establish the bounds on the PMR for long rod EM KE packages. Initial UK designs of EM KE launch package have been of the circular bore, 'base-push', type where the armature is positioned behind the projectile. A comprehensive programme has resulted in a good understanding of the PMR bounds for this configuration. More recent studies have focussed on circular bore, 'mid-ride' concepts, where the armature is situated near the mid-point of the shot and there is potential to attain further reductions in PMR. The paper presents an overview of the UK KE launch package studies together with a more detailed assessment of the expected PMRs.

INTRODUCTION

The UK Defence Evaluation and Research Agency (DERA) has an extensive capability for the design of conventional gun launched armour piercing, fin-stabilised, discarding sabot (APFSDS) kinetic energy anti-tank projectiles. The capability encompasses internal ballistics prediction, penetrator materials technology, sabot design, shot/barrel interaction modelling, aeroballistics and accuracy, and terminal effectiveness assessment via hydrocode modelling. The theoretical capability is reinforced with trials programmes, both strength of design and armour defeat, such that an extensive body of experimental data has been collected.

As implied above, maximising the performance of a KE penetrator to defeat a threat armour is reliant on a 'systems' approach - the terminal effectiveness being dependent on an array of system parameters which interact in a complex fashion. For example, in a conventional gun, the propellant charge requirement must be optimised with respect to the gun type (chamber volume and operating pressure) and the shot mass to achieve the best muzzle velocity.

A kinetic energy long rod is launched with a sabot, which fills the space between the rod and the bore, converting combustion pressure into a distributed force along the length of the rod. The sabot is discarded at the muzzle and constitutes parasitic mass. The parasitic mass ratio (PMR, the mass of discarded components to total shot mass) has therefore become a key indicator of shot design efficiency. Typically a PMR of about 0.45 is possible for a depleted uranium (DU) rod with an aluminium alloy sabot of 'saddleback' configuration[1]. This figure can be reduced by changing to a 'double-ramp' configuration[2], by using high strength rod materials, or by using lightweight sabots. A fibre reinforced plastic (FRP), double-ramp sabot can offer PMR values of around 0.3. However, to take advantage of a lower PMR requires considerable interaction with the remainder of the system: a longer rod with a double-ramp sabot needs a suitable combustion chamber and the necessary stowage; a higher muzzle velocity, attributable to lower shot mass, needs an optimised charge.

Current UK interest in the emerging electromagnetic gun technology is as a contender for the main armament of a future land combat system. Given the military need for more readily deployable forces (the US FCS and the UK FRES initiatives), great attention is being focussed on air-portable armoured vehicles with a robust capability to defeat enemy threats (Ref 1). EM gun technology has many attractive features, including:

- Low recoil (of critical concern for a light vehicle).
- Improvements in survivability by elimination of energetic materials from the vehicle.
- Reduction in logistic drag by elimination of energetics from the supply chain.
- Enhanced target defeat by providing hypervelocity launch velocity.

[1] 'Saddleback' refers to the sabot configuration where the main pressure bulkhead/obturator is near the back of the shot. Most of the rod is launched in compression and only a small section of rod carrying the fin is subjected to tensile stress.

[2] 'Double-ramp' is the sabot configuration where the main pressure bulkhead is about half way along the rod. A short saddleback section is complimented by a rear ramp subjected to combustion pressure. More of the rod is launched in tension than in saddleback designs.

DERA has been researching electromagnetic launch technology on behalf of UK MoD for the last 10 years, drawing on its conventional gun expertise and enhanced by investment in large scale EM launch facilities, principally at Kirkcudbright (which is the only facility in the world capable of launching EM projectiles and flying them out to long ranges). A systems approach has been taken and, as a consequence, significant advances in EM launch technology have been achieved (Refs 2, 3, 4).

Reducing the parasitic mass ratio for an EM gun launched projectile is a significantly greater challenge than for a conventional projectile. The EM projectile must fulfil an additional function, that of conducting a high electrical current across the rails, which implies the need for metallic components (thereby increasing the PMR significantly). In the light of this, a PMR goal of 0.5, somewhat higher than for conventional projectiles, has received common acceptance by the EM projectile community (eg Ref 5). The current paper describes the UK progress with large calibre EM projectile designs with particular emphasis on minimising the PMR towards the goal of 0.5.

One of many tools which has been developed to aid the study has been an analytical model for estimating the PMR, taking into account the sabot/penetrator material properties and the influence of the armature mass. This tool is described in the first section. Next, the UK programme in EM gun projectiles is presented in more detail, followed by design proposals for EM projectiles with reduced PMR. Details of relevant firings of experimental armatures is complimented by the results of EM modelling. Finally the use of alternative bore shapes, other than round, is discussed in terms of the impact on sabot designs.

EM GUN PROJECTILES - OVERVIEW

Projectile Configurations

As with conventional guns, EM gun projectiles have two principal configurations: base-push and mid-ride. In a base-push design, the armature pushes the shot from behind. This is similar in concept to the saddleback design of conventional rounds.

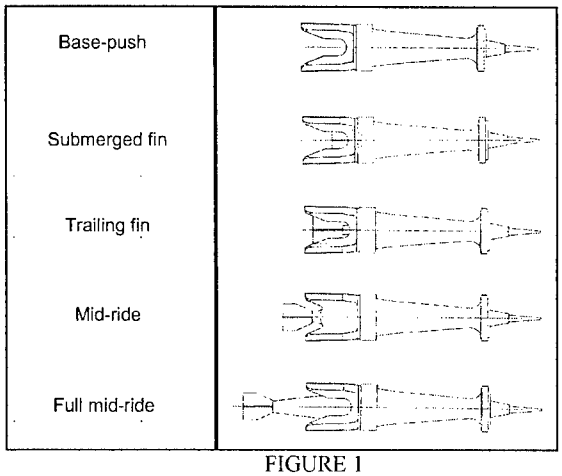


FIGURE 1

The mid-ride design has the armature situated (approximately) mid-way along the penetrator, and the sabot possesses both saddleback and rear ramps. The key difference between this concept and the double-ramp conventional shot is that the rear ramp of the EM projectile is not subjected to combustion pressure. The evolution from base-push to full mid-ride encompasses a range of design configurations depicted in Fig 1.

The initial UK work was performed with circular-bore, base-push projectiles with separate armatures to allow read-across of design data from conventional rounds and independent armature development. The design principles used for EM projectiles were similar to those for powder gun projectiles. The ratio of penetrator length to penetrator diameter (L/D) for conventional rounds is typically in the range 15 to 35. Similar values of L/D have been considered for UK EM gun projectiles.

Parasitic Mass Ratio Estimation

It is possible to derive an analytical expression for the parasitic mass ratio of an idealised base-push projectile subjected to axial acceleration. The following assumptions are necessary:

- The axial strain in the penetrator is equal to the axial strain in the sabot (Ref 6).
- The penetrator of length L has an overhang equal to L_o at the front of the projectile which is not supported by the sabot.
- The penetrator cross-sectional area, A_o, is constant along its length.
- The stress in the penetrator, when supported by the sabot, is constant and equal to the stress at the base of the front overhang.
- The stress states in the rod and sabot are due only to the effect of body forces arising from axial acceleration.

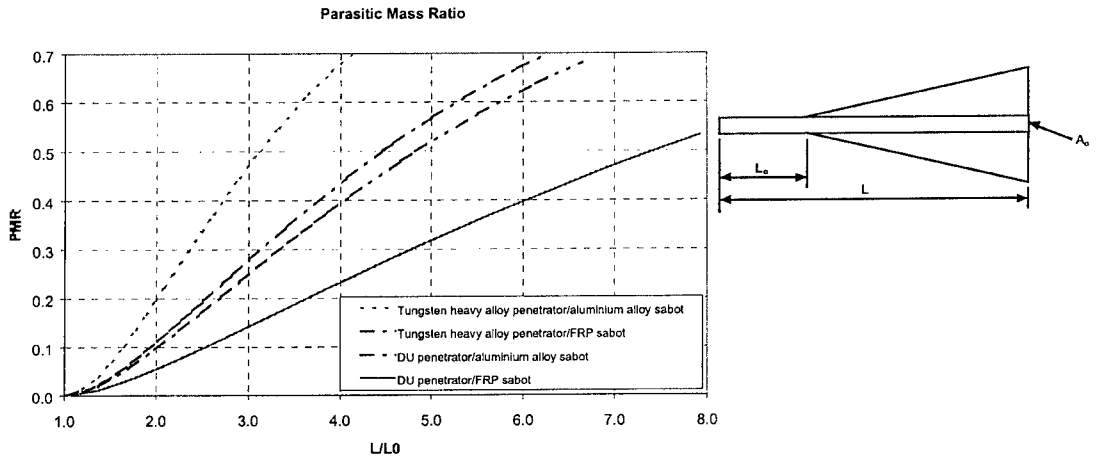


FIGURE 2

Fig 2 illustrates how the projectile PMR varies for idealised constant stress sabots as a function of the ratio L/L_o (penetrator length/penetrator front unsupported length) considering different rod and sabot materials.

The relationships embodied in Fig 2 are for wedge-shape, base-push sabots of circular cross-section. By symmetry about the basal plane, they are also applicable to mid-ride sabots with penetrator length 2L and front and rear L_o overhangs. At a typical value of $L/L_o = 4$, the use of a fibre reinforced plastic for the sabot instead of aluminium alloy reduces the PMR by 0.24 for a tungsten alloy penetrator and 0.15 for a depleted uranium rod. Changing from a tungsten heavy alloy penetrator to a DU penetrator is slightly more effective, with a reduction in PMR of about 0.29 for an aluminium alloy sabot, and 0.2 for an FRP sabot. The PMR is not a function of penetrator length to diameter (L/D) ratio based on this formulation. The influence of L/D is only apparent in real designs because the front and rear bore riders must extend from the penetrator to a fixed bore diameter.

These calculations illustrate trends in PMR considering different rod and sabot materials whilst deliberately excluding the mass of the armature. Adding an armature to a base-push shot significantly increases PMR as discussed below.

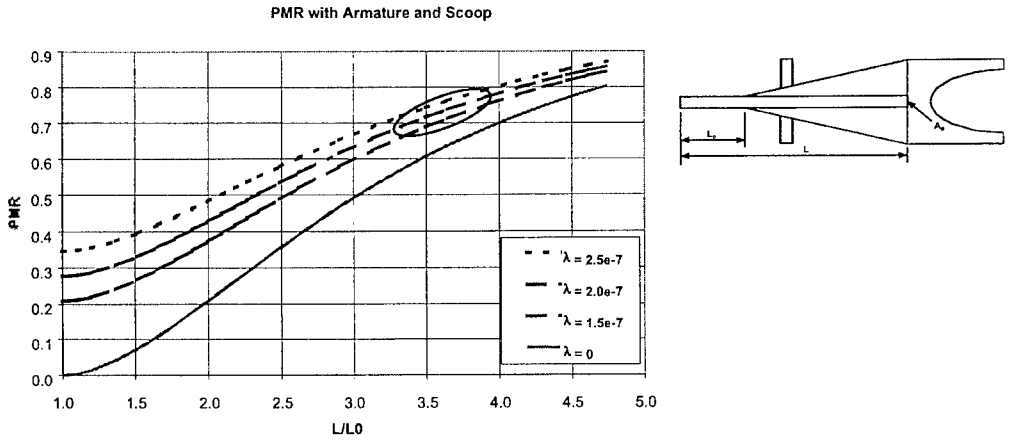


FIGURE 3 - Aluminium alloy sabots - $\lambda = V/(L' \times g)$ in SI units

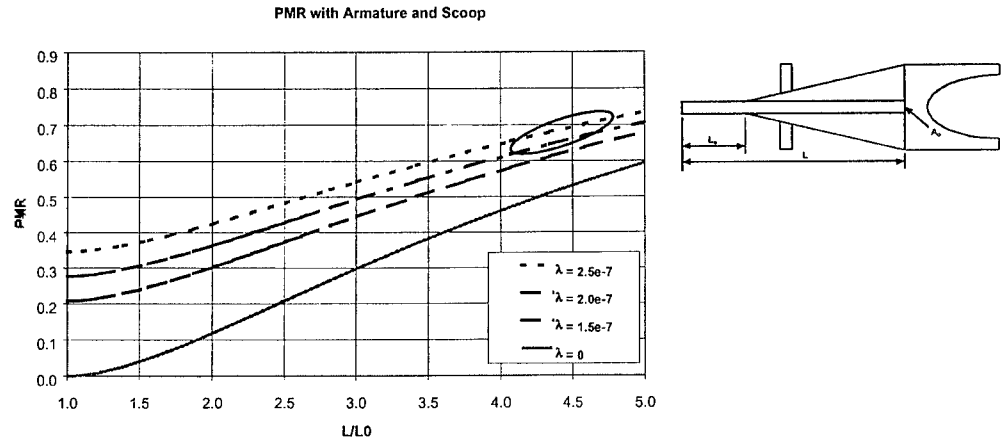


FIGURE 4 - FRP sabots - $\lambda = V/(L' \times g)$ in SI units

Figures 3 and 4 depict the variation in PMR as a function of L/L_o for base-push EM projectiles with tungsten alloy penetrators having aluminium and FRP sabots respectively.

The analysis is the same as presented in Fig 2 except that the masses of an air-scoop (front bore-rider) and an armature are now included. It is additionally assumed that:

- An appropriate size of gun is available, and that together with its power supply, the system will enable the chosen acceleration and velocity combination to be realised.
- The air-scoop is assumed to have the same diameter as the base of the sabot.

The armature mass has been estimated by first evaluating

$$A_A^2 = \frac{2M_S V}{L' g} \tag{1}$$

where A_A is the minimum current carrying cross-sectional area of the armature assuming a uniform current distribution, M_S is the total shot mass, V is the muzzle velocity, L' is the barrel inductance gradient and g is the specific action for the armature material. The specific action for various armature alloys has been evaluated from

$$g = \int \frac{\rho C_p}{\varepsilon} dT \tag{2}$$

where C_p is the specific heat, ρ is the density and ε is the electrical resistivity. In Eq (2), ε and C_p are taken as functions of temperature. Values of C_p for pure aluminium and a range of aluminium alloys have been determined by DERA from room temperature up to melt, and beyond, by experiment. The correlation between A_A and the armature mass is determined from limit-case EM gun firings at both 40mm calibre and 90mm calibre.

Usually the bore of the gun would be slightly larger than the sabot base size. The error involved in estimating the scoop mass using the sabot base diameter is considered small because the annulus between the scoop and the bore would be mostly filled with a lightweight insulating material, typically a suitable grade of nylon.

As before, PMR is a function of L/L_o, but now the parameter $\lambda = V/L'g$ is included to size the armature. A range of λ values have been included to cover typical combinations of V, L' and g. The special case of $\lambda = 0$ corresponds to a base-push shot without an armature and should be compared with the corresponding result in Fig 2 to assess the effect of the mass of the air scoop on PMR. Also of interest are the intercepts at the y-axis for the various λ values. Here, PMR_o values can be obtained for projectiles comprising rods of length $L = L_o$ and their armatures, but which do not require sabots.

The mass of an armature typically adds ~0.1 to the PMR of aluminium sabotted shot at a sensible value of L/L_o (ie ~ 4). The effect is more pronounced for FRP sabotted shots where the PMR is increased by ~0.15 at $L/L_o = 4$ by including the armature. Inspection of Fig 3 shows that a PMR of 0.5 is only possible with aluminium alloy sabotted rounds if very short rods are considered. At a PMR of 0.5, lightweight FRP sabots can (theoretically) increase L/L_o by about a third compared to an aluminium alloy sabotted projectile. The relationships depicted in Figs 3 and 4 are not exact (finite element analysis of designs would provide a better answer), but do indicate the correct trends, namely that it is very difficult to achieve respectable PMRs for base-push EM shots, and that the mass of the armature is significant in this respect.

Achieving hypervelocity with the same length barrel as a conventional gun increases the duration of the accelerating forces. The laminated, 90mm calibre, International Applied Physics (IAP) laboratory gun at Kirkcudbright was found to impart severe balloting (lateral acceleration) loads to projectiles as they travelled along the barrel under the extended action of the acceleration force combined with increased velocity (Ref 2). Thus additional parasitic mass over conventionally fired, ordnance velocity, projectiles is required for two reasons: the mass of driving armature behind projectile; and the higher transverse balloting forces. The latter is not reflected in the theoretical treatment of Figs 3 and 4 but is usually manifested in the need for a shorter front overhang, less than the L_0 required to otherwise size the sabot.

Armature Development

The development of low-mass armatures with improved electrical performance has always been recognised as a key factor in the success of EM gun technology. Early UK base-push armature designs were of the C-shape type, weighing some 1.2kg at 90mm calibre. As expertise grew, aided by the unique capability at Kirkcudbright to recover fired armatures, this mass was reduced to approximately 0.8kg. Further mass reductions were demonstrated but at the expense of earlier transition. Typical engineering weight-saving measures such as drilling holes, tapering dimensions and chamfering corners were all tried with mixed success.

In the light of this, the UK MoD has funded a dedicated research programme covering armature materials. The technical approach has been to combine the mechanical properties sought with the possibility of manufacturing armatures having preferential current flow to minimise ohmic heating in critical regions. The programme included the development of methods for characterising mechanical, electrical and thermal properties of candidate armature materials subjected to launch-type conditions, together with thermo-electromagnetic modelling of armatures and the development of a micro-mechanics design code to predict anisotropic electrical properties. The four key areas of investigation have been:

- Joining of dissimilar metals.
- Dispersion hardened and particulate reinforced metal matrix components.
- Continuous fibre reinforced metal matrix components.
- Porous refractory metals.

Multi-material armatures are perceived to offer the advantages associated with tailored thermal and electrical properties and several examples have been fired successfully.

EM GUN PROJECTILES - BASE-PUSH

The UK commenced large calibre EM gun research with an extensive history in round-bore conventional guns and projectiles. This background, coupled with the fact that the US had already amassed a database of 90mm calibre EM launch packages, led to the choice of 90mm round-bore as the preferred calibre type.

The UK EM launch packages are designated by the 'U' series nomenclature. The early designs were base-pushed and used a 'C' shaped armature of aluminium alloy to drive the shot

from behind. Whilst this configuration is not particularly mass efficient, it was chosen to allow independent development of shot and armature. Some of the packages feature fibre reinforced plastic sabots; the remainder using high strength aluminium alloy. The high specific strength and stiffness of FRP is well known and translates in this application to a lower parasitic mass. Thus for a given launch energy, faster and/or heavier penetrators can be fired with an FRP sabot compared to an aluminium alloy one.

The velocity regimes for the first three 90mm round-bore EM projectiles U1, U2 and U3 were all above $2000ms^{-1}$. The shot mass constraints implied by the 32MJ capacitor bank immediately made the use of lightweight FRP sabots mandatory for the higher velocity rounds U1 and U2.

The aluminium alloy sabotted U3, and its fin-stabilised variant U4, have been used to successfully demonstrate strength of design and repeatability when fired from the IAP barrel at Kirkcudbright and the Task B gun at Green Farm (Ref 7). The PMR for U4 is high at 0.78, but the use of composite sabots permits lower PMRs and longer rods to be fired at tactical velocity.

The second generation of UK lightweight EM gun projectiles, U7 and U9, were similar to U2 and U1 respectively, but used alternative manufacturing methods for the FRP sabots.

All of the above FRP sabotted designs have flare stabilised sub-projectiles. The third generation of lightweight EM shots, represented by U10, was typified by longer rods and the move towards fin stabilisation.

All UK base-push projectiles are first tested for strength of design in powder gun firings to axial accelerations well in excess of what is required for a hypervelocity launch from an EM gun. Clearly, it was not possible with powder guns to test both peak accelerations and required velocities at the same time.

Of particular note are the EM gun firings at the US Green Farm facility of U7 and U9 (Fig 5) at velocities considerably in excess of $2000ms^{-1}$ - including the fastest launch of a tactical KE launch package.

Bore straightness and stability under firing loads have long been recognised as poor in existing EM launchers when compared with conventional powder guns. A major consequence is that lateral accelerations (ie balloting forces) are thought to be some five to 10 times higher during an EM launch than those experienced during a conventional powder gun firing. The bore of the 90mm IAP barrel at Kirkcudbright is not particularly straight or round and the bore shape changes with each shot (although considerable improvements have been made to this barrel recently, Ref 2). Both the U7 and U9 projectiles have suffered nose tip failures when fired from the IAP barrel, a failure mode noted by other researchers (Ref 8).

The lowest shot parasitic mass achieved to date for a base-push launch package was 0.66 for the U10v2 projectile with FRP sabot and mid-length penetrator. This design has been launched successfully to its design acceleration from a conventional gun, and is awaiting an appropriate quality of EM barrel before it is fired. Obviously lower parasitic mass values can be achieved for lower accelerations and shorter penetrators. The rod size in U10v2 was chosen as being the optimum to achieve the best penetration for a given breech energy, bore size and sub-projectile diameter. Figure 6 shows EM projectiles U7, U9, U10v1 and U10v2 together with their parasitic mass ratios (calculated including armatures). It should be noted that the rounds pictured have a wide range of penetrator lengths and different muzzle velocities, yet the PMRs are in a relatively tight band from 0.66 to 0.74.

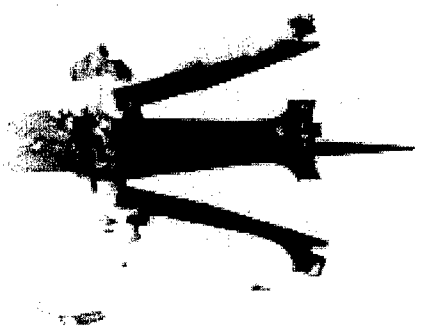


FIGURE 5

Projectile	PMR	
U7	0.74	
U9	0.69	
U10v1	0.70	
U10v2	0.66	

FIGURE 6

The parasitic mass ratio of base-push projectiles remained high, even with composite sabots, and a move towards mid-ride concepts was made. Again, the knowledge accumulated from conventional gun firings of double-ramp sabotted rounds was used to good effect.

EM GUN PROJECTILES - MID-RIDE

Design Concepts

More mass efficient EM gun projectiles can be designed with a mid-ride configuration. Instead of the armature being at the back of the round, in a mid-ride shot the armature is positioned part-way along the sabot so that some of the penetrator is towed behind the shot in tension. This shape is similar to a double-ramp sabot configuration sometimes used in conventional projectiles eg US M829 A2.

Three types of mid-ride sabot construction can be envisaged:

- All-metallic with combined sabot/armature functionality.
- An all-metal concept with selective FRP reinforcement introduced into regions where high electrical conductivity is not required.
- An FRP sabot with integrated metallic armature.

Examples of all three types have been investigated to assess their parasitic mass ratios and the most promising schemes have been analysed fully by finite element analysis to check for strength of design. All of the design schemes are for a conventional two-rail launcher and feature at least one split line in the sabot/armature aligned with the rail-to-rail centre line.

The best parasitic mass ratio for a shot with a mid-range L/D rod is estimated as 0.58, achieved using an FRP sabot. This is an improvement on base-push designs, but (assuming that the proposed scheme would be successful) is still some way from reaching the goal of PMR = 0.5. The key to reducing parasitic mass further is to understand how the armature can be made lighter and this requires extensive thermo-electromagnetic and structural modelling using the finite element method.

The most efficient mid-ride projectile scheme proposed (0.58 parasitic mass ratio) requires the parasitic mass to be reduced by a further 27% before the PMR = 0.5 goal can be achieved. Even with a mid-ride design this is clearly a difficult goal to meet given the present rod length, rod diameter and acceleration specification. Increasing the rod diameter, reducing the rod length and reducing the launch acceleration would simplify this task. These decisions are critically dependent on the ability to model the overall system trade-offs (Ref 9).

Firing Trials

Experiments to date have examined all-metallic, mid-ride constructions. U13 and U14 are aluminium alloy sabotted mid-ride designs with integral armatures, the former being a development proof shot, the latter being a fully functioning APFSDS shot.

The proof shot projectile designated U13v1 was developed to examine the erosion and magnetic effects on parts of the penetrator and fin which extend into the plasma environment between the armature legs. This one-piece proof shot with integral armature and trailing core section enables a variety of fin materials to be fired and recovered intact for technical analysis. U13v2 is a split design having two aluminium alloy sabot petals enabling integral armature performance and sabot discard to be assessed. Further development has led to the U14 (Fig 7), a full APFSDS shot, which represents the first practical step in the UK towards an EM gun-launched, mid-ride projectile. The parasitic mass ratio of this projectile is at present 0.68 which is comparable to the FRP sabotted, base-push U10v2 (albeit U14 is not designed to equivalent acceleration levels).

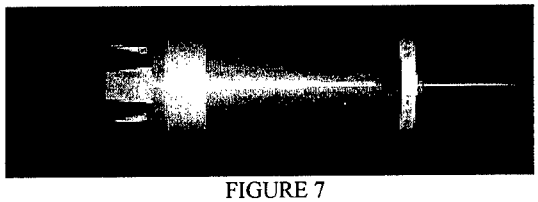


FIGURE 7

Mid-Ride Armature Development

All of the FRP sabotted mid-ride concepts described above feature armatures with a central, longitudinal hole to allow the rear sabot ramp section to pass through. The presence of a hole in the armature reduces its strength and current carrying capacity.

Figure 8 shows the result of 3D EM modelling of a standard armature and one modified with a central hole at peak current during a 1.5MA current pulse. Contours of specific action, relative to the specific action for the armature material, have been calculated on the diametral plane of minimum cross-section (Fig 9).

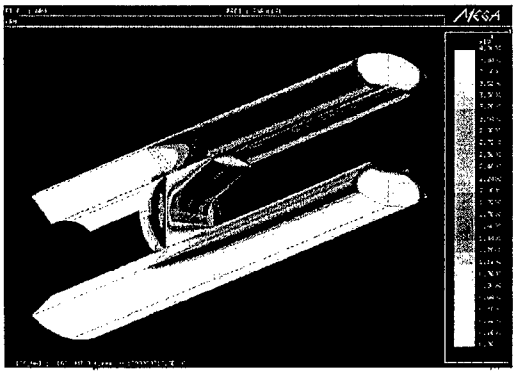


FIGURE 8A: Armature without central hole

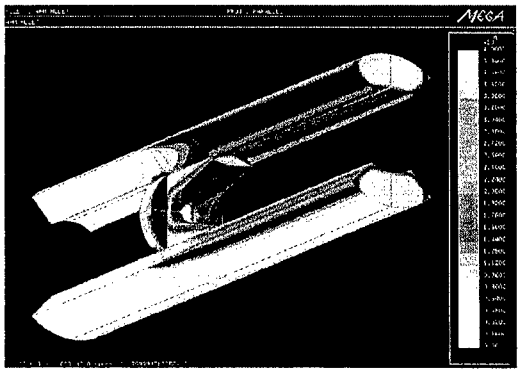


FIGURE 8B Armature with a central hole

The standard armature has a 'specific action concentration factor' of 5.1 compared to 6.9 for the armature with the central hole, both relative to the specific action assuming a uniform current distribution,

$$g = \left(\frac{I}{A_A}\right)^2 dt \tag{3}$$

where I is the input current.

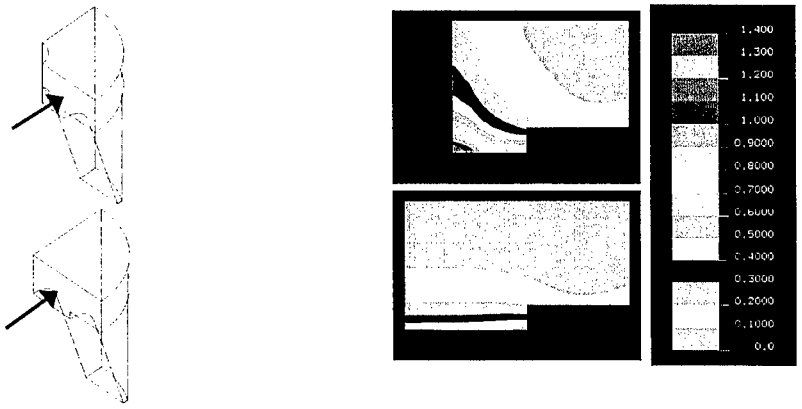


FIGURE 9

Armatures containing central longitudinal holes of various diameters have been fired at representative action levels. Providing that the hole was not too large, the effect on performance was minimal, though at higher velocities and energies the armatures tended to split in two and distort under the large internal magnetic forces present in the armature.

Figure 10 shows the effect of the action concentration around the hole on a recovered armature - visible microstructural changes in regions where the specific action of the armature material has been exceeded correlate well with the EM modelling for a comparable current pulse (Fig 9).

A more realistic mid-ride style armature was fired containing a tapered glass reinforced plastic plug representing the sabot. Although the armature was fired as a base-push design behind a U9 proof-shot, the amount of armature material removed is representative of the FRP sabotted mid-ride designs discussed above. The recovered armature is shown in Fig 11 having been successfully fired at $1500ms^{-1}$. Clearly there is still some way to go to reach hypervelocity and it is thought that a similar, yet multi-material, design might provide a solution.

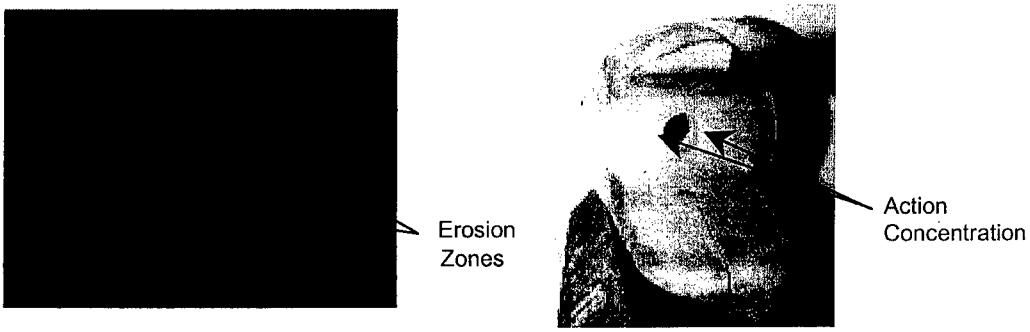


FIGURE 10



FIGURE 11

The EM armature modelling and firing trials are being used to gain a better understanding of the relationship between A_A from Eq (1) and the dimensions of functional armatures.

EM GUN PROJECTILES - BORE SHAPE

Circular (ie round) bores were chosen initially for compatibility with existing powder gun design methodologies and with previous US work. With base-push projectile designs, round-bores work well, and transition velocities over $2000ms^{-1}$ can be achieved. However, with mid-ride concepts, round-bore armatures have restricted space for a trailing penetrator scheme to work properly. Selecting a rectangular geometry may improve this situation as well as increasing the barrel inductance gradient (relative to a round-bore) to reduce the electrical load into the armature. Also the current distribution across the rail from edge-to-edge is more uniform, reducing the severity of the concentration at the rail corners.

Analysing and manufacturing bore shapes other than round presents further challenges to the projectile community. Numerical models become much more complicated and fully 3D analyses are essential. Simple rectangular-bore barrel designs can be manufactured, though

final surface finishing is not as easy as for round-bores. If there is a requirement to move to some form of elliptical or combined flat/round-bore shape (Ref 2), then serious consideration would have to be given to the production of such shapes, regardless of their potential paper benefits.

Figure 12 shows that an elliptical cross-section sabot, assuming an isotropic sabot material, is as effective at controlling rod stress as a sabot of circular cross-section whilst maintaining the same PMR. This finite element analysis suggests that the PMR relationships in Fig 2 still hold for mildly non-circular, aluminium alloy sabot cross-sections.

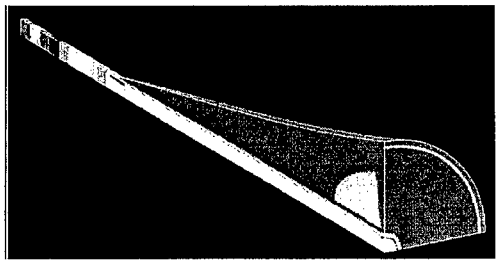


FIGURE 12A: ¼ model circular sabots

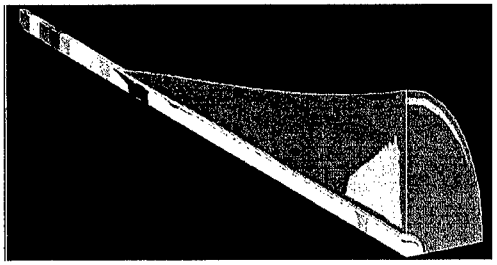


FIGURE 12B: ¼ model elliptical sabots

An elliptical cross-section sabot is not an unreasonable choice for a rectangular-bore barrel providing a natural transition between the bore and the circular cross-section penetrator. Elliptical flight bodies also offer some potential from the aerodynamic viewpoint. With non-circular sabots, careful consideration must be given to the unusual shear stress distribution arising from the non-axisymmetric sectional stiffness; this may cause problems with some anisotropic composite materials.

CONCLUSIONS AND NEXT STEPS

This paper has illustrated the complexities associated with the development of EM projectiles for the direct-fire KE application. A number of important lessons can be learned:

- EM projectiles cannot compete with conventional projectiles in terms of parasitic mass ratio, given present understanding. It will be a major challenge to achieve a parasitic mass ratio of less than 0.58 for a round-bore EM launch package containing a meaningful L/D penetrator.
- Moving to a more oblate bore cross-section (eg extended oval, elliptical) offers a potential advantage in PMR, in that the L' of the gun is increased and the armature needs to carry less electrical energy. Alternate aerodynamic flight bodies become possible within such envelopes, but at the expense of greater complexity in manufacture of both launcher and projectile.
- Within the UK, the ability to recover fired armatures has contributed significantly to an improved understanding of the fundamental physics being employed, and in the development of thermo-electromagnetic modelling tools with greater fidelity. Good progress has been made in this direction, though further improvements will aid the evolution of launch packages which may prove intractable otherwise.

- The armature/sabot materials and launch package geometry technologies are a long way from maturity and there is a need (and every likelihood) of some significant breakthroughs before a formal commitment to the development and procurement of an EM weapon system is initiated.

ACKNOWLEDGMENTS

This paper has been written on behalf of the entire UK EM Gun project team at DERA and within MoD, whose inputs to the work described here are gratefully acknowledged. Particular thanks are given to Colin Hunwick, Ben Watkins and Grant Hainsworth.

REFERENCES

1. Robert J. Taylor, "Influence of Combat Vehicle System Constraints on EML Technology Development," *IEEE Transactions of Magnetics, Vol 35, No. 1,* 473-478, January 1999
2. M. J. Hinton, A. Howard, N. R. Cooper, D. K. Wallington and M. A. Firth, "Concepts for Fieldable Electromagnetic Gun Barrels, to be presented at " *10th U.S. Army Gun Dynamics Symposium, P42,* 23-26 April 2001
3. David Haugh, "An Update on the UK Electric Gun Research Programme," *IEEE Transactions of Magnetics, Vol 33, No. 1,* 17-20, January 1997
4. Doug Kirkpatrick and David Haugh, "Launching Tactically Configured Solid Armature Projectiles from Large and Medium Calibre Railguns - Results from the DRA Test Programme," *IEEE Transactions of Magnetics, Vol 33, No. 1,* 109-114, January 1997
5. Alexander E. Zielinski and Paul Weinacht, "Improved Integrated Launch Package Ballistic Performance," *IEEE Transactions of Magnetics, Vol 35, No. 1,* 124-129, January 1999
6. B. Burns, L. Burton and W. Drysdale, "Methodologies for Forecasting Sabot Mass for Advanced Gun and Projectile Systems," *Ballistics Research Laboratory Report, BRL-TR-3387,* September 1992
7. David Haugh and Doug Kirkpatrick, "Large Calibre Armature Firings at Green Farm Electric Gun Test Facility," *IEEE Transactions of Magnetics, Vol 33, No. 1,* 68-73, January 1997
8. Timothy E. Hayden, Rolf Dethlefsen and John H. Price, "Effective Launch Package Integration for Electromagnetic Guns," *IEEE Transactions of Magnetics, Vol 31, No. 1,* 150-155, January 1995
9. Scott Fish, Todd McGall and Erik Howard, "Launch Package Mass and Pulsed Power Energy Estimation for Subcalibre Electromagnetic Railgun Projectiles," *IEEE Transactions of Magnetics, Vol 33, No. 1,* 63-67, January 1997

USE OF THE SIMBAD GUN DYNAMICS CODE FOR MODELLING THE IN-BORE DYNAMICS OF EM LAUNCHERS

D.W. Lodge[1], and A.M. Dilkes[1]

[1] *Defence Evaluation & Research Agency, Chobham Lane, Cherstey, Surrey, KT16 0EE, UK.*

Generic SIMBAD models of various Electro-Magnetic (EM) launchers have been used in the UK for studying model the in-bore phase and launch accuracy issues of such systems. Although many of features of the EM environment are not modelled with any degree of complexity, SIMBAD still provides a useful tool for investigating some of the dominant material and geometric influences on the in-bore dynamics and launch accuracy.

Modifications to the SIMBAD code allowed for the simulation of asymmetrical electro-magnetic forces acting on the projectile. Other modifications allowed for the simulation of some of the time varying asymmetries in the forces on the projectile. These have demonstrated that there may be additional EM influences contributing to in-bore projectile balloting.

Comparative performance data was produced for three shot designs (U4, U7 and U9 projectiles) simulated being fired from the 90mm IAP and Task C launchers, and highlighted their typical in-bore performance characteristics. Transverse accelerations on the projectiles showed typical peak values of 6,000g. Higher values and degradation in projectile performance was demonstrated due to increasing wear and distortion in the launcher's core when experimental bore straightness and wear were included.

Initial values for projectile exit conditions from the launchers were produced, which demonstrated increased sensitivity of shot jump, pitch and pitch rate in the vertical plane and some important differences between projectile designs.

INTRODUCTION

The Defence Evaluation and Research Agency (DERA) has conducted applied research for the UK Ministry of Defence over the past five years into the use of Electro-Magnetic (EM) launchers and projectiles. One strand of this work has investigated the firing dynamics of the system in relatively simple terms using the existing 'Gun dynamics' code of SIMBAD [1]. Previous to this, limited studies had been conducted using RAMA [2] to model the US 90mm SPARTA gun [3] and with SIMBAD to model a generic 90mm projectile [4].

EM gun systems differ in several important respects from conventional gun systems, namely: anisotropic composite barrel structures, hyper-velocity in-bore projectile dynamics and interaction of rapidly varying electromagnetic, thermodynamic and mechanical deformation fields. These features cannot be modelled directly with any degree of complexity within the

SIMBAD code. However, its use does provide a tool for investigating some of the predominant material and geometric influences on the system dynamics for low computational cost and rapid solution, thus allowing for investigations into a wide variety of input parameters.

Over a period of three years, work was performed on the following: adding code to account for some of the special effects of the EM launchers and projectiles; refining the input data used for the SIMBAD model, and performing basic sensitivity studies to establish data on a number of gun and projectile designs. In particular work has concentrated on the 90mm IAP and Task C launcher systems firing the U4, U7 and U9 shot variants.

MODELS

Using commercially available software (Solid Edge CAD [5], Algor FEA [6] and Ideas FEA [7]), numerous CAD and FEA models of the launcher and projectile components were built (see Figures 1 to 3 below). These are typical techniques used to generate launcher and projectile input data for the SIMBAD models.

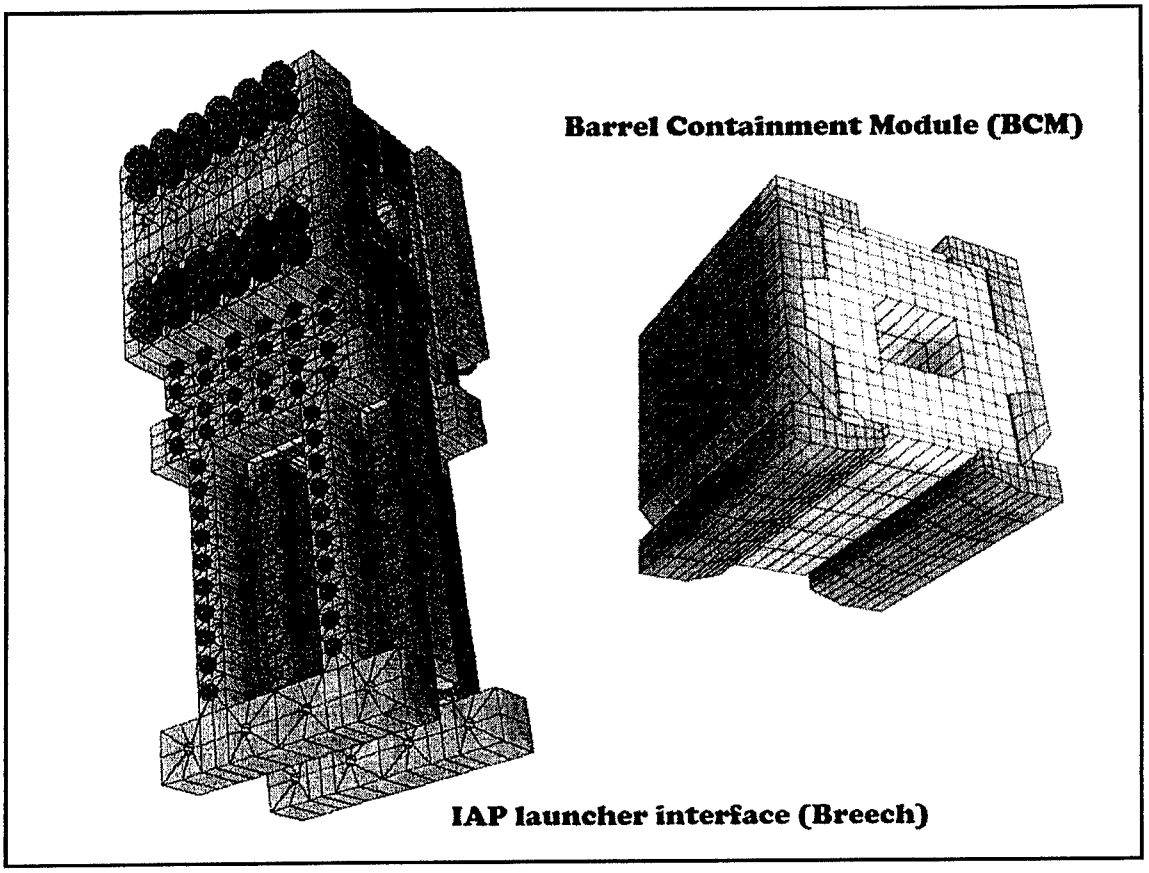


FIGURE 1. Algor FEA 'brick' models of the IAP launcher interface and BCM.

The CAD models are able to provide accurate mass properties for components e.g. mass, centre of mass, inertia. This can be used directly in SIMBAD for items such as the projectile's

armature which were represented as 'lumped masses', and indirectly to check mass data generated by SIMBAD, such as overall projectile mass. The FEA models are able to provide stiffness data for component-to-component interfaces e.g. projectile/barrel contact stiffnesses, elevating gear stiffness, and indirectly to check the frequency response of the model components, e.g. modal analysis of overall projectile assembly using various boundary condition constraints.

IAP BARREL

There are several ways in which the IAP launcher could have been modelled within SIMBAD. The approach adopted in this instance assumed that the majority of the bending stiffness within the barrel structure is derived from an 'I' section support beam running the length of the launcher and two 'U' section connecting beams running down the sides of the Barrel Containment Modules (see Figure 2). This also assumes that both the core and the BCMs do not contribute greatly to the bending stiffness.

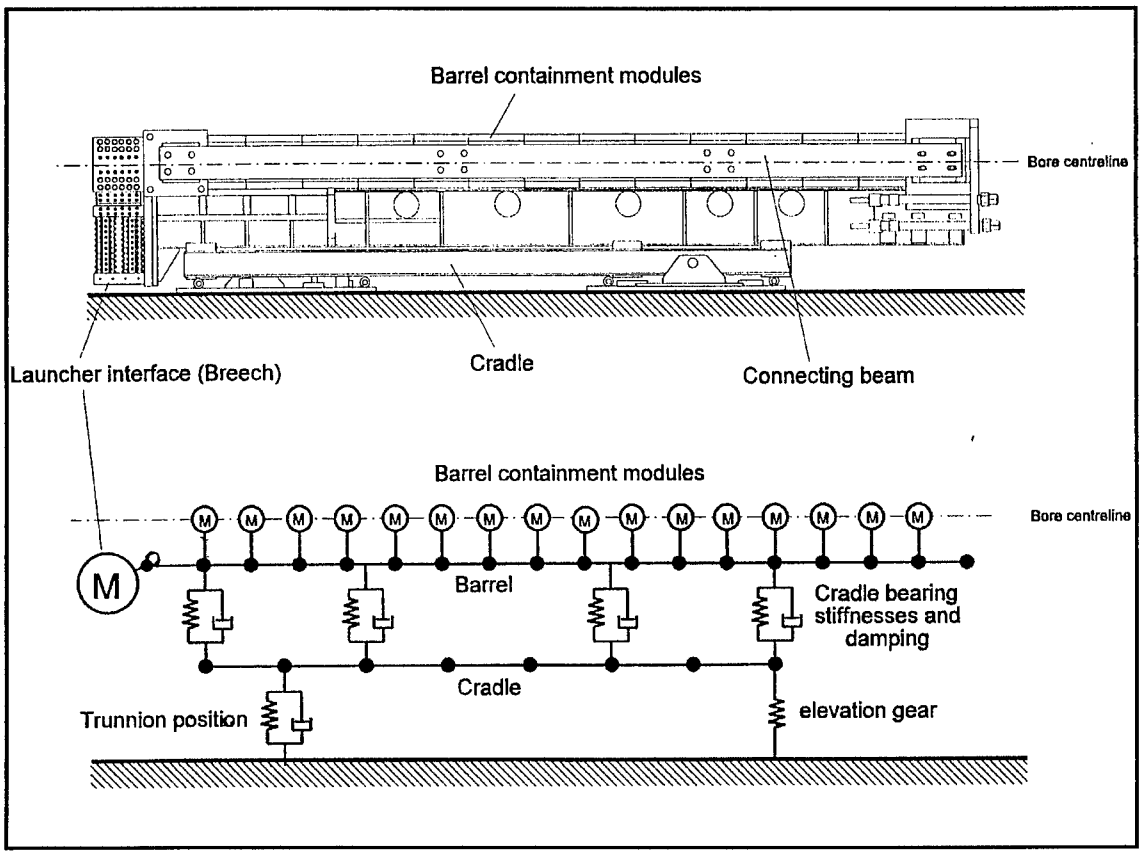


FIGURE 2. SIMBAD FEA 'beam' element model of the 90mm IAP EM launcher.

The first of these assumptions was backed up by a simple comparison of the bending stiffness of the support beams with that of the copper-G10 core, assuming the latter to be a contiguous unit of similar length. From simple theory the ratio of the stiffnesses was found to be 200:1. The mass and inertia of the core, approximated from modelling to be in the order of

552.0 kg [6], was not ignored but added to the 'lumped masses' of the BCMs described below.

BARREL CONTAINMENT MODULES (BCMs)

The fourteen BCMs of the IAP launcher are designed to hold the copper-G10 core in place. The assumption that the BCMs were not contributing to the structural bending stiffness of the barrel was based on experimental evidence from firings which indicated that these behave and move independently of one another, and possibly of the support and connecting beams, during in-bore shot travel. Due to this, and the compact nature of their structure, they were modelled most effectively in SIMBAD as lumped masses. These lumped masses are added at the relevant barrel nodes so their gross behaviour on the barrel structure was included.

The barrel nodes of the SIMBAD IAP barrel model were modified accordingly by redefining the offsets of centroid position of the cross-section from the bore centreline, i.e., the true position of any node is x, $y+y_{offset}$, $z+z_{offset}$. In this instance the y offset was a constant -0.3225m to account for the mismatch between the apparent and real bore centrelines.

To try and optimise the effects the BCMs have on the structure, the number of barrel beam elements was initially limited to 17, thus allowing for nodes 3 through to 16 to accept the mass of one BCM each. The code was later modified to allow for 63 elements to represent the barrel thus allowing experimental barrel bore straightness to be better represented.

TASK C BARREL

The first model constructed for the Task C EM Gun analysis was a 3D linear brick element model of the Task C composite barrel. The Task C barrel is complex in its construction and the information gathered detailing its internal structure was limited. The second FEA model used linear beam elements to construct the model of the composite barrel. Two models were constructed. The first used multiple beam element sections to represent the separate materials associated with the composite barrel, i.e. copper rails, insulator, laminate containment structure and outer skin. The second variant combined the properties of the first model to produce single beam elements representing the cross section of the Task C barrel. Data from this model was then used to produce the SIMBAD gun dynamics model.

To analyse the behaviour of the composite barrel, free-free normal modes analyses were performed to calculate the natural frequencies and mode shapes for each of the barrel models constructed. Results (see Table 1) showed that there was good correlation between the natural frequencies for the first two bending modes of the brick and beam barrel models. The multiple beam element model produced closer values of natural frequency than the single section beam model to the brick element model.

As a further check linear static analyses were performed to predict the bending moment stiffness of the barrel models. Each analysis supported the barrel as a simple cantilever beam, then applying a load to the other end of the structure. The results (see Table 1) showed a better correlation between the bending moment stiffnesses of the two beam models giving good confidence in the models. Again the stiffnesses are slightly higher than the brick model but this can be expected due to modelling assumptions and simplifications that were made.

TABLE 1. Predicted natural frequencies for the Task C barrel models.			
Mode type↴ / Model Type →	IDEAS 'Brick' element model	IDEAS 'Beam' element model	SIMBAD beam element model
Natural Frequency (First Bending, Hz)	16.82	17.44	18.04
Natural Frequency (Second Bending, Hz)	49.47	51.84	57.07
Natural Frequency (Third Bending, Hz)	94.30	104.6	115.51
Natural Frequency (Fourth Bending, Hz)	161.01	174.47	193.00
Bending moment stiffness (Nm/rad)	5.544E+10	6.413E+10	6.343E+10

The Task C cradle was constructed as a detailed FEA model using linear 'shell' elements. The SIMBAD cradle model was created using 'beam' elements. Certain assumptions and approximations were made during construction of this model in order to produce an accurate comparison with the detailed shell element model. Cross-sectional properties were obtained from the 'shell' element model at selected intervals along its length and converted into beam elements. Lumped masses were used to represent the saddles at the relevant nodal positions on the 'beam' element model. A mass property comparison between the 'shell' and 'beam' element cradle models showed good correlation in mass, inertias and C of M.

A normal modes analysis was performed for the elevating mass models (barrel and cradle) with cradle-to-ground boundary conditions in place. The natural frequencies of the structure were obtained and are shown in Table 2 below.

TABLE 2. Predicted natural frequencies for the Task C elevating mass models.		
Mode type↴ / Model Type →	IDEAS 'Brick' element model	SIMBAD 'beam' element model
Vertical First Bending (Hz)	32.0	39.3
Horizontal First Bending (Hz)	51.9	56.4
Vertical Second Bending (Hz)	75.8	72.2
Vertical Third Bending (Hz)	83.2	86.3

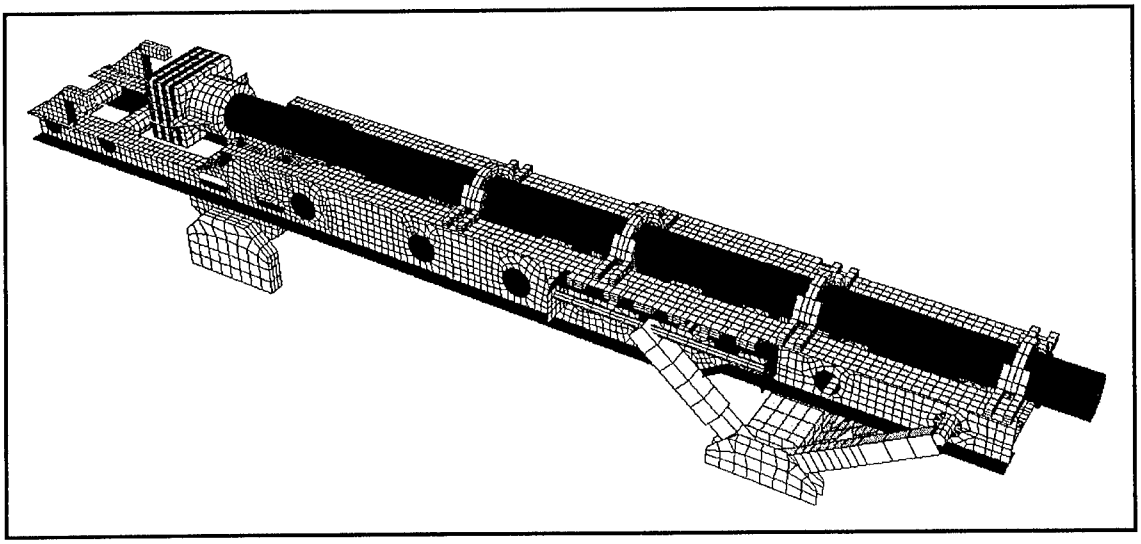


FIGURE 3. IDEAS FEA 'brick' and 'shell' element model of the Task C EM launcher.

APFSDS PROJECTILES

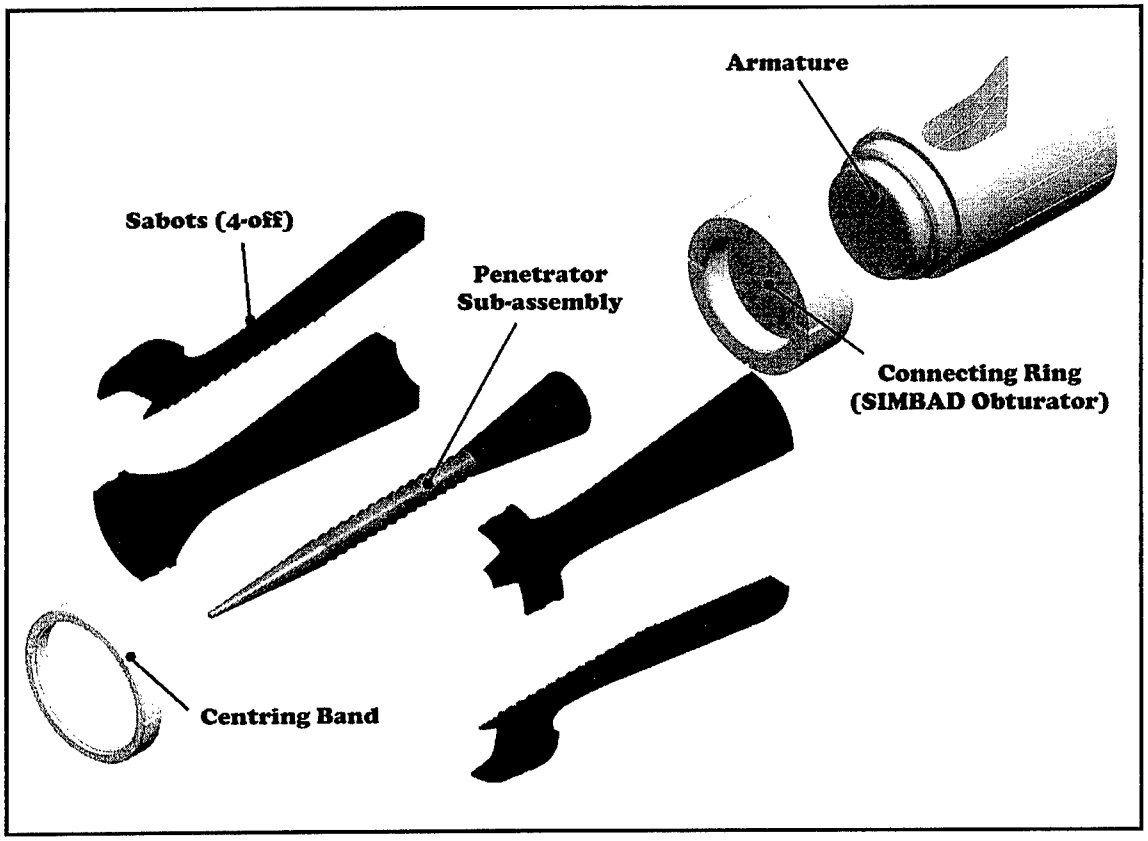


FIGURE 4. Components of the EM APFSDS projectiles.

Preliminary use of the IDEAS and Algor FE analysis software was undertaken when constructing the EM projectiles. Using 'brick' element models of the full projectile assemblies, the U4, U7 and U9 projectiles were analysed with and without the armature connected and compared to the equivalent SIMBAD 'beam' element models (see Figure 5 below). Table 3 below shows some typical results obtained from a free-free modal analysis comparison without the armature connected. As might be expected, the U7 variant has the higher natural frequencies since it is the shortest in length. Also, the carbon composite sabot of the U7 and U9 is slightly stiffer than that of the aluminium sabot of the U4.

All projectiles were modelled as two-piece (sabot and penetrator) shots within SIMBAD (See Figure 6 below). Typical assumptions for this type meant that all four sabot petals are composed of a single piece of material; all screw threads between components, e.g. between the sabot and penetrator core, are based on the mean thread depth for the components interface; all components exhibit isotropic material properties.

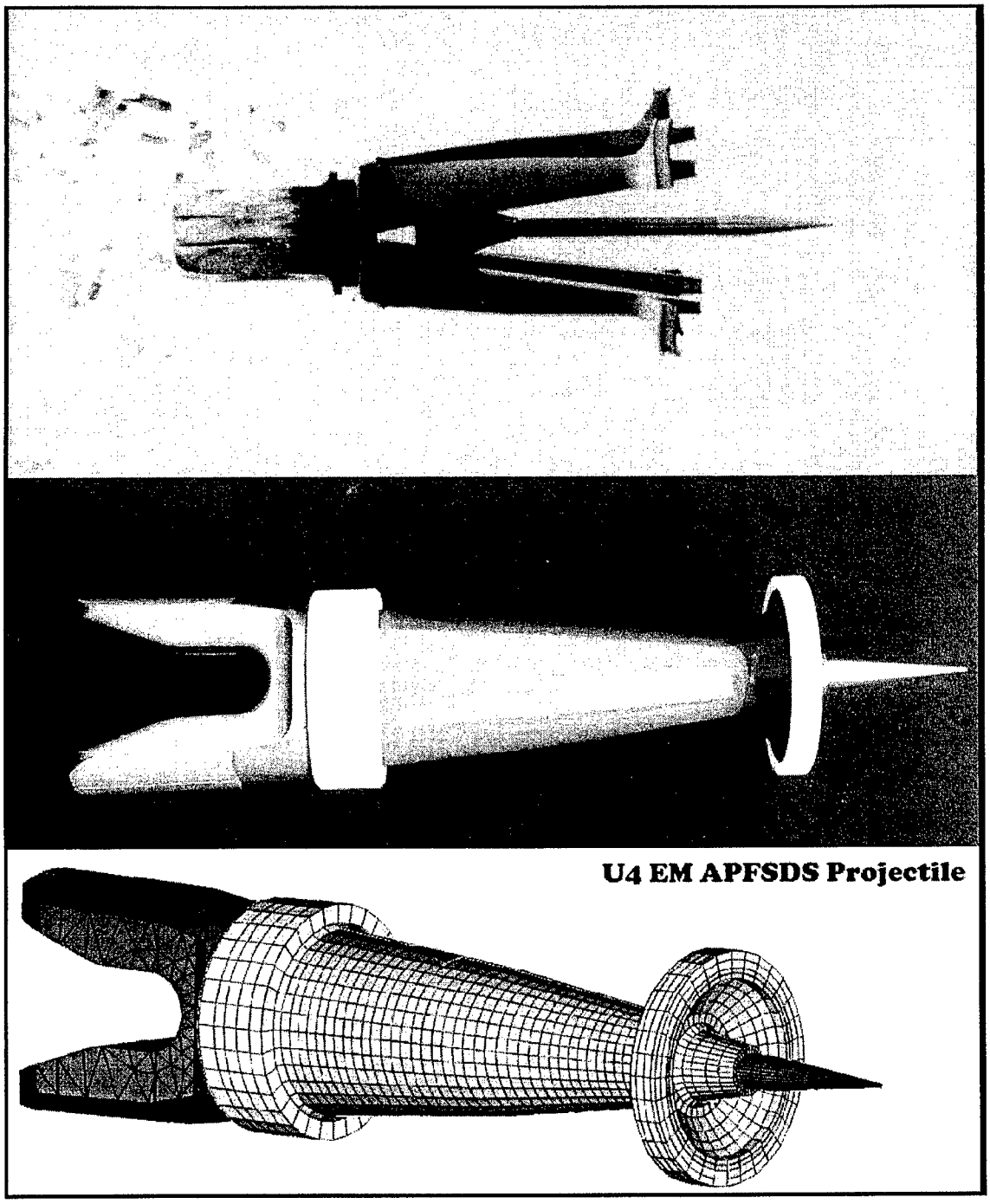


FIGURE 5. Typical IDEAS FEA 'brick' element model of the U4 EM projectile.

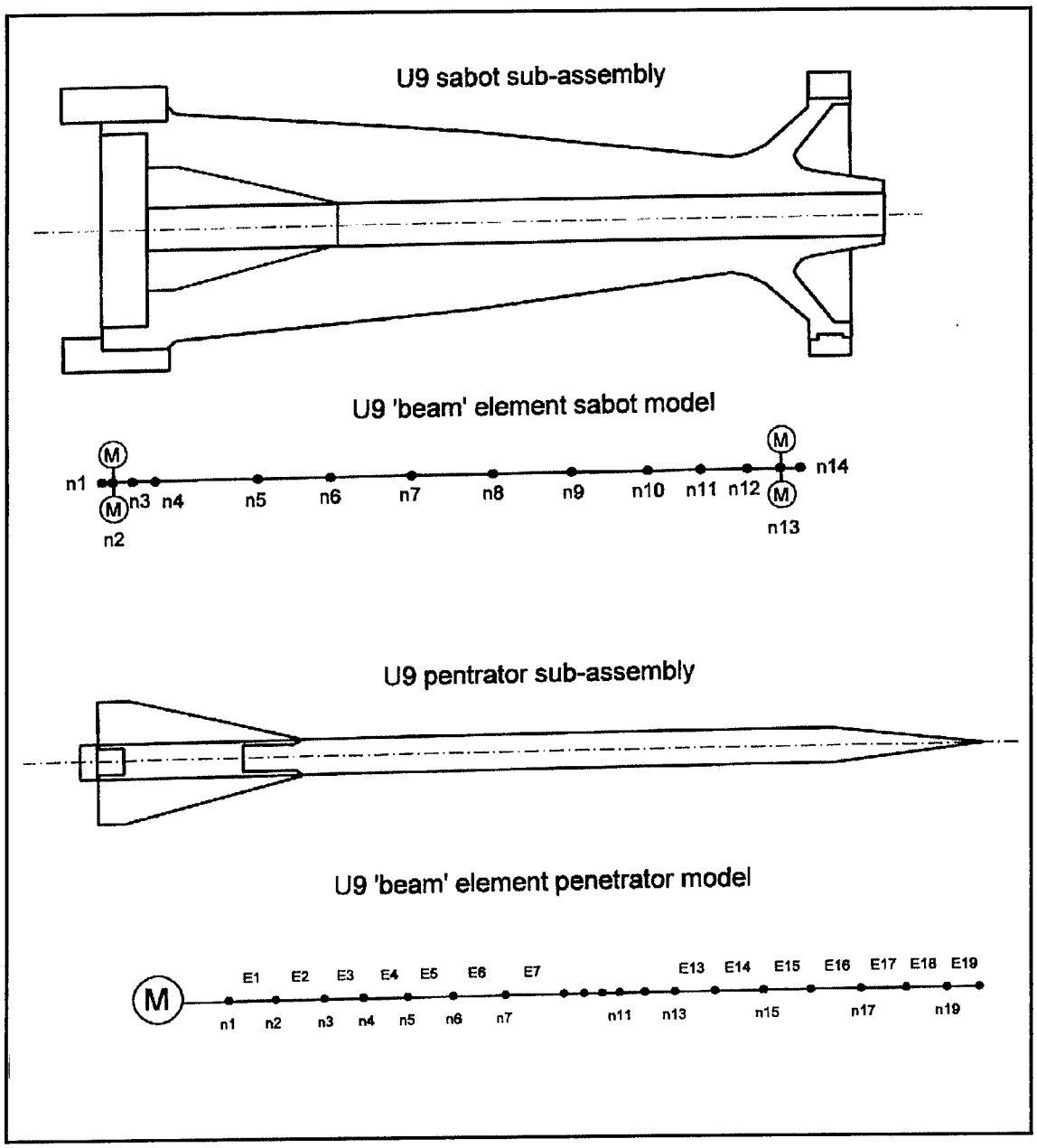


FIGURE 6. Example of SIMBAD 'beam' element model for the U9 APFSDS projectile.

TABLE 3. Free-free natural frequencies of the U4, U7 and U9 projectiles, less armature.						
Mode Type	U4		U7		U9	
	Brick (Hz)	Beam (Hz)	Brick (Hz)	Beam (Hz)	Brick (Hz)	Beam (Hz)
Bending 1	1966	1964	2020	2207	1558	1528
Bending 2	2304	2134	2966	3153	2607	2491
Bending 3	4097	3586	4905	5389	4099	4235
Bending 4	7329	7874	-	-	-	-

PROJECTILE STIFFNESS CALCULATIONS

The contact stiffnesses used in SIMBAD between the projectile and the barrel are one of the most critical areas when considering the in-bore dynamics of the shot. For the purposes of the SIMBAD gun dynamics simulation, a significant simplification is made in their representation, and is achieved using a series of spring/damper elements acting between nodes on the shot and barrel models. Stiffness values were calculated for the following parts of the projectile: connecting ring (SIMBAD obturator or driving band) radial and moment stiffnesses, front centring band radial stiffness and armature radial stiffnesses.

2D and 3D FEA models of the projectile components were constructed in IDEAS to calculate static deflection and hence stiffness. The values found varied between projectile and are summarised in Table 4 below.

TABLE 4. Projectile stiffness values used for the U4, U7 and U9 APFSDS projectiles.				
APFSDS Projectile	Radial centring band (N/m)	Radial connecting ring (N/m)	Radial armature (N/m)	Moment connecting ring (Nm/rad)
U4	8.800E+07	5.450E+08	1.000E+07	2.560E+05
U7	1.250E+08	2.420E+08	0.939E+07	3.750E+06
U9	7.500E+07	3.100E+08	0.960E+07	1.240E+05

The increased thickness of the U7 connecting ring compared to that of the U4 and U9 gives rise to a lower radial stiffness but a much higher moment stiffness, which can be confirmed by simple analytical calculations. The armature radial stiffnesses vary little between the projectile variants as expected because physical dimensions vary little between them.

ADDITIONAL ELECTROMAGNETIC LOADING EEFECTS

One difference that is apparent between a conventional gun and an EM gun is the method by which the recoil force is passed into the launcher. In a conventional gun the force of the gas pressure on the breech face pushes the recoiling mass rearwards. This is simplified in SIMBAD by the application of this pressure force on the breech node (normally node 1).

At the time this work was performed the method of recoil force application on an EM rail launcher was still not fully understood, but one theory suggested it was transferred to the barrel at the point at which the projectile's armature was within the core. The recoil force was

thus seen to travel with the shot up the barrel. Subsequent work has shown this to be incorrect, with this type of model more representative of a coil gun than a rail gun. The main recoil effect in an EM rail gun is still believed to act primarily at the breech. However, for this study both the 'conventional' and 'travelling' recoil force models were used in the SIMBAD analysis.

Two further modelling approaches were also used to demonstrate possible additional second order effects that the time varying Electro-Magnetic field is having on the projectile during its in-bore travel. These have not been derived from first principles, and as such they were merely used to demonstrate possible mechanisms by which additional pitch and yaw may be induced in an EM shot. Modelling of variable armature contact was concerned with the possible variation in the armature-rail contact surface during in-bore travel. In a conventional gun, the horizontal component of the applied shot base force (F_H) is given by Eq (1):

$$F_H = F_B \, . \, \alpha_y \tag{1}$$

where F_B is the shot base force in the x direction and α_y is the rear band yaw angle with respect to the barrel and assumed to be small. In the armature of an EM gun the contact between rail and armature will vary depending on the yaw angle. It can be reasoned that as the yaw angle increases the surface area of contact on one side of the armature increases, whilst on the other it decreases. This leads to a different current flow in the two halves of the armature and a change in the current density, leading to an increase in the horizontally applied force on the shot. In simple terms this was modelled by adding an additional force to Eq (1), defined here as the "EM shot force yaw constant" (K_y):

$$F_H = F_B.\alpha_y.(1 + K_y) \tag{2}$$

To induce initial yaw in the projectile a small C of M offset was introduced into every SIMBAD run.

The other attempt at modelling additional secondary EM effects concerns the point of application of the shot base force. If the projectile and armature's horizontal axis is coincident with the barrel's then the current flow will flow evenly through the armature. As the shot and barrel axes move apart, the current path will move also. In a conventional gun, if the shot moves upwards by δ_y, the point of application of the shot base force will remain approximately in the centre of the round, i.e., on the shot's horizontal axes. Due to the changes in the current flow, it could be argued that this is no longer the case in an EM projectile, and that the point of application will move further, creating an additional pitching moment on the projectile. To observe the sensitivity of this effect the relative shot displacement is multiplied by a "EM offset base force constant" (K_o).

RESULTS

This paper is a summary of the work conducted over a three-year period. Within this time numerous studies were conducted with the models that have been described in the above

paragraphs. Due to the volume of data generated by the SIMBAD model, the following section highlights only some of the more interesting results of the SIMBAD dynamics studies.

IAP LAUNCHER MOTION

The amount of vertical movement in the barrel is very small, as the structure is extremely stiff. A maximum of ~0.8 mm is seen in the 'travelling recoil' model at the muzzle towards shot exit. For the 'breech recoil' model, the flexure of the barrel centreline appears to be relatively benign. In the 'travelling recoil' model, the profile shows greater displacements with higher dynamic curvatures induced in the barrel. It should be noted that this is due in part, to the limited number of elements used to represent the barrel. Barrel displacements are approximately 1000 times lower in the horizontal plane due to there being no off-axis masses.

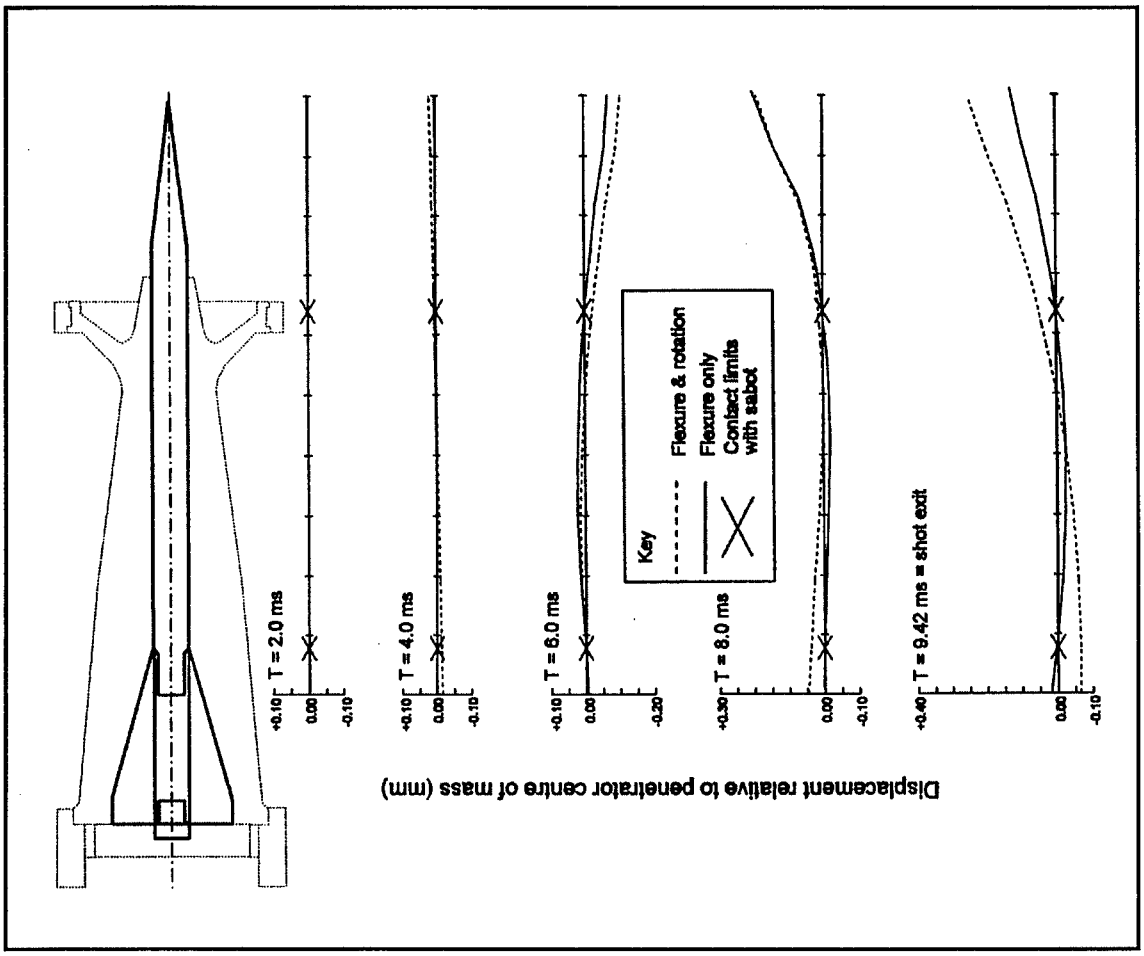


FIGURE 7. SIMBAD predicted U4 penetrator bending from an IAP launcher firing.

PROJECTILE MOTION

Figure 7 presents dynamic shapes in the vertical plane of a U4 penetrator fired from the IAP launcher with the 'travelling recoil' model. Each plot shows two penetrator shapes: pure flexure of the rod (solid line) and flexure and rotation of the rod (dotted line). The primary mode of vibration in the rod is that of the fundamental (first mode) frequency, distinguished by the 'cantilever' bending of the forward section of the penetrator forward of the sabot-penetrator contact point. Maximum flexure of the penetrator tip away from the neutral axis is in the order of 0.2 mm (travelling recoil) and 0.05 mm (breech recoil).

LATERAL SHOT LOADINGS

Transverse or lateral accelerations on an EM projectile during in-bore motion were predicted from the SIMBAD models for numerous conditions. Differences were particularly marked between the two recoil types. For the conventional 'breech recoil' peak accelerations were less than 2,000g. Only at the breech did the shot receive a 'kick' and a maximum acceleration of 3,500g was seen. For the 'travelling recoil' model the magnitude of the accelerations saw a peak of nearly 20,000g. Further analysis showed this to consist of two dominant frequencies: a relatively low frequency (0.3 kHz) probably associated with barrel motion, which produces a 10,000g peak, and a higher frequency (10.0 kHz) which increases the overall acceleration to 20,000g. These values are much higher than the design strength of the projectile. If the projectile were experiencing such accelerations it would almost certainly be breaking in-bore.

As a simple demonstration that these acceleration levels would break the projectile the bending and shear stresses within the penetrator for the in-bore phase were calculated. The point at the front of the penetrator-sabot interface (node 7) was chosen as one of the most likely areas of failure in shear (or bending). Maximum shear stress on the neutral axis was calculated. Shear stress at this point is plotted in Figure 8 for the two recoil models. For the 'breech recoil' model maximum shear stress values of 0.10GPa are recorded. For the 'travelling recoil' model maximum values of 2.0GPa are seen. The shear strength value of tungsten (assumed to be 0.87GPa), marked on the plot is crossed several times, indicating probable failure of the rod in shear.

SHOT EXIT PREDICTIONS

Table 5 shows some examples of shot exit conditions of a U4 projectile fired from the IAP launcher. Whilst predicted gun and shot jump figures are different between the 'conventional' and 'travelling recoil' models the standard deviations (SDs) for these exit parameters are not. Shot pitch and shot pitch velocities however show SDs that are far higher in the 'travelling recoil' model. This indicates lower launch accuracy and consistency in this model. More importantly the results show that these shot exit conditions are very sensitive to the recoil model type and that more effort is required to understand the issues of recoil force modelling in the EM gun if the models are to be more accurate.

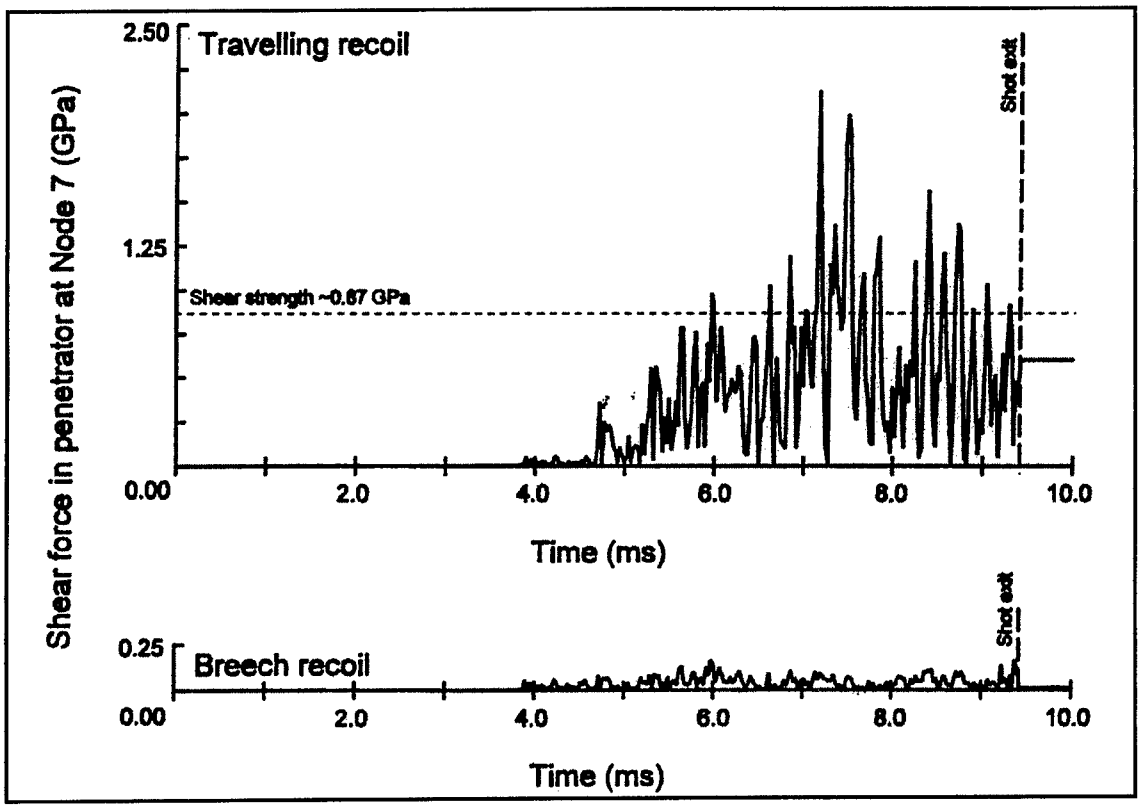


FIGURE 8. SIMBAD predicted U4 penetrator shear stress from an IAP launcher firing.

TABLE 5. Typical shot exit conditions for the two recoil models, U4 from IAP launcher.

Model		Vert. Gun Jump mils	Horiz. Gun Jump mils	Vert. Shot Jump mils	Horiz. Shot Jump mils	Shot Pitch angle mrad	Shot Yaw angle mrad	Shot Pitch Vel. rad/s	Shot Yaw Vel. rad/s
Breech recoil	Mean	-0.466	-0.055	-0.319	0.008	0.388	0.001	1.959	0.000
	SD	0.102	0.026	0.192	0.010	0.079	0.000	0.400	0.000
Travelling recoil	Mean	-1.064	-0.020	-0.758	0.011	0.685	0.001	1.671	0.001
	SD	0.041	0.018	0.115	0.010	0.621	0.000	1.694	0.001

PROJECTILE COMPARISONS

Overall, the in-bore dynamic behaviour of all three projectiles fired from the IAP launcher appeared to be similar. Subtle variations were seen in frequency responses of the various sub-assemblies, particularly the penetrator, which is to be expected due to the geometrical differences of the three projectiles.

The U4 projectile saw marginally higher forces, velocities and displacements in general. However, analysis of the vertical lateral acceleration of the sabot indicates that the U7 sees peak accelerations twice that of either the U4 or U9. The U7 and U9 also see higher

penetrator displacements relative to the sabot than the U4, again indicating higher loads at the sabot-penetrator interface.

The longer wheel-base of the U9 does not appear to impart more in-bore stability to the overall design as might have been expected. This is probably due to the greater influence of the launcher motion on the shot than a conventional gun system.

ARMATURE STUDIES

Studies were performed specifically to investigate the armature effects on projectile in-bore motion.

It is known from experimental firings that the armature is severely eroded during the in-bore phase and that its reduction in mass can be significant. A simple test in SIMBAD of reducing the armature mass by 40% appeared not to significantly alter the overall in-bore behaviour other than at shot exit. Here, sabot pitch angles were significantly different when armature mass was varied. Barrel motion heavily influences the behaviour of the projectile prior to shot exit, which in turn is a function of the SIMBAD barrel model and the launcher's geometry. It is probable that this apparent variation is due to one or both of these factors.

Variations in the position of the armature C of M and armature inertias showed negligible changes to projectile in-bore behaviour. This would be expected, as for example a change of 25% to the armature's inertia, results in a change of 10% to the projectile's pitch inertia. This leads to a change of approximately 4% to the pitch/yaw frequency, which is believed to be too small to be noticeable.

Changes in the contact stiffness between the armature and the bore were initially believed to be one of the more significant factors affecting EM projectile behaviour, since similar studies in conventional gun system indicated so [7,8]. For the IAP launcher in the vertical plane this did not appear to be the case. Despite using a large variation in armature stiffness only a marginal change in sabot/projectile response was observed. A much greater variation was seen in the horizontal plane. Decreasing the stiffness altered the yaw of the projectile, but the general behaviour was similar to the baseline. Increasing the armature stiffness had a much more marked effect, and the yaw angle was much lower for the majority of the in-bore travel.

The non-symmetry in the geometry of the armature and thus its contact stiffness appears to have an effect on projectile in-bore dynamics. In particular it appears that the more sensitive axis is that which runs through the legs. This is an important point to note, as the orientation of the projectile can be specific to each launcher. The contact stiffness of the armature may be time-position dependent and 'non-linear' due to any plasma layer that forms between armature and copper rails and should be considered when modelling its stiffness in SIMBAD.

CONCLUSIONS

Modelling of the in-bore dynamics of a number of EM projectiles fired from two EM launchers using the SIMBAD gun dynamics code. The code was modified extensively from its use on conventional gun systems simulation to account for some of the effects unique to the EM environment. Modelling has shown that amongst other factors projectile exit conditions are most sensitive to the choice of recoil force model used ('conventional' or 'travelling' recoil), the

magnitude of the time varying 3D asymmetric EM projectile loadings, and bore centreline profile and wear.

In the IAP launcher, the behaviour of the barrel model is the predominant influence in the behaviour of the projectiles in-bore due to a heavy muzzle mass dominating the response of the barrel. All projectiles see higher forces, accelerations and displacements towards the end of in-bore travel. In-bore dynamic behaviour of all three projectiles studied were similar. Subtle variations were seen due mainly to their geometrical differences.

Non-symmetry in the geometry of the armature and thus its contact stiffness appear to have an effect on projectile in-bore dynamics. In particular it appears that the more sensitive axis is that which runs through the legs. This is an important point to note since the orientation of the projectile in the bore can vary with each EM launcher system.

ACKNOWLEDGMENTS

The authors wish to acknowledge the work of Mr D.N Bulman of Danby Engineering Ltd., Mr S.F. Storey of Simatics Ltd. and the firm of Temati Ltd. for their contribution to the work contained within this presentation.

REFERENCES

1. *SIMBAD Manual (Version 28).* Danby Engineering Ltd. May 2000.

2. *Gun barrel dynamics computer simulation (RAMA) documentation (version 80).* SMMCE/LS/060/1473, RMCS Shrivenham. April 1991.

3. BULMAN, Prof. DN & STOREY, SF. *EM gun, an investigation into the dynamics during the launch process using the SIMBAD gun dynamics program.* Report No. Simatics/EMGUN/0696, Simatics Ltd. June 1996. UK RESTRICTED - COMMERCIAL.

4. CAMPBELL, P. *The influence of bore profile and contact stiffness on the in-bore/exit dynamics of an EM gun launched projectile.* DRA/FVS-WD/CR9439/1.0, DRA(Ch). December 1994. UK RESTRICTED - COMMERCIAL.

5. EXELL, AJ. *Theoretical calculation of the peak centring band loading of a 90mm APFSDS EM-Gun round (preliminary report).* Group Working Paper CR/FV&S/065/92, DRA(Ch). March 1992. UK RESTRICTED.

6. *IDEAS master series 3*, SDRC Operations Inc., 1996.

7. LODGE, D W & THOMAS, A R. *A SIMBAD analysis of the in-bore dynamics of the U4 APFSDS projectile in the 90 mm IAP EM gun.* DERA report No. DERA/LS3/TR9768/1.0, June 1997, UK RESTRICTED - COMMERCIAL.

8. LODGE, D W & THOMAS, A R. *A Theoretical comparison of the in-bore dynamics of the U4, U7, and U9 APFSDS EM projectiles using SIMBAD and IDEAS.* DERA report No. DERA/LS3/TR980078/1.0, March 1998, UK RESTRICTED - COMMERCIAL.

9. LODGE, D W & THOMAS, A R. *A dynamic analysis of the P4/4 APFSDS projectile fired from the 140 mm EXP 45 high velocity gun.* DERA report No. DERA/LS3/TR970183/1.0, September 1997, UK RESTRICTED - COMMERCIAL.

10. LODGE, D W & BLATCHFORD, P W. *An initial study into the instrumentation of a 120 mm L23A1 proof shot for measuring in-bore projectile motion.* DRA technical report DRA/LS3/TR9712/1.0, February 1997, UK RESTRICTED - COMMERCIAL.

© British Crown copyright 2000. Published with the permission of the Defence Evaluation and Research Agency on behalf of the Controller of HMSO.

RESULTS OF A STUDY FOR A LONG RANGE COILGUN NAVAL BOMBARDMENT SYSTEM*

Steve Shope, Jeff Alexander, Walt Gutierrez, Ronald Kaye, Marc Kniskern, Finis Long, David Smith, Bob Turman, Barry Marder, Albert Hodapp Jr. and Richard Waverik

*Sandia National Laboratories, Albuquerque**, NM,87185*

We have evaluated the feasibility of a long range bombardment coilgun launcher and a suite of compatible projectiles. We will present an analysis of the technical feasibility, engineering, and systems implementation issues for shipboard mounting and utilization. Some of the key issues that will be presented are prime power requirements, energy storage, target lethality, ground support, and critical issues. Ranges to be studied are hundreds of nautical miles. At the conclusion of the study we will have sufficient analysis and information to define the requirements and plan for a demonstration program.

*This work was supported by Navy CTO (Order No. N00014-00-F-0452) and DARPA (Contract No. DE-AC04-94AL85000

**Sandia is a multiprogram laboratory operated by Sandia Corporation, a Lockheed Martin Company, for the United States Department of Energy under contract DE-AC04-94-AL85000.

INTRODUCTION

This paper presents a technical analysis of an enhanced range gun capability for naval surface combatants, based on the concept of an electromagnetic coilgun. The technology base to provide such capability has been demonstrated with small-scale launch experiments, and requires additional development to provide full functionality.

The primary elements of an electric gun are the power source, an energy storage device, a power peaking device, and the conversion elements from electric to kinetic energy. With the potential for very high muzzle velocity, in the range of 2.5 km/s with this electromagnetic coilgun, dramatic new force projection capabilities are possible: This concept gives surface combatants very long-range weapon delivery capability, to 300 NM. It provides time critical delivery of a few minutes from firing to impact (2 minutes to 100 NM, 6 minutes to 300 NM). No explosive powder or propellant is required for the rounds; the ship's propulsion system provides the prime power for the gun. This provides a simplification of logistics, large improvement in the rounds load-out capacity, and simplifies stores handling and re-supply at sea. It provides increased penetrator round and kinetic energy round lethality as a result of the higher impact velocity. It provides flexibility for use of multiple projectile types from the same weapon.

MISSION REQUIREMENTS

Navy mission for littoral and strategic strike will continue to move in the direction of increased range and increased rate of fire on target, using rapid response, cost-effective means. Improved gun technology could aid in this mission, particularly with the potential for hypervelocity, and thus longer range guns based on electromagnetic launch technology [1,2,3,4]. The launch velocity is not constrained by the expansion velocity of the high pressure gas that is the basis for all conventional guns, relying instead on electromagnetic pressure developed from electrical power. For this study we assumed there would be two classes of targets. The first would be hard targets such as bunkers or heavily armored vehicles. The second class was soft targets such as personnel or light armored vehicles. These hard and soft targets allowed us to define projectile types that would be used in the coilgun.

COILGUN

In a coilgun, kinetic energy is imparted to the projectile though a series of sequentially switched coils. The coilgun projectile has no electrical contact, Figure 1, since it couples magnetically, and the forces within the coil are such that the projectile tends to be self-centered within the launch barrel and is magnetically levitated on the launcher centerline. This centering force minimizes wear on the barrel.

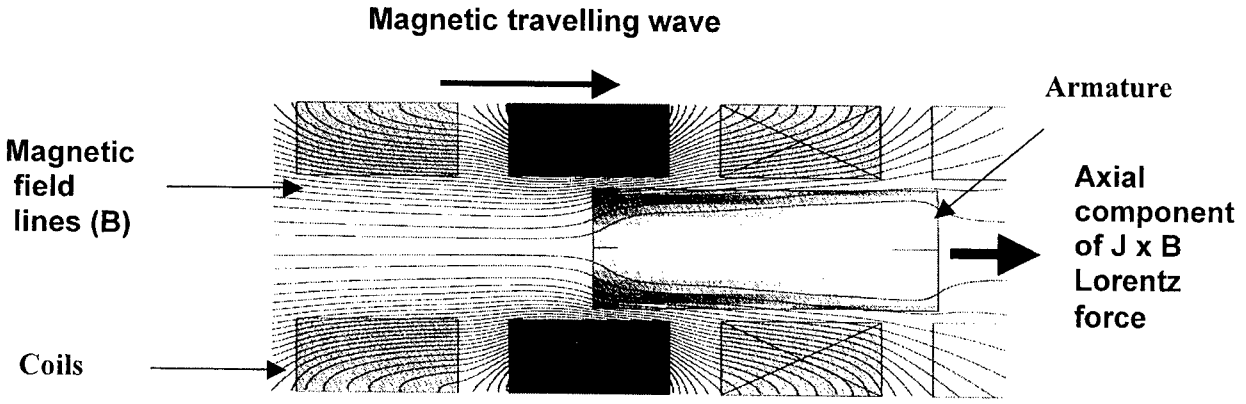


FIGURE 1. Coilgun propulsion comes from interaction of the magnetic field from the coil and the induced currents in the armature. A traveling magnetic wave is created by sequentially switching power into the coils.

In a coilgun, very high launch pressure can be maintained uniformly over the entire length of the gun barrel. The resulting uniform acceleration allows very high velocities to be achieved with the shortest possible barrel. The average pressure in any gun is the muzzle energy of the projectile divided by the volume of the bore. In a coilgun, this pressure is contained by embedded copper windings in the coils. Making high strength coils is the fundamental challenge for coilgun designers; for it is this feature that determines the length of the gun. Test coils in earlier experiments withstood about 1.1 kbars of average pressure [5]. In these experiments velocities in excess of 1 km/s were achieved with a 5-cm diameter, 240-gram aluminum

projectile in a 1.6-meter gun. The experiments demonstrated coil strength, operating reliability and controllability, and benchmarking of simulations.

REQUIREMENTS AND ASSUMPTIONS

For this study of the long range coilgun, analyses were limited to the following requirements:

1. 15, 30, 60, or 75 kg flight vehicles
2. 2 to 3 km/s muzzle velocities
3. 15 and 20 m gun length
4. 6 shots/min firing rate

The mass of the launch package is the combined mass of the flight vehicle delivered to the target, the armature winding and its support structure, and the sabot that couples thrust from the armature to the vehicle and supports it in the gun bore. The size of these individual components were estimated as a function of armature diameter based on the assumptions that:

1. maximum radial pressure on the armature is equivalent to that on the coil but directed inward generating a compressive hoop stress,
2. a boron/epoxy composite shell retaining the radial load has a maximum operational compressive hoop strength of 1.75 GPa,
3. the carbon/epoxy composite axial load transfer ring has a maximum operating shear strength of 319 MPa if the armature thrust is coupled to the flight vehicle structure through a tailored shear interface to the case, and
4. the copper armature wire occupies 40% of the armature winding crossection with carbon epoxy composite as the balance.

The SLINGSHOT circuit simulation code was used to calculate the electrical, dynamic, and thermal performance of the coilgun using lumped elements for the coils[6]. Velocities that can be achieved in 15 and 20 m length gun with these launch packages are shown in Figure 2 as a function of armature diameter and flight vehicle mass. From this scaling and earlier scalings performed in the study an armature outer diameter of 30 cm was selected for concept evaluation. The coil concept developed in this study builds upon the previous design by adding coolant channels for heat transfer from the winding allowing operation at 6 pulses per minute in steady state. Like the coil developed in 1993, the total winding is a set of individual nested helical winding layers electrically in series. The nested helix uses multiple layers of wires to reduce current density and ohmic heating. To limit the temperature rise the windings were constructed of litz cable to provide as much conductor in each layer as possible. Litz cable is constructed of insulated wire strands twisted in such a way that results in a uniform current distribution across them. Each layer consists of many insulated wires in parallel that occupy the entire circumferential area. The number of wires and number of turns in each layer is consistent with the requirements for the inductance of that coil depending upon its position in the gun. Feeds to the winding inner and outer layers are the azimuthally distributed wires of the winding directed radially outward.

SLINGSHOT simulations and thermal analysis show heating rates of coils vary from 71 to 9 kW from the breech to muzzle of the gun with 90% of a 225 stage gun at 20 kW or less. The required coolant flow per coil is 75 l/min (20 gal/min) or less except for the first 20 coils at the breech end. The required coolant flow rate at the breech end is 1400 gal/min. Estimates of wire temperature from SLINGSHOT and steady-state heat transfer calculations indicate that the

wire conductor peak temperature can be kept below 100°C thus not affecting the strength of the fiber composites. The coolant manifold will be located on the outside of the coil structure.

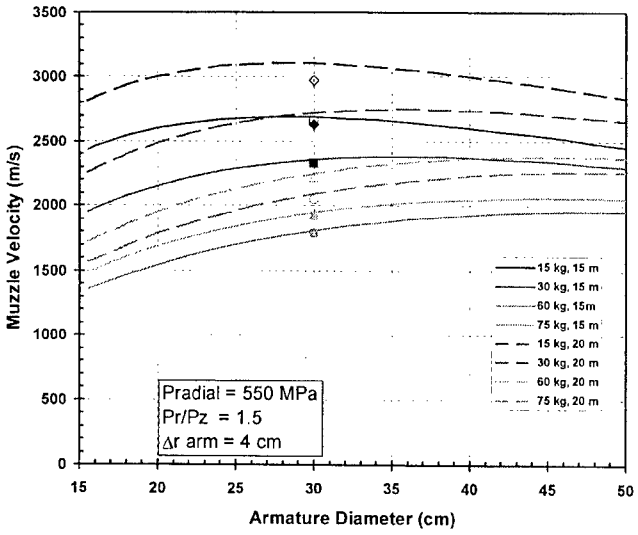


Figure 2. Velocity scaling as function of armature size and flight vehicle mass. Results of SLINGSHOT calculations plotted at 30 cm diameter demonstrate that a coilgun can be configured to meet the criteria of the scaling. SLINGSHOT calculations were performed with armature winding initially cooled to 77°K.

Given the number of winding layers, the radial thickness of the reinforcing shells is determined from the total radial and axial forces on the coil, and a linear load distribution that is assumed as a function of radius over the build of the coil. The radial build of each shell is tailored to work the fiber composite to a maximum operating stress equivalent to the root-mean-square of the axial and hoop stresses from these applied loads. Axial shear loads are compared to the maximum composite shear and the number of winding layers adjusted if necessary. The total radial build and conductor fill fraction of the coils is tabulated as an input to the detailed coil specification for the final SLINGSHOT calculation. Details of the concept are shown in Figure 3, which illustrates a crossection of three stator coils, a composite barrel, location of radial cooling channels, and the armature at the base of the flight vehicle. The variation of coil parameters over the length of a 15 or 20 m gun is shown in Figure 4 for coils with reinforcement shells constructed of PBO/carbon fiber/epoxy composite. The minimum number of turns in the winding was set at two to keep bank current on the order of a megamp or less. As seen in the chart, most of the gun is constructed of coils similar to the muzzle design, and the first 20 coils have significantly greater radial build. Although not considered here, more optimal solutions may use individually tailored capacitor banks for these early stages to reduce the coil build and improve coupling to the armature. Velocity and acceleration profiles for the coils discussed above are shown in Figure 5. The input file for this run defines a 20 m long coilgun, but velocity values at 15 m are of interest to fit destroyer platforms. Total launch mass of 94.7 kg is comprised of a 60 kg flight vehicle, 17.4 kg, 30 cm OD armature conductor (calculated by the code), and 17.3 kg for armature structural support and sabot. Capacitor banks for each coil are

charged to 40 kV and bank energy increases just under 4% over groups of 50 coil stages. The initial temperature of the copper armature winding is 77°K to reduce the resistance of that circuit.

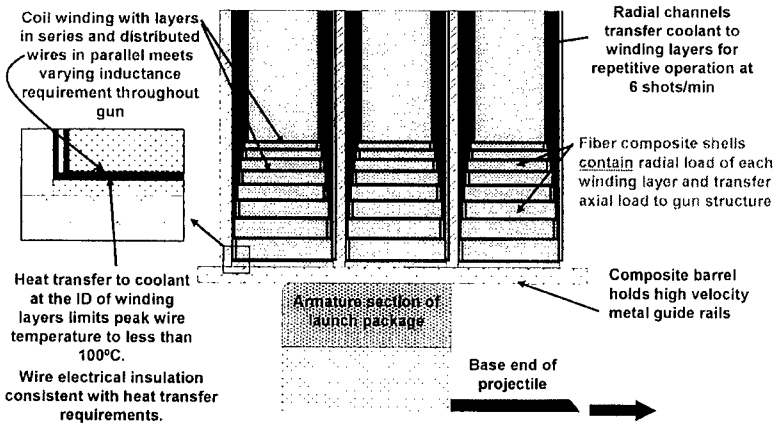


Figure 3. Crossection of 3 nested helix coils and the armature at the base end of the projectile flight vehicle. Radial and axial coolant channels occupy 50% of the circumferential area with spacers filling the balance for mechanical support.

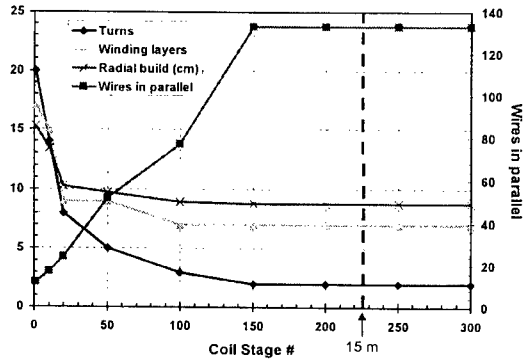


Figure 4. Variation of coil parameters from the breech to muzzle of a 15 or 20 m gun for SLINGSHOT simulation assuming PBO/carbon fiber/epoxy reinforcement shells. All coils have the same winding length of 49 mm at 58 mm center-to-center spacing.

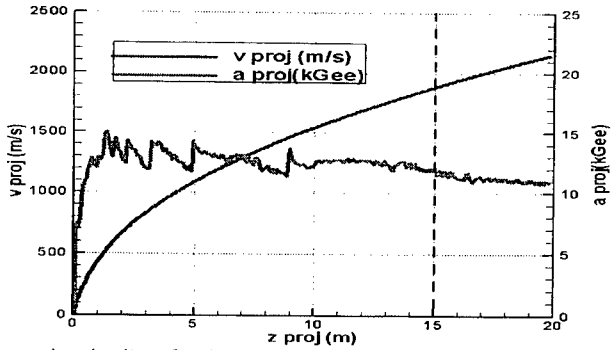


Figure 5. Acceleration and velocity of a 95 kg launch package consisting of a 30 cm OD armature initially at 77°K, sabot structure, and 15.5 cm OD, 60 kg flight vehicle. Total initial stored energy in the 15 m gun of 225 coil stages is 464 MJ.

The 15 m length coilgun accelerates the 95 kg launch package at about 13 kgees to a velocity of 1.9 km/s in 17.6 ms. The 15 m length gun is comprised of 225 coil stages and the 20 m gun has 300 stages. The current in each stator coil is opened after one full current cycle at a time of a current zero to recover part of the magnetic energy and limit coil heating.

Cryogenic cooling of only the armature winding reduces the ohmic losses resulting in a long time-constant for the decay of induced current. Muzzle velocities for armatures at liquid nitrogen temperature of -193°C are about 13% greater than that achieved with a room temperature initial condition. This represents an increase in muzzle energy of 25 to 30%. Cryogenic cooling of the stator was not considered.

PROJECTILES

A representative projectile design and aerodynamic model were developed to provide realistic simulations of trajectory performance for comparison with mission requirements. Ballistic performance results are presented for 15-kg, 30-kg, 60-kg and 75-kg bodies. A 60-kg reference projectile was scaled, assuming constant packaging density, to obtain the sizes for the other identically shaped projectiles in the set. The ballistic coefficient for the 60 kg reference projectile was 5900 psf at 2 km/sec. Choice of the reference projectile shape, size and mass was based on requirements for long range, hard and soft target missions and on results of a preliminary packaging study. The study was focused on a projectile design that could meet ballistic performance requirements and provide adequate warhead volume using a current Navigation Guidance and Control (NG&C) system design and current heat-protection technology. Results indicate that a 155-mm diameter is desirable for relieving NG&C and thermal-protection packaging constraints to achieve acceptable warhead volume. Results of the coilgun simulation determined an armature diameter of 30.0 cm would give the best performance. The choice of 155 mm projectile diameter would also allow the use of fixed guiding fins and takes advantage of current 155 mm technology.

The Reference Projectile model, shown in Figure 6, was created to explore packaging, sabot interface, aero-heating and flight performance requirements. This fin-stabilized ogive-cylinder shape provides a near optimal balance between minimum supersonic drag and maximum payload volume. Addition of a boattail, to further reduce drag, is dependent on unresolved packaging and sabot interface constraints. Choice of a 60-kg mass and 155-mm diameter was based on three factors: assuring sufficient warhead volume; results of a packaging

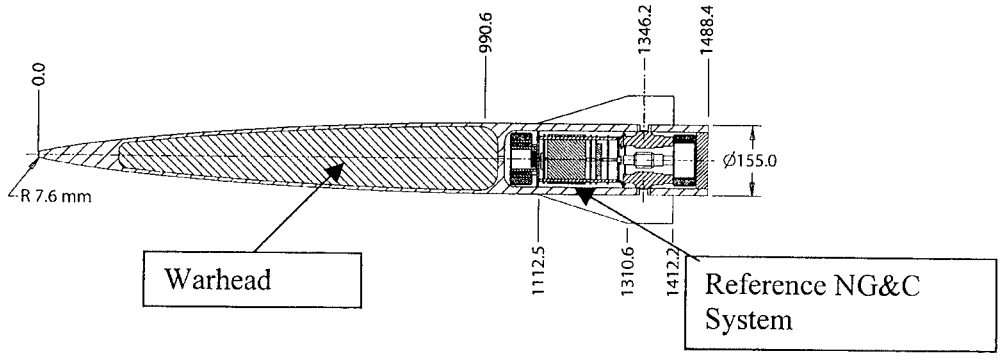


FIGURE 6. 155 mm diameter 60 kg reference projectile.

study, and on Mission Scenario requirements. An aerodynamic model has been developed to provide realistic simulations of performance and aero-heating for projectiles of this shape. The reference 60-kg projectile shape was scaled to 15-kg, 30-kg, and 75-kg sizes, assuming constant packaging density (3-g/cc). Therefore, the smaller less massive projectiles have lower ballistic coefficients. The Trajectory Analysis and Optimization Software (TAOS) was used for the projectile performance in our analysis[7]. The code simulates point mass and rigid-body trajectories for multiple vehicles. Results, based on muzzle velocities for total accelerated mass (projectile, sabot and armature), indicate that the coilgun system should be able to deliver projectiles on target at supersonic velocities over a band of range that extends from tens of nautical miles (nm) out to a maximum that approaches 300-nm. This is demonstrated for projectiles that maneuver on ascent from a fixed quadrant elevation (QE) gun (51-deg, max range. Significant cross range can be achieved, with a small sacrifice in impact velocity at a given range, by maneuvering to change azimuth during ascent, see Figure 7. The 15-kg projectile appears to be capable of reaching 300-nm by maneuvering on descent to extend its 280-nm ballistic range. Results are given in Table 1 for dependence of range on projectile mass and launch velocity. Muzzle velocity was increased for a given mass by increasing the gun tube length from 15-m to 20-m. Muzzle velocities were derived assuming a pusher sabot and using realistic accelerated masses for each projectile. Note that maximum range for the 15-kg projectile approaches the 300-nm requirement. It is very likely that the projectile could maneuver during descent to the extend range to 300-nm. Note also that maximum ballistic range for the 60-kg and 75-kg projectiles exceed the 100-nm requirement for the Mission Scenario. Results of our feasibility study indicate that a projectile may be developed in the near future to satisfy the Mission Requirements for 100-nm plus range, 50-nm per-minute delivery time, and a large payload volume.

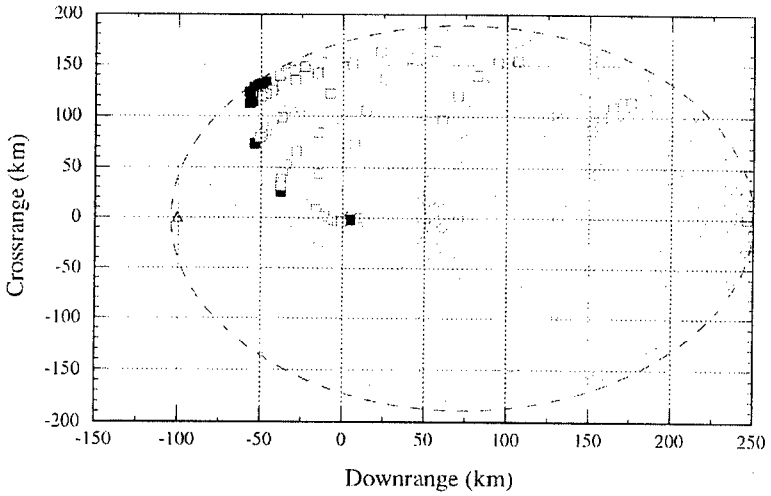


FIGURE 7. The field of fire for a maneuvering projectile.

TABLE 1. Effects of Mass and Velocity on Range

	15-M TUBE			20-M TUBE		
Projectile Mass, kg	Velocity, km/sec	Range, km	Range, nm	Velocity, km/sec	Range, km	Range, nm
15	2.55	338	182	3.00	520	281
30	2.23	276	149	2.53	390	210
60	1.80	188	101	2.00	245	132
75	1.70	172	93	1.90	220	119

ENERGY STORE

The projectile mission places requirements on the coilgun, and the gun performance and design, in turn, puts requirements on the coil driver circuits, which may vary along the length of the gun. Our concepts have been based on a maximum charge voltage of 40 kV that is consistent along the whole length. A requirement for 2 MJ per module suggests a total bank capacitance of 2.5 mF. To keep the modules simple and compact, we have targeted an average module energy density of 4 J/cc, assuming one 1-MA class switch per module. With a nominal capacitor packing fraction of 50%, we require a capacitor energy density of 8 J/cc.

There has been a dramatic increase in the energy storage capability of capacitors in the past ten years, and this trend is expected to continue over the next decade. For the conservative design an average module energy density of 4 J/cc translates into about 8 J/cc for the capacitors, which appears to be achievable. TPL, Inc. of Albuquerque have developed a siloxane polymer film with a higher dielectric constant (~9) and breakdown strength (15-16 kV/mil) than the polypropylene that is used in the typical discharge capacitors. In collaboration with Aerovox Corp., they fabricated a number of small capacitors in which 2 to 3 J/cc has been demonstrated.[8] They feel like they should be able to exploit all the properties of their new polymer and demonstrate 30 to 50-kJ capacitors within three years. An energy density of at least 7.5 J/cc is anticipated.

Jaycor, Inc. in Huntsville, AL and Vanderbilt University in Nashville, TN have collaborated to apply Polycrystalline Diamond Film (PDF) technology to develop HED capacitors. The capacitor application is in its infancy, but the PDF analysis and technology has at least a strong ten-year history behind it.[9] The PDF diamond is considered to be the best thermal conductor (20 W/cm-C), highest electrical insulator (>30 MV/cm), highest temperature compatibility, and hardest material. Its dielectric constant of 5.5 (higher than most plastics and oils, and the ε_r = 3.5-4 DLC process developed for Wright Patterson AFB) [10] coupled with the high voltage breakdown threshold makes it attractive as a possible HED capacitor. Developers have established an energy density goal of 30 J/cc, which is still a factor of four below the theoretical limit.

A single switch for each 2-MJ capacitor bank module (225 for a 15-m gun) would conduct peak currents up to 1 to 1.2 MA and transfer approximately 100 Coulombs per shot. The faster discharge circuits require upper limits on the inductance and closed switch resistance of about 100 nH and 1 mΩ, respectively. The switch electrodes will need to be actively cooled, especially for extended scenarios at a rate approaching 20 kJ per shot. There exist a few candidate switches that have demonstrated performance parameters near our coilgun circuit

requirements. Satisfying the module closing switch specifications should not require any significant development. If this switch could be opened after energizing the coil approximately 30% of the capacitor energy could be recovered. This would be a significant volume and weight reduction in the energy store.

SHIP INTEGRATION AND OPERATIONS

The Navy will be building a new 21st century land-attack destroyer, the DD-21. The weapons will be the most advanced available. For this reason the DD-21 was chosen for conceptual layouts of a fixed gun and a trainable gun. The current design could be retrofitted to the Arleigh Burke class destroyers. All design dimensions and parameters were taken from the previous sections. The results of this parametric evaluation are shown in Table 2. A plot of the range versus the projectile kinetic energy is shown in Figure 8. It can be seen from the table and these plots that attractive gun parameters can be achieved at reasonable sizes and weights.

TABLE 2. PARAMETRIC EVALUATION

Coilgun Concepts

KE	V	Projctle mass	Armtre &sabot Mass	Coil Bore	Barrel Parameters Lngth	Mass	Gun Mount	Rounds Mass	Energy and Power Stored Energy	Energy S Mass	Power & Thrml contrl Mass	System Tonnes	Range
MJ	km/s	kg	kg	m	m	Tonnes	Tonnes	Tonnes	MJ	Tonnes	Tonnes	Tonnes	NM
80	2.2	15	18	0.2	11	5	7	55	200	62	13	142	125
150	3	15	18	0.2	20	9	13	55	375	118	24	219	270
150	2.5	30	18	0.2	20	9	13	81	375	118	24	245	210
190	2.4	30	35	0.3	15	15	22	109	475	149	30	325	180
290	2.8	30	43	0.34	20	25	38	123	725	226	46	458	280
190	2	60	34	0.3	15	15	22	158	475	148	30	373	130
330	2.5	60	45	0.35	22	28	42	176	825	258	53	557	230
220	2	75	35	0.3	20	19	29	185	550	172	35	440	140

Assumptions:
Energy Storage Density = 8 J/cc, 4 J/gm, 50% volume fraction
Power striplines/cables = 0.25 x Energy Storage mass
Number of Rounds Stored = 1400
Power Density (gas turbine/alternator genset) = 0.3 kg/kw
Power based on 6 shots per minute
Thermal Control = 0.5 kg/kw
Gun Mount = 1.5 barrel mass

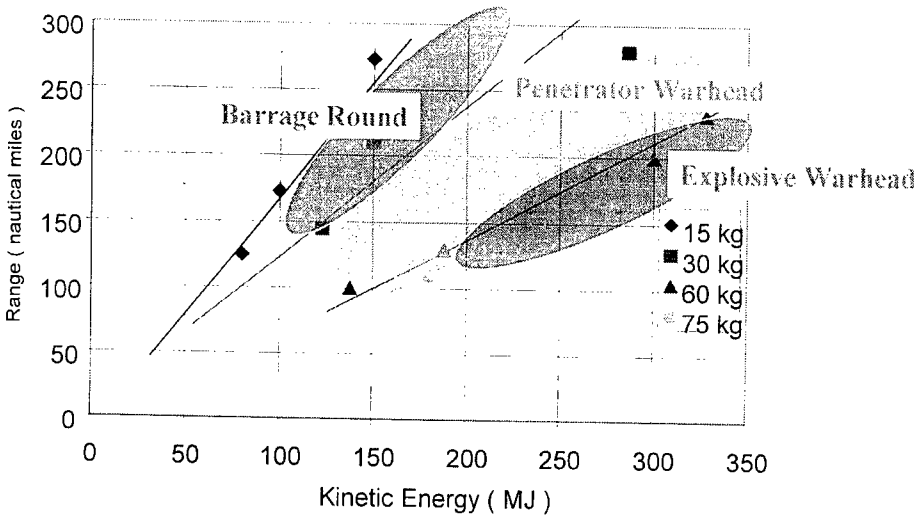


FIGURE 8. The projectile range for varied mass and the initial projectile kinetic energy.

CONCEPTUAL SHIP LAYOUT

The gun barrel is 15m long and 32 cm inside diameter. The capacitors have an energy storage density of 8J/cc and an average energy storage density of 2-4J/cc. The projectile with armature and sabot is 1.5 m in length. The gun length in both options was 15m. Both concepts have their advantages and disadvantages. For both designs the energy storage (total of 450 MJ) is four parallel rows of capacitors with the switches and cabling located between the rows. At 6 shots per minute this will require 45 MW of conditioned power. This could come from ship

Two mounting options were investigated; a fixed and rotating mount, Figure 9. The fixed mount option is angled at 51 degrees elevation for maximum trajectory. The layout of the gun barrel (15 m), energy storage, and projectiles are based on parameters discussed in the previous sections. An advantage of this layout is in the gun placement, which can be entirely below deck, reducing the radar cross-section.

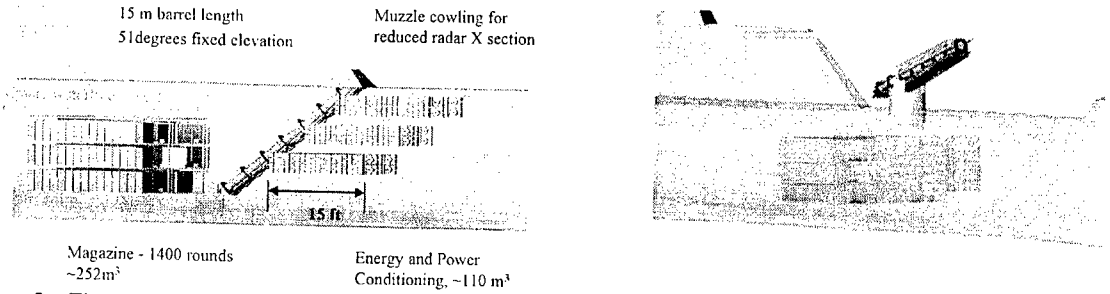


Figure 9. Fixed gun layout is on the left showing the location of the energy store, barrel and magazine. The rotating turret is shown on the right.

For targeting the ship will have to be maneuvering in the proper direction or the projectile guided to target. A plot of the field of fire was shown in Figure 6. While there is some penalty for maneuvering it is a viable option and increases the ship versatility with instantaneous retargeting. It also will simplify the construction and maintenance as well as reduce the gun costs.

The gun parameters for the trainable gun layout are the same as those for the fixed gun. This option has the advantage of rapidly changing target coordinates and reduces the maneuverability requirements on the projectile. The capacitive energy storage can be placed below the waterline. This option does have a higher radar cross section during firing. To reduce the cross section when not in use it could be lowered to deck level or below. This does complicate the design, construction, and increase costs. It also increases the number of power feeds required for the muzzle section. To keep the inductance low it would require twenty-eight parallel sets of cables to power the end coils. All leads would have to have extra slack in them to allow for the turret to rotate and elevate.

CRITICAL TECHNICAL ISSUES

There are a several critical technical issues that must be resolved to bring this capability into operational reality. The first issue for the coilgun launcher is a demonstration of firing control at full velocity. The maximum velocity tested at Sandia to date is at 1.0 km/s.

The next critical issues for the gun launcher itself is, with the combination of high pressure, high heat load, high electric fields, and high stresses within the coils and the integrated barrel structure. These issues are thought to be manageable within the coil design concept that has been presented. Choice of materials (preferably light-weight, high strength composites) is also a challenge to insure that mechanical strength, insulation and thermal properties are all optimized.

Energy storage system design and the size of the energy storage device are also critical issues. In these concept designs, we have extrapolated the current proven capacitor technology to a level of 8 J/cc. This level is anticipated to be achievable on the time-scale of 3 to 5 years on the basis of the trend of current development efforts on three technology fronts, using siloxane polymers, vacuum deposited thin film diamond, and cryogenic ceramic dielectrics.

Design and development of projectile maneuvering capability is a critical issue for the high-speed, long-range projectile. For long-range accuracy, terminal maneuvering will be required, particularly for rounds that require high accuracy, such as a kinetic energy penetrator. Analysis indicates that control surface area from the concept design projectile will be adequate for the maneuvering needed. The projectile maneuvering requirement for a fixed gun concept is within the capability of the control surfaces shown in the projectile concept design. Maneuvering at near-full muzzle velocity also introduces an added amount of aerodynamic heating. Simulation results indicate that aerodynamic heating problems can very likely be overcome with available materials for 155 mm class projectiles launched at < 2.5 km/sec higher velocities and smaller size present a challenge.

SUMMARY

We have developed a conceptual design of a coilgun that will fit on a destroyer. Layouts for a fixed and trainable gun are both feasible. Both layouts rely on capacitor technology reaching 8 J/cc. Projectile ranges and mass are in regions of interest for littoral and inland mission support. The total system weight will adapt to the DD-21. Additional design work needs to be done with Naval Architects to ensure full compatibility with the DD-21.

The coilgun design work has addressed thermal and mechanical design issues and found coils can be designed to meet mission requirements of 100-300 nm. Suitable projectile designs have also been evaluated for use in a coilgun, and again found to satisfy mission requirements for hard and soft targets. Guidance, thermal issues, and trajectories for 15 to 75 Kg have been analyzed.

We have identified critical technical issues that must be resolved to bring this capability into operational reality. We did not find any critical areas that would prevent the deployment of a long-range coilgun.

REFERENCES

[1]. R. J. Lipinski, "Long-range Gun Induction Launcher," Sandia National Laboratories report to Vic Dawson, Center for Naval Analysis, November 1991.

[2]. Dent, Philip A., et. al., "Advanced Strike Platform Concept: Feasibility Assessment of a Linear Induction Electromagnetic Launcher on a Naval Surface Combatant," David Taylor Research Center Report DTRC/SD-91-05, June 1991.7

[3]. W. A. Walls, at al, "Application of Electromagnetic Guns to Future Naval Platforms", IEEE Transactions on Magnetics, Jan 1999, pp 262 –266.

[4]. David Foxwell, "Renewed Naval Fire Support," Janes International Defense Review, September 1997, pp 83 – 87.

[5]. R.J. Kaye et al., "Design and Evaluation of Coils for a 50 mm Diameter Induction Coilgun Launcher, " IEEE Trans. Mag., vol. 31, no. 1, January 1995, pp. 478-483.

[6]. Shokair,I. R., Cowan, M., Kaye, R. J., and Marder, B. M. "Performance of an Induction Coil Launcher", from the proceedings of the IEEE Transactions on Magnetics Conference, Vol. 31, No. 1, January 1995.

[7]. David E. Salguero, "Trajectory Analysis and Optimization Software (TAOS), SAND-99-0811, Sandia National Laboratories, Albuquerque, NM, Jan 1999.

[8]. Private communications with Hap Stoller, Kirk Slenes, and Lew Bragg, TPL, Inc., Albuquerque, NM, 13 Sep 00.

[9]. J. L. Davidson, et. al., "CVD Diamond, A Unique Dielectric, Semiconductor and Thermal Conductor for Electronic Applications," Interface, The Electrochemical Society Magazine, Oct 95.

[10]. K Systems Patented process (5,844,770, December 1, 1998) for Diamond-Like Carbon thin films developed under an Air Force SBIR Phase II Program with WPAFB. Contact: Dr. Richard L.C. Wu, Vice President, K Systems Corporation, Beavercreek, Ohio.

Critical Velocity of Electromagnetic Gun in Response to Projectile Movement

Jerome T. Tzeng[1]

1. US Army Research Laboratory, Attn: AMSRL-WM-MB, Aberdeen Proving Ground, MD 21005-5066

ABSTRACT

A model is developed to investigate the dynamic response of an electromagnetic (EM) rail gun, induced by a moving magnetic pressure during launch of projectiles. As the projectile velocity approaches a critical value, resonance can occur and cause high amplitude stress and strain in the rail at the instant and location of projectile's passage. In this study, governing equations of a railgun under dynamic loading conditions are derived that illustrate a lower-bound critical velocity in terms of material properties, geometry, and barrel cross-section. That represents the worst case or a lower bound solution for the structure under a dynamic loading condition. A study is then performed to show the effect of these parameters on the critical velocity of the barrel. Accordingly, the model that accounts for projectile velocity and gun construction can be used to guide and improve barrel design.

INTRODUCTION

A strain of very high amplitude and frequency, commonly referred to as dynamic strain amplification, develops in a conventional gun tube due to the passage of the projectile. The phenomenon is caused by the resonance of flexural waves when the moving pressure approaches the velocity of wave propagation in the gun tube. The resonance response in an isotropic cylinder attributed to a moving pressure load has been investigated by Taylor [1], Jones and Bhuta[2], Tang [3], and Reismann [4]. Simkins [5] investigated the dynamic response of flexural waves in steel gun tubes, as very large strains have been observed in a 120mm tank gun barrel. Hopkins [6] applied finite element analysis to obtain a solution in a more complex taper geometry. Tzeng and Hopkins[7] investigated the dynamic strain effect in cylinders made of fiber-reinforced composite materials overwrap with a metal liner. Tzeng [8] extended the research to study fracture in the composite gun tube due to the dynamic response.

In this paper, an analytical solution was developed to obtain the critical velocity of an EM rail gun barrel attributed to dynamic loading conditions. Dynamic response could be a concern particularly since a fieldable EM barrel has to be a lightweight construction with hypervelocity launch capability. Figure 1 shows a schematic of an EM rail gun cross section

and loading condition [9]. The rail and insulator (typically ceramic or polymer composite) were contained and supported by a containment structure. The rails are in compression due to the EM force acting on the rail and reaction force resulting from the containment structure. Furthermore, the magnetic force in the rail is discontinuous at the location of projectile armature where the electrical current passes through. The discontinuity of the force causes local bending moment and shear stress in the rails near the armature location. The pressure front will move along the rails as the projectile moves down through the barrel. Accordingly, dynamic stress and strain occur as the projectile movement approaches the critical velocity of the railgun.

ANALYSIS

Consider a railgun cross section as shown in Figure 1. The rail has a rectangular cross section and is mechanically supported by a rigid material, a containment structure, and insulation material [10]. The structural response of the rail can be modeled as a beam sitting on an elastic foundation as shown in Figure 2. Accordingly, the rail is the beam and the support from the insulation material and containment is modeled as an elastic foundation. It is assumed that structural interaction between the rail and the containment is modeled through the elastic constant. The magnetic pressure traveling at the speed of the projectile on the rail can be expressed as a Heaviside step function. The governing equation for the rail gun subjected to a moving pressure can then be derived as follows:

$$m\frac{\partial^2 w}{\partial t^2}+EI\frac{\partial^4 w}{\partial x^4}+kw=q[1-H(x-Vt)], \tag{1}$$

Here, w is the lateral displacement, dependent upon time, t, and axial position coordinate, x, m is the mass per unit length and is equal to ρBh, ρ is the density of rail material, and B and h are the width and thickness of the rail, respectively. E is the modulus of rail material and I is the moment of inertia of the rail cross section. The elastic constant, k, due to the elastic foundation will be derived in a later section. The loading function, $q(1 - H(x-Vt))$ in Equation (1), represents the magnetic pressure front traveling along the rail with a constant velocity V, represented by a Heaviside step function, $H(x-Vt)$. The magnetic pressure q, is assumed to be constant also. Accordingly,

$$\begin{aligned} q(1-H(x-Vt) &= 0 \qquad when\ x>Vt \\ &= q \qquad when\ x\le Vt \end{aligned} \tag{2}$$

Eq.(1) can be solved using separation of variables with the assumption of

$$w(x,t)=\phi(t)\theta(x) \tag{3}$$

Accordingly, the left-hand side of Equation (1) can be rewritten to solve the homogeneous solution as follows:

$$m\ddot{\phi}\theta + EI\phi\theta'''' + k\phi\theta = 0 \tag{4}$$

The critical velocity of the beam (rail) can be derived from the characteristic function and the particular solution from Equation (3) as

$$V_{cr}^2 = \frac{1}{\sqrt{3}}\frac{1}{\rho}\sqrt{\frac{h}{B}}\sqrt{E}\sqrt{k} \tag{5}$$

Equation (5) shows that the critical velocity of a railgun subjected to a moving pressure front is a function of the rail geometry, density, and elastic modulus. In addition, the support from the containment structure has great influence on the dynamic behavior of the rail. Critical velocity increases with the elastic modulus of the rails and the stiffness of containment structures. From a design point of view, a launcher constructed with high stiffness, lightweight, and a large moment of inertia is preferred for dynamic loading conditions.

The elastic constant of foundation, k, can be calculated from the containment structure if the coupling effects of the insulation material (ceramic in general) are neglected. We consider a circular containment of a unit length subjected to concentrated loads at the inner surface of a cylinder as shown in Figure 3(a). Accordingly, the concentrated loads are calculated from the summation of resulting magnetic pressure. Since both the containment geometry and loading conditions are symmetrical, the structural response can be calculated from the free body shown in Figure 3(b). The stiffness of the containment at the location of the concentrated load can then be obtained from the strain energy of the curved beam shown in Figure 3(b). Neglecting the shear contribution, the strain energy can be expressed as follows:

$$U = \int_0^{\pi/2} \frac{N^2 R}{2A_c E_c} d\theta + \int_0^{\pi/2} \frac{M_a^2 R}{2I_c E_c} d\theta \quad , \tag{6}$$

Where N is the normal force, M_a is the moment resulting from the concentrated load, and R is the mean radius of the containment. A_c, I_c, and E_c are the cross sectional area, the moment of inertia, and elastic modulus of containment, respectively. N and M_a can then be derived as follows:

$$N = \frac{P}{2}\cos\theta \tag{7}$$

and

$$M_a = \frac{PR}{2}(\cos\theta - \frac{2}{\pi}) \tag{8}$$

Therefore, the strain energy of the quarter containment can be calculated in terms of concentrated load P, material properties, and geometry. Based on Castigliano's theorem, the

displacement at the location of the loading "P" can then be derived from the derivative of the strain energy with respect to the "P" as follows:

$$\delta_p = \frac{\partial U}{\partial P} = \frac{\pi PR}{16 A_c E_c} + \frac{\pi PR^3}{16 I_c E_c}\left(1 - \frac{8}{\pi^2}\right) \tag{9}$$

Where I_c is the bending moment of inertia calculated from a unit length of containment (curved beam) shown in Figure 3, which is equal to $\frac{1}{12} bt^3$ (b=1); where b and t are the length and thickness of the containment, respectively. E_c is Young's modulus of the containment. The stiffness constant of the containment can then be defined as follows

$$k = \frac{1}{\delta_p} \quad \text{, and} \quad P = 1 \tag{10}$$

NUMERICAL RESULTS

A baseline test case is used to obtain critical velocity for a parametric study. The gun is composed of a pair of aluminum rails, ceramic insulation, and a steel containment. The aluminum rail has a cross section of 12.5mm (0.5 inch) thick by 76.2mm (3.0) inch high. The containment is 12.5mm (0.5 inch) thick. The parameters required for the simulation are listed in Table 1:

Table 1: Mechanical properties and geometric parameters of the rail and containment

Rail (Aluminum)			
Modulus (E)	*Thickness (h)*	*Height (B)*	*Density (ρ)*
68.95 GPa	*12.5×10^{-3} m*	*76.2×10^{-3} m*	*2750 kg/m3*
Containment (Steel)			
Modulus(Ec)	*Thickness (t)*	*Mean Radius (R)*	
206.85 GPa	*12.5×10^{-3} m*	*63.5×10^{-3} m*	

The stiffness of the containment can be obtained from Equations (9) and (10) by application of a unit concentrated pressure load. The inverse of deflection at the center of rail (δ_p) yields the stiffness, k, as follows:

$$k = 1 / \delta_p = 3.48 \times 10^9 \, Pa \, .$$

The k represents the spring constant of foundation for the entire rail height of 76.2 mm (3.0 inch). The critical velocity of the barrel can then be calculated from Equation (5) as follows:

$$V_{cr} = 1148\ m/sec$$

The critical velocity is strongly dependent on the cross section geometry and the mechanical properties of rail and containment. The model is based on the assumption of no structural coupling effects from insulation materials. It is a reasonable assumption since the bonding between rail and insulation is friction. Parametric studies are performed to compare the baseline case that is constructed with aluminum rails and a steel containment as listed in the Table1.

Figure 4 shows the effects of rail thickness on the critical velocity of railguns. The geometry of containment and all material properties are identical to the baseline case. The increase in the moment of inertia of the rail will enhance the bending stiffness of the rail. Accordingly, the critical velocity increases with the thickness of the rail. However, the critical velocity does not increase linearly. It varies with only a power of 0.25. The stiffness of containment also has strong effects on the critical velocity of the railgun. Figure 5 shows the effect of containment thickness on the critical velocity of the railgun. A thicker containment provides higher stiffness and structural support for the rail. Accordingly, the deflection of containment decreases as it is subjected to magnetic pressure from the rails. Mathematically, it is modeled as the stiffness of foundation, k, which increases as illustrated in Equation (5). The effect of the containment stiffness on the critical velocity is not linear either. It varies with a power of 0.75.

The effect of rail material properties on the critical velocity is illustrated in Figure 6. A combined effect on the dynamic behavior due to the density and elastic modulus of rail is illustrated using some potential material choices. The baseline case is 7075 aluminum alloys. Three different conductor materials are examined. GIGAS24 is an advanced aluminum alloy with a higher modulus of 88.25 GPa (12.8 Msi). The density is about the same as the 7075 aluminum. Accordingly, a higher critical velocity is obtained due to the increase of modulus. Glidcop is aluminum oxide dispersion strengthened cooper. It has a high modulus of 172.4 GPa and a high density of 8900 kg/m^3 material. The critical velocity turns out to be lower than the 7075 aluminum due to the high density. Finally, aluminum reinforced with aluminum oxide (Al_2O_3) fiber (45% volume fraction of fiber content) is used for comparison. The modulus and density of this material are 165.5 GPa (24 Msi) and 3400 kg/m^3, respectively. The combination of high modulus and low density gives a high critical velocity.

CONCLUSIONS

The dynamic behavior of an EM barrel can be modeled with reasonable assumptions as a rail sitting on an elastic containment. The derived solution illustrates effects of important design parameters and material properties on the critical velocity of barrel, which can be applied for barrel design under dynamic conditions. A high magnitude of cyclic stress can occur that might cause damage in the rail, accelerate growth of defect, and eventually shorten the rail life significantly. The dynamic phenomenon is particularly crucial if gun barrels are

designed to be a lightweight and fieldable system with hypervelocity capability. The developed model provides a meaningful tool to guide barrel design that accounts for dynamic response due to a moving projectile.

REFERENCE

1. Taylor, G. I., "Strains in a Gun Barrel Near the Driving Barrel of a Moving Projectile," A.C. 1851/Gn. 104, U.K. Ministry of Supply, London, England, March 1942.
2. Jones, J. P. and Bhuta, P. G., "Response of Cylindrical Shell to Moving Loads," *Journal of Applied Mechanics*, Vol. 31, Trans, ASME, Vol. 86, Series E, March 1964, pp. 105 - 111.
3. Tang, S., "Dynamic Response of a Tube Under Moving Pressure," *Journal of the Engineering Mechanics Division Proceedings of the ASCE*, October 1965, pp. 97-122.
4. Reismann, H., "Response of a Prestressed Cylindrical Shell to Moving Pressure Load, Development in Mechanics," *Solid Mechanics - Proceedings of the Eighth Midwestern Mechanics Conference*, Pergamon Press, Part II, Vol. 2, 1965, pp. 349-363.
5. Simkins, T. E., "Response of Flexural Waves in Gun Tubes," Tech. Report ARCCB-TR-87008, US Army ARDEC, Benet Weapons Laboratory, Watervliet, NY, July 1987.
6. Hopkins, D. A., "Predicting Dynamic Strain Amplification by Coupling a Finite Element Structural Analysis Code with a Gun Interior Ballistic Code," BRL-TR-3269, US Army Ballistic Research Laboratory, APG, MD, September 1991.
7. Tzeng, J. T., and Hopkins, D. A., "Dynamic Response of Composite Cylinders Subjected to a Moving Internal Pressure," *Journal of Reinforced Plastics and Composites*, Vol. 15, No. 11, November 1996, pp 1088-1105.
8. Tzeng, J. T., "Dynamic Fracture of Composite Overwrap Cylinders", *Journal of Reinforced Plastics and Composites*, Vol.19, No.1, 2000, pp.2-14.
9. Tzeng, J. T., "EM Launcher Structural Design and Material Selection," IAT TN 0191, Institute of Advanced Technology, the University of Texas at Austin, July 2000.
10. Zielinski A., "Integrated Launch Package Design with Condition for Reduced Joule Demonstration", ARL-TR-2315, Jan. 2001.

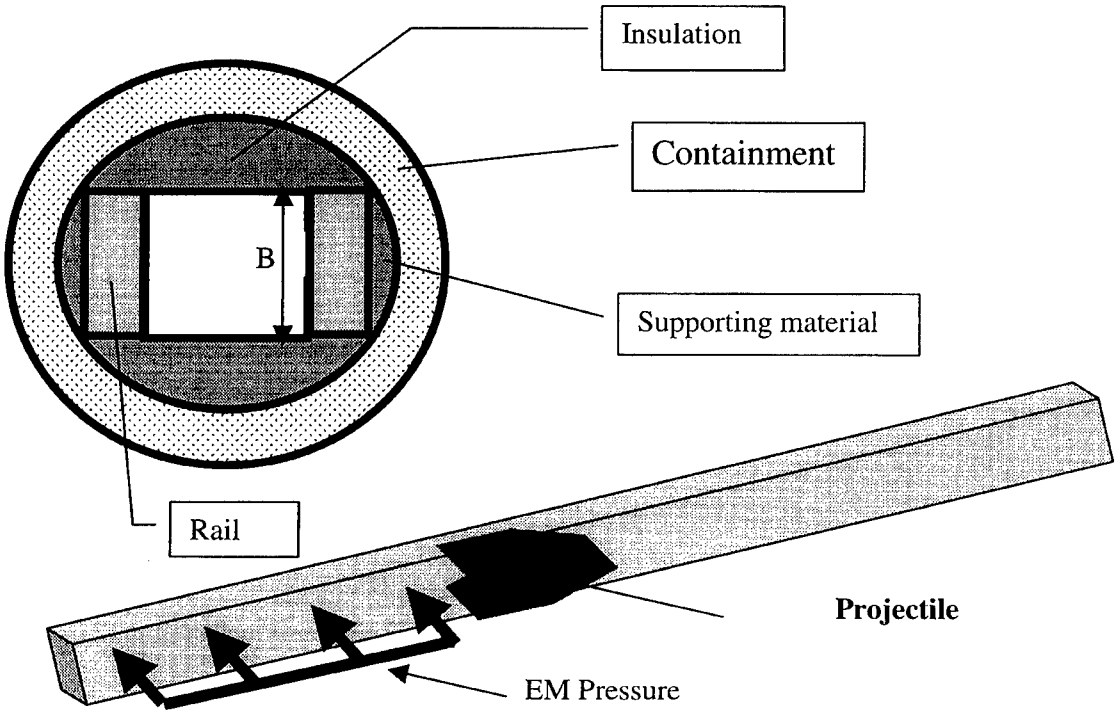


Figure 1: A schematic of EM Gun Cross Section, Rail, and Loading Conditions

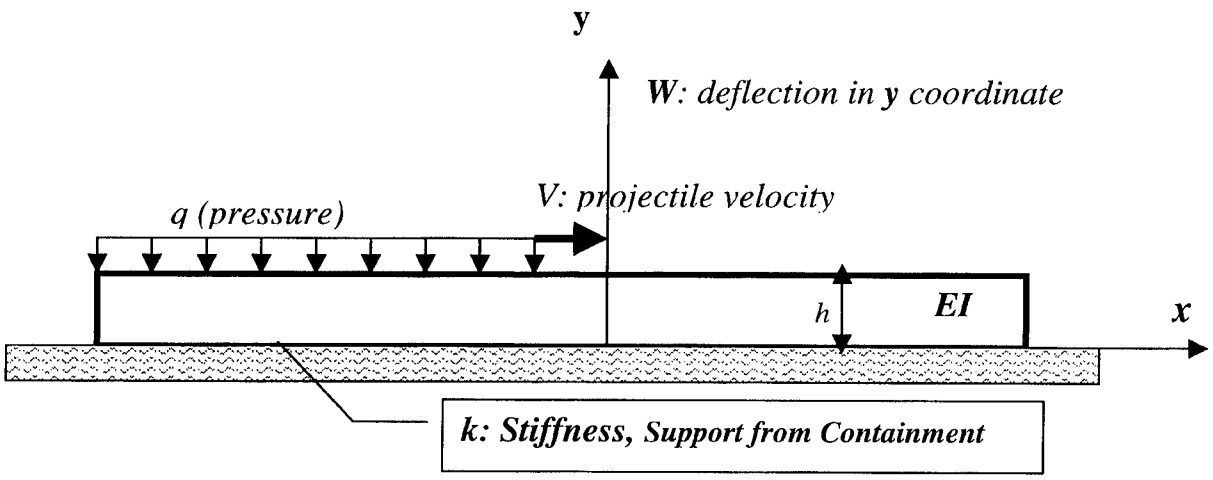


Figure 2: Coordinate System and Model Simulation

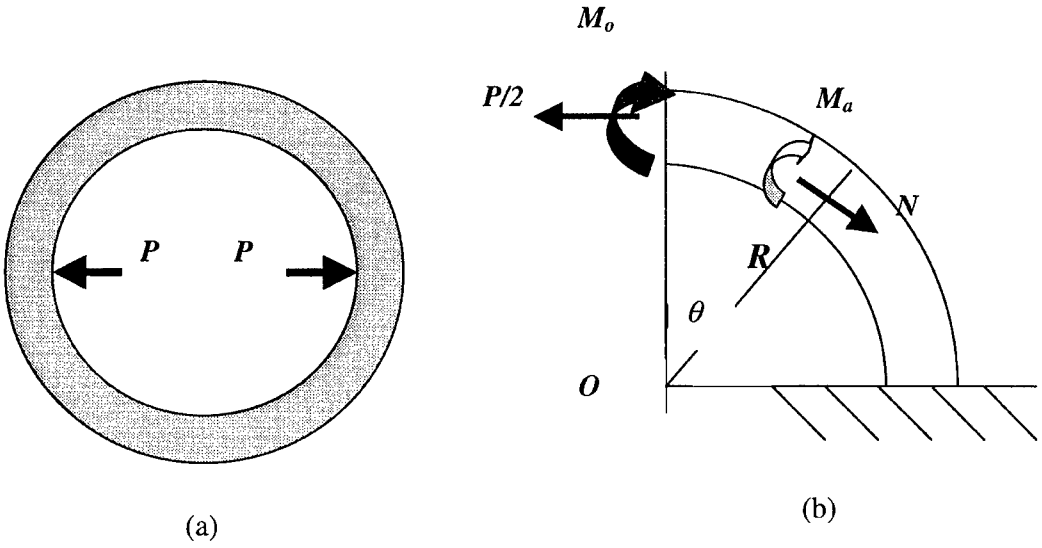


Figure 3: Modeling of Containment Stiffness

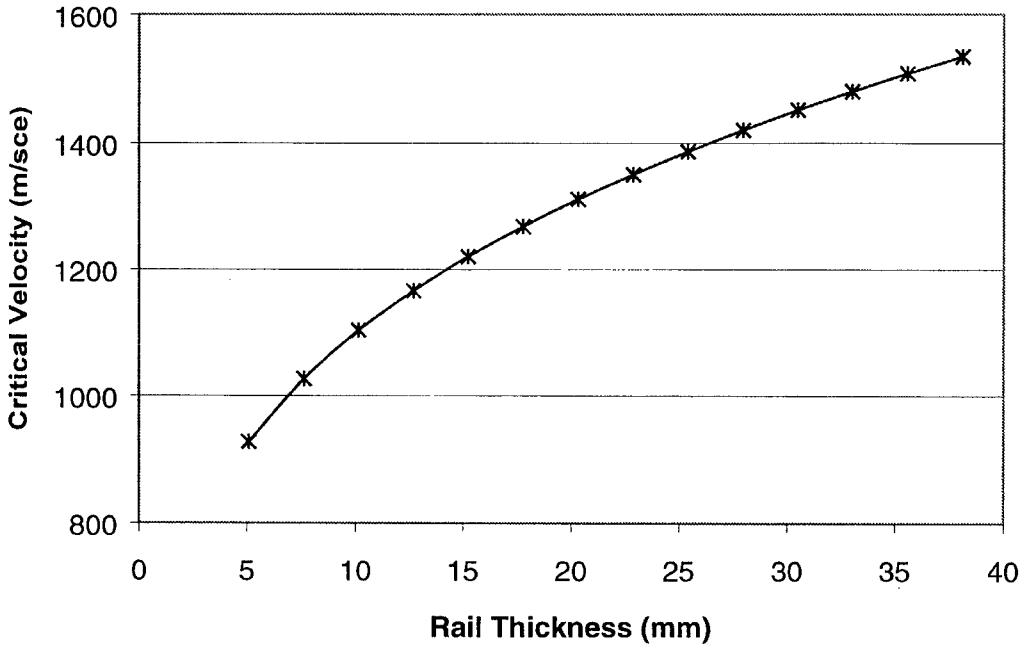


Figure 4: Effects of the rail thickness on the critical velocity

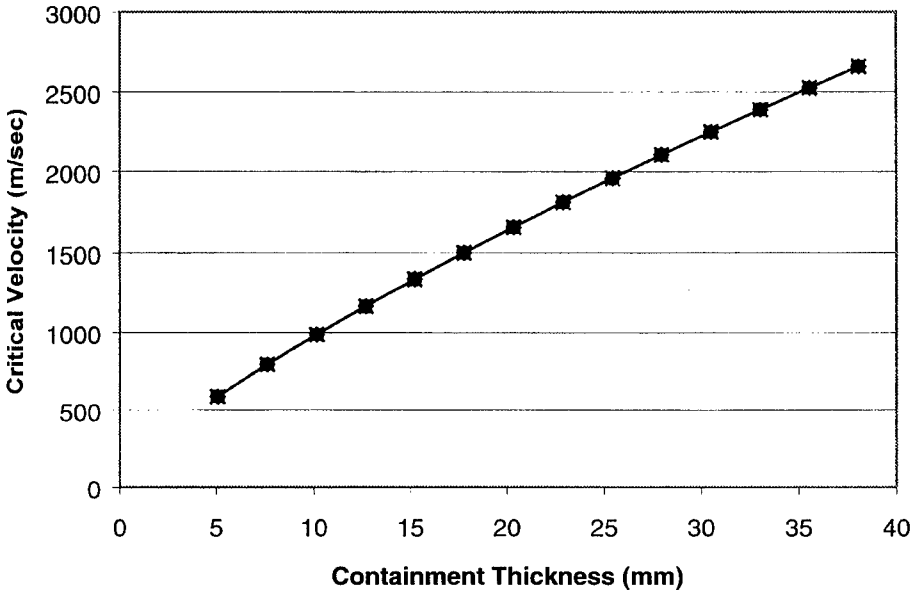


Figure 5: Effects of the containment thickness on the critical velocity.

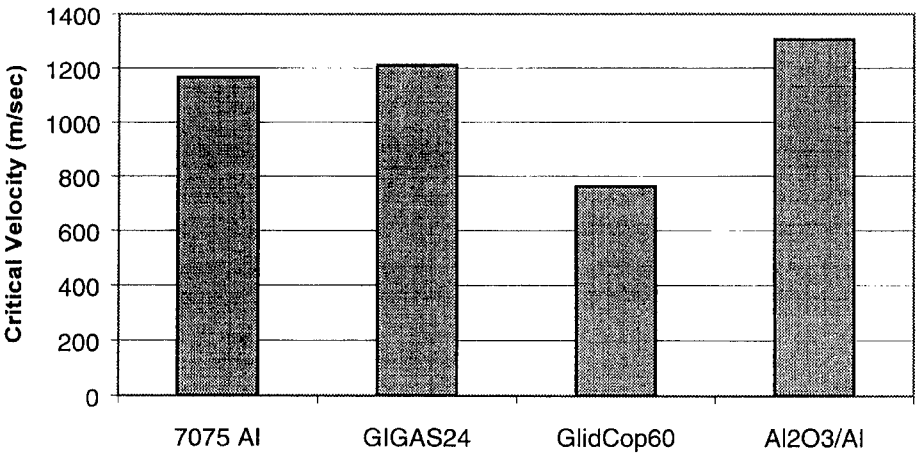


Figure 6: Effects of the rail material properties on the critical velocity.

REINFORCED METAL STRUCTURAL JACKETS FOR ADVANCED GUN BARRELS

Mr. James M. Burnett[1]
Horst Gigerenzer[1]
Eric Pennell[1]
Craig Dampier[2]

[1]*Triton Systems Inc.*
200 Turnpike Rd.
Chelmsford MA 01824

[2]*CDR USN RET*

High performance reinforced metals are being developed that have a series of desirable properties for gun barrel structural jacket applications. The two materials of interest are reinforced aluminum and reinforced titanium. Both of these materials possess very high strength, high fatigue resistance, high temperature resistance, and low density. Ongoing work to apply these promising materials to high performance gun barrels includes diffusion bonding to specified liners, material characterization, development of appropriate gun modeling tools, autofrettage/prestressing parameter development, and dynamic analysis of performance in the composite structure. This paper discusses ongoing work to integrate these materials into large caliber gun barrels.

1. Introduction

The Naval Surface Fire Support (NSFS) and Surface Strike community has identified a need for an extended length barrel for a 5 in./MK 45 weapon system upgrade and a need for an Advanced Gun System (AGS) that is based on the 155mm crusader barrel. These advanced gun barrels are being developed to provide fire support to troops in near-shore and far-inland battle scenarios. The new mission requirements include extended range, increased rates of fire, the use of rocket-assisted projectiles, and high impetus, high temperature propellants. This enhanced Naval Surface Fire Support Mission has placed additional demands on gun barrel materials and designs, requiring them to be stronger and longer, without significant increases in mass moment of inertia. High specific strength, high specific stiffness barrel materials that can be integrated into the manufacture of these large caliber weapon systems are required to achieve the expanding NSFS mission requirements.

Fiber reinforced titanium and fiber reinforced aluminum have been under development for aerospace applications and appear to be eminently suitable for the NSFS mission requirements for gun barrel applications. These metal matrix composites have outstanding tensile, fatigue, and thermal properties [1,2,3,4,5,6] and are currently under development for integration into gun barrels. As shown in FIGURE 1, these materials are being integrated as a structural jacket over a steel liner in large caliber gun barrels. Fabricating these structural jackets with *steel* liners was chosen as the first logical step to gun integration to minimize the development effort required prior to initial qualification and testing. New revolutionary liner technologies not using steel as a base can be integrated into these structural jacket materials after the parallel efforts are completed. Integration technologies are currently under investigation from the perspective of the liner technology. This approach separates the technology efforts so that an efficient transition to existing weapons systems can take place without making the new (liner and structural jacket) materials systems co-dependent.

The titanium and aluminum matrix composites are both high specific strength materials, but due to the great difference in their thermal properties and performance, are being targeted at two different gun systems.

The titanium matrix composite (TMC) is being primarily developed as the muzzle

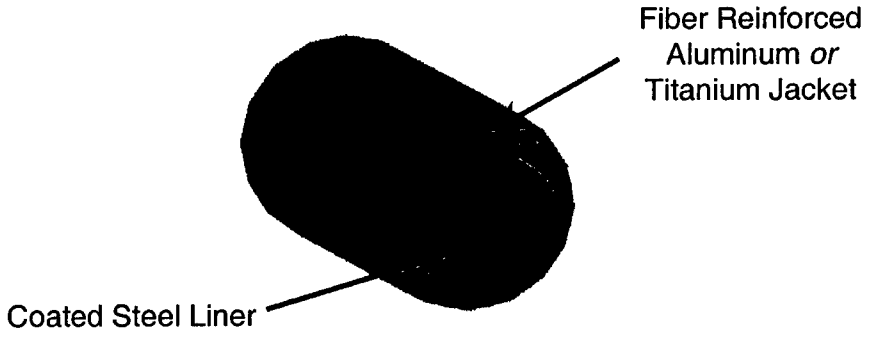


FIGURE 1 Schematic of reinforced metal gun barrel cross section.

extension for the MK 45 due to its very high strength and high temperature fatigue performance. In this application, the TMC will be used to reinforce a significant portion of the gun barrel near the muzzle to extend the length of the 5 in./Mk45 barrel from 62 caliber to at least 70 caliber without increasing the mass-moment-of-inertia of the barrel. Due to the very high specific strength of this material, the mass of the barrel can be allowed to increase while maintaining the current mass moment of inertia. This allows the new extended caliber barrel to be used with the existing MK45 mount.

The aluminum matrix composite (AMC) material is being developed to support the Advanced Gun System effort by developing the nextel fiber reinforced aluminum material for application along the entire length of the AGS barrel. The reinforced aluminum has a high specific strength and high thermal conductivity. The high thermal conductivity of the AMC significantly reduces the thermally induced stress across the barrel below that of a monoblock steel barrel allowing the barrel thickness and autofrettage levels to be increased.

The important aspects related to material properties, material processing, gun fabrication integration (including full scale gun fabrication), and initial gun design are being developed for both the TMC and AMC material systems.

2. Titanium Matrix Composite Structural Jackets

The titanium matrix composite is a continuous fiber reinforced monotape consisting of continuous SCS-6 silicon carbide fibers in a Ti-6Al-2Sn-4Zr-2Mo-.08Si (Ti-6242) matrix.[7] The silicon carbide fibers have tensile strengths ranging from 600 ksi for the SCS-6 fibers to 1,000 ksi for the Ultra-SiC fibers. Both fibers have a modulus of 60 Msi. The SiC filaments have a diameter of 0.0056 inches and the composite volume fraction ranges between 0.35 and 0.40. A typical microstructure of the titanium matrix composite material is shown in Figure 2. The dark core at the center of the filaments is the carbon core used in the chemical vapor deposition process during fiber fabrication. The dark outer layer of the filament is a carbon rich coating that aids adhesion between the Ti-6242 matrix and the fiber. [8,9,10]

The TMC material was chosen for its high strength, high temperature resistance, low density and excellent fatigue properties. The material properties of the TMC are shown in TABLE 1. The gun steel data is 4340 steel tempered to a tensile strength between 160 and 180

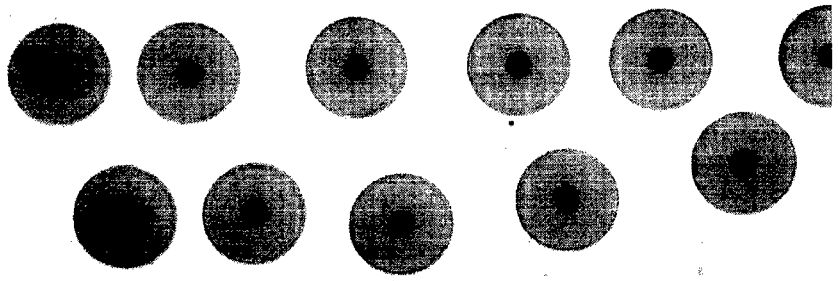


Figure 2 Cross Section of Consolidated TMC

TABLE 1 Material properties of TMC material

Material	Density $(lb/ft)^3$	Tensile Yield Strength (ksi)		Elastic Modulus (MSI)		Coefficient of Thermal Expansion (PPM/°C	
		72°F	800°F	72°F	800°F	72°F	800°F
Gun Steel	489	Tempered to 160-180	<140 <60 @ 1000°F	29	24	11.2	13.5
Ti 6242 SCS-6 (35% by volume)	252	190	145	29	26.5	≅ 4.5-5	≅ 3.5-4
Ti 6-4 Ultra SCS (29% by vol)	252	321	245	29	26.5	≅ 4.5-5	≅ 3.5-4

ksi. As indicated by the table, the specific strength of the SCS-6 based TMC is more than two times that of the 4340 steel and the Ultra SiC based TMC is over three times the specific strength of 4340 steel. This high specific strength makes the TMC materials ideal candidates for the structural jacket muzzle extension for the MK 45. The low density, combined with high strength allows the design of a muzzle extension that does not increase the mass moment of inertia of the extended barrel, allowing the use of existing mounts. In addition to high strength, the TMC material will withstand over 100,000 cycles at stress levels over 100 ksi at a temperature of 1,000°F. The 4340 steel has a tensile strength of less than 60 ksi at 1000°F. [11]

The TMC is fabricated using a two-step process. First, the silicon carbide fiber is wound on a stainless steel drum and plasma sprayed with titanium alloy. This forms a tape with uniaxially oriented fibers placed accurately on center to form a consolidated tape with a 0.375 volume fraction and a thickness of 0.014 inches. Initially, the plasma sprayed tape is 70% dense. To form a fully consolidated component, the multiple layers of plasma sprayed tape are placed in a hot isostatic pressing (HIP) tool. The HIP tool is evacuated down to $1*10^{-5}$ torr and welded closed using E-Beam welding. The HIP tool is placed in the HIP vessel and subjected to a temperature between 1650°F and 1750°F and a pressure between 15,000 and 30,000 psi. Consolidation takes place when the HIP tool deforms to compress the TMC layup. As the HIP tool deforms, the titanium tape layers are diffusion bonded together to form a fully dense composite. Dimensional control over the HIPped component is achieved through the design of the HIP tool itself. The HIP tool design for the structural jacket is shown in FIGURE 3.

In the structural jacket application on the Mk 45 gun muzzle, the primary orientation of the fibers is in the hoop direction to maximize the hoop strength of the composite jacket. The HIP tool was designed with a substantial outer mandrel and a much thinner inner mandrel, forcing the inner mandrel to expand into the composite layup against the relatively stable outer mandrel. This was desired so that the fibers would be loaded in tension rather than compression during consolidation and ensured that the fiber orientation remained normal to the cylinder axis.

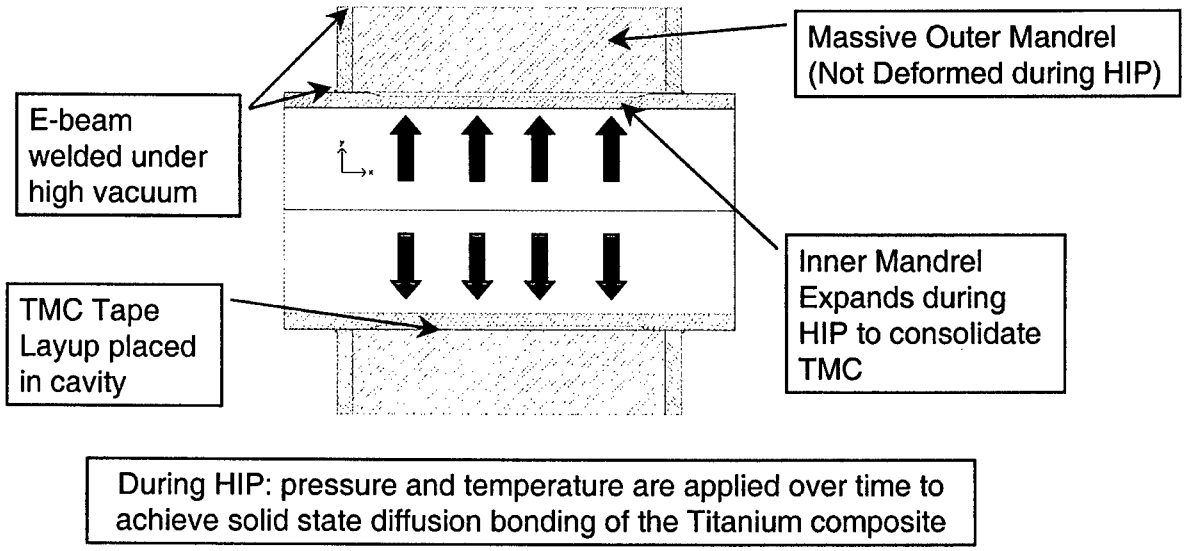
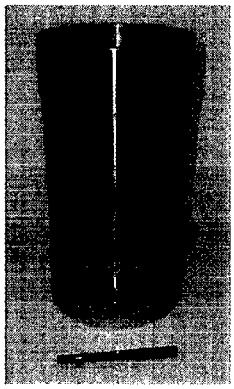


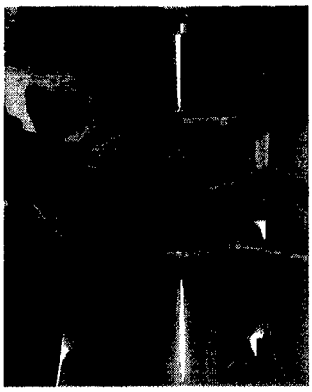
FIGURE 3 HIP tool design

A series of photographs showing the assembly of a 6-in-diameter cylinder is shown in FIGURE 4. After HIPping, the fully dense TMC jacket is excised from the HIP tool by machining.

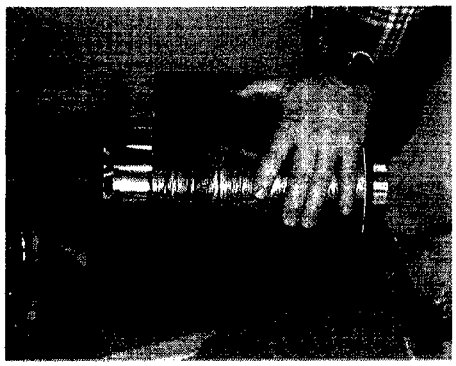
The TMC structural jacket must be integrated onto the muzzle of the gun barrel while maintaining the steel liner and TMC heat treatments. The options for joining the jacket to the liner include shrink fitting and autofrettaging the jacket into place. This allows the TMC and the steel liner to be fabricated and heat treated separately, prior to joining. This prevents the problems associated with press fitting the jacket over the steel. The longest HIP vessel available governs the length limit for the muzzle extension jacket, currently measuring 119-inches-long. This is long enough to extend the Mk 45 mod 2 from 54 to 77 calibers and the mod 4 from 62 to 85 calibers.



Inner Mandrel



TMC Tape wrapping



Final HIP tool assembly

FIGURE 4 Processing steps for TMC fabrication

3. Aluminum Matrix Composite Structural Jackets

The aluminum matrix composite structural jacket is pressure infiltration cast alumina fiber reinforced aluminum. The fiber reinforcement is Nextel™ 610 high purity alumina at a volume fraction of approximately 0.65. The alloy is high purity aluminum. This material was chosen for its high strength, high fatigue resistance, and high thermal conductivity. FIGURE 5 shows a micrograph cross section of the composite material. The material properties are shown in TABLE 2.

The primary reason for integrating this material as a structural jacket in the AGS barrel is its high thermal conductivity, maximizing the heat transfer from the bore surface, keeping the bore cool, and minimizing the thermal stress across the barrel wall. Reduction in bore temperatures increases bore life while reduction in thermal stress increases fatigue life, thus effectively increasing both major factors governing barrel life.

Active cooling of the AGS barrel is required to minimize bore temperatures and the bore erosion caused by the high firing rate NSFS mission. Active cooling allows the bore surface temperature to be kept low, increasing bore life. Although active cooling significantly increases bore life, it dramatically increases the heat flux through the barrel, causing a significant increase

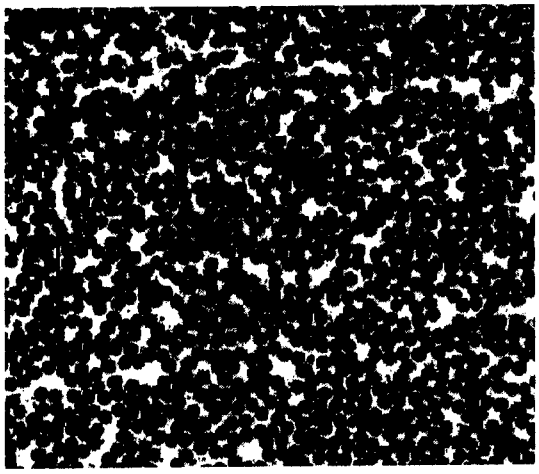


FIGURE 5. Typical cross-section of Triton Systems' Al/Nextel 610/60f composite.

TABLE 2 Material properties of AMC material

Tensile Strength	240 ksi
Compressive Strength	500 ksi
Density	3.4 g/cc
Modulus	35 msi
Biaxial Composite Fatigue (0-90)	30+ ksi runout 10^7 cycles –same at 700 F
Thermal conductivity	120 W/mK
Specific stiffness	3 times greater than 4340 steel
Specific strength	3.85 times greater than 4340 steel

in thermally induced stress.

Heat flux in conventional barrels is limited by free convection in air, while actively liquid cooled barrels have a much higher heat flux due to the higher heat transfer coefficient of forced liquid systems. This high heat flux generates a high ΔT across the barrel wall due to the limited thermal conductivity of steel. The temperature drop through a thick wall tube is related to the thermal conductivity of the material and the ratio of the inner to outer radii. For comparison purposes, FIGURE 6 shows the temperature profile of the barrel cross section using a steady state heat transfer analysis. For comparative purposes, the curve indicating the lowest bore surface temperature is for an all reinforced aluminum barrel and the upper curve is for an all steel barrel. The intermediate curves represent a jacketed barrel with a .5-in-thick steel liner and a 2.25-in-thick steel liner. For these calculations the heat flux and the cold wall temperature were held constant for comparison purposes. The shallower slope of the aluminum curve is directly related to the difference in thermal conductivity between the steel liner and the reinforced aluminum jacket.

In addition to lowering the bore temperature, the high ΔT across the all-steel barrel wall induces a high compressive stress at the bore and a high tensile stress at the outer surface. The expansion of the relatively hot inner elements is constrained by the cool outer elements. At the steady state heat flux levels of the AGS, the compressive stress developed at the bore surface can approach 100 ksi. This high thermally induced stress places limits on the autofrettage levels attainable if bore collapse is to be prevented. This limit on autofrettage levels causes the prestress to be less than desired during cold fire situations.

The thermally induced stress in all-steel actively cooled barrels is high due to the low thermal conductivity of steel. This thermal stress can be minimized, and the bore surface temperatures further reduced through the use of a high thermal conductivity reinforced aluminum structural jacket. As indicated in FIGURE 6, the high thermal conductivity AMC material significantly reduces the ΔT across the barrel wall resulting in a nearly 50% reduction in thermally induced stress. The reduction in thermally induced stress allows the autofrettage levels

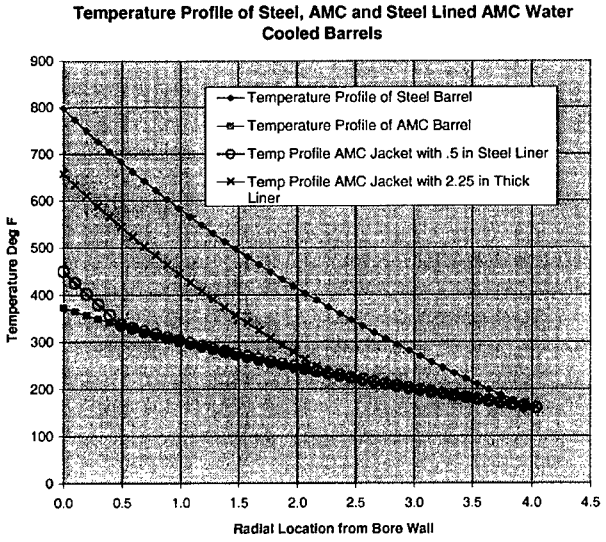


FIGURE 6 Actively Cooled Barrel Temperatures

with the AMC jacketed barrel to be increased, thereby allowing an increase in autofrettage levels and a concomitant improvement in fatigue life for the barrel.

Autofrettage of Steel Lined AMC Jacketed Barrels

The separate fabrication of the AMC structural jacket and the steel liner will be used to fabricate the gun barrel. In this process, the heat treatments of both the steel and the structural jacket are performed separately, and joined using either heat shrinking or autofrettage. This concept solves a number of issues associated with the fabrication of a large-scale gun barrel, including:.

- Inspection of the liner and jacket separately
- Provides greater control over autofrettage stresses on the liner
  - OD of steel machined
  - ID of AMC jacket machined
  - ID of steel liner independently machined
- Allows greater strains on outer elements of steel

Analysis

Thick wall cylinders are able to sustain an internal pressure that is no greater than the yield strength of the material used. As the wall thickness approaches infinity, the hoop stress on the bore becomes equal to the internal applied pressure. This is due to the uneven stress distribution across the thick wall, causing inner elements to carry more tensile stress than outer elements. It is desired to redistribute these stresses across the barrel wall section so that the tensile load is carried more evenly, causing an increase in the fatigue limit and strength of gun barrels. Stress redistribution is accomplished by placing the bore surface into a state of residual compression and the outer elements into a state of residual tension. This reduces the maximum hoop stress on the inner elements of the gun barrel and increases the allowable internal pressure along with the fatigue limit for the structure. In the gun barrel application, bore surface compression also aids in the prevention of cracks that develop under harsh service conditions. Bore surface compression is attained in monoblock steel barrels through autofrettage. In the autofrettage process, the inner elements at the bore surface are overstrained into the plastic regime by swaging, leaving the bore in a state of high residual compression.

It is desired to use the swage autofrettage process to generate these internal compressive stresses in the AMC jacketed gun barrel to attain the advantage of prestressing the bore. The important factors to be considered when establishing a method to achieve autofrettage in this structure are:

- Strains required for the attainment of suitable autofrettage
- Strain at plastic deformation of the steel liner
- Strain to failure of the composite structural jacket
- Stress state at the steel/jacket interface

When the swage passes through the layered barrel composite the bore is strained into the plastic range and the interface is strained to a somewhat lesser extent. The extent of the strain at the interface is dependent upon the bore strain and the liner thickness. Interface strain decreases with increasing liner thickness.

The gun barrel consists of a steel cylinder directly wrapped in an all-hoop direction with MMC. During autofrettage, stress applied to the bore of the steel liner causes the material to plastically deform. Once the applied stress equals the yield stress of the steel, plastic deformation begins. With increase in stress, the depth of plastically deformed material moves further into the material. This "front" of plastically deformed material is called the elastic-plastic interface. Subsequent removal of the applied stress results in residual stresses produced by the elastic spring-back of the material.

The system is modeled as an internally pressurized cylinder. Calculating the bore deflection at a particular pressure makes the translation to the autofrettage process. This deflection represents the radial interference created during the swaging process.

The analysis breaks down into three parts; elastic-plastic, fully plastic, and unloading analysis. Elastic-plastic refers to analysis where the elastic-plastic interface has not moved completely through the steel liner. Fully plastic refers to analysis of a fully yielded steel liner. Unloading analysis predicts the residual stresses produced by the elastic spring-back. The maximum shear stress yield criterion is utilized and linear strain hardening is assumed.

The analysis will look specifically at the 6.1 inch gun and the bulk of the equations used in this exercise were obtained from Chen [12]. The variable definitions are shown in FIGURE 7.

Elastic-Plastic Analysis

The independent variable is the radial location of the elastic-plastic interface. All other parameters are functions of this depth of plastic deformation. The required internal pressure for a given depth of plastic deformation is determined. The effect of the metal matrix composite (MMC) jacket on the behavior of the steel liner is characterized by calculating an interface pressure. This is the pressure on the outer diameter of the steel liner and inner diameter of the MMC jacket, created by stressing the MMC jacket. Once the internal pressure and interface pressure are known, all the stresses, deflections and strains can be determined as functions of the depth of plastic deformation.

Fully Plastic Analysis

The next level of the analysis is fully plastic. In this range, the elastic-plastic interface has moved through the entire section of the steel. The controlling variable in this case is internal

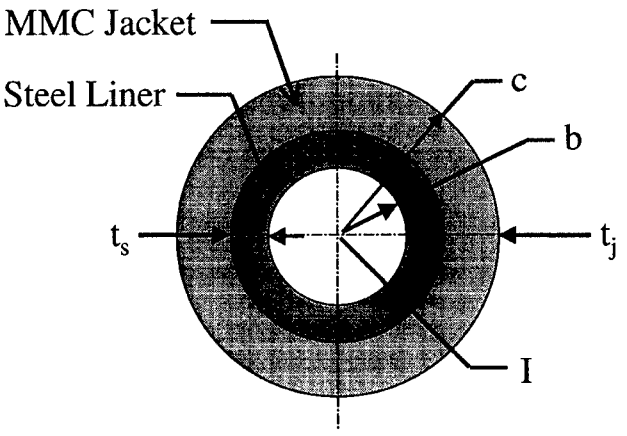


FIGURE 7 Variable definitions used for analysis

pressure. The interface pressure is determined and all stresses, deflections and strains are found subsequently.

Unloading Analysis

The residual stresses, strains and final geometry of the barrel are determined by this analysis. The unloading pressure is simply the negative value of the internal pressure, and this is used to determine the unloading interface pressure. Unloading stresses, deflections and strains are calculated, and added to the initial deformation values to determine the residual magnitudes.

155mm Gun Analysis

A critical relationship to be determined is what level of autofrettage will the barrel accept without fracturing the AMC jacket. The strain at failure of the AMC jacket loaded uniaxially in the fiber direction is 0.6%. For the hoop orientation of the gun jacket application, this translates into a maximum hoop train at the steel jacket interface of no more that 0.6%. The following illustrates the relationship between radial interference and the strain at the steel liner-MMC jacket interface.

FIGURE 8 demonstrates the ability of the steel liner to be fully plastically deformed without fracturing the AMC jacket. Thinner sections of steel yield higher interface strains for a given radial interference during swaging. For example, the 0.5-inch-thick liner can sustain just over a radial interference of 0.025 inches. The 2-inch-thick liner can sustain a radial interference of over 0.05 before overstraining the composite jacket. The associated residual stresses obtained at the bore are illustrated in FIGURE 9.

FIGURE 9 plots interface strain against hoop stress at the bore for three liner thicknesses. All curves are cut off at the maximum interface strain of 0.6%. The curves show that compressive hoop stress from zero to over 150,000 psi can be attained without failing the jacket for all liner thicknesses. The design space for autofrettage of the AGS barrel is wide open, and sufficient levels of autofrettage stress are obtainable with the thinnest sample analyzed.

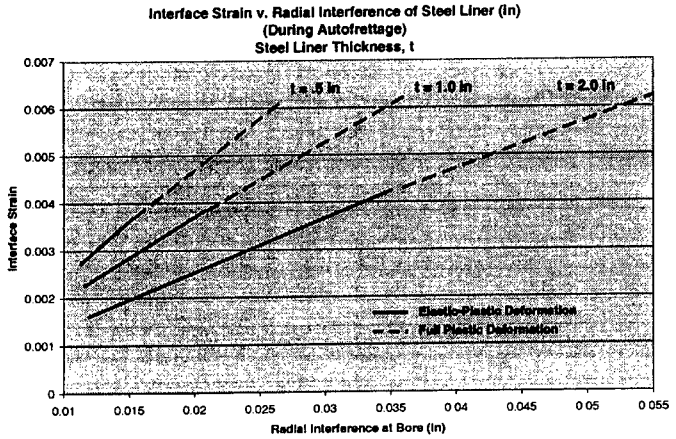


FIGURE 8 Interface Strain during Autofrettage

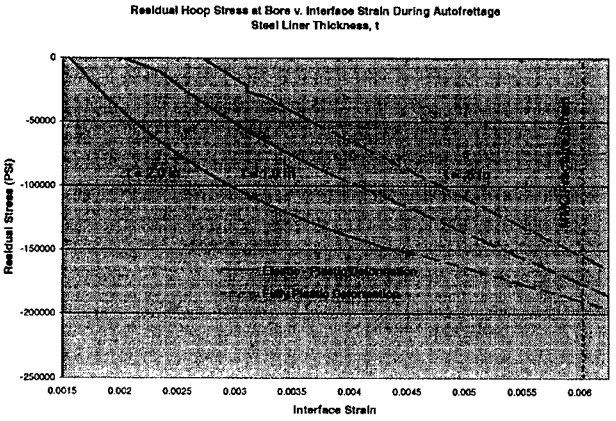


FIGURE 9 Residual Stress at Bore

The associated residual stresses at the steel liner-MMC jacket interface are shown in FIGURE 10. This figure shows that full plastic deformation is necessary to obtain any residual compressive stresses at the interface. Thinner sections of steel yield larger residual compressive stresses for a given interface strain during autofrettage. It is not clear at this writing if it is necessary to generate compressive hoop stress in the steel to achieve long barrel fatigue life.

Residual radial stresses do not occur at the bore, but the associated residual stresses at the interface are shown FIGURE 11. The major feature of this graph is the large shift in radial interfacial stress that occurs when the deformation transforms from elastic to plastic. It is necessary to generate radial stress at the interface to ensure sufficient load transfer between the liner and jacket material. As this graph shows, the design space is there at well below the strain limit of the jacket material to preload this interface in radial compression.

This analysis shows that significant residual compressive radial stresses are obtained for small interface strains during autofrettage. These stresses diminish by an approximate factor of 10 when full plastic deformation is reached. The magnitudes of the stresses for the three samples are very close, differing by only about 15,000 psi throughout the entire range of strain. The

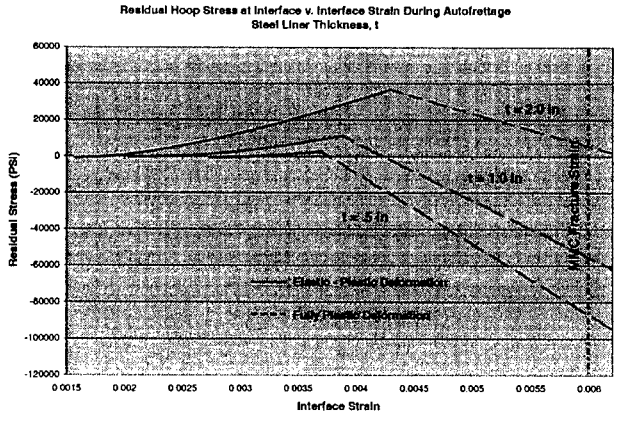


FIGURE 10 Residual Hoop Stress in Steel at Interface.

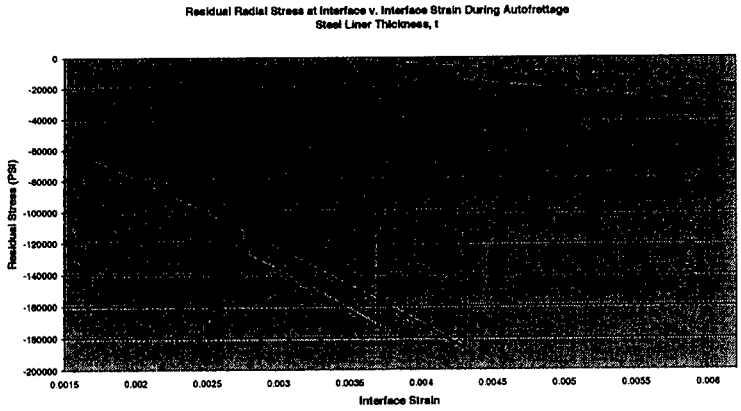


FIGURE 11 Residual Radial Stress at Interface

thinner sections provide slightly higher residual radial stresses prior to full plastic deformation, but yield lower levels after the liner becomes fully plastic.

The preceding analysis indicates that there is considerable design space for optimizing the autofrettage of the AGS barrel to desired levels.

Subscale Sample Fabrication

In a recently completed program, small-scale samples of AMC jacketed cylinders were pressure infiltration cast and then successfully autofrettaged. This was demonstrated by the fabrication of two-layer composite cylinders, as shown in **FIGURE 12**, followed by machining and swage autofrettage in a press. Results showed that the steel liners took on a permanent set (plastically deformed) as desired, and that the reinforced aluminum jackets remained in the elastic regime, as desired. All samples were fabricated on steel liners with a 1.5-in-outside diameter and a reinforced aluminum jacket with a 1.9-in-outdside diameter. Sample sizes were kept small to keep tooling costs down.

3.2Autofrettage Of Reinforced Aluminum Jacketed Samples

To keep tooling costs down, one swage was machined and hardened. It was designed with a lead diameter slightly less than the composite samples, a 2-degree taper and a smaller top section that allowed the swage to fall through the sample at the completion of the swaging stroke.

The swage assembly is shown in FIGURE 13. The swage jig has a center hole slightly larger than the maximum swage diameter to allow the swage to fall through at the completion of the pressing stroke. It also has a 0.050-in-counterbore that just fits the outside diameter of the samples, so that the assembly is kept on center during the swage process.

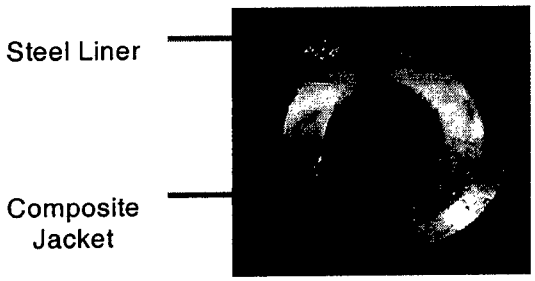


FIGURE 12 Pressure Infiltration Cast AMC Over Steel

All samples were fabricated from the same casting. The bore diameters were final machined

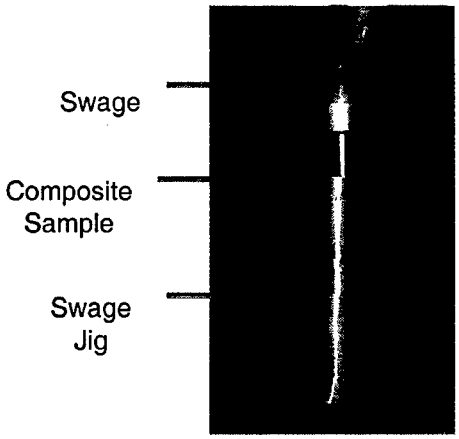


FIGURE 13 Swage Autofrettage Process

to tolerances of ± 0.0005 to ensure that the predicted strains would be achieved during autofrettage.

FIGURE 14 is a photograph of the jacketed samples after autofrettage. The sample on the left was strained to levels just below the strain limit of the jacket. The sample on the right was subjected to interface strains above 0.6%, the strain limit for the composite jacket and was expected to crack, as indicated.

4. Conclusions

The reinforced titanium is under development for a muzzle extension of the 5"62-caliber Navy gun to 70 calibers by fabricating a muzzle extension that provides a barrel with the same mass and moment of inertia as the 5" 54-caliber barrel. The processes to diffusion bond the reinforced titanium to the 4340 gun steel liner are being developed. Developments for the near future include the fabrication of full bore hoop specimens for impulse and high temperature fatigue testing.

The reinforced aluminum is under development as a structural jacket in the Advanced

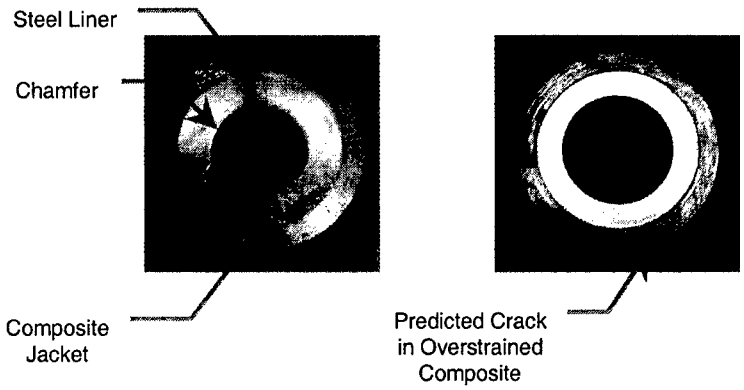


FIGURE 14 Autofrettage samples

Gun System (AGS) barrel. In this case, the high conductivity of the reinforced aluminum is being used to reduce thermally induced stress in this actively cooled barrel. By applying the high conductivity structural jacket to the AGS barrel, bore temperatures are reduced significantly and the delta T between the outer cold wall and the inner bore surface are reduced. The reduction in delta T between the outer and inner walls reduces thermally induced stress by as much as a factor of four. These factors open the design space in the autofrettage levels and in the cooling system for the AGS barrel. The ultimate effect is that the bore and fatigue life are both increased for this barrel. The work to date has successfully shown that the reinforced aluminum can be autofrettaged without overstraining, and can be used to successfully reduce bore temperature and thermal stress in the AGS barrel. Additional future effort includes the development of a large scale manufacturing approach, the verification of those approaches by fabrication of full section barrels, and development of computer design tools for behavior prediction in the AGS gun barrel environment.

ACKNOWLEDGMENTS:

The authors would like to thank the sponsors of these efforts for their ongoing input and continued support. Mr. Rodney Hubbard of the Naval Surface Warfare Center Dahlgren Division, and Mr. Dan Holmes of the Naval Surface Warfare Center Port Hueneme Detachment-Louisville are currently the technical points of contact for these efforts. We would also like to thank Mr. Mike Hermanson of UDLP, Mr Paul Conroy of ARL and Roger Ellis of the NSWC-DD for their ongoing suggestions and input that have been so helpful in keeping the effort focused on the point of greatest need for the gun systems involved.

REFERENCES:

[1] K. Upadhya, "High Performance Metal and Ceramic Matrix Composites", ed.K. Upadhya (Warrendale, PA: TMS, 1994). P. 237

[2] I.A. Ibrahim, F.S. Mohamed, and E.J.Lavernia, (Journal of Materials Science), (1991), p. 1137

[3] T. Saito, T. Furuta, and T. Yamaguchi, Recent Advances in Titanium Matrix Composites, ed. F.H. Froes and J. Storer (Warendale PA : TMS, 1995), p. 33

[4] R.A. Mckay, P.K. Brindly, and F.H. Froes, JOM. 42 (5) (1991), pp. 23-29

[5] Carl Zweben, JOM, 50 (6) (1998), pp. 47-51

[6] H.E. Deve and C. McCullough, JOM, 47 (7) (1995), pp. 33-37

[7] H. Gigerenzer and A. Kumnick, "Low Pressure Induction Plasma Spraying of Titanium Metal Matrix Composites SCS-6/Ti6Al-4V and SCS-6/Ti6Al-2Sn-2Zr-2Mo" Materials Research Society Symposium Proceedings, Vol 190, San Francisco Spring Meeting, April 17-19, 1990

[8] X.J.Ning and P.Pirouz, "The Microstructure of SCS-6 SiC Fiber" Journal of Materials Research Volume 6, No. 10, October 1991

[9] Suplinskas, R.J., "Manufacturing Technology for silicon Carbide fiber," AFWAL-TR-84-4005, 1983

[10] Textron Specialty Materials, "Continuous Silicon Carbide Metal Matrix Composites" Data Sheet

[11] ASM Handbook Volume 1, "Properties and Selections: Irons and Steels" Ninth Edition, American Society for Metals 1978, Metals Park Ohio

[12] Peter C.T. Chen "Non-Linear Analysis of a Pressurized Steel Cylinder Jacketed with Metal Matrix Composite" ARCCB-TR-92026

INVESTIGATION OF TUNGSTEN, COPPER, AND SILVER ALLOYS WITH INDIUM AT THE RAIL-ARMATURE INTERFACE ON A RAILGUN TEST BENCH

D. Gillich[1] and W. Maier[2]

[1] *United States Military Academy, Department of Physics, West Point, NY 10996*
[2] *Naval Postgraduate School, Physics Department, Monterey, CA 93940*

With the advent of electrically propelled ships, the Navy is now considering the use of electric power to launch projectiles in support of maritime land attack. Bore wear is one of the most significant challenges for a naval railgun program. The interface between the armature and rails is the most stressed point of a railgun because it transitions to liquid under high current densities. This liquid interface causes rail and projectile material to redistribute unevenly thereby produces rail degradation. Various combinations of tungsten, copper, and silver alloys were tested for rail and armature materials to determine which combination resulted in minimum damage during firing. The least degradation was observed with a silver-tungsten projectile and copper-tungsten rail: 10% loss in projectile mass for a current density of approximately 86 kA/cm^2. Indium at the interface protected the rails and projectile from damage at current densities under 21.5 kA/cm^2.

1 INTRODUCTION

One of the major challenges facing electromagnetic launch (EML) railguns is the degradation of the rail and armature during firing. This degradation is caused by uneven redistribution of material due to the liquid interface that forms at the rail-armature interface. In this paper we investigate the use of tungsten, copper, and silver alloys for rail and armature materials to determine which combinations result in minimum rail degradation.

We begin in Section 2 by providing the motivation for our work. We outline the apparent paradigm shift in the Navy's interest in the use of EML technologies as the basis for future weapon systems. In Section 3, we study the idea of using an interface material that will melt without damaging the rails or armature while acting as a "conductive lubricant" for the projectile.

A theoretical model is presented in Section 4 that allows us to determine the material parameters that are important for reducing rail degradation. Section 5 contains information about our experimental setup. We conclude Section 5 with a brief outline of the experiment. Experimentation was done in two phases: high current firing tests and low current density tests. In Section 6, we will present our procedure and experimental results for each of the two phases. Finally, concluding comments will appear in Section 7.

2 MOTIVATION: ARMY VERSUS NAVY APPLICATIONS

For two decades, the United States Army has conducted research in the field of EML railguns. The main focus has been on developing a "tank-killer" gun capable of defeating armor through direct-fire engagement with high-velocity projectiles (2-3 km/s). Within the past few years, the Army has further defined requirements to develop a launch platform that weighs less than 19,000 kg and is capable of being deployed in a C-130 aircraft. Given this new requirement, Army researchers are now focusing their efforts on developing more compact pulsed-power supplies and lighter yet stronger barrels [1].

In the past, the Navy's official position on the adoption of railgun technology has been to monitor the Army's railgun program. Recent developments, however, have increased interest in EML technology as the basis for future weapon systems. Currently, the Navy is considering EML technology for the mission of indirect fire in support of the littorals [2].

The origin of this paradigm shift in the Navy's focus is the Railgun Technology Assessment Report published by the Center for Naval Analysis (CNA) in 1998. In this report, reviewers determined that EML technology is sufficiently advanced to warrant further investigation for naval use. The CNA "recommends that the Navy pursue basic rail(gun) technology and provide modest funding to support a more detailed analytical study by the Navy's technical community, regarding the cost and effectiveness of railguns for maritime land attack"[2].

The Navy is also building electric propulsion ships with the advent of the destroyer, DD-21. In an electric ship, the EML railgun system can share its power supply with the electric propulsion system. This arrangement will save space and fuel as well as provide the opportunity to easily redirect tremendous amounts of energy [3].

The Navy's requirements for an EML railgun are different from the Army's. As mentioned earlier, the Army is developing a direct-fire system primarily designed for short, line-of-sight distances. The Navy, on the other hand, is interested in indirect firing engagements with extended range capabilities. Fig 1 gives an outline of the parameters that the Navy is considering for an EML railgun.

Range: 550 to 750 km (300 to 400 nmi)	Firing Rate: 6 rounds/min
Projectile Mass: 60 to70 kg	Power Use: ~ 60MW (at max range and rate)
Barrel Length: ≤ 15 m	Time of Flight: ~ 8 min (at max range)
Muzzle Velocity: 2.5 to 3.5 km/s	Cost: ≤ ~ $5K per round
Impact Velocity: 1.5 to 2.5 km/s	

FIGURE 1 Performance Parameters for a Notional Land Attack EM Gun [3].

3 RAIL-ARMATURE INTERFACE

The interface between the armature and the rails is a highly stressed location in an EM launcher: joule and frictional heating cause melting at the interface. This heating is associated with ablation on the rails or even gouging at hyper-velocities (velocities greater than 1.5 km/s) [4]. The change of the rail/armature interface to liquid is simply referred to as

transition. "Reliable prevention of transition has proven difficult because no validated physical model of transition has been demonstrated" [5].

The Electromagnetic Armament System Focused Technology Program (EMAS FTP) has established exact parameters concerning the amount of ablation or bore growth (change). "The program requirement is a 0.4% of the bore diameter growth (change) over a 1000-shot life, which is equivalent to 0.2 μm of deposition per shot" [4]. The traditional combination of an aluminum projectile on copper rails yields about 25μm of deposition per shot, distributed unevenly on the rails.

When considering gouging at hyper-velocities, the effect of this liquid interface is not as easily understood. Researchers believe that a liquid interface may prevent or delay gouging at velocities over 1.5 km/s. However, the EML community lacks full understanding of the exact nature of the effects of a liquid armature-rail interface [4].

In the absence of a physical model to predict and prevent transition, researchers have adopted a trial-and-error approach to determine compatible rail and armature combinations. The central point to this type of approach is to determine what material parameters are relevant to the problem and to make an educated guess as to what combinations or materials are likely to yield successful results. Very likely, harder and more refractive materials will be less susceptible to melting and gouging.

As stated, the interface between the rail and armature changes to liquid under high current densities. The focus of the investigations being done at the Naval Postgraduate School in Monterey, California is to test different interface materials to reduce degradation of the rail or armature. By selecting materials that have low melting points, low vapor pressure, and high boiling points, we hope to find an interface material that will melt without damaging the rails or armature. This interface material must also act as a "conductive lubricant" for the projectile.

This idea is not entirely new. In 1972 a doctoral student at the Australian National University, J.P. Barber, dipped a copper projectile in lead-tin alloy (common solder) and fired the projectile with very little damage to the rails or base projectile. However, subsequent firing failed to reproduce the original results. As a suggestion for further research, Barber includes the use of "laminated projectiles dipped in a lower melting point material than solder (e.g. indium)" [6].

Another Australian, A.J. Bedford, conducted research in 1984 with different materials at the rail-armature interface. He tested copper rails (standard Cu-0.6%Cd alloy) that were plated with various materials and used a plasma armature (aluminum foil) to initiate firing. Bedford found that rails plated with zinc and tin gave promising results in terms of rail damage. He also concluded that "the behavior of Sn and Zn coatings in resisting deep arc damage, probably by melting and flowing, also suggests avenues for more investigation" [7].

4 THEORETICAL MODEL

When considering which materials are best to prevent degradation of the rail or armature, we must first determine what material properties pertaining to heat conduction are important. To get a rough estimate of these parameters, in what follows, we will ignore any conduction of heat due to friction.

The quantity of heat, dQ, required to change the temperature of a material of mass m an amount dT is given by

$$dQ = mcdT \tag{1}$$

where c is the specific heat of the material. When a quantity of heat dQ is transferred to a material in a time dt, the rate of heat flow, or power, is

$$P = \frac{dQ}{dt}. \tag{2}$$

Combining equations (1) and (2) we find that

$$P = mc\frac{dT}{dt}. \tag{3}$$

Now let us consider a small element of material with cross-sectional area A and length dx. We can express the mass of the material as

$$m = \rho A dx \tag{4}$$

where ρ is the mass density. If a current flows through the material, the electrical power dissipated is

$$P = I^2 R \tag{5}$$

where R is the resistance of the material. This resistance can be also be expressed in terms of a small element of length dx as

$$R = \frac{dx}{\sigma A}. \tag{6}$$

Here σ is the conductivity and A is the cross-sectional area through which the current flows. This allows us to combine equations (3)-(6) to obtain an expression for the current in terms of the material parameters, i.e.,

$$I^2 = \rho c \sigma A^2 \frac{dT}{dt}. \tag{7}$$

To get an idea of how these material parameters affect the momentum of the armature, we can obtain an expression for the current through the armature using the Lorentz force law, $F = \frac{1}{2}L'I^2$, and Newton's second law, $F = m\frac{dv}{dt}$. Doing so, we obtain

$$I^2 = \frac{2m}{L'}\frac{dv}{dt} \tag{8}$$

where L' is the inductance gradient. Combining equations (7) and (8) allows us to express the momentum, dp, of the armature in terms of material parameters

$$dp = mdv = \frac{\rho c \sigma A^2 L'}{2} dT . \tag{9}$$

To maximize the momentum we must maximize the right hand side of equation (9). For a rough approximation we will keep the specific heat, c, constant. Hence, the best materials for armature use are found through the material parameters $\rho c \sigma \Delta T$. Here we have replaced the infinitesimal temperature, dT, by ΔT. If we furthermore consider the mass of the armature to be constant we see that the material parameters which are important are the change in temperature of the armature, ΔT, and the conductivity, σ. The other variables that appear in equation (9) are parameters of the railgun geometry.

Tables 1 and 2 below give pertinent data concerning possible materials to be investigated. In Table 1, T_m is the melting temperature, T_b is the boiling temperature, and ΔT_m is the difference between room temperature (taken to be 20° C) and the melting temperature. We use ΔT_m for rail and armature materials because we do not want the rail or the armature to melt.

TABLE 1Rail/Armature Material Data [8]

Material	T_m (°C)	T_b (°C)	ρ (g/ml)	c (cal/g-°C)	σ (1/μΩ)	ΔT_m (°C)	ρcσΔT (cal/ml-μΩ)
Al	660	2450	2.7	0.215	0.382	640	142
Cu	1083	2595	8.96	0.092	0.593	1063	520
Mo	2610	5560	10.2	0.061	0.19	2590	306
Ag	960	2210	10.5	0.056	0.616	940	340
W	3410	5930	19.3	0.032	0.181	3390	379

In Table 2, T_m is the melting temperature, T_b is the boiling temperature, and ΔT_b is the difference between room temperature (taken to be 20° C) and the boiling temperature. We take this difference because we want the material at the interface to melt without boiling off. This will allow us to neglect any latent heat in our expression for equation (1).

Table 2 Interface Material Data [8]

Material	T_m (°C)	T_b (°C)	ρ (g/ml)	C (cal/g/°C)	σ (1/μΩ)	ΔT_b (°C)	ρcσΔT (cal/ml/μΩ)
Zn	419	906	7.14	0.091	0.167	886	96.1
Ga	30	2237	5.9	0.079	0.058	2217	52.4
In	156	2000	7.3	0.057	0.111	1980	78.5
Sn	232	2270	7.3	0.054	0.088	2250	68.3

5 BASIC EXPERIMENTAL COMPONENTS

5.1 Railgun Test Bench

A small test bench was constructed to test various materials at the rail-armature interface, Fig 2. The test bench was primarily made out of a phenolic with 4"-long by 1"-wide copper rail inserts. The test material is mounted on the end of the copper insert with screws as shown in Fig 3.

Given the dimensions of the railgun test bench, the inductance gradient is roughly estimated to be

$$L' = 8.9 \times 10^{-8} \left(\frac{henries}{meter} \right).$$

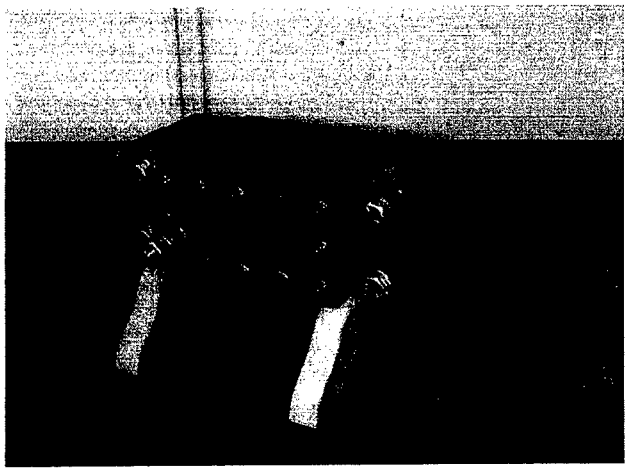


FIGURE 2 Railgun Test Bench

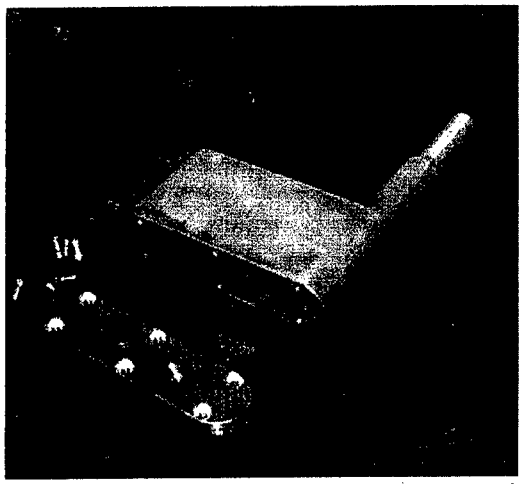


FIGURE 3 Copper Pole Piece with Test Rail Material

5.2 Power Unit

The power supply consists of two 830 μF capacitors rated at 10kV in parallel, two TVS-40 vacuum switches, and a diode crowbar circuit to prevent reverse charging of the capacitors. This pulse-power supply is capable of producing up to 200 kA of current and 80 kJ of energy [9]. To prevent failure in the crowbar circuit three strings of six DA24 F2003 high power avalanche diodes were installed. Proper installation of these diodes, manufactured by ABB Semiconductors AG of Lenzburg, Switzerland, require a mounting force of 20 kN at the center of the devices. Special mounting clamps were ordered from ABB Semiconductors and the three strings of diodes were installed, as seen in Fig 4. The internal inductance of the circuit was measured to be 2.4μH. We found that the period of this circuit is 0.4 ms and the resonant frequency of the circuit is 2.5 kHz.

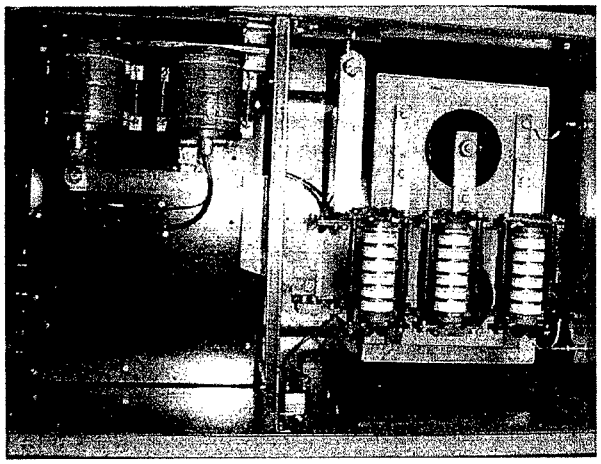


FIGURE 4 Power Unit

5.3 Projectile Design

The projectiles were designed to ensure constant contact between the rail surface and the armature. Two different designs were used. The first had a straight edge at the interface as shown in Fig 5. This provided a 0.6 cm^2 area at the interface. The 60° notch in the back of the projectile is designed to allow the projectile to expand when the Lorentz force drives the rails apart during firing.

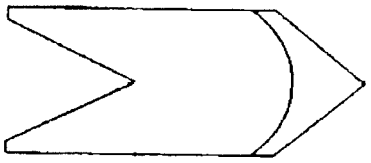


FIGURE 5 Solid Armature

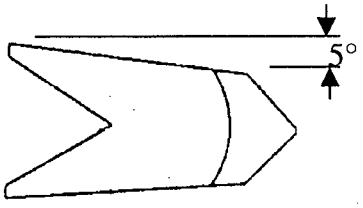


FIGURE 6 Hybrid Armature

The second type of armature is a hybrid armature, Fig 6. This design is fundamentally identical to the solid armature except for a 5° slope at the interface. The material in contact with the rails melts and turns into a conductive plasma, which may fill in the back of the projectile to provide the Lorentz force. Essentially, this design sacrifices the rear most portion of the projectile to melting while the bulk of the projectile remains undamaged.

Both types of armatures were used for high current density experiments while only the solid armature was used for low current density experiments. Table 3 provides the average projectile masses for the test materials before firing.

TABLE 3 Average Projectile Mass of Test Materials

Material	Average Mass
Al	0.81 g
Cu	2.50 g
CW 75	3.60 g
SW 50	4.60 g
Mo	3.43 g

5.4 Outline of the Experiment

Initial testing of materials using the railgun test bench was completed in two phases. Phase I was designed to stress the investigated materials with extremely high current densities. Under these conditions, the hope was to gain insight into which rail-armature material combinations are more suitable to use in the EML environment. These tests were also used to investigate the use of the test bench as a railgun by providing enough current to fire the projectile. During phase II the capacitor voltage was reduced, and materials were investigated at lower current densities. With these experiments, the value of the current at the point at which materials began to melt and/or move via the Lorentz force was determined.

The materials used for early firing tests were the traditional combination of bar stock copper rails with aluminum projectiles. After the railgun test bench fired successfully, other materials were tested. The primary materials used were copper-tungsten and silver-tungsten alloys for the armature and rails. The interface material was indium.

The data that was gathered during these tests is rudimentary. One of the shortcomings of this test bench is the lack of advanced diagnostics for gathering data.

6 EXPERIMENTAL PROCEDURES AND RESULTS

6.1 High Current Firing Tests

6.1.1 Procedure

The projectiles were started from rest approximately one inch from the end of the rail giving an effective rail length of three inches. The mass and size of the projectiles were measured before and after firing and the changes were calculated. The mass and the face-to-face width of the armatures were measured using a Mettler Macro-Balance, Model H 15 and a Mitutoyo Digimatic Caliper, 500 series, respectively. We also visually inspected the

surfaces of the rails after each shot and recorded general observations. Additionally, some of the shots were video taped and photographed.

The current was measured using a Pearson wide band current monitor, Model 1330. To convert from the voltage reading received from the Hewlett Packard Infinium oscilloscope, Model HP 54845A, to determine the maximum current, I_{max}, the following formula was used

$$I_{\max} = \frac{(\max V)(92.58)}{0.005}(A) \tag{10}$$

where (max V) is the maximum voltage reading off the oscilloscope. We measured the correction factor for the two 20 dB attenuators to be 92.58. The term, 0.005, is the V/A conversion factor read off the data plate on the Pearson current monitor. We also used commercial computer simulation software, MicroSIM Eval8, to verify that the measured maximum voltage, (max V), and the calculated maximum current, I_{max}, were in agreement with the expected values. Fig 7 depicts a typical current output plot from the oscilloscope. A Shooting Chrony chronograph, Beta Model, was used to measure projectile velocity.

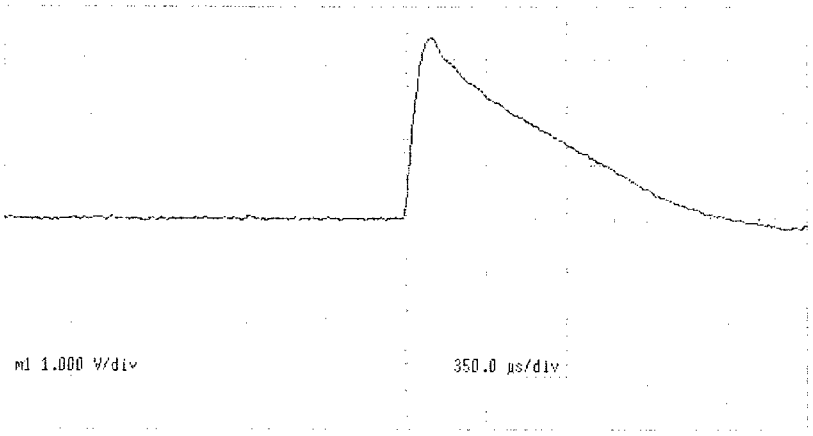


FIGURE 7 Oscilloscope Wave Form
(63 kA Current –Voltage Plotted on Ordinate Axis, Time Plotted on the Abscissa Axis).

6.1.2 Results and Discussion

Various combinations of rails and armatures were tested at different currents ranging from 48 kA to 67 kA. Table 4 summarizes the data collected for numerous shots.

Tests with aluminum armatures on copper rails yielded the predicted results. The copper rails were virtually undamaged but had a large amount of ablation from the projectile. The losses to the projectile in both mass and size were significant. Indium at the interface did not significantly change these results; in fact, for the tungsten alloy material combinations, a greater loss to the projectile was recorded.

Pure copper or aluminum armatures fired on silver-tungsten or copper-tungsten rails yielded worse results than aluminum on copper. The copper and aluminum broke down under Joule heating and extreme losses to the projectile in both size and mass were observed.

Table 4 Firing Test Data (S – Solid Projectile and H – Hybrid Projectile)

RAIL	Projectile (Solid/ Hybrid)	INTER FACE	V_0	I_{max}	% LOSS SIZE	% LOSS MASS	COMMENT
Cu	Al (S)	None	3 kV	No Reading	6 %	17.5%	Al Ablation on rails Chronograph-771 m/s
Cu	Al (S)	None	4 kV	51 kA	11%	21%	Al ablation on rails
Cu	Al (S)	None	4 kV	51 kA	14%	30%	Al ablation on rails
Cu	Al (S)	In	4 kV	51 kA	10%	25%	Al/In ablation
Cu	Al (S)	Al/In	4 kV	52 kA	21%	41%	Severe ablation on rails
Cu	Al (H)	None	4.5kV	56 kA	25%	32%	Severe ablation on rails
SW 65	Cu (H)	None	4 kV	52 kA	20%	24%	Minimal ablation on rails
SW 65	Cu (H)	In	4 kV	51 kA	22%	26%	Cu/In ablation on rails
SW 50	Al (S)	None	5 kV	63 kA	100%	100%	Projectile disintegrated - plasma out the bore
SW 50	Al (S)	None	4.5 kV	58 kA	25%	48%	Severe Al ablation on rails
SW 50	CW 75 (H)	None	5 kV	63 kA	15%	11%	Very little ablation on rails See Fig (4.7).
SW 50	CW 75 (H)	None	5 kV	66 kA	14%	17%	Very little ablation on rails
SW 50	CW 75 (H)	In	5 kV	63 kA	21%	19%	CW/In ablation on rails
CW 75	Cu (H)	In	5kV	62 kA	20%	26%	Chronograph-2894 m/s See Figure (4.6)
CW 75	SW 50 (H)	None	5 kV	62 kA	18%	19%	Half the projectile fractured
CW 75	SW 50 (H)	None	4 kV	52 kA	11%	10%	Rail gouge, little projectile ablation
CW 75	Mo (S)	None	4 kV	49 kA	7%	7%	Gouge on (-) and ablation on (+) rails

While firing a copper projectile on copper-tungsten rails with an indium interface, a chronograph reading of 2.9 km/s was obtained. We calculated the maximum feasible speed of the projectile given its mass and the energy in the system and determined that the projectile could not have traveled that fast. Upon reviewing videotape of the shot, we observed an indium/copper plasma spray traveling ahead of the projectile at a much greater speed. This spray triggered the chronograph, which was then unable to detect the velocity of the projectile itself.

Using combinations of the copper-tungsten and silver-tungsten yielded the most promising results given extremely high current densities. These projectiles were generally less ablated and had their original shape after exiting the railgun test bench, Fig 8. We concluded that the copper-tungsten, CW 75, melts before the silver-tungsten, SW 50. Again, projectile loses were slightly greater with the indium interface.

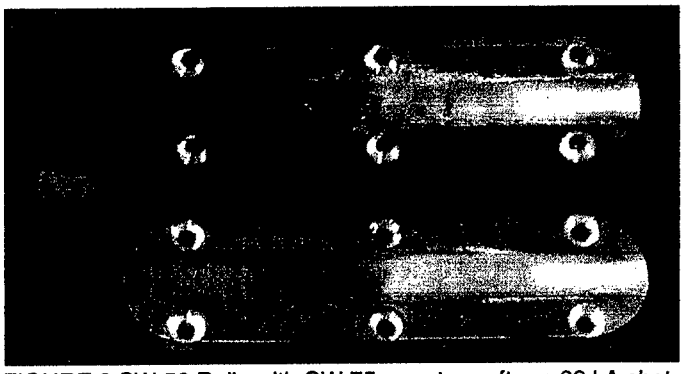


FIGURE 8 SW 50 Rails with CW 75 armature after a 63 kA shot.

The combination of SW 50 armature on CW 75 rails proved to be the most successful at high current densities using hybrid projectiles. With these shots, the projectile remained intact with material loss at the back of the hybrid projectile while the rail lost very little material through the breakdown of the CW 75. The material data for these materials is presented in Table 5.

TABLE 5 Copper/Silver-Tungsten Alloys Material Data

Copper-Tungsten Typical Properties				
Mi-Tech	Nominal Composition % Weight	Rockwell Hardness	Electrical Conductivity % IACS	Density GMS/CC
CW70	30 Copper- 70 Tungsten	90 B	50	14.18
CW75	25 Copper- 75 Tungsten	94 B	48	14.70
Silver-Tungsten Typical Properties				
SW50	50 Silver - 50 Tungsten	70B	65	13.4
SW65	35 Silver - 65 Tungsten	87B	53	14.5

Note: %IACS is International Annealed Copper Standard (i.e. %IACS of 50 means that CW70 has conductivity equal to 50% the conductivity of copper), Mi Tech Metals Inc. Indianapolis, IN

Finally, molybdenum projectile material on tungsten alloy rails must be investigated further. The amount of loss to the projectile is a promising result. However, the projectile velocity was noticeably slower since the projectiles fell short of the target sump in three shots. The low conductance of molybdenum may have caused this marked decrease in speed.

6.2 Low Current Density Tests

6.2.1 Procedure

After reviewing current literature discussing the parameters necessary for an operational naval railgun, we determined that the current densities imposed in phase I of this experiment were much higher than necessary.

A recently published paper by the Institute for Advanced Technology uses the parameter: "I'=I/h as a measure of linear current density on the inner surface of the rails that carry current (where h is the height of the rail at the inner bore from one insulator to the other)" [10]. In this paper, the authors give a conservative estimate for I'

$$I'=30\ (kA/mm) \tag{11}$$

Given this estimate and assuming h = 5" (127 mm) for a typical five-inch Naval gun,

$$I=3810\ (kA) \tag{12}$$

We further assume a 30 cm contact length between the projectile and rail to give a contact area of 381 cm^2. For a naval railgun the current density should then be about

$$\frac{I}{Area}=10\left(\frac{kA}{cm^2}\right). \tag{13}$$

For the railgun test bench this current density, given the 0.6 cm^2 projectile contact area, yields a current of 6 kA, which equates to roughly a 250 V charge on the capacitors in our power supply.

To verify that equation (13) is a good assessment, we calculated another estimate from the Lorentz force equation and Newton's Second Law

$$\frac{1}{2}L'I^2 = ma \tag{14}$$

Here we assumed a 50 kg projectile and an average acceleration of 38.5 kilogees [10]. We calculated an estimate of the inductance gradient assuming, radius of 5 cm and a bore width of 12.7 cm. We get

$$L' = 5x10^{-7} \quad \left(\frac{henries}{meter}\right) \tag{15}$$

Given the inductance gradient, the mass, and acceleration, we find the current, I, to be

$$I = 8.7x10^6 \text{ (A)} \tag{16}$$

Thus, given a contact area of 381 cm^2

$$\frac{I}{Area} = 23\left(\frac{kA}{cm^2}\right). \tag{17}$$

When comparing the two estimates above, equation (13) to equation (17), we find that the values are in agreement to within a factor of two.

During this phase of experimentation, the voltage of the capacitors was lowered, thereby reducing the current. Using the tungsten alloy materials, we determined at which voltage and current density the materials transitioned. Based on materials available and results found in phase I, we used CW 70 rails with SW 50 armatures. Solid armatures were used to ensure that there was a 0.6 cm^2 contact area with the rails. An indium interface between the same rail and armature combination was also investigated.

6.2.2 Results and Discussion

The projectile was placed in the bore to ensure a constant metal-to-metal contact between the armature and the rails, but was also able to accelerate when force was applied to it. We could then determine at what current densities the Lorentz force would initiate motion. Table 6 gives the results of this experiment.

The data suggests that the materials begin to break down at around 36 kA/cm^2. At 56 kA/cm^2, the projectile begins to accelerate under the Lorentz force before succumbing to joule heating and welding to the rails. A current density of 56 kA/cm^2 equates to roughly 34 kA given the railgun test bench parameters. This current density is roughly 5 times higher than necessary, given the estimate for naval railgun use in equation (13). At currents over 33

kA, the projectile appears to accelerate over a greater distances but also inflicts greater damage on the rails and armature.

We replicated the experiment with indium at the interface between the same combinations of materials. An electric hot plate was used to melt the indium. The melted

TABLE 6 SW50 Armature on CW 70 Rails

Voltage on Capacitor (V)	Current Density (kA/cm^2)	Results
500	10	No change in projectile or rail.
1000	22	No change in projectile or rail.
1600	36	Small contact-spot (0.012" diameter) on armature and rail.
2000	44	Armature welded to a 0.094" diameter. Weld spot is 0.17" from the back of projectile.
2500	56	Armature appears to have moved 0.36" before welding to a 0.129" diameter. Weld spot is 0.17" from the end of the projectile.
2500	54	Armature appears to have moved 0.04" before welding to a 0.4" diameter. Weld spot appears across the contact area of the projectile.
3000	64	0.52" movement. Welded to a diameter of 0.15". Weld spot is 0.17" from the back of the projectile.

indium was then applied to the contact face of the projectile by dipping the projectile into the liquid. As a result, an average of 0.127 grams and 0.0185 inches of indium was non-uniformly melted onto the projectiles. During each shot, plasma was ejected from the railgun test bench, however, the projectile failed to accelerate (except on one shot). Table 7 summarizes the results of subsequent firing test.

The results here are promising. Comparing these results to those in Table 6, we see a significant reduction in loss to the projectile. Indium evidently protects the rails and projectile from damage at lower current densities.

TABLE 7 SW 50 Armature on CW 70 Rails with Indium Interface

Voltage on Capacitor (V)	Current (kA)	Loss in size	Loss in mass	Results
500	5	No data	No data	No damage to rail/projectile except for indium loss
1000	12	10%	4%	No damage to rail/projectile. Indium completely gone off projectile.
1000	13	1%	1%	No damage to rail/projectile. Some indium left on the projectile.
1000	13	3%	2%	Welded to (-) rail. No damage to (+) rail and after extraction little damage to (-) rail. Projectile has some indium left.
1250	15	7%	1%	Small amount of pitting on rails. Indium gone off the projectile.
1500	18	4%	2%	More severe pitting on rails. 0.66" movement of projectile. Indium gone off the projectile.
2000	26	5%	2%	More severe damage to rails. Projectile slightly damaged, indium gone.

Comparison of data in Table 6 and Table 7 also implies that the tungsten alloy materials melt at lower currents with the indium interface than without it. The Lorentz force appears to accelerate droplets of liquid indium faster than the projectile. Arcing between the projectile and the rails after the indium interface has left the bore may cause rail and armature materials to melt at lower currents. This effect would also explain the slightly higher percentage of losses, seen in Table 4, with an indium interface at higher current densities.

A maximum current of 13 kA, which equates to a current density of 21.5 kA/cm^2, is apparently where the rail/projectile material begins to break down. Again, this current density is up to 2 times greater than what is apparently necessary for naval railgun use. A projectile must be designed to keep the indium interface from blowing by the projectile before the Lorentz force is able act.

7 CONCLUDING COMMENTS

Initial testing of materials on a railgun test bench yielded promising results. Tungsten alloys were tested for the rail and armature materials; with a SW50 (50% W - 50% Ag) projectile and CW75 (75% W - 25% Cu) rail combination yielding the best results in our tests. Indium at the interface does protect the rails and projectile from damage at lower current densities. The projectile design must be improved. Indium may need to be better integrated into the projectile. This may allow the Lorentz force to act upon the projectile as a whole before the interface material blows past the projectile.

An investigation into different alloys at the interface may also prove to be beneficial. Materials that have an extensive plastic range may be more advantageous than the pure indium used here. Completely different interface materials also need to be investigated. Table 2 provides a list of possible materials.

ACKNOWLEDGMENTS

This paper is adapted from a Masters Thesis written by D. Gillich [11]. We are grateful for the support received from the Naval Postgraduate School on this work. We extend our deepest gratitude to Don Snyder, George Jaksha, and Gary Beck. Without their ingenuity and dedication this work would not have been possible. We'd also like to thank LT Mark Adamy for his assistance in the lab and his continuing work with the railgun project at NPS. Keith Aliberti is also gratefully acknowledged for his careful reading of the manuscript and his many useful comments.

REFERENCES

1. Ogorkiewicz, R.M., *In Search of Lighter, Smaller Electric Guns for Future Tanks,* Jane's International Defense Review, Vol. 032, Issue: 001, pp. 1-6, 1999.
2. Center for Naval Analysis Report CRM 98-74, *Railgun Technology Assessment*, by Kohlberg, I. and Bomse, pp. 3-15, 1998
3. Luke, I.T. and Stumborg, M.F., *The Operational Value of Long Range Land Attack EM Guns to Future Naval Forces,* submitted for publication to IEEE Transactions on Magnetics, pp. 1-4, 1999
4. Persad, C., Yoh, A., Prabhu, G., White, G., and Eliezer, Z., *On the Nature of the Armature-Rail Interface: Liquid Metal Effects*, IEEE Transactions on Magnetics, Vol. 33, No. 1, pp. 1140-145, 1997
5. Persad, C., *Solid Armature Performance: A Progress Report 1980-1990*, IEEE Transactions on Magnetics, Vol. 33, No. 1, pp. 134-139, 1997
6. Barber, J.P., *The Acceleration of Macroparticles and a Hypervelocity Electromagnetic Accelerator,* Doctoral Dissertation, The Australian National University, Canberra, A.C.T., March 1972
7. Bedford, A.J., *Rail Damage and Armature Parameters for Different Railgun Rail Materials,* IEEE Transactions on Magnetics, Vol. MAG-20, No. 2, pp. 352-355, 1984
8. Table of Periodic Properties of the Elements, Sargent-Welch Scientific Company, 1968
9. Lockwood, M., *Design and Construction of an Expandable Series Trans-Augmented Electromagnetic Railgun*, Master's Thesis, Naval Postgraduate School, Monterey, California, June 1999
10. McNab, I.R., Fish, S., and Stefani, F., *Parameters for an electromagnetic Naval Railgun,* Institute for Advanced Technology, The University of Texas at Austin, IAT.P 0367, pp. 1-6, 1999
11. Gillich, D., *Design, Construction, and Operation of an Electromagnetic Railgun Test Bench*, Master's Thesis, Naval Postgraduate School, Monterey, California, June 2000

CONCEPTS FOR FIELDABLE ELECTROMAGNETIC GUN BARRELS

M. J. Hinton[1], A. Howard[2], N. R. Cooper[2], D. K. Wallington[3], and M. A. Firth[3]

[1] *Future Systems Technology Division (FST), DERA, Fort Halstead, UK*
[2] *Structures and Materials Centre, FST Division, DERA, Farnborough, UK*
[3] *Centre for Defence Technology, FST Division, DERA, Fort Halstead, UK*

Point of Contact: Professor M. J. Hinton, Director of Technology (Operations),
FST Division, Fort Halstead, Sevenoaks, Kent, TN14 7BP, UK
Telephone: 44 (0) 1959 514946
Fax: 44 (0) 1959 516059
e-mail: mjhinton@dera.gov.uk

© British Crown Copyright 2001. Published with the permission of the Defence Evaluation and Research Agency on behalf of the Controller of HMSO. This work was carried out as part of Technology Group 01 of the UK MoD Corporate Research Programme.

The Defence Evaluation and Research Agency (DERA) is investigating EM gun technology on behalf of the United Kingdom Ministry of Defence for possible application to future armoured land vehicles. The UK has achieved considerable success with large calibre, laboratory-weight launchers at the Electromagnetic Launch Facility at Kirkcudbright. The development of 'fieldable' EM guns is less advanced, mirroring the picture elsewhere in the world. One approach taken by the UK has been to consider how technology, currently being applied to conventional (ie powder) gun barrels, can be combined with the best aspects of the laboratory EM barrels into fieldable EM launcher concepts. In this paper the new EM barrel concepts are compared with conventional barrels and laboratory EM launchers in terms of mass, flexural stiffness, muzzle droop and inductance gradient, the latter parameter being a key driver of launcher electrical efficiency. Both circular and non-circular bore shapes are considered. The role of lightweight, fibre composite containment structures is highlighted in order to produce weapons of comparable mass and muzzle droop to a conventional tank gun.

INTRODUCTION

Electromagnetic (EM) launch technology can be divided into the sub-categories of 'rail launchers' and 'induction launchers'. The latter can be further divided into 'coil guns/launchers' and 'linear induction launchers'. In recent years the majority of weapons related EM launch technology research, in the UK and around the world, has concentrated on rail launchers. Furthermore, the research has focussed upon the use of EM launch technology

for the hypervelocity launch of direct fire kinetic energy (KE) ammunition. The primary motivation is enhanced terminal effectiveness.

With the move towards improved strategic mobility, and consequently lighter platforms, the primary exploitation route for EM launch technology is currently considered to be as a main armament for a future land combat system. In addition to enhanced lethality, EM launch offers further benefits including (i) a reduction in trunnion pull (recoil impulse) compared with an equivalent performance conventional (ie powder) gun and (ii) the elimination of chemical propellant, providing improved survivability, enhanced tactical mobility (reduced logistic drag) and increased battle tempo.

The requirements for such a weapon system include the need for compatibility with future light(er) weight vehicles (Ref 1) and the lethality to defeat future enemy combat systems. Also desirable would be any improvements accrued in survivability or sustainability due to adoption of the weapon system. EM launch provides enhanced target defeat through the hypervelocity launch of KE projectiles. Coupled with novel KE projectile development, this should ensure robust defeat of enemy targets.

EM launch technology has been studied at various times in the past, and during the recent era (1980s onwards) a considerable amount of information has been gathered. It is evident from the literature (Refs 2, 3 and 4) that the current status of much of the required technology (power supply, launcher, launch package) is still at the experimental stage. Consequently there is a something of a gap between current research programmes and that which is required to achieve the tactical advantages in the operational environments described above.

Considering specifically EM gun barrel technology, successful launchers (ie those capable of firing tactical projectiles at hypervelocity) remain as heavyweight laboratory structures which would be impossible to deploy in combat. Much lighter designs are required - similar in mass to conventional powder guns.

In parallel with EM launcher development, the UK has investigated the technology required to lighten conventional gun barrels using fibre composites, namely tensioned overwraps and flexural stiffening. This paper describes how the UK's composite materials technology, previously applied to conventional barrels, translates to the designs of fieldable EM launchers.

The next section describes progress in the construction and use of large-calibre launchers capable of firing tactical projectiles. This is followed by a review of present-day UK launchers, together with details of the development that has made them into multi-shot devices. Subsequently, the UK's advanced conventional barrel programme is described including the application of tensioned overwraps and thermal management, illustrating the logical extension of these technologies to the design of lightweight fieldable EM launchers. Finally, new concepts for lightweight EM launchers based on the novel use of tensioned overwraps are described. A parametric study of existing and proposed launchers is presented showing progressive development in launcher design with reference to mass, muzzle droop and inductance gradient. The benefits of thermal management for EM launchers also are discussed.

A BRIEF HISTORY OF THE DEVELOPMENT OF EM LAUNCHERS

The initial work on railguns was motivated by the curiosity of physicists ie as 'interesting physics experiments'. The first railguns were designed to allow rapid re-builds. They typically had a square or rectangular-bore cross-section, formed from tightly clamped and bolted core components, and required minimal machining either before or after assembly. The rails were made of plain copper, a natural first choice (given its good electrical conductivity and availability in flat bar form) but susceptible to gouging at relatively low velocities (often below $1kms^{-1}$). Gouge formation became a major focus of the early work, so experimental programmes were embarked upon whereby the gun was rebuilt after every single shot. This routine satisfied the need to have a 'perfect' bore condition for each projectile launch, but carried the inevitable penalty of a readily strippable gun ie a general lack of structural rigidity.

As EM gun technology advanced, a second phase of 'more applied physics experiments' was embarked upon in the late 80's, with interest beginning to focus on the launch of projectiles with a meaningful military utility. Given that almost all gun-launched projectiles, to date, have been circular in cross-section, there was a natural move towards the development of round-bore EM launchers. The US Task B 90mm guns of the late 80s were the first significant exponents of round-bore EM technology at a relatively large calibre. The two launchers (one at Green Farm in California and the other at the Centre for Electromechanics in Texas (CEM)) differed completely in their design. The Green Farm gun (Ref 5) is relatively simple in its design, is fairly easy to rebuild but has relatively low radial stiffness. The CEM gun (Ref 6) has high radial and axial stiffness, a pressurised design which does not lend itself to rapid rebuild cycles, and a mass of around 30 tons.

Attempts to attain a reduction in mass from the CEM barrel were made with the Sparta 90mm guns (Refs 7, 8), where hydraulic pressure was used to maintain a state of compression in alumina ceramic segments surrounding the core. The approach was similar to that employed in the CEM Task B gun but with the outer, thick steel, pressure vessel of the Task B gun replaced by a stainless steel tube of minimal thickness supplemented with a composite over-winding. Firing trials showed up severe limitations in the Sparta barrels, but a number of useful design lessons were learned as a result.

Round-bore EM guns require post-assembly machining, usually by honing. This operation demanded a significant investment in machinery and operators. Because of the engineers' desire for as good a bore condition as possible for their shots, the Task B guns were generally re-honed after every firing (certainly in the early days). This produced a gun with an ever-growing bore size and a slow shot rate - one or two shots per week being typical. Nevertheless the two workhorse Task B guns, together with the expertise of the support teams, have contributed immensely to the development of the technology.

By the time that the UK Electromagnetic Launch Facility (EMLF) at Kirkcudbright came on line in 1993, a considerable amount of knowledge had been built up on large calibre EM firings. A generation of laboratory EM barrels has followed, using thin steel laminates to contain the core. The UK has fired several hundred EM shots in laminated steel EM barrels of different calibres in the 90s, confirming their suitability as laboratory guns. The challenge now is to introduce acceptable flexural properties, whilst also improving the core's radial stiffness and electrical properties and, most importantly, reducing the overall mass.

REVIEW OF UK EM LAUNCHERS

LAM40 5m and 8m Barrels

A 5m long, 40mm calibre laboratory barrel was conceived for installation at Fort Halstead in 1994 to help with rail and insulator materials selection. The design featured laminated steel containment, copper rails and glass/epoxy (GRP) insulators.

A technique was developed to build laminated containment modules by forming a structural bond between the steel plates. The adhesive used also provided the necessary plate to plate electrical insulation. Later this construction method was used to build an 8m long, 40mm calibre barrel at Kirkcudbright for high velocity firings. This design of module represented a major improvement in barrel structural integrity. To date in excess of 75 shots have been fired in these barrels with no deterioration of the modules observed. The rail material is copper-chrome-zirconium and full-length GRP pultruded insulators have been employed with excellent results.

90mm IAP Launcher at Kirkcudbright

This barrel was supplied to the UK EMLF at DERA in 1993 by International Applied Physics (IAP). It is an 8m long steel laminated construction with the original laminations secured by tack welds on their periphery. Laminated modules, approximately 0.5m long, are clamped in pairs, one above and one below the bore, to form the containment. A number of such pairs of modules complete the 8m length. Originally, the bore was formed from pure copper rails and the insulators were manufactured from an electrical grade of glass fibre reinforced plastic known as 10G40 (Tufnol). The use of a harder rail material, copper-chromium-zirconium, reduced the incidence of gouging thereby increasing the working velocity to 2000ms^{-1} (Ref 9). Alternative 10G40 insulator configurations have been tried to improve the bore dilation stiffness. However the dimensions in which the 10G40 insulator material is manufactured meant that joints were required along the length of the barrel which inevitably absorbed honing fluid and copper swarf leading to breakdown of the insulation.

The welded containment modules showed signs of deterioration after the first few shots (Fig 1). Individual steel plates deformed, both in the plane of the plate and in a warping mode. Shear displacement of the laminated assemblies occurred, similar to a pack of cards. Movement was also apparent between individual modules and between the modules and the support structure.

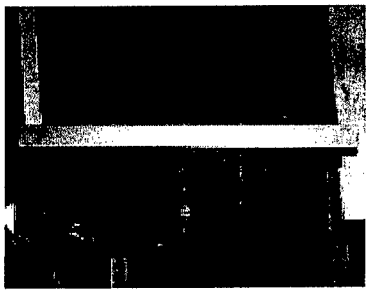


FIGURE 1

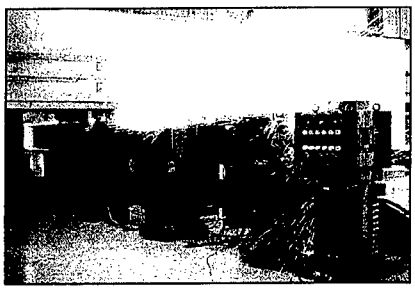


FIGURE 2

The cable attachment (Fig 2) was asymmetric below the centreline of the launcher, producing bending forces in the structure that were sufficient to cause permanent deformation of components. This effect has been noted for future launcher designs, where balanced forces will be essential to prevent deleterious effects on the structure and shot accuracy. The supporting I-beam also buckled forward of the breech interface.

Since its installation at DERA, the 90mm IAP launcher has been subjected to continuous development. The bowed module plates (Fig 1) did not compromise the radial stiffness of the launcher, but posed increasing difficulties during assembly. The original tack-welded containment modules of the IAP 90mm barrel were gradually replaced with structurally bonded modules (Fig 3) like those of the LAM40, but with thinner steel plates and bond lines to improve the barrel inductance gradient. The new laminated modules have been keyed to the sub-frame to prevent axial motion under firing load.

The insulators have evolved from segmented 10G40 through to full-length pultruded designs. The muzzle has been significantly strengthened to prevent damage from muzzle arc. The supporting I-beam has been extensively modified and reinforced to eliminate bending. A revised breech design with cable attachment either side of the launcher centreline has been fitted to reduce out-of-balance forces (Fig 4).

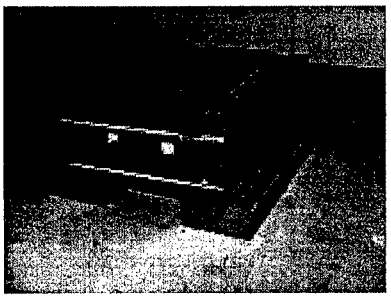


FIGURE 3



FIGURE 4

The limitations of the IAP 90mm launcher are now well known, but the progressive improvements have increased the launch energy to 8MJ, from an earlier limit of 5MJ, and have extended the life of the core components. Despite the difficulties encountered, over 210 shots have been fired to date at velocities of around $2000ms^{-1}$, which was exceeded on many occasions. Nowadays, the launcher is honed once after building but not after subsequent firings.

The development programme described above illustrates the difficulty of constructing multi-part launchers, especially if are they are required to be easily rebuilt. The lessons learnt from the laboratory launchers are now being applied to the design of fieldable launchers.

90mm Task C Launcher at Kirkcudbright

This US (designed and built by CEM, (Ref 10)) barrel currently installed at the EMLF uses a laminated construction that has metal plates retained by a glass fibre reinforced composite overwrap. The rail material is are Glidcop, an oxide dispersion strengthened copper alloy produced by powder metallurgy, with fine alumina particles in the copper matrix. The insulators are full-length pultrusions of GRP featuring a braided skin over a core of uni-directional fibres. The rails and insulators are retained in position with a thin, shrink-fit, insulator before shaped steel plates are slid over the assembly. The plates are adhesively

bonded to each other, firstly in 5cm thick sub-assemblies, and then into 1m sections to form the 8m long barrel. The core and containment are bonded together by impregnating the entire assembly with epoxy resin. The steel plates primarily contain the rail loads during firing, with an additional thick, glass reinforced plastic overwrap providing structural stability and some degree of flexural stiffening. The whole barrel is mounted on a laboratory support structure. The Task C launcher (Fig 5) has been used at Kirkcudbright for proof firing projectiles approaching their design pressure and has also confirmed the results of the earlier accuracy trials from the IAP launcher.

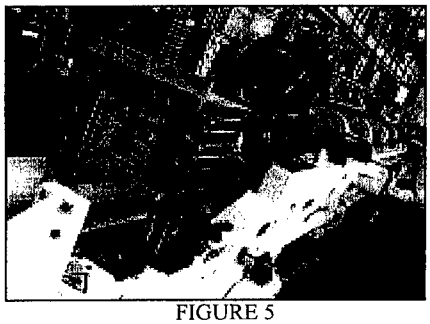


FIGURE 5

ADVANCED UK CONVENTIONAL BARREL TECHNOLOGY

Selective strengthening and/or selective stiffening a steel tank gun barrel with advanced fibre composite materials has been the subject of much research in the UK. The technology is an extension of tensioned overwrap methods successfully applied to rocket motor construction (Ref 11).

The specific strength and specific stiffness advantages of composites over gun steels (in excess of 5:1) suggest that significant improvements in barrel performance could be gained by their use in gun barrel design. Compared to an all steel barrel, the higher specific strength of composites could be used to produce a gun barrel that has either a lower mass, or a higher working pressure for the same weight, or is longer for the same trunnion balancing moment. Alternatively, a combination of such benefits could be realised. Similarly, the higher specific stiffness of composites could be used to improve the accuracy of the gun system by reducing muzzle droop and increasing the natural frequency of the barrel. Furthermore, the local cross-section stiffness of the barrel could be modified to aid local tuning of the dynamic response.

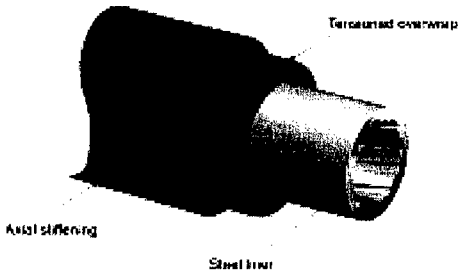


FIGURE 6

The technology developed by the UK comprises a carbon fibre composite wound under tension around a conventional gun steel liner. A diagram, identifying the various features of such a barrel, is shown in Fig 6.

The steel liner provides the wear and flame resistance, the pressure seal, and can accommodate the rifling if required. The function of the tensioned composite overwrap is to increase the hoop strength of the barrel, enhancing the pressure containment, and the outer sleeve increases flexural stiffness.

The UK has addressed the following fundamental issues that have enabled the potential benefits of this technology to be quantified, leading to the ability to optimise overwrapped gun barrel designs:

- A considerable amount of heat energy (in excess of 50% of the total available energy in the propellant) is released each time a round is fired. A significant portion of this heat is absorbed into the barrel, where it is dissipated via conduction and surface convection. Hence the thermal conductivity and heat capacity of the barrel will have a major impact on the barrel temperatures. Since fibre composites with organic matrices (e.g. epoxy resins) have a low thermal conductivity and heat capacity when compared with steel, there is a danger that the composite overwrap will fail to dissipate the heat at an adequate rate. This could result in barrel temperatures far exceeding those found in current all-steel guns. Note that temperatures in excess of 200-250°C are not untypical on the outside surface of a gun.
- To enable the composite overwrap and the steel liner to be used efficiently, bearing in mind the significant difference between their operating strains (steel <0.4, composites >1%) it is essential that the overwrapped barrel is in a state of pre-stress; compressive in the liner, tensile in the overwind. Furthermore, the presence of this pre-stress also alleviates the thermal expansion mis-match problems, particularly at low temperature, where the steel will contract significantly more than the tensioned overwrap.
- The fatigue life of overwrapped barrels needs to be commensurate with that for the all-steel barrels. Pre-stressing the liner is essential in meeting this requirement.
- Accurate structural analysis procedures must be developed in order to design an efficient thick-walled, metal lined, composite overwrapped gun tube. These procedures need to take into account anisotropic material properties, the pre-stress induced during fabrication and the differential thermal expansion behaviour.

In order to address the key technical areas associated with this technology, a comprehensive R & D programme was initiated in 1987. To ease the technical risks and to provide confidence in the 'guns community', the programme was divided into the following phases:

- Development of a PC-based gun barrel design package to provide the structural analysis, barrel heating, frequency and droop calculations with easy to use pre- and post-processors applicable to composite overwrap barrels.
- Overwrap material selection considering both fibre types and high temperature resin systems.
- Laboratory evaluation of 30mm and 120mm calibre overwrapped barrel sections in static and fatigue tests.

- Firing trials of overwrapped 30mm calibre 'RARDEN' and 120mm calibre tank guns with barrel heating and dispersion assessment.

Application of Gun Barrel Design Software

The software has been used to study overwrap technology in relation to 30mm, 40mm, 120mm calibre and 140mm calibre barrels. Useful improvements to mass, droop and frequency response have been predicted. Certain scenarios permit the barrel length to be extended giving useful improvements to range and accuracy. The highest rates of fire are predicted to cause cook-off problems that might require thermal management. Full details of the phased development programme are reported elsewhere (Ref 12).

Thermal Management

Barrel heating can prevent sustained high rates of fire with modern artillery. Firstly, the barrel may become hot enough to cause charge 'cook off' (~180°C) and/or melting of the shell filling (80°C). Secondly, high temperatures can cause unacceptable wear rates, and in extreme cases, a loss of mechanical strength of the barrel materials.

During the firing cycle of the gun, approximately 5% of the charge energy is imparted to the inside surface of the barrel wall as heat. This heat is conducted through the barrel wall and is dissipated to the atmosphere through natural convection from the exterior barrel surface. Due to the poor heat transfer to the surrounding air, the rate of heat loss from the barrel is low compared to the rate of heating. As a result, rapid or sustained firing will quickly heat the barrel to a temperature beyond that which the ammunition can be safely loaded and fired. In extreme circumstances the gun may be out of action for periods up to 24 hours before its temperature returns to ambient.

Considering artillery systems, studies have shown that improved performance will require greatly increased charge energies. The current levels of heat input to AS90 (the UK's in service 155mm, self-propelled, howitzer) is around 2.4MJ (per shot), with near future systems 2.7MJ and next generation 4.2MJ.

A system study has indicated that active thermal management could be of 'high' benefit to the AS90 system. Benefits are expected to be a higher sustained rate of fire with reductions in risk of cook-off, barrel wear at the commencement of rifling, barrel bend, bore choke, muzzle velocity variations and thermal signature.

The UK programme at DERA continues to investigate thermal and structural testing of full-calibre, 155mm, mid-wall cooled barrels (Fig 7).

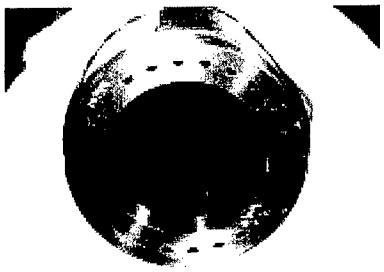


FIGURE 7

DEVELOPMENT OF FIELDABLE EM BARREL CONCEPTS

Research to date has focussed on enhancing the structural integrity of the existing launcher systems, whilst developing construction methods and materials applicable to future, lightweight, electrically efficient, fieldable EM barrels. Construction methods have centred on overwound designs as a logical extension of the expertise developed for conventional barrels. Structural stability and bore dilation under dynamic loading are key factors in determining the projectile launch dynamics, accuracy and dispersion inherent in a gun system. Consequently, launcher concepts are analysed using structural and electromagnetic finite element modelling and the results are validated by instrumented trials using short barrel test sections.

Specific technologies under consideration include tensioned overwraps, both organic fibres and metals, and methods for pre-loading the core in compression using hydraulics. Short lengths of promising core containment concepts have been built and tested to begin to identify a practical configuration for an advanced EM barrel, working towards a fieldable system. Parametric studies (mass breakdown, stiffness, barrel droop, frequency response, etc) have been performed for existing EM barrel configurations and future barrel concepts. Whilst the parameters might not match future specifications in absolute terms, they are felt to be sufficiently representative to demonstrate the relative merits of the various EM launcher concepts.

Laboratory EM launchers have been made previously with varying degrees of bore radial stiffness, both less than and greater than conventional ordnance. However, none of them has provided any significant inherent flexural stiffness; this is the predominant additional requirement of a fieldable launcher. Lightweight materials with high strength and modulus are candidates for fieldable launcher construction. However, many promising materials are not available in the size required, and often the available materials data is not relevant to EM launcher design. DERA has ongoing programmes to develop appropriate forms of materials, and acquire materials data for the design of fieldable launchers.

Design Concepts

Four concepts for 90mm calibre fieldable barrels have been produced in outline. For the barrel cross-section shown in Fig 8, the flexural stiffness is provided by a fabricated structure which is independent from the hoop-wise composite tensioned overwrap containment. The insulators are of a two-part construction to provide the advantages of both GRP and ceramics. The inner insulator is sufficiently elastic and dimensioned such that the pre-stress applied by the overwrap will compress it against the rail. The outer insulator is a stiffer non-conductive material, which enables the amount of pre-stress required from the containment to be provided without deforming the bore geometry. With this configuration, the pre-stressed inner insulator moves with the rail during firing.

The fabricated longitudinal support would also facilitate the integration of the barrel into the vehicle using a conventional cantilever cradle mounting arrangement.

In the launcher configuration shown in Fig 9 the copper rail/ceramic insulator interface has been keyed longitudinally to minimise relative displacement under firing load. During manufacture, an insulating material would be wound around the core (not shown in the schematic) after which an insulated steel wire overwrap is added to react the dilation of the rails and insulators during firing. The next outer layer is of tensioned composite overwrap to

augment the steel windings. Finally, a steel or titanium fabricated structure will be clamped round the barrel to provide flexural support.

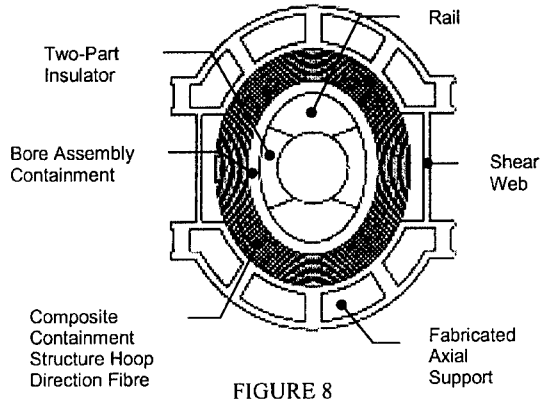


FIGURE 8

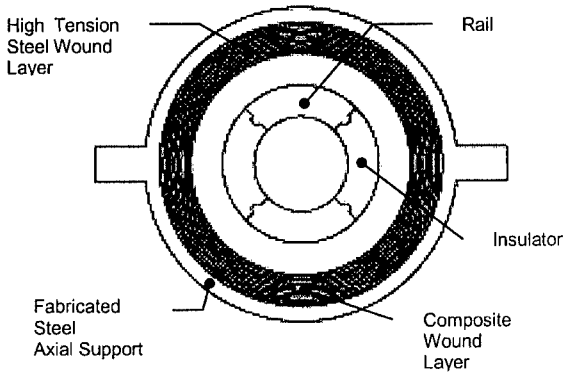


FIGURE 9

The composite elliptical containment shown in Fig 10 may provide a better method of controlling rail movement than circular overwrapped designs and the rail configuration employed increases the inductance gradient compared to contemporary 90mm launchers. The latter is a significant result since system study modelling has shown that launcher efficiency is the most important factor contributing to overall system efficiency. The proposed barrel features a high performance carbon fibre reinforced plastic (CFRP) overwrap and a carbon fibre composite, longitudinally stiffened sleeve whose thickness is calculated to obtain muzzle droop comparable to a conventional 120mm tank gun barrel. As yet the barrel cross-section is assumed to be constant along the length, but a future development will be to reduce weight and decrease droop further by reducing rail and containment size nearer the muzzle.

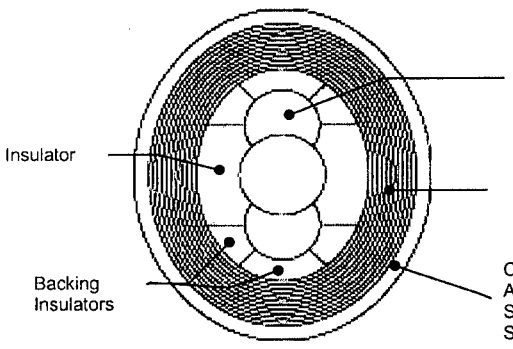


FIGURE 10

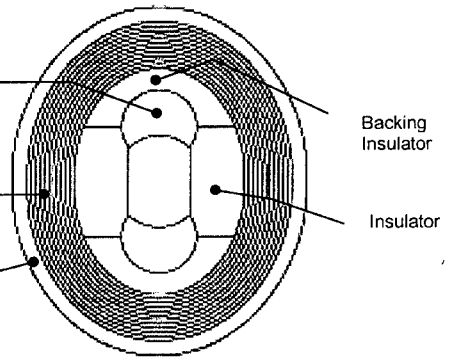


FIGURE 11

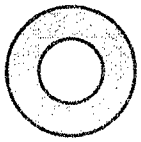
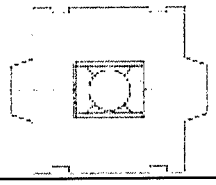
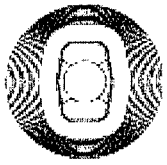
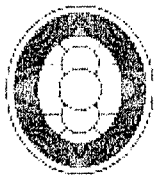
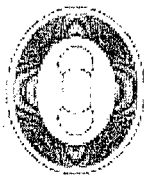
The UK effort has concentrated mainly, to date, on round-bore EM projectiles and guns. Rectangular-bore guns have certain advantages over round-bore configurations (Ref 13). For example, the efficiency of electrical contact is probably higher for a rectangular-bore because the current is distributed more evenly across the rail width. Muzzle droop may be less because the rails can be positioned more favourably with respect to the neutral axis of the

barrel in bending. The inductance gradient may be higher depending on the ratio of rail spacing to overall rail width. However, containment design for a rectangular-bore is likely to be more difficult, as will be bore finishing operations such as honing. An elliptical-bore (to match the elliptical containment described above) has similar disadvantages because of difficulties with bore finishing. However, a hybrid 'oval' bore, where the rails of a round-bore launcher are moved further apart, would have a desirable inductance gradient whilst the flat sides of the oval would ease the structural design of insulators thereby permitting higher rail pre-load. Projectile design is simplified being an evolution of successful round-bore designs and the possibility of shot rotation in-bore would be avoided. Such a scheme is shown in Fig 11.

EM Launchers Parametric Study

Table 1 contains the results of a parametric study of present EM launchers and lightweight EM launcher schemes in relation to the L30, 120mm calibre barrel fitted to the UK Challenger 2 main battle tank. Barrel length, mass, flexural stiffness, droop under self-weight and inductance gradient have been evaluated to enable realistic comparisons to be made between the various designs.

Table 1

Barrel Design	Total Barrel Mass	Flexural Stiffness EI	Tip Deflection*	L' Value (μH) from Stored Energy	Barrel Cross-Section
120mm calibre Challenger 2 L30 In-service conventional barrel	1.00	1.00	1.00	-	
IAP 90mm calibre laminated laboratory barrel	8.92	7.38	2.21	0.455	
TASK C 90mm calibre laminated laboratory barrel, glass/epoxy overwrap	1.91	0.64	5.44	0.461	
90mm calibre composite barrel concept with fabricated steel support	1.14	2.11	0.99	0.367	
90mm calibre wire wound barrel concept with steel tube support	1.46	1.49	1.79	0.136	
90mm calibre elliptical overwrap barrel concept with longitudinally stiffened external sleeve	1.28	2.33	1.00	0.486	
100mm calibre oval-bore barrel concept with elliptical overwrap and longitudinally stiffened external sleeve	1.32	2.49	0.97	0.518	

* - Assuming barrel is encastré at the breech-end. EM barrels assumed to be 8m long

For the EM launchers, the mass has been determined from finite element models of the cross-sections and the barrel length. The flexural stiffness (EI) is the summation, for all components, of the product of the Young's modulus in the axial direction and the second moment of area about the neutral axis of the barrel in bending. Tip deflection is calculated assuming that the barrel is supported as a cantilever and using the appropriate formula based on Engineers' Bending Theory (Ref 14). The barrel inductance gradient, L', has been estimated from electromagnetic finite element modelling of the barrel section; this technique correlates well with published data (Ref 10).

The laboratory launchers LAM90 and, to a lesser extent, Task C, are included to emphasise how heavy and flexible such designs are, and that their deployment as fieldable barrels, ie without their laboratory stands, is completely unrealistic. The laminated steel construction method used appears inappropriate for lightweight barrels.

The four fieldable barrel concepts proposed all feature tensioned overwrap technology combined with separate flexural stiffening. Their masses are comparable with that of a conventional 120mm barrel, as are their tip deflections. It is noteworthy that the oval-bore, fully composite, barrel has an increased L' of 0.518, compared to the round-bore designs. The wire-wound barrel concept has a disappointing L' value of $0.136\mu Hm^{-1}$ at present. However, this concept is part of an ongoing development programme investigating active management of bore dilation. Controlling the rail movement during firing is extremely difficult with overwrapped barrels. For example, Task C barrel contains the rail loads mostly by the steel laminations; the overwrap only providing additional structural stability. However, the predicted rail dilation for the composite overwrapped, oval-bore, barrel (Fig 11) is commendably low at about 1.2 times the breech-end bore dilation at the gun design pressure for L30, considering a typical hypervelocity EM gun firing scenario. The bore dilation is affected by many elements of the barrel design, but is strongly influenced by the choice of insulator material.

Hydraulic Bore Loading

Understanding the movement of the core components during firing is fundamental in the design of fieldable EM launchers. Finite element modelling of candidate barrel sections has been backed-up by bore dilation measurements on barrel sections. In order to simulate the internal forces that act in the launcher during firing, a bore loading mandrel has been developed which applies a load evenly along the launcher rail length. This mandrel has been successfully demonstrated up to levels of pressure equivalent to the working pressure in a conventional tank gun barrel. The force distribution has been validated through tests in a thick-walled steel cylinder, instrumented with strain gauges and non-contact fibre-optic displacement sensors, Fig 12.

Pre-loading the core of the EM launcher in compression can be used to control bore dilation during firing. The two principal methods that have been investigated are so-called 'flat jacks' (Ref 15) and tension overwinding (described previously). A flat jack (Fig 13) comprises two plates, seam welded about their edges and pressurised internally. Flat jacks have been successfully incorporated into a 90mm laminated launcher module to pre-load the core. The jack is placed directly behind the rail and reacts against the containment module. The behaviour of the core components, in particular the insulators, can be assessed using this technique.

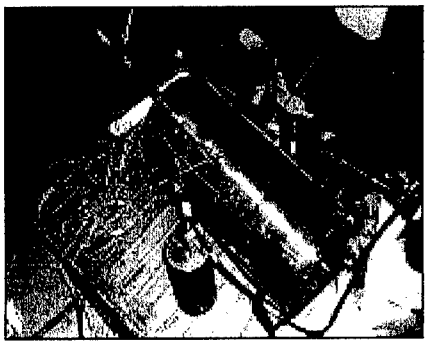


FIGURE 12

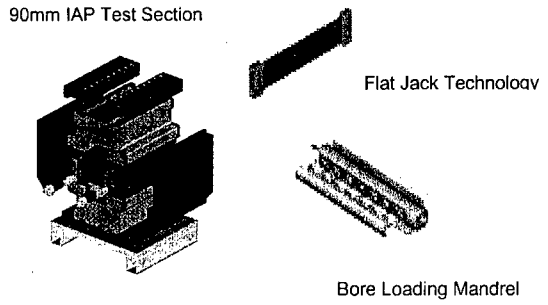


FIGURE 13

Thermal Management and Rail Materials

The present generation of EM launchers uses monolithic rails with uniform properties along the whole length and across the whole section. There are at least three separate sections along the length of the barrel requiring different properties - the insertion region, the high current density region and the exit. The rail containment in the high current density region needs to be much stiffer than other regions of the barrel and redistribution of the mass in the form of tapered rails would seem appropriate. However for accuracy, the exit region, which is subjected to lower current densities, must retain dimensional precision. Steel might be useful here as it would also provide resistance to gouging.

Co-extrusion of rail materials appears attractive and samples of aluminium-cored copper have been procured. EM modelling has shown (Fig 14) that in a round-bore gun, the current density is higher at the edges of the rails than in the interior, allowing a lighter, lower conductivity material to be introduced into the core. Clearly the weight-saving is advantageous in the design of a fieldable launcher.

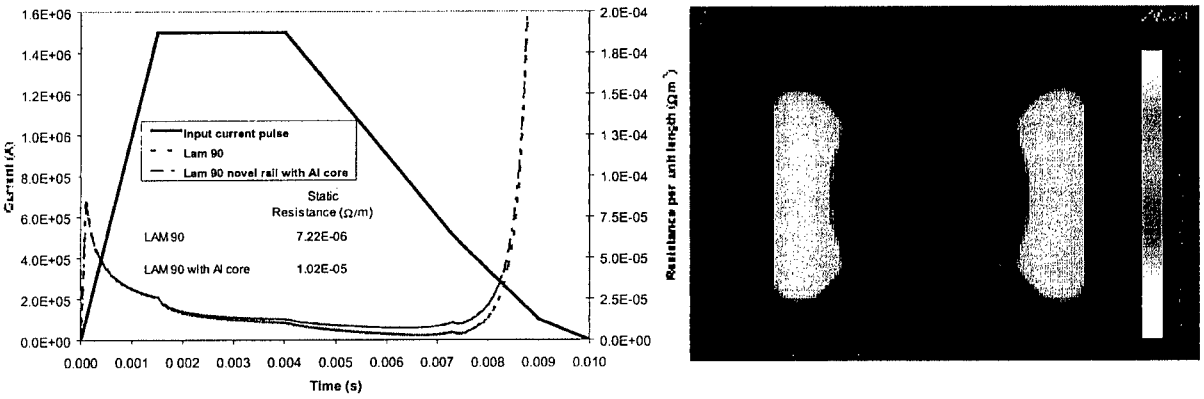


FIGURE 14

The techniques described earlier for the thermal management of conventional barrels are likely to be required for fieldable EM launchers. Thermal management of the rails would seem essential to minimise changes in rail conductivity under variable ambient conditions, to control the increase in rail temperature during repeated firings, and possibly to increase the conductivity and strength by suitable cooling below ambient temperatures. Water cooling may reduce rail wear by ensuring that any melting is immediately quenched back to solid alloy. Operating at modest cryogenic temperatures could provide considerable advantages, even if the high-current density section only was cooled. It may allow considerable improvements in system efficiency permitting hyper-velocities to be achieved for tactical projectiles without recourse to exotic materials, if the engineering and practical issues can be overcome.

CONCLUSIONS AND NEXT STEPS

The brief history of EM launcher developments, provided in this paper, serves to indicate that much of the technology still remains rooted in 'physics experiments', for reasons that are readily understood. There is a significant challenge in front of the community to move the debate towards concepts which can be translated into 'fieldable EM Guns' in the true sense of the words. Whilst the remaining fundamental physics issues should not be underestimated (eg when/if transition in-bore is acceptable), the level of maturity is now sufficient to switch attention elsewhere.

The intent of this paper has been to indicate that the conventional (ie powder) gun design community is not static, and recent advances in that arena may well form the basis for bridging the technology gap which the EM gun community must cross, if it is to have a future. It is now timely to begin to address the practical gun design issues, those of stiffness, mass distribution, materials selection, fabrication route, shot/barrel dynamics and mounting within a vehicle. The singular most effective next step is to bring together the physicists and gun designers such that the next generation of EM launchers is designed and built to be a prototype 'towards fieldable' EM launcher, and not another 'physics experiment'.

ACKNOWLEDGMENTS

This paper has been written on behalf of the entire UK EM Gun project team at DERA and within MoD, whose inputs to the work described here are gratefully acknowledged. Particular thanks are given to Ben Watkins and Michael Royle, for their extensive analytical work underpinning the EM barrel concept comparisons, described in the paper.

REFERENCES

1. Robert J. Taylor, "Influence of Combat Vehicle System Constraints on EML Technology Development," *IEEE Transactions of Magnetics, Vol 35, No. 1,* 473-478, January 1999
2. K. G. Cook et al, "Subscale Rotor Spin Testing for Compulsator Component Development," *IEEE Transactions of Magnetics, Vol 35, No. 1,* 277-282, January 1999

3. John M. Juston, "A High Performance Railgun Launcher Design," *IEEE Transactions of Magnetics, Vol 33, No. 1,* 566-570, January 1997
4. Alexander E. Zielinski, "Improved Integrated Launch Package Ballistic Performance," *IEEE Transactions of Magnetics, Vol 35, No. 1,* 124-129, January 1999
5. S. Rosenwasser, "Recent Advances in Large Railgun Structures and Materials Technology," *IEEE Transactions of Magnetics, Vol 27, No. 1,* 444-451, January 1991
6. R. Zowarka et al, "9MJ Laboratory Gun and Range at the University of Texas at Austin," *IEEE Transactions of Magnetics, Vol 25, No. 1,* 653-661, January 1989
7. M. Holland et al, "Advanced Railgun Experimental Test Results and Implications for the Future," *IEEE Transactions of Magnetics, Vol 29, No. 1,* 419-424, January 1993
8. Vrable et al, "Design and Fabrication of an Advanced Lightweight High Stiffness Railgun Barrel Concept," *IEEE Transactions of Magnetics, Vol 27, No. 1,* 470-475, January 1991
9. D. Munday, D. G. Jones and K. J. A. Mawella, "Metallographic Studies on Rails Removed from the DRA Electromagnetic Launch Facility at Kirkcudbright," *5th European Symposium on Electromagnetic Launch Technology, Toulouse, France,* Paper No. 93, 10-13 April 1995
10. J. J. Hahne, J. H. Herbst and J. L. Upshaw, "Fabrication and Testing of a 30mm and a 90mm Laminated, High L' Railgun Designed and Built at CEM-UT," *IEEE Transactions of Magnetics, Vol 31, No. 1,* 303-308, January 1995
11. J. Cook, A. Groves, R. Hayman, A. Howard, "Modern Approach to Overwound Structures," *Plastics, Rubber and Composites, Vol 28, No. 5,* 259-267, 1999
12. M. J. Hinton et al, "Advanced Materials for Gun Systems, to be presented at," *10th U.S. Army Gun Dynamics Symposium, Plenary paper,* 23-26 April 2001
13. Richard A. Marshall, "Railgun Bore Geometry, Round or Square," *IEEE Transactions of Magnetics, Vol 35, No. 1,* 427-431, January 1999
14. Warren C. Young, "Roarke's Formulas for Stress and Strain," Published by McGraw-Hill Book Company, 1989
15. M. D. Werst et al, "Design and Testing of a Rapid Fire, Lightweight, Ultrastiff Railgun for a Cannon Calibre Electromagnetic Launcher System," *IEEE Transactions of Magnetics, Vol 31, No. 1,* 365-370, January 1995

LARGE CALIBER GUN TUBE MATERIALS SYSTEMS DESIGN

J.S. Montgomery[1], and R.L. Ellis[2]

[1] *U.S. ArmyResearch Laboratory, Aberdeen Proving Ground, MD 21005*
[2] *U.S. Naval Surface Warfare Center, Dahlgren, VA 22448*

The requirements of future gun systems have put increasing demands on the materials of construction. Our knowledge of the gun tube service environment and materials now allows us to use a materials systems design approach to design new gun systems.

The gun tube environment and current gun tube materials, properties, dimensions, and fabrication methods will be reviewed, as well as the erosion test methods that have been used to characterize the in-bore environment. Fatigue, erosion and muzzle wear are the three predominant reasons for gun tube retirement, and each of these phenomena will be examined.

The materials systems design approach will be used to examine a number of possible materials systems designs for advanced gun systems, and we will highlight the strengths and weaknesses of these designs.

BACKGROUND

For the purposes of this paper, we will only be considering the gun tube subsystem, not the gun carrier subsystem, the propellant subsystem, or the projectile subsystems. In actual practice, the design of a gun system must take these components into consideration, and, ideally, all should be designed simultaneously. If one examines existing "successful" gun systems, one sees that most had their gun, propellant and projectiles designed at about the same time. It is beyond the scope of this paper to consider gun system components outside the tube subsystem. Furthermore, we will only be considering large caliber gun tubes. These are tubes that are typically greater than 40 mm caliber, and are used in the tank gun (direct fire) and in the artillery (indirect fire) roles. Gun tube designs that use artificial cooling of the gun tube by forced liquid cooling of the jacket or evaporative cooling of the bore will not be considered, but these features may be easily incorporated in the analysis.

Because gun tubes have been around a long time, they have undergone an evolutionary optimization. The wise man pays careful attention to this before attempting a "revolutionary" approach to materials design. An excellent background on gun tube design may be found in the AMC pamphlet [1].

The perspective of this paper will be framed in the language of systems design as applied to materials. For a background on this, the reader is referred to the many papers by G.B. Olson and his students [2-9]. The one-page flow-block diagram for a tank gun is shown in Figure 1. Any materials system can be examined in terms of PROCESSING/ MANUFACTURING, STRUCTURE/COMPOSITION, PROPERTIES/BEHAVIOR and PERFORMANCE/FUNCTIONS. COST is located on one end next to PROCESSING/

MANUFACTURING, because this step is normally associated with the greatest cost. On the other end, near PERFORMANCE/FUNCTIONS is VALUE. This is the value that the system provides to the user. Cost is very important to the gun tube materials system design, because if a gun system becomes too costly compared with the value provided to the user by a competing type of system (such as missiles), the user will vote with his wallet (assuming a free market).

We break the gun tube down radially into three components or zones: the coating, the liner and the jacket. A gun tube may have all three of these components made from the same material (many do), or, at the other extreme, it may have a continuous gradation of materials from the coating through the liner to the jacket. This is known as a functional gradient material, or FGM. There are past and present Army and Navy SBIR programs whose objective is to produce a FGM gun tube.

Currently, all fielded gun systems (that the authors are aware of) use tubes that are monobloc steel, except the .50 cal M2 machine gun, which has a Stellite insert. The steel is generally a low alloy medium carbon Ni-Cr-Mo steel tempered in Stage III. Steel is an excellent material for this application because it possesses the necessary specific strength, is somewhat resistant to erosion, is fabricable, and inexpensive. In service, it behaves predictably and repeatably.

Before WWII, the service life of gun tubes was generally based on fatigue. As performance increased during that war, thermochemical erosion of the bore became the determining factor of service life. This trend has shown no signs of abating. Throughout the gun's life, the amount of erosion is measured with various kinds of mechanical gages. At some point the amount of erosion exceeds a certain limit, based on prior testing, and the tube is retired from service. Ultimately, however, the performance attributes that are degraded by erosion are dispersion and muzzle velocity. Erosion would play no role in gun tube (or propellant) materials design if it did not degrade these valuable performance attributes.

COATINGS

The coating is the most difficult part of gun materials systems design. The list of required and desired properties is long, and a material that satisfies the list completely does not exist. Trade-offs must be made, and that is where systems design comes in. There are also very constraining requirements of the coating process. The process must be able to produce a coating with extremely good adhesion, to the point where it is considered to be metallurgically bonded. In welding terms, it must have 100% joint efficiency. To this end, some interface mixing is desirable. Because large caliber gun tubes will continue to be made from autofrettaged quench-and-tempered low-alloy steel into the foreseeable future, the coating process must not heat the steel substrate to above the stress-relief temperature of about 400°C. There are geometrical and produceability constraints as well. The process must be able to coat the inside of a tube as small as 90 mm and as long as 9 m. If the tube is rifled, it must be able to coat the sides of the rifling. Finally, the process should allow the whole tube to be coated within one 8 hr shift.

It is very difficult to adequately simulate the gun environment for the purposes of coating testing. Furthermore, a particular gun system will have a unique propellant gas chemistry, wall temperatures, heat input to the barrel, ballistic cycle time and duty cycle. A capacitive discharge or excimer laser can simulate the thermal pulse. A vented combustor or ballistic compressor can simulate the thermal pulse, the propellant chemistry and the gas

cross-flow velocity. Pin-on-disc testing can simulate the mechanical forces and rotating band wear in a gun tube, although the higher sliding speeds are difficult to obtain. Adhesion/ cohesion can be checked by scaled-up scratch testing. After a series of these kind of laboratory tests have been conducted, coatings are generally tested in a subscale gun system before the investment is made in large caliber.

Adhesion/Cohesion

The coating must possess complete adhesion when produced and throughout its service life, since coating life determines gun tube life. The coefficient of thermal expansion should be similar to or higher than substrate, so that when the tube heats, there is no stress acting to pull the coating off. The modulus of the coating should be similar to or lower than substrate so that when the tube is stressed by firing, the stress is transferred to the substrate. There should be no chemical reaction with substrate. This is a difficult requirement to meet: the coating is in intimate contact with the substrate, and the couple is heated by firing. Most materials couples will react, or at least, will interdiffuse. It is desirable for the coating to be under a residual compressive stress. Such a stress state will promote adhesion. "Cohesion" is the cohesiveness of the coating layer itself. It does no good to have complete adhesion if the coating separates (delaminates) within the coating layer.

Chemical Barrier

Once a coating can be made to stick, it must provide a chemical barrier for the substrate against the erosive effects of the hot propellant gasses. The coating must be free from cracks as-produced and in service. Any cracks will be exploited by the very aggressive environment of propellant gasses during firing, and the substrate will be attacked. These cracks will also be wedged and racheted open by microscopic debris during firing, and after firing, the substrate can be attacked by simple corrosion. There should be a low solubility of the elements hydrogen, carbon, nitrogen and oxygen if these will degrade the substrate (as in the case of steel). The coating should also have a low reactivity to these elements, that is, there should not be a large negative free energy of reaction at the temperatures, pressures and chemistry encountered during firing. The CO/CO_2 ratio of the propellant gasses is typically used to measure their carburization potential, and for fielded solid propellants is in the range of about one to ten. Liquid propellant LP 1846 has a very different CO/CO_2 ratio, about 0.02. This is very oxidizing, and leads to rapid erosion of the combustion zone materials. When the propellant was modified by adding just 4.76% fuel (TEAN), the CO/CO_2 ratio increased to about 0.4, decreasing the rate of erosion of PH13-8Mo by over 16 times [10].

Thermal Barrier

The coating also serves as a thermal barrier, insulating the substrate from the damaging effects of heat input from high temperature propellant gasses. A good thermal barrier should have a low thermal conductivity and a high heat capacity. Additionally, it should be thermally stable and "heat resistant." This term encompasses a number of properties, including: a high melting point, a high hot hardness, thermal shock resistance, and

a lack of phase transformations throughout the service temperature envelope (typically, -60°F to the melting point). The thermal properties of the coating, along with its thickness, should prevent phase transformation or reaction of the substrate. It does this by damping out the high temperature pulse. In the case of a steel substrate, the martensite → austenite phase transformation occurs at about 727°C. When this temperature is exceeded, the transformation causes a discontinuity in the thermal expansion coefficient, resulting in large local strains. Because the steel is also soft at this temperature, the strain is taken up plastically rather than elastically. On rapid cooldown, such as in a gun, the plastically-deformed austenite transforms back to martensite. This martensite, however, is hard and brittle, and so cracks instead of plastically deforming to accomodate thermal stresses on further cooling. This is called heat checking. Obviously, this phase transformation really wreaks havoc with the integrity of the coating. It will tend to thermal fatigue and crack the coating, as well as promote de-adhesion.

Mechanical Properties

The coating/liner must be strong enough at the service temperatures to withstand the forces imposed by the projectile (rotating and obturator bands and bourellet) and the propellant gas "wash." If the tube is rifled, there must be sufficient strength to support the rifling torque. Furthermore, a high velocity rifled gun tube is subject to muzzle wear [11]. The coating/liner should possess enough strength to withstand this kind of mechanical wear. Rotating band wear is accelerated by a rough bore surface. If the band wears out before muzzle exit, there will be projectile steel sliding against the bore, leading to muzzle wear. The coating/liner must be smooth enough to preclude premature band wear-out.

Candidate Coating Materials and Processes

A coating material that possesses all these properties does not exist at present. If one looks at the periodic table of the elements and their phase diagrams, one can generate a fairly short list of candidate materials in two classes: (1) refractory metals and (2) ceramics. There does not appear to be any intermetallics that have melting points high enough to compete with these two classes.

The refractory metals are Cr, Nb, Mo, Ta, W and Re. Electroplated chromium has worked well in the past, but it has some undesirable features. Its melting point is not very high, and as an electroplate it is too thin to insulate the underlying steel. Because it is thin, it does not damp out the thermal pulse, so that the underlying steel transforms. This promotes chromium cracking; cracking leads to coating failure. If it is plated thicker, the tensile residual stresses in the plate (inherent in the process) and low adhesive strength cause the coating to spall off. Unalloyed Nb is too soft, and its alloys have not been explored as a coating material. The advantages are that its modulus is similar to steel, and it is not as expensive as other refractory metals. Molybdenum tends to be easily embrittled by hydrogen. Alloys of Mo-Re show better ductility, but are expensive. Tantalum has been shown to work well unalloyed, and even better alloyed. However, it is the second-most expensive refractory metal. Tungsten and its alloys are very difficult to process, and easily embrittled by hydrogen. Rhenium is the most expensive refractory metal by far. It has been shown to promote ductility when used as an alloying agent in the other refractory metals.

It is instructive to examine the impact of coating material cost on the cost of gun tubes. For example, to coat a 120 mm M256 tank gun with 0.5 mm of material for its entire length is a volume of about 500 cm^3 of coating material. Using the 2001-2002 Alfa catalog [12], the price of each candidate material was used to roughly calculate the material cost of the coating. The least expensive forms of the pure elements were chosen for this exercise.

TABLE 1. Coating Materials Cost Calculations

Element	Form	Cost $/gm*	Density g/cm^3	Mass Req'd (g)	Coating Cost ($)
Cr	Broken plate	0.69	7.1	3550	2450
Nb	0.75 in rod	0.24	8.6	4300	1030
Mo	0.5 in rod	0.36	10.2	5100	1840
Ta	0.5 in rod	1.58	16.6	8300	13100
W	0.5 in rod	0.48	21.0	10500	5040
Re	0.2 in rod	25.8	19.3	9650	249000

*reference: 2001-2002 Alfa catalog [12]

These calculations will change if an alloy is used, if the material cost of the precursor form used is different, if the thickness of the coating is different, if the gun tube is partially coated, or if there is any amount of coating removed during final machining. It is readily apparent that rhenium is a non-starter solely based on cost, although it may be used as an alloying element. It is also readily apparent that there is a significant cost savings if a niobium alloy can be used.

The oxide, carbide and nitride ceramics can have extremely high melting points with excellent chemical resistance. Because of this, there have been a few attempts to use ceramics as coatings. Their downfall in the past has been poor adhesion, poor thermal and mechanical shock resistance [13].

There are many, many coating processes. Most of them can be removed from further consideration based on the manufacturing constraints above. As stated above, electroplated chromium has been perfectly adequate in the past. Unfortunately, the other refractory metals cannot be plated from aqueous solution. They can be deposited from fused salts, but this anneals the steel substrate [14, 15]. Thermal spraying of various types is feasible, but they either anneal the substrate or do not possess enough adhesion/cohesion in the service environment [16]. High rate magnetron sputtering shows promise [17]. Ion beam assisted deposition is too slow to build up the required thickness [18]. CVD produces a very uniform adherant coating, but currently operates at a temperature that anneals the substrate [19]. Laser cladding exhibits excessive mixing of the coating material with the substrate [20]. And so on. The coating process that best meets the above requirements is explosive bonding. A thick coating can be deposited with perfect adhesion very rapidly with negligible heating of the substrate. The refractory metal can be an alloy, but it must possess "enough" ductility. It is not difficult to integrate into the manufacturing sequence.

Under an ARO-ARL Phase II SBIR, TPL, Inc. explosively bonded tantalum on three 25 mm M242 Bushmaster barrels. Two of these barrels were test-fired at Aberdeen Test Center the week of 26 March 2001 with funds provided by the Naval Surface Warfare Center. The ammunition used was from the initial lot of M919 APFSDS-T, without the ablative paste. This lot was not fielded. It uses superhot HES9053 propellant that has an adiabatic

flame temperature of about 3700 K. This cartridge resembles a scaled-down high-performance tank gun cartridge. Standard Bushmaster barrels last 200-300 rounds with this ammunition. A no-twist rifled barrel and a smoothbore were tested, using the same firing schedule as was used with standard barrels. The rifled barrel was still serviceable after 600 rounds. The remaining 1385 rounds were fired through the smoothbore, and it continued to show good dispersion. Inspection of this barrel following testing showed that it only just started to breach the tantalum cladding. This barrel demonstrated a life in excess of five times the life of a standard barrel.

LINER

As opposed to the coating, the liner must be a stressed part of the gun tube. This may be part of a monobloc gun tube, or part of a built-up gun tube. The liner must have a high specific strength and a high fracture toughness. It should be under a residual compressive stress to maximize the mechanical efficiency of the gun tube. The amount of residual stress necessary depends on the liner's mechanical properties. It should have some amount of heat resistance (high melting point, retains modulus and strength). A low thermal conductivity and high thermal shock resistance are also advantageous.

Liners generally have been steels (16-inch Naval gun) or Stellite (.50 cal M2 machine gun). There have been numerous programs to use ceramics as liner materials. These have failed in the past because of the quality of the ceramic, and the inadequate axial preload in the guns tested. Another problem is the liner "walking" out of the jacket, or moving around inside the jacket as the gun is fired and thermally cycled. Also, heat-shrinking does not generate compressive residual stresses comparable to autofrettage. Coextrusion, as well as gas pressure bonding of a liner with a jacket have been tried [21], but these become difficult (expensive) in large caliber applications.

Built-up gun tubes are inherently expensive, especially as one goes up in size. Two-piece (liner-jacket) tubes that are accurately machined and heat-shrink-fit together are the most difficult to manufacture. These can be less expensive if the liner is made up of short sections. The cost of a built-up gun tube can be significantly reduced and the liner-jacket interface can be improved if a jacket can be wrapped around a liner.

JACKET

The jacket may also be part of a monobloc or built-up gun tube. Its materials requirements are similar to those of the liner: a very high specific strength and high fracture toughness. As a consequence of mechanical equilibrium, it will be under a residual tensile stress. It should also have a reasonable melting point and a high thermal diffusivity to dissipate waste heat faster.

Jacket materials have generally been high strength steels; they are predictable materials, and designers feel comfortable with them. They are inexpensive. The next best pressure vessel material is filament-wound graphite-epoxy composite. The polymer-matrix composites would be excellent low-weight alternatives to steel, except they do not possess the melting/decomposition point necessary in combination with their low thermal diffusivity. If the liner has sufficiently low thermal diffusivity, more heat is kept in the propellant gasses and less is put into the tube. There are some ceramics that possess a low thermal diffusivity

with good mechanical properties. ARDEC has an SBIR program that is exploring the combination of a ceramic liner that is put under the required preload by a polymer-matrix composite jacket.

Metal-matrix composite jackets [22, 23] have been tried with some success, but their inherent expense, coupled with their difficulty in manufacture has put them out of reach in the past. This may be changing with the inexpensive Nextel 610 fiber by 3M, and a program at ARL is examining this prospect.

"PAPER" GUN TUBES

Based on the above analysis, we are now in a position to design gun tube materials on paper. We will examine a tank gun tube, an artillery gun tube, an aircraft machine gun tube, and a mortar tube.

Tank Gun Tube

The tank gun barrel envisioned is similar to the existing 120 mm M256. It is a smoothbore, firing AP and HE projectiles with polymeric obturator bands. The "paper gun" has an autofrettaged monobloc high strength steel liner/jacket similar to the M256. However, it makes use of increased lethality propellant, which has a high adiabatic flame temperature, and so is quite erosive to steel. Electroplated chromium provides inadequate protection, since the substrate steel melts under the propellant's high flame temperature. Instead, a thick refractory metal is explosively-bonded to the steel substrate. How this would be produced is shown in Figure 2. The explosive bonding process must occur after the barrel forging has been heat-treated, autofrettaged, and the bore rough machined. The wall thickness must be fairly thick during explosive bonding, or else there will be plastic deformation of the tube. If a full-length clad is required, this difficulty can be obviated by the use of a suitable momentum trap around the thinner parts of the barrel.

Artillery Gun Tube

The "paper" artillery barrel is an artificially-cooled smoothbore, firing folding-fin high capacity projectiles with polymeric obturator bands. It is also an autofrettaged monobloc high strength steel liner/jacket with an explosively-bonded coating. The manufacturing sequence is similar to that for the paper tank gun tube in Figure 2.

However, if it must fire the existing inventory of 155 mm projectiles, it must be rifled. While the explosively-bonded coating can be made as thick as the depth of rifling, it must also be able to transmit the rifling torque to the projectile. It is unknown at this time whether a sufficiently strong refractory metal can be successfully bonded. The alternative is to initially produce a rounded rifling profile (similar to what is currently done for chromium electroplated rifled tubes). The refractory metal is bonded over that, and the tube is finish rifled. The difficulty of following the original rifling with the finish rifling tooling is acknowledged. The manufacturing sequence is shown in Figure 3.

Aircraft Machine Gun Tube

Although this application is not large caliber, it makes sense to present some ideas here. Ordinarily, a barrel that is lighter than a steel barrel is not really desirable due to stability issues. However, aircraft design places a high value on weight, and aircraft are inherently unstable firing platforms anyway. These guns are typically rifled with a progressive twist, and fire projectiles with polymeric or metallic rotating bands. For this application, the "paper" gun tube has no coating. It has a zirconia or silicon nitride ceramic liner with a graphite-epoxy composite jacket. The jacket is wrapped in tension over the liner, putting the necessary pre-stress (hoop and axial) on the liner. An ARDEC SBIR and a proposed ARL program are currently addressing this kind of a gun tube. The manufacturing sequence is shown in Figure 4.

Mortar Tube

Mortar and recoilless rifle barrels should also be lightweight. Titanium alloys have been tried for each [24, 25], but they suffer from extremely rapid erosion. An explosively-bonded refractory metal coating would prevent this. However, because it is a fairly thin-walled tube, the proper momentum trap must be devised to prevent the tube from plastically deforming during bonding. The tube gets quite hot in service during maximum firing rate, so the titanium must be a high temperature alloy, such as TIMETAL® 1100 or TIMETAL® 21S. The manufacturing sequence is shown in Figure 5.

An ARL program is currently examining the feasibility of using metal-matrix composites as a jacket material for mortars. These could be pressure cast around a steel liner. However, the required fatigue, thermal fatigue and high temperature fatigue must be demonstrated.

SUMMARY

There have been countless gun tube materials design experiments over the past century. Our level of understanding of the materials property requirements and materials processing, and the materials science and systems design that ties the two together allows us now to design gun tube materials systems that optimize value and cost. Using these principles, four gun tube materials systems (a tank gun, an artillery piece, an aircraft machine gun, and a mortar) were designed.

ACKNOWLEDGMENTS

The authors wish to thank Bob Lowey and Tom Schilling of TPL, Inc. for their interaction on explosive bonding Rick Snow and David Byron of MagTech, Inc., Shel Cytron of ARDEC and Andy Wereszcak of ARL have provided valuble insight into the use of ceramics in gun tubes. Conversations with Paul Conroy and Charlie Leveritt of ARL have been invaluble to our understanding of interior ballistics and propellants.

REFERENCES

1. "Research and Development of Materiel, Engineering Design Handbook, Gun Series, Gun Tubes," AMCP 706-252, U.S. Army Materiel Command, Washington DC (1964).

2. G.B. Olson, "Materials Design: An Undergraduate Course," *Morris E. Fine Symposium*, TMS-AIME, Warrendale, PA (1991) pp. 41-48.

3. C.J. Kuehmann, J. Cho, T.A. Stephenson and G.B. Olson, "Systems Design of High Performance Steels," in *Sagamore Army Materials Research Conference Proceedings: 40th*, E.B. Kula and M.G.H. Wells, eds. U.S. Government Printing Office, Washington DC (1994) pp. 337-355.

4. C.J. Kuehmann and G.B. Olson, "Computer-Aided Systems Design of Advanced Steels," in *Proceedings of an International Symposium of Phase Transformaaations During the Thermal/Mechanical Processing of Steel -- Honoring Professor Jack Kirkaldy*, E.B. Hawbolt et al. eds., Metallurgical Society of the Canadian Institute of Mining, Metallurgy and Petroleum, Vancouver BC (1995) 345-356.

5. G.B. Olson, "Materials Design: Building a Better Martensite," in *C.M. Wayman International Conference on Displacive Phase Transformations and Their Applications in Materials Engineering*, TMS-AIME, Warrendale PA (1996).

6. G.B. Olson, "Brains of Steel: Designing Metallurgists," *ASM Alpha Sigma Mu Lecture*, ASM, Metals Park OH (1996).

7. G.B. Olson, "Systems Design of Hierarhically Structured Materials: Smart Steels," in *Proceedings of an International Forum on Creation of Super Metallic Materials Consisting of Amorphous, Nanoscale and Mesoscopic Structures*, R&D Institute of Metals and Composites for Future Industries (RIMCOF), Tokyo, Japan (1997).

8. C.J. Kuehmann, "Gear Steels Designed by Computer," Advanced Materials & Processes, May 1998, ASM, Metals Park OH.

9. Erik Davis, "Forging the Dragonslayer," *Wired Magazine*, 9.02 (February 2001), San Francisco CA. Also http//www.wired.com/wired/archive/9.02/dragonslayer.html.

10. W.H. Reitz, L.S. Ingram, Shieh, J.S. Montgomery and A. Fish, "Combustion Zone Material Erosion Combatibility Assessment of XM46 Liquid Propellant," in *FY1998 Liquid Propellant Technology Program Final Report*, U.S. Army Research Laboratory, Aberdeen Proving Ground MD (1999).

11. R.S. Montgomery, "Muzzle Wear of Cannon," *Wear*, V. 33 (1975), pp. 359-368.

12. "2001-2002 Materials Catalog," Alfa Aesar Company, Ward Hill MA (2001).

13. I.C. Stobie, R.P Kaste, B.D. Bensinger, T.L. Brosseau and R.J. Ward, "Screening Gun Tube Coatings' Response to Combustion Gases, Ballistic Research Laboratory Technical Report ARBRL-TR-02396, Aberdeen Proving Ground MD (1982).

14. I. Ahmad, G.J. Janz, J. Spiak and E.S. Chen, "Electrodeposition of Refractory Metal Coatings (Tantalum and Columbium) from Fused Salt Electrolytes," in *Proceedings of the Tri-Service Gun Tube Wear and ErosionSymposium*, U.S. Army Armament Research and Development Command, Dover NJ (1982).

15. P.D. Aalto, G.P. O'Hara and G. D'Andrea, "Advaanced High Performance Guns with Refractory Liners for Erosion Resistance," in *Proceedings of the Tri-Service Gun Tube Wear and ErosionSymposium*, U.S. Army Armament Research and Development Command, Dover NJ (1982).

16. J.S. Montgomery, unpublished research on HVOF and plasma sprayed coatings (1999)

17. J.F. Cox, High Rate Sputtering of Tantalum onto Steel," in *Proceedings of the Tri-Service Gun Tube Wear and ErosionSymposium*, U.S. Army Armament Research and Development Command, Dover NJ (1982).

18. J.K. Hirvonen, private communication (1997).

19. J.A. Sheward, "Erosion Resistant Coatings for Gun Bore Protection," in *Proceedings of the Tri-Service Gun Tube Wear and ErosionSymposium*, U.S. Army Armament Research and Development Command, Dover NJ (1982).

20. R.B. Beal, J. Dolega, E. Chester and T. Watmough, "Gas-Pressure Bonding of Multilayer Gun Barrels," Rock Island Arsenal Technical Report SWERR-TR-72-42, Rock Island IL (1972).

21. J. McCay, unpublished research (2000).

22. R. Hasenbein, E. Hyland and G. Cunningham, "Metal Matrix Composite-Jacketed Cannon Tube Program," Benet Laboratory Technical Report ARCCB-91027, Watervliet NY (1991).

23. E. Troiano, "Applications of Advanced Materials to Cannon Production," Benet Laboratory Technical Report ARCCB-92026, Watervliet NY (1992).

24. J.J. Burke, "Historical Monograph: Ordnance Corps Titanium Program 1946-61," Watertown Arsenal Monograph MS-39, Watertown MA (1962).

25. R.S. Montgomery, "Wear of Titanium Alloy in Mortar Tubes and Effect of Anodizing (Declassified)", Watervliet Arsenal Technical Report WVT-7013, AD 509 634L, Watervliet NY (1970).

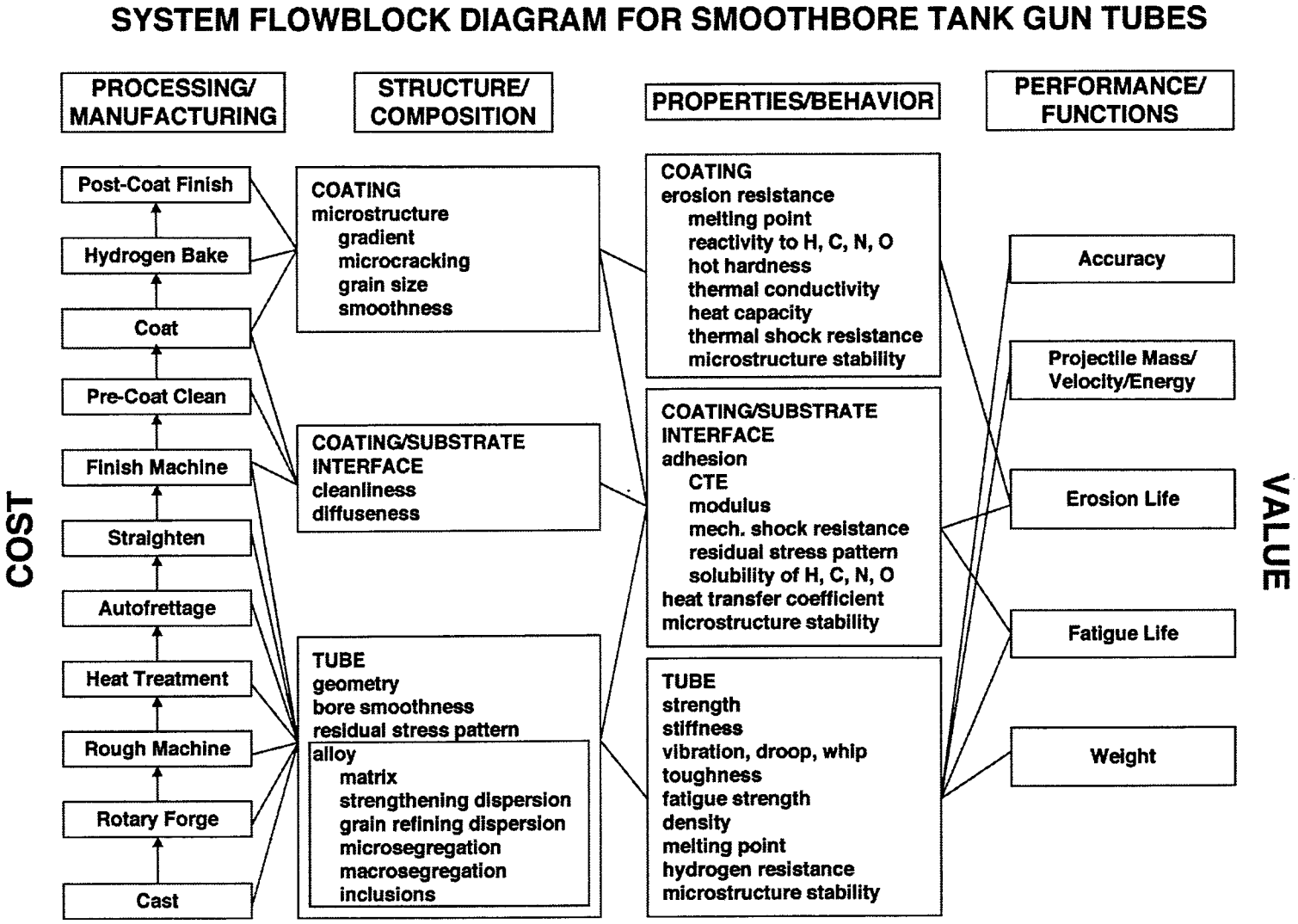


Figure 1. Tank Gun Tube Flow-Block Diagram

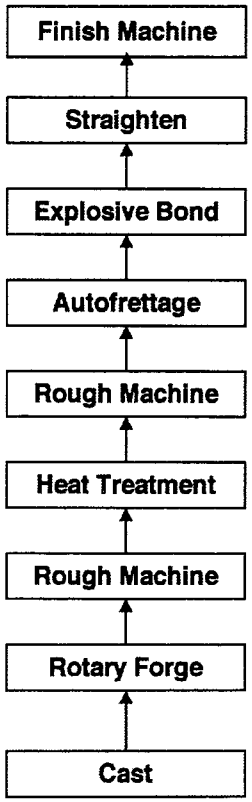


Figure 2. Manufacturing Sequence for a"Paper" Tank Gun Tube

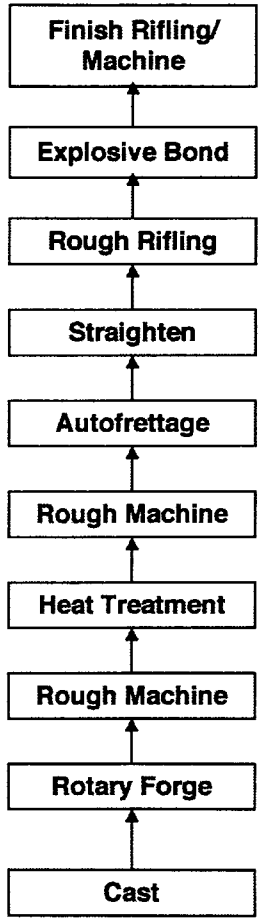


Figure 3. Manufacturing Sequence for a"Paper" Artillery Gun Tube

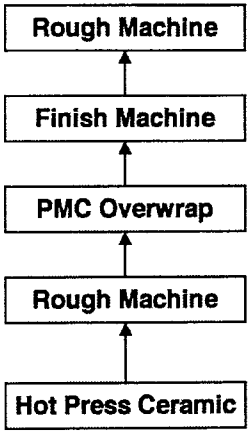


Figure 4. Manufacturing Sequence for a"Paper" Aircraft Machine Gun Tube

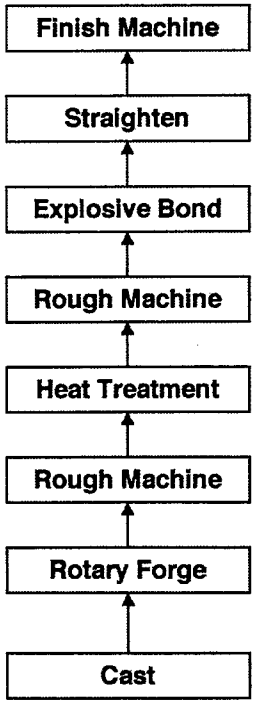


Figure 5. Manufacturing Sequence for a"Paper" Mortar Tube

OFF THE SHELF TECHNOLOGY FOR GUN BARREL STRAIGHTNESS MEASUREMENT
10TH U.S. ARMY GUN DYNAMICS SYMPOSIUM

J. Garner,[1] and T. Marrs,[2] T. Erline,[3] and M. Bundy[4]

[1] *U.S. Army Research Laboratory, Aberdeen Proving Ground, MD 21005*
[2] *Aberdeen Test Center, Aberdeen Proving Ground, MD 21005*
[3] *U.S. Army Research Laboratory, Aberdeen Proving Ground, MD 21005*
4 U.S. Army Research Laboratory, Aberdeen Proving Ground, MD 21005

Gun barrel straightness is one of several manufacturing variables that must be held to a specified tolerance. Therefore, barrel centerline measurement is a necessity. In the past, centerline measurement techniques have been developed specifically for this application, and production of such machines has been made on a small quantity basis. This paper will describe the application of an off-the-shelf, three-dimensional laser tracker system, manufactured by Spatial Metrix Corporation (SMX), to measure the bore centerline of a 120-mm tank gun barrel. An introduction/tutorial on barrel straightness terminology, coordinate systems, and the level of precision required for such measurements is presented. A side-by-side comparison is then made between the SMX-based measurement and the standard/conventional measurement of several barrel centerlines, with the pros and cons of each system noted.

INTRODUCTION

It has long been asserted that barrel centerline shape substantially affects gun accuracy. Projectile developers are quick to request and select tubes that exhibit smooth centerlines to ensure the least amount of in-bore disturbance possible to their designs. Tank trainees also desire near-norm centerlines since their qualification tests (tank table tests) could be jeopardized by atypical tubes. Thus, the ability to acquire and access centerline data is important to researchers as well as users.

TERMINOLOGY & METHODOLOGY

Barrel straightness is defined by specifying the path of the barrel's symmetry axis. This can be determined, for example, by measuring the location of a bore-centered target as it moves down the tube. It is common practice to reference the bore centerline to either a line drawn through the center of the bore at its end points, Fig. 1a, or a line drawn through the center of the bore at its support points, Fig. 1b (the latter definition [b] is adopted here). Watervliet Arsenal (WVA) gun centerline measurements are typically done in accordance with Figure 1a. This method is chosen because a maximum bend of 2 mm over the entire length is described by a maximum radius (basically``y'' from the line joining the breech and muzzle

centers) calculation at any one point. Figure 1a shows only the ``y" distance to the centerline as ``x" deviation contributions are typically much smaller.

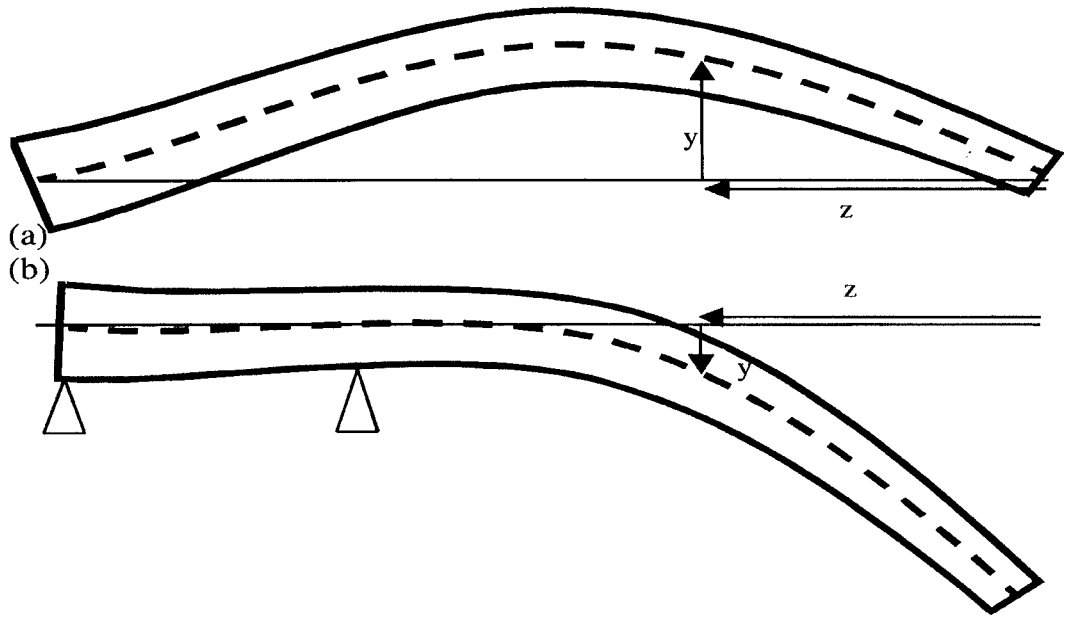


Figure 1. Two Methods of Specifing Barrel Curvature: (a) Relative to a Line Through the First and Last Bore Center Measurements, or (b) Relative to a Line Through the Bore Center at Its Support Points.

Barrel centerline measurements must account for gravity effects as well as nonstraightness of the bore. These attributes are separated by subtracting measurements of the tube at 12 o'clock and 6 o'clock orientations. The difference is the barrel centerline. The removal of the centerline deviations from a measurement reveals the gravity effects or , "droop" as it is termed. Tube measurements are taken every 200 mm. A barrel acceptance criteria states that the tube centerline, excluding droop, must not vary by 0.5 mm over a 600mm distance, or by 2 mm over the entire length of the tube (1,2). These criteria created the need for a coordinate system that is easily understood and descriptive. The result was simply to have a translating "X-Y" (2-D) coordinate at each measurement location. Positive Y is upward and positive X to the right. A self-centering target is moved down the tube and its displacement from a virtual perfect centerline noted. Measurements are performed with the tube held in the same manner as in the tank. These zero points are located at 670 and 1850 mm from the rear face of the tube. Neither the Aberdeen Test Center (ATC)or WVA measurements include the chamber area and are simply for the projectile travel length. The centerline plots, such as Figure 1, begin at 230 mm (near the muzzle) and end at 4630mm (near the bore start). Unfortunately, ATC measurements are taken in reverse of WVA as their measurements begin near bore start and end near the muzzle. ATC has adhered to making measurements in the

same bore locations as WVA for easy barrel comparison and the figures presented follow this convention. ATC protocol is to take 3 measurements and use an average. As noted, the straightness measurements are composed of X and Y displacements as the measurement devices move down the tube. The selected figures that follow simply give ``Y'' measurements, since the elevation plane is where the largest deviations are commonly measured.

OPTICAL CENTERING TECHNIQUE

An older method for estimating gun tube straightness is the optical method (3). This method requires an alignment telescope and a backlit target on a bore-riding carrier. This method's accuracy is largely dependent on the skill of the operator. The optical method is time consuming due partially to setup. The error involved is most easily reduced by averaging measurements. Figure 2. is derived from a set of optical measurements. The differences in the passes for the elevation graph are primarily caused by differences in resolving the motion of the target. The differences between the graphs are on the order of 0.10 mm (.004 inches).

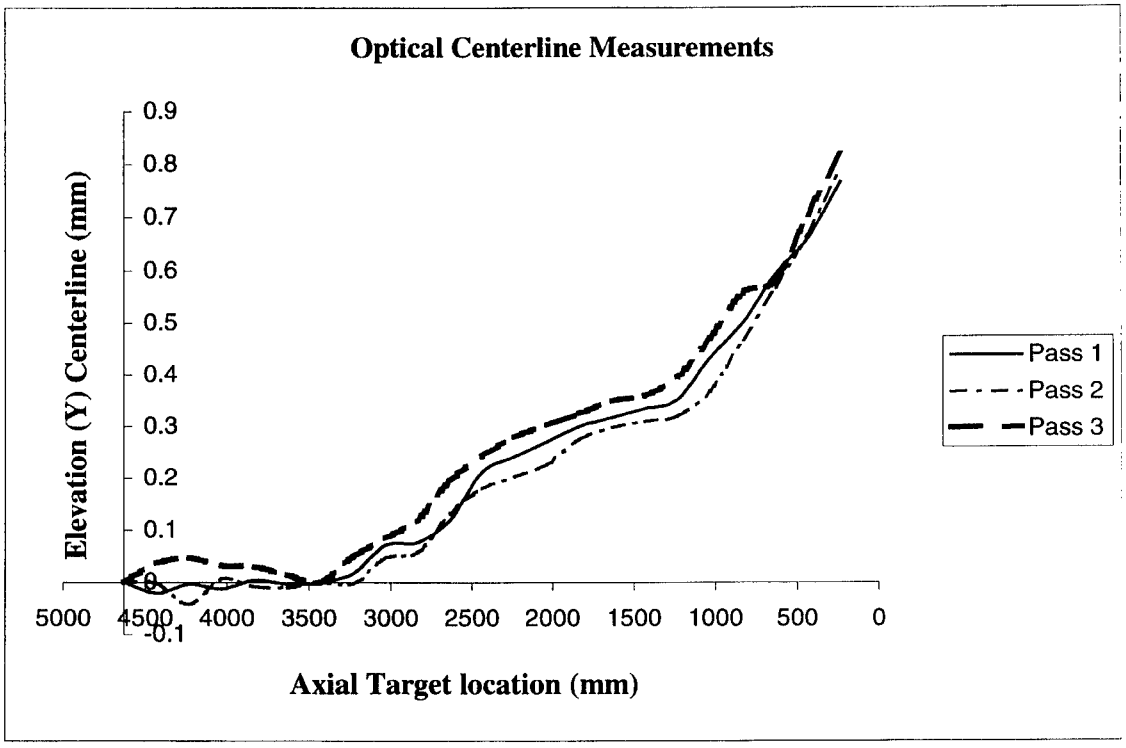


Figure 2. Typical tube centerline elevation (Y) deviations using the optical method.

A step toward reducing the operator influences is offered in the Gun Tube Inspection Station (GTIS) method.

GTIS MEASUREMENT TECHNIQUE

The 120mm tank gun tube straightness is initially measured with a laser device, known as the GTIS (located at the manufacturing plant in Watervliet Arsenal, NY) (4,5,6). These measurements involve sensing the location of a laser spot on a target and the motion of

the target relative to the reference laser beam, as the target moves down the bore. The laser emitter fixture and the target are initially aligned (to establish a reference centerline) at the muzzle and bore start. The target resolution, as to where the laser beam strikes it, is governed by the amount of pixels the target has and the spread of the beam. Ascertaining where the beam strikes the target requires the determination of the center of the beam. While the laser beam is a focused source, its spread at distance dictates that an averaging procedure be used to compute where the beam center actually is. This equipment generally produces consistent results. Unfortunately the system requires warm-up over the course of 20-30 minutes. Measurements done before this warm-up period is complete show a bias not found in later readings. Concerns have also been expressed as to inaccuracies occuring from a rotation of the target head as it traverses the barrel. These are small but nonzero. Operator error is generally minimized over the optical method. One drawback of the GTIS equipment is that it has shown maintenance deficiencies. This state of affairs forced ATC to use the optical method more frequently than the GTIS equipment. Figure 3 shows a set of GTIS measurements for an L55 barrel.

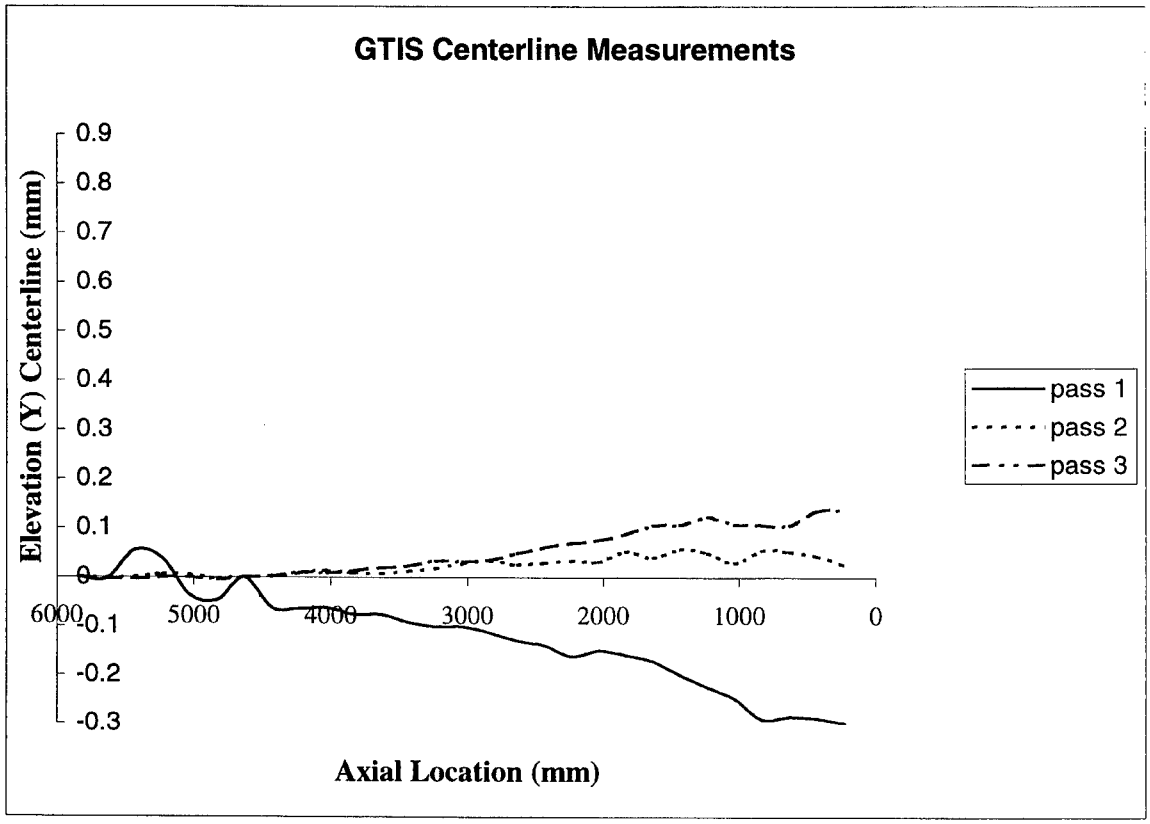


Figure 3. GTIS Centerline Elevation Measurements on an L55 barrel.

SMX MEASUREMENT TECHNIQUE

The Spatial Metrix (SMX) laser metrology system offers a host of improvements over the current gun tube measurement methods. A picture of the system is shown in Figure 4. The system uses a single tracking head which follows a Spherically Mounted Reflector

(SMR). This is opposed to laser based triangulation methods that require the setup of 2 receiving heads. The setup for the SMX system requires environmental conditions of over 40 and below 110 F (7). These restrictions are based on the ability of the equipment to modulate the laser beam such that it produces a constant wavelength of light. Operator checks are also required to assure that angular measurements and optical return power levels are satisfied. Checks for point closure (the ability to remeasure a point and get the same value as that obtained previously) are easily performed by returning to measured points and noting differences (if any) from prior measurements. Tolerance levels can be input to warn of potentially inaccurate readings. These setups and verifications take approximately 20-30 minutes to perform. The SMX system uses interferometry measurements from the laser beam returns to determine the location of the SMR. The SMR is positioned in a fixture mounted to the same self-centering target apparatus used in the optical method discussed previously. Centering of the SMR on the target is done once by the centering of a nest, in which the SMR rests. During measurement, the SMR is moved to the preset axial locations used under the GTIS and optical measurement practices, and measurements are taken. Because the receiving head of the SMX system tracks the SMR's motion it continously measures location at a 1 kHz rate. It records this data when instructed and then averages the most recent

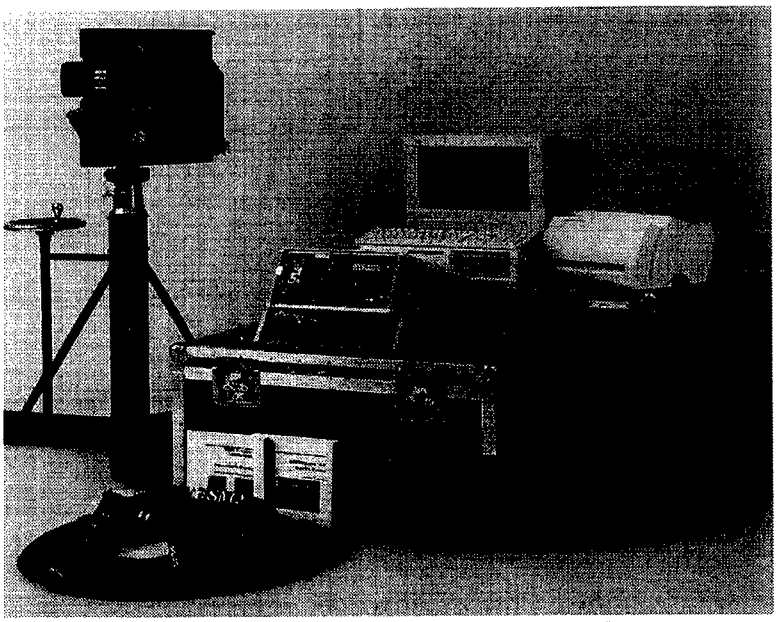


Figure 4. The SMX Tracker 4500 metrology system.

measurements to minimize the effect of spurious readings. Accuracies of approximately .0001 inch are realizable when measuring centerlines with the SMX system. This compares to a .001 inch accuracy using the optical method. Recording data with the SMX system simply requires the push of a button once the SMR is located at the desired measurement points. The burden of having to optically judge the change in location of the target center is removed, and the operator's biggest concern is assuring that readings occur at the proper axial points. Making centerline measurements in this manner (once the system is setup) is a 5 minute process. Other data acquisition techniques using the system may further reduce the measurement time to less than a minute. These techniques have not been pursued to date. A

comparison with previous methods is more obvious when axial measurement points are identical, and this temporarily precludes the use of the advanced method. These more advanced techniques also require slightly more familiarization with the system. They will eventually be employed. The removal of the judgement of target motion has also tremendously increased the repeatability of the measurements. This makes the system equally effective to all users with reasonable skill. Perhaps the best feature of the new measurement technique is the removal of pencil and paper for recording measurements. The measurements are stored electronically and are readily transferable to graphing packages for review. Furthermore the data is easily transferable via electronic means to interested parties. The elimination of computer data entry to facilitate dispersal is key to speeding the process and eliminating human error. Perhaps the most daunting attribute of the system is the $145,000 cost. This cost is easily offset in the amount of time saved in measurement, and data transmission and manipulation. New system costs are always a changing attribute as they typically drop over time as a technology becomes more accepted. The choice of accessories also impacts the cost of the system.

While other tasks are not discussed here, there are many other uses. The portability of the system and its ease of use make it ideal for accurate test instrument location surveys, fragment dispersal, damage measurements, and rapid contour and part characterizations as well. These uses also potentially offset the high cost.

Figure 5a offers the same graph shown in Figure 2. with the SMX data set superimposed for easy comparison to previous data set. The SMX data falls within the envelope of the optical measurement plots and is so repeatable that variations between passes are difficult to detect. The repeatability of the data is shown in Figure 5b. Small differences can be detected but these may arise from not matching axial location perfectly.

Figure 5a. Comparison of Optical measurement technique to SMX method.

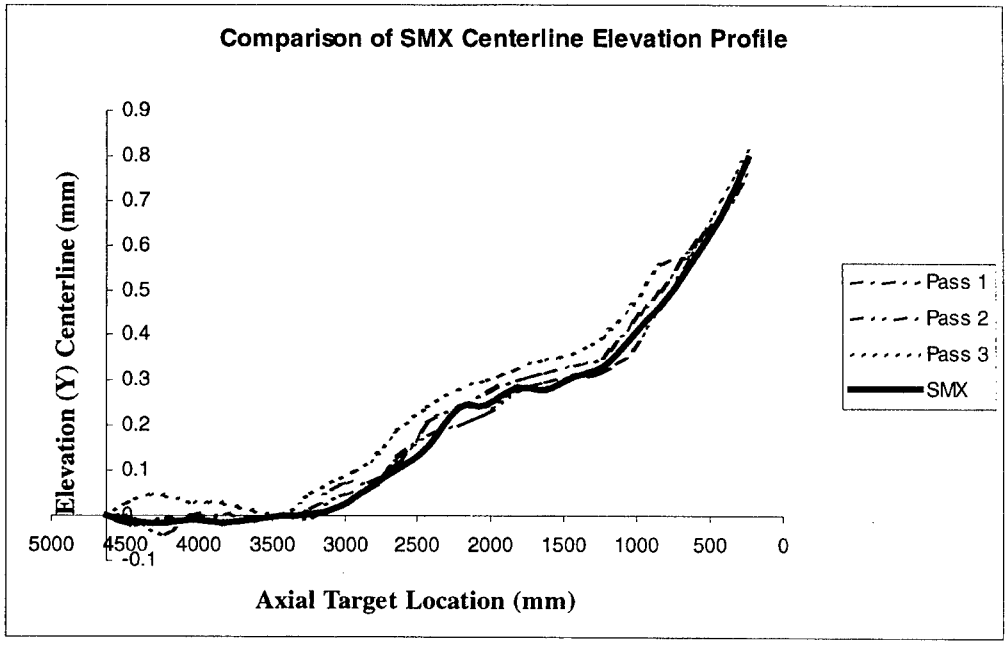
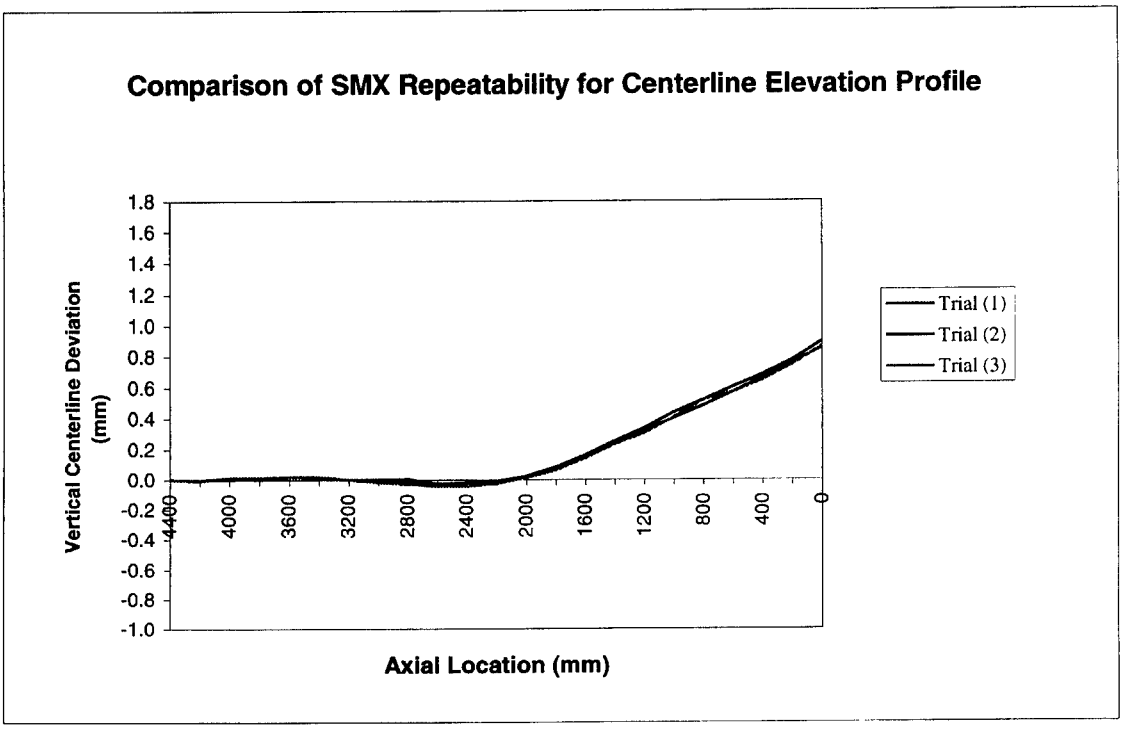


Figure 5b. Comparison of Repeatability of SMX method.



The difference detectable is perhaps .01 mm Lastly the maintenance required for the SMX system is a once per year cleaning and "tuning" of the optics and electronics. Spare parts (such as extra SMR's) are included as desired in the purchase package. SMR's generally get damaged as they are handled most frequently.

CONCLUSIONS

The SMX system is a significant advancement in the science of measuring gun tube centerlines. It conservatively allows bore measurement to proceed 10 times faster with a similar advance in data processing speed and distribution. The repeatability of the SMX system almost argues against doing more than one pass, though multiple passes are still performed to add an increased level of certainty to the data (multiple passes are also reasonable in light of the fact that each pass takes only 5 minutes). The SMX system's ease of use should expand the potential set of users as well. Enhancements to allow the measurement of tube diameter at axial locations with the SMX system are also in process. Despite the SMX system cost, it is a worthwhile step forward in accurately measuring gun attributes.

REFERENCES

1. 120mm, M256 Gun Tube Drawing 12528311, Sheet 1, Note 4, and Sheet 3, Note 1, US Army Armament Research and Development Command, Watervliet, New York, 1980

2. Military Specification MIL-C-13931, Cannon: General Specification for, paragraph 6.3.4, 1980

3. Weddle, A. L. "Methodology Investigation of Gun-Tube Straightness Measurements,"Aberdeen Proving Ground USACSTA-6439, October 1986.

4. Howd, C. A., "In-Process Straightness Measurement of Gun-Tubes," Watervliet Arsenal WVA-QA-9101, August 1991.

5. Wilkerson, S. A., "A Consistent Method for Determining Gun-Tube Straightness on the M256 120mm Gun," Proceedings of the 7th U. S. Army Symposium on Gun Dynamics, May 1993.

6. "Cannon Straightness Measurement", unpublished document received from Ken Insco, WVA, July 1991.

7. "SMX Tracker 4000/5000 Operator's Guide" SMX document 922-00-007 Rev. E Sec 10-3, 1999.

PERFORMANCE ENHANCEMENT AND HEALTH MONITORING OF A MEDIUM CALIBER GUN SYSTEM USING OPTICAL FIBER BRAGG GRATING SENSORS

C. LaVigna[1], J. Bowlus[1], H. Kwatny[1], S. Chen[2], H. Zhang[2], and S. Cytron[3]

[1] *Techno-Sciences, Inc., Lanham, MD 20706.*
[2] *University Of Maryland, College Park, MD 20742.*
[3] *U.S. Army TACOM-ARDEC, Picatinny Arsenal, NJ 07806-500.*

In this paper we present a novel Fiber Bragg Grating based system to provide real time monitoring of Round Exit Velocity (REV). REV can be used for automatic fuse setting in air burst munitions and as an indication of gun system performance. The REV data provided by this system can also be used to improve aiming accuracy, and to monitor barrel wear and corrosion. In this research, a prototype REV measurement system was designed, fabricated and tested on the 25 mm M242 Bushmaster cannon. Live fire tests were conducted in single shot and burst modes with various service rounds. The results of these test showed that measured REV was accurate to within 2-3% of a reference muzzle velocity radar reference system. The results also showed that REV could be accurately measured for each round in a burst at the standard M242 burst firing rates of 100 and 200 rounds per minute. The sensor system adds negligible mass to the weapon system and it is rugged and reliable.

INTRODUCTION

The purpose of the research was to develop a system to measure round exit velocity from measurements taken while the round is still in-bore through the use of surface mounted fiber optic strain sensors. The capability to monitor in the field, in real-time, the Round Exit Velocity (REV) for medium (and large) caliber cannons would be useful for improving gun system performance, for determining barrel health, and for enabling automatic fuse programming (setting) for air burst rounds.

Important measures of gun system performance include round impact accuracy and dispersion. One of the significant factors affecting the impact accuracy on target of a given round for a modern cannon is the accuracy of the azimuth and elevation coordinates computed by the fire control system. The computation of these coordinates is typically accomplished by means of solution of a set of external ballistic equations in which the REV of the projectile is a critical input. Currently, in most fielded gun systems (some field artillery systems are the exception), REV is not directly measured. Instead, it is estimated based on nominal ammunition requirement specifications. These specifications typically specify the REV mean and standard deviation requirements for qualifying rounds fired from a standard barrel at a nominal temperature. However, in the field, many factors such as ammunition temperature, barrel temperature, and barrel wear, to name a few, can affect REV. High ammunition temperature can affect the propellant burn rate resulting in a 5-10% increase in pressure and REV. Elevated barrel temperatures can affect the interior ballistics and cause bore expansion leading to blowby of propellant gases resulting in variations in REV on the order of 5%. Finally, barrel wear can cause

substantial REV reduction and increase in dispersion. Wear can lower REV by as much as 10-20% [1].

Since the accuracy of the ballistic solution for a given round depends in part on the accuracy of the REV estimate for that round, and since it is not possible to measure the REV for a given round prior to its firing, it is critical that the REV estimate be based on the best REV statistical data available for the current gun system and ammunition conditions. This means that a system that continuously measures REV should be able to provide a better estimate of the current REV statistics than the nominal qualification data and therefore a better REV estimate from which to compute the external ballistic solution.

In addition to improving the accuracy of the round impact by increasing the accuracy of the fire control ballistic solution, real-time REV monitoring can provide an indirect indication of barrel health and wear. Trends in the REV mean and standard deviation can be analyzed online, in real-time, and compared to acceptable values to determine the remaining useful life of the barrel. This differs from typical current useful life methods, which rely on tallying the number of rounds fired from a given barrel to determine when to change out a barrel.

Finally, on-line real-time REV monitoring can be employed in a real time automatic fuse programming system for air burst munitions on automatic medium caliber canons, such as the 25 mm M242 gun system. In this type of a system, the REV sub system would be integrated with the gun fire control system and an inductive based fuse setting system that would communicate time to destruct information to a timer-based fused munition shortly after it left the muzzle. A system such as this could enable automatic programming of fused rounds for each and every round in a burst.

In view of these potential benefits, the purpose of the research was to develop a system to measure the exit velocity of a round from measurements taken while it is still in-bore through the use of surface mounted fiber optic strain sensors. The research approach included designing, analyzing, fabricating and testing a fiber optic based strain sensor system for measurement of REV in medium caliber gun barrels. This system, called the Optical Fiber Round Velocity (OFREV) measurement system is based on the following operating principles. In typical gun systems, immediately after ignition, the propellant gases generate very high levels of pressure (>50 ksi for the M242 system) and start to accelerate the projectile down the bore of the gun barrel. As the projectile moves, the gas pressure behind it generates a moving hoop strain wave, i.e., the pressure causes a measurable increase in the diameter of the barrel and this disturbance moves with the projectile. As the projectile nears the muzzle of the barrel, the acceleration slows and a nearly constant velocity is reached. This velocity can be estimated from the hoop strain wave by measuring the elapsed time for the strain wave to pass between two barrel-surface mounted (located near the muzzle) strain gages of known separation distance. The system essentially works as a speed trap, timing the hoop strain wave and computing the velocity by dividing the strain gage spacing by the measured elapsed time to obtain the average velocity of the projectile in the bore between the sensors. Since the projectile experiences a small additional acceleration for the short distance between the strain sensor closest to the muzzle and the unvented portion of the muzzle brake, a correction factor based on empirical live-fire test results is added to the measured velocity to arrive at the REV.

Current Techniques for Measurement of REV

There are a number of techniques currently employed by the ballistic community to measure REV in field and laboratory environments. In the field, muzzle velocity radars are

employed on some field artillery systems to measure REV of the outgoing round. The M94 Muzzle Velocity Radar (MVR) system, currently fielded by the U.S. Marines, employs a flat phased array antenna typically mounted onto the non-recoiling structure of a howitzer gun system. This system directly measures the velocity of the outgoing projectile via Doppler shift. For laboratory environments, yaw screens, inductive timing rings (also used in the field on the Oerlikon system), bore pressure transducers and strain gages are often employed for measurement of REV. Yaw screens and inductive rings are similar in application in that they are used to measure the passage of a projectile through two inductive coils. Typically, the coils are mounted a short distance away from the muzzle and measure REV by timing the passage of the projectile between two screens (or rings). Knowing the distance between the screens or rings and the elapsed time of travel between them, one can compute REV. For the bore pressure transducers method, two transducers are inserted into drilled and tapped holes in the barrel and are employed to detect the onset of the high pressure propellant gas wavefront as it moves down the barrel. Typically, the transducers are mounted to the barrel near the muzzle with a nominal spacing. REV is computed similarly to the yaw screen method. Another common method for measurement of REV in laboratories is based on metal foil strain gages. In this method two strain gages are attached to the surface of the gun barrel and are employed to detect the hoop strain pulse moving with high-pressure propellant gas wavefront that accelerates the projectile. Again, the REV is computed in the same method as the previous techniques.

Analysis of REV Measurement Systems for a Field Weapon Application

The previously mentioned REV measurement techniques for application on a fielded weapon system have several inherent disadvantages. The MVR is expensive ($25K replacement cost for M94 system), bulky, complex, and actively emits radar pulses. It also has a major operational drawback in that REV is measured when the projectile is in flight which is too late for integration to the inductive fuse setting system for setting of the fuse for that particular round.

The mounting and placement locations of yaw screens and inductive rings make their use difficult for application on a fielded gun system. Since the screens or rings need to be located outboard of the muzzle, a structure attached to the gun which holds them out into the projectile path would be required. In this location, the screens or coils would be subjected to the shock, vibration, temperature, and pressures generated by the muzzle blast. In order to withstand these considerable effects, the structure to hold the coils would need to be substantial and therefore heavy. The Oerlikon system mentioned in a previous section uses such coils in its design. The addition of significant mass at the end of the gun barrel adversely affects the gun barrel flexure dynamics leading to an increase in flexure induced aiming errors and limits the performance of the gun stabilization system.

The use of pressure transducers is also not well suited for this application. Barrel mounted pressure transducers require drilling holes from the outer surface directly into the barrel bore which presents barrel reliability and safety problems for use in the field on a combat weapon system.

Finally, foil strain gages are not well suited for this application. The use of electrical-resistance strain gages for ballistic research dates as far back as the early 1940's [2]. However, while they are useful for some types of ballistic research such as triggering for high-speed cameras and indirect measurement of in-bore pressures, they have significant drawbacks in this application, such as; slow data capture rates of measurement instrumentation, non-automated measurement techniques and sensor error due to electromagnetic interference (EMI). However,

the use of fiber optic strain sensors for REV measurement enables the application of this well tested concept without any of the drawbacks of foil sensors noted above.

Advantages of Fiber Optic Based Sensors System for REV Measurement

Optical fiber based sensor systems provide the following advantages important to the ballistics community. Firstly, because optical fibers are compact (5~10 μm core surrounded by a cladding of 125μm, which is only slightly thicker than a human hair). Secondly, optical fibers are mechanically robust. The mechanical strength of the optical fiber has been measured to be 5~7Gpa, which is about 7 to 10 times that of carbon steel. The use of optical fibers has been reported in applications spanning wide temperature ranges from cryogenic (-270°C) up to nearly 1000°C [3]. Examples of the use of high strength optical fiber in harsh operating conditions include pay-out fiber in TOW anti-tank missiles [4] and fiber temperature and pressure sensor inside downwells of oil fields. [5] Additionally, optical fibers are light and flexible which enables the fiber to be attached or embedded to most structures without affecting the functionality of the host. Finally, optical signals are immune to electromagnetic interference inherent in explosive environments. This property enables optical fiber-based sensors to avoid the extensive measures normally required to shield the sensors, lead wires and processing instrumentation, which often leads to a bulky and heavy system.

OFREV SYSTEM DESIGN

Internal Ballistic Phenomenon

Various dynamic and thermodynamic interactions take place among the gun barrel, propellant, projectile and external environment during an internal ballistic event. After ignition, the rapidly burning propellant creates a very high pressure inside the barrel bore behind the projectile [6]. This pressure accelerates the projectile and induces various strain phenomena in the walls of the gun barrel. One of the phenomena produced is a moving dilation in the hoop strain at the rear of the projectile that moves with the projectile as it travels from the breach to the muzzle. The proposed REV measurement system measures the velocity of this hoop strain dilation phenomenon as a means for measurement of the projectile velocity

In order to evaluate and optimize the design of the REV measurement system it is necessary to understand the motion of the projectile in the bore and the strain produced in the barrel during the firing process. These data can be obtained from live-fire tests or from internal ballistic model predictions. For this research, barrel surface strain and temperature data was obtained from a report describing live-fire tests of the M242 conducted at the Armament Technology Facility (ATF) 300 m Range at Picatinny Arsenal, NJ [7]. The strain and temperature data in this report were useful in determining the expected levels of strain and temperature during firing which are important parameters for the overall system design. Also of significance for the design is the velocity profile of the projectile in-bore. A simplified model of the internal ballistic dynamics and in-bore velocities was constructed using the data that was available.

Optical System Design and Principle of Operation

The fiber optic REV measurement system has the primary function to measure the elapsed time for the hoop strain wave to pass each of two barrel-surface mounted strain sensors. As mentioned previously, in this system optical Fiber Bragg Grating (FBG) sensors are employed as the strain sensing elements and an instrumentation system composed of fiber optic and electric components to convert the signals produced by the sensors into useable voltages for post processing (The operational principles of FBG's are described later in this paper.). For the M242 cannon the OFREV system design requirements included a maximum projectile velocity of 1400 m/s, a velocity measurement resolution of < 1% of maximum projectile velocity (i.e., 14 m/s), to withstand shock and vibration commensurate with live fire of a limited number of single rounds and a small number of bursts, and to withstand temperatures only moderately higher than ambient.

In addition to these requirements, the expected levels of strain and strain rates generated during live fire are important for optical system design. Based on the results of live fire testing reported by [8], the maximum strain levels at the expected sensors locations for the M242 gun system are estimated to be in the range 600-1000 με and the strain rates as high as 500 με/μs. Consequently, the strain resolution requirement for the system in order to meet the 1% velocity measurement resolution listed above was determined to be 100 με.

In the design process several system configurations were evaluated to arrive at a feasible design, which is shown schematically in Fig. 1. As can be seen in the figure, the design consists of two FBG's fabricated into a single fiber, an FBG-based notch filter, a broadband source, a coupler, a photo detector amplifier and a PC with A/D card.

The main objective of the design process was to produce a system of minimal complexity and cost that met the requirements described above. In order to achieve this, the design possesses two significant features: multiplexing of the FBG's and a demodulation scheme using an FBG-based notch filter. Multiplexing the FBG's into a single fiber results in a single channel system in which the FBG's are interrogated independently thereby reducing the need for two channels of sensor signal demodulation optics and electronics. Employing the FBG-based notch filter results in a very simple configuration in which the sharp rising edge of the hoop strain wave can be detected at a sharp step in light intensity output (this will be seen later in the results of the prototype laboratory testing).

Also of major consideration in the design optimization process were the repeatability and complexity of fabrication of the FBG-based notch filter, an optical component that filters the reflected signal from the fiber strain sensors. Several different signal filtering methods and optical filter types were investigated during the design and prototype fabrication tasks. This effort resulted in a novel filter fabrication design using a standard phase mask

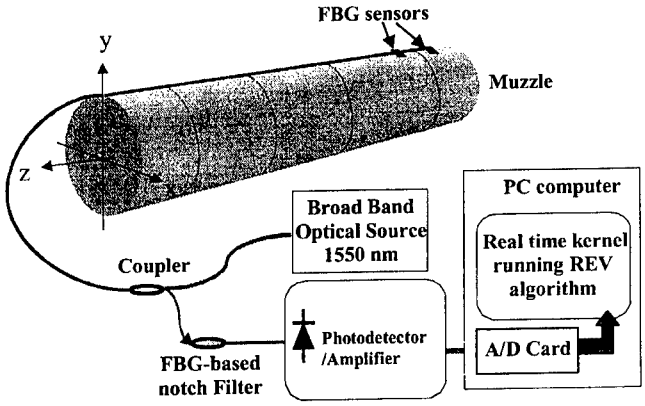


FIGURE 1: REV system configured on gun barrel.

illuminated by a 244 nm wavelength IR laser using an iris.

The remaining system design task involved development of the photo detector/amplifier, which is the instrumentation that converts the optical intensity into a useable voltage signal. In this task an amplifier was designed to interface with an MRV purchased photo detector. The amplifier was designed to have a 2 MHz bandwidth and a gain to ensure an output in the 1-5 volts range based on the expected light input to the photo detector.

The underlying principle of operation of the OFREV measurement system is quite straightforward. The sensors utilize the optical technology of the FBG, which consist of a length of optical fiber where the core of the fiber has been modified using a laser to obtain a modulation in the refractive index of the core. FBG's operate by acting as a wavelength selective filter for light passing through it and reflects a single wavelength called the Bragg wavelength, λ_B. The Bragg wavelength is related to the grating pitch, Λ, and the mean refractive index of the core, n, by

$$\lambda_B = 2\Lambda n \qquad 1)$$

Both the fiber refractive index (n) and the grating pitch (Λ) vary with changes in strain (ε_{zz}) and temperature (ΔT), such that the Bragg wavelength shifts left or right in wavelength space in response to applied thermal-mechanical fields. For a Bragg grating sensor bonded to the surface of a structure, the strain and temperature are related to the change in the Bragg wavelength by

$$\frac{\Delta\lambda_B}{\lambda_B} = P_e\varepsilon_{zz} + [P_e(\alpha_s - \alpha_F) + \zeta]\Delta T \qquad 2)$$

where α_s and α_f are the coefficients of thermal expansion of the structural material and fiber, respectively, and ζ is the thermal-optic coefficient, and P_e is the strain-optic coefficient [9,10]. The Bragg gratings are oriented so that they are sensitive to hoop strain, i.e., they are aligned perpendicular to the barrel axis around the outer surface of the barrel and epoxied in place. This design transfers the fast rising hoop strain from the barrel surface to the sensor. Thus it enables detection of the moving projectile as it reaches each sensor. The hoop strain dilation is detected as it passes a Bragg grating by monitoring the shift in λ_B.

By positioning the two strain sensors at a fixed separation, L, near to the muzzle and measuring the time difference, Δt, of the onset of the shift in λ_B, the REV can be estimated as

$$V_{re} = L/\Delta t \qquad 3)$$

From (3), we can calculate the minimum time resolution, $d\Delta t$, required in order for the sensing system to measure the REV to the required resolution, dV_{re}/V_{re} and express it as

$$d\Delta t = (L/V_{re})(dV_{re}/V_{re}) \qquad 4)$$

Assuming L= 0.25m, V_{re}=1400 m/s and dV_{re} = 7.8 m/s, we can obtain the minimum time resolution of the sensing system as 1μs, which translates to a sensor bandwidth of 1MHz. It is important to note that the REV measurement requires high speed, not high accuracy for the two Bragg grating strain sensors and the detection system, i.e., the sensor system needs to be capable

of detecting the onset of the shift in λ_B with a resolution of 1μs but does not need to accurately measure the amount of shift.

In order to meet this high-speed requirement an innovative method for detection of the shift in λ_B, was developed. The method developed consists of employing an optical notch filter with a precisely defined optical transmission spectrum in the configuration shown in Fig. 1. The spectrum of this filter is shown in Fig. 2 and is employed as follows. First, consider the case where there is no strain on either of the sensors. Light from the source passes through the coupler and a portion of it is reflected back by each of the Bragg gratings. The intensity spectra of the reflections are shown in Fig. 2. Notice that two peaks at slightly different wavelengths characterize the spectra, one for each of the sensors. The reflected light then passes through the notch filter and into the photo detector. The photo detector outputs a current that is linearly proportional to the optical *power* that it receives. Due to the shape and location in wavelength space of the notch filter, see Fig. 2, both of the intensity peaks are extinguished by the notch filter. This figure illustrates how the two peaks fit inside of the notch, which effectively blocks the transmission of optical power at these wavelengths. Therefore, no light reaches the photo detector and its output is its quiescent level. When the weapon is fired and the hoop strain dilation reaches Bragg grating sensor no. 1 it is subjected to tensile strain stretching the sensor and increasing λ_B. As λ_B increases, outside the influence of the notch filter, light is transmitted through the notch filter and into the photo detector. This effect is shown in Fig. 3. Due to the sharp slopes of the notch filter transmission spectrum and the Bragg grating reflection spectrum, even a small shifting of λ_B, produces a significantly large change in the light reaching the photo detector. Therefore, when the hoop strain dilation reaches sensor no. 1 a sharp step is seen in the photo detector output current (The laboratory test results from the Phase I prototype indicate that we will be able to detect a strain event with resolution down to 100 με or less).

As the hoop strain dilation reaches the Bragg grating sensor no. 2 it also experiences an increase in λ_B and another step increase in the light power reaching the photo detector occurs. This effect is shown in Fig. 4. The time response curve expected from the sensor system as the hoop strain dilation passes both sensors is illustrated in Fig. 5.

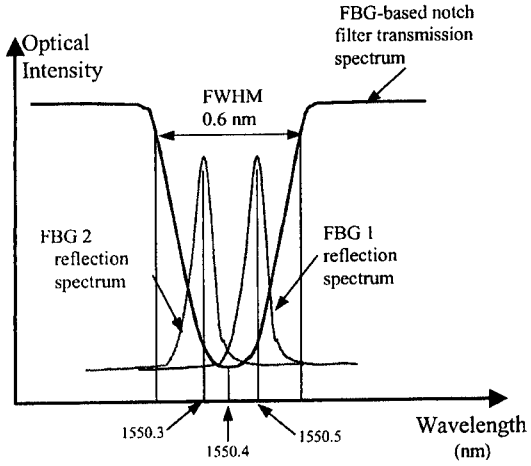


FIGURE 2: Optical intensity spectra for FBG's and FBG-based notch filter in the unstrained condition

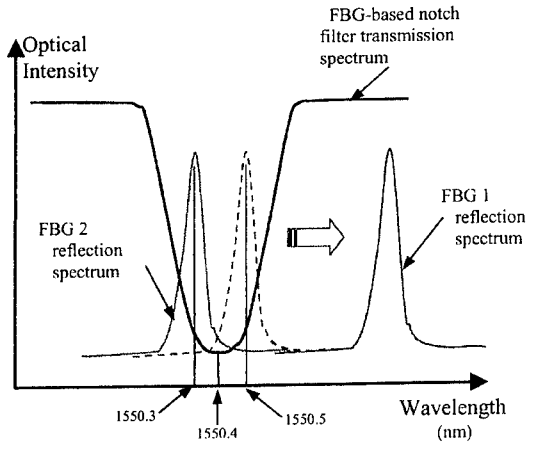


FIGURE 3: Optical intensity spectra for FBG's and FBG-based notched filter when FBG 1 is strained.

Prototype System Fabrication

In order to evaluate the feasibility of the proposed system design a prototype system was fabricated. The FBG's and FBG-based notch filter were manufactured at the fiber optics laboratory at the Smart Materials and System Research Center (SMSRC), University of Maryland. Bragg gratings were fabricated by exposing the fiber to a periodic intensity profile produced by coherent interference with Bragg wavelength of 1550.9 and 1550.7, respectively. The FBG-based notch filter was fabricated using single mode fiber and a unique fabrication process using a reduce diameter (2 mm) UV laser for fringe writing with a standard phase mask. This was achieved by passing the laser light through an iris before the phase mask interface. The overall effect of this procedure was to increase the full width half maximum (FWHM) length (from 0.1 nm to 0.9 nm) of the wavelength spectrum to band stop, under non-strain conditions.

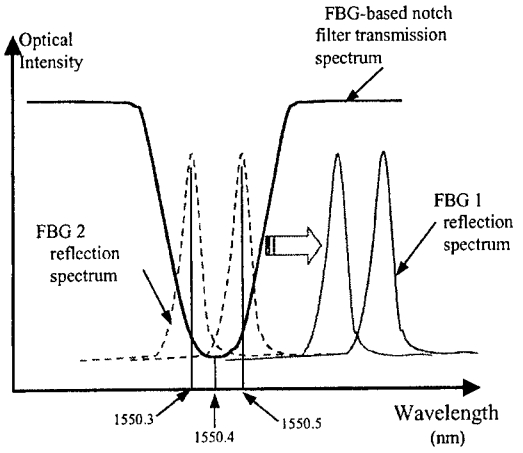


FIGURE 4: Optical intensity spectra for FBG's and FBG-based notch filter when FBG 1 and FBG 2 are strained.

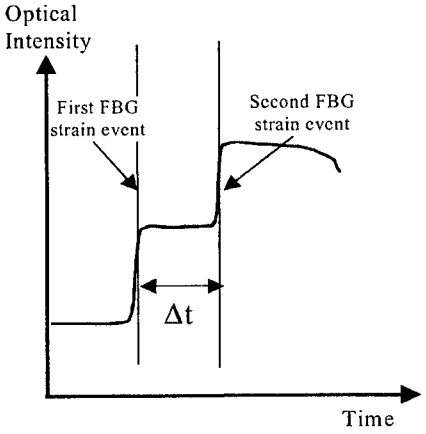


FIGURE 5: Expected optical output intensity time history for successive straining of FBG 1 and FBG 2

Arrangement of FBG Strain Sensors on M242 Gun Barrel

The results of the sensor placement analysis indicated that to achieve the velocity measurement accuracy and resolution targets, the sensor should be mounted as close to the muzzle as possible and spaced at least 10 cm apart. Using the results of this analysis, the sensors on barrel no. 1 were located on the barrel with the sensor closest to the muzzle being located approximately 4.5 cm inboard of the muzzle and with a sensor-to-sensor spacing of 20 cm. In order to evaluate the system performance with the sensors at the minimum spacing, the sensors on barrel no. 2 were spaced 10 cm apart, with the sensor closest to the muzzle also located at approximately 4.5 cm in board of the muzzle. For both barrels, the sensors were orientated perpendicular to the axis of the gun barrel to measure hoop strain.

LIVE-FIRE TESTING OF OFREV MEASUREMENT SYSTEM

Testing Description and Procedures

Live fire tests were conducted on two OFREV equipped M242 25-mm gun barrels. Barrel no. 1 was equipped with both an OFREV system and a foil strain gage system. The foil strain

gages were mounted in close proximity to the OFREV strain sensors to enable system debugging and performance evaluations. The spacing of the two OFREV strain sensors (and the foil strain gages as well) was 20 cm with the strain senor mounted closest to the muzzle being located within approximately 4.5 cm of the muzzle. Barrel no. 2 was equipped with an OFREV sensor system with 10 cm spacing of the OFREV strain sensors and also, like barrel no. 1, with the strain senor mounted closest to the muzzle being located within approximately 4.5 cm of the muzzle. The outputs from each system were connected simultaneously to a high-speed (1 MHz sample rate) digital oscilloscope and a National Instruments PC-based DAQ card installed in a Pentium PC host. The oscilloscope was connected to a laptop for data storage. The LabView system enabled direct streaming of the captured data to the PC hard drive.

In order to evaluate the accuracy of the OFREV measurements a Weibel Scientific W-680I Doppler Analyzer was used as a reference. This system tracks the projectile as it leaves the muzzle and computes the muzzle velocity based on its trajectory. The system is limited to measurement of the muzzle velocity of the first round in a multiple round burst

Testing Description and Results

Several test were conducted for each of the barrels using different ammunition types and under single and burst shot modes. Table 1 provides important characteristics of the tests conducted, indicating the test no., barrel no., round type, and firing mode (single shot or burst) for each of the tests. During each of the tests listed, data was collected from the OFREV, strain gages (for Barrel no.1 only), and the Weibel MVR system. For the tests involving burst mode, it was only possible to measure the muzzle velocity of the first round in the burst using the MVR.

The data from each of the tests were analyzed to compute the estimated round exit velocity (or muzzle velocity). This was done by examining the OFREV output for each of the tests and graphically estimating the width of the OFREV output signal pulse.

TABLE 1: Test characteristics.

Test No.	*Barrel No.*	*Round Type*	*Firing Mode - Single/Burst (rate)*
Test1	1	M793	Single
Test2	1	M793	Single
Test3	1	M793	Single
Test4	1	M793	Single
Test5	1	M793	Single
Test6	1	M793	Single
Test7	1	M793	Single
Test8	1	M793	Single
Test9	1	M793	Single
Test10	1	M793	Single
Test11	1	M793	Burst – 2 Rnds (100 rpm)
Test12	1	M791	Single
Test13	1	M910	Single
Test14	1	M793	Burst – 5 Rnds (200 rpm)
Test15	2	M910	Single
Test16	2	M910	Single
Test17	2	M910	Burst – 3 Rnds (100 rpm)
Test18	2	M793	Single
Test19	2	M793	Burst – 20 Rnds (200 rpm)

Single Shot Firing Mode Tests

Fig. 6 illustrates a typical time response curve generated by the OFREV system during the firing of a single round. Table 2 shows the estimated REV, reference REV, and error percentage for each of the single shot tests conducted. OFREV data were not available for Test1, Test7, and Test16 due to data collection triggering problems. The average error in the estimated REV for the tests shown in the table is 2.2 %. The errors for Test2 and Test3 were high due to optical fiber sensor temperature calibration related issues. After these issues were resolved, the average error dropped to 1.6 %. This error compares well with an OFREV system design accuracy target of 1 %.

Burst Shot Mode Firing Tests

The burst mode data was analyzed according to the same procedure as the single shot mode data. This analysis was performed for as many shots in the burst as possible. Due to errors introduced when the barrel temperature increased during firing, only the first several shots in a burst could be analyzed. Table 3 shows the round type, estimated REV, reference REV, and error percentage for each of the shots in a burst in which there was valid data. Note that the Weibel MVR was limited to measurement of the REV of the first round in a burst. Consequently, the error of the OFREV measurement was only computed for the first round. Inspection of the data in Table 3 for the rounds after the first for each burst indicates an increase in the error if we assume that the reference velocity for each of the rounds is close to that of the first round in each burst. This is most likely due to heating of the barrel and is an expected effect since the system design did not include temperature compensation features. The effects due to the increase in temperature can be seen in Fig. 7, which shows a typical OFREV time response curve for a burst mode test (Test14). Note that the average level increases as the rounds are fired. This rise is related to an increase in the temperature of the barrel, which induces thermal strain in the system.

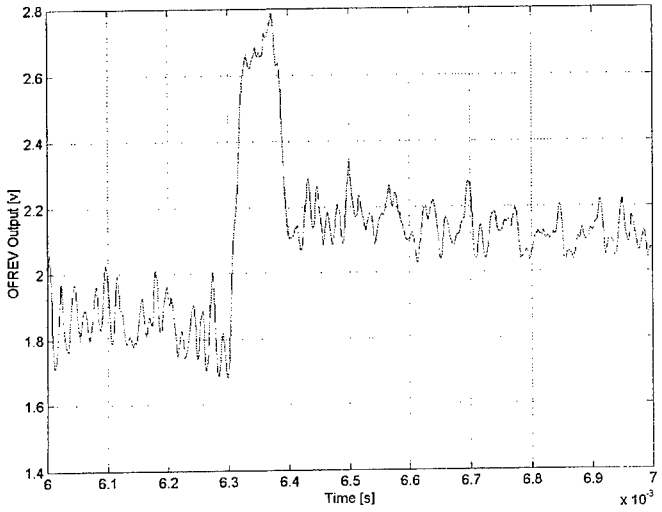


FIGURE 6: Typical OFREV system output response for a single shot.

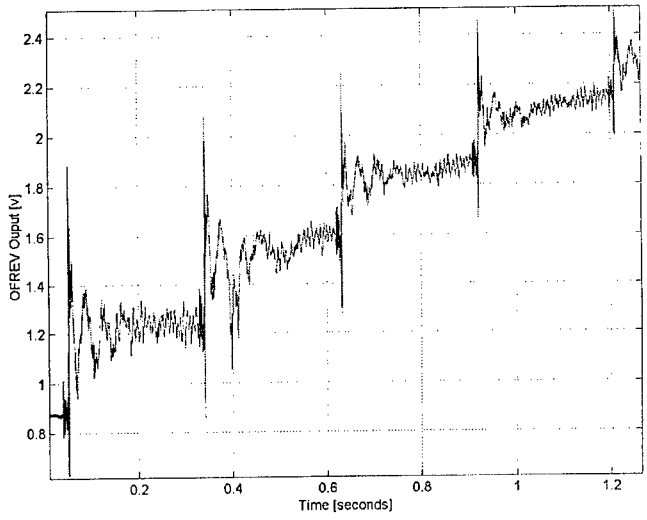


FIGURE 7: Typical OFREV output for a burst (Test 14)

Also, the data from the burst mode tests indicates that the system response is sufficiently fast with adequate resolution to enable measurement of REV for each round in a burst at firing rates of 100 and 200 rounds per minute. Automation of the elapsed time data extraction for the OFREV will enable real time REV measurement under burst mode for air burst munition applications.

The results of the testing also indicate that the system was sensitive to changes in temperature as the barrel is heated during firing, especially for multiple round bursts. This effect can be minimized using barrel attachment techniques that thermally isolate the optical sensor.

CONCLUSIONS

A prototype system was designed, fabricated and tested under live fire indoor test range conditions on an M242 25 mm cannon. The OFREV system performed quite well in the live fire tests. The results of the 19 firing tests of over 40 rounds showed that the system could measure the REV to within 2-3% of the reference MVR system for the three different types of rounds. It is likely that an improvement in the system accuracy could be achieved by taking into account the additional unmeasured acceleration from where the velocity measurement was made (the OFREV system essentially computes the average projectile velocity between the strain sensors) to outboard of the muzzle, since the projectile is still experiencing a small acceleration in this region.

In addition to achieving good accuracy, the OFREV system demonstrated an output waveform very suitable for automated feature extraction. The shape of the system output signal pulse generated by a firing event was sharp with a high signal-to-noise ratio, which will make it very conducive to a high-speed automatic elapsed time extraction algorithm.

Finally, the system held up quite well under the shock and thermal loads generated during the firing of over 40 rounds, including the high velocity M910 and M791 rounds. The fiber sensors did not break nor was there any evidence of failure in the adhesive used to bond the sensor to the barrel.

TABLE 2: Results of OFREV round exit velocity estimates for single round tests

Test No.	*Round Type*	*OFREV estimated REV (m/s)*	*Weibel reference REV (m/s)*	*Error (%)†*
Test1	M793	N/A	1102.3±1.2	
Test2	M793	1025.6	1093.2±1.4	-6.2
Test3	M793	1043.4	1090.5±1.3	-4.3
Test4	M793	1085.8	1093.8±1.1	-0.7
Test5	M793	1073.0	1090.2±1.6	-1.6
Test6	M793	1082.3	1090.5±1.5	-0.8
Test7	M793	N/A	1085.9±1.9	
Test8	M793	1076.4	1095.4±1.4	-1.7
Test9	M793	1077.6	1090.3±1.8	-1.2
Test10	M793	1078.2	1097.2±1.2	-1.7
Test12	M791	1303.8	1338.4±1.2	-2.6
Test13	M910	1496.2	1498.2±1.3	-0.1
Test15	M910	1439.1	1506.1±2.4	-4.4
Test16	N/A	N/A	1501.1±2.0	
Test18	M793	1078.0	1089.8±1.4	-1.1

† Error computed based on nominal Weibel reference REV value.

TABLE 3: Results of OFREV round exit velocity estimates for multiple round burst tests

Test No. (round no. in burst)	*Round Type*	*OFREV estimated REV (m/s)*	*Weibel reference REV (m/s)*	*Error (%)†*
Test11 (1)	M793	1082.3	1090.7±1.7	-0.8
Test11 (2)	M793	1033.3	N/A	
Test14 (1)	M793	1060.8	1088.4±1.7	-2.5
Test14 (2)	M793	1005.5	N/A	
Test14 (3)	M793	1027.3	N/A	
Test14 (4)	M793	1032.4	N/A	
Test14 (5)	M793	1026.6	N/A	
Test17 (1)	M910	1425.8	1513.3±2.1	-5.8
Test17 (2)	M910	1469.6	N/A	
Test17 (3)	M910	*	N/A	
Test19 (1)	M793	1106.8	1094.9±1.7	-1.1
Test19 (2)	M793	1158.3	N/A	
Test19 (3)	M793	1091.4	N/A	
Test19 (4-20)	M793	*	N/A	

† Error computed based on nominal Weibel reference REV value.
* Data not available due to elevated barrel temperatures.
Note: Reference values only available for first round in burst due to Weibel MVR limitation.

ACKNOWLEDGEMENTS

This work was supported by a U.S. Army SBIR Phase I grant under contract number: DAAE30-00-C-1019. Special thanks for support and guidance to the staff of TACOM-ARDEC at Picatinny Arsenal, NJ.

REFERENCES

1. S. Cytron, personal communications, March 30, 2001.
2. Flynn, Paul D., "Application of Strain Gages to Ballistics Problems," Frankford Arsenal Report no. FA-TA-74008, August 1974
3. Morse TF 1999, He Y and Luo F, "An optical fiber sensor for the measurement of elevated temperatures", Proceeding of 13th Optical fiber sensor conference, Kyongju, Korea, SPIE proc. Vol 3746, pp.54-57.
4. Culshaw, B. 1988, Dankin, J., *Optical Fiber Sensor: Systems and Applications*, Vols. 1 and 2, Artech House, Norwood, MA.
5. Kersey AD 1999, "Optical fiber sensors for downwell monitoring applications in the oil and gas industry", Proceeding of 13th Optical fiber sensor conference, Kyongju, Korea, SPIE proc. Vol 3746, pp.326-331.
6. Tzeng, Jerome T, and Hopkins, David A, "Dynamics Response of Composite Gun Tubes Subjected to a Moving Internal Pressure," U.S. Army Research Laboratory Report no. AR-TR-889, October 1995.
7. Aesoph, Michael D, Czarnek, R, and Miller, C, "Advanced Gun Barrel Technology Initiative: Instrumentation and Testing Report for a Modified Unlined M242 Barrel," National Center for Excellence in Metalworking Technology, Contract N00140-92-BC49, Test Report, September 30, 1996.
8. James, Stephen W, Fuller, Stephen R., Crompton, C., and Tatam, Ralph P., "Transient Strain Monitoring on a Gun Barrel Using Optical Fibre Bragg Grating Sensors," SPIE Conference on Laser Interferometry IX: Applications, San Diego, CA, July 1998.
9. Sirkis, J.S. 1993, "A Unified Approach to Phase-Strain-Temperature Models for Smart Structure Interferometric Optical Fiber Sensors: Part I-Development," *Optical Engineering*, 32 (4), pp. 752-761.
10. Meltz, G. R. 1989, Morcy, W. W., and Glen, W. H., "Formation of Bragg Gratings in Optical Fibers by a Transverse Holographic Method," *Opt. Letts.*, 14, pp. 823-825.

INVESTIGATING UHF TELEMETRY FOR ELECTROMAGNETIC LAUNCHERS

S. Levinson[1], L. Burke[2], M. Erengil[1], and J. Faust[2]

[1] *Institute for Advanced Technology, 3925 W. Braker Lane, Suite 400, Austin, TX 78759*
[2] *U.S. Army Research Laboratory, Aberdeen Proving Ground, MD 21005*

This paper describes an experimental investigation of the feasibility of microwave telemetry for conveying diagnostic information collected during and after launch from an electromagnetic (EM) gun. The study focused on extending the Hardened Subminiature Telemetry Sensor Systems (HSTSS) technology for use in EM launch environments. While HSTSS technology has already been successfully demonstrated in high-g, high-pressure launch environments in conventional gun systems, it has not yet been tested in an EM gun environment, where the launch accelerations are generally higher and where the projectile can be exposed to high magnetic fields and EM transients. In this work, ultra high frequency (UHF) telemetry measurements were made at fixed locations in the magnetized bore of the Medium Caliber Launcher (MCL) at the IAT to assess the effect of the EM environment on telemetry and the HSTSS-like components. The data show that UHF FM signals can both propagate and be received in this non-optimal environment. Signals were received with minimal loss after propagating along the entire bore as well as through the containment wall. To examine the effect of high, transient magnetic fields on HSTSS-like components, the telemetry package was located both ahead of and behind a stationary armature, with the latter case simulating the higher fields in an EM launch with a muzzle shunt. The results showed that, in an EM launch without a muzzle shunt, the telemetry package could be positioned far enough ahead of the armature such that there would be no interference in the received telemetry signals. However, when a muzzle shunt was simulated, there were momentary disruptions in the transmitted signal coincident with fast rising, transient magnetic fields. The use of a thick metallic cylindrical shield surrounding the telemetry components reduced the induced voltages due to transient magnetic fields somewhat and slightly improved the observed telemetry signal.

INTRODUCTION

To aid in the research and development of projectiles for EM gun systems, there is a need for on-board instrumentation. Both in-bore and free flight phenomenon must be measured and understood. Parameters such as, but not limited to, setback acceleration, balloting, pressure, yaw/pitch rate, and spin need characterization. For smart munitions, on-board diagnostics may also be needed to monitor the performance of seeker or inertial measurement unit sensors. On conventional gun systems this information is routinely gathered using an on-board telemetry system. Until recently these telemetry systems have been expensive and limited to large caliber projectiles. However, under the U.S. Army's Hardened Subminiature Telemetry and Sensor

System (HSTSS) program a new family of rugged, low cost telemetry components is being developed.

The HSTSS program, a tri-service program scheduled to complete all development contracts in FY03, is currently developing state-of-the-art telemetry components and subsystems for missile and ballistic applications. The goal of the program is to provide lower cost, user configurable telemetry components for making in-flight measurements of standard and smart munitions. Products being developed include a transmitter chip set, a data acquisition chip set, a reference oscillator, power sources, various sensors, and electronic packaging techniques for the ballistic environment. All of the devices are available in their lowest form of packaging (e.g., integrated circuit die) and are being designed to survive setback accelerations greater than 100,000 G's. To date, the program has fielded telemetry systems for the Multiple Launch Rocket System (MLRS), Advanced Kinetic Energy Projectile Program, and the DERA ETC gun programs. HSTSS is now being considered for electromagnetic launchers (EML) to provide on-board diagnostics for an EM launched projectile [1].

Unlike conventional gun systems, EM gun systems have the added complexity of high, transient electric and magnetic fields during the launch phase that may affect the performance of the on-board electronic systems, particularly the RF link. There are at least two additional considerations for wireless telemetry when it is used as an on-board diagnostic on an EML, such as the Medium-Caliber Launcher (MCL). The dimensions of the MCL bore and containment structures are approximately those of a rectangular waveguide having a 3.75 GHz cutoff for the lowest-order propagating mode - significantly higher than the carrier frequency (2.2 GHz) used in the HSTSS. It will be determined whether microwave energy can propagate inside as well as through the MCL bore structure, which is also effectively closed on one end by a conducting armature. Secondly, during any EM launch there is significant transient magnetic field - which may render the on-board electronics at least temporarily inoperable. For some configurations of the MCL, for example, such fields reach 10's of T at a rate 10's of T/ms in regions where HSTSS electronics would be located.

The objective of this study is to evaluate the feasibility of using an on-board telemetry system in this harsh environment. A series of stationary tests were conducted using a very simple analog RF link to (1) determine limitations in transmission through the EM launcher and containment structures, and (2) characterize the performance of the telemetry link during and just after the application of high magnetic field transients. The remainder of this paper reviews the test methodology, describes the telemetry module, and summarizes the results.

PRELIMINARY STUDIES

Quiescent Railgun Environment

The high currents in a railgun result in large transverse forces on the rails that must be resisted by an external containment structure. The MCL uses a close-fitting structure composed of insulated metal laminations, as shown in Fig 1. The laminations allow a change in the magnetic field to propagate into the lamination gap at the speed of light while diffusing into steel laminations on the order of 2-μs [2]. Thus, on the time-scales associated with EM launch dynamics (> 20-μs), the containment structure is essentially transparent to the transverse field. However, the close proximity of the rails and laminated-steel containment form a complicated,

difficult-to-analyze UHF telemetry environment, and accurate estimation of the UHF energy propagating through the containment is an expensive calculation.

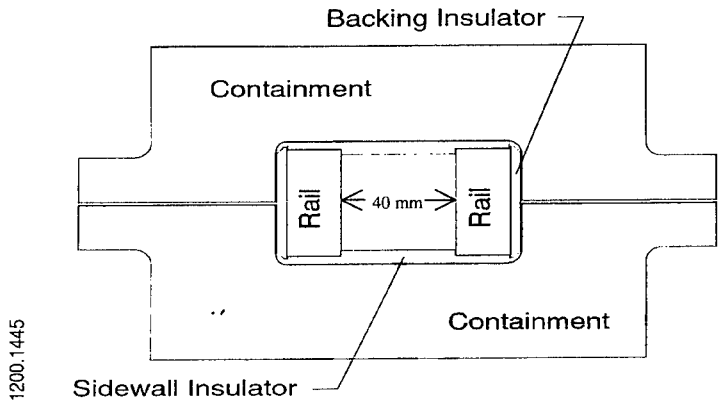


FIGURE 1. Cross-section of the Medium Caliber Launcher is shown viewed down the barrel. The parts marked 'containment' are made of stacks of 1.5-mm thick steel laminations.

In Ref [3], a simple experimental investigation on the MCL demonstrated that UHF signals will both propagate and be detected in a quiescent EM launcher environment. Those measurements were conducted using a continuous wave UHF transmitter and a spectrum analyzer each connected to a dipole antenna, positioned inside and/or outside of the MCL bore. In that study, neither the transmitter nor the receiver were exposed to EM railgun transients; nor were the measurements conducted in the presence of an armature, where the effect of the MCL, acting as a waveguide that is closed on one end, could be investigated. Nevertheless, the results indicated that the effect of the MCL rails and laminated containment structure was minimal. The reduction in the received UHF signal level was only about 5-10 dB over the length of the 10-m barrel compared to that of equidistant out-of-bore measurements, regardless of the receiving antenna position. Thus, in Ref [3], no fundamental roadblocks associated with the railgun and containment structure were identified.

Magnetized Railgun Environment

An equally important concern is the effect of the applied transient magnetic field on the telemetry link. In typical MCL experiments, 200-300 g launch packages are accelerated up to 2500 m/s over the first few meters of a 7-m long launcher. The driving current rises to about 1.0 MA peak in about 500 ms, persists at a plateau for a few milliseconds, and then decays to several hundred kilo-Amp by the time the launch package leaves the gun. The schematic in Fig 2 shows the rails, the armature, driving current and magnetic field lines that are perpendicular to the current flow. The bore geometry used in this study was 1.575x1.575 in (40 x 40 mm) in cross-section and 50-in long. The rails, which were made of 6061-T6 Aluminum (¾-in x 1¾-in cross-section), were separated by a 6061-T6 Aluminum block (1¾-in in height and 1-in in axial extension) acting as a stationary armature. The schematic in Fig 3 shows the basic experimental configurations used in the present study.

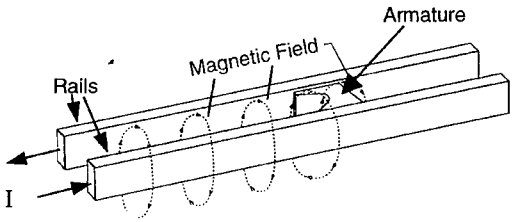


FIGURE 2. A schematic diagram is shown of the armature and rails of the Medium Caliber Launcher (containment not shown). At the bore center, magnetic field lines are perpendicular to the bore axis.

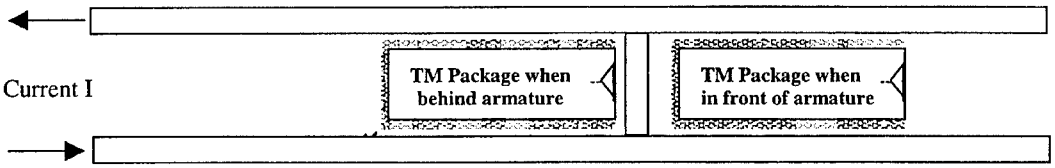


FIGURE 3. Shown is a schematic diagram of the fixed Aluminum armature and Aluminum rails used to assess the magnetic fields that would be exposed to the telemetry system The magnetic containment (not shown) is also present. The locations of telemetry transmitter package are shown at two locations tested in the telemetry experiments. Metal, cylindrical magnetic shields surrounding the package and used in several of the tests are indicated by the "▓" pattern.

When a projectile is launched with a railgun, the voltage induced on electronic components on board is the result of two terms: one proportional to the rate of change of magnetic flux and the other proportional to the projectile velocity. While field measurements associated with a stationary armature offer only a limited approximation of comparable dynamic railgun fields, they were determined in Ref. [4] to provide an order of magnitude estimate of the magnetic flux density (**B**) and the induced voltage, which is proportional to d**B**/dt. Figs 4 and 5 show the applied current waveforms, and the peak magnetic flux densities along the bore centerline, respectively. At locations behind the stationary armature, the peak value of |**B**| was 1.6 T and the peak value of |d**B**/dt| was 6 T/ms. As expected, except in the vicinity of the armature, the magnitude of the magnetic field was essentially independent of axial position and directly proportional to the peak current level at 16 T/MA. At locations ahead of the armature, **B** was markedly reduced. The peak in **B** was nearly an order of magnitude lower at 1.5-2 armature heights ahead of the trailing edge of the armature, and was more than two orders of magnitude lower at 4.5-5 armature heights, as illustrated in Fig 5.

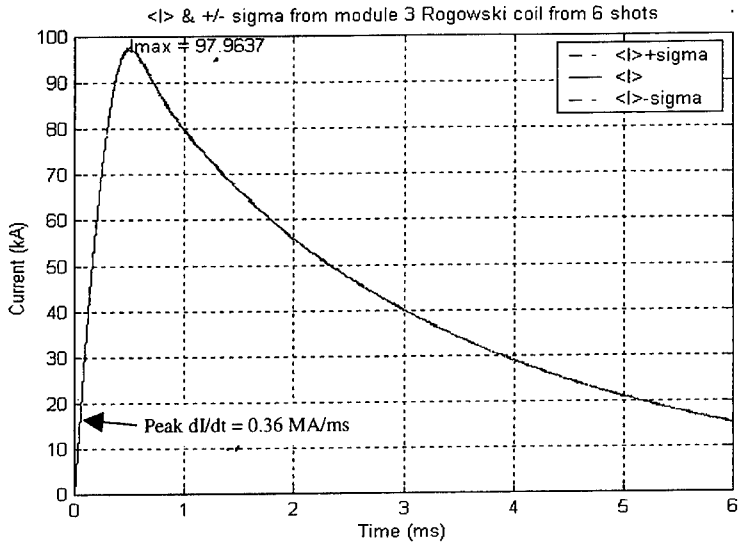


FIGURE 4. Measured railgun current waveforms from Ref. [4] are shown that were used to obtain measurements of the stationary magnetic flux density **B** in the bore center. For a 100 kA peak current, the peak current growth rate was 0.36 MA/ms. The corresponding peak in **B** was 1.6 T, normal to the bore axis, and the peak value of d**B**/dt was 16 T/MA × 0.36 MA/ms = 6 T/ms.

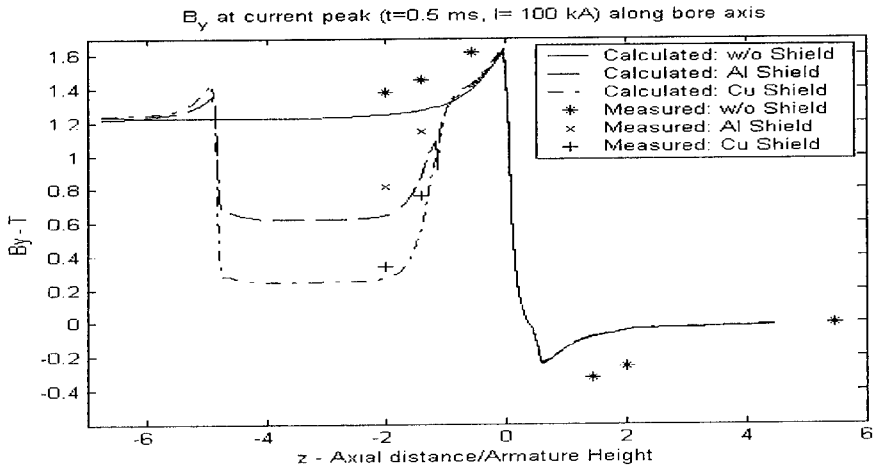


FIGURE 5. Measurements and EMAP3D calculations of the magnetic flux density were made for three different shield cases, which occupied a region 1-5 armature heights behind the trailing edge of the armature [4]. The peak component (perpendicular to bore axis) of **B** is shown during the current peak.

In a railgun launch, if the armature current is not zero at exit, an electrical arc will form as the armature leaves the gun and may cause a number of undesirable consequences, most of which can be alleviated with the use of a muzzle shunt [5]. Unfortunately, when a muzzle shunt is employed, significantly larger EM transients will develop ahead of the armature as the magnetic flux is compressed between the armature and the muzzle shunt. The magnetic field transients induced because of a muzzle shunt are difficult to measure or calculate accurately. However, the muzzle voltage, normally 10-30 V on the MCL, has been measured in kilovolt ranges when such a shunt is attached [6]. Thus, the use of a muzzle shunt in an EM launcher

may subject the launch package to extremely high voltage transients and have dire consequences for the on-board instrumentation in the telemetry package.

One potential solution is the use of a magnetic shield. The ability of a hollow, metallic cylinder to mitigate the effects of the high, transient EM field was also explored in Ref [4]. Two hollow, 6½-in long, 1/10-in thick cylindrical shields, closed on one end, were tested. One was made of Al7075 and weighed 130 g, the other was made of ETP Cu and weighed 430 g. As expected, the greatest reduction in the magnetically induced voltage was achieved by the more conductive and heavier copper shield. Compared to the case with no shield, the induced peak voltages were reduced by more than 80% during initial current rise (i.e., < 100 μs). However, after 250 μs, the induced fields were no longer attenuated by the shields. If necessary, improved shielding may be obtained with more sophisticated shield design; however, significant weight penalties could render the use of shields impractical. Nevertheless, their effect on telemetry was also investigated in this study.

TELEMETRY EXPERIMENTS

The telemetry experiments were conducted by placing the transmitter module inside the MCL bore and closed containment structure. The frequency modulated (FM), UHF signal was transmitted to two side-by-side receivers located outside the bore, and recorded digitally for subsequent analyses. In this section, the telemetry module and receivers are first described. Telemetry measurements - conducted in a full length, quiescent railgun environment in the presence of a conducting armature - are discussed next. Finally, telemetry in a magnetized railgun bore is examined. Here, the effect on the telemetry is investigated by analyzing the carrier frequency shift and the frequency spectrum of the received, modulated sub-carrier signal with changes in 1) antenna orientation, 2) telemetry transmitter module (TM) location, 3) **B** inside the bore, and 4) magnetic shielding.

Telemetry Transmitter and Receiver

The TM shown schematically in Fig 6 and photographed in Fig 7 was made up of boards and commercial components previously used in other telemetry systems. The module, powered by a regulated, 10-cell 170mAh Ni-Cd battery, is an FM/FM system that was used without modulating the sub-carrier oscillator (SCO). The SCO is a 225-kHz ± 15% voltage-controlled oscillator (QuadTron VCO) - used at its lower band-edge (~192 KHz). The signal was amplified before it was used to modulate the 2.2-GHz carrier produced by a second VCO made by Pacific Monolith (PMI VCO). This UHF signal was then amplified by a Celeritek power amplifier to produce about 17dBm (50 mW), and then fed by a probe to a 50-mil rectangular patch antenna. The dimensions of the antenna were nominally 860 mils by 1024 mils, with the feed point inset 331 mils for impedance matching. This module was entirely encapsulated in STYCAST insulating material with only the antenna and battery connector exposed. The encapsulated package and batteries were also enclosed by magnetic shields in some of the tests, as illustrated in Fig 3, above.

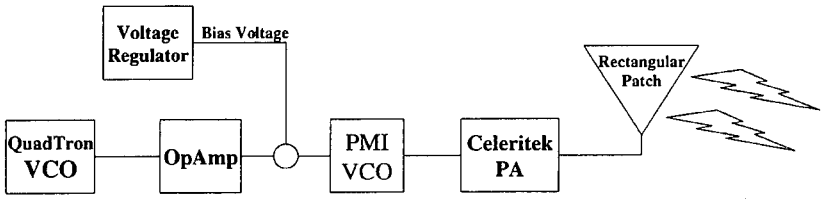


FIGURE 6. A schematic diagram of telemetry transmitter module tested in this analysis is shown.

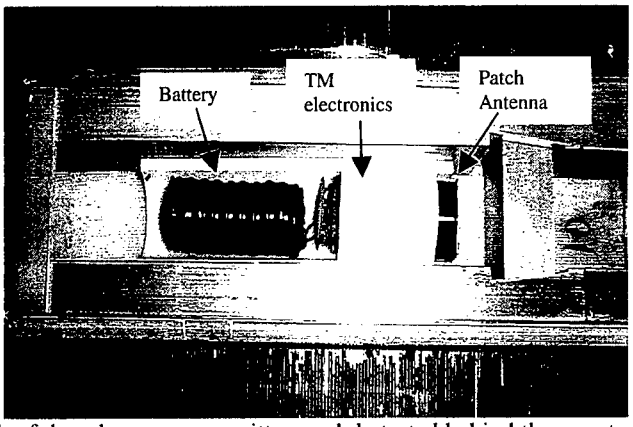


FIGURE 7. A photograph of the telemetry transmitter module tested behind the armature in this analysis is shown. With the upper sections of the containment-structure and magnetic shield removed, the TM package, armature and rails are visible.

Two similarly oriented receiving antennae were placed within a meter of each other, and positioned to detect the telemetry signal, as shown schematically in Fig 8. A spectrum analyzer connected to antenna 1 was used to establish the optimum positioning of both antennae by continuously providing the carrier noise levels of the received UHF signal. The receiver was used to demodulate the received signal, which was digitized and stored for subsequent analysis.

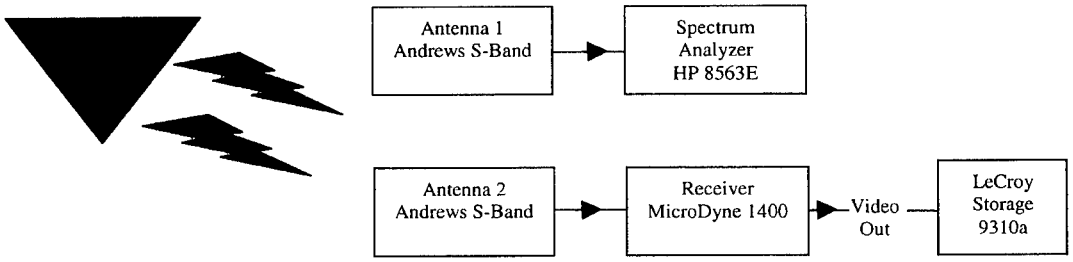


FIGURE 8. A schematic diagram of telemetry receiver tested in this analysis is shown. Signal and noise levels were measured with the spectrum analyzer to optimize positioning of both receiving antennae. Experimental measurements of the demodulated signal detected by the MicroDyne receiver were digitized and recorded by the LeCroy oscilloscope for analyses.

Telemetry Measurements in the Quiescent MCL

Experiments were first conducted under quiescent conditions to ascertain the interference effects of the rail and containment structure in the presence of a conducting armature, which effectively closed one end of the MCL "waveguide". Measurements corroborated those obtained in [3], and further established that signals transmitted from the telemetry package - placed in

front of a conducting armature at positions throughout the full 7-m bore - were readily received and demodulated using receiving antennae positioned several feet outside the bore, anywhere from 50 to 345 inches from the transmitting antenna. Extremes in the signal/noise levels versus antennae separation were mild, varying only a few dB, and the MCL containment structure was observed to reduce the signal level by only about 10 dB.

Telemetry Measurements in a Magnetized Bore - TM Package ahead of the Armature

The reminder of the experimental analyses considered telemetry in a magnetized bore with the containment structure in place. The TM package was first placed in front of the armature (as illustrated in Fig 3), with the patch antenna at the muzzle end of the package at 4½ armature-heights from the armature's trailing edge - a relatively practical arrangement if it is to be launched with a standard KJ200 armature on the MCL without a muzzle shunt. The receiving antennae were positioned outside the bore and containment structure about 10-ft from the package. Telemetry measurements were recorded for a number of tests, with currents varying from 0 to 100 kA, and both with and without magnetic shields.

The SCO signals were analyzed by forming spectrogram plots. These were generated by sub-dividing each 10-s (250k) data record into 328-μs (8k) sub-records. The sub-records were 50% overlapped, with a Hamming window applied before calculating each digital Fourier transform (FFT). Every FFT had a 12.5 MHz Nyquist frequency and a 3-kHz fundamental frequency, but each plot was frequency limited to 500 kHz and amplitude limited to a minimum of -75 dB relative to the peak. The origin of the time axis corresponds to the beginning of each current pulse, where spectra at positive times describe the telemetry measurements just after the current pulse was applied.

The spectrograms corresponding to the conditional extremes investigated in front of the armature are shown in Fig 9, where the Aluminum shielded TM package was used and no current was applied to the railgun, and in Fig 10, where an unshielded TM package was used and 100 kA was applied. The received modulation signal peaked at 192.6 kHz in all of these cases, with the first harmonic clearly visible at 385 kHz, about 25 dB below the fundamental. No change or degradation was observed for any of the measurements in which the telemetry package was placed in front of the armature.

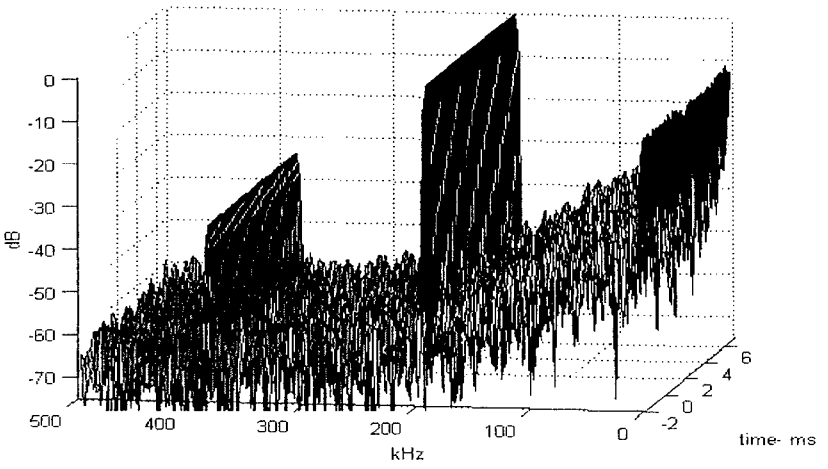


FIGURE 9. Spectrogram of the demodulated Telemetry signal transmitted from an Aluminum-shielded TM package 4.5 arm heights in front of armature. There was no railgun current (I = 0).

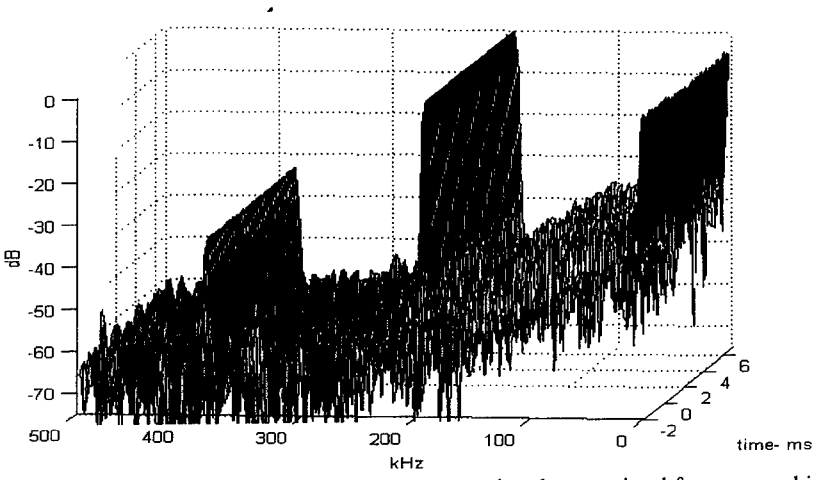


FIGURE 10. Spectrogram of the demodulated Telemetry signal transmitted from an unshielded TM package 4.5 arm heights in front of armature. The peak railgun current I was 100 kA.

Telemetry Measurements in a Magnetized Bore - TM Package behind the Armature

The magnetic field transients had to be increased significantly in order to affect changes in the received telemetry signal. This was accomplished by placing the TM package directly behind the armature, with the patch antenna at the muzzle end of the package, positioned 0.45 armature-heights behind the armature's trailing edge, as illustrated in Fig 3. For the same 100-kA railgun current, the magnetic fields and induced voltages in this region were more than 2-orders of magnitude higher than the corresponding fields and voltages in regions ahead of the armature, as discussed above.

When the telemetry module was exposed to these higher field transients, a dc shift in the receiver's video output was observed. Such a change occurs when there is a corresponding shift in the carrier frequency. Because of the FM modulation scheme used, any change in the transmit frequency corresponds to a voltage shift after demodulation. The amount of voltage shift on the output was controlled by the video gain of the receiver, which for these measurements was about 3 V/MHz. The intermediate frequency (IF) bandwidth of the receiver was set to allow it to frequency demodulate the UHF signal within a (locking) window of about $\pm$ 2 MHz.

The measured frequency shifts of the received signal are shown as a function of time in Fig 11 for three magnetic-shield examples when a 100 kA current pulse was applied. The origin of the time axis corresponds to the beginning of each current pulse. The frequency shift in the case without a shield was somewhat different from those in the other two cases. It had a sharp, positive frequency shift, which was coincident with the rise in magnetic field, and remained positive for times less than 0.3 ms. The frequency shift in the case with the copper shield was the smallest of all, but persisted for the longest time – consistent with the longer magnetic diffusion time associated with this more conductive shield.

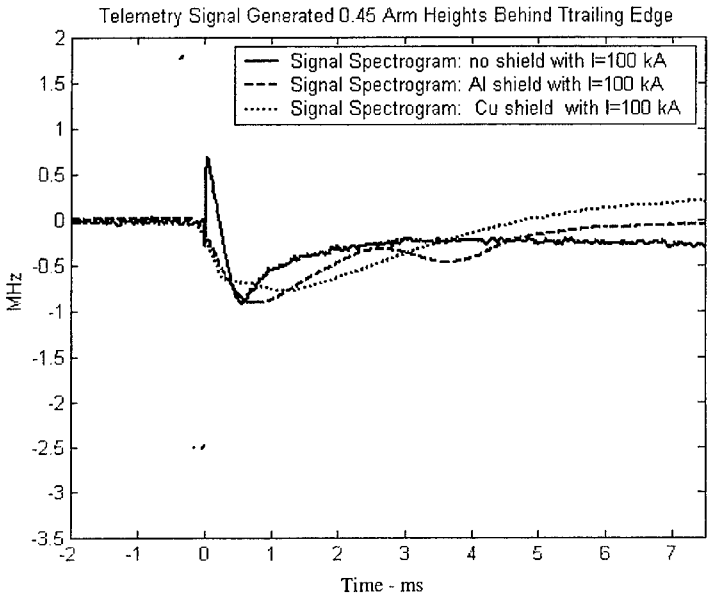


FIGURE 11. Measured (received) carrier frequency shifts, shown for different TM shields, were caused by magnetic field transients behind the armature.

More significant frequency shifting was observed when 1) the TM signal polarization was changed by rotating the patch antenna by 90° with respect to the rails, and/or 2) when **|B|** was increased by a factor of three by increasing railgun current. Two such examples are shown as a function of time in Fig 12, along with one of the previous cases, the 100-kA current, Aluminum shielded case with the original antenna orientation, for reference. In these two cases, the effects of the antenna rotation and/or the increase in **|B|** are so large that the telemetry link is lost temporarily.

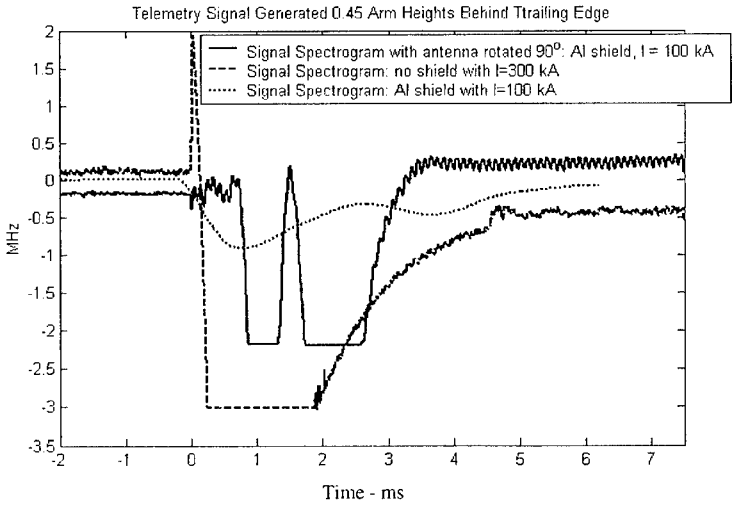


FIGURE 12. The measured (received) carrier frequency shifts become clipped if the TM antenna is rotated 90°, or if the current waveform shown in Fig 4 is increased by a factor of 3.

Spectrograms of the demodulated signal for the five high field transient cases corresponding to Figs 11 and 12 are shown in Figs 13-17. The results in Figs 13-15, which correspond to the cases having no shield, an Aluminum shield, and a Copper shield, respectively, show that the 192.5 kHz received modulation signal and its first harmonic had neither frequency nor amplitude deviation. Both were essentially unaffected by the high field transients - even as the carrier frequency was shifted by 1 MHz. Although a low-level broadband noise more than 50 dB below the received signal level emerged during the high magnetic field rise, only the lowest frequency components (< 20 kHz) were affected over the times during which the carrier frequency shifted (see also Fig 11). The results in Figs 16 and 17, which correspond to the cases where the TM antenna was rotated by 90°, and where |B| was increased by a factor of 3, respectively, show that the telemetry link was lost completely due to large frequency shifting (see also Fig 12). However, the modulated signal recovered in all cases - undistorted in both frequency and amplitude and coincident with the recapture of the telemetry link.

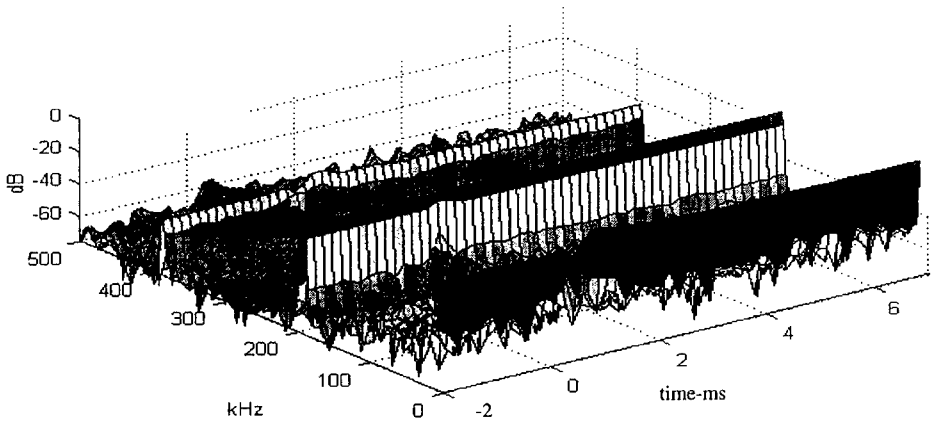


FIGURE 13. Spectrogram of the Received Signal with no magnetic shield, peak current I=100 kA.

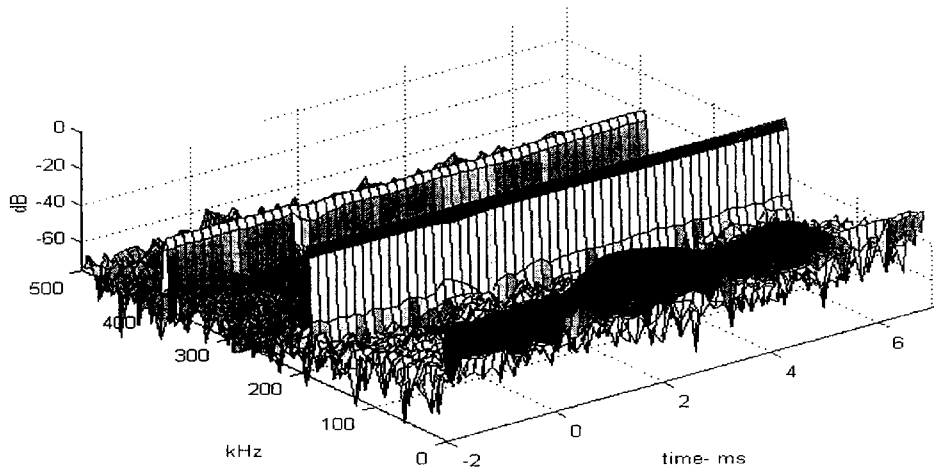


FIGURE 14. Spectrogram of the Received Signal with Al magnetic shield, peak current I=100 kA.

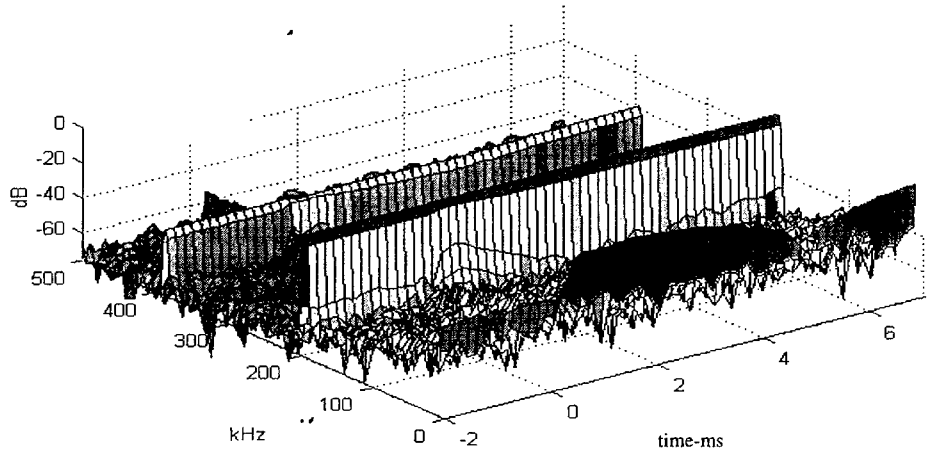


FIGURE 15. Spectrogram of the Received Signal with Cu magnetic shield, peak current I=100 kA.

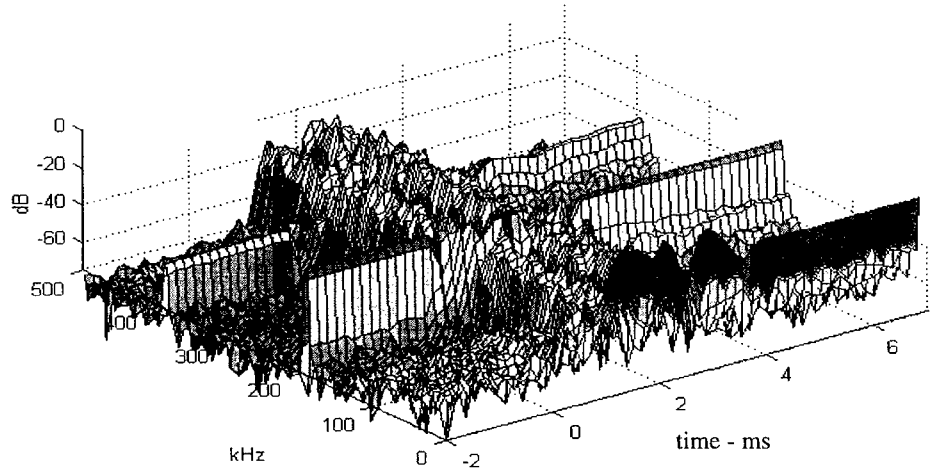


FIGURE 16. Spectrogram of the Received Signal with TM antenna rotated 90 deg, no magnetic shield.

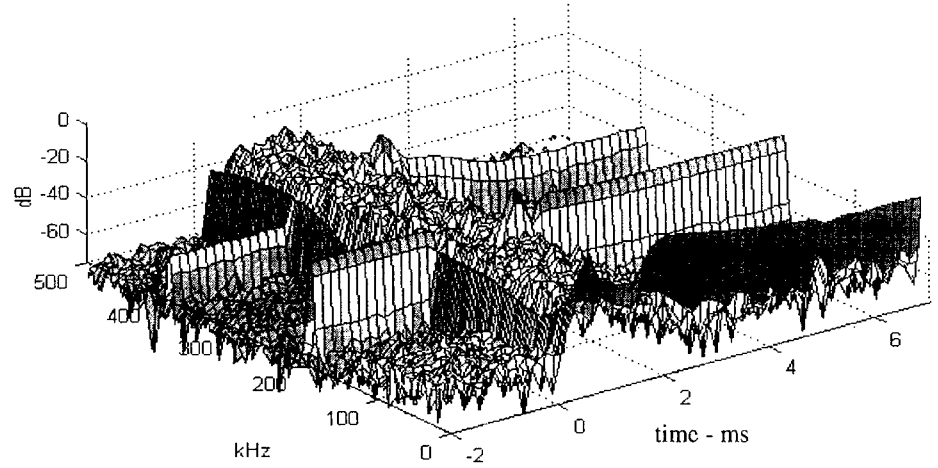


FIGURE 17. Spectrogram of the Received Signal with neither antenna rotation nor magnetic shield, peak current = 300 kA.

Discussion

Possible reasons for a frequency shift of the transmitter are 1) frequency pushing of the VCO due to a power supply fluctuation or 2) frequency pulling of the VCO because of an effective impedance change and/or induced voltage on the transmitting antenna. Loss of the telemetry link will occur whenever the telemetry signal experiences a frequency shift that is larger than the tuning bandwidth of the receiver or whenever there is a failure of the TM package. The telemetry link always recovered in this investigation. So, while it is conceivable that the TM package may have only suffered a transient failure each time the telemetry link was temporarily broken, it is more likely that the transmitter carrier frequency shifted outside the tuning bandwidth of the receiver causing loss of data.

For the two 100 kA cases in Fig 12 - where the test conditions were identical except for a 90° rotation of the TM antenna, the telemetry link temporarily broke only when the antenna was rotated. As the diagram in Fig 18 illustrates, the TM patch antenna is normally oriented to transmit the signal with the H plane aligned in quadrature to the strongest component of the railgun's magnetic field transient. This orientation minimizes coupling of the antenna with that field component; however, if it is rotated by 90°, coupling is maximized. Thus, the primary cause of the temporary loss of the telemetry link in this study can probably be attributed to coupling to the antenna of the large, transient B field.

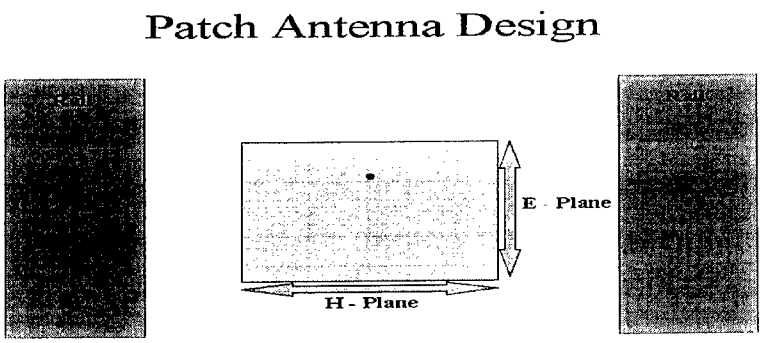


FIGURE 18. The telemetry signal polarization is shown - viewed into the railgun barrel - for the normal orientation of the patch antenna. The magnetic field from the railgun is strongest and aligned with the E-Plane at the barrel center. If the antenna is rotated 90°, the H-plane is aligned with the strongest magnetic component of the railgun.

SUMMARY AND CONCLUSIONS

An experimental investigation has been conducted to analyze the feasibility of using telemetry techniques in conjunction with on-board diagnostics for EM launchers. It was determined that microwave energy propagates without difficulty inside as well as through the MCL barrel, which is surrounded by a laminated containment and closed on one end by a conducting armature. The magnetic field transients associated with active EM launches were simulated in stationary experiments with magnetic fields in the bore increasing at rates as high as

17 T/ms up to peak levels of 4.8 T. Aluminum and copper cylinders surrounding the telemetry transmitter were also investigated to assess their effectiveness as magnetic shields.

The results of this study indicate that telemetry can likely be performed successfully in an EM launch - and should be evaluated further using the actual HSTSS components as they become available. There were two cases observed where telemetry failed after losing frequency lock of the signal: 1) when an inappropriate transmitting antenna orientation was used or 2) in a configuration which produced an exceedingly high, transient magnetic field. In both cases, recovery occurred after 2 ms, suggesting that - at a minimum - telemetry might be used once the projectile exits the EM launcher's barrel.

Several steps can be taken to avoid and/or mitigate both kinds of failures in future measurements. Using proper antenna polarization will help eliminate a failure due to the coupling of magnetic energy into the TM antenna. Failure due to excessive frequency deviations can be minimized by increasing the IF bandwidth to allow the receiver to track larger shifts in frequency. Additional improvements to this system in an EM environment include:

- Incorporating an isolator between the antenna and transmitter
- Using a highly frequency-selective antenna coupling to the transmitter (e.g., EM coupling)
- Employing a smaller, improved antenna design – e.g., one in which less of the railgun's off-axis magnetic field can couple to the antenna

Other areas that need to be addressed for the EM gun environment include:

- Technology dependent sensors (i.e., piezoelectric, piezoresistive, etc.)
- Signal conditioning and encoding circuits (digital & analog)
- Battery and power conditioning technologies
- Printed wiring board layout, component orientation, and board interconnect

Both in-bore and free flight measurement systems should be realizable for EM gun projectiles. The highly integrated components being produced by the U.S. Army's HSTSS program coupled with continued EM gun research and development activities will make telemetry a practical solution for on-board measurements in EM gun systems.

ACKNOWLEDGEMENTS

The authors would like to acknowledge Paul Snowden and John Goutier of the Institute for Advanced Technology for their technical support and operation of the MCL, and Mr. Phillip Peregino and Mr. Charles Mitchell of the U. S. Army Research Laboratory for their excellent mechanical design and fabrication support. Mr. Robert Wert and Mr. Nathaniel Hundley, also of the Army Research Laboratory, are also recognized for their electronic fabrication and testing support. In addition, the authors would like to thank the HSTSS Project Director, Mr. Dennis Schneider, of the U.S. Army Simulation Training Instrumentation Command for funding a significant portion of this research study.

This work was supported by the U. S. Army Research Laboratory (ARL) under contract DAAA21-93-C-0101.

REFERENCES

1. William D'Amico, "Telemetry Systems and Electric Gun Projectiles," William P. D'Amico, *Magnetics*, **37,** Jan. 2001
2. Jerald V. Parker and Scott J. Levinson, "Loss of Propulsive Force in Railguns with Laminated Containment," *IEEE Trans. Mag. 35*, 442-446, Jan. 1999
3. Scott Levinson, "Measurements of UHF Propagation in the MCL, Part 1: Quiescent Evaluation," IAT.TN.0196, July 2000.
4. Scott Levinson, Mehmet Erengil, Jonah Faust, and Larry Burke, "Evaluation of Magnetic Shields for Instrumented Launch Packages," IAT.TR**265** Apr 2001.
5. Jerald V. Parker and Scott J. Levinson, "Muzzle Arc Control Using and Inductive Shunt," IEEE Trans. Magn. 33, pp.594-598 Jan. 1997 .
6. Private discussions with Francis Stefani and Trevor Watt, concerning muzzle shunt experiments they conducted on the MCL at the IAT in Sept. 2000.

USE OF AN INSTRUMENTED 120MM PROJECTILE FOR OBTAINING IN-BORE GUN DYNAMICS DATA

D.W. Lodge[1], and A.M. Dilkes[1]

[1] *Defence Evaluation & Research Agency, Chobham Lane, Cherstey, Surrey, KT16 0EE, UK.*

Simulation work undertaken by DERA to investigate the dynamic behaviour of gun systems during firing has predominantly used the existing package of SIMBAD. In-bore behaviour of the projectile has had little experimental data to increase confidence in the modelling predictions. A programme of work was started in 1996 for the UK MoD with the aim of designing, building and firing a number of instrumented projectiles, the final objective being to obtain data with which to validate a model of the Challenger 2 MBT L30 gun system.

The UK design consists of a 16-channel data-logger, which captures the information during in-bore motion together with a specially designed battery assembly. Data is stored on board and downloaded once the projectile has been recovered. Instrumentation consists of six accelerometers and six displacement transducers for the purposes of measuring overall projectile motion as well as in-bore balloting of the projectile relative to the barrel.

Three projectiles were fired from a smoothbore 120mm L30 gun system in March 2000 and retrieved using over-water recovery. The last round was fired with a muzzle velocity of 1550m/s resulting in a peak acceleration of 42,000g. All data-loggers and accelerometers survived the launch along with a number of the displacement transducers. Although the data gathered proved insufficient for full model validation purposes, important lessons were learnt regarding instrumentation components, particularly battery design and assembly. These lessons are being incorporated into a series of instrumented firings planned for a 90mm electro-magnetic launcher.

INTRODUCTION

The Defence Evaluation and Research Agency (DERA) has conducted applied research for the UK Ministry of Defence over many years into the accuracy and consistency of conventional gun systems and projectiles. One strand of this work investigates the in-bore dynamics of the system using the gun dynamics codes such as SIMBAD [1, 2].

An initial study into technology [3] of possible use in the instrumented projectile was conducted in 1994. The overriding conclusion was that the best method for obtaining data would be by the use of onboard transducers connected to a data recorder (logger), with the latter being retrieved from a fired projectile and the data downloaded. Work in other areas of the DERA had successfully used onboard recorders, in measuring projectile fin temperatures during free flight [4]. Work prior to 1995 had centred on the use of a 155mm artillery shell

[5], since the useable volume within a 155mm shell was more than adequate for the purposes of housing the proposed instrumentation. Two schemes for mounting the data recorder in the nose and in the base of the round were formulated. The simple data recorder and accelerometer package recorded a maximum axial deceleration of 3,000g, well below the expected axial acceleration during firing of 20,000g or more but was sufficient to demonstrate a simple "proof of principle" for gun fired projectiles.

Due to subsequent budgetary limitations the 155mm work was dropped as it was felt that sufficient knowledge and experience had been gained to transfer the technology directly to a large calibre Main Battle Tank (MBT) type gun.

A clear definition of the requirements of an 'instrumented carrier projectile' for the validation of the gun dynamics shot models was required. With this in mind, input data values used in the SIMBAD dynamics codes to model the British Army's L23A1 APFSDS projectile fired from their L11 120mm gun system (Challenger 1) were revised and checked. Selected sensitivity studies were conducted aimed at obtaining predictions on the typical and peak displacements, velocities, accelerations and forces experienced by the L23A1 APFSDS projectile during its in-bore travel.

CARRIER PROJECTILE CONSIDERATIONS

Since 120mm APFSDS ammunition remains the primary nature of shot used by the British Army, it was logical to validate the modelling work using such a projectile. There is one immediate problem apparent when looking at any APFSDS projectile for use as an instrumented carrier, which is that on exit from the gun the projectile splits into several components. Use of the penetrator as a data-logger carrier would not be feasible as safe recovery is almost impossible. Both penetrator and sabot petals had insufficient internal volume to house the proposed data-loggers and battery. A 140mm round was also considered but still resulted in insufficient space [6].

The nearest workable type of projectile that could be used was the L23A1 proof shot. Though this was not specifically designed to exhibit similar dynamic behaviour to the L23A1 it had similar mass properties and identical methods of obturation so that an identical charge (L8) could be used. The obvious advantage of the proof shot is that it is not designed to break up on shot exit, allowing for full use of the internal volume and allowing the design to be kept axis-symmetric along the shot's axis of travel. An axis-symmetric design has two notable advantages. Firstly, overall centre of mass and inertia can be controlled to give close agreement with the L23A1 APFSDS projectile. Secondly, the data logger, power supply and transducers can be mounted along the axis of rotation, which if fired from a rifled barrel will reduce the amount of rotational acceleration on these components.

PROJECTILE CAPTURE

One consideration, tied closely to the choice of carrier projectile and its design, is the method by which any such projectile will be ultimately recovered. There were several possible methods:

- vertical trajectory recovery;
- over water recovery;

- over snow recovery;
- on-board projectile telemetry;
- sand butt recovery.

Although there were good and bad reasons for all of the above, Over Water Recovery (OWR) was chosen, as the DERA site at Shoeburyness had such facilities. This method involves firing over a shallow estuary at high tide so that the water provides a softer impact, waiting for the tide to go out and then recovering the projectile from the exposed ground.

MODELLING STUDIES

A comparison of the L23A1 APFSDS projectile with a possible 'instrumented carrier projectile' candidate, i.e. L23A1 proof shot was made [6]. The aim of this work was to determine to what extent changes in mass, stiffness, inertia etc. affected the dynamic response during firing. Both static and dynamic analyses, using Ideas [7], Algor [8], and SIMBAD were used for this purpose and to obtain definitive statements on the typical and 'worst case' accelerations, velocities and displacements of the L23A1 projectile for use in determining the specifications necessary for the instrumentation package. (See Figure 1 below).

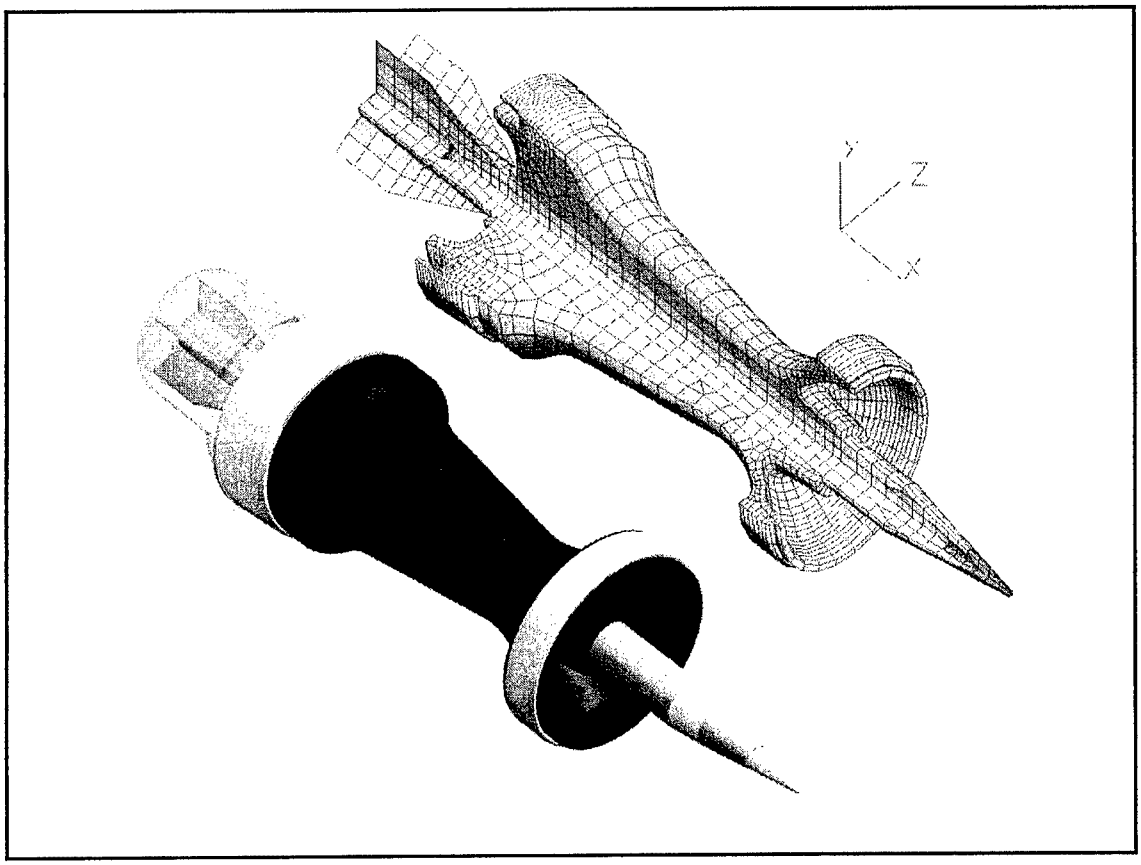


FIGURE 1. CAD & FEA models of the L23A1 APFSDS for use in the modelling studies.

The comparison of the dynamic response of the two projectiles was undertaken using SIMBAD. Numerous runs were performed to fully assess the two projectiles with the aim of finding a 'worst case' result for each projectile so that an upper limit on the specifications for the various transducers could be made.

Axial shot acceleration was seen to reach a maximum of 36,900g. Lateral accelerations of 920g and 770g were seen in the APFSDS and proof shot respectively. Instantaneous accelerations, which also include that due to pitch/yaw, gave peak accelerations of 2,040g in the APFSDS round and 1,940g proof projectile.

Runs simulating the projectiles fired from smoothbore and rifled barrels showed that the differences in projectile response between a rifled and smooth bore barrel were smaller than the differences caused by other effects. This indicated that the use of a smoothbore gun was an option for gaining data to verify shots models fired from a rifled barrel.

Bore profile or barrel straightness has been shown to be one of the most important factors that affect the gun dynamics models. It is believed to play an equally important role in real gun systems and may be the major contributor to differences in barrel MPIs. To demonstrate its effects, and to check to ensure that the maximum values of shot motion were not exceeded, experimental bore profile data for the vertical and horizontal planes were introduced into the L11 barrel model. The particular barrel bore profile used was that of one known to produce a particularly harsh response in the shot. Most importantly, instantaneous lateral acceleration on the projectile in the vertical plane increased to give values of 3,100g and 2,100g in the APFSDS and proof projectile respectively.

In summary the worst case values based on the use of experimental bore straightness data to which any instrumented projectile needed to survive and measure are given in Table 1 below. The acceleration along the barrel for these simulations is of the order of 37,000g and is by far the predominant motion. This was the maximum acceleration that the all transducers were designed to survive and operate under.

Table 1. Peak values of criteria for measurement.

Property	Maximum value
Absolute C of M bounce displacement	±8.0mm
C of M bounce wrt barrel axes	±0.8mm
Absolute C of M pitch/yaw angle	±2.5mrad
Absolute C of M pitch/yaw angular rate	±7.5rad/s
C of M pitch/yaw angle wrt barrel axes	±2.5mrad
Absolute transverse acceleration	±2,038g
Maximum frequency content of transverse accelerations	3.0 kHz to 4.0 kHz
Absolute axial velocity (shot exit)	1542m/s ±25m/s
Absolute axial acceleration	36,878g
maximum rotational acceleration (slipping band)	79,300rad/s^2
maximum rotational velocity (slipping band)	53Hz (333rad/s)
maximum centripetal acceleration (slipping band)	6653m/s^2 (678g)
Sabot/proof body transverse bending	±0.02mm
Breech pressure	434MPa
Shot exit time	10.50ms
Time to first axial & transverse motion	2.23ms
Time to 1%, 10% & 100% of maximum axial acceleration	2.63ms, 4.13ms, 6.38ms
Maximum distributed force on the driving band	±1.0MN
Maximum distributed force on the centring band	±3.0kN

INSTRUMENTATION

ACCELEROMETERS

Feasibility studies [3] indicated that accelerometers were the most appropriate transducer for in-bore measurement. One important consideration was cross-axis sensitivity. With a typical value of 5%, this would equate to a measurement error in the lateral plane almost as large as the expected accelerations. Also any slight pitch or yaw of the projectile (or a accelerometer misalignment) will introduce a component of the axial acceleration into the transverse measurement axis. If the axial acceleration is 37,000g then a pitch/yaw angle of 2.5 mrad will result in a transversely mounted accelerometer detecting a component of this acceleration equal to 92g. Although this is sufficiently small (3-5%) not to swamp the signal being measured, it is not a negligible effect, and represents a significant amount of noise.

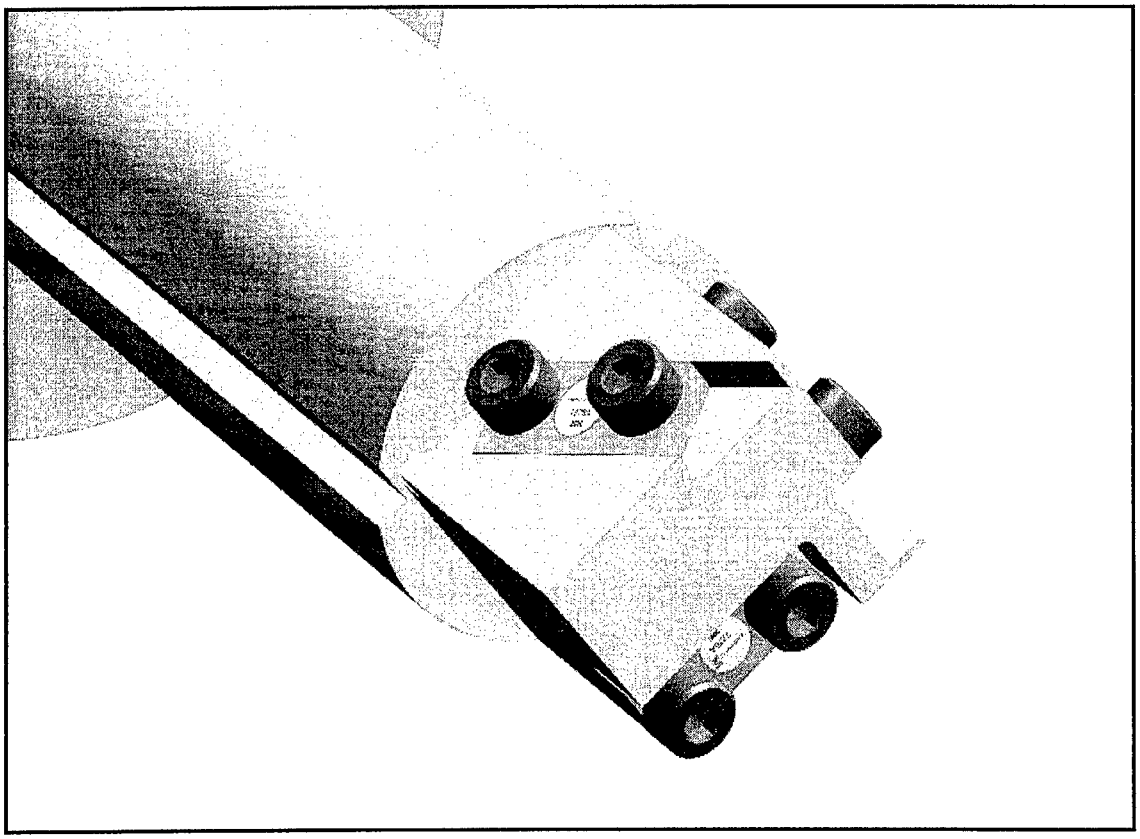


FIGURE 2. Accelerometer mounting on instrumentation carrier.

Of the possible accelerometers currently available, only the Endevco 7270A piezo-resisitive accelerometers could meet the specification [9]. The 7270A-20K (20,000g range, 60,000g limit) was the accelerometer of choice. Of the 18 accelerometers used in the final firings the mean cross-axis sensitivity was measured at 1.71% with a standard deviation of 0.41%. At worst (40,000g axial acceleration) this would give an additional 680g ±330g due to cross-axis sensitivity. This could be removed from the results though, knowing the exact cross-axis-

sensitivity for each accelerometer and having measured the axial acceleration. To fully minimise the cross-axis sensitivity, the accelerometers measuring in the transverse (lateral) plane were mounted at an angle of 30 degrees to the axial acceleration. (See Figure 2).

DISPLACEMENT TRANSDUCERS

To measure projectile motion relative to the barrel, displacement transducers were chosen. No commercially available transducers were readily available. However, a capacitive type known to work up to 5,000g was sourced from a firm (Si-Plan Electronics Research Ltd.). These were modified such that they would withstand accelerations up to 50,000g [10] (See Figure 3). Using these at two locations on the projectile body would allow both displacement and rotation of the projectile to be calculated.

These could not easily be used in a rifled barrel, which made the use of a smoothbore barrel essential. Also, bore wear needed to be minimised and carefully measured, as the resolution of these devices was sensitive enough to detect bore wear of 0.01mm (10μm).

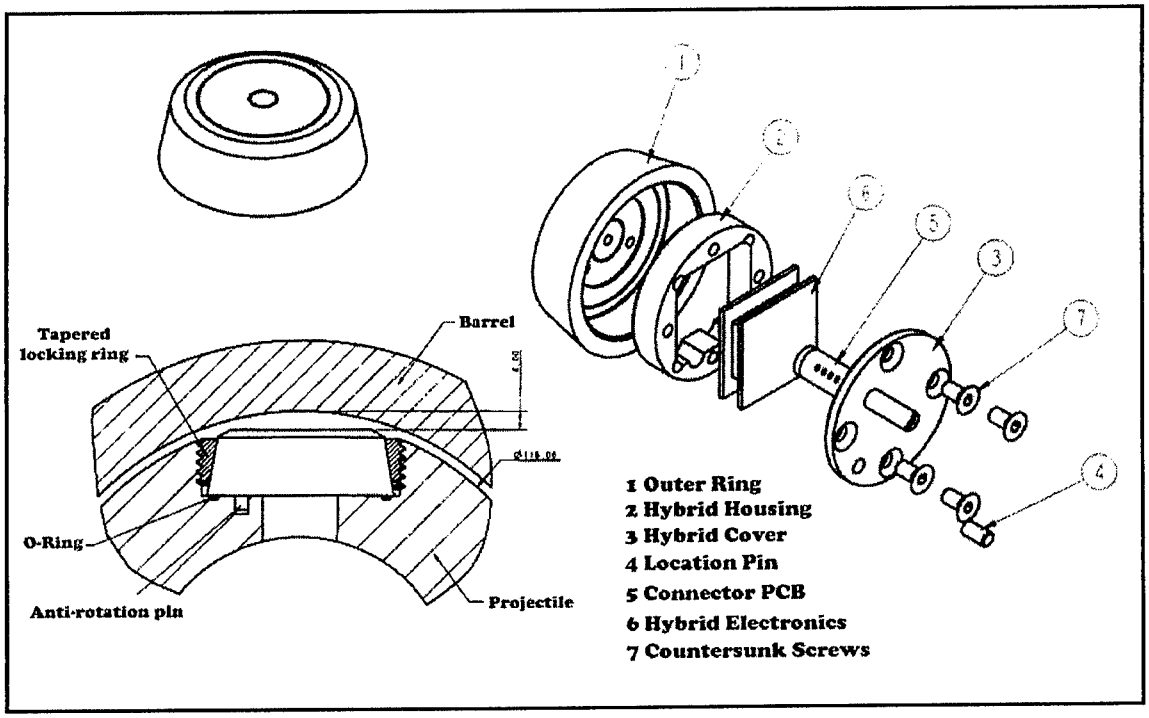


FIGURE 3. Exploded view of displacement transducer and detail of assembly into projectile.

DATALOGGER AND BATTERIES

The data recorder chosen was designed and manufactured by DERA in association with Deltatek Defence Ltd. It is a 16-channel, 12-bit, solid state device. It was designed to withstand a maximum 50,000g-shock load. Similar designs had been tested and withstood

80,000g [4]. It was hard mounted centrally in the instrumentation carrier sub-assembly by 'potting' compound introduced in a vacuum to reduce voids in the mixture.

A relatively simple battery pack was designed to supply power to the data-logger and transducers. This was constructed from standard Nickel-Cadmium (Duracell type) batteries arranged in stacks within a Nylon and aluminium bobbin and hard mounted in place in a similar fashion to the data-logger. The design was such that it formed a ring, which surrounded the main instrumentation carrier sub-assembly (See Figure 4). This ensured that the cable runs from battery to transducers were minimised.

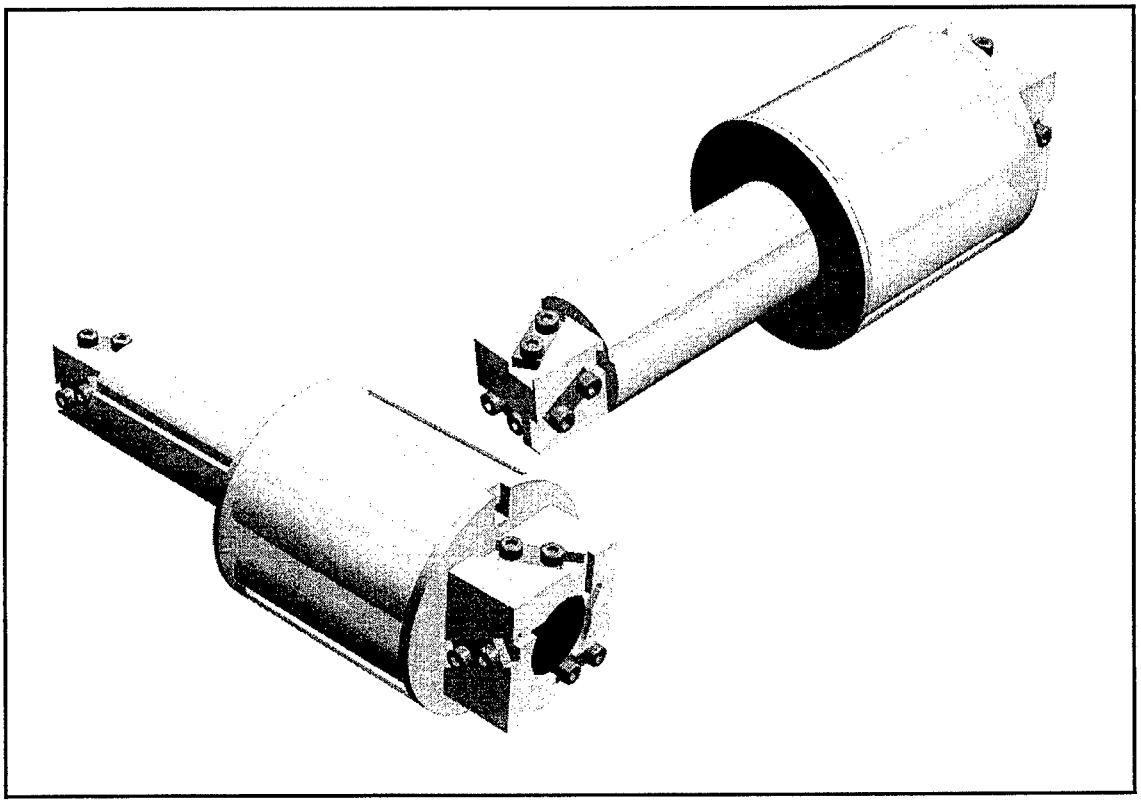


FIGURE 4. Instrumentation carrier and battery pack.

There were initial concerns about the battery life and ability of the battery to keep the logger's memory powered until recovered. Subsequent testing showed that for a standard firing, the battery would keep running for approximately 3 hours, long enough for data recovery.

The final overall design is shown in Figure 5. The package consisted of six Endevco accelerometers, six Si-Plan capacitive displacement transducers, one 16 channel DERA-Deltatek data-logger and a battery unit. All transducer cabling was encapsulated in potting compound during construction. Just prior to firing, the battery was connected to all transducers and logger through access in the front of the round. Trigger levels etc. on the data-logger were set using a laptop PC connected to the logger. The end cap was then screwed in place, using a rubber O-ring seal to prevent ingress of seawater.

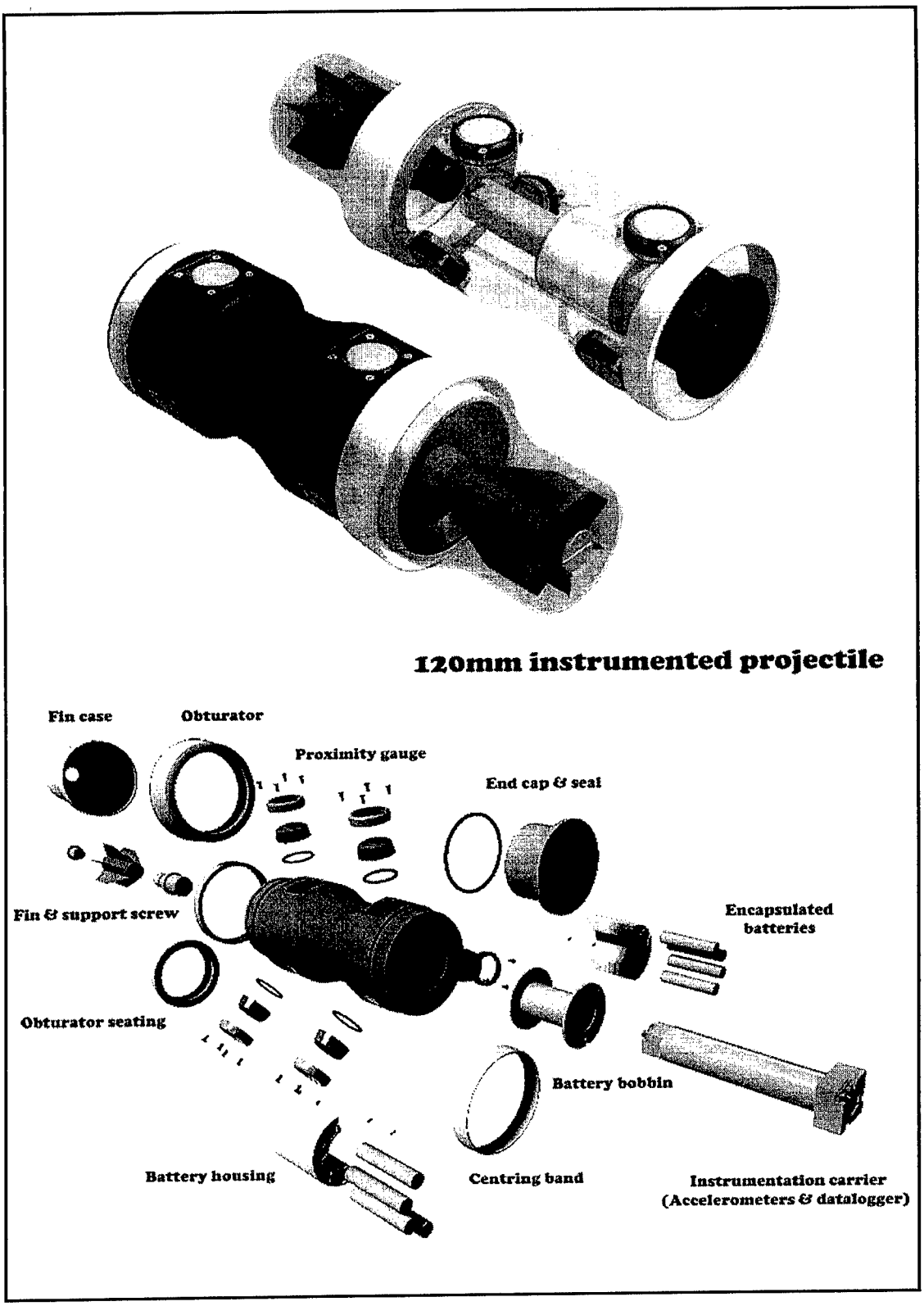


FIGURE 5. Exploded view of the 120mm instrumented projectile.

EXPERIMENTAL FIRINGS

A firing trial for the instrumented projectiles took place in March 2000 at DERA Shoeburyness, UK [11]. A smoothbore 120mm gun system fixed to a firing stand was used. In all other respects the gun system was identical to the Challenger 2 L30.

Modified L8 charges were used as the propellant. These were adjusted to give the correct muzzle velocities required for the projectiles. Three instrumented rounds were fired. All three were recovered successfully using the OWR method.

The first round was fired at a reduced muzzle velocity (24,000g). Before firing it was found that the end cap would not screw fully into the projectile body and the O-ring seal was not fully compressed. Despite this it was still fired. However, after recovery it was found that some water had penetrated into the instrumentation compartment and had 'short circuited' the batteries. A small amount of data was recovered from the data-logger before the batteries failed completely. Further checks showed that the data-logger and all accelerometers were still fully functional, though only one of the displacement transducers was found to be operational.

The second round was also fired at a reduced muzzle velocity (24,000g), due to the problems experienced with the first round. Examination of the recovered data revealed that the data-logger had triggered prior to its in-bore travel and only low level noise was present on each channel. It is not known what caused the false trigger. Further checks showed that the data-logger and accelerometers were still fully functional along with two of the displacement transducers. Testing of the battery showed this was also working correctly.

The final round was fired at a higher muzzle velocity (42,000g). On recovery, it was found that a short circuit in the battery prevented access to the data-logger. By supplying external power the data was recovered. On examination of the data, all channels were found to contain corrupted signals in the form of a square wave signal. Checks showed that the data-logger and accelerometers were still fully functional. Later x-rays of the battery revealed that several cells in the logger's battery circuit had collapsed (see Figure 6). This was probably due to a void in the potting compound around the cells. The other two battery circuits were fully functional.

CONCLUSIONS & RECOMMENDATIONS

Three 120mm instrumented proof shot rounds were built and fired from a smoothbore L30 gun system. Unfortunately, data on the in-bore motion of the projectile was not obtained due to three completely different failures modes of the instrumentation: water ingress into the battery/instrumentation compartment; false triggering of the data-logger and; cell collapse and failure within the battery.

However, all three data-loggers were fully functional after firing, together with most of the accelerometers. A small number of displacement transducers also survived. The overall design of the instrumented projectile appeared to have performed well. In addition all three rounds were launched with zero spin.

Some simple component level testing may have reduced the risk of instrumentation failure, particularly for the battery and displacement transducers, and some simplification of the design to reduce the complexity of the assembly procedure.

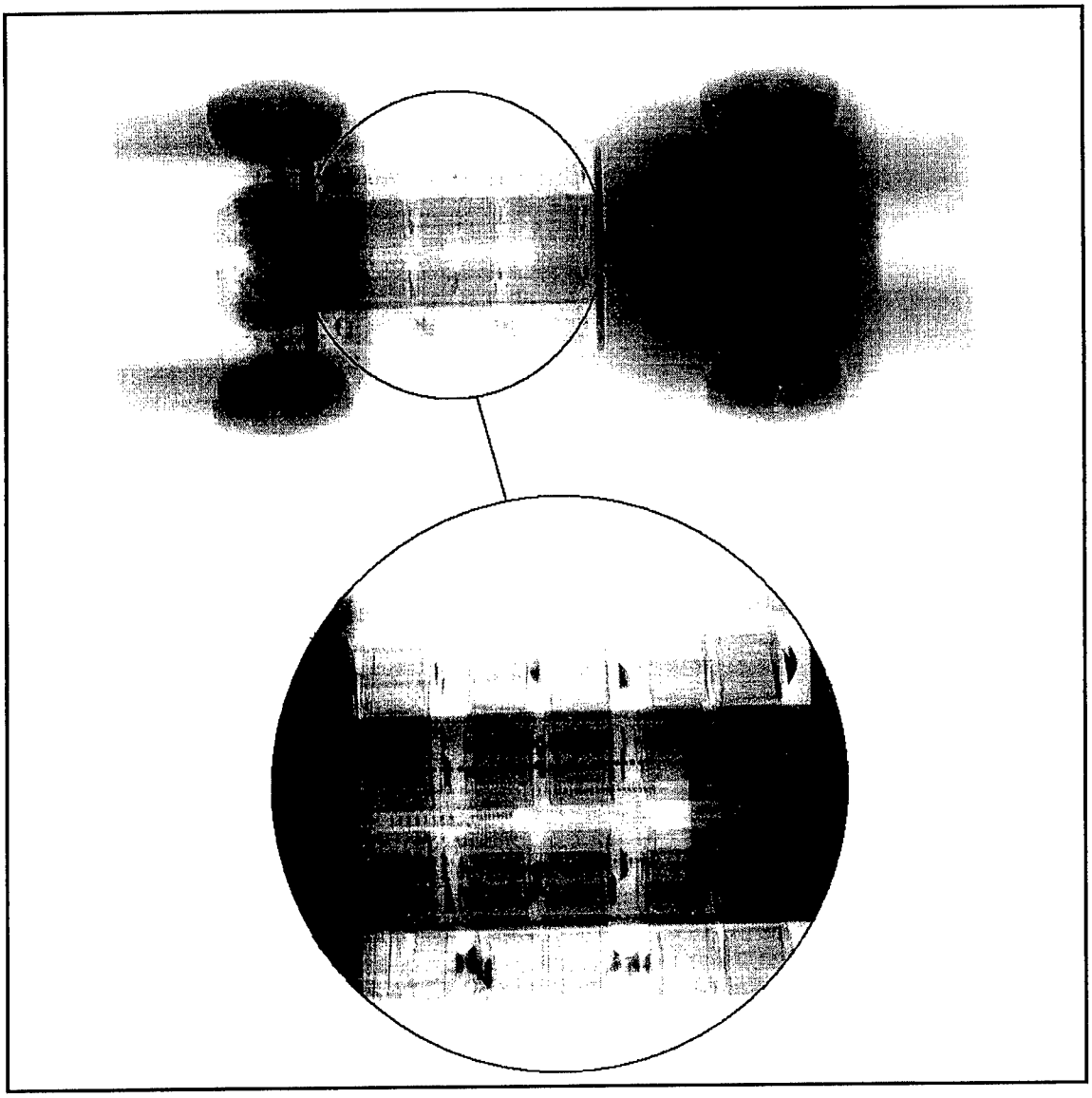


FIGURE 6. X-ray of fired projectile, highlighting battery failure.

A further trial was planned for this year but a funding cut has meant that this will not take place. Collaboration with other nations is the probably the best method now for validating the gun dynamics codes as other countries have similar programmes aimed at gaining experimental in-bore data [12,13].

These lessons are being incorporated into a series of instrumented firings planned for a 90mm electro-magnetic launcher.

REFERENCES

1. *SIMBAD users manual - version 28.* Danby Engineering Ltd., May 2000.

2. BULMAN, Prof. DN. *The in-bore bending dynamics of long rod projectiles.* 13th International Symposium on Ballistics, Stockholm, Sweden, 1992.

3. POPAT, B. *Feasibility study of in-bore projectile motion measurements.* DRA customer report DRA/FV&S4/CR9419/1.0, May 1994. UK RESTRICTED - COMMERCIAL.

4. FOSTER, GJ, EDWARDS Prof. JA, & COOPER, PH. *CAN3 projectile programme - Trial No. W7/B/24/93 Datalogger strength of design.* DRA report, October 1994. UK/CAN RESTRICTED - COMMERCIAL.

5. YOUNG, DG, CALVERT, B, & PEDRICK GA. *In-bore measurement feasibility study.* DRA customer report DRA/LS(LSF1)/CR9618/1.0, February 1996. UK RESTRICTED - COMMERCIAL.

6. LODGE, D W & BLATCHFORD, P W. *An initial study into the instrumentation of a 120 mm L23A1 proof shot for measuring in-bore projectile motion.* DERA technical report DERA/LS3/TR9712/1.0, February 1997, UK RESTRICTED - COMMERCIAL.

7. IDEAS Master Series 7.0. SDRC Operations Inc., 1999.

8. *Algor Docutech CD ROM.* Algor Inc. Pittsburgh, May 1999.

9. *Endevco model 7270A data sheet.* Meggitt Aerospace.

10. *Detailed design report for a prototype displacement transducer.* Contract LSF/E30035. Si-Plan Electronics Research Ltd. March 1998. UNCLASSIFIED.

11. TAYLOR, WM & PRING, A. *120mm Instrumented projectile over water recovery.* DERA report DERA/Ranges(Shb)/CR0658/1.0, July 2000. UK RESTRICTED.

12. ROTACHER, T & GIGER, B. *High G ballistic flight data recorder.* 18th International Ballistics Symposium, November 1999.

13. PHILLIPS, M. *HSTSS Quarterly - April 2000.* HSTSS Project Office.

© British Crown copyright 2000. Published with the permission of the Defence Evaluation and Research Agency on behalf of the Controller of HMSO.

VISUAL CHARACTERIZATION OF WEAR IN LARGE CALIBER WEAPONS

Dominick Salafia

Metrology and Simulation Division
Materiel Test Center
U. S. Army Yuma Proving Ground
Yuma, Arizona 85365

Abstract: As part of the Army Test and Evaluation Command (ATEC) the Metrology and Simulation Division at the U.S. Army Yuma Proving Ground (USAYPG) has the mission to measure and record the detrimental effects of firing conventional and experimental munitions on large caliber cannon tubes. The primary objective is to ensure that the weapon to be fired will safely meet mission requirements for the quantity and energy of the munitions under live fire testing. One aspect of this mission is to conduct physical measurements on rifled and smooth bore cannon tubes. The measured value is compared to the acceptable tolerance; from this the disposition of the weapon is then determined.

In the past physical measurements were taken with a "star gage". The star gage is used to measure wear on rifled cannon tubes. This device measures the wear of the reference "land and groove" at the zero and 90-degree positions respectively. Although this method offers a high degree of precision, faults that exist at other positions are not recorded. As a result of this limitation, wear phenomena such as erosion or build up could not be quantified. Recent developments in barrel measurement instrumentation have expanded the analytical capabilities of the status quo. Instead of two data points, 2000 data points may be measured from 0 to 360 degrees. From this data, tooth profiles for rifled barrels and wear in smooth bore cannon tubes may be displayed and three-dimensional models may be developed. Different algorithms have been developed to display collected data from a variety of perspectives. The resulting types of perspectives and the visual characterization of different types of wear will be examined in the body of this paper.

INTRODUCTION

In order to maximize safety, and to accurately assess the performance of conventional and experimental muntions, regulation dictates that physical measurements be performed to gage the wear induced from firing. Figure 1 defines the terminology and conventions subsequently used in the body of this paper. Inspections normally occur at specific distances with respect to the "origin of rifling" for the weapon being tested. The origin of rifling (OR) is usually indicated as d=0 and zero degrees corresponds to top dead center or 12 o'clock. Subsequent measurements down the bore are positive. Figure 2 shows the tooth profile at the OR for a 155mm cannon tube measured radially from the centerline of the bore. The displacement between 120 degrees and 330 degrees indicates wear on the lands. A three-dimensional model may be constructed by adjusting for the twist of the rifling and piecing the data together linearly using a Delaunay triangulation method [1,2]. Figure 2 illustrates this methodology. Although the raw data is useful for generation of computer models, the amount of data is cumbersome to process and not easily interpreted by the untrained eye. By reducing the data to 48 land and groove radii, the data processing is faster and produces clearer results. Averaging the radial values with respect to lands and grooves reduces the data. Using this method, the wear effects between firing missions

may be quantifiably visualized. Groove radial analysis, land radial analysis, land/groove height radial analysis, percent wear analysis and a comparative analysis showing the cumulative effect of firing an additional 496 rounds through a 155mm cannon tube will be illustrated and discussed. The standard statistical analysis may be applied to the data from each measurement position. This discussion will focus on three dimensional analysis techniques and how this method may be used to gage the increase in wear from mission to mission.

DEFINITION OF TERMS AND CONVENTIONS

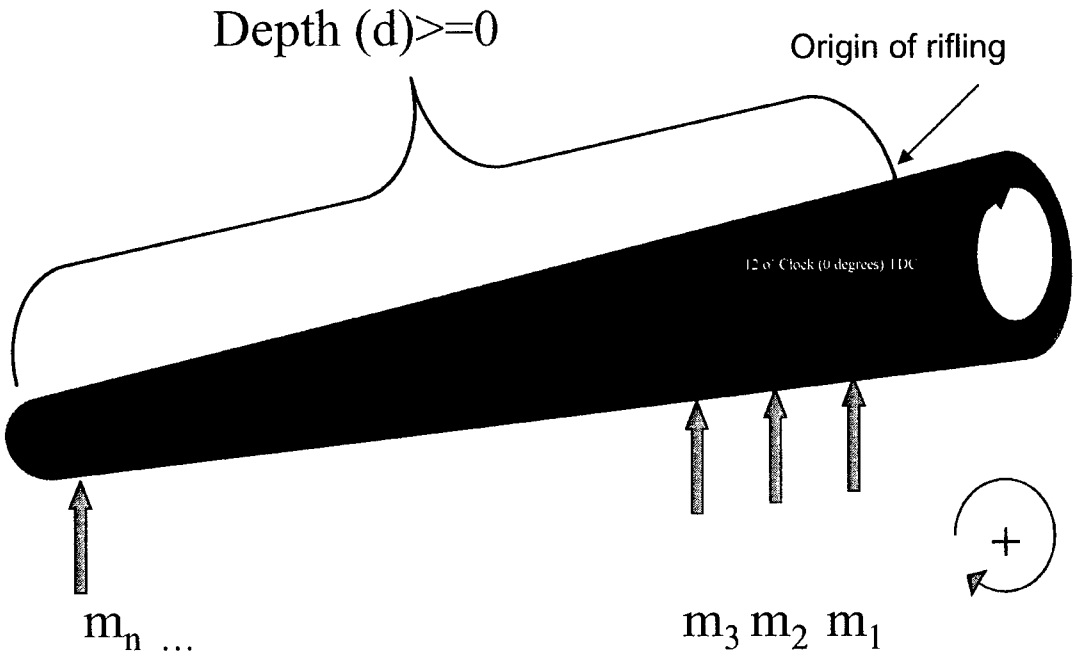


FIGURE 1 Definition of Terminology and Sign Conventions.

The parameters shown in Figure 1 are defined as follows:

Origin of Rifling (OR): The point at which the commencement of full rifling begins.

Depth (d): The length down the bore at which the measurement is taken in millimeters. The origin of rifling is designated as d=0.

$m_1 \ldots m_n$: An index of measurements at a specific depth.

12 o' Clock: Zero degrees top dead center (TDC) of the cannon tube with positive rotation clockwise.

MODELING

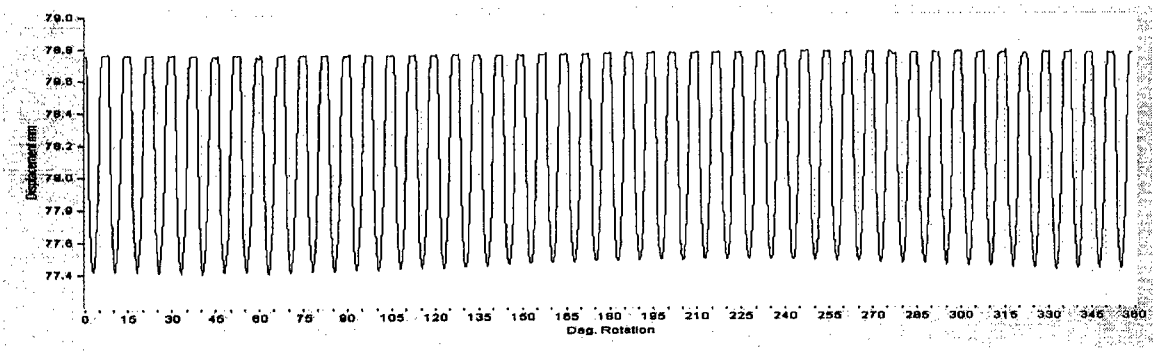


FIGURE 2 Tooth Profile at Origin of Rifling (OR), Depth=0

As indicated in Figure 3., the protuberance on the first groove represents a loss of material. In the corresponding density (top view) plot the chrome loss shows as a darker line at approximately 7 degrees rotation. Loss of land material (tooth wear) is indicated by the different intensities at approximately 3 degrees and 11 degrees rotation respectively

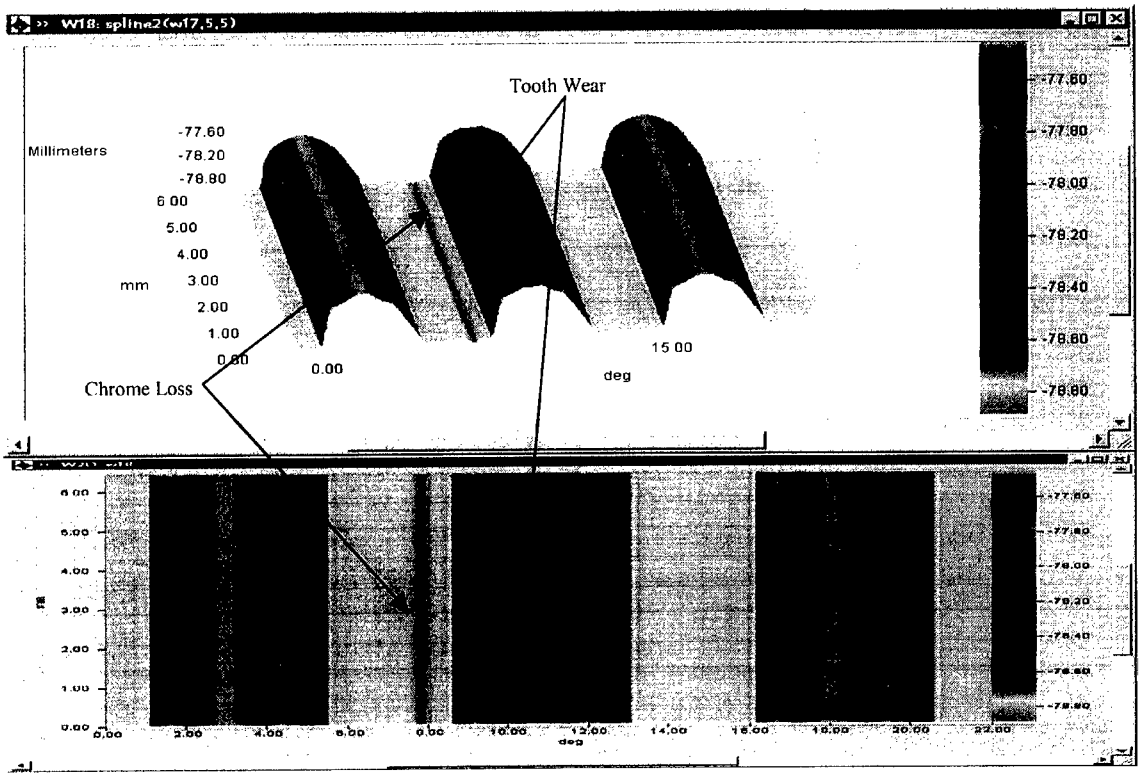


FIGURE 3 Three Dimensional Tooth Profile and corresponding Density plot.

RADIAL ANALYSIS

Let us now examine the effect of firing 496 rounds through a tube. The data at 2060 rounds will serve as a baseline measurement. The advantages and disadvantages for each type of analysis will be discussed.

Three Dimensional Groove Radial Analysis

The reduced data may be represented as a surface plot with corresponding top view (contour plot). Since most of the wear is on the rifling (lands), the groove radius is consistent with the manufacturing tolerance of the weapon. This is a useful technique for acceptance of new cannon tubes. Since the grooves see a minimal amount of wear throughout the lifetime of the weapon, this radius is expected to remain consistent. An example of summary statistical calculations is shown in Figure 4. Subsequent measurements can then be compared to the baseline data (ideally a new gun tube). Although this is a poor indicator of wear, this is a useful method to visualize and quantify any buildup of material in the grooves.

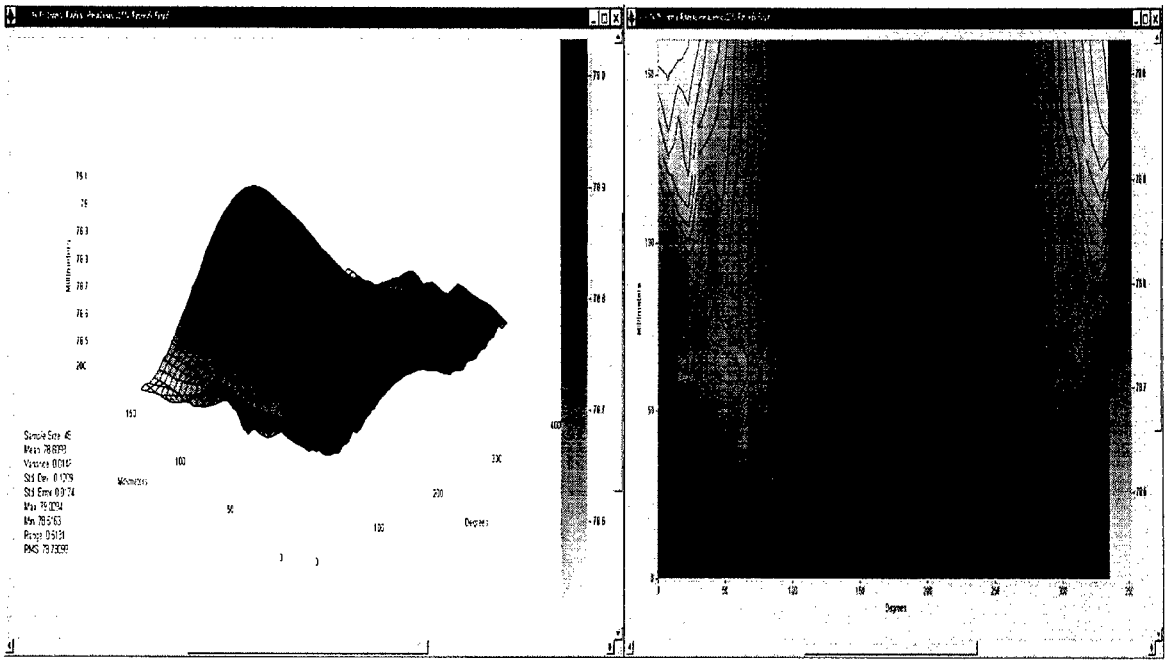


FIGURE 4. Land Radial Analysis 3 Dimensional Surface plot and corresponding top view

Three Dimensional Land Radial Analysis

Figures 5 and 6 illustrate wear on the lands. Unless the person viewing the data is familiar with measurement tolerances, the degree of wear measured is not clearly evident. However people such as inspectors and test engineers would notice significant wear about the zero degree position.

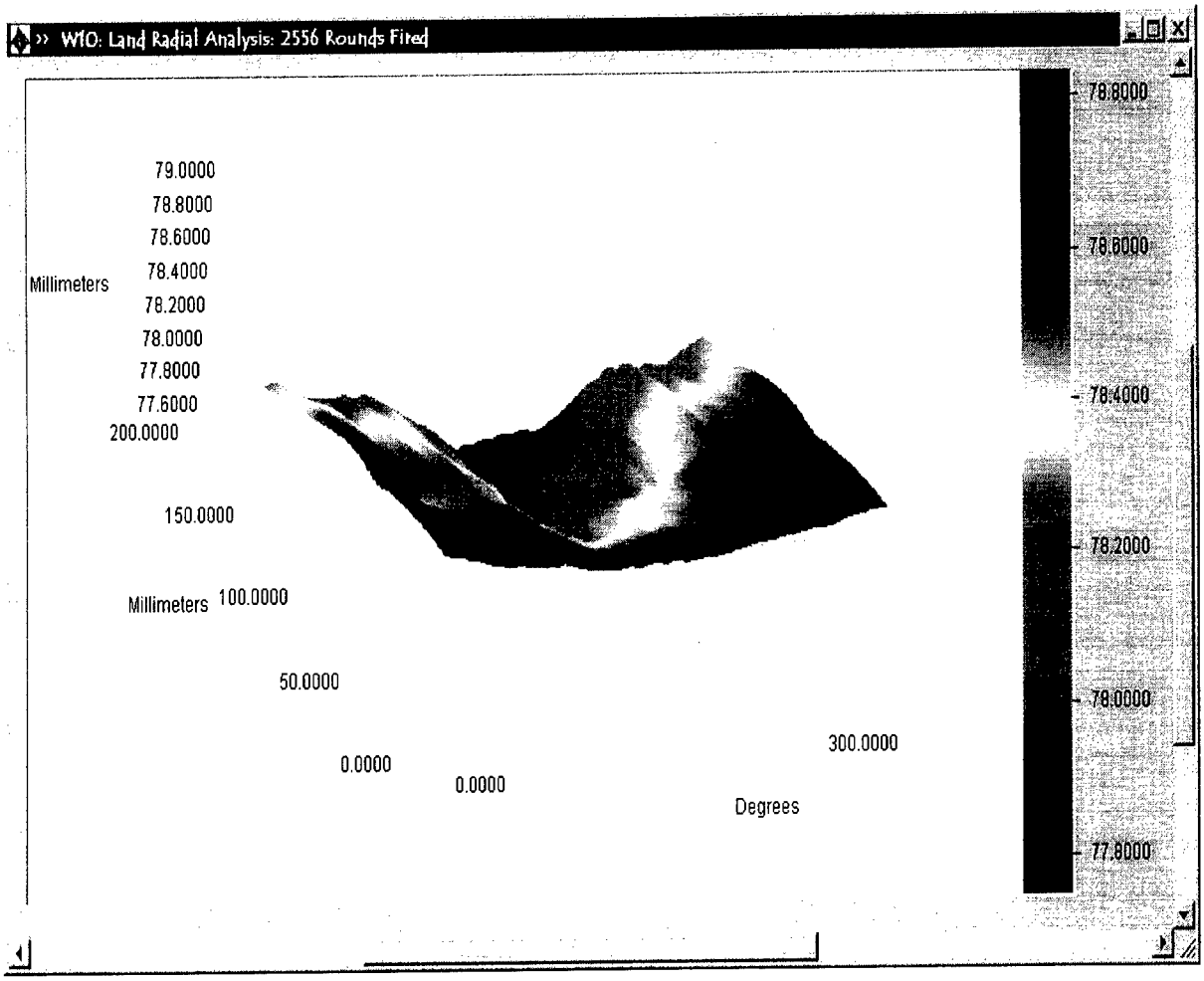


FIGURE 5 Land Radial Analysis 3 Dimensional Surface Plot

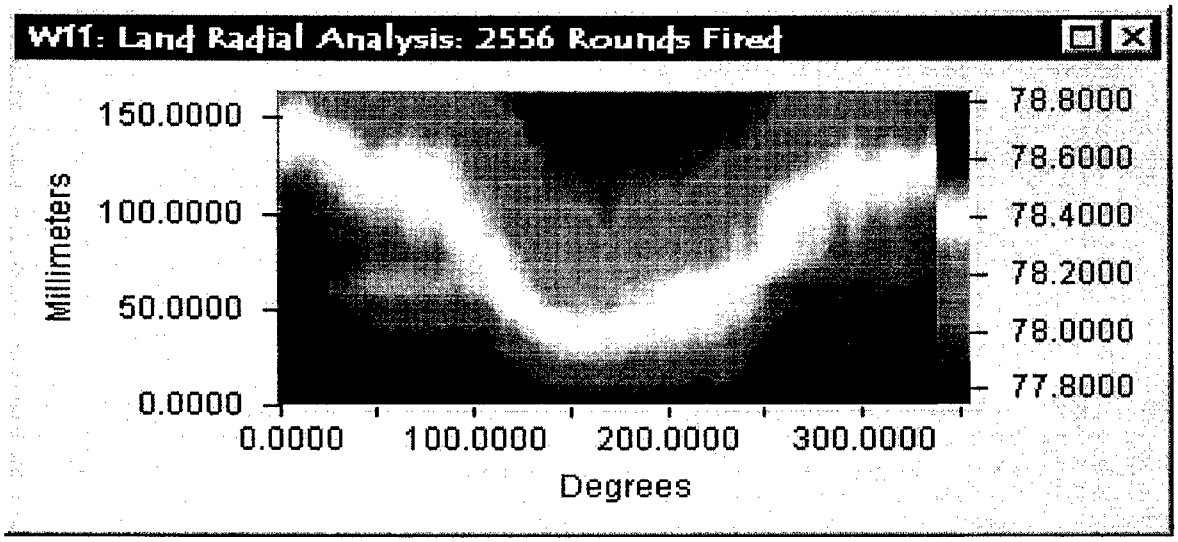


FIGURE 6 Land Radial Analysis corresponding top view

Three Dimensional Land/Groove Height Analysis

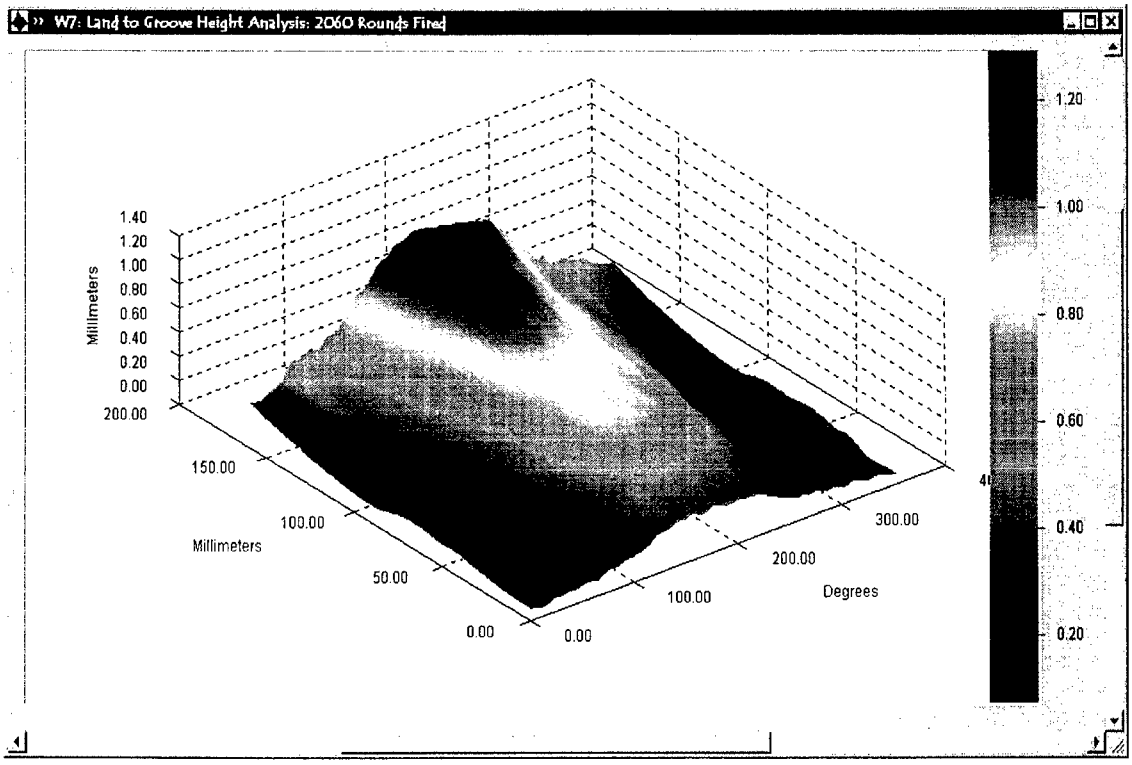


FIGURE 7 Land/Groove Height Analysis 3 Dimensional Surface Plot

This analysis is the most indicative of wear with respect to the weapon under test [3]. The relation of land to groove heights is plotted as a three-dimensional surface with the corresponding top view Figures 7 and 8. Note that the height is approximately zero at the zero degree (12 o'clock) position indicating a significant tooth loss and that this weapon is nearly at the deadline criteria [4]. This method still requires that the analyst is familiar with the tolerances and deadline criteria for this particular weapon.

PERCENT WEAR ANALYSIS

In order to compare and to quantify the degree of wear induced from mission to mission on a particular cannon tube, the land to groove height is normalized with respect to the nominal land to groove height. The model, caliber and manufacturing process determines this value. The value used in this discussion was obtained from the inspection history of the cannon tube. Normalization maps the data into a 0 to 100 percent scale by calculating the percent difference from the measured value versus the nominal land to groove height Figure 9 shows the wear pattern at 2556 rounds and 2060 rounds respectively.

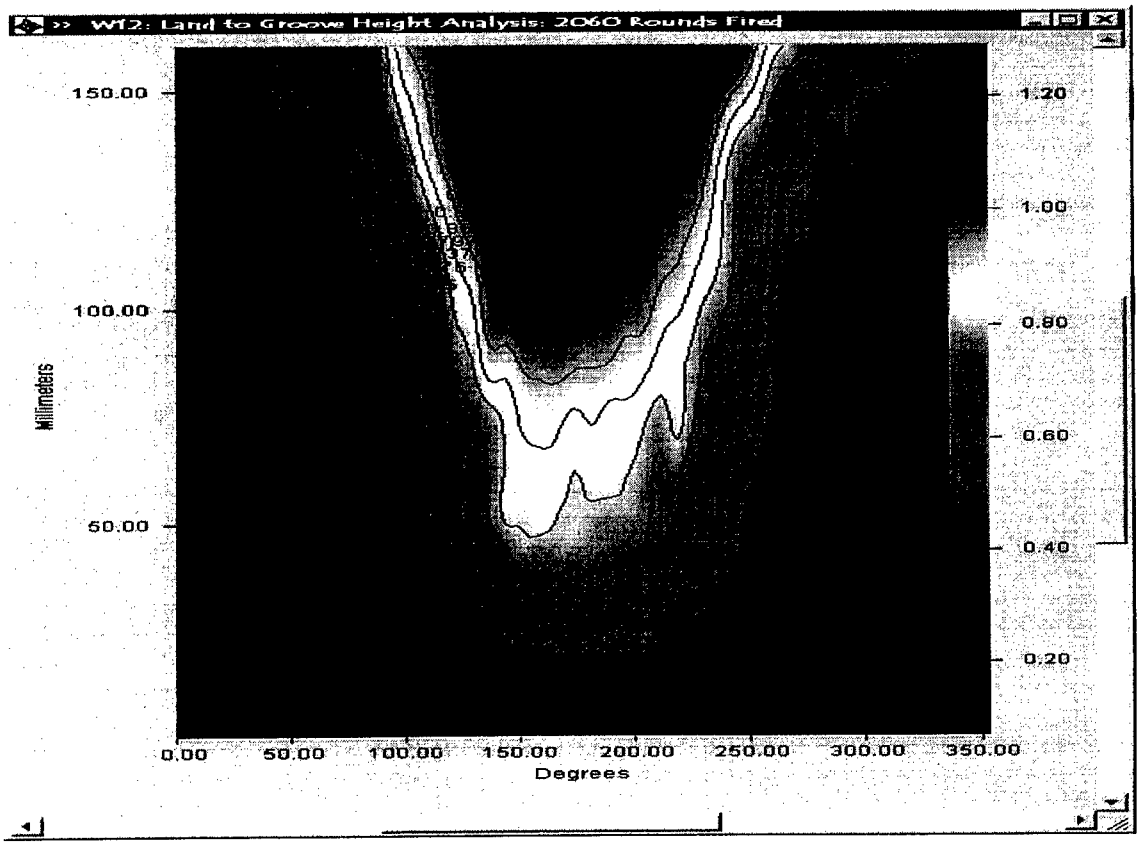


FIGURE 8 Land/Groove Height Analysis Top View with labeled contour lines

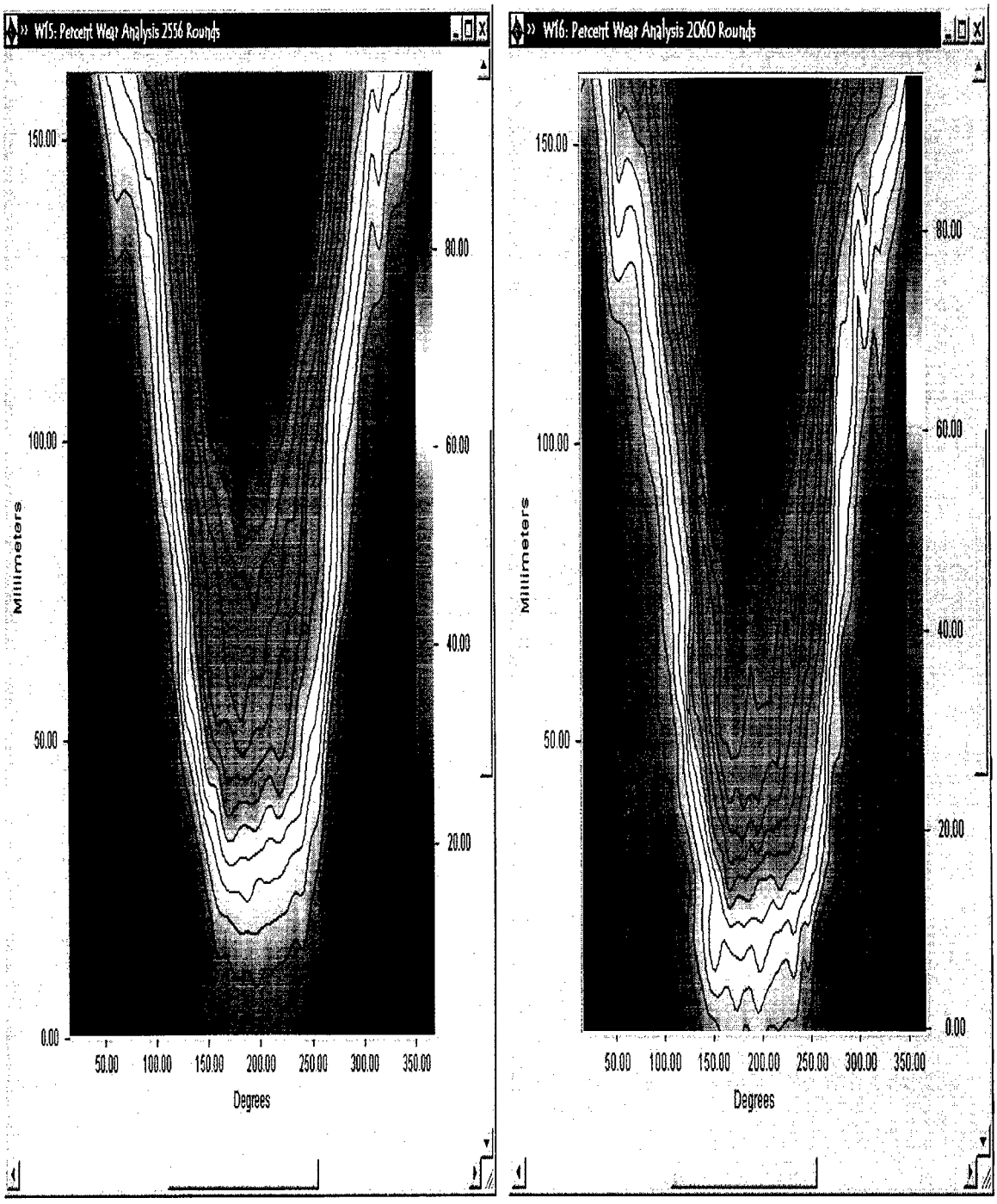


FIGURE 9 Comparison of Normalized Wear Maps at 2556 and 2060 Rounds Fired

The above illustrations show the effect of firing 496 rounds. Notice that the wear is progressing up the cannon tube. Since most of the wear occurs at 0 degrees (12' o' clock) the wear pattern may be rotated 180 degrees and plotted with respect to o'clock position (Figure10).

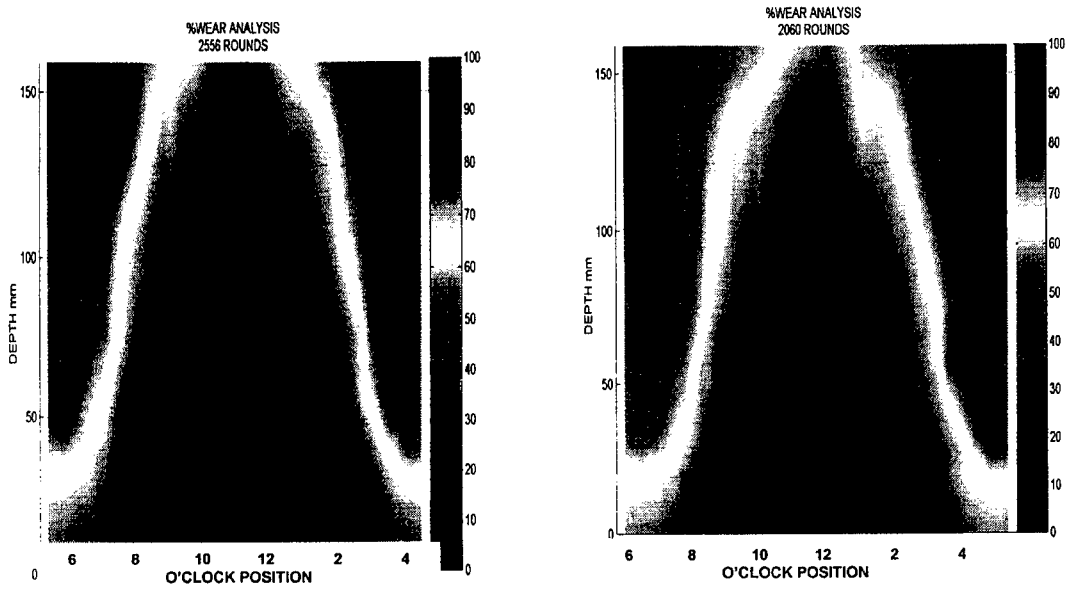


FIGURE 10 Normalized Wear Pattern rotated 180 Degrees

The wear incurred by firing 496 rounds is the difference of the maps in Figure 10 and is portrayed in Figure 11 with respect to o'clock position.

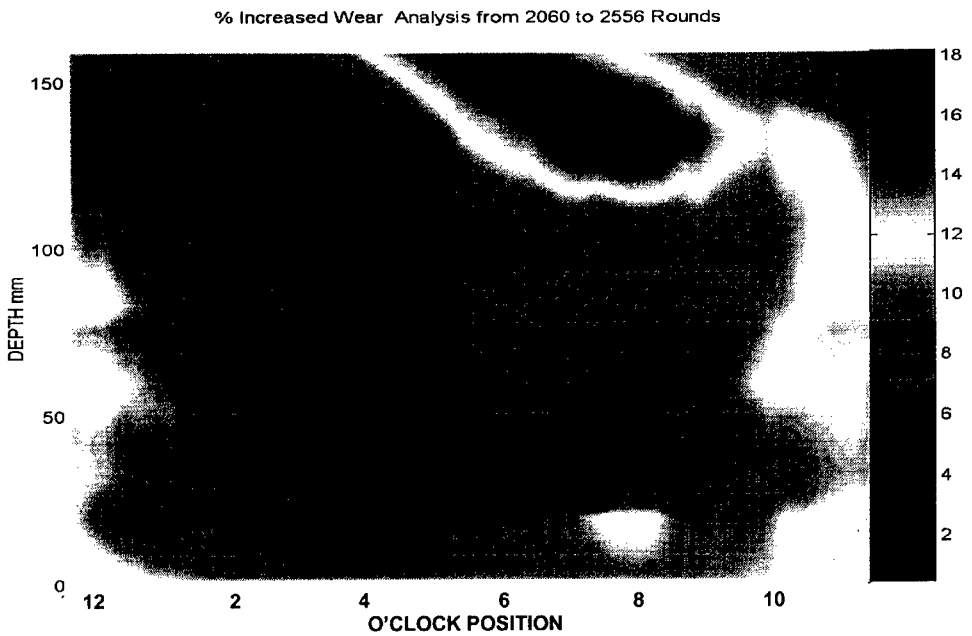


FIGURE 11 Map of Percent Increased Wear illustrating the effect of firing 496 Rounds

DISCUSSION

As illustrated above the analyst may now easily quantify wear patterns as a function of the number and/or type of munitions fired. Although the entire gun tube may be mapped by the same methodology, the author feels that the methodology is best exemplified by concentrating in the area where most of the wear will occur. The above analysis was performed with a commercially available software package. The analyst may use all of the potential of the software package to expand the scope of the analysis or to easily automate the analysis and explore new methodologies. If the illustrations are confined to grayscale, some of the impact that color has to offer is somewhat diminished. Albeit, even with this limitation, the reader may notice distinct wear patterns. The comparative analysis in Figure 11 readily illustrates and quantifies the location and severities of wear incurred by the additional firing of 496 rounds. By starting with new cannon tubes as a baseline, cross-referencing the type and quantity of munitions tested, and incorporating visual inspection (borescope) one can conduct a long-term controlled experiment to generate a computer wear model.

CONCLUSION

The advent of measurement technology in the arena of munitions testing has provided a means to visually characterize and gage the effect of testing on the weapon. A historical database is planned such that a computer model may one day simulate the effect of virtual firing missions. The above methodology, as well as the standard two-dimensional analyses may be tied into the Wear Analysis Database [5] currently in use at the U.S. Army Yuma Proving Ground. In closing, it is the opinion of the author that this technology has the potential to serve as a valuable tool in the U.S. Army's initiative to enhance overall operations, minimize developmental costs, and ensure safer operations by the use of computer generated models.

REFERENCES

1. Sandwell, David T. "Biharmonic Spline Interpolation of GEOS-3 and SEASAT Altimeter Data", *Geophysical Research Letters,* 2, 139-142, 1987.
2. Watson, David E., Contouring: *A Guide to the Analysis and Display of Spatial Data,* Tarrytown, NY: Pergamon (Elsevier Science Inc.): 1992.
3. Davis, Terry L. Lead NDT Inspector, USAYPG, verbal consultation
4. HQ, Dept. of Army and Air Force, TM9-1000-202-14: TO11W2-17-5-1
5. Salafia Dominick, DeLeon Norberto and Outlaw James F. , "Automation of Wear Analysis for Large Caliber Weapons". AIP Conference Proceeding #497, pp346-351, June 1999
6. Salafia Dominick, "Visualization of Wear in Large Caliber Weapons" (*et al), Proceedings* 10^{th} Annual Symposium on Nondestructive Characterization of Materials, pp 365-370. June 2000

Stereo at the speed of light: high-speed digital stereo imaging at up to 100 million frames per second

Donald R. Snyder [a], Air Force Research Laboratory, 101 W. Eglin Blvd., Eglin AFB, FL 32542
Eugene R. Chenette [b], Roger D. Hudson, R. P. Young Jr., Sverdrup Technologies, Eglin AFB, FL, 32542
David W. Gardner, Dalsa/SMD, 5055 Corporate Plaza Dr., Colorado Springs, CO 80919
Peter E. Nebolsine [b], Physical Sciences, Inc., 20 New England Business Park, Andover, MA 01810

ABSTRACT

When shutter speeds approach a nanosecond you set your experiment up using a tape measure. Light-in -Flight imaging takes over when the length of the pulse and the shutter time can relate to a distance of two or three meters. This paper addresses the development of next generation ultrahigh speed digital imaging system and their application to stereo photography of ballistic, penetration, fragmentation, and spray events. Applications of high speed imaging from 1000 to 100 million frames per second are discussed along with the software used to evaluate various experimental methods. Applications range from ultra-high resolution still imaging using a laser strobe to laser illuminated digital movies.

Keywords: ballistic, impact, terminal ballistics, 3D imaging, crack propagation, stereo, laser photography, high speed photography, million frame per second, CCD, multi-pulse laser.

INTRODUCTION

While performing initial acceptance trials for new high-speed digital imaging systems it became apparent that in the process of evaluating two cameras we were generating stereo pair. Initial experiments indicated that the resulting 3D images provided almost as much insight into the ballistic experiments being performed as had our previous work in ballistic holography. As we developed each new high-speed sensor, we captured data in parallel. This has allowed us to begin an evaluation of digital stereo imaging as an engineering tool. From this initial work we demonstrated the integration of light sources, ultra-high resolution and ultra-high speed digital imagers, analysis software and display technology to fully utilize this new capability.

EXPERIMENTAL METHOD AND FACILITY

The Terminal Effects Laser Camera Center (TELCC) is a terminal ballistics research and evaluation facility at Bldg. 410 Eglin AFB, Florida. This facility was developed by Air Force Research Laboratory personnel to support development of several generations of holographic and high-speed electronic imaging systems. The facility is being transitioned for operational support to the Joint Munitions Test Project (Chicken Little). It is comprised of two gun tunnels with instrumentation bays adjacent to the launch and impact areas. Projectiles are launched from powder or air guns into targets of interest. The facility has capabilities to support several sets of digital cameras utilizing two imaging ports with armored glass windows to protect the optics. Timing is provided by sets of infrared light emitting diode screens that generate projectile velocity. Precision counters and pulse generators from Cordin and Stanford Research are utilized to generate the delays necessary to trigger the cameras and light sources exactly when the projectile is in the field of view. In most facilities the flash from impact or energetic materials reacting overpowers the camera resulting in poor image quality or saturated images. We have developed and perfected the use of Laser photography to overcome incandescence of object and impact flash. By use of 3 to 10 nanometer narrow-bandwidth laser interference filters combined with fast shutter mechanisms we have been able to reject most of the undesirable light. Both projectiles and fragments can be launched at various velocities and caliber's up to 40mm.

(a) Fellow SPIE; Contact Information: D. Snyder, email: fastcam1@quixnet.net/Tel: (850) 689-2122 (b) Member SPIE

An integrated, high-speed photographic system combining a high-repetition rate, pulsed ruby laser and high-framing rate CCD cameras has been demonstrated. Individually, the laser and cameras have been discussed previously and each was developed under the Small Business Innovative Research (SBIR) sponsorship through the Air Force Research Lab (AFRL). This paper presents for the first time dynamic digital stereo images captured at up to 1 MHz using the two elements integrated as a high-speed photographic system .

The laser and camera were integrated with the range master control clock, completing the high-speed, laser-based image acquisition system. The Bay-10 gun range at Eglin Air Force Base has the capacity for firing 30 mm rounds at up to 3,200 ft/s (e.g., A10 cannon).

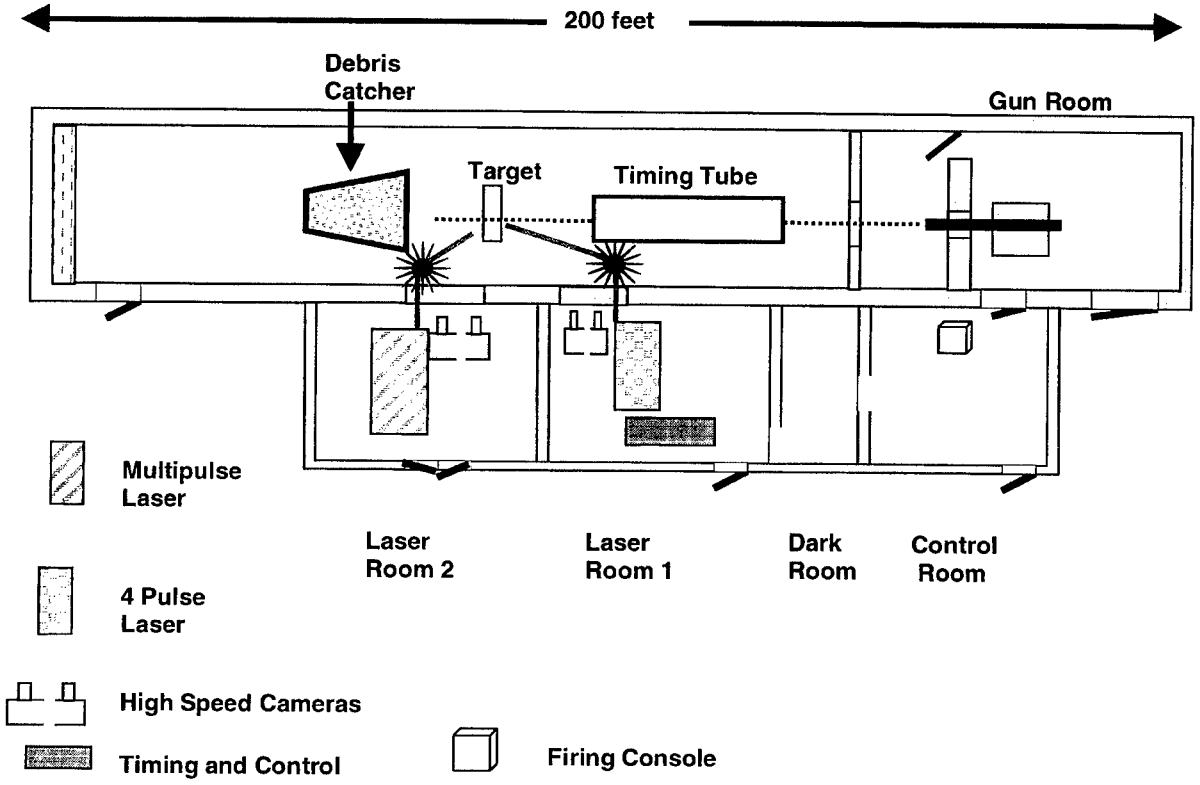


Figure 1. Terminal Effects Laser Camera Center at Interior Ballistics Facility Bay 10.

CAMERAS

The initial cameras used in our investigation were the Silicon Mountain Design (SMD) Mach1- 1000 frame per second -512 by 512 digital camera. For still imaging we used the SMD/ Dalsa 4M4 - 2K by 2K focal plane sensors with 12 bit sensitivity. Soon after our initial experiments we developed a technique using an image mask over the charge coupled device chip to generate a 256 by 256 pixel -1 million frame per second digital camera. Images are stored under a mask so that shifting image down by one row hides the previous image. Up to 68 images on a 2K by 2K-focal plane sensor are possible. The original camera was not image intensifier shuttered (ungated). This sensor resulted in the prototype million frame per second camera, the SMD/Dalsa 64K1M. To further stop motion blur and permit outdoor operation we then developed s high-resolution image intensifier (GEN IV) and demonstrated shutter times down to 3 nanoseconds. Light from the laser moves at about 1- foot per nanosecond. For the highest speed ballistic events, 10 kilometer per second or 10mm/microsecond, a small object only moves 0.1 millimeters in a 10-nanosecond exposure time. This combination of fast shuttering using image

intensifiers and fast strobe flash using laser illumination stops all motion blur. We found that we also needed to diffuse the light to prevent noise from speckle. In various experiments we tried ground glass, tissue paper, and finally to our amazement a holographic diffuser from Physical Optics Corporation that almost completely diffused the beam with little attenuation.

For documentation of the various ballistic experiments, prototype Mach1-1000fps digital 10bit cameras and 64K1M million frame per second digital cameras were used with flood lights and the laser illumination system respectively. For high resolution still imagery, SMD 4M4 un-intensified 4 million pixel digital cameras and SMD/Videoscope million pixel digital cameras with a 3 nanosecond image intensifier shutter were used to capture data. These were mounted on crossbars and adjustable pan and tilt heads to provide for the desired stereo base separation and alignment.

The ultrahigh speed cameras were the prototype un-gated 64K1M Silicon Mountain Design (SMD) cameras with 17 frames of data. Sixteen of the frames are normally used for data and one for the active or open frame. With normal illumination this frame is open during readout and integrates ambient light until the mechanical shutter closes. With laser strobe this 17th frame becomes useful for data, or in a number of configurations a final still frame with multi-exposure from laser pulses. It is possible to configure the test so that the 16 initial frames each record a pulse with up to 10 or so multi-strobed images layering in the last image. This has been used for particle imaging velocimetry applications and to determine the rate of expansion of debris cloud volume growth when the particles are sub-resolved. The camera puts out a pulse train corresponding to the integration time for each image. The timing relative to synch pulse input is approximately 150 to 200 nanoseconds delay for the first frame. The integration time varies somewhat with frame rate, from 600 nanoseconds per frame at 1 microsecond interframe rate (1Mfps) to 8.8 microseconds at 10 microsecond interframe rates (100Kfps)

The imaging sensor in the prototype 64K1M is based on the Thomson CSF-type 7887 Frame Transfer CCD. The basic CCD is a 1K by 1K frame transfer array with custom timing and a metallic aperture mask applied by SMD to define the active pixels and storage registers. For 17 frames in active optical operation this results in approximately 61680 effective pixels for 248 by 248 pixel resolution. With this resolution the straight-line spacing would be 17 pixels or 238 microns for a rectangular sample arrangement. To maximize resolution, the pixel aperture mask openings are staggered to provide a 4 pixel maximum separation between active pixels. With 14-micron pixels, the aperture provides for a 9.5 (+/- 1) micron openings to help minimize cross-talk with the high laser illumination levels. With the staggered mask approach the resulting "pitch" is 56 microns between pixels. The 12 bit dynamic range and high sensitivity of the camera electronics significantly improves imaging performance and helps compensate for the "loss" of active area. A stair-step pattern of the CCD mask is implemented so that every 16 pixels horizontally and 17 pixels vertically starts a new subarray. The stair-step approach results in a pitch of image from the offset in the sampling spacing of pixels to maximize resolution. Due to the stagger, the resulting image has a roll of 14 degrees in the output image. This is compensated in the test set up with a mechanical wedge in the camera mount. The camera uses an imaging technology frame grabber in a standard personal computer and operates using SMD IMAP™ software. The resulting 12 bit files can be viewed a composite sheet as the figures in the paper, a movie file, or individual 12 bit TIF format files. Provision was also made to convert the 12 bit images into scaled 8 bit TIF format files. The camera integration time is user generated by even microsecond intervals resulting in frame rates of 1M, 500K, 333K, 250K, 200K, 166K, 142K, 125K, 111K, 100K, and slower by 1/M microsecond rate. The delay for the last frame is set to prevent premature readout while experiment generated light is present that would result in smear. Provision for a liquid crystal or mechanical shutter has been incorporated in the prototype while image converter shutters have been implemented in the final ULTRA series of cameras.

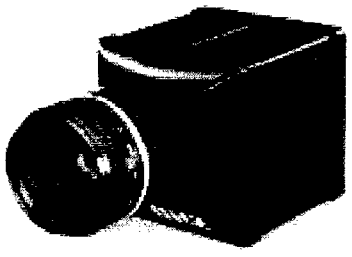


Figure 2. SMD64k1M Million Frame per Second Camera

Imager Format	256 x 256 x 17 frames monochrome
Dynamic range	12 bits
Pixel cell size	56 μm x 56 μm
Sensitivity	8 μV/e
Size	3.9" L x 3.7" W x 3.7" H
Operating Temperature	0 – 45 ° C
Weight	850 gm
S/N Ratio	70 dB
Power consumption	20 W
Dark current	~ 8 nA/cm^2
Lens mount	C or F mount
Frame rates	1M, 500K, 333K, 250K, 200K, 166K, 142K, 125K, 111K, 100K, and slower by 1/M microsecond rate
Readout rate	Up to 60 image sequences per second

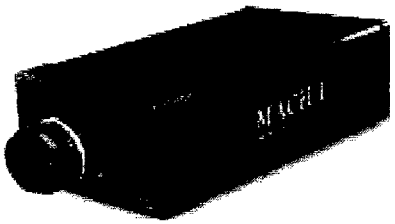


Figure 3. Mach 1 Camera, 512 by 512 pixel 1000 frames per second, 10 bit dynamic range, 1024 frames storage.

An integrated, high-speed photographic system combining a high-repetition rate, pulsed ruby laser and high-framing rate CCD cameras has been demonstrated. Individually, the laser and camera have been discussed previously and each was developed under the Small Business Innovative Research (SBIR) sponsorship through the Air Force Research Lab (AFRL). This paper presents for the first time dynamic digital stereo images captured at up to 1MHz using the two elements integrated as a high-speed photographic system.

The laser and camera were integrated with the range master control clock, completing the high-speed, laser-based image acquisition system. The Bay-10 gun range at Eglin Air Force Base has the capacity for firing 30 mm round at up to 3,200 ft/s (e.g., A10 cannon). The tests presented in this paper were conducted using NATO 7.62mm rounds at approximately 800 m/s.

ILLUMINATION

Two lasers with a 694.3-nanometer output are used for illuminating the experiments. The first is a Lumonics HLS-4 flash lamp pumped ruby laser with peak output of 10 Joules. This system was developed for holographic applications and has capability to deliver up to 4 pulses in an 800-microsecond period. The nominal pulse width for this system is 15 nanoseconds. This system is used for high resolution still photography with the unshuttered SMD/DALSA 4M4 - 4 million pixels cameras, the SMD/Videoscope 1K by 1K pixel- 3 nanosecond cameras, and for use with the new HADLAND/IMCO ILS-4 10 nanosecond camera. Single pulses or multiple flashes per exposure are used to capture a blur free image/sequence of images.

For motion capture a two stage amplification repetitively Q-switched ruby laser was developed by Physical Sciences Inc. (PSI) in partnership with Continuum Electro-Optics Inc. under the Small Business Innovative Research program with the Air Force Research Laboratory (AFRL/MNMF). The oscillator stage incorporates the multiple Q-switching technology intracavity allowing for series addition of amplification stages. The current version of this laser uses two amplification stages and a novel pulse former to maintain pulse to pulse energy stability within the macropulse envelope.

The laser is capable of generating a train of 68 pulses at 500 kHz operation with micropulse energy of ~350 mJ each (>25 J for the macropulse). The test reported herein required less than 50% of this capability or ~100 mJ per pulse. The laser was

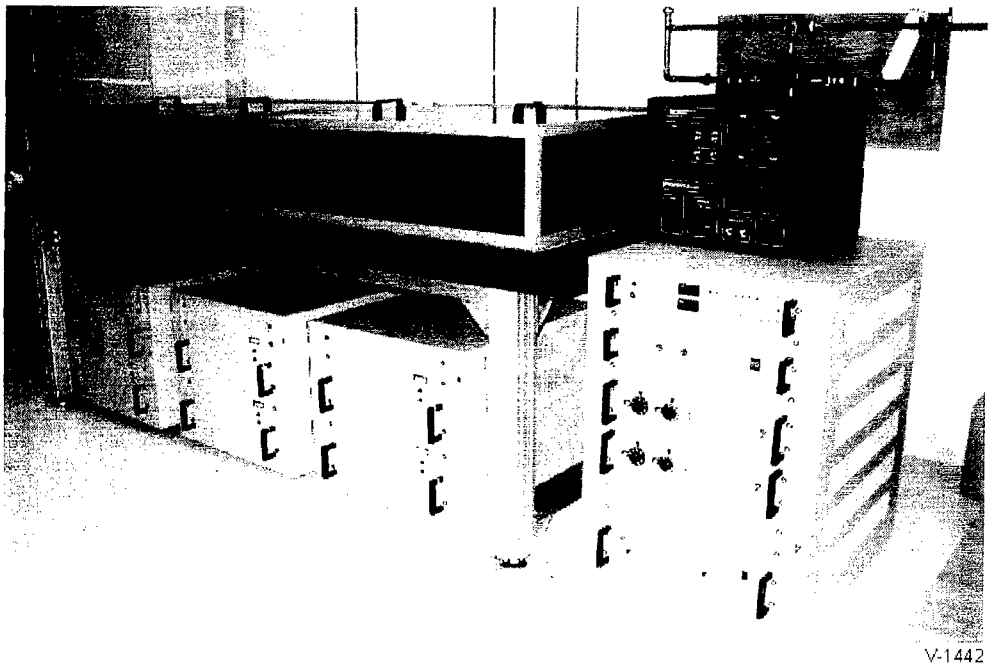


Figure 4. Physical Sciences/Continuum Inc. 1 Million PPS Laser Illuminator System

selected as the master time control because the laser pulse could be located in time with high precision (<1 ns jitter) relative to a secondary laser output trigger. The laser pulse occurred at the end of the Q-switch open time, as previously shown by the authors. Recent advances in the camera trigger system allowed precise synchronization of the laser pulse and camera open shutter time. Data are presented showing this synchronization.

Q-switching of a laser cavity is normally done once to obtain a single giant pulse. This is usually done near the end of the flashlamp pump when the population inversion in the rod is at its highest. To obtain multiple pulses, the laser cavity is repetitively Q-switched over a period of time for which the gain is greater than the losses associated with the laser cavity. It

has been found that the laser cavity can be repetitively Q-switched with resulting pulses formed, for approximately the same duration in which the laser will emit when free running.

Typical applications for high speed imaging systems require large area illumination, on the order of 1000 cm^2. Diffusers are also incorporated to remove laser speckle from the image. A low power negative lens and ground glass diffuser were incorporated into the optical train as shown in the following figure. Here the beam exiting the laser room has approximately a 1" diameter. The resulting illumination area on the target is on the order of 2500 cm^2. Most exposures were acquired with a target to camera distance of about 4 meters. Tokina 35mm (150 to 500mm) zoom lens (f5.6/f32) were used on the cameras. Field of view varied from 250 mm to 75 mm. Most exposures were made at f/11 to f/16. Provision for filtering ambient light with ruby laser line filters and neutral density filters from Andover Optics was made. The ruby line filters were also used to reject light from the impact flash during tests with metal objects. Speckle was controlled using lens tissue sandwiched between two layers of 3 mm thick ground glass. Later tests made use of a holographic polymer diffusers from Physical Optics Corporation. A much higher light transmission (over 90%) was obtained by use of the thin polymer.

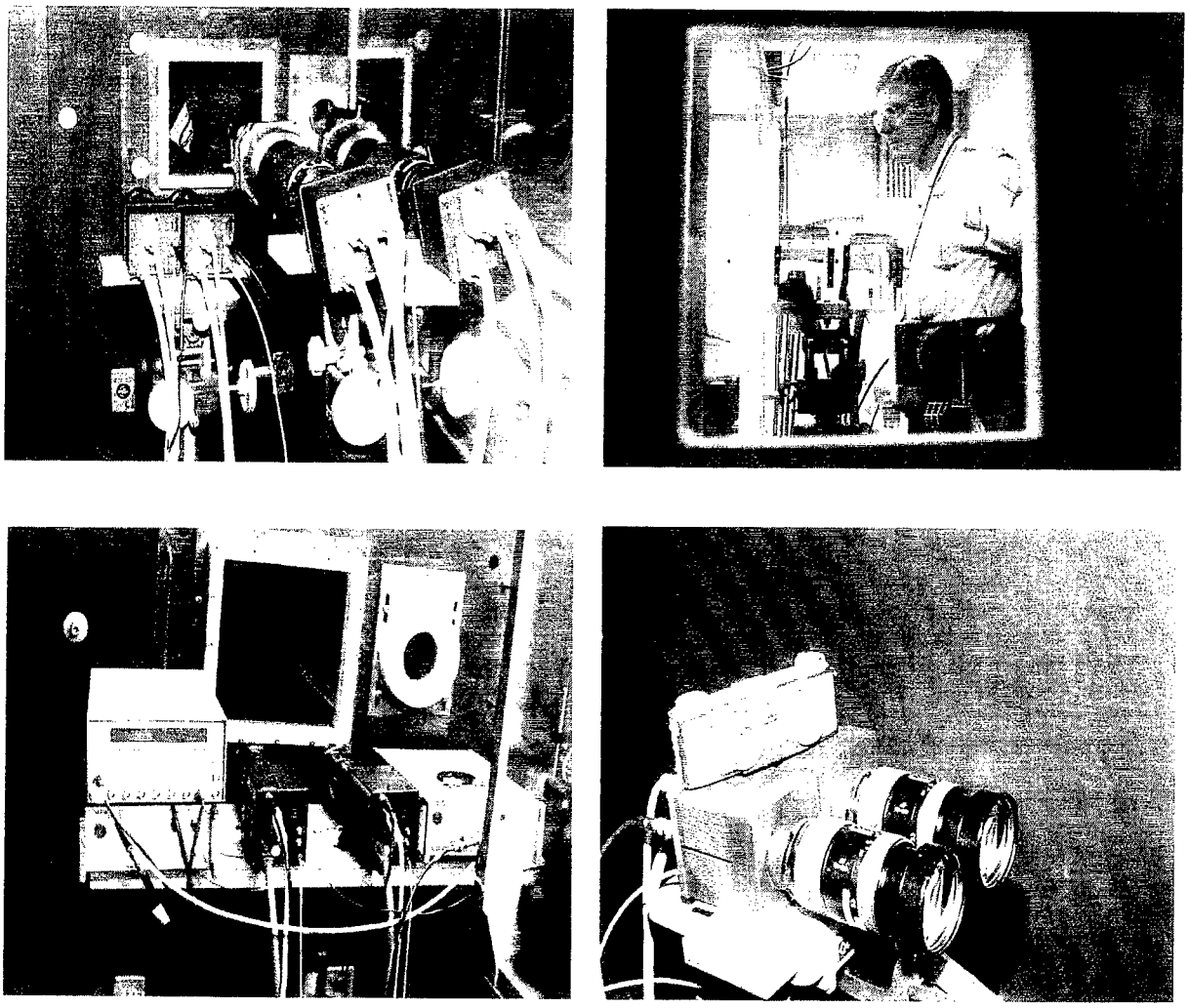
SOFTWARE

Various software is used in the generation and analysis of the stereo images. IMAP is the native package that is used on the SMD/Dalsa data acquisition system to capture and store the image in native 12 bit, 8 bit, or 16 bit files. For the movie sequences IMAP provides the ability to create a sequence of individual TIF or BMP files from the raw image. IMAP has dynamic range mapping, flat field correction, and some limited image processing. Adobe Photoshop or Image-Pro is then used to adjust each image, matching the image sizes for slight variations in rotation and focal length. From the corrected images stereo pair are produced in several formats using different commercial software applications. For simple anaglyph or .jps type images, 3D Stereo Image Factory Plus from SOFTreat is used as well as DEPTHCHARGE Developers Studio with 3D STUDIO MAX plug-ins from VREX. Platypus Animator from C Point Pty. Ltd., is used to create AVI or MPEG files from the resulting anaglyph image sequences. NEOTEK has provided a useful measurement program as a part of their 3D imaging and analysis suite. The KnowledgeVision Composer and Presenter package has integrated a 3D cursor for X,Y, and Z measurements of the position of an item while being displayed in stereo using liquid crystal shutter
Advanced software packages that are being evaluated to photogrammetrically correct and measure items in the image pairs are FotoG-FMS from Vexcel Corporation, PhotoModeler 3.1 from EOS Systems Inc., and Shapecapture 3.1 from Shapequest, Inc. In addition to making measurement of the position of items, these software applications are used to create 3D CAD models. These generate solid models in wire-frame or bitmapped 3D for export into Autocad or other engineering applications. The key intent to translate the velocity, position, and shape from the imagery data into the frame of reference for the modeling and simulation engineering CAD tools that the analyst is using.

For the measurement of particle motion in stereo, Flowmap Stereo from DANTEC, Inc. is being evaluated. This software is designed to import laser strobed stereo images for Particle Imaging Velocimetry. Instead of typical planar PIV for two-dimensional flow, Flowmap provides true 3-vector information on the direction of each particle.

DISPLAY

Data are displayed on Viewsonics 21-inch color monitors (P815) using customized shutter glass emitters from Stereographics and from Neotek. Crystal Eyes,Neotek, and VRex liquid crystal glasses are used to view the data in 3D for presentation and analysis. Often for viewing and for group presentation anaglyph glasses (Red-left and Blue-right lenses) are used and provide satisfactory results. A few of the more art-like images (Edgerton ballistic photo reproductions) have been converted over to hardcopy in 3D courtesy of San Francisco Imaging, Inc. using the Stereo Jet polarized laminate process. This has provided interest results for both permanent hardcopy display and projection using overhead projectors and silvered projection screens.



Clockwise:

Figure 5. High Resolution 4 Million Pixel Stereo Pair and Million Frame Per Second Stereo Pair.

Figure 6. Laser Interference Narrow Band Filters for rejection of ambient and experiment generated flash.

Figure 7. 1950's Stereo Realist Camera and 4 Million Pixel Digital Stereo System

Figure 8. 3 Nanosecond Image Intensified 2K by 2K Pixel prototype camera for light in flight experiments

IMAGES

The first images shown below are from field experiments with the 1000 frame per second digital camera system. Two systems were mounted on a common platform and used for evaluation of stereo imaging in the field. A water tank experiment with plexiglass windows was designed to observe projectile penetration and pressure deformation due to generated shockwaves. The second set of images are from an experiment with a professional golf instructor striking a ball into a plexiglass shield in front of the cameras. This experiment used two different configuration cameras and the difficulting in converging the images is a result of slightly different scale factors for the CCD image sensor and excessive toe-in. The third set of images are from a 7.62 mm projectile at 2800 feet per second. This image pair is extracted from the movie captured at 1 Million frames per second with the SMD 64K1M unintensified camera. The PSI multipulse laser was used to frame the images and prevent blur during the 1 microsecond integration time. The 10 nanosecond laser pulse prevents any

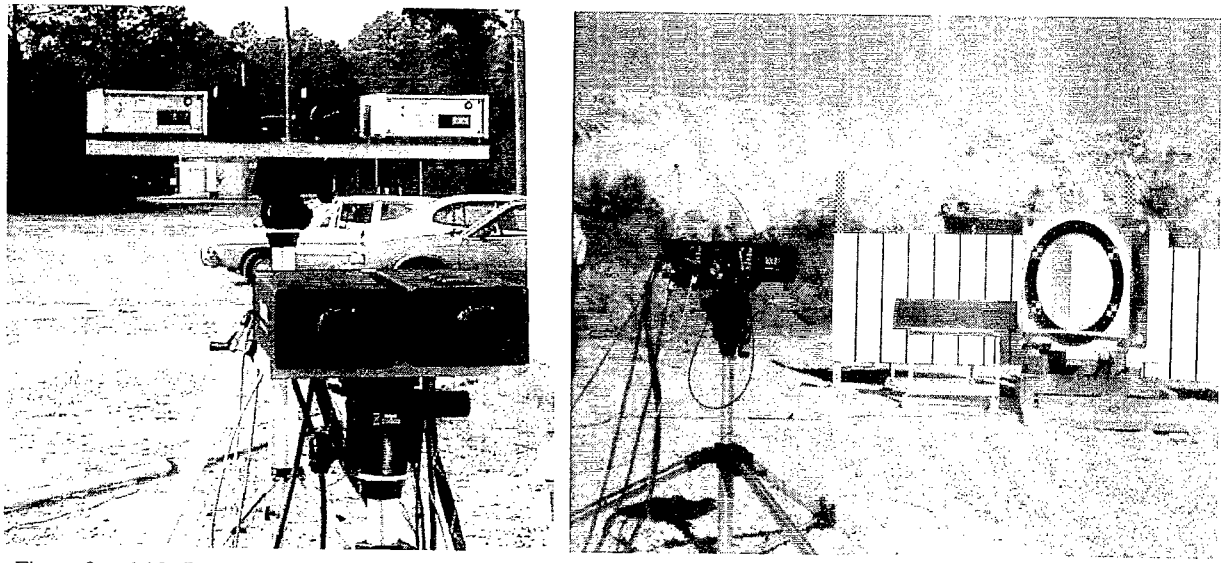


Figure 9 and 10. Range configuration for 1000 frame per second and million frame per second stereo experiments.

motion from being detected while the sensor is shifting from one frame to the next. The final image set is from a extremely high velocity impact using the gated 1K by 1K sensors. These images represents 3 nanosecond exposures of the fine cloud of aluminum particles resulting in a small pellet impacting a satellite skin. This experiment simulated micrometorite impact on a satellite skin or the space station. No flash is noted in the image where normally the image would be totally saturated from the burning aluminum particles.

These images are set for viewing with a Stereoscope viewer such at those inexpensive ones available from Hubbard Scientific, P.O. Box 760, Chippewa Falls, WI, 54729. Reproduction may skew the scale factor. A high quality copier can shrink or enlarge the images until they adjust for the correct inter-pupillary distance.

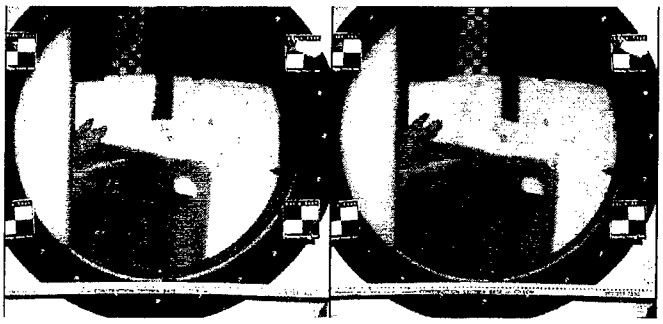


Figure 11. 1000 frame per second capture of projectile penetrating water tank at high velocity.

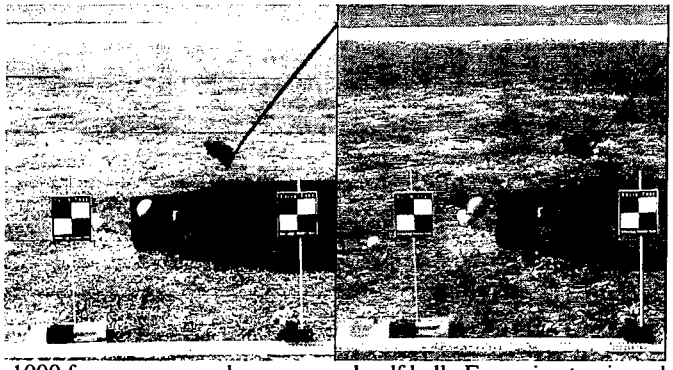


Figure 12. Experiment with two 1000 frame per second cameras and golf ball. Excessive toe-in and scale factor difference.

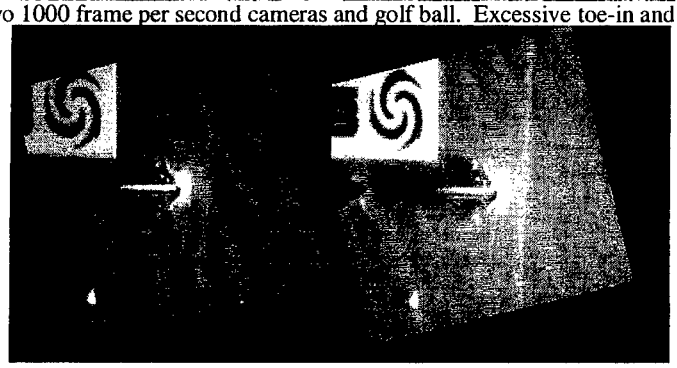


Figure 13. Million frame per second capture with laser photography of projectile penetration of target card.

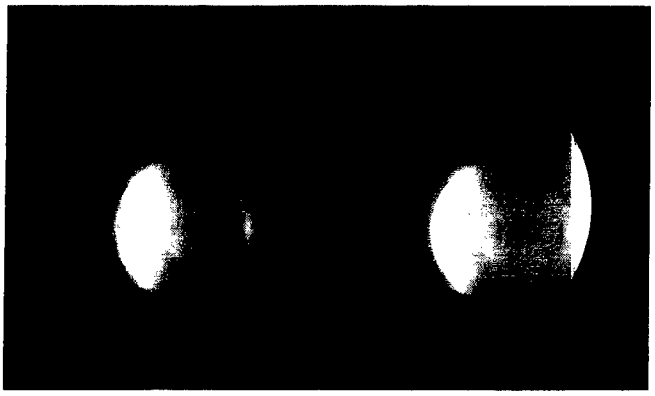


Figure 14. Hypervelocity Impact at several kilometers per second into aluminum sheathing. Note no impact flash.

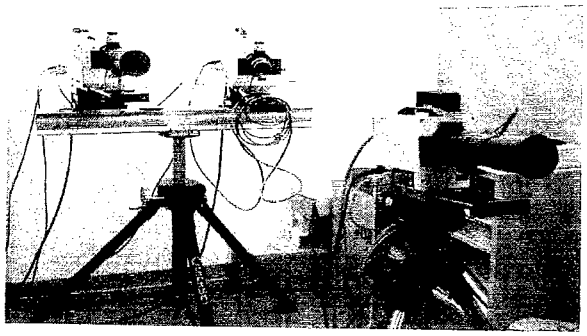
NEW TECHNOLOGIES

Based on the prototype experiments and systems we are currently finishing development of a new series of cameras optimized for stereo laser photography. We have been jointly developing these systems with Dalsa/SMD; DRS Hadland/IMCO; and Atomic Weapons Establishment of the U.K.

The first system is the ILS-4. This system is comprised of a fast decay phosphor 40mm image intensifier (GEN II) coupled to a Dalsa 4M4 camera with a 2K by 2K sensor. Shutter times down to 10 nanoseconds are possible to freeze the fastest moving projectile. As in all the new cameras a viewfinder between the optical system and camera allows precise focus and alignment. This system is capable of accepting up to 63 triggers for multiple exposure of small particles crossing the field of view for PIV and debris tracking applications.

The second system is the ULTRA 17. With 17 frames and 512 by 512 pixel resolution this camera was designed to provide the resolution indicated from the earlier experiments with the SMD 64K1M. The same type of aperture mask is applied to a Thomson 7889 CCD to provide on chip storage. Limitations in the vertical-clocking rate for this CCD has limited the frame rate of the ULTRA 17 to 150,000 frames per second. This however is sufficient for most ballistic experiments where projectiles are moving at rates of 1 to 4 millimeters per microseconds.

The ULTRA 68 is capable of capturing 68 frames of data at 500,000 frames per second. The initial version of this sensor has a resolution of 256 by 256 pixels. A dual image intensifier configuration provides for shuttering down to 20 nanoseconds and amplifications for capturing images at this high rate. A unique beam-splitter arrangement projects the imaged field onto the face of the segmented photocathode of the intensifer. While half the CCD is being exposed the other half is being shifted, clearing space for new images. Very high burst rates in sequences of 4 images are possible.



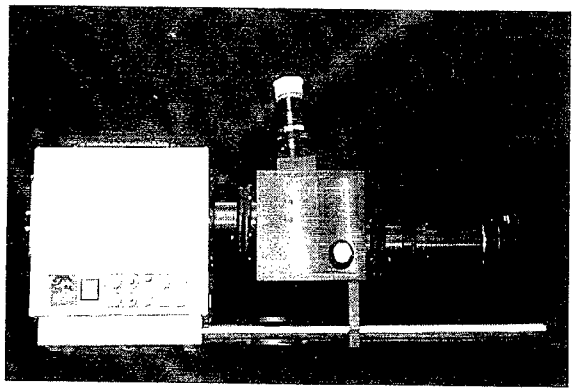


Figure 15 and 16. ULTRA 8 - 100 Million Frame Per Second Stereo System, ULTRA 17- 150,000 Frame Per Second Stereo System and ULTRA 68- 500,000 Frame Per Second 68 Frame System.

The ULTRA 8/ULTRA 8 STEREO was designed to provide the highest performance needed for ballistics or high energy physics. Up to 9 images at 600 by 600 pixel resolution can be captured on the large 2K by 2K charge coupled device sensor at rates up to 100 Million Frames per Second. The two stage 40mm image intensifier provides fast shuttering down to 20 nanoseconds and amplification for capturing data with the short pulses from the laser. As shown two Ultra 8 cameras are mounted on a positioning system with precision tilt, yaw, roll and stereo base separation. The entire system is mounted on a heavy duty Quik-Set tripod with geared head for field use. Through the lens focusing is accomplished with the viewfinder and two slots are available in front of the sensor for neutral density and laser interference filters. The current design for all sensors includes direct connect to a PC controller via frame grabber or with a fiber interface board for remote operation.

We also are beginning development of a single 7K by 4K CCD sensor for macro-still laser photography using a range-finder type beamsplitter. This camera will have a single Pentax medium format aperture with image splitting prisms, turning mirrors, and objective lenses. This system is in final design and will be reported in subsequent proceedings.

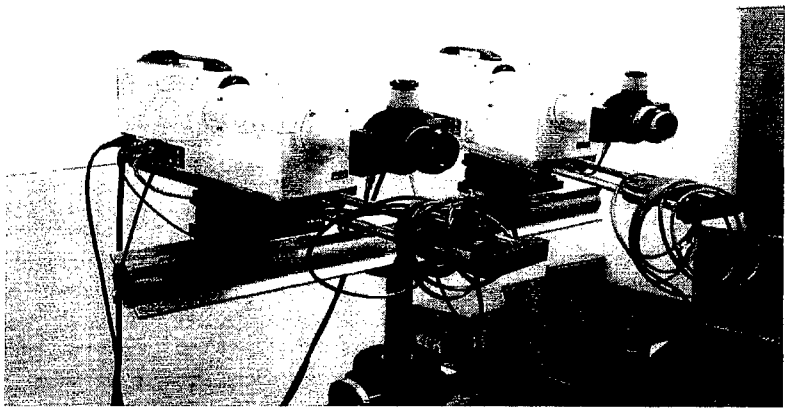


Figure 17. ULTRA 8 100 Million frame per second Stereo system with crossbar and precision attitude adjustment system.

BIBLIOGRAPHY

Huntley, J. "High-Speed Laser Speckle Photography- Part I and II", J. Opt. Eng., Vol. 33(5), 1994.

Ellis, A.T. and Forney, M.E. "Application of a Ruby Laser to High-Speed Photography", Proc. of IEEE, Vol. 51(6), 1963.

Buescher, B.J. Jr., Bruck, H.A., Deason, V.A., Ricks, K.L. and Epstein, J.S., "Dynamic Moire Interferometery", Proc. of 22nd Intn'l. Conf. On High-Speed Photography and Photonics, Sante Fe NM, 27Oct.-1Nov., 1996.

Lempert, W. R., Wu, P.F., Zhang, B., and Miles, R. B., ``Pulsed-burst laser system for high-speed flow diagnostics," presented at 34th Aerospace Sciences Meeting and Exhibit, AIAA 96-0179 (Jan 1996).

Howard, N.E., Gardner, D.W., Snyder, D.R., "Million Frame per Second CCD Camera with 16 Frames of Storage" Ultrahigh- and High-Speed Photography and Image-based Motion Measurement, Proc. SPIE, Vol. 3173, pp. 40-47, 1997.

Grace, J.M., Nebolsine, P.E., Goldey, C.L., Chahal, G., Norby, J., Hertitier, J-M. "Repetitively Pulsed Ruby Lasers as Light Sources for High-Speed Photography", J. Opt. Eng., Vol. 37(8), Aug., 1998.

Goldey C. L., Grace, J. M., Nebolsine, P. E. , and Huntley, J. H., ```Ruby laser repetitively pulsed at rates up to 500 kHz containing etalons and amplifications," in Solid State Lasers VII, Proc. SPIE 3265, pp. 144-154 (Jan. 1998).

Grace, Jeffrey M.; Nebolsine, Peter E.; Snyder, Donald R.; Howard, Nathan E., and Long, J.R.; " Integration of a high-speed repetitively pulsed laser with a high-speed CCD camera," in High-Speed Imaging and Sequence Analysis, Proc. SPIE Vol. 3642, p. 133-141, (May 1999).

"Dynamic Ballistic Impact Events Imaged at 500 kHz Using Laser-Based Image Acquisition", Jeffrey M. Grace, Peter E. Nebolsine, Donald R. Snyder, Eugene R. Chenette, SPIE Vol. 3968, High Speed Imaging and Sequence Analysis, Photonics West, January 2000.

Physical Optics Corporation, Torrance, California, "Holographic Light Shaping Diffusers", http://www.poc.com/hgram/index.htm.

"A high-speed, eight-frame electro-optic camera with multipulsed ruby laser illuminator", L. L. Shaw, L. L. Steinmetz, W. C. Behrendt, J. B. Sonderman, G. K. Beer, L. G. Seppala, & E. Romero, Lawrence Livermore National Laboratory, Livermore, Ca; K. Mikkelson, Sandia National Laboratory, Albuquerque, NM; Proceedings of the 16th International Congress on High Speed Photography and Photonics , Strasbourg, France, August 27-31, 1984

COMPLETE BORE CENTERLINE EXTRACTOR AND SURFACE MAPPER

R. Von Wahlde[1], T. Erline[2], M. Kregel[3], and M. Bundy[4]

[1] *U.S. Army Research Laboratory, AMSRL-WM-BF, Aberdeen Proving Ground, MD 21005*
[2] *U.S. Army Research Laboratory, AMSRL-WM-BC,Aberdeen Proving Ground, MD 21005*
[3] *Kregel Technical Services, Aberdeen, MD 21001*
[4] *U.S. Army Research Laboratory, AMSRL-WM-BC,Aberdeen Proving Ground, MD 21005*

Currently, a bore-riding laser target is used to measure gun barrel centerlines. A reference line is established from the center of the breech to the muzzle. The target is positioned at a number of stations down bore and the deviation of the centerline is determined. While accurate, the method requires the average of multiple measurements and physical contact with the barrel. A new measurement device that accurately and quickly finds the entire gun barrel centerline at once is being designed. It consists of an instrumented, sub-caliber, in-bore tube extending the entire length of the barrel. Non-contact displacement gauges are positioned lengthwise on the external surface of the tube. Rotating the in-bore tube provides a map of the surface from which the centerline can be extracted. Flaws in the bore surface and out-of-roundness can also be detected. The proof-of-principle experiments on this new technique are reported here.

INTRODUCTION

During manufacture, every tank gun barrel is measured for straightness, to ensure that it meets a specified tolerance before it is released for field use. Some fielded barrels undergo additional straightness measurements. For instance, since centerlines are known to be a factor in ammunition accuracy, barrels used for ammunition lot acceptance tests have their centerlines re-measured. Likewise, in the field of gun dynamics research, understanding the projectile-barrel interaction requires a knowledge, and therefore an accurate measurement of, the barrel centerline. Measurement of the bore profile has always been both an operational requirement and a useful research tool. Presented in this paper is: a brief description of the current centerline measurement methods, followed by a discussion of the new centerline technique. Next, the centroid finding algorithm is described in some detail. Finally, there is a quick description of what can be found about the bore surface and detection of bore out-of-roundness, followed by the conclusion.

CURRENT MEASUREMENT METHODOLOGY

Currently, laser devices, such as the Gun Tube Inspection Station (GTIS) located at Watervliet Arsenal, and a portable version at Aberdeen Test Center (ATC), are used to measure centerlines. Briefly, a reference line is established from the center of the breech to a bore-riding laser target at the muzzle. The target is positioned at a number of stations down the bore and the deviation of the laser beam from the center of the target is determined. (A more detailed description of techniques for centerline measurements as practiced now and in the past can be found in these references [1]-[5].)

Normally, the centerline is compiled from the average of multiple GTIS measurements. Figure 1 shows a sample centerline in the horizontal plane from three separate passes of ATC's GTIS. The cumulative system error as the target bore rider moves in the barrel is on the order of 0.2mm at the muzzle end. Typically, point-to-point measurements can fluctuate by ± (0.05 to 0.1) mm from one pass to another.

A NEW CENTERLINE MEASUREMENT TECHNIQUE

A new measurement device that accurately and quickly finds the entire bore centerline at once, with minimal physical barrel contact, is being designed. The proposed device (Fig. 2) is an instrumented in-bore sub-caliber tube that extends the entire length of the gun bore. Non-contact (eddy current probe) displacement gauges are positioned lengthwise on the external surface of the tube. Rotating the in-bore tube provides a map of the surface from which the centerline can be extracted. Flaws in the bore surface can also be detected as well as bore out-of-roundness.

The eddy current probe is essentially a small wire coil (usually potted in a non-conductive substrate) through which a high frequency current flows, setting up an electromagnetic field that induces eddy currents in any nearby conductive materials (e.g., metals). The induced current in the conductive specimen creates its own electromagnetic field, counter to the probe/coil field. The electromotive effects of the induced field on the probe circuit can be decoded and used to estimate (precisely) the distance between the probe and the nearby sensed surface. Such probes are sold commercially, and widely used in industry to monitor —for example—machine vibration.

The measurement tube in which the eddy-probe gauges are placed will be a lightweight and extremely stiff composite structure, minimizing its droop. Any remaining bend will be accounted for by calibrating the tube. The tube will be supported at the breech and the muzzle. A servomotor positioned at the breech-end will rotate the tube on bearings. In the first design, the displacement gauges will be located axially every 200mm, with the first station located 230mm from the muzzle. Although more stations could be included or the instrumented tube could be incrementally moved axially (which would provide a more detailed bore map), this set-up will emulate the current GTIS measurement operation.

Diagonal pairs of probes can be used at each measurement station to provide two independent measurements. Probe cables will exit the measurement tube through a hollow shaft at the muzzle end.

CENTERLINE EXTRACTION

Military Specification, MIL-C-13931, [6] defines bend in a machined gun barrel as the deflection, excluding droop, from a theoretical straight line extending between the bore centers at the origin of the bore and at the muzzle end. Droop is the deflection of the tube due to gravity. According to additional specifications for the 120mm, M256 barrel [7], the straightness tolerance for the gun tube is:

> *Overall Straightness: The bend, excluding droop, in the bore portion of the tube shall not cumulate over 2mm over the entire bore length.*
> *Incremental Straightness: The bend, excluding droop, in the bore portion of the tube shall not exceed 0.5mm in any 600mm interval.*

Figure 3 illustrates the straightness specifications in terms of modern drafting practices [8]. It means that the centerline must lie within a 4.0-mm cylinder for the total bore length and within a 1.0-mm cylinder over any 600-mm length. These are exacting tolerances but the measurement technique must be capable of resolving the centerline with even greater accuracy.

Figure 4 shows a sample bore profile obtained by an eddy current probe and angle encoder at one station with one rotation of the measurement tube. Note, a constant value has been subtracted from all radial measurements to make the deliberately-imposed gouges more prominent in this plot. The center of the bore area, relative to the rotation axis of the tube, is found through an iterative minimization algorithm. In this algorithm, the rotation center serves as the initial estimate for the centroid location assumed at the point (X0=0, Y0=0). The standard deviation of the radius, termed the SigmaRadius, is computed for all the data points in the circumferential direction.

Figure 5 illustrates the minimization technique used for both the horizontal, X, and vertical, Y, planes. The candidate centroid is then shifted a small amount, delta, in the positive and negative directions, both horizontally and vertically. The SigmaRadius is found for each of these new points (X0,Y0+delta), (X0,Y0-delta), (X0+delta,Y0), and (X0-delta,Y0). A quick parabolic fit method finds the point at which SigmaRadius is a minimum (Xmin0,Ymin0) which becomes the starting point for the next iteration (X1= Xmin0,Y1=Ymin0). The process is repeated a number of times until the centroid does not change to any significant degree. Figure 6 shows how quickly the algorithm converges to a fixed point.

Because the algorithm is driving the solution to a minimum, the actual magnitude of the standard deviation is not important. If a large random error creeps into the eddy current probe data or the angle encoder data, the error at each measurement location can be tolerated, because a large number of measurements are taken for each position within the rotation.

Figure 7 shows the centerlines obtained for a short (6") barrel section in the horizontal and vertical planes. The centerline is down and to the right of the rotation axis of the instrumented tube. The error at each measurement station is not additive to the total error and does not accumulate as the bore-riding laser target effect does. These data were acquired several times with more than one eddy current probe. The repeatability is very good. The precision of the measurement is in the range of 0.005 to 0.05 mm, much smaller than the current GTIS error.

BORE SURFACE MAPPING

Figure 8 shows a portion of a bore surface map compared to the actual bore section. The eddy current probes are readily able to detect gouges and missing chrome. The displacement data easily show the machined gouge in the figure. The thickness of the chrome is on the order of 0.1 to 0.2 mm. This too is within the range of accuracy of the displacement guages.

OUT-OF-ROUNDNESS DETERMINATION

Figure 9 shows a greatly exagerated example of how an out-of-round bore would be detected. The radius would appear cyclic as a function of rotation. Also, the standard deviation of the radius would provide a measure of this variability. In this way, the out-of-roundness of the bore could be determined.

CONCLUSIONS

The findings thus far seem to indicate that a device can be built that will find centerlines more easily and accurately than the current laser method. Recent experiments with a short section of an M256 barrel demonstrated that eddy current probes on an instrumented sub-caliber tube could be used to readily map the bore surface. The algorithm used for finding the actual center at a mapped axial position converges quickly to an accurate solution. This device would also have the capabilty to detect flaws such as gouges and missing chrome along the bore surface. In addition, out-of-roundness in the barrel can be determined in the measurement process. Further experiments with a full-scale measurement tube, in an actual gun barrel, are planned.

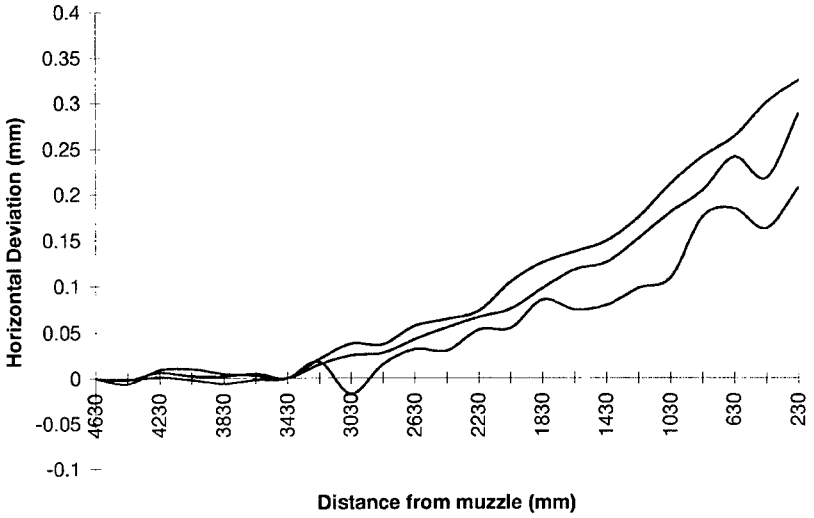


FIGURE 1. Sample Gun Tube Horizontal Centerline, 3 GTIS Measurements.

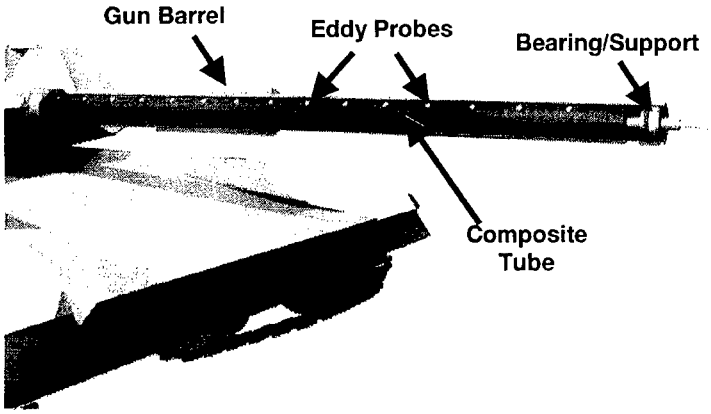


FIGURE 2. Full Bore Centerline Measurement Tube.

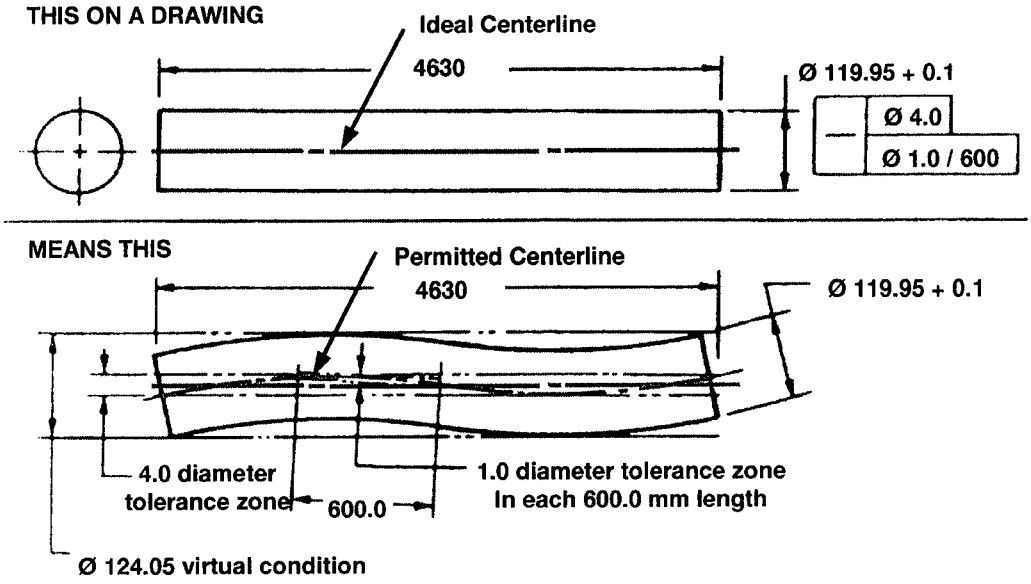


FIGURE 3. Centerline Tolerance Zone.

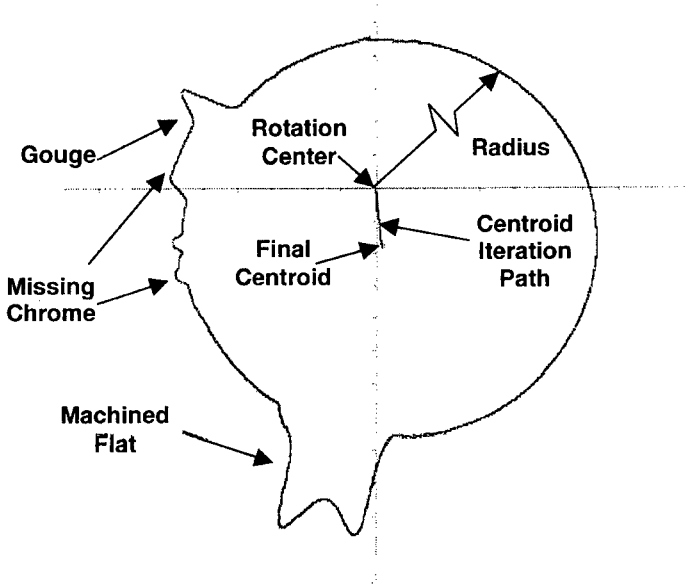


FIGURE 4. Sample Bore Profile.

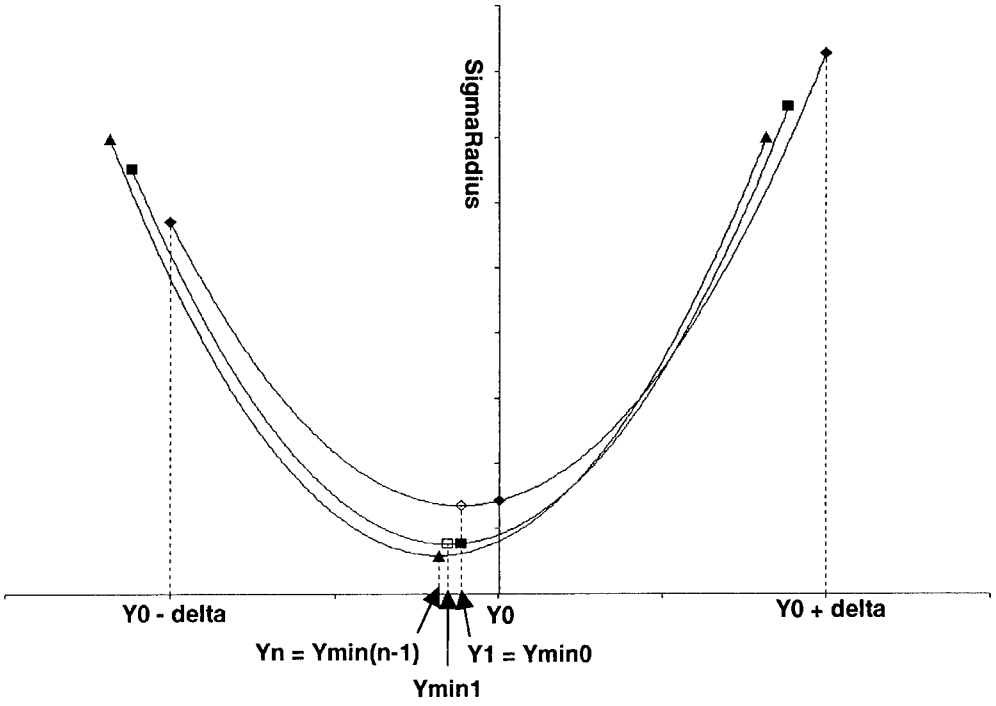


FIGURE 5. Schematic Depiction of the Minimization Technique.

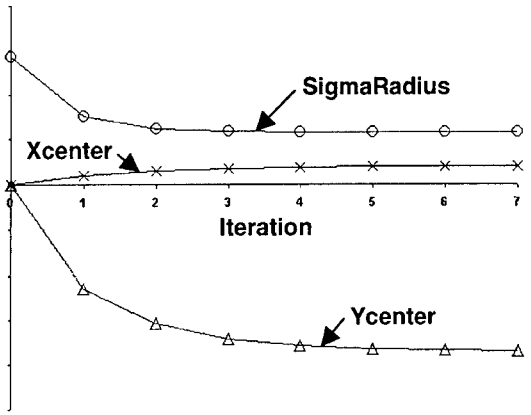


FIGURE 6. Solution of the Centroid Algorithm vs. Number of Iterations.

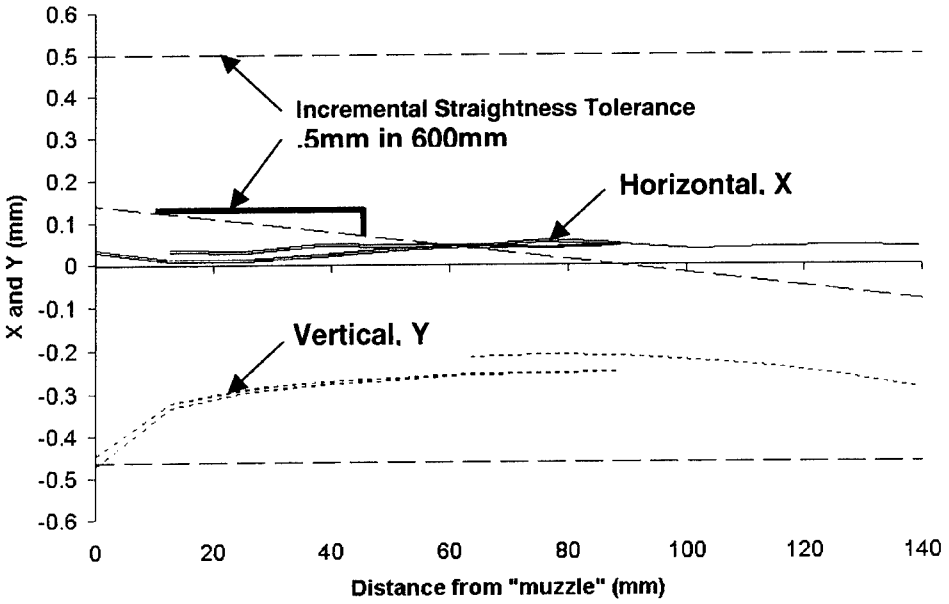


FIGURE 7. Short Gun Tube Section Centerline.

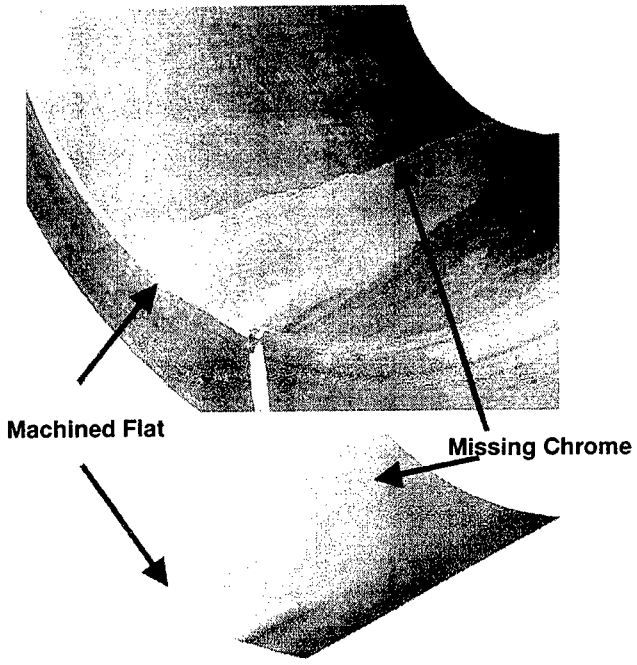


FIGURE 8. Bore Surface Map.

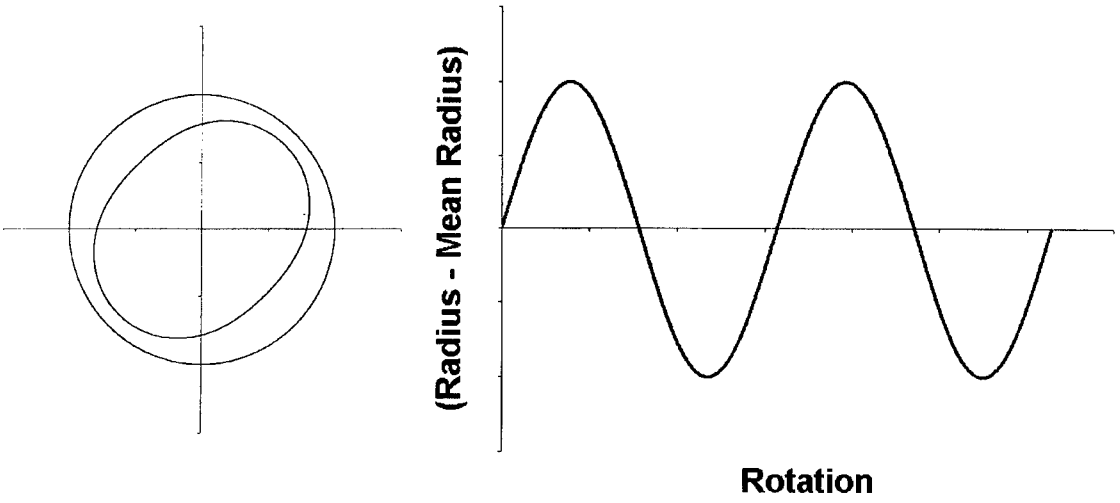


FIGURE 9. Out-of-Roundness.

REFERENCES

1. Weddle, A. L. "Methodology Investigation of Gun-Tube Straightness Measurements," Aberdeen Proving Ground USACSTA-6439, October 1986.
2. Howd, C. A., "In-Process Straightness Measurement of Gun-Tubes," Watervliet Arsenal WVA-QA-9101, August 1991.
3. Wilkerson, S. A., "A Consistent Method for Determining Gun-Tube Straightness on the M256 120mm Gun," Proceedings of the 7th U. S. Army Symposium on Gun Dynamics, May 1993.
4. "Cannon Straightness Measurement", unpublished document received from Ken Insco, Watervliet Arsenal, July 1991.
5. Garner, J., T. Marrs, T. Erline, and and M. Bundy, "Off the Shelf Technology for Gun Barrel Straightness Measurement," Proceedings of the 10th U. S. Army Symposium on Gun Dynamics, May 2001.
6. Military Specification MIL-C-13931, Cannon: General Specification for, paragraph 6.3.4
7. 120mm, M256 Gun Tube Drawing 12528311, Sheet 1, Note 4, US Army Armament Research and Development Command, Watervliet, New York, 1984
8. Modern Drafting Practices and Standards Manual, Genium Publishing Corporation, Schenectady, NY, 1988

OPTIMIZING A SLINGATRON-BASED SPACE LAUNCHER USING MATLAB®

M. Bundy[1], G. Cooper[2], S. Wilkerson[3]

[1]*U.S. Army Research Laboratory, Aberdeen Proving Ground, MD 21005*
[2]*U.S. Army Research Laboratory, Aberdeen Proving Ground, MD 21005*
[3]*U.S. Army Research Laboratory, Aberdeen Proving Ground, MD 21005*

A slingatron is the name given to a propellantless mechanical means of launching a projectile. To date, slingatrons are only conceptual in nature, but their potential use as a ground-to-space launch mechanism for unmanned payloads is under investigation. Slingatrons can be configured in a variety of geometries; one form consists of a spiral track (or launch tube) that gyrates at a constant frequency about a set radius. Under proper conditions (design parameters), a projectile entering the spiral at its small-radius end will undergo nearly constant tangential acceleration before exiting. The differential equations governing the motion of the projectile within the spiral are highly non-linear, making the optimum design solution non-intuitive. This report describes how the slingatron works from first principles, then uses the numerical integration procedures within the computer software environment of Simulink® and MatLab® to search for and identify the optimum design solution parameters based on structural dynamics and mechanical design considerations.

PURPOSE OF STUDY

The cost of launching payloads into space is currently around $10,000 per pound. Although this expense may be acceptable for manned space missions, it can be a curtailing financial burden for other potential enterprises. Less expensive, alternative methods of launching acceleration-insensitive bulk items into space is thus an area of interest. The slingatron is a proposed (propellantless) means of launching objects for such missions (Tidman et al. [1], Tidman [2,3], Tidman and Greig [4]). This study describes the operational principles of the slingatron and investigates the range of possible design solutions using Matlab and Simulink software; thus, bounding the physical scale of this mechanical device.

OPERATIONAL PRINCIPLES OF A SLINGATRON LAUNCHER

Those who played with a hoola-hoop as a child, and remember how the sound of the ball's speed within the hoop increased with the gyration rate of the hips, might recognize the similarity with a projectile in a slingatron. Figures 1–3 show the progression of forces in action in going from uniform circular motion to circular slingatron (or, hoola-hoop-type) motion. Specifically, Fig 1 displays uniform circular motion of a ball of mass m about a circle of radius D, with velocity $\vec{v}$, and centripetal force $\vec{F}_D$ (all of constant magnitude).

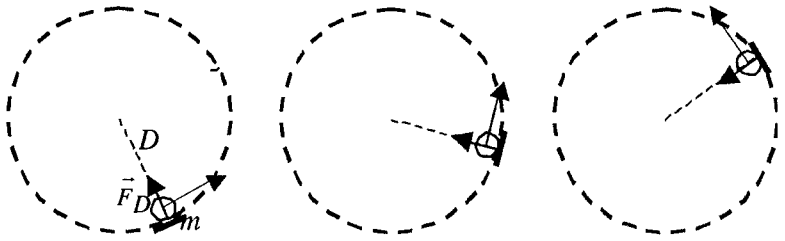


FIGURE 1. Uniform Circular Motion.

The speed of the ball in Fig 1 can be increased by orienting the normal force acting on the ball so that it has a tangential as well as a centripetal component. This could be done by envisioning a rotating wedge as shown in Fig 2. As the circular speed of the ball increases under the tangential force, so too must the angular velocity of the supporting wedge, as well as the normal force of the wedge on the ball, illustrated in Fig 2. (Note, if γ in Fig 2 is positive, the speed will increase; if γ is negative, it decreases; and when $\gamma = 0$, the speed stays constant, equivalent to Fig 1).

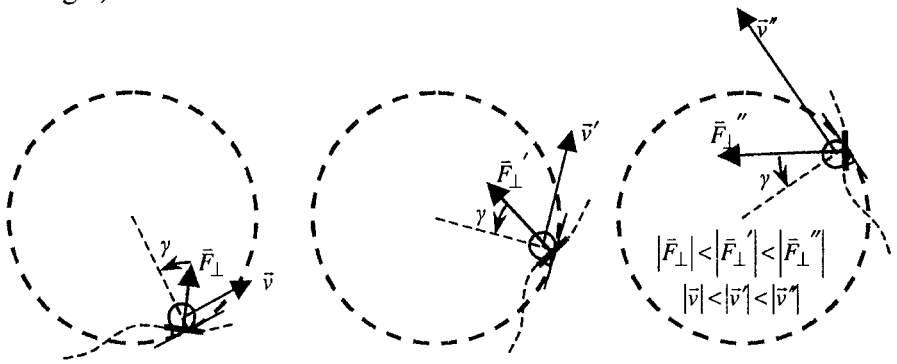


FIGURE 2. Non-Uniform Circular Motion Created by the Tangential Force Component of a Rotating Wedge (or Wave).

The effect of the rotating wedge (or wave) on mass m in Fig 2 can be duplicated by employing a gyrating ring of radius R, and therein lies the operational principle of the circular slingatron (or hoola-hoop), as shown in Fig 3. As indicted in the illustration, the gyrating ring can provide the same boundary geometry and normal force as the wedge. Like the wedge, the frequency of gyration, $\dot{\psi}$, must increase in order for the ring to maintain its support for, stay in phase with, the object.

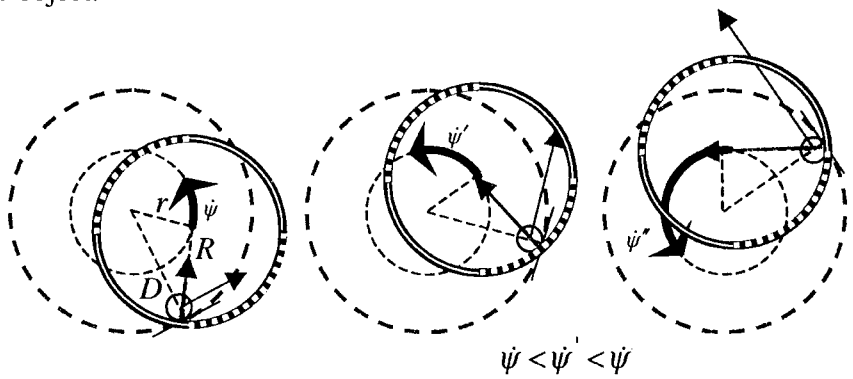


FIGURE 3. Non-Uniform Circular Motion Created by a Gyrating Ring.

In addition to the hoola-hoop, Fig 4a, swirling liquid in a cup by moving the hand in a circular pattern (oxidizing wine in glass, for instance) is another practical example, Fig 4b, of the same effect. In this case, the wave in the fluid moves up and around the sides of the cup/glass. (As a practical exercise, hand swirling liquid in a cup reveals how important the gyration phase angle is to maintaining, or increasing, the wave speed/amplitude.)

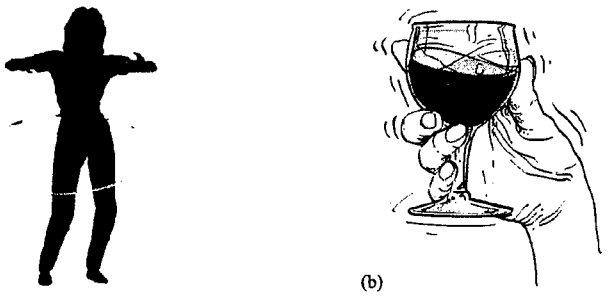


FIGURE 4. Slingatron-Like Motion of (a) a Hoola Hoop or (b) Swirling Liquid in a Glass.

Unlike the wedge in Fig 2, which rotates with the object, the ball in Fig 3 must execute circular motion within the gyrating ring. This relative motion can be detected in the illustration by observing that the ball is in contact with different shaded arc lengths along the gyrating ring as it moves about it's circular path of radius D. Thus, a frictional force of the track on the ball needs to be considered. Figure 5 shows the general orientation of the normal and frictional force on the object, as well as specifying a set of reference angles. It can be said that the ring radius, R, lags the gyration radius, r, by the phase angle $\theta\ (=\psi - \varphi)$.

Thus far, the discussion has been limited to a circular slingatron track. However, such a configuration poses the practical problem of designing a mechanical gate to release the projectile after it reaches the sought after speed, e.g., earth-to-space "escape" velocity. For this reason, an open-ended spiral slingatron is a more feasible projectile-launching track geometry.

Making the conceptual transition from a circular to a spiral slingatron is facilitated by viewing a spiral that is composed of interconnected semicircular arc lengths, Fig 6(a). At any given location, the track is moving within a gyrating circular path, as it was in Fig 5. Here, however, the radius of the circular arc changes every half-revolution, so that an object moving within the launch tube must accelerate in order to complete one revolution in phase with gyrating track, Fig 6(b). Thus, it is conceivable that (under the right normal and friction force conditions) the object can accelerate, even if the period of gyration is constant.

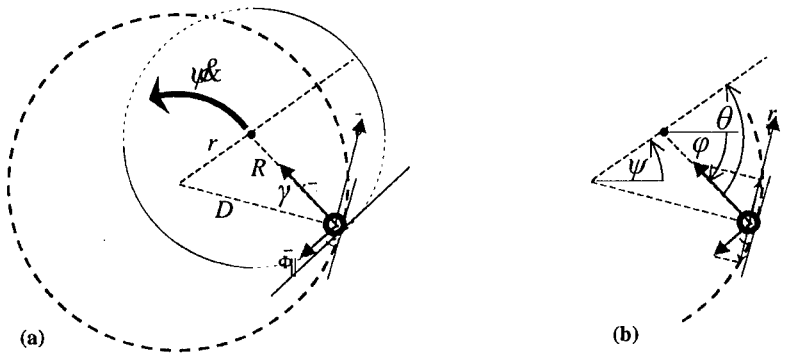


FIGURE 5. (a) Normal and Frictional Force, With (b) Tangential Components, of the Ring on the Mass.

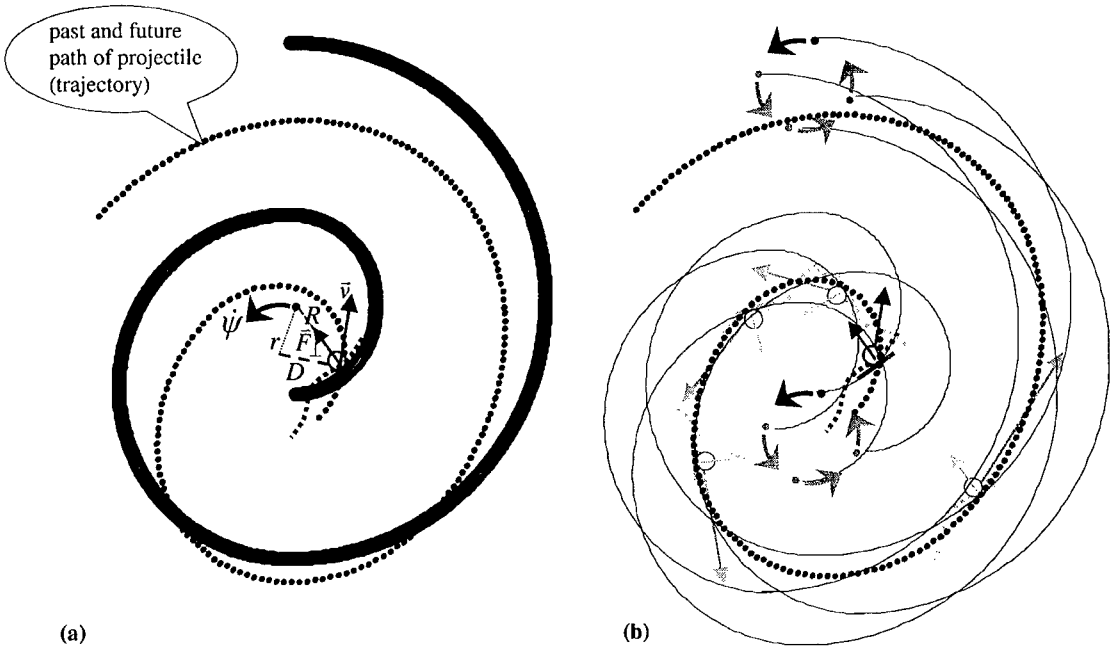


FIGURE 6. Spiral Slingatron, (a) Initial and (b) First Four Quarter-Cycle Gyration Conditions.

EQUATION OF MOTION FOR A SLINGATRON LAUNCHER

The trajectory of the object in Fig 6 is redrawn in Fig 7, with the track and the object in motion suppressed to facilitate visualization of the object's velocity, force, and angular orientation. Unlike the gyrating ring of Fig 5, where the normal force was always directed toward the center of the ring, the direction of the normal force in the gyrating spiral depends on the spiral geometry, $R = R(\phi)$. It can also be characterized by the angle β (Fig 7), defined below. Note that if R does not change with time (or ϕ), the spiral is actually a circle and $\beta = 0$.

$$\beta = \tan^{-1}\left(\frac{\dot{R}}{R\dot{\phi}}\right) = \tan^{-1}\left(\frac{1}{R}\,\frac{dR}{d\varphi}\right) \quad . \tag{1}$$

Aided by Fig 7, the x- and y-components of Newton's second law of motion for an object of mass m in the spiral slingatron are:

$$\begin{aligned} m\,\ddot{x} &= \left|\vec{F}_{\perp}\right|\cos\{\phi-\beta-\pi\} - \left|\vec{F}_{\parallel}\right|\sin\{\phi-\beta-\pi\} \\ &= \left|\vec{F}_{\parallel}\right|\sin\{\phi-\beta\} - \left|\vec{F}_{\perp}\right|\cos\{\phi-\beta\} \end{aligned} \quad . \tag{2}$$

$$\begin{aligned} m\,\ddot{y} &= \left|\vec{F}_{\perp}\right|\sin\{\phi-\beta-\pi\} + \left|\vec{F}_{\parallel}\right|\cos\{\phi-\beta-\pi\} \\ &= -\left|\vec{F}_{\perp}\right|\sin\{\phi-\beta\} - \left|\vec{F}_{\parallel}\right|\cos\{\phi-\beta\} \end{aligned}$$

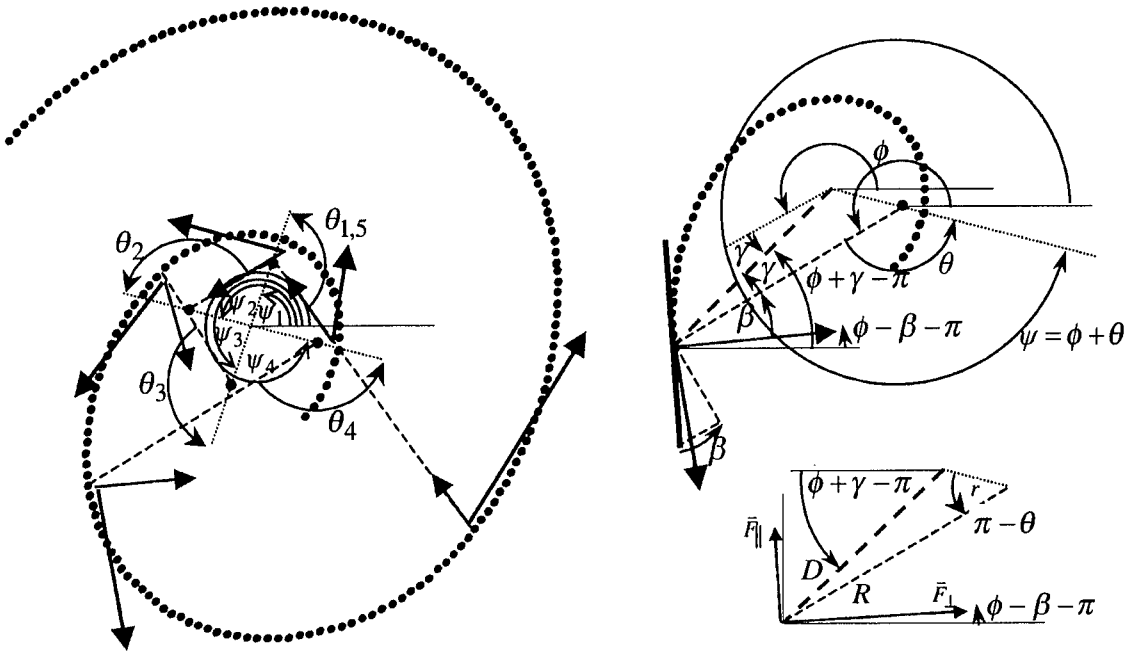


FIGURE 7. Kinematics of a Spiral Slingatron Trajectory.

In general, the force parallel to the track is not only due to track friction, but air friction/drag as well; therefore, assume that

$$\left|\vec{F}_{\parallel}\right| = \mu\left|\vec{F}_{\perp}\right| + PA \quad , \tag{3}$$

where μ is the coefficient of friction between the circulating mass (ball) and the gyrating track. P is the average frontal air pressure, and A is the object's frontal cross-sectional area. Using Eq 3 in Eq 2 yields:

$$m\ddot{x}\left(\sin\{\phi-\beta\}+\mu\cos\{\phi-\beta\}\right)+m\ddot{y}\left(\mu\sin\{\phi-\beta\}-\cos\{\phi-\beta\}\right)=PA \quad . \tag{4}$$

Furthermore, in keeping with the geometry designations of Fig 7, the x and y components of the objects location can be written as

$$\begin{aligned} x &= r\cos\{\psi\}+R\cos\{\phi\} \\ y &= r\sin\{\psi\}+R\sin\{\phi\} \end{aligned} \tag{5}$$

Bearing in mind that r is constant, and $R = R(\phi)$,

$$\ddot{x} = \ddot{\phi}\left[\frac{dR}{d\phi}\cos\phi - R\sin\phi\right] + \dot{\phi}^2\left[\frac{d^2R}{d\phi^2}\cos\phi - 2\frac{dR}{d\phi}\sin\phi - R\cos\phi\right]$$

$$-\ddot{\psi}\,[r\sin\psi] - \dot{\psi}^2\,[r\cos\psi] \qquad , \qquad (6)$$

$$\ddot{y} = \ddot{\phi}\left[\frac{dR}{d\phi}\sin\phi + R\cos\phi\right] + \dot{\phi}^2\left[\frac{d^2R}{d\phi^2}\sin\phi + 2\frac{dR}{d\phi}\cos\phi - R\sin\phi\right]$$

$$+\ \ddot{\psi}\,[r\cos\psi] - \dot{\psi}^2\,[r\sin\psi]$$

Combining Eq 6 and Eq 4 yields the equation of motion for the spiral slingatron, viz.,

$$R\,\ddot{\phi}\,[\tan\beta(\mu\cos\beta - \sin\beta) - (\cos\beta + \mu\sin\beta)]$$

$$+R\,\dot{\phi}^2\left[\left(\frac{d\tan\beta}{d\phi} + \tan^2\beta - 1\right)(\mu\cos\beta - \sin\beta) - 2\tan\beta\,(\cos\beta + \mu\sin\beta)\right]$$

$$+r\ddot{\psi}\begin{bmatrix}\sin\beta\{\sin(\psi-\phi) - \mu\cos(\psi-\phi)\} \\ -\cos\beta\{\cos(\psi-\phi) + \mu\sin(\psi-\phi)\}\end{bmatrix} \qquad , \qquad (7)$$

$$+r\dot{\psi}^2\begin{bmatrix}\cos\beta\{\sin(\psi-\phi) - \mu\cos(\psi-\phi)\} \\ +\sin\beta\{\cos(\psi-\phi) + \mu\sin(\psi-\phi)\}\end{bmatrix} \quad -\frac{PA}{m} = 0$$

with β given by Eq 1.* Note, if the spiral collapse into a circle, then $\beta = 0$ and the equation of motion for a circular slingatron becomes,

$$\ddot{\phi}R + \dot{\phi}^2\mu R + r\ddot{\psi}[\cos(\psi-\phi) + \mu\sin(\psi-\phi)] - r\dot{\psi}^2[\sin(\psi-\phi) - \mu\cos(\psi-\phi)] + \frac{PA}{m} = 0 \qquad . \qquad (8)$$

In this investigation, the only solutions of interest are those for which the gyration rate is steady, i.e., $\dot{\psi}$ is constant. (It is envisioned that size of the spiral slingatron required for earth-to-space launch will be so massive, that it would be difficult to provide such a large

* With the exception of the pressure term, Eq. 7 agrees with the equation of projectile motion in a gyrating and evacuated spiral launch tube, as derived by D. A. Tidman in his unpublished notes, dated November 11, 1997.

structure with any substantial angular acceleration over the short time period that the projectile traverses the launch tube.) Looking for solutions with $\ddot{\psi} = 0$ means the motion of an object in the spiral slingatron will conform to

$$R\ddot{\phi}\left[\tan\beta(\mu\cos\beta - \sin\beta) - (\cos\beta + \mu\sin\beta)\right]$$

$$+ R\dot{\phi}^2\left[\left(\frac{d\tan\beta}{d\phi} + \tan^2\beta - 1\right)(\mu\cos\beta - \sin\beta) - 2\tan\beta\,(\cos\beta + \mu\sin\beta)\right] \quad . \quad (9)$$

$$+ r\dot{\psi}^2\begin{bmatrix}\cos\beta\left\langle\{\sin(\psi-\phi) - \mu\cos(\psi-\phi)\} \equiv \{\sin(\theta) - \mu\cos(\theta)\}\right\rangle \\ \\ + \sin\beta\left\langle\{\cos(\psi-\phi) + \mu\sin(\psi-\phi)\} \equiv \{\cos(\theta) + \mu\sin(\theta)\}\right\rangle\end{bmatrix} - \frac{PA}{m} = 0$$

Clearly, this differential equation of motion is non-linear. A numerical solution is the only one possible. To this end, the numerical integration techniques within Matlab and Simulink (both marketed by Mathworks Inc.) are used here to solve the problem. However, before invoking these solution algorithms, both μ and P need further clarification. For simplicity, the straightforward analytical expression given in Eq 10[†] will be used for the average frontal pressure on the object in the slingatron, viz.,

$$P = \frac{P_\infty \gamma(\gamma+1)M^2}{2} \quad . \quad (10)$$

Here, M is the Mach number of the projectile through the air ahead of it, in which the gas pressure is P_∞, $\gamma = 1.4$, and the sound speed is 335 m/s. Under these conditions, it was found that air drag can significantly retard the acceleration of the projectile, unless the launch tube is partially evacuated. Since this study is primarily interested in finding the range of possible solutions, it was assumed from the outset that the launch tube could be pumped down to a pressure of $P_\infty = 0.01$ atm $= 1.01\text{x}10^3$ N/m^2.

The friction coefficient, μ, is also found to play a significant role in determining the size and speed of the slingatron needed to achieve the requisite earth-to-space escape velocity, assumed here to be 8 km/s. Tidman [6] has obtained experimental data on μ for speeds up to 2 km/s; a curve fit to that data yielded Eq 11. Until a broader range of data can be sampled, Eq 11 will be utilized to compute μ as a function of the object's velocity.

$$\mu = \frac{0.12}{1.0 + 2.43\times10^{-3}\,|\vec{v}|} \quad (11)$$

[†] This expression can be derived from Equation 3.5, page 64, of Liepman and Roshko [5], in the limit of $P/P_\infty >> 1$, i.e., high object/projectile velocity.

SOLVING THE EQUATION OF MOTION

Spiral Slingatron Parameters

Since $\dot{\psi}$ is the angular rate at which the spiral track gyrates, it is not a variable, but rather, a parameter of the problem. Likewise, the radius of gyration, r, is a parameter, as is the mass, m, and cross-sectional area, A, of the projectile. Depending on the geometry of the spiral, its description can involve several parameters, for instance, a circle requires one parameter—the radius. For simplicity, a two-parameter Archimedes spiral is assumed here, of the form

$$R(\phi) = a\,\phi + R_o \quad , \tag{12}$$

where a and R_o are the two parameters. Initial conditions are also needed to specify the starting angles, ψ_o and ϕ_o, as well as $\dot{\phi}_o$. Thus, in total, there are 9 parameters that need to be specified in order to unambiguously solve Eq 9. However, not all of these parameters are varied in this exploratory investigation. In particular, ϕ_o is taken to be a constant, thereby defining a reference axis; also, the mass m is taken to be a constant, as is the projectile's cross-sectional area A. Furthermore, it is assumed that $\dot{\phi}_o$ is the same as $\dot{\psi}$, i.e., there is no initial time rate of change in the phase angle, θ. Hence, the number of parameter that will be varied in this study is reduced from 9 to 5.

Solution Results

Although a large range of solutions will ultimately be explored, a small subset is chosen first, in order to demonstrate that some parameters have more influence on the solution than others. With this in mind, the initial range of parameters is taken to be:

$$\begin{array}{lll}
\dot{\psi} = \dfrac{7\pi}{2}, \dfrac{9\pi}{2}, \dfrac{11\pi}{2} \text{ rad/s} & & \text{r} = 7.5,\ 9.5,\ 11.5 \text{ m} \\
\dot{\phi}_o = \dot{\psi} & & \text{R}_o = \text{r}+8,\ \text{r}+10,\ \text{r}+12 \text{ m} \\
\left.\begin{array}{l}\psi_o = \dfrac{\pi}{8}, \dfrac{\pi}{10}, \dfrac{\pi}{12} \text{ rad} \\ \phi_o = 0 \text{ rad}\end{array}\right\} \theta_o = \dfrac{\pi}{8}, \dfrac{\pi}{10}, \dfrac{\pi}{12} \text{ rad} & & \text{a} = 0.175\times\text{r},\ 0.225\times\text{r},\ 0.275\times\text{r m} \\
\text{m} = 1{,}000 \text{ kg} & & \text{A} = 0.086 \text{ m}^2
\end{array} \quad , \tag{13}$$

A command procedure was written (containing a series of nested loops), whereby the computed Simulink solution of Eq 9 (using Eqs 1, 10, and 11, for β, P and μ, respectively) is obtained for each of the 243 combinations of parameters/initial conditions set out in Eq 13. A solution for $\phi(t)$ was considered acceptable, for the purpose of launching a projectile into space, if the computed value of the projectile's speed within the spiral track, viz.,

$$
\begin{aligned}
|\vec{v}| &= \sqrt{\dot{x}^2 + \dot{y}^2} \\
&= \dot{R}^2 + (r\dot{\psi})^2 + (R\dot{\phi})^2 + (2\dot{\psi}\,\dot{\phi}\,R\,r)\cos\theta - (2\dot{\psi}\,\dot{R}\,r)\sin\theta \\
&= (\dot{\phi}\,a)^2 + (r\dot{\psi})^2 + \left([a\phi + R_o]\dot{\phi}\right)^2 + (2\dot{\psi}\,\dot{\phi}\,r\,[a\phi + R_o])\cos\theta - (2\dot{\psi}\,\dot{\phi}\,a\,r)\sin\theta
\end{aligned}
\quad , \qquad (14)
$$

reached 8 km/s, at any time. Out of the 243 solutions, only 90 produced a projectile speed of at least 8 km/s. One such solution,

$$
\begin{aligned}
&\dot{\psi} = \frac{11\pi}{2}\ \text{rad/s} && r = 5.5\ \text{m} \\
&\dot{\phi}_o = \dot{\psi} && R_o = r + 12\ \text{m} \\
&\left.\begin{aligned}\psi_o &= \frac{\pi}{12}\ \text{rad} \\ \phi_o &= 0\ \text{rad}\end{aligned}\right\} \theta_o = \frac{\pi}{12}\ \text{rad} && a = 0.275 \times r\ \text{m} \\
&m = 1{,}000\ \text{kg} && A = 0.086\ \text{m}^2
\end{aligned}
\quad , \qquad (15)
$$

yielded the results shown in Fig 8.

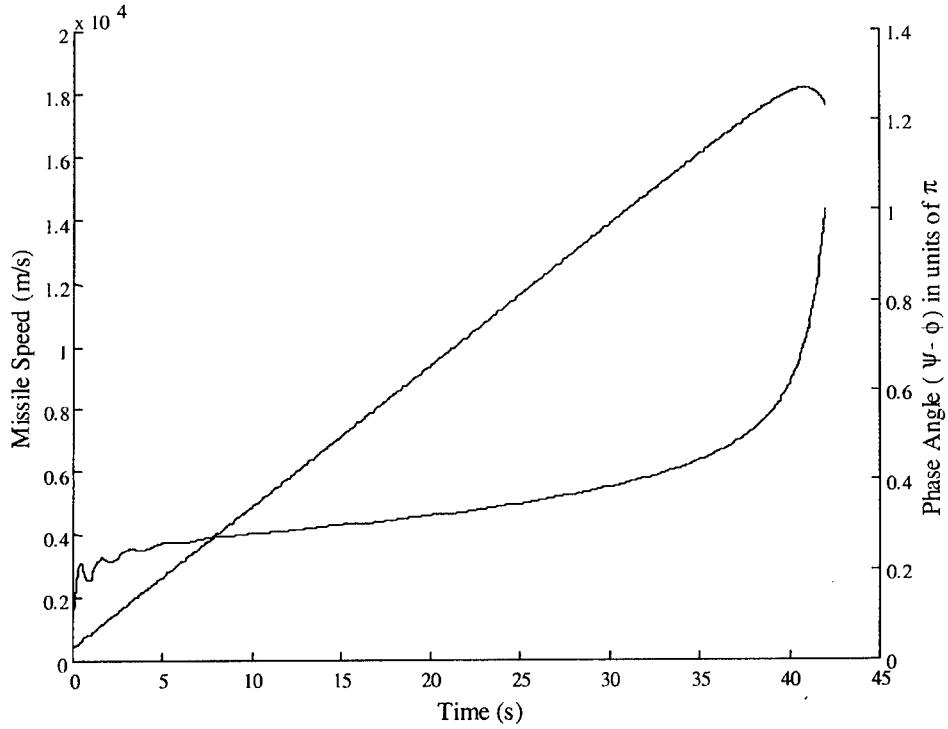


FIGURE 8. Velocity and Phase Angle vs. Time, Based Upon the Simulink Solution of Eq (9) for the Conditions of Eq 15.

It appears from Fig 8 that the solution for the missile's speed, Eq 14, increases in a near-linear fashion, almost independent of the phase angle, $\theta = \psi - \phi$, until such a time (~40 s) that the phase angle exceeds some critical value, here ~0.6 π rad (~108 deg), above which it grows rapidly while the speed declines. However, the decline in speed in this case occurs well above the sought after launch velocity of 8 km/s, which requires ~17 s for this particular set of slingatron parameters. Figure 9 plots the acceleration of the projectile in the tangent and normal directions to the spiral. Although it is the non-zero tangential acceleration that gives rise to the speed increase in Fig 8, it can be seen that this component is minor in comparison to the acceleration that the projectile undergoes in the direction normal to the track (e.g., ~100 g's vs. ~14,000 g's at the time the projectile reaches 8 km/s).

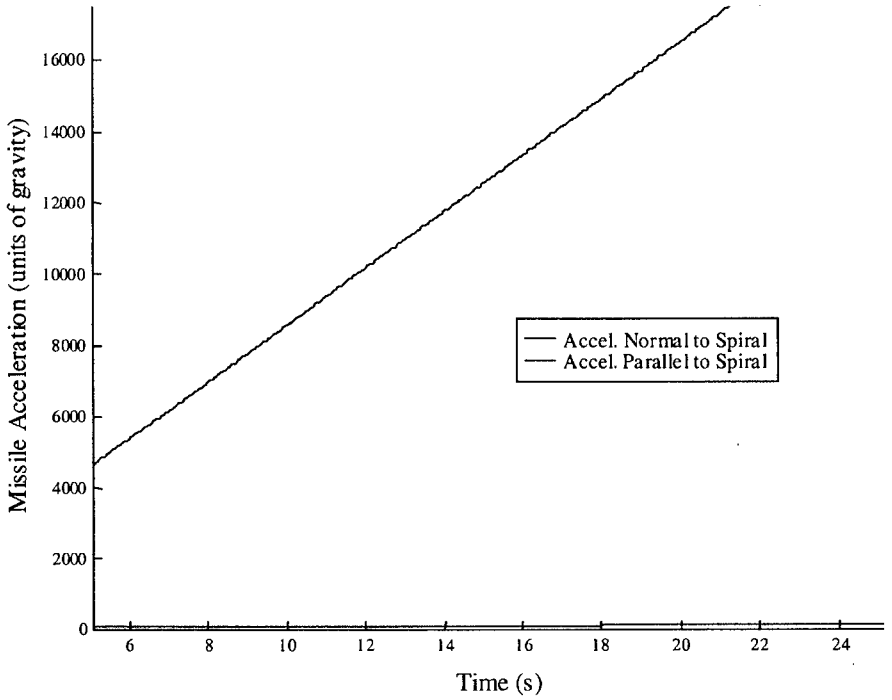


FIGURE 9. Acceleration vs. Time, Based Upon the Simulink Solution of Eq (9) for the Conditions of Eq 15.

The high acceleration of the projectile normal to the track requires a large normal force, creating a substantial wall pressure, displayed in Fig 10. In practice, a track formed from steel pipe would require a considerable wall thickness to accommodate this level of pressure. A finite element model was formulated to analyze the problem. In particular, a time varying pressure load was swept across one side (180 degrees) of the inner surface of a steel tube, Fig 11, assumed to be hinged at both ends. A plot of the peak hoop (circumferential) stress in the tube as a function of wall thickness is shown in Fig 11, for various pipe thicknesses. For example, if a wall pressure of 10 ksi was required to change the projectile's direction in the spiral track, then it would generate a peak inner surface hoop stress of ~6–7 ksi in a 2 in thick wall. (For reference, 70 ksi is considered a safe hoop-stress level in gun barrel steels.) In the pressure vessel industry, a simple rule of thumb for gauging wall thickness is (Dorf [7]):

$$\text{Wall Thickness (in)} = \frac{\text{Applied Normal Pressure (psi)} \times \text{Inside Cylinder Radius (in)}}{\text{Allowable Stress (psi)} - 0.6 \times \text{Applied Normal Pressure (psi)}} \quad , \quad (16)$$

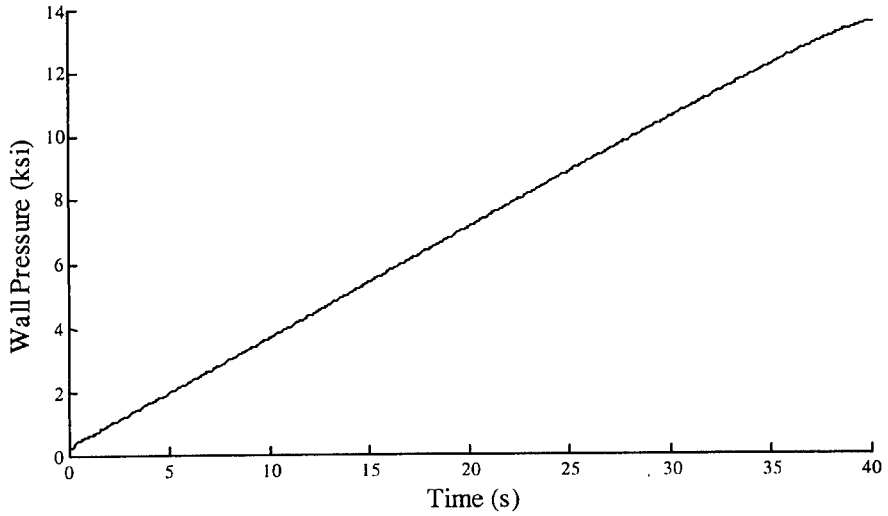


FIGURE 10. Projectile-Track Interface Pressure vs. Time, Based Upon the Simulink Solution of Eq (9) for the Conditions of Eq 15.

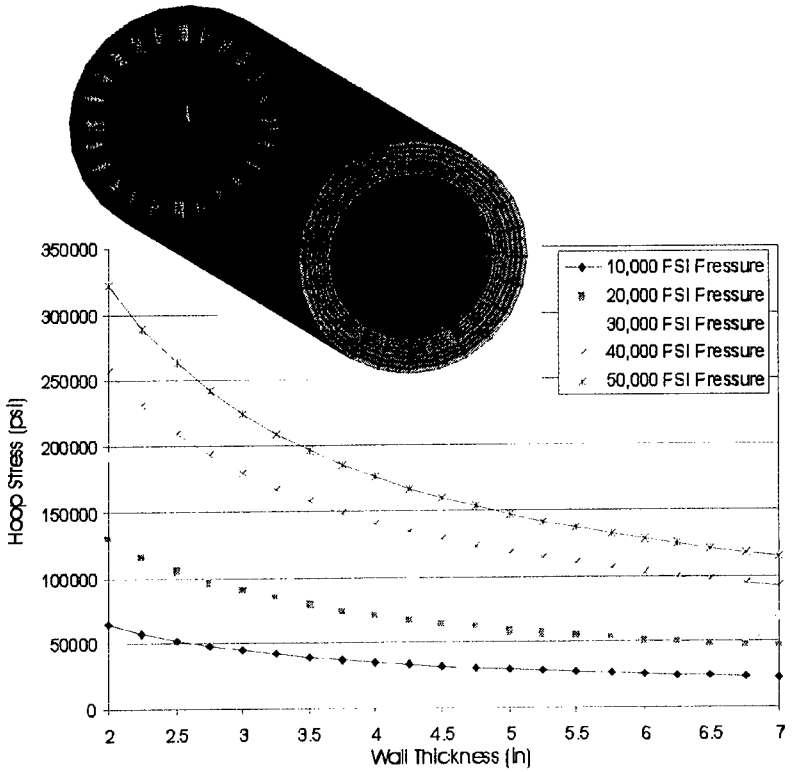


FIGURE 11. Peak Inner Surface Hoop Stress vs. Wall Thickness, for Various Semi-Circular, Inner-Wall Pressure Loadings, in AISI 4340 Steel Pipe.

In order to compute the total weight of a Slingatron track, the total track length needs to be determined. Figure 12 shows the cumulative arc (track) length vs. time for the same Simulink solution as that of Figs 8–11. At 17 s (~8 km/s) the spiral length is ~ 43 mi. Although not shown here, wall pressure vs. track length could also be resolved from the Simulink solution. Similarly, assuming a pipe-like track design made from steel that can safely tolerate a hoop stress of 70 ksi, with inner diameter (from A in Eq 15) of 25 in (0.64 m), Eq 16 can be invoked to provide wall thickness vs. arc length. It was thus determined, that 43 mi of track would weight ~17,000,000 lbs, or, 8,500 tons.

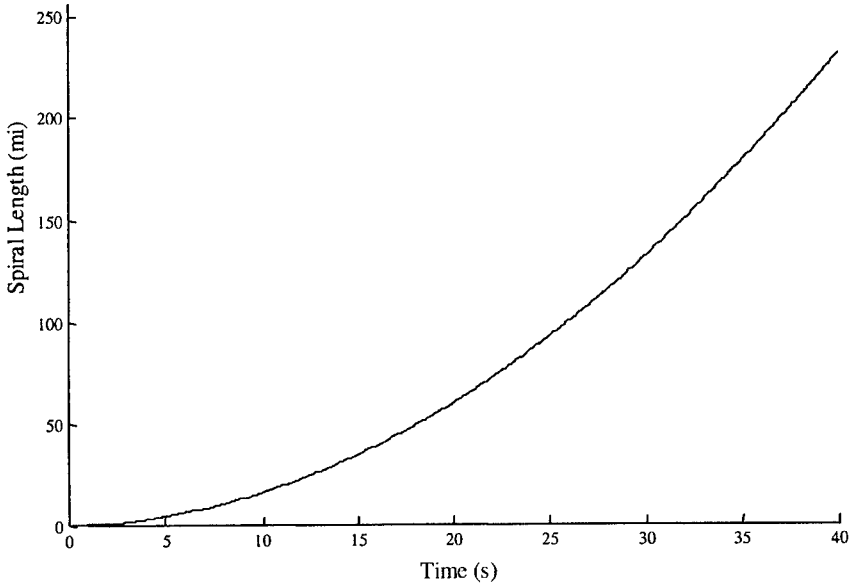


FIGURE 12. Track Length vs. Time, Based Upon the Simulink Solution of Eq (9) for the Conditions of Eq 15.

Upon closer inspection, it was noticed that within the 90 parameter-sets that yielded successful solutions, variation in θ_o and R_o did not strongly affect the outcome. To illustrate this, Fig 17 plots solutions derived from the following subset of Eq 13,

$$\dot{\psi} = \frac{11\pi}{2} \text{ rad/s} \quad ; \quad \dot{\phi}_o = \dot{\psi} \quad ; \quad r = 5.5 \text{ m} \quad ; \quad R_o = r+12 \text{ m}$$

$$a = 0.275 \times r \text{ m} \quad ; \quad m = 1{,}000 \text{ kg} \quad ; \quad A = 0.086 \text{ m}^2 \qquad . \quad (17)$$

$$\left.\begin{array}{l} \psi_o = \frac{\pi}{8}, \frac{\pi}{10}, \frac{\pi}{12} \text{ rad} \\ \phi_o = 0 \text{ rad} \end{array}\right\} \theta_o = \frac{\pi}{8}, \frac{\pi}{10}, \frac{\pi}{12} \text{ rad}$$

As indicated, these three cases differ from each other only by the initial phase angle θ_o.

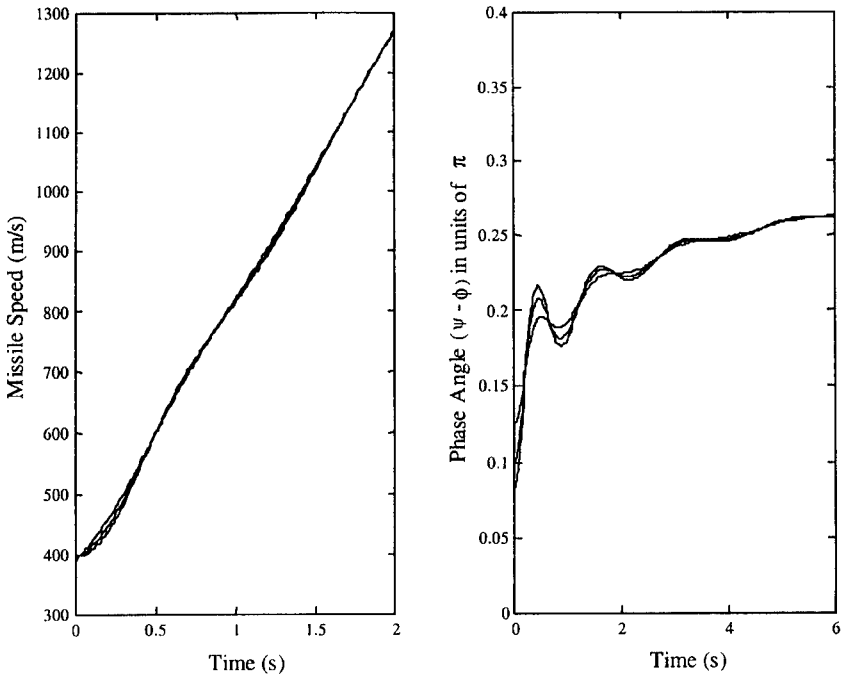


FIGURE 13. Speed and Phase Angle vs. Time, Based Upon the Simulink Solution of Eqs (9) and (17).

As can be seen from Fig 13, variation in the phase angle dampens out, as did its effect on the solution for the projectile's speed. Likewise, though not plotted here, variation in phase angle did not produce significant changes in the total track length, nor did it noticeably affect the plot of wall pressure vs. time. A similar result was found to hold for variation in R_o, viz., significant changes in the initial spiral radius produced insignificant change, over time, in the projectile speed, track length, and wall pressure.

In summary, of the 243 parameter-sets specified in Eq 13, only 90 yielded a solution that produced a projectile speed of 8 km/s (or more). Of these 90, there was a subset of 10 that yielded notably different values for the track length and wall pressure; for each of these 10, there were 9 variations in θ_o or R_o that only slightly perturbed the length and pressure profiles.

In addition to track length and wall pressure, another factor that must be considered in evaluating a practical slingatron design would be the speed at which the spiral track gyrates. For instance, the higher the frame speed, the more energy is expended doing work against air resistance/drag. Furthermore, the higher the structural speed, the higher the loads on moving parts (e.g., bearings) and the more wear and maintenance that can be expected. Figure 14 plots the frame speed vs. wall pressure and track length for the 90 successful launch solutions of Eq 9. The inset plot shows the 10 most unique solutions, demonstrating that variation in θ_o and R_o is not needed to capture the gross range of solutions.

The most desirable solution is the one that has a low track speed, low wall pressure, and short track length; not surprisingly, concurrent minimums in these three parameters appears unachievable. Thus, a compromise has to be made, two of the three desirable traits must be favored at the expense of the third, or, less than minimum values must be accepted for all three factors. For example, from Fig 14, if a maximum wall pressure at projectile exit of 6 ksi could be tolerated, then a minimum spiral length of 43 mi, gyrating at a minimum circular speed of 95 m/s could be achieved. On the other hand, if the maximum wall pressure was set

at 5 ksi, it would necessitate a minimal spiral length of 66 mi with a frame speed of 78 m/s. Also shown in Fig 14 are three solutions where the pressure is 5 ksi and the frame speed is 78 m/s, but the track lengths are vastly different, at 66 mi, 80 mi, and 102 mi, respectively. Although these three designs accomplish the same effect (viz., launching the projectile at 8 km/s), the difference in their costs (one being 40% shorter than the other) would be tremendous; thus proving the potential benefit of this type of parametric analysis.

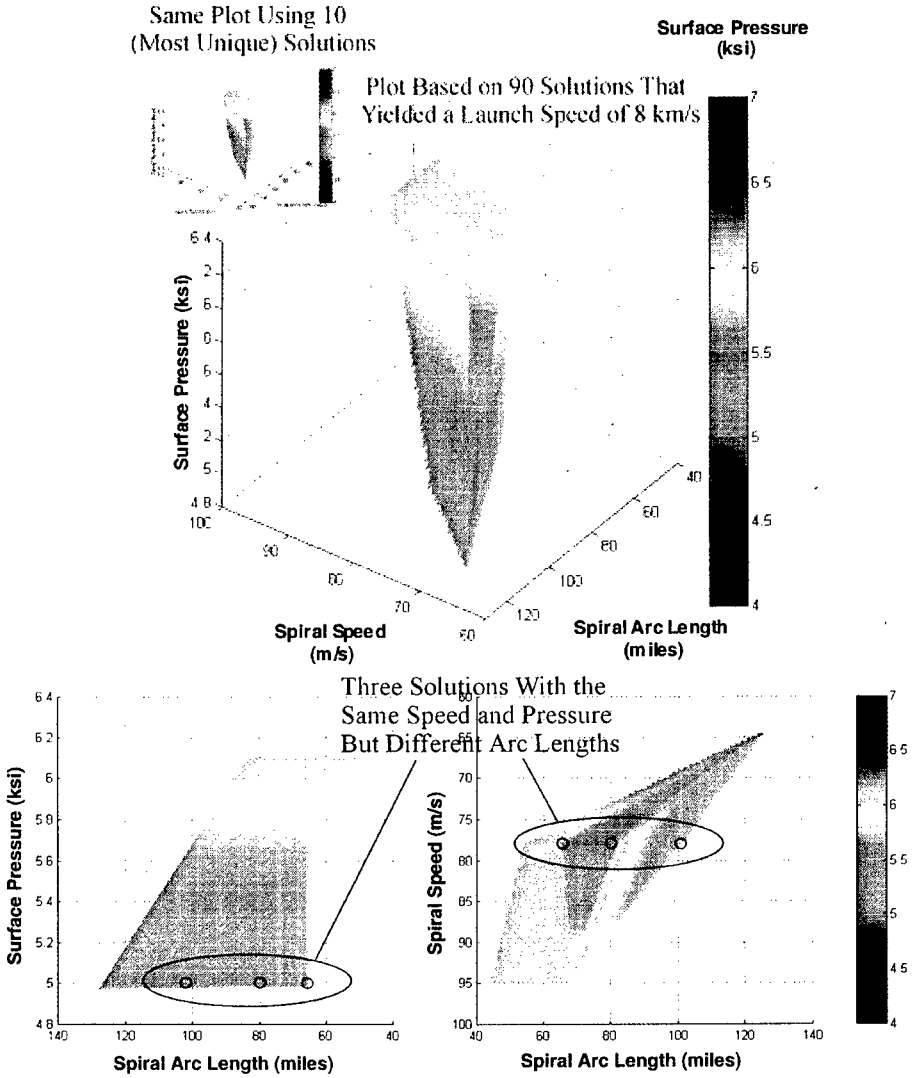


FIGURE 14. Wall Pressure vs. Spiral Speed vs. Spiral Track Length, Based Upon Es (9) and (13).

The relatively small range of parameters specified in Eq 13 has been used to demonstrate (via Figs 8–14) the methodology by which Simulink can be utilized to search for favorable solutions to the problem of a slingatron-based earth-to-space projectile launch, from an engineering-practical vantage point. Although Fig 14 shows a solution surface, the range of parameters upon which it was derived, viz., Eq 13 (with its 243 possibilities), is not all-inclusive. Are there other parameter sets that might produce even better (easier to produce and

maintain) solutions/designs? To answer this question, a broader range of parameters needs to be examined. In order to explore the widest possible range of solutions with the minimum computer time and resources, it is sensible to distribute the collection of parameters in accordance with their degree of influence on the solution. As indicated by the likeness of the 10-solution subset to the full 90-solution assembly in Fig 14, variation in the parameters θ_o and R_o does not produce significantly different results. Therefore, it makes sense to narrow the range of these two parameters and widen the range for the remaining three, viz., the gyration speed parameter, $\dot{\psi}$, the gyration radius, r, and the parameter governing the tightness of the spiral, a. Accordingly, the 18,375 parameter-sets of Eq 18 were examined and (as will be shown) found to yield a range of solutions that liberally bound the region of practical interest.

$$\begin{aligned}
&\dot{\psi} = \frac{\pi}{2}(2n_1 - 1)\,\text{rad/s}\ ;\ \text{for}\ n_1 = 1{:}35 && R_o = r + 4\ \text{m}\\
&r = n_2 - 0.5\ \text{m}\ ;\ \text{for}\ n_2 = 1{:}35 && \dot{\phi}_o = \dot{\psi}\\
&a = (n_3 - 0.5)\times 0.05\times r\ \text{m}\ ;\ \text{for}\ n_3 = 1{:}15 && m = 1{,}000\ \text{kg}\\
&\left.\begin{aligned}\psi_o &= \frac{\pi}{40}\,\text{rad}\\ \phi_o &= 0\ \text{rad}\end{aligned}\right\}\theta_o = \frac{\pi}{40}\ \text{rad} && A = 0.086\ \text{m}^2
\end{aligned} \qquad (18)$$

Out of the 18,375 different combinations of parameters, there were 16,178 successful solutions (of Eq 13 for $\phi[t]$) that yielded a projectile speed (Eq 14) of at least 8 km/s. Fig 15 is the counterpart of Fig 14, displaying all 16,178 solutions.

Clearly, a structural speed that is greater than the speed of sound (~335 m/s) is impractical, neglecting these cases would eliminate the majority of the solutions indicated in Fig 15. A more reasonable speed might be several hundred meters per second slower. Searching the solution set, Fig 16 shows a subset plot of 600 solutions where the structural speed of the track was < 140 m/s and the track length is < ~100 mi.

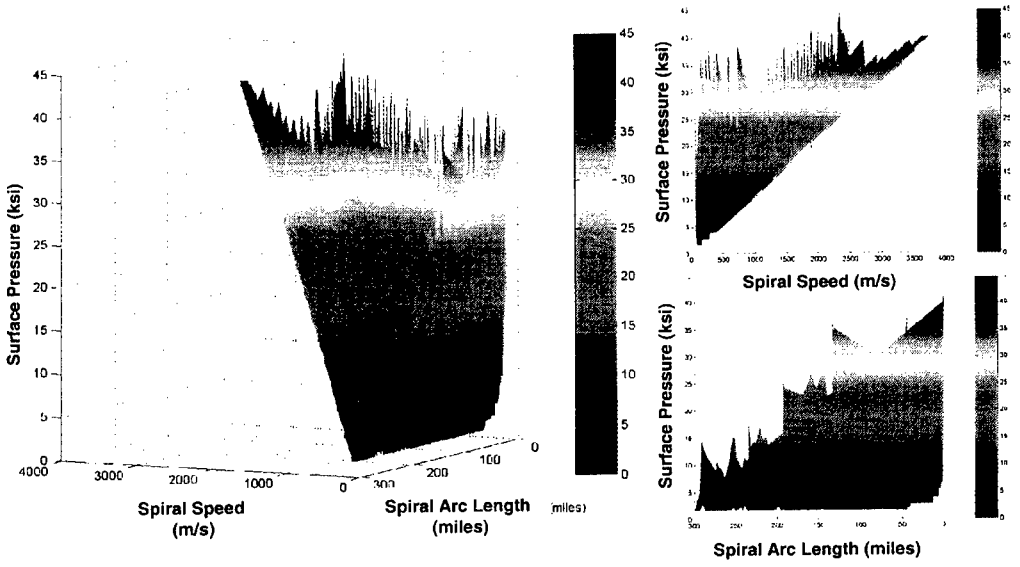


FIGURE 15. Wall Pressure vs. Spiral Speed vs. Spiral Track Length, Based Upon Eqs (9) and (18).

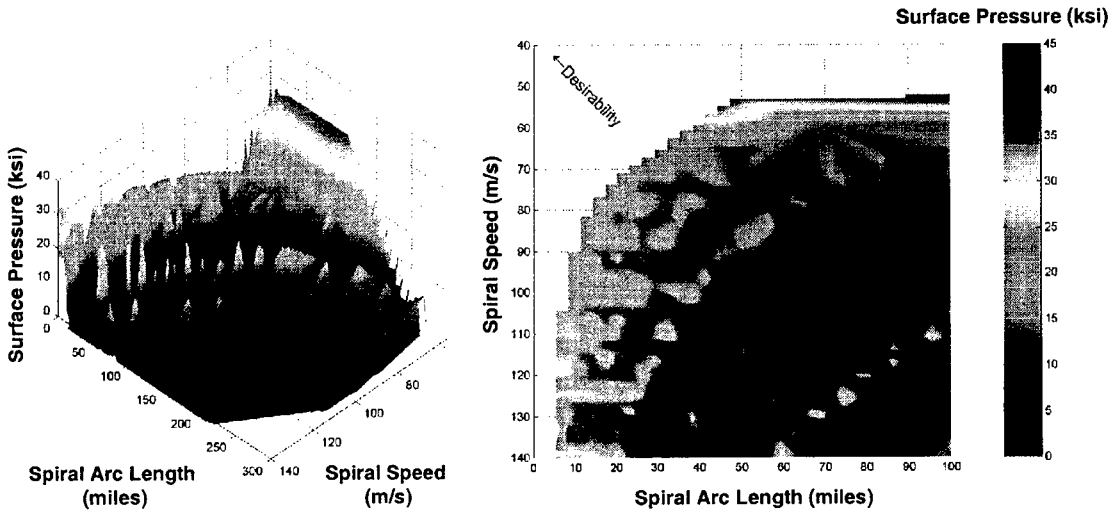


FIGURE 16. Wall Pressure vs. Spiral Speed vs. Spiral Track Length, Based Upon Eqs (9) and (18).

At the upper speed end in this subset is a solution ($n_1 = 2$, $n_2 = 30$, $n_3 = 13$) where the structure is moving at 139 m/s (313 mph), the peak wall pressure is below 2 ksi, and the track length is a, relatively, moderate 54 mi. Based on the same approach used to determine the 8,500-ton track weight in the previous (95-m/s, 6-ksi, 43-mi) example, this designated-upper-speed-limit, 54-mi track would weigh a relatively low 2,700 tons.

At the low speed end, a solution exists ($n_1 = 34$, $n_2 = 1$, $n_3 = 2$) where the track motion is slowed down to 53 m/s; the track length remains in the middle ground at 48 mi, but the wall pressure peaks at 37 ksi. The estimated weight of this lower-speed-limit track is high, at 107,000 tons.

A more all-around-moderate solution ($n_1 = 7$, $n_2 = 4$, $n_3 = 6$) would have the track moving at 72 m/s, with a wall pressure of 7 ksi, and a track length, again in the mid-range, at 50 mi. The estimated weight of this track would be 12,200 tons.

Perhaps the best solution compromise for structural speed, peak wall pressure, length, and weight is one ($n_1 = 10$, $n_2 = 3$, $n_3 = 7$) that produces mid-range values for the frame speed, at 75 m/s (170 mph), wall pressure, at 11 ksi, weight, at 10,500 tons, and a low-end track length of 28 mi. (For reference, this slingatron would be the weight-motion equivalent of two fully-loaded medium-sized river barges, each circling at ~5 hz around an ~8 ft radius.)

Although the evidence is anecdotal, the values for n_1, n_2, and n_3 in the four practical-solution examples described above and tabulated below (spanning the high, moderate, and low frame speed regimes) illustrate that the range of n_1 and n_2, from 1–35, and n_3, from 1–15, was broad enough to capture the majority, if not all, of the most practical slingatron designs.

SUMMARY

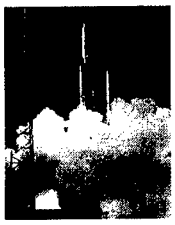
This report provides a physical explanation of the mechanism by which the mechanical device, referred to as a slingatron, akin to a hoola-hoop, can be used to launch a projectile into space. Furthermore, using the software program called Simulink (a complementary program to Matlab) the non-linear differential equation of motion for a spiral slingatron design was solved

for a large range of input parameters. These solutions were sorted based upon whether or not the slingatron design could accelerate a 1000-kg, 0.64-m diameter projectile to at least 8 km/s (assumed to be a sufficient speed to place such a payload into space). Finally, the most physically reasonably of these successful solutions were down-selected. A case in point, it was found that a spiral track 28 mi long weighting 10,500 tons having a structural speed of ~170 mph could be used to launch such a projectile into space.

With the type of information provided in this study (viz., structural speed, wall pressure, and track length), a more detailed track-design analysis could begin, leading to, among other things, a total-dollar (or per-payload-pound) cost estimate for a slingatron-based earth-to-space launch system.

Table 1. Examples of the "Most Practical/Optimum" Slingatron Track Designs

Minimum Values	Structural Speed (m/s)	Wall Pressure (ksi)	Track Length (miles)	Weight (U.S. tons)
A	139	2	54	2,700
B	53	37	48	107,000
C	72	7	50	12,200
D	75	11	28	10,500

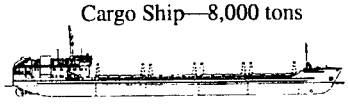


Titan IV Rocket —340-380 tons



International Space Station —520 tons

500-ft Fully Loaded Cargo Ship—8,000 tons



Large Steel River Bridge—10,000 tons



1000-ft Fully Loaded Aircraft Carrier — 80-100,000 tons



Golden Gate Bay Bridge — 200,000 tons



REFERENCES

[1] Tidman, D. A., R. L. Burton, D.S. Jenkins, and F.d. Witherspoon. "Sling Launch of Materials into Space." *Proceedings of 12th SSI/Princeton Conference on Space Manufacturing*, ed. By B. Faughnan, Space Studies Institute, Princeton, NJ, pp 59–70, May 4–7, 1995.

[2] Tidman, D. A. "Sling Launch of a Mass Using Superconducting Levitation." *IEEE Transactions on Magnetics*, vol. 32, no. 1, pp 240–247, January, 1996.

[3] Tidman, D. A. "Slingatron Mass Launchers." *Journal of Propulsion and Power*, vol. 14, no. 4, pp 537–544, July–August, 1998.

[4] Tidman, D. A. and J. R. Greig. "Slingatron Engineering and Early Experiments." *Proceedings of the 14th SSI/Princeton Conference on Space Manufacturing*, ed. By B. Faughnan, Space Studies Institute, Princeton, NJ, pp 306–312, May 6–9, 1999.

[5] Liepman, H. W., and A Roshko. "Elements of Gasdynamics." John Wiley & Sons, Inc., New York, Eq 3.5, page 64, 1957.

[6] Tidman, D. A. "The Spiral Slingatron Mass Launcher." *Proceedings of the 10th U.S. Army Gun Dynamics Symposium*, April 23-26, 2001.

[7] Dorf, R. C. "The Engineering Handbook." CRC Press Inc, Boca Raton, FL, page 85, 1996.

Numerical Simulations of the Slingatron

G. R. Cooper[!], D. A. Tidman[*], M. Bundy[!], S. Wilkerson[!]
[!]U.S. Army Research Laboratory, Aberdeen Proving Ground, Maryland 21005-5066
[*]ALCorp., 6801 Benjamin Street, McLean, VA 22101

Abstract

The slingatron mass accelerator is described for several track configurations (shapes), and numerical simulations of this accelerating mass traversing a given track configuration are presented. The sled is modeled as a point mass that interacts with the slingatron track using both a conventional and a new empirical velocity dependent friction law. The closed loop circular slingatron was found to produce high maximum sled velocities provided the gyration angular speed is always increasing. In contrast several spiral shaped slingatron tracks reveal that high maximum sled velocities are obtainable with the gyration speed held constant. In fact, a slingatron constructed out of semi-circles is shown capable of generating high velocity sleds in such a way that no initial sled injection is necessary. Choosing the proper initial gyration phase with an empirically determined friction model allows the mass sled to gain ever-increasing velocities when placed in a semi-circle slingatron. The sled bearing pressure and its total acceleration are examined and presented.

Nomenclature

$\mathbf{A}$ =	acceleration vector
$A_{//}$ =	$\mathbf{n}$ component of $\mathbf{A}$
$A_{\perp}$ =	$\mathbf{m}$ component of $\mathbf{A}$
D =	sled diameter
$\mathbf{F}$ =	force vector acting on sled $F = \lvert\mathbf{F}\rvert$
$F_{//}$ =	$\mathbf{n}$ component of $\mathbf{F}$
$F_{\perp}$ =	$\mathbf{m}$ component of $\mathbf{F}$
f =	spin frequency of gyration vector
$\dot{f}$ =	time derivative of gyration frequency f
$\mathbf{i}, \mathbf{j}, \mathbf{k}$ =	Cartesian unit triad
L =	sled length
M =	mass of sled
$\mathbf{m}$ =	normal unit vector on concave side of track
$\mathbf{n}$ =	normal unit vector anti-parallel to the track
P =	bearing pressure
$\mathbf{R}$ =	sled radius vector $\lvert\mathbf{R}\rvert = R$
$\mathbf{r}$ =	gyration vector $\lvert\mathbf{r}\rvert = r$
s =	displacement
t =	time
V =	velocity $V = \sqrt{\dot{x}^2 + \dot{y}^2}$
$\hat{V}$ =	relative sled velocity

$x =$	abscissa of sled
$y =$	ordinate of sled
$\alpha =$	orientation angle $= \phi - 2\pi\lfloor(\phi/2\pi)\rfloor$
$\delta =$	differences between upper and lower semi-circle radii
$\theta =$	lock-in angle
$\gamma =$	ratio of specific heats
$\lambda =$	radius of curvature
$\mu =$	coefficient of friction
$\rho =$	diameter of circle
$\phi =$	orientation of **R**
$\psi =$	orientation of **r**
$\psi_0 =$	initial value of ψ
$\lvert\ \rvert =$	absolute value
$(\,)' =$	$d(\,)/d\phi$
$(\dot{}) =$	$d(\,)/dt$
$\langle\ \rangle =$	average value
$\times =$	vector product
$\lfloor x \rfloor =$	greatest integer $\leq x$

Introduction

A mechanical method for accelerating a mass to high velocities has been proposed by D. A. Tidman[2] using a device called the slingatron[1]. Several closed loop slingatron configurations have previously been examined. For these configurations the accelerated mass (called a sled in this report) interaction with the slingatron track was modeled with magnetic levitation[1] or with a mechanical friction force that is proportional to the normal force exerted by the track[2] on the sled. This report presents numerical simulations of slingatrons having several different track configurations. The sled and track interaction continues to be treated as a normal force friction model but now the friction coefficient, μ, is either a constant or an empirically determined function depending on the sleds velocity relative to the slingatron track.

These simulations reveal that the mass can be accelerated to very high velocities for each track configuration (track shape) examined here. Generally, the calculations show that spiral shaped slingatrons will produce high velocities for constant gyration speeds and the single loop circular slingatron will produce high velocities for sufficiently high gyration acceleration. We emphasize that the main reason this happens is that the sled locks into a constant phase angle as it transverses the slingatron track. When this occurs the sleds velocity is optimally increased for each 2π revolution of the sled. This will continue until the frictional force dominates the component of the Coriolis force that is parallel to the slingatron track. However, there are cases where parameters can be chosen so the parallel component of the Coriolis force is always greater than the force due to friction. In such cases one will find that the non-relativistic sled velocity increases indefinitely. In the spiral slingatrons lock-in occurs almost instantaneously while for the single loop circular slingatron lock-in occurs after a sufficient amount of time has passed.

Theory

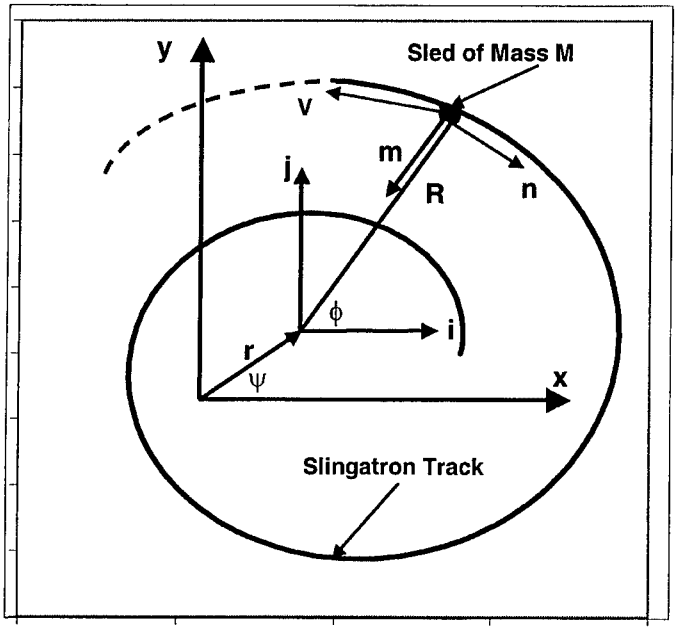


Figure 1 Schematic of a general slingatron

Figure 1 shows a sled of mass M moving along a track with position $\mathbf{R}+\mathbf{r}$ and corresponding velocity $\mathbf{V}=\dot{\mathbf{R}}+\dot{\mathbf{r}}$. The sleds velocity is assumed large enough so that it stays in contact with the track at all times. In fact, the velocity may be large enough to cause mass loss due to abrasion or evaporation, i.e.. $\dot{M}\neq 0$. The force $\mathbf{F}$ acting on the sled can be written as $\mathbf{F}=F_{\perp}\mathbf{m}+F_{//}\mathbf{n}$ where $\mathbf{m}$ and $\mathbf{n}$ are unit vectors pointing normal (toward the concave side of the track) and anti-parallel to the track. Therefore, $\mathbf{n}=-\mathbf{R}'/R'$ and $\mathbf{m}=\mathbf{n}\times\mathbf{k}$ for unit vector $\mathbf{k}$ pointing out along the normal to the plane of the track. Calling the unit vectors along the abscissa and ordinate $\mathbf{i}$ and $\mathbf{j}$ allows the momentum equations, see Fig. 1, to be written as

$$\begin{aligned}\left(\dot{M}\dot{x}+M\ddot{x}\right)&=-\left(\sin\phi\left(F_{\perp}R'-F_{//}R\right)+\cos\phi\left(F_{\perp}R+F_{//}R'\right)\right)\Big/\sqrt{R'^2+R^2}\\ \left(\dot{M}\dot{y}+M\ddot{y}\right)&=-\left(\sin\phi\left(F_{\perp}R+F_{//}R'\right)+\cos\phi\left(F_{//}R-F_{\perp}R'\right)\right)\Big/\sqrt{R'^2+R^2}\end{aligned}\qquad(1)$$

with Cartesian coordinates (x,y) in the $(\mathbf{i},\mathbf{j})$ plane which are constrained so that

$$\begin{aligned}x&=R\cos\phi+r\cos\psi\\ y&=R\sin\phi+r\sin\psi\end{aligned}\qquad(2)$$

The parallel force $F_{//}$ is assumed to be caused by friction and therefore the standard friction model is represented as

$$F_{//} = \mu(\hat{V})F_{\perp} \ni \hat{V} = |\dot{\phi}|\sqrt{R'^2 + r^2} \tag{3}$$

for which $\hat{V}$ is the sled velocity relative to the track. Now solving Eqs. (1) for $F_{\perp}$ and $F_{//}$ and then including Eq. (2) and Eq. (3) results in the following differential equation

$$\begin{aligned}\ddot{\phi} = &-\frac{\dot{\phi}^2\left(\mu\left(R^2 - RR'' + 2R'^2\right) + R'(R + R'')\right)}{R^2 + R'^2} \\ &+\frac{\left(\left(M\left(\ddot{\psi} + \mu\dot{\psi}^2\right) + \dot{M}\dot{\psi}\right)\sin(\psi - \phi) + \left(M\dot{\psi}^2 - \mu\left(M\ddot{\psi} + \dot{M}\dot{\psi}\right)\right)\cos(\psi - \phi)\right)rR'}{M\left(R^2 + R'^2\right)} \\ &+\frac{\left(\left(M\left(\dot{\psi}^2 - \mu\ddot{\psi}\right) - \mu\dot{M}\dot{\psi}\right)\sin(\psi - \phi) - \left(M\left(\ddot{\psi} + \mu\dot{\psi}^2\right) + \dot{M}\dot{\psi}\right)\cos(\psi - \phi)\right)rR'}{M\left(R^2 + R'^2\right)} \\ &-\frac{\dot{M}\dot{\phi}}{M}\end{aligned} \tag{4}$$

Equation (4) is general enough to account for many slingatron configurations as long as the motion takes place in the **i, j** plane. The configurations are obtained by specifying the ϕ dependence of the vector $\mathbf{R}(\phi)$ giving the shape of the slingatron track. The friction coefficient, $\mu(\hat{V})$, the time dependent mass, $M(t)$, and the gyration angle, $\psi(t)$, must also be given in order to numerically integrate Eq. (4)

Circular Slingatron

This report considers several possible track configurations all of which treat the length of the gyration arm, $|\mathbf{r}| = r$, as a constant. The first consideration is the circular slingatron[1,2] defined by

$$|\mathbf{R}(\phi)| = \text{constant}. \tag{5}$$

In general we have found that any slingatron will optimally accelerate a sled to high velocities whenever the lock-in angle, $\theta = \psi - \phi$, is very close to constant i.e.

$$\begin{aligned}&\dot{\theta} \approx 0 \text{ hence} \\ &\dot{\psi} \approx \dot{\phi} \text{ and } \ddot{\psi} \approx \ddot{\phi}\end{aligned} \tag{6}$$

Using the constraints given by Eq. (5) and Eqs. (6) simplifies Eq. (4) to the following expression

$$\begin{aligned}&\ddot{\phi} = b\dot{\phi}^2 \\ &b = \frac{r(\sin\theta - \mu\cos\theta) - \mu R}{r(\mu\sin\theta + \cos\theta) + R}\end{aligned} \tag{7}$$

for constant μ and M. . This is easily integrated to give us the sleds velocity $V = \sqrt{\dot{x}^2 + \dot{y}^2}$ as

$$V = \frac{\left|\dot{\phi}(0)\right|\sqrt{2rR\cos\theta + R^2 + r^2}}{\left|1 - \dot{\phi}(0) b\, t\right|}. \tag{8}$$

A plot of Eq. (8) is shown in Fig. 2 for $\theta = \pi/4$ $\phi(0) = 0$ and $\dot{\phi}(0) = \pi$. One can see that the non-relativistic velocity V becomes infinite at the time $t_\infty = 1/\dot{\phi}(0)b$ whenever we force θ to be constant[1,2].

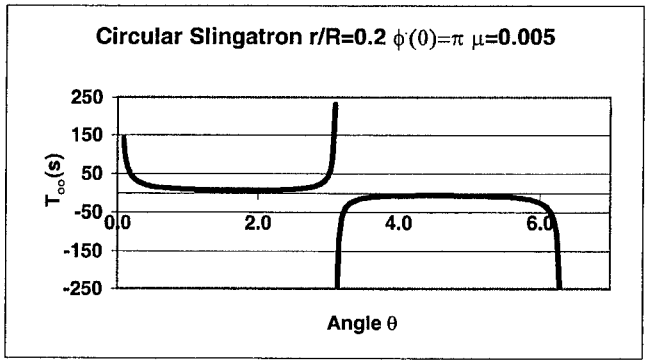


Fig. 2 Velocity vs. time for the circular slingatron

The values of t_∞ change rapidly in regions where $\theta \approx \pi n$, $n = 0,1,2\cdots$ and therefore a plot of $t_\infty(\theta)$ is given in Fig. 3.

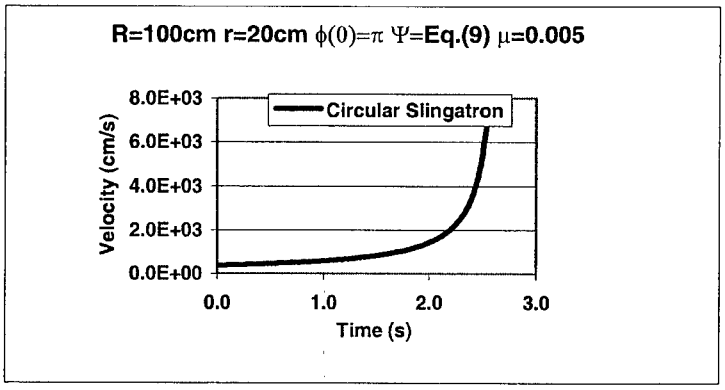


Fig. 3 $t_\infty(\theta)$ vs. time for the circular slingatron

Equation (7) shows that $b = 0$ whenever

$$\theta = \pm 2\tan^{-1}\left(\sqrt{(\alpha^2-1)\mu^2+\alpha^2} \mp \alpha/(\alpha-1)\mu\right) \pm \pi\, n,\ n = 0,1,2 \qquad (9)$$
assuming $(\alpha^2-1)\mu^2+\alpha^2 \geq 0$

These results used in Eq. (8) produce two time independent velocities given by $V = \left|\dot{\phi}(0)\right|\left|\sqrt{(\alpha^2-1)\mu^2+\alpha^2} \mp 1\right| / \sqrt{\mu^2+1}$. A small amount of algebra reveals that constant velocities occur when the normal force becomes so large that friction prevents the sled from accelerating along the circular track. Hence, the sleds velocity stays constant.

Instead of demanding the constraints given by Eqs (6) lets now consider a circular slingatron with an accelerating angular gyration speed such that

$$\psi = \psi_0 + 2\pi f\, t + \pi \dot{f}\, t^2. \qquad (10)$$

Numerically integrating Eq. (4), subject to Eq. (10), produces the velocity, with initial conditions $\phi(0) = 0$ and $\dot{\phi}(0) = 2\pi f$, plotted in Fig. 4. Here we see that high velocities are obtained for $\dot{f} \neq 0$.

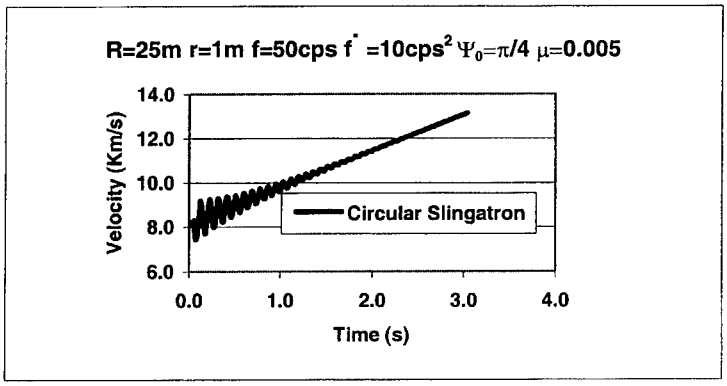


Fig. 4 Velocity vs. time for the driven circular slingatron

The corresponding lock-in angle, $\theta = \psi - \phi$, found in Fig. 5 becomes relatively constant when sled velocities become large.

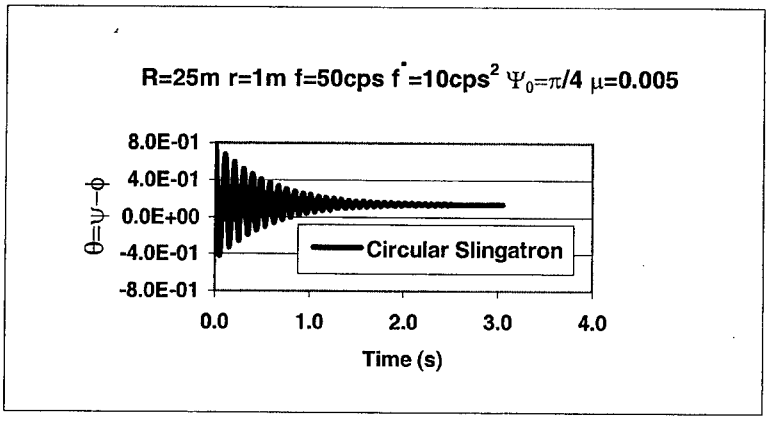


Fig. 5 Lock-in angle vs. time for the driven circular slingatron

Even though high sled velocities can be obtained with a circular slingatron it is encumbered with the difficulty of creating an easy exit port for the high-speed sled. To alleviate this mechanical difficulty we will next examine possible open loop spiral slingatrons.

Archimedes Spiral Slingatron

We now focus our study on configurations that are not closed loop slingatrons. In particular, we examine spiral shaped tracks having open ends, which have the advantage of an easy exit for an accelerated sled entering free flight. Following Tidman[2] we first examine an Archimedes spiral shaped slingatron track given by

$$R = R_i + r\phi \sin(\psi_0) \tag{11}$$

for which the constant R_i is the initial radius and spacing between adjacent spirals is determined by $\sin(\psi_0)$. The gyration speed is now held constant so that the expression given in Eq. (10) is replaced with

$$\psi = \psi_0 + 2\pi\, f\, t\,. \tag{12}$$

Tidman[3] presents a first order analysis for a sled with $\dot{M} = 0$ and μ held constant. Putting Eq. (11) into Eq. (4) and keeping first order terms, i.e. terms first order in $O\left(\frac{r}{R}, \mu\right)$, leads to the simple equation with $\theta = \psi - \phi$

$$V'/V = (r\sin(\theta))/R(\phi) - \mu\,. \tag{13}$$

Integrating this result shows that the average increase in velocity, ΔV, for the sled during a 2π revolution of a single spiral leads to the following expression for averaged quantities

$$\Delta V/\text{cycle} \approx 2\pi\langle V\rangle\left[(r\sin(\theta))/\langle R(\phi)\rangle - \mu\right]. \tag{14}$$

With this motivation we now place Eqs. (10-11) into Eq. (4) and follow with numerical integration to produce the velocity plot, $V(t) = \sqrt{\dot{x}^2 + \dot{y}^2}$, found in Fig. 5. The initial conditions are $\phi(0) = 0$, $\dot{\phi}(0) = 2\pi f$ and the sled mass plus the coefficient μ are both held constant.

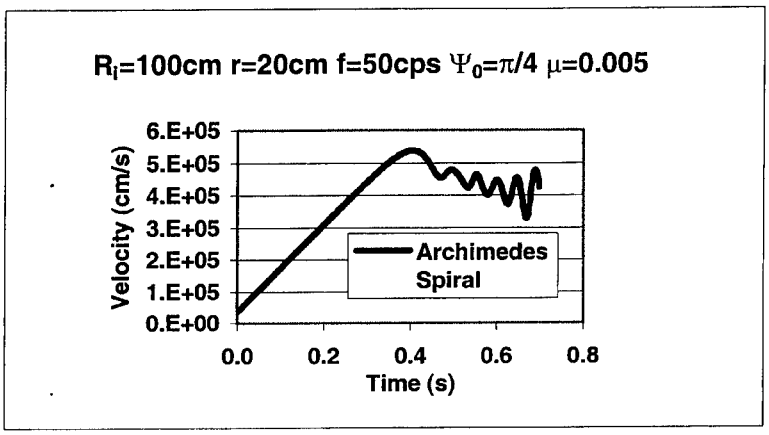


Fig. 6 Velocity vs. time for the Archimedes spiral slingatron

We immediately see that the maximum velocity has the same order of magnitude as that found for the circular slingatron, see Fig. 2, but does so in far less time and requires no acceleration of the gyration arm. The radius $R(\phi)$ changes so that the lock-in angle, θ, stays relatively constant until the sled has reached its maximum velocity as shown in Fig7.

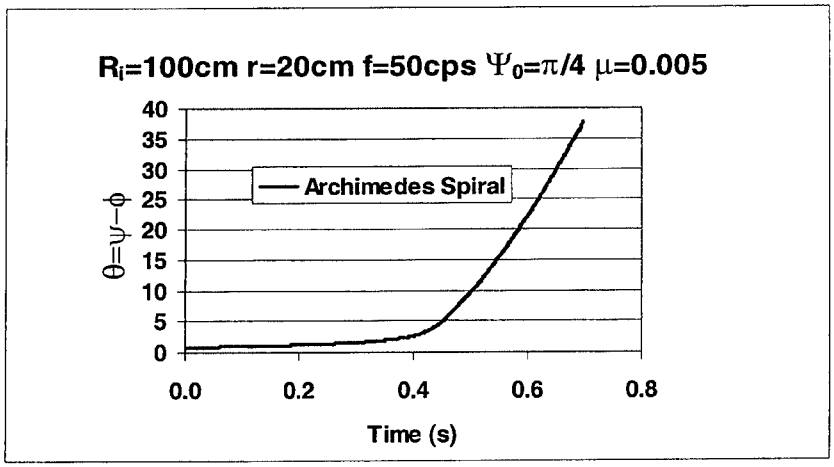


Fig. 7 Lock-in angle vs. time for the Archimedes spiral slingatron

Inspecting Eq. (14) one can infer that the maximum velocity occurs where the frictional force, between the sled and track, balances the parallel component of the Coriolis force as the sled moves along the spiral track. A plot presented in the following section will provide numerical confirmation of this conclusion.

Semi-Circle Slingatron

The next slingatron configuration examined, is constructed using a sequence of semi-circles[3] having increasing radii, see Fig. 8.

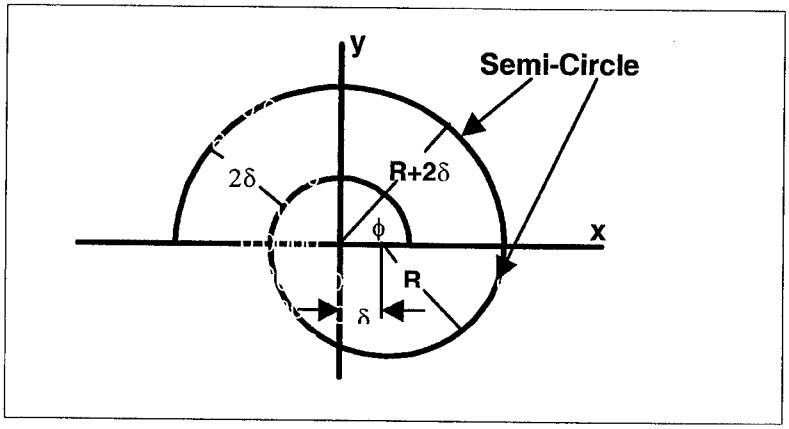


Fig. 8 Schematic of the semi-circle slingatron

We note this slingatron continues to have the sled exit advantage found for the Archimedes slingatron. However, this track has the added advantage in that large sled velocities can be obtained without the need of initial sled injection, i.e. $\phi(0)=0$ and $\dot{\phi}(0)=0$, provided the slingatron has been scaled up to a sufficiently large size. All of the previous slingatrons plus the small-scale high frequency version of the present slingatron require initial sled injection, $\dot{\phi}(0)\neq 0$, in order to obtain large maximum velocities. Because of these advantages a more thorough investigation including sled pressure loads and an empirical friction model, incorporating mass loss $\dot{M}<0$, is presented. According to Fig. 8 the semi-circles in the upper half plane are described by

$$\begin{aligned} R &= R_i + 2\,\delta\lfloor \phi/2\pi \rfloor \\ R' &= 0 \\ R'' &= 0 \\ \delta &= \pi\, r \sin(\psi_0) \end{aligned} \tag{15}$$

and applying the law of cosines to this geometry we find for the semi-circles in the lower half plane having center coordinates at $(\delta,0)$ are described as

$$R = \delta\cos(\phi) + \sqrt{(R_i + 2\delta\lfloor\phi/2\pi\rfloor + \delta)^2 - \delta^2\sin^2(\phi)}$$
$$R' = \frac{\delta R\sin(\phi)}{\delta\cos(\phi) - R} \qquad (16)$$
$$R'' = \frac{R'^2 + 2\delta R'\sin(\phi) + \delta R\cos(\phi)}{\delta\cos(\phi) - R}$$

Putting Eq. (15) and Eq. (16) into Eq. (4) followed with numerical integration leads to sled velocities shown in Fig. 9.

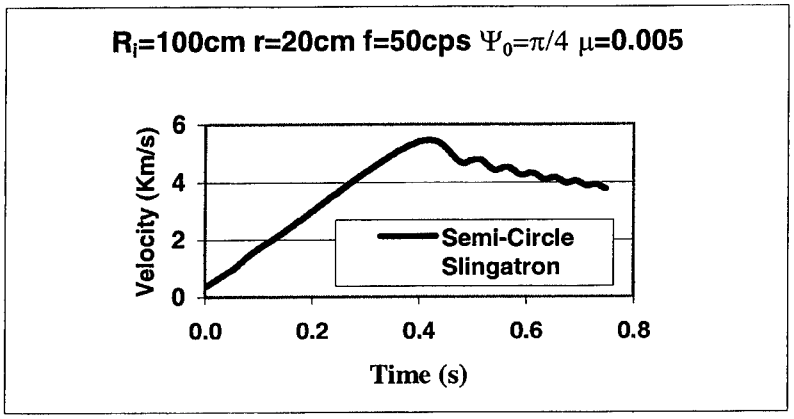


Fig. 9 Velocity vs. time for the semi-circle slingatron

This high frequency small-scale slingatron, i.e. $f = 50\text{cps}$ and $R_i = 100\text{cm}$, is subjected to the conditions $\phi(0)$, $\dot{\phi}(0) = 2\pi f$, $\dot{M} = 0$, and $\mu = 0.005$. Figure 10 tells us again that the lock-in angle θ diverges, from nearly a constant value, after the time, t, where the sled reaches its maximum velocity.

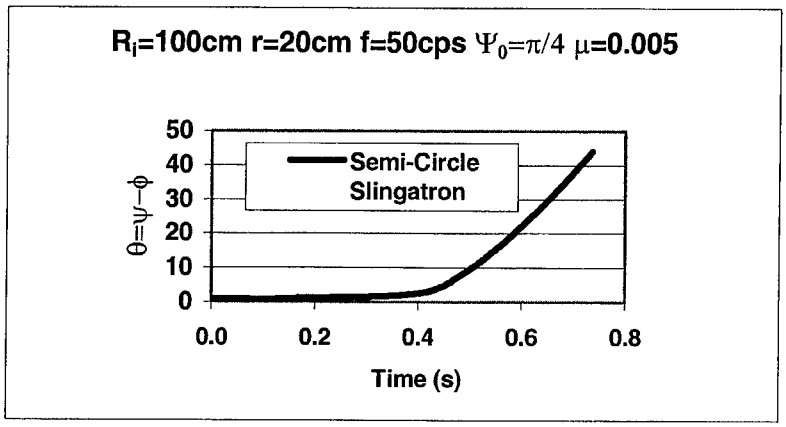


Fig. 10 Lock-in angle for the semi-circle slingatron

An important simplification, when constructing a semi-circle slingatron, occurs when we consider a large-scale version, i.e. $f = 11\text{cps}$ and $R_i = 400\text{cm}$, of this slingatron. For these cases we can generate large maximum velocities without the need for an initial sled injection velocity. An example of this is depicted in Fig. 11 such that $\phi(0) = 0$, $\dot{\phi}(0) = 0$ and the sled mass as well as the friction coefficient are still held constant.

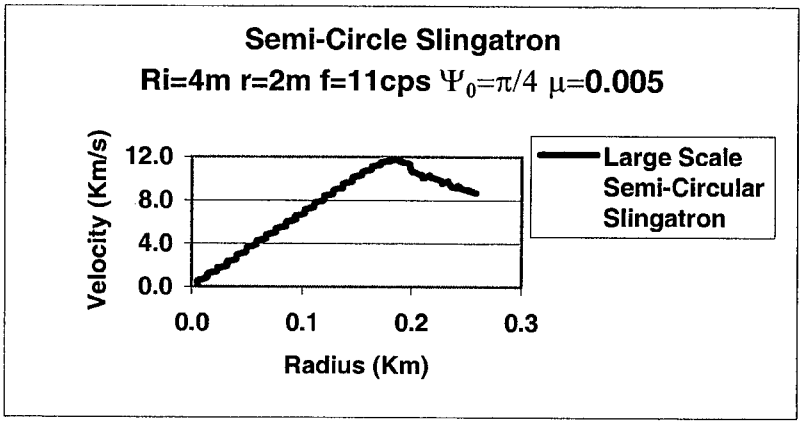


Fig. 11 Velocity vs. radius for the large-scale semi-circle slingatron

This plot has the time axis replaced by radial distance to indicate the size of this large-scale example. In contrast we note that the small-scale version, of this slingatron, still requires a non-zero initial sled velocity, $\dot{\phi}(0) \neq 0$, in order to obtain a significantly larger maximum sled velocity.

To address a more realistic slingatron one should consider the interaction between the sled and the slingatron track. Therefore, we will assume that the sled is covered with material that abrades, $\dot{M} < 0$, as it moves along the track, in such away that the removed mass acts as a lubricant. As the velocity increases the abraded particles may become a liquid bearing and at still greater velocities the liquid will eventually evolve into a gas or even a plasma. To date only a preliminary experimental investigation of the friction coefficient, $\mu(\hat{V})$, dependence on the sleds relative speed $\hat{V}$, has been carried out by Tidman[3]. The preliminary data for a lexan sled indicate that

$$\mu(\hat{V}) = \frac{0.152}{(1+3.16\hat{V})} \qquad (17)$$
$$\hat{V} = \dot{\phi}\sqrt{R'^2 + R^2}$$

where $\hat{V}$ is measured in Km/s, ranging up to a maximum velocity of 2.0 Km/s. The corresponding value of $\dot{M}$ is still very suspect but the preliminary data gives the following estimation

$$\dot{M} = -\frac{M\hat{V}}{50\pi R(\phi)}. \qquad (18)$$

Tidman[2] has suggested that if the velocity, and therefore the bearing pressure between the track and the sled, is large enough to cause the abrading mass to gasify one might then assume

$$\dot{M} = -\frac{\mu M\hat{V}}{\gamma(\gamma-1)R(\phi)} \qquad (19)$$
for lexan $\gamma \approx 1.25$

The two estimates found in Eqs. (18-19) are plotted in Fig. 12 while assuming the friction coefficient given by Eq. (17) remains true for all velocities.

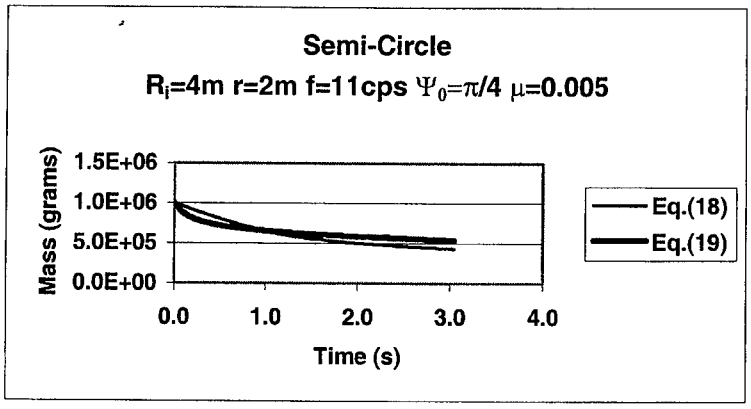


Fig. 12 Sled mass vs. time for the semi-circle slingatron

Figure 13 shows the velocity results for a constant mass sled plus the two cases where $\dot{M} \neq 0$ given by Eqs. (18-19). Since there is no discernable difference between the three cases we will select $\dot{M} = 0$ for the remainder of this paper.

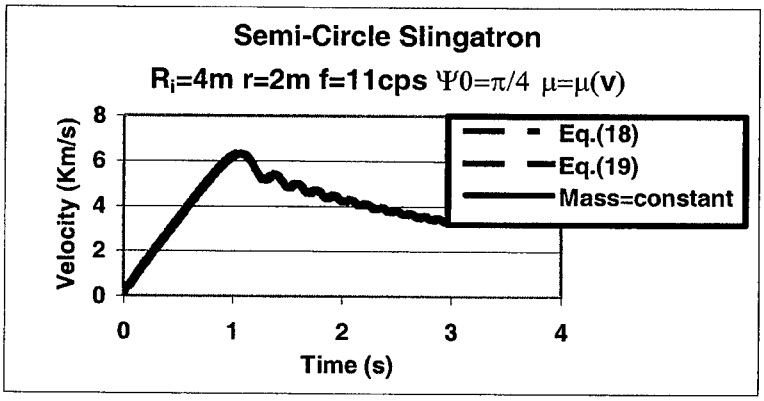


Fig. 13 Velocity comparision vs. time as functions of M and $\dot{M}$

This selection should not be taken as a general conclusion since the present results stem from two simple $\dot{M}$ models. All that we can claim here is that the dynamics represented by Eq. (4) are weekly dependent on our two $\dot{M}$ models. A more in-depth study of the bearing physics may reveal that $\dot{M}$ cannot be ignored in a more elaborate friction model and therefore $\dot{M}$ must be included in the momentum equations.

To demonstrate the importance of the friction model we next compare our empirical model, Eq. (17), to the constant friction model $\mu = 0.005$. Figure 14 has an example comparison of the sled velocity using initial conditions $\phi(0) = 0$ and $\dot{\phi}(0) = 0$ for these two models.

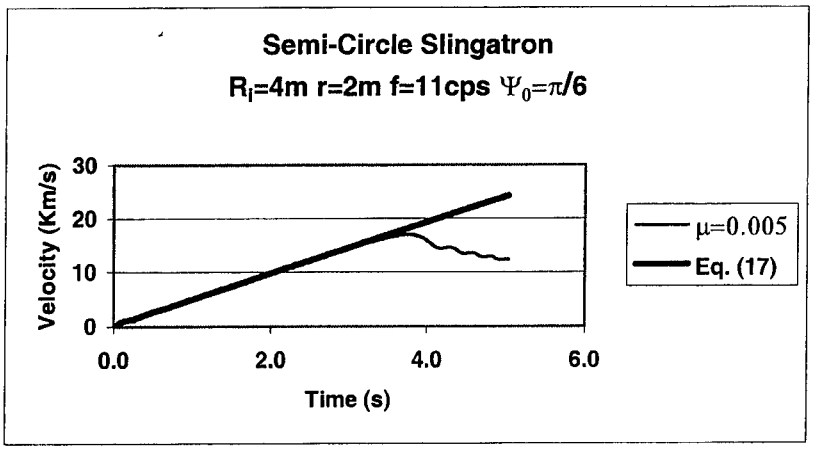


Fig. 14 Velocity comparison vs. time as a function of μ

We see that Eq. (17) and the initial phase $\psi_0 = \pi/6$ can lead to classically unlimited velocities imparted to the sled. This is an example force due to friction never becomes large enough to overcome the parallel component of the Coriolis acceleration.

To gain insight into the magnitudes of the bearing pressure exerted by the sled on a semi-circle slingatron one can examine a typical right cylinder shaped lexan-coated sled having length L and diameter D. Assuming that the ablating material exerts a uniform pressure along the half lateral surface of the sled facing the slingatron track, one will find the pressure P is easily calculated to be $P = F_\perp / DL$. An example of bearing pressure, for a sled with initial mass $M = 1.0 \times 10^3 Kg$, plotted as a function of time is presented in Fig. 15.

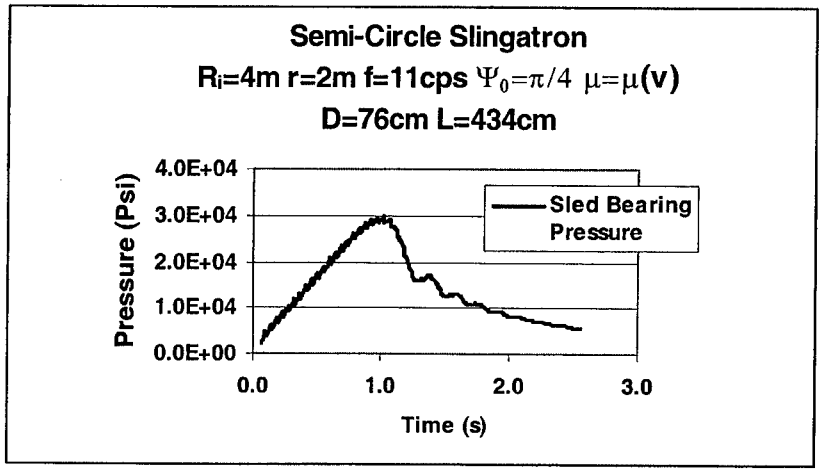


Fig. 15 Sled bearing pressure vs. time for semi-circle slingatron

Calculating the sleds acceleration along the unit vectors **m** and $-\mathbf{n}$ while the traversing the slingatron track may also prove useful to the designer. Remembering that the normal component of the acceleration is always pointing toward the concave side of the track we can find its magnitude from $A_{\perp} = V^2/\lambda$. An example, for the large-scale slingatron, is shown in Fig. 16.

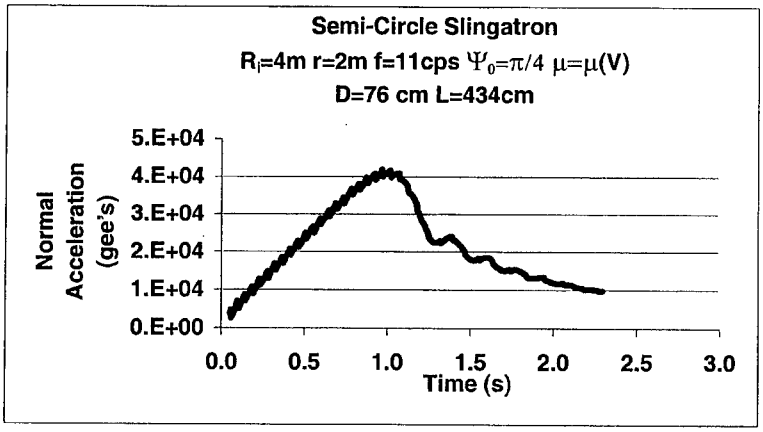


Fig. 16 Normal component of acceleration vs. time for the Semi-Circle Slingatron

In a similar fashion the parallel component of acceleration, $A_{//} = -\ddot{s}$, is plotted in Fig. 17 where for comparison we also plot $|F_{\perp}|/M$.

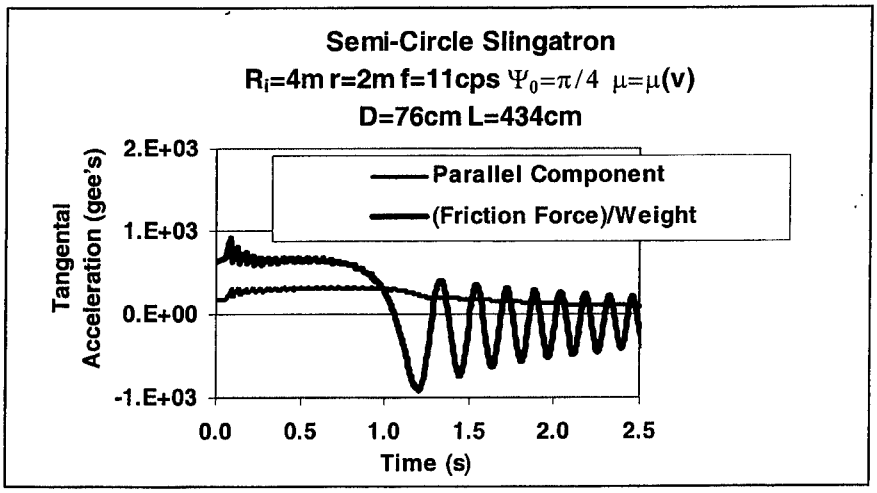


Fig. 17 Comparison of parallel component of acceleration and friction force/weight vs. time

Comparing Fig. 16 with Fig. 17 verifies that the time t where the maximum velocity is found is also the time where friction force per unit mass equals $A_{//}$, thus substantiating the conclusion mentioned above.

Examining the curvature of the semi-circle slingatron shows that $\mathbf{R}''$ is not continuous at the points, $\phi = n\pi$, $n = 0,1,2\cdots$, where the upper half plane semi-circles meet the lower half plane semi-circles, see Eqn. (15-16). However, these discontinuities of the sleds acceleration are not severe enough to cause numerical integration problems of Eq. (4).

Further Illustrations

Before leaving the topic of spiral shaped slingatrons we will give results for two other familiar spiral shaped tracks. Both of these configurations have the non-zero initial velocity, $\phi(0) = 0$ and $\dot{\phi}(0) = 2\pi f$. The first is the parabolic spiral given by

$$R(\phi) = R_i + r\sin(\psi_0)\phi^2. \tag{20}$$

A velocity plot for this is given in Fig. 18

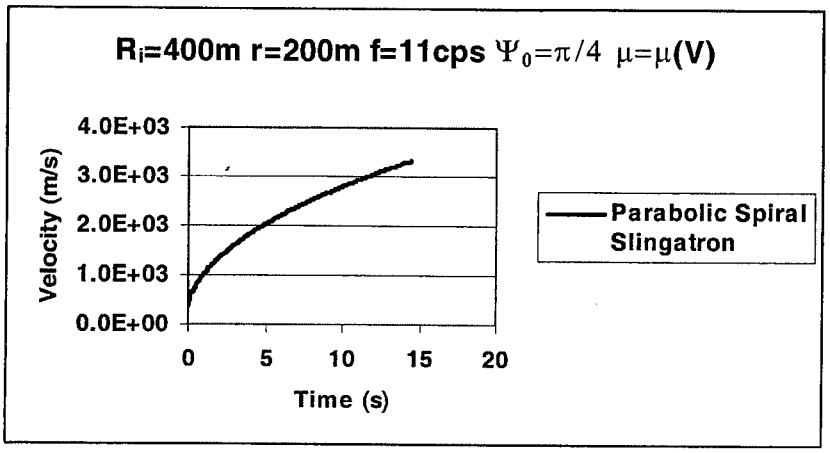


Fig. 18 Velocity vs. time for the parabolic spiral slingatron

for which the friction coefficient μ is modeled using Eq. (17). The last case considered is the logarithmic spiral given by

$$R(\phi) = R_i + r\sin(\psi_0)\ln(\phi). \tag{21}$$

The velocity for this spiral is presented in Fig. 19 where again the coefficient μ is calculated using Eq. (17).

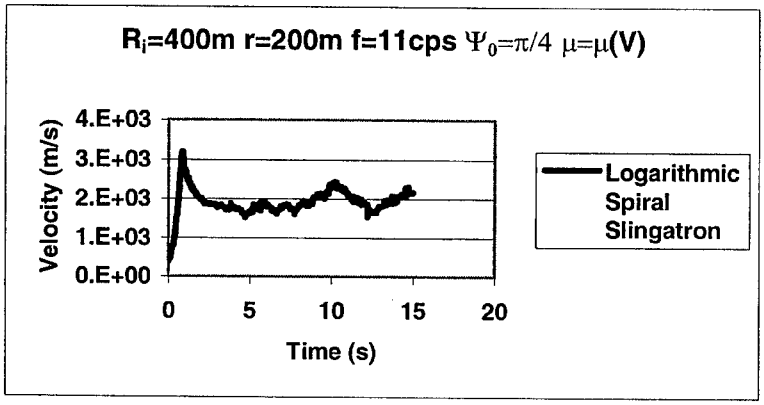


Fig. 19 Velocity vs. time for the parabolic spiral slingatron

One can see from the last two plots that a wide variety of choices for, $R(\phi), r, \psi$ and f, are possible to obtain large maximum sled velocities. These choices offer considerable flexibility when faced with design constraints for a spiral shaped slingatron.

Conclusion

The closed loop circular slingatrons require the gyration arm, r, to accelerate, $\ddot{\psi} > 0$, in order for the mass sled to reach substantial maximum velocities. As time progresses the sled is optimally accelerated as indicated by the lock-in angles θ approaching nearly a constant value. Experience from generating computer simulations, for the closed circular slingatron, reveal that initial sled velocities close to $\dot{\phi}(0) = 2\pi f$ are necessary in order to gain substantial sled acceleration.

The spiral slingatrons are able to produce sufficiently large maximum sled velocities using only constant angular gyration speeds, $\ddot{\psi} = 0$. All of the small-scale spiral slingatrons require initial injection velocities in the neighborhood of $\dot{\phi}(0) = 2\pi f$ in order to gain large maximum speeds. However, the large-scale version of the semi-circle slingatron has an additional favorable feature in that it can generate large maximum velocities with zero initial injection sled velocities. This will make such slingatrons mechanically easier to build. Examination of the bearing pressure and the corresponding magnitude of the sled acceleration give insight into the stress levels that the sled and spiral track must endure.

The empirical friction model shows that the maximum velocity is very sensitive to $\mu(\hat{V})$. Furthermore, we found unlimited sled velocities for a proper choice of the parameter ψ_0. There are a variety of choices regarding the spiral shape, $R(\phi)$, as well as the parameters $r, \dot{\psi}, \psi_0$ and f that one can make in order to produce a large range of maximum sled velocities. Even though the results given here strongly suggest that spiral shaped tracks are the most desirable, the optimal spiral configuration is still an unanswered question. Experiments and further modeling to address the high velocity dependence of $\mu(\hat{V})$ are slated to take place in the near future.

References

[1]Tidman, D. A. "Sling Launch of a Mass Using Superconducting Levitation", IEEE Transactions on Magnetics, Vol. 32, No.1, 1996, pp 240-247

[2]Tidman, D. A. "Slingatron Mass Launchers", Journal of Propulsion and Power, Vol. 14, No. 4, pp. 537-544, July-August, 1998. See also Tidman D. A., US Patents 5,699,779, Dec. 1997: 5,950,608, Sept. 14, 1999; and 6,014,964, Jan. 18,2000.

[3]Tidman, D. A. "private communication" and notes."

SLINGATRON: A HIGH VELOCITY RAPID FIRE SLING

D. A. Tidman

Advanced Launch Corporation, 6801 Benjamin Street, McLean, VA 22101-1576
datidman@starpower.net

The mechanics of a spiral slingatron mass accelerator is discussed, together with some experiments to measure the sliding friction and mass loss of projectiles in such a machine. The potential utility of this machine for defense applications is also discussed, including examples of 1 kg and 50 kg projectiles launched at 3 km/sec. The device appears capable of high launch velocity with repetitive fire without over-heating the steel guide tube, since hot high-pressure gas is not used. It could derive power from a turbine that burns kerosene and it fires projectiles without propellant cartridges. Angular dispersion of emerging projectiles can be minimized, but would be larger than for conventional guns. However, projectiles that are smart enough to reduce dispersion of the projectile stream would suffice for many applications. Smart projectiles would also be needed for any gun capable of the long-range missions available due to high launch speed.

INTRODUCTION

A mechanical mass accelerator concept called a slingatron has been proposed by the author [1-5] and computer models developed by Tidman [2], Cooper et al [6], and Bundy et al [7] for the dynamics of both spiral and circular versions of this machine. Here we first summarize the dynamics. A new approach to the mechanics is then discussed that is useful for the potential defense applications of a spiral slingatron in which a projectile (or stream of projectiles) could be accelerated to high velocity.

The device consists of a spiral steel tube (Fig.1) mounted on swing arms distributed along it so that the entire tube can be propelled so that it gyrates around a small circle of radius r with a *constant* gyration frequency f cps. The machine transfers stored inertial energy directly into projectile kinetic energy with no intermediate steps, and work is done on a projectile sliding through the spiral because the accelerator tube is continually pulled inward at the projectile location against the centrifugal force of the projectile. The accelerating force experienced by the projectile is an example of a coriolis force and is proportional to the projectile mass. As the projectile swings out around the spiral into turns of increasing radius R, it also maintains phase stability with the small-radius gyration of the entire tube. This phase locking enables it to move out around the spiral turns with the same frequency f so that its increasing velocity V is approximately equal to $2\pi Rf$. The device can be viewed as a mass cyclotron [2].

The dynamics is similar (but not identical) to whirling a mass around at the end of a string as in a conventional sling, but with the string growing in length so that the whirling frequency, f cps, is constant. However, there is a basic difference in that there is no string to break under tensile stress in the slingatron. Instead, the guide tube can contain

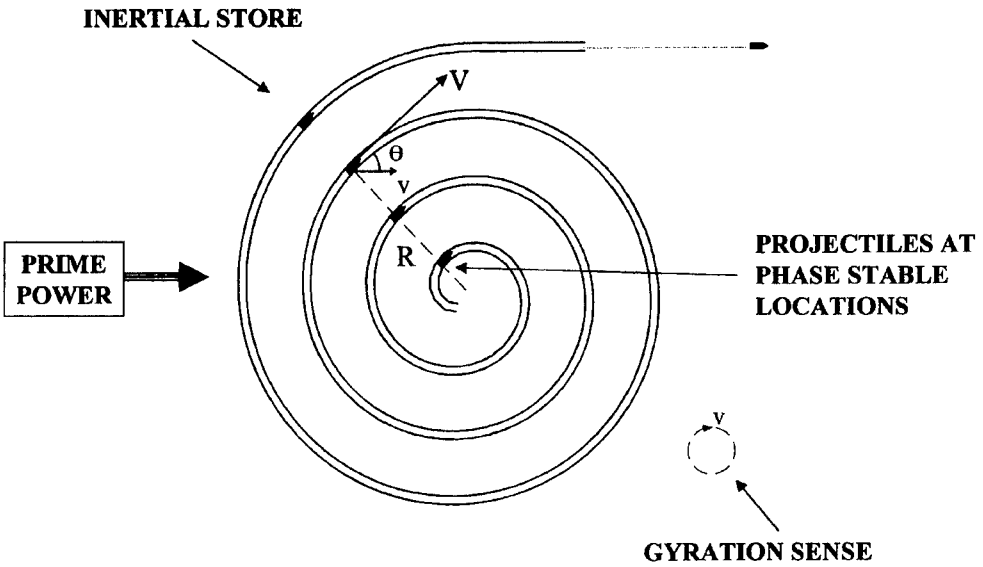


FIGURE 1. A Spiral Tube mounted on Distributed Swing Arms (not shown) that propel the entire spiral around a Small Gyration Circle of radius r with a Constant Frequency f cps and the sense shown. Projectiles fed into the Spiral Entrance are pushed forward by the Closed Breech and accelerate through with a Stable Relative Phase Angle θ and Increasing Speed $V = 2\pi Rf$.

the projectile to much higher speeds since the mechanical impulse delivered per unit length, $mV/R \cong 2\pi mf$, is approximately constant along the spiral. The tube wall thickness can thus remain constant along the spiral.

Note that if one treats the tube as an elastic beam supported at intervals on swing arms, the driving force per unit length in the beam deflection equation swept by a point mass m would be $(mV^2/R)\delta(x - Vt) = \Sigma mf\delta(t - x/V) \rightarrow \Sigma mf\delta(t)$ as $V \rightarrow \infty$, i.e., a uniform impulse for segments traversed with V >> transverse wave speeds. The projectile wave drag due to the elastic response of the track is also small for all speeds.

Experimentally, we have repeatedly fired 0.738 gram lexan projectiles at 5.2 km/sec into curved 1020 steel tube (OD = 0.5, ID = 0.3, wall thickness of 0.1in.) and a radius of curvature R = 30 inches, so that a force of 2.7 tons sweeps around the tube with a contact bearing pressure of 1.37 kbars, and with no discernable effect (except to slightly smooth the tube asperities). A static force of this magnitude would permanently deform the tube.

For most defense slingatrons a single conventional motor could be used to propel the gyration, and for larger systems distributed motors could be used to swing the spiral around its gyration circle and continuously supply inertial energy globally to the spiral for extraction by an ongoing stream of projectiles passing through the spiral. The launcher could be operated as a rapid-fire device with a maximum shot frequency equal to the gyration frequency f (assuming the prime power is available), and for a given design its system mass is approximately proportional to mV^2, [5].

No gun injector is needed. A projectile inserted into the spiral entrance with the breech closed behind it will accelerate through the spiral. It will acquire its initial speed when the tube is moving forward at the projectile location, so that the projectile initial speed (acquired from the breech block) is the same as the gyration speed $v = 2\pi rf$. In this case it is also necessary for the first turn of the spiral to have a radius of curvature that is no more than a few times the gyration radius, and an interior diameter slightly larger than the projectile diameter so that the projectile can negotiate the first turn. A mechanical feed of projectiles into the entrance can then maintain the supply of projectiles.

Note also that the absence of hot propellant gas in the guide tube allows a higher velocity, projectile mass, and fire rate, than conventional guns without overheating the guide tube. A slingatron also has no appreciable muzzle blast or EMP, other than what might arise from the drive motor. Although the spiral guide tube is long, it could be constructed from segments with tapered entrances at the connections. The machine is not sensitive to the exact shape of the spiral, which could approximate an Archimedes spiral.

The two basic issues involved in construction of a slingatron are the sliding friction coefficient of the projectile (with its attendant mass loss), and implementation of the mechanical system needed to propel the gyration.

APPROXIMATE RELATIONSHIPS FOR THE DYNAMICS

The approximate equations listed here are useful for guideline purposes as a supplement to the computer models based on more exact equations. An approximate equation of motion for the projectile in a spiral sling can be obtained, Fig.1, by equating the rate of energy gain for the projectile, $(d/dt)(0.5mV^2)$, to the power used to pull against the projectile centrifugal force $(mV^2/R)v\sin\theta$, minus the power dissipated by the projectile sliding friction, $\mu mV^3/R$. Note, all three of these powers neglect higher order terms in the small quantities r, v, and μ, and for this discussion we also assume that the projectile mass m is constant. The result is

$$dV/dt \cong (V^2/R)(vV^{-1}\sin\theta - \mu), \qquad (1)$$

where R is the guide tube radius of curvature at the projectile location, V the projectile speed in the spiral tube, v the constant gyration speed (assumed $<< V$), and θ is the phase angle between the vectors **v** and **V**. It is also assumed that projectile drag due to residual gas in the guide tube is negligible, so that μ is simply the sliding friction coefficient. We also consider only spirals for which the gap between neighboring turns is a constant.

We see from equation 1 that the key to achieving a high projectile velocity is to mechanically implement a high gyration speed v, and for the projectile to have a small coefficient of sliding friction and to lose only a moderate amount of its mass to supply the gas film on which it slides.

When the exact equations for the dynamics are solved numerically, one finds that for most of the range $0 < \theta < \pi/2$, the projectile is stably trapped in a traveling potential well and advances around the spiral turns with an angular frequency V/R approximately equal to $v/r = 2\pi f$, i.e., acceleration occurs. Provided the friction term μ remains smaller than $v\sin\theta/V$ (because μ is decreasing with increasing V), the angle θ undergoes only

small oscillations about (and a small cumulative displacement in) its stable value to accommodate changes in the relative magnitudes of the coriolis and friction terms. Phase locking occurs, Fig. 1, because if a perturbation causes the projectile to move too fast its relative phase θ decreases and the gyration velocity component perpendicular to the tube at the projectile location decreases (as does the rate at which work is done against its centrifugal force) and the projectile falls back, and conversely if it moves too slowly its relative phase θ increases so the projectile experiences a larger accelerating force and catches up. Computer models and analysis show that friction damps oscillations about the stable relative phase as the projectile advances through the spiral.

As long as this situation prevails, and acceleration continues, it suffices to assume

$$V/R \cong 2\pi f = v/r. \qquad (2)$$

For a spiral designed with constant gaps ΔR between its turns, the velocity gain per turn, ΔV, is also approximately constant, in which case

$$\Delta V \cong 2\pi(v\sin\theta - \mu V), \qquad \Delta R \cong 2\pi(r\sin\theta - \mu R)\,, \qquad (3)$$

and the relative phase θ changes slightly to accommodate the change in μ. For example, for a gyration speed v = 200 m/sec and $\theta = \pi/3$ with m constant and friction negligible, the gain in velocity per turn would be $\Delta V \cong 1$ km/sec. A more complete list of approximate formulas for the case m = constant has been given earlier [5], and exact equations and computer models for the dynamics in references [2,6,7] with [6] including discussion of projectile mass loss.

Finally note that the guide tube has a radius of curvature R that goes from R_{in} for the inner turn to R_{out} for the outermost turn. If the projectile consisted of a perfectly rigid cylinder of length l_p, it would be supported in the tube on its two ends with its mid-section above the tube surface a height δh given approximately by $\delta h/l_p \cong l_p/8R << 1$. However, δh becomes sufficiently small after passing through the first 1 or 2 turns, and the centrifugal force sufficiently large, that projectile elasticity provides the small amount of flexure (well below its elastic limit) needed to push it into tight contact with the tube along the projectile length. As the projectile travels farther out through the spiral its flexure decreases as R increases, and could be reduced to zero at exit by gradually straightening out a segment of tube and bringing its ID down to fit the projectile diameter just before the exit.

MECHANICAL DESIGN

The slingatron is subjected to two kinds of stress, Harris [8] and Tapley [9], namely quasi-static stresses due to gyration and a traveling impulse due to the projectile. Impulsive stresses can be treated approximately using an energy method, or by using detailed codes. In this section we briefly discuss only the gyration machinery and leave a safety margin so that a range of applicability that includes the traveling impulse of the projectile could be experimentally determined.

In order to swing the entire spiral around its gyration circle of radius r, the guide tube is attached to swing arms via clamps that turn on tapered roller bearings as shown in Fig. 2. These bearings allow the entire spiral to roll around its gyration circle while keeping its orientation the same, i.e., it gyrates but does not spin. The swing arms could be oblique to the gyration plane of the spiral tube, which allows them to be spaced more closely along the tube without mutual collision occurring, which in turn allows a higher swing speed without shear of the guide tube. Close packing of the clamps also avoids resonance between the gyration frequency f and transverse elastic vibrations of the tube segments. For example in Fig. 2 they are shown spaced so that the tube segment length between the centers of adjacent clamps is $L_{seg} = r$. For early experiments however, it might be simpler to swing the arms in a plane with $L_{seg} \cong 1.5r$.

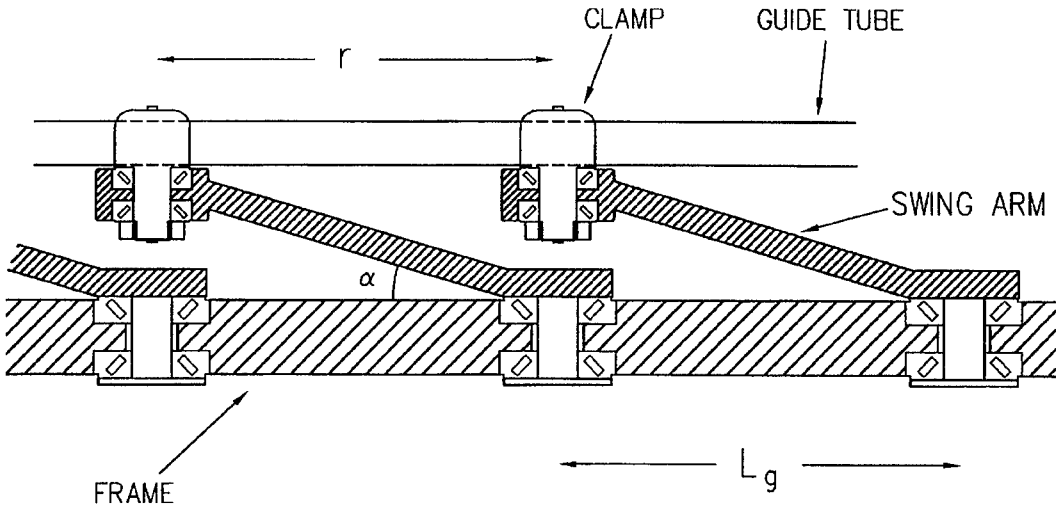


FIGURE 2. Distributed Swing Arms are shown Oblique to the Spiral Plane for Close Packing along the Guide Tube for Maximum Swing Speed. Arms could alternatively be deployed both above and below the guide tube. The arms have a cross-sectional area A that is larger at the frame (they are wider plates going into the page) and A decreases along the arm toward the end that clamps to the tube.

Swing Arms and the Potential for High Gyration and Projectile Speeds

We consider the case in which the arms in Fig. 2 swing in a plane, i.e., $\alpha = 0$, which can also be viewed as an approximation for long swing arms with a small finite value for α. The arms then experience tensile stress that remains approximately parallel to a swing arm as it swings around the gyration circle. If we choose to use 4340 (Q&T, 315C) steel for the arm, a design strength of T = 120,000 psi can be assumed, which is approximately its fatigue endurance limit for cycled stress (even though this stress is not cycled). This allows some added strength for the traveling impulse delivered by the projectile sweeping around the spiral.

If we design the arm with a cross-sectional area A(r) that decreases going away from the frame so that its tensile stress T is constant in the arm, i.e., there is no parasitic mass being carried in the arm, we find the result $A(r) = A_o\exp(-2\pi^2\rho f^2 r^2/T)$, where ρ is the steel density and A_o the cross-section at the frame. The swing speed is then

$$v = 465[\ln(A_o/A)]^{1/2} \quad \text{meters/sec,} \qquad (4)$$

and the mass m_{load} that can be carried at the end of the arm (consisting of the tube segment, clamp, bearings, and steel to retain the bearings) is given by $m_{load} = AT/(4\pi^2 rf^2)$.

However, the clamps and guide tube experience stresses that are both cycled and in the shear direction, so that more complicated geometrical factors are involved in their stress distributions. For these components we choose a design strength S = 60,000 psi for 4340 steel.

Consider the maximum average shear stress at the clamped ends of a tube segment of length $(L_{seg} - L_{clamp})$ between clamps of length L_{clamp} and density ρ propelled around a circle of radius r with a frequency f cps. This stress is $2\pi^2 f^2 \rho r(L_{seg} - L_{clamp})$ so that the maximum speed with which the tube segment can swing around is,

$$v(max) = (2Sg_E r/\rho(L_{seg} - L_{clamp}))^{0.5} = 320(r/(L_{seg} - L_{clamp}))^{0.5} \quad \text{meters/sec,} \qquad (5)$$

where we used $g_E = 386$ in/sec^2, $\rho = 0.289$ lbs/in^3, and could allow the clamp to be tapered and extend a length L_{clamp} along the tube for tube support so that the tube segment effective length shown in Fig. 2 is reduced.

In summary we see that very high swing speeds are possible. For example for v = 300 m/s the projectile velocity gain per spiral turn follows from (3) as $\Delta V = 1.6$ k/s/turn, neglecting friction and assuming a phase locked angle $\theta = \pi/3$. Conceivably a future machine using advanced materials (in a reduced pressure environment) might achieve a swing speed of v = 1 km/sec, in which case $\Delta V = 5.4$ km/sec/turn, i.e., V = 21 km/sec in four turns! But a first-generation machine is likely to operate in the range $v \sim 200$ m/s.

There will be some binding of the motion due to clamping of the tube at multiple locations, but as the spiral gains speed the centrifugal forces rapidly become dominant as the tube pulls outward against the swing arms, as was found in a small machine [2].

Reciprocating Machinery for Synchronous Drive

Consider first the case of a *single* swing arm with its shaft bearing anchored in a drive plate as shown in Figure 3(a). If the drive plate is propelled in a small radius circular motion, energy can be pumped into the swing arm rotational motion. This swing arm motion can be stably phase-locked with the drive plate motion just as for a conventional sling (in which ones hand replaces the plate) or for a projectile accelerating in a gyrating spiral as discussed earlier.

Thus if a number of such swing arms were anchored in a drive plate as in Figure 3(b), they could *all* be synchronously accelerated (once started) by a small-amplitude circular motion of the drive plate, regardless of possibly differing masses and swing arm lengths. This phase stability allows a complete spiral guide tube, clamped by distributed swing arms as in Figure 3(c), to be accelerated up to a high gyration speed while maintaining

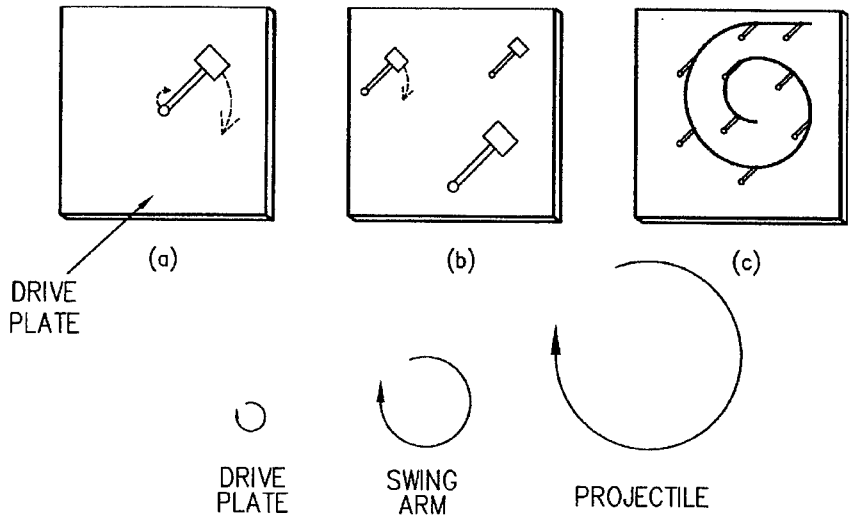


FIGURE 3. Phase Stability maintains Synchronization of the Swing Arms propelled by a Small-Amplitude Circular Motion of a Drive Plate. The Plate Motion is the same as one makes by hand in whirling a Conventional Sling.

synchronization along the guide tube length. No other provision for synchronization between the arms is needed. Guide tube stiffness suffices to start the motion of the spiral in a synchronized state, and phase locking maintains it thereafter.

Another way to view this is to regard Figure 3(a) as simply an example of a small mass orbiting about a larger mass, and tied together by a swing arm. Assume for the moment that the system is not being driven and that the drive plate is confined to slide in a plane with frictionless bearings at its four corners. These two masses then cycle around each other in a plane, and the end of the swing arm moves around a circle of radius r and the heavier plate moves around a smaller circle of radius δr. Note that these *radii* are *independent* of the gyration speed. Also, although the centrifugal forces can become large, they are balanced and distributed internally in the coupled system, just as for a top spinning about its center of mass.

Figures 4 and 5 show an example utilizing this drive principle in which a single automobile engine is used to power the small-amplitude drive plate motion. The drive plate is captured at its four corners by bearings that constrain its motion to a horizontal plane. This restraint involves a relatively small oscillating vertical force (moment) due to

the fact that the drive plate and the guide tube cycle in planes that are slightly displaced from each other. Two camshafts propel the circular motion of the drive plate but do not experience the large internal centrifugal forces provided they push the drive plate around a circle of radius equal to the natural cycling radius of the drive plate.

The system is essentially a two-stage sling. The cams at the ends of the two vertical shafts in Fig 5 propel the drive plate around a small circle, and the drive plate in turn slings the spiral around a larger circle, and the spiral slings the projectile around and even larger radius path with very high speed. All three of these motions occur at the same frequency but with ascending velocities, and the sling motions are phase stable. Also, little energy would be stored in the drive plate motion.

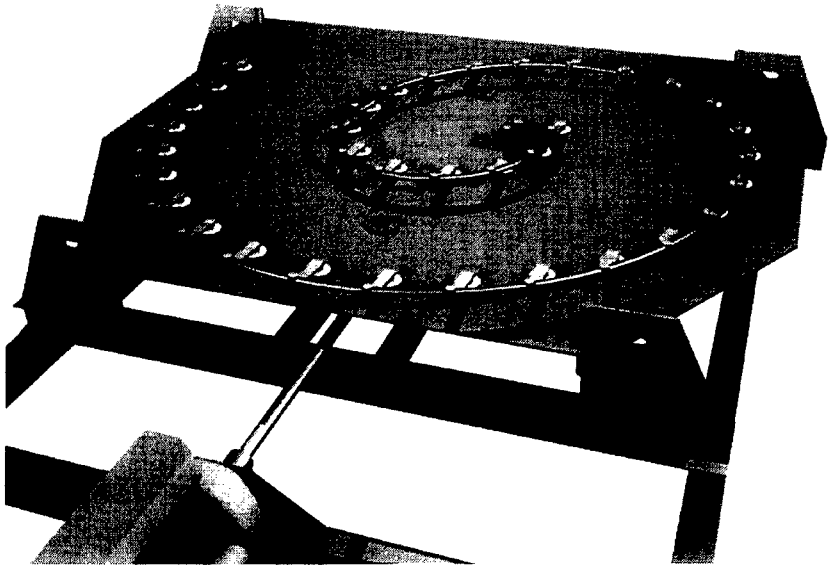


FIGURE 4. Concept for a 1.5-Turn Spiral Experiment Powered by an Automobile Engine. Two Vertical Camshafts under the plate power the plate motion and are shown in Figure 7. A small Clip of Cartridges is shown for supplying a Short Burst of Projectiles. The Drive Plate could have holes to make it lighter.

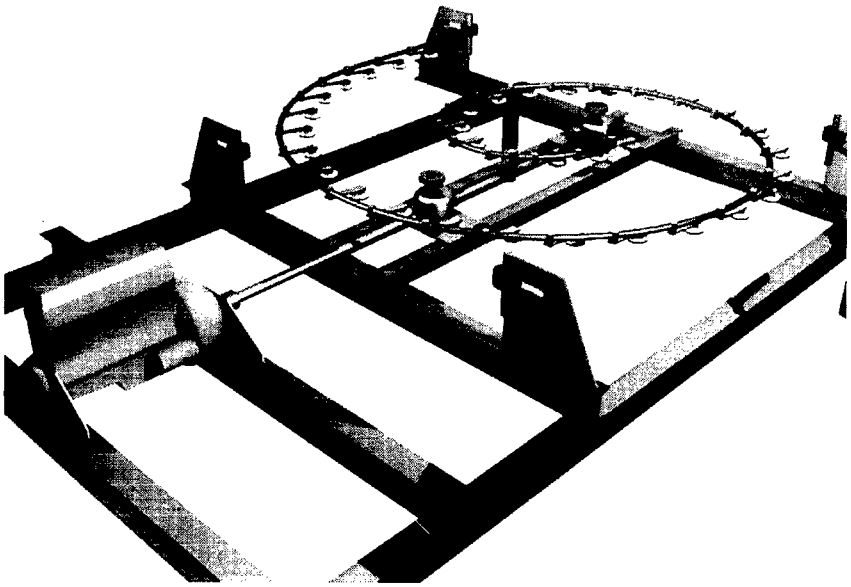


FIGURE 5. The same system as Figure 6 but with the Drive Plate removed to show the Motor Shaft passing through two Gear Boxes with their Vertical Camshafts that propel the Drive Plate.

Role of Air Drag

The gyrating components consisting of the swing-arms, guide tube, clamps, etc, experience aerodynamic drag as they swing around the gyration circle at speed v. In addition, the projectile will snowplow air (and in rapid fire cases also bearing gas) in the guide tube, but this could be vented through slots on the inner side of the curved tube as shown in the table top machine in Fig. 4 of Ref. 2.

For a rapid-fire system the power inputs required to drive the system typically have relative magnitudes (Power to Maintain Projectile KE Stream) > (Aerodynamic Swing-Drag Power) > (Roller Bearing Friction Power of Drive Modules). This assumes a drag coefficient $C_D \sim 1$ for the arms, clamps, and guide tube, and also assumes that the fire rate is > 0.1f. Although one could reduce the swing drag by streamlining the design of the gyrating components to reduce C_D, this might not be worth doing for the case of a rapid-fire system since the prime power input required is in any case dominated by the kinetic energy power of the projectile stream.

For spirals designed for extremely high projectile velocity (e.g., physics experiments) one could eliminate air drag by enclosing the entire system in a reduced-pressure environment. These involve long tapered swing arms with high swing speeds v.

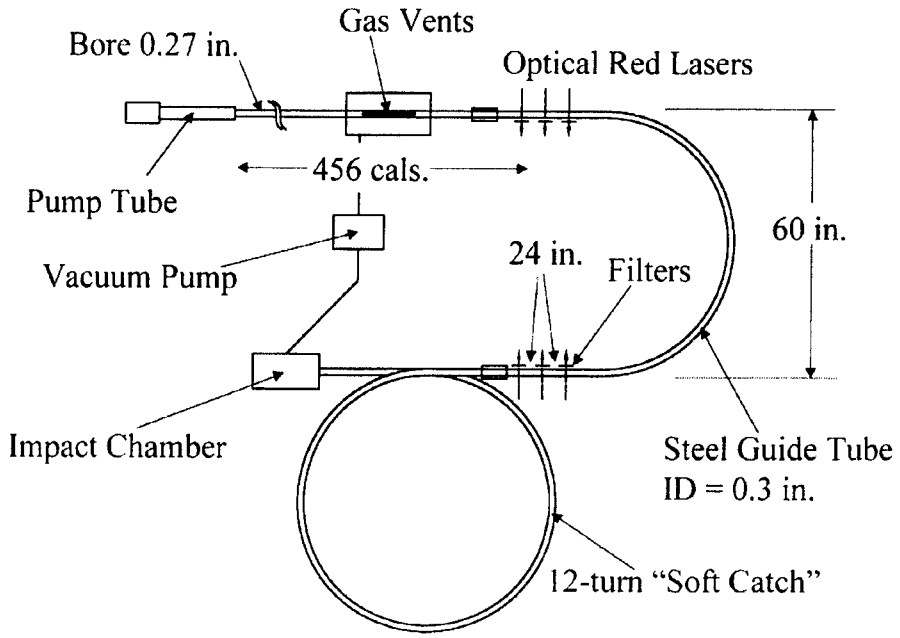


Figure 6. Layout of the Sliding Friction and Mass Loss Experiment.

SLIDING FRICTION AND MASS LOSS EXPERIMENTS

Here we give a brief summary of experiments described more fully in Ref 10. Figure 6 shows the layout of the experiment used to obtain data for the projectile velocity loss and mass loss due to friction up to ~ 4 km/sec. It consists of a 2-stage light gas gun of small bore size, namely 0.27 inches, that fired lexan projectiles of mass 0.738 grams into evacuated semicircular guide tubes of various radii, after which the projectile came to rest in a 12-turn ring that functioned as a soft catch .

The laser triplets located at the input and output ends of the semicircular guide tube provided a measurement of the projectile velocity V_{in} going into the curve, and V_{out} leaving the curve. As the projectile passes through the semicircle it is pushed against the outer wall of the tube which results in a frictional force $-\mu mV^2/R$. In Fig.7 we plot data for the quantity $\pi^{-1}\ln(V_{in}/V_{out})$, as a function of the average velocity $V = 0.5(V_{in} + V_{out})$ around the semicircle, and in all cases the velocity loss $V_{in} - V_{out}$ was small compared with V_{in}. The relationship of $\pi^{-1}\ln(V_{in}/V_{out})$ to μ follows from equation 1 (with $v = 0$) but generalized to include a drag term due to bearing gas accumulated on the projectile nose, and also to allow for projectile mass loss. Converting the time derivative d/dt to Vd/dx, and integrating along the projectile path around the semi-circle then gives,

$$\pi^{-1}\ln(V_{in}/V_{out}) = \mu - (2\pi)^{-1}\ln(m_{in}/m_{out}) + 0.25\pi d^2 R\langle P_{nose}/(mV^2)\rangle \ , \qquad (6)$$

where the subscripts in and out indicate the projectile velocity or mass either entering or leaving the semicircular tube section, d is the projectile diameter, R the radius of the semicircular tube, P_{nose} the reverse pressure from the dusty gas mass that accumulates on

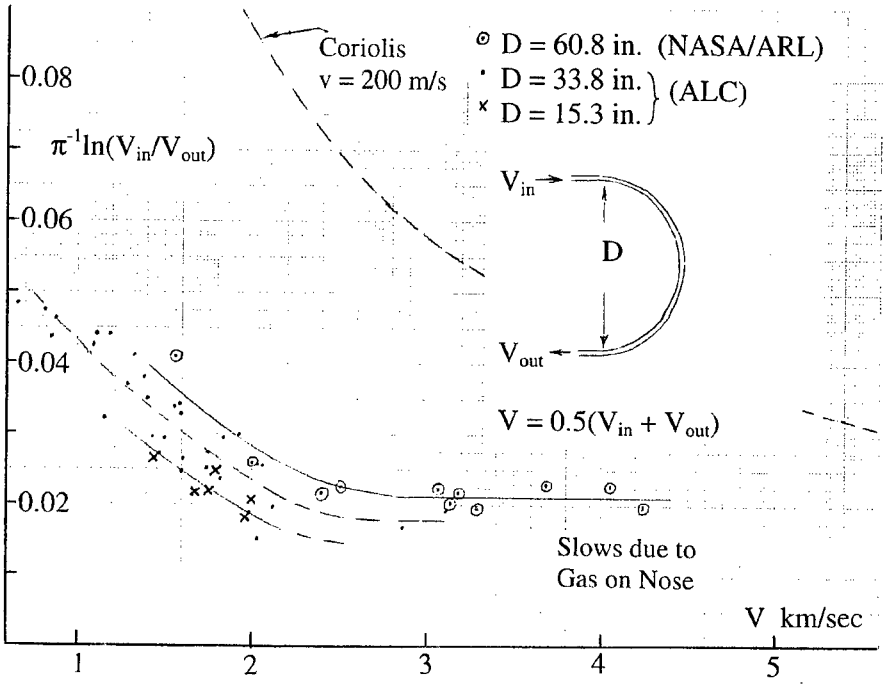


FIGURE 7. Velocity Slowing Data for 0.738 gram lexan Projectiles fired through a Semicircular Arc of Steel Tube for several values of the Arc Diameter D = 2R and Injected Velocities V_{in}. The Relationship of the Quantity Plotted to the Friction Coefficient is given by equation 6.

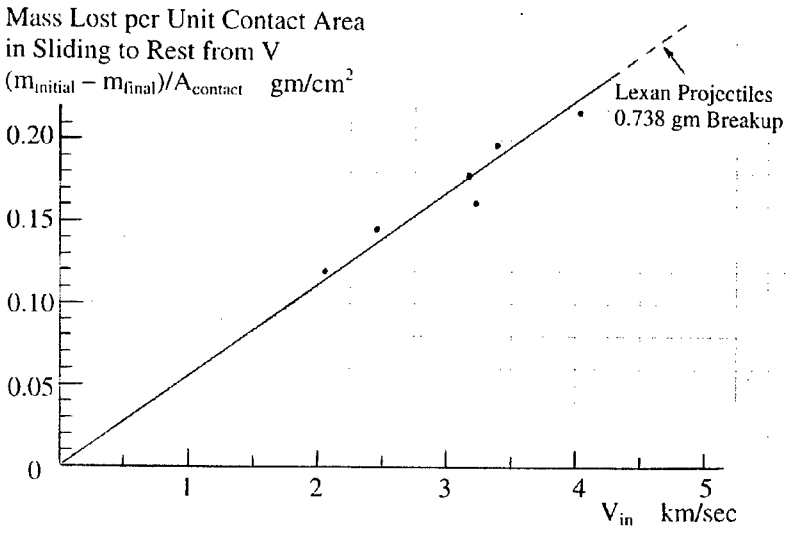


FIGURE 8. Mass Loss Data for 0.738 gram Lexan Projectiles that Slide to Rest in a Multi-Turn Soft Catch . For V_{in} = 3.5 km/sec about 50% of the 0.738 gram Projectile had Ablated Away, and above 4 km/sec the Projectiles Broke Up so data could not be obtained. For a Slingatron accelerating Identical Projectiles with a Net Force α times the Frictional Drag, one expects < α^{-1} times the above loss.

the projectile nose, and <> represents an average value of the argument integrated around the semicircle. The left side of equation 6 is the quantity plotted in Figure 7, and it is only equal to the friction coefficient in the limit that there is zero ablated mass from the projectile and also zero snowplowed dusty gas accumulated on the projectile nose. Figure 8 shows the mass loss of projectiles that were recovered from the soft catch .

Measurement of the asperity heights and microscopic examination showed that after repeated traversals by lexan projectiles up to ~ 5 km/sec, the track had become slightly smoother and harder, but use of a single 2.4 km/sec Al projectile resulted in shallow gouges [11].

POTENTIAL DEFENSE APPLICATIONS

Although the slingatron concept is in the design and computer-modeling phase, we note that it would have several advantages if it works as theorized. First, it is a simple mechanical device that does not involve a flow of high temperature high-pressure gas in the guide tube. The result (from the thermal calculations below) is that it appears capable of launching large mass projectiles at high velocity and high fire rates without overheating the guide tube, and without muzzle blast or EMP except from the drive motor.

Second, the accelerating coriolis force continues to provide projectile acceleration at high speeds, provided the sliding friction coefficient continues to decrease at least as 1/V with increasing velocity. This force is experienced along the length of an elongated projectile, and not just on its base. Third, the slingatron could be powered by a standard technology motor (internal combustion, turbine, or electrical) that continuously provides

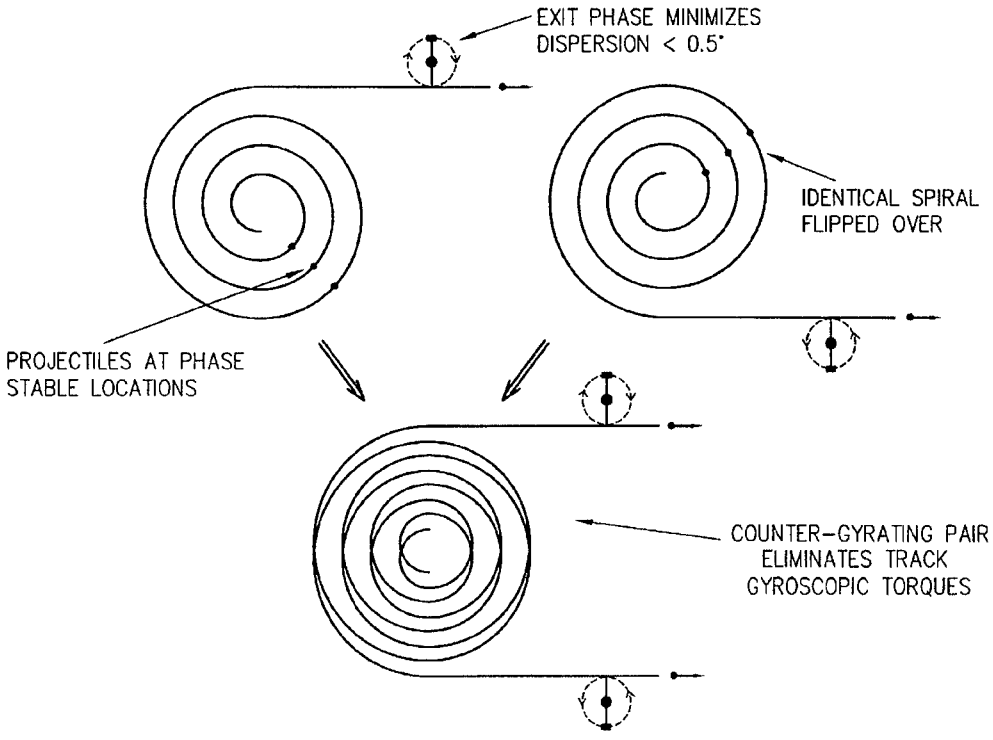


FIGURE 9. Two Counter-Gyrating Spirals that can be Re-Directed as a Unit without Precession-Inducing Torques. The Linear Exit Sections are chosen to have a length so that the Phase-Locked Projectiles Exit when the Swing Velocity is Parallel to the Tube, to Minimize Angular Dispersion at Launch.

energy to the spiral, which in turn directly couples its inertial energy into projectiles passing through the spiral. Finally, the device appears capable of accelerating a continuing stream of smart projectiles through the spiral with the maximum rate being limited by either the gyration frequency or the available power.

Figure 9 shows an arrangement in which 2 counter-gyrating spirals are assembled so that as a unit they can be swiveled for aiming without causing precession-inducing torques, and Figure 10 shows a concept of a rapid-fire slingatron based on this arrangement in which a turbine is shown powering the system.

The counter-gyrating spirals shown in Fig 9 are mounted on opposite sides of a common drive-plate structure, and the drive-plate would undergo a small-amplitude *linear* oscillation in response to the pair of counter-gyrating spirals. Ratchets could ensure that the spirals turn in opposite directions, and the drive plate ensures their locked frequency. Thus the pair of counter-gyrating spirals could be brought up to speed by a single high-powered motor that drives a small-amplitude linear oscillation of the drive plate. (This differs from the circular motion of the drive plate discussed in the context of a design for an experimental test in Figs 4 and 5.)

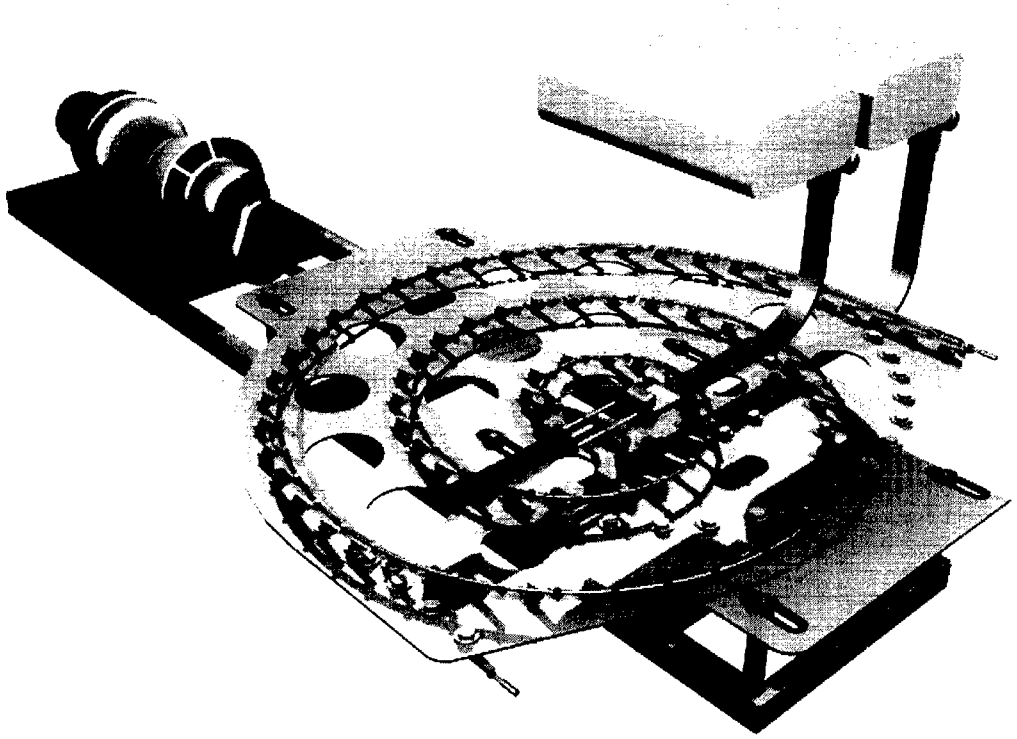


FIGURE 10. Concept for a Continuous-Fire Dual-Spiral Slingatron powered by a Turbine that Drives a Small-Amplitude Linear Oscillation of a Single Drive Plate. The Counter-Gyrating Spirals are located on opposite sides of the Drive Plate. It consumes kerosene and air and fires projectiles without cartridges.

Projectile Feed System

An example is shown in Fig 11. It consists of a loading block that is propelled by an electrically controlled piston along 2 rods on which it executes a linear oscillation with its maximum speed equal to the gyration speed v. The fire rate could thus be controlled, with a maximum of 0.5f to reduce stresses. The loading block picks up a projectile from a feed chute when the block reaches its maximum amplitude and has zero speed. The loading block then pushes the projectile (past a retaining stop) into the spiral entrance when the block and the spiral are moving adjacent and parallel with velocity v.

Example 1: 1kg Smart Projectiles Launched at 3 km/sec from a 40mm Tube.

Here we consider the case in which the prime power supply has sufficient power to provide a continuous fire rate that might suffice for some long-range missions. This enables one to directly power the spiral with a single prime power supply without any intermediate power-conditioning step, as shown in Fig 10.

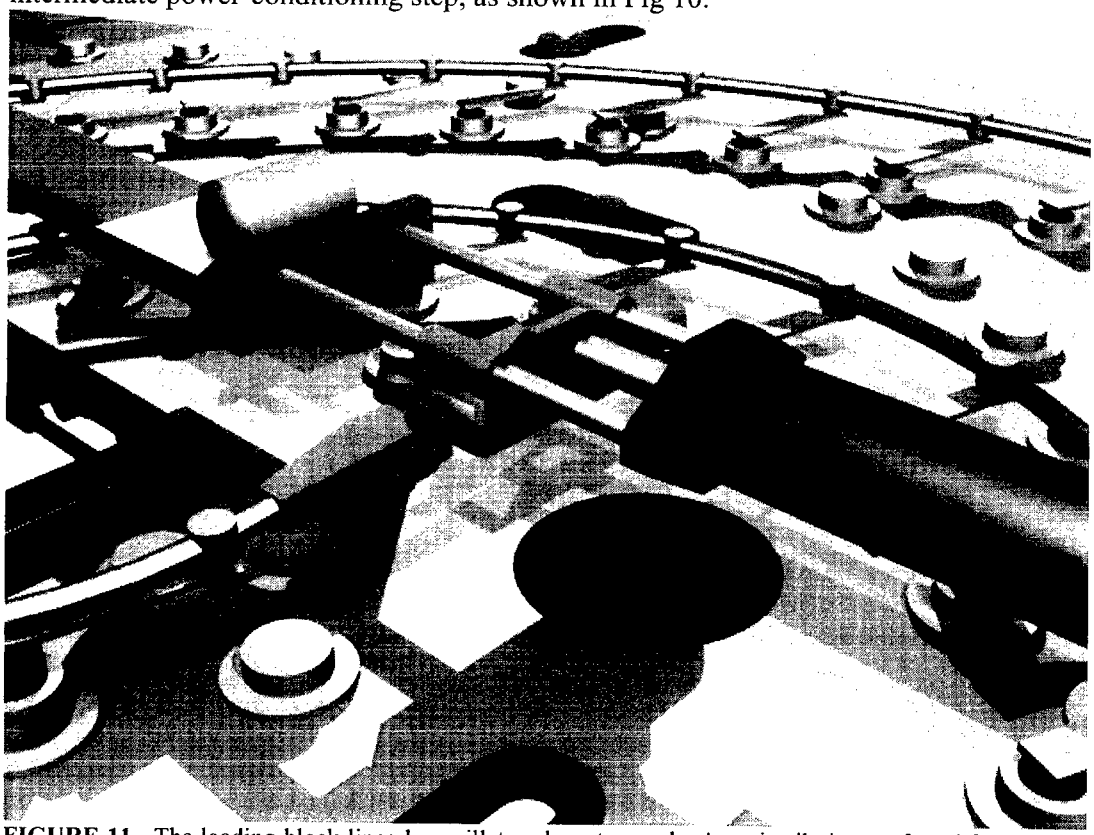


FIGURE 11. The loading block linearly oscillates along two rods. A projectile is transferred from a feed chute into the loading block when it is at its maximum amplitude, and subsequently pushed into the spiral entrance when the block and spiral entrance are moving parallel to each other with the same swing speed v.

For example, note that a single turbofan engine used on a 747 plane puts out 27.5 MW of power and weighs 4 tons. Assuming a turbine power unit with these numbers (without the bypass fan), and a launch efficiency of 50%, the slingatron could maintain a

continuous stream of smart 1 kg 3 km/sec projectiles with a fire rate of f_{shots} = 3 shots/sec, that might suffice for some ground-to-air-missions.

An example of a set of numbers for such a machine are: swing speed v = 200 m/sec, frequency f = 90 cps, tube ID = 4 cm and OD = 6 cm, swing radius r = 35.4 cm, final radius of curvature R = 5.31 meters, velocity gain per turn ΔV = 1.088 km/sec, number of turns in the spiral = 2.75, projectile diameter $d_p \sim 4$ cm, length l_p = 32 cm, and average mass density ρ_p = 2.5 gm/cc. Note, larger f gives a smaller R, e.g., f = 120 cps and V = 2.5 k/s gives R = 3.32 meters which would be suitable for a mobile platform.

Example 2: 50 kg Smart Projectiles Launched at 3 km/sec.

For this larger example, we note that 250MW turbines exist for example in some power generation plants. Assuming the same ~ 50% efficiency, a single turbine of this power could launch a steady stream of 50 kg projectiles at 3 km/sec with a continuous fire rate of 1 per 1.8 seconds.

Heating of a Spiral Slingatron Tube Used for a Continuous Stream of Shots

Although the slingatron delivers a relatively small thermal load into its guide tube, some heating does occur which we now estimate. In a continuous fire situation, repeated traversals of the track by projectiles will cause the track surface temperature to increase due to projectile sliding friction. Each projectile will impart a thermal pulse to the track and leave in its wake a temperature spike immediately behind the projectile. The track surface then cools as heat diffuses deeper into the tube wall until traversed by another projectile. This process continues and gradually increases the average temperature of the track. However, if this average heating occurs slowly enough, heat can diffuse through the guide tube wall and be removed from the outer surface by convection into the air through which it gyrates, in which case further temperature increase of the inner wall ceases. Here we derive some simple formulas for the spike and average temperature increases of the track and the potential for heat removal for continuous operation of the launcher. The projectiles are assumed to be simple cylinders of length l_p and diameter d comparable to the inner diameter of the guide tube.

The friction power dissipated by a single projectile is $\mu mV^3/R$ where R is the local radius of curvature of the guide tube. This power is shared by evaporation and heating of bearing gas from the projectile contact surface, and heating of the track throughout the semi-circular contact arc $\pi d/2$ swept out by the projectile. The contact pressure and friction power density are assumed constant throughout the half-cylinder contact surface of the projectile, and a fraction F of this friction power goes into track surface heating.

During a stream of shots the swept track experiences thermal flux pulses of duration l_p/V and power per unit area q, with a frequency f_{shots}, where $A = \pi d l_p/2$ is the projectile contact area. The power density q in a thermal pulse, and the average power <q> per unit area into the track area swept by repeated traversal pulses, are thus

$$q = \mu F m V^3/(AR) = \pi \mu F \rho_p d f V^2 ,$$
$$<q> = \mu(mV^2/R)(2Ff_{shots}/\pi d) = \pi \mu F \rho_p l_p d f f_{shots} V . \quad (7)$$

For the case of a constant heat flux q entering the surface of an infinitely thick slab of material (in this case steel), the heat diffusion equation has a simple solution for the increase in surface temperature $T_s(t)$ over its initial value T_o, namely

$$\Delta T(\text{degrees K}) = T_s(t) - T_o = 2qt^{1/2}(\pi\rho_s c_s \kappa_s)^{-1/2} = 0.84q(\text{watts/cm}^2)t_{scc}^{1/2}, \quad (8)$$

where for steel the parameters are, specific heat $c_s = 0.460$ Joules/(gmK), density $\rho_s = 7.83$ gm/cm^3, and thermal conductivity $\kappa_s = 0.502$ watts/(cmK). Combining (7) with (8) gives the temperature spike increase immediately behind a projectile, and the average increase in the track temperature of the track after many traversals, namely

$$\Delta T(\text{spike}) = 0.84q(l_p/V)^{1/2} = 8.34\mu F\rho_p fd(l_p V^3_{km/sec})^{1/2},$$
$$<\Delta T> = 0.84<q>t^{1/2} = 0.0264\mu F\rho_p d l_p f f_{shots} V_{km/sec} t^{1/2}, \quad (9)$$

where temperature rises are in degrees K, q in watts/cm^2, and in the final expressions on the right of (9) lengths, mass densities, frequencies, and times are in cgs units except for the velocities that are in km/sec as indicated. Note that f is constant throughout the spiral, so that $\Delta T(\text{spike})$ is proportional to $\mu V^{3/2}$ and $<\Delta T>$ to μV. If μ decreases with increasing V, then these increases in track temperature become less dependant on V.

Consider example 1 given in the preceding section, namely 1 kg projectiles launched at 3 km/sec at 3 per second, i.e., $f_{shots} = 3$ and use the slingatron numbers given in example 1. We will also assume that the sliding friction coefficient μ of such large projectiles at V = 3 km/sec is 0.005 and that the fraction of dissipated friction energy going into the guide tube is F = 0.2. For this choice using equation 9 we find $\Delta T(\text{spike}) =$ 221 K, and $<\Delta T> = 6.84t^{1/2}$ for which the average temperature would go up by ~ 216K after 1000 seconds i.e., after 3000 shots. Such a slow average heating would have time to diffuse through the tube wall for disposal so the machine could be operated continuously.

Finally, from the scaling section in Ref. 5, one can multiply all the linear dimensions of a given design by the same number and one has a larger machine that is geometrically similar and as viable mechanically as the smaller machine from which one scaled. However, the temperature increase formulas (9) scale differently. Specifically, as m increases as α^3, the spike temperature increase ΔT behind the projectile increases as α (note $f \sim \alpha^{-1}$), and $<T>$ stays the same independent of α provided the shot rate f_{shots} is chosen to be proportional to f. Thus very large projectiles could also be launched with low thermal energy transfer to the guide tube wall, depending on experimental data for the friction coefficient μ and the fraction F of friction power transferred to track heating.

SUMMARY

The dynamics, mechanics, friction, and thermal physics of the spiral slingatron mass accelerator concept have been discussed, and projectile streams of high velocity appear possible and potentially useful for a variety of industrial, space, and energy

applications. Long tapered swing arms provide high swing speeds with lower gyration frequencies and may provide a path to extremely high projectile speeds.

If smart projectiles could be manufactured that were cheap and effective, and the slingatron works as theorized, such systems might also have a useful defense role. Projectiles would not have to individually strike a distant target, but need to be only smart enough to narrow down the rapid-fire stream and perhaps fragment on final approach.

ACKNOWLEDGMENTS

This work was supported by the Advanced Launch Corporation, including the sliding friction experiment up to 2 km/sec using a powder gun. The extension of the friction experiment into the velocity range above 2 km/sec using a light gas gun was supported by NASA via U.S. Army Contract/Order No. DAAD17-00-P-0710 with UTRON Inc. The author also wishes to thank Mr. Paul Westmeyer of the NASA-GSFC, many scientists at the U.S. Army Research Laboratory and UTRON Inc., Mr. Mark Kregel, and Dr Jonathan Jones of NASA-MSFC, for useful discussions.

REFERENCES

1. D. A. Tidman, Sling Launch of a Mass Using Superconducting Levitation, *IEEE Transactions on Magnetics*, Vol. 32, No. 1, January, 1996, pp 240-247 (accepted Dec. 28, 1994).
2. D. A. Tidman, Slingatron Mass Launchers, *Journal of Propulsion and Power,* Vol.14, No. 4, pp 537-544, July- August, 1998.
3. D. A. Tidman and J. R. Greig, Slingatron Engineering and Early Experiments, *Proceedings of the 14th SSI/Princeton Conference on Space Manufacturing*, May 6-9, 1999, ed. by B. Faughnan, publ. by Space Studies Institute, Princeton, NJ, pp 306-312.
4. D. A. Tidman, Method and Apparatus for Moving a Mass in a Spiral Track, *US Patent No. 6,014,964*, January 18, 2000.
5. D. A. Tidman, The Spiral Slingatron Mass Launcher, *Proceedings of the Space Technology and Applications International Forum,* February 11, 2001, publ. by the American Institute of Physics.
6. G. R. Cooper, D. A. Tidman, and M. Bundy, Numerical Simulations of the Slingatron, *submitted to the 10th U.S. Army Gun Dynamics Symposium*, April 23-26, 2001, Austin, Texas.
7. M. Bundy, G. R. Cooper, and S. Wilkerson, Optimizing a Slingatron-Based Space Launcher Using Matlab, *submitted to the 10th U. S. Army Gun Dynamics Symposium*, April 23-26, 2001, Austin, Texas.
8. Cyril M. Harris, Shock and Vibration Handbook, *publ. by McGraw Hill, Fourth Edition,* 1996.
9. B. D. Tapley, Eshbach's Handbook of Engineering Fundamentals , *publ. by John Wiley & Sons, Fourth Edition,* 1990.
10. D. A. Tidman, A Scientific Study on Sliding Friction Related to Slingatrons, *ALC Tech Note 2001-1*, Final Report for U.S. Army Contract No. DAAD17-00-P-0710, 2/20/01.
11. F. Stefani and J. V. Parker, Experiments to Measure Gouging Threshold Velocity for Various Metals Against Copper, *IEEE Trans. Magnetics,* Vol. 35, Jan 1999, pp. 312-316.

Author Index

A

Ahmadian, M. 9
Alexander, J. 320
Allaei, D. 121
Anderson, W. 224
Appleton, R. 9

B

Bowlus, J. 406
Bulman, D. N. 133
Bundy, M. 398, 465, 474, 491
Burke, L. 418
Burnett, J. M. 341

C

Campion, B. 80
Chabalowski, C. 224
Chen, P. C. T. 213
Chen, S. 406
Chenette, E. R. 454
Coats, D. 236, 265
Conroy, P. J. 224, 258
Cooper, G. R. 474, 491
Cooper, N. R. 291, 369
Cytron, S. 406

D

Dampier, C. 341
Dilkes, A. M. 152, 305, 433
Dillon, R. 236
Dreizin, Y. A. 279
Dunn, S. 236, 265
Durocher, R. 107

E

Edge, H. L. 193
Ellis, R. L. 385
Erengil, M. 418
Erline, T. 398, 465

F

Faust, J. 418
Ferries, J. G. 133
Firth, M. A. 291, 369
French, J. 236

G

Gardner, D. W. 454
Garner, J. M. 25, 176, 200, 398
Gast, R. 37
Gigerenzer, H. 341
Gillich, D. 355
Guidos, B. J. 25, 160
Gully, M. 107
Gutierrez, W. 320

H

Haugh, D. 291
Hinton, M. J. 291, 369
Hodapp Jr., A. 320
Hoppel, C. P. R. 176
Howard, A. 369
Hudson, R. D. 454

J

Johnson, A. W. 258

K

Kathe, E. L. 37, 140, 236, 247
Kaye, R. 320
Kniskern, M. 320
Kregel, M. 465
Kwatny, H. 406

L

LaVigna, C. 406
Leach, M. 213
Leveritt, C. S. 258
Levinson, S. 418
Littlefield, A. 140
Livecchia, C. D. 160
Lodge, D. W. 152, 305, 433
Long, F. 320

M

Maier, W. 355
Marcopoli, V. R. 49
Marder, B. 320
Marrs, T. 398
Mattice, M. S. 121
Montgomery, J. S. 385

N

Nebolsine, P. E. 454
Newill, J. F. 160, 176, 200
Ng, M. S. 49
Nusca, M. J. 224

O

O'Hara, G. P. 67
O'Hara, P. 265

P

Patton, B. J. 25
Pennell, E. 341
Petitpas, E. 80
Pflegl, G. 265
Plostins, P. 200

R

Randrianangaly, I. 80
Renard, J. 80
Rickard, C. 265

S

Salafia, D. 444
Schmidt, E. M. 193
Shope, S. 320
Smith, D. 320
Sneck, H. J. 92
Snyder, D. R. 454
Soencksen, K. P. 176, 200
Sopok, S. 236, 265

T

Tarnowski, D. J. 121
Tedesche, M. 107
Testa, R. 121
Tidman, D. A. 491, 509
Turman, B. 320
Tzeng, J. T. 332

V

Von Wahlde, R. 465

W

Wallington, D. K. 369
Waverik, R. 320
Weise, T. H.G.G. 1
Wells, C. R. 49
Wilkerson, S. 474, 491
Witherell, M. 236

Y

Young Jr., R. P. 454

Z

Zhang, H. 406